Biosensors

Biosensors

Edited by

Pier Andrea Serra

Intech

Published by Intech

Intech
Olajnica 19/2, 32000 Vukovar, Croatia

Free online edition of this book you can find under www.sciyo.com
Additional copies can be obtained from:
publication@sciyo.com

First published February 2010
Printed in India

Technical Editor: Teodora Smiljanic
Cover designed by Dino Smrekar

Biosensors, Edited by Pier Andrea Serra
p. cm.
ISBN 978-953-7619-99-2

Preface

A biosensor is defined as a detecting device that combines a transducer with a biologically sensitive and selective component. When a specific target molecule interacts with the biological component, a signal is produced, at transducer level, proportional to the concentration of the substance. Therefore biosensors can measure compounds present in the environment, chemical processes, food and human body at low cost if compared with traditional analytical techniques.

This book covers a wide range of aspects and issues related to biosensor technology, bringing together researchers from 11 different countries. The book consists of 16 chapters written by 53 authors. The first four chapters describe several aspects of nanotechnology applied to biosensors. The subsequent section, including three chapters, is devoted to biosensor applications in the fields of drug discovery, diagnostics and bacteria detection. The principles behind optical biosensors and some of their application are discussed in chapters from 8 to 11. The last five chapters treat of microelectronics, interfacing circuits, signal transmission, biotelemetry and algorithms applied to biosensing.

I want to express my appreciation and gratitude to all authors who contributed to this book with their research results and to InTech team that accomplished its mission with professionalism and dedication.

Editor

Pier Andrea Serra
University of Sassari
Italy

Contents

1

Enzyme-based Electrochemical Biosensors

Zhiwei Zhao[1] and Helong Jiang[2]
[1]*Southeast University,*
[2]*State Key Laboratory of Lake Science and Environment, Nanjing Institute of Geography and Limnology, Chinese Academy of Sciences, China*

1. Introduction

A biosensor can be defined as a device incorporating a biological sensing element connected to a transducer to convert an observed response into a measurable signal, whose magnitude is proportional to the concentration of a specific chemical or set of chemcials (Eggins 1996). According to the receptor type, biosensors can be classified as enzymatic biosensors, genosensors, immunosensors, etc. Biosensors can be also divided into several categories based on the transduction process, such as electrochemical, optical, piezoelectric, and thermal/calorimetric biosensors. Among these various kinds of biosensors, electrochemical biosensors are a class of the most widespread, numerous and successfully commercialized devices of biomolecular electronics (Dzyadevych et al., 2008). In this chapter, we will focus on the enzyme-based electrochemical biosensors since enzyme electrodes have attracted ever-increasing attentions due to the potential applications in many areas.

Enzyme-based electrochemical biosensors have been used widely in our life, such as health care, food safety and environmental monitoring. Health care is the main area in the biosensor applications, such as monitoring blood glucose levels and diabetics by glucose biosensors. Besides, the reliable detection of urea has potential applications for patients with renal disease either at home or in the hospital. Industrial applications for biosensors include monitoring fermentation broths or food processing procedures through detecting concentrations of glucose and other fermentative end products. The sensitive detection of phenolic compound is an important topic for environmental research because phenolic compouds often exist in the wastwaters of many industries, giving rise to problems for our living environment as many of them are very toxic.

This chapter is on the enzyme-based electrochemical biosensors, which will begin with a section for enzyme immobilization methods due to their important roles in biosensors. The next section will focus on the recent advances in enzyme-based electrochemical biosensors. Nanomaterials play an important role in recent development of enzyme-based biosensors, thus some popular fabrication methods of nanomaterials will be briefly described towards their applications in nanomaterials synthesis. The emphsis of this chapter is on the recent advances particularly nanomaterials-based biosensors. Some important and intelligent nanomaterials including gold, ZnO, carbon nanotube and polypyrrole will be presented in a way to the current achievements in enzyme-based electrochemical biosensors. The last section of this chapter will discuss challenges currently faced to practical applications.

2. Enzyme immobilization methods

In order to make a viable biosensor, the biological component has to be properly attached to the transducer with maintained enzyme activity. This process is known as enzyme immobilization. Biosensors are usually designed with high enzyme loading to insure sufficient biocatalyst activities, and the enzymes are provided with an appropriate environment to sustain their activities. The local chemical and thermal environment can have profound effects on the enzyme stability. The choice of immobilization method depends on many factors, such as the nature of the biological element, the type of transducer used, the physicochemical properties of the analyte and the operating conditions in which the biosensor is to function, and overriding all these considerations is necessary for the biological element to exhibit maximum activity in its immobilized microenvironment (Singh et al., 2008). A detailed information on advantages and drawbacks of different methods for enzyme immobilization could be found in the literature (Buerk 1993; Eggins 1996; Nunes & Marty, 2006). Generally, there are 4 regular methods for enzyme immobilization and they are briefly described as shown below:

1. **Adsorption**: It is the simplest and fastest way to prepare immobilized enzymes. Adsorption can roughly be divided into two classes: physical adsorption and chemical adsorption. Physical adsorption is weak and occurs mainly via Van der Waals. Chemical adsorption is stronger and involves the formation of covalent bonds. Many substances adsorb enzymes on their surfaces, eg. alumina, charcoal, clay, cellulose, kaolin, silica gel, glass and collagen. For this method, there are good examples in the section of 3.2.1 of this chapter, in which physical adsorption is mostly used for enzyme immobilization in ZnO-based glucose biosensors.
2. **Entrapment**: It refers to mixture of the biomaterial with monomer solution and then polymerised to a gel, trapping the biomaterial. However, this method can give rise to barriers to the diffusion of substrate, leading to the reaction delay. Besides, loss of bioactivity may occure through pores in the gel. The gels commonly used include polyacrylamide, starch gels, nylon, silastic gels, conducting polymers, etc.
3. **Covalent bonding**: In this method, the bond ocuurs between a functional group in the biomaterial to the support matrix. Some functional groups which are not essential for the catalytic activity of an enzyme can be covalently bonded to the support matrix. It requires mild conditions under which reactions are performed, such as low temperature, low ionic strength and pH in the physiological range.
4. **Cross-linking**: For this method, usually, biomaterial is chemically bonded to solid supports or to another supporting material such as cross-linking agent to significantly increase the attachment. It is a useful method to stabilize adsorbed biomaterials. Glutaraldehyde is the mostly used bifunctional agent. The agents can also interfere with the enzyme activity , especially at higher concentrations.

3. Enzyme-based electrochemical biosensors

3.1 Fabrication techniques for nanomaterials

Recent years witness the vigorous applications of various nanomaterials in the development of biosensors. Nanomaterials are generally referred to the materials with dimensions ranging from 1 to 100 nm, which have some special physicochemical characteristics resulting from their “small” size structures. Nanomaterials make contribution to the

improvement of the performance and stability of enzyme electrodes in the electrochemical biosensors, which can be fabricated by many various techniques. The generally used techniques for nanomaterials in biosensor applications are described briefly as follows.

Wet chemical route, also called chemical solution deposition, is one of the most widely used to fabricate nanomaterials, especially nanoparticles. For wet chemical route, solution of chemical species will be involved during the process, which thus differs from dry chemical route. Briefly, it uses a liquid precursor, usually a solution of organometallic powders, dissolved in an organic solvent. Chemical reactions then occur in order to get purposeful product(s). It is a quite common method to be used for nanomaterials fabrication, especially in the application of electrochemical biosensors.

The vapor-liquid-solid method is based on a mechanism for the growth of nanostructural materials with one-dimension from chemical vapor deposition, such as nanowires. It is generally very slow for a crystal to grow through direct adsorption of a gas phase onto a solid surface. During vapor-liquid-solid process, this problem is overcome by inducing catalytic liquid alloy phase to rapidly adsorb a vapor to supersaturation levels, and thus crystal growth can subsequently occur from nucleated seeds at the liquid-solid interface. The physical characteristics of nanowires grown in this manner is closely associated with the size and physical properties of the liquid alloy.

Hydrothermal synthesis is a method to synthesize crystalline materials from high-temperature aqueous solutions at high vapor pressures. The chemical reaction occurs in a vessel, which is separately from ambient environment. Hydrothermal synthesize will drive those hardly-dissolved compounds under normal conditions to dissolve in the solution under special conditions followed by recrystallization. The method can be used for the large crystal growth with high quality, where good control over composition is required. This method has been used for the fabrication of nanomaterials with low-dimentions.

The sol-gel process, strictly, belongs to a wet-chemical technique (chemical solution deposition) for material fabrication. This process uses a chemical solution as the precursor for an integrated network (or gel) of either discrete particles or network polymers. The sol evolves towards the formation of a gel-like system with two phases (a liquid phase and a solid phase), whose morphologies range from discrete particles to continuous polymer networks. A drying process is generally required to remove the remaining liquid phase, during which a significant amount of shrinkage and densification occur. The precursor sol can be either deposited on a substrate to form a film or used to synthesize powders. The sol-gel approach is a cheap and low-temperature technique that allows for the fine control of the product's chemical composition.

Thin films are thin material layers ranging from fractions of a nanometre to several micrometres in thickness. There are many popular deposition techniques for thin film deposition, such as evaporation, sputtering, chemical vapor depositions, etc. For example, evaporation in vacuum involves two basic processes: evaporation of a hot source material and then condensation of the material vapor on the cold substrate surface in the form of thin film. The average energy of vapor atoms reaching the substrate surface is generally low (i.e. tenths of eV) and thus normally results in a porous and little adherent material. Sputtering entails the bombardment of a target with energetic particles (usually positive gas ions), which causes some surface atoms to be ejected from the target. These ejected atoms deposit onto the substrates in the vicinity of the target. The target can be kept at a relatively low temperature, and sputtering is especially useful for compounds or mixtures. Chemical

vapor deposition is done through exposure of the substrate to one of several vaporized compounds or reactive gases. A chemical reaction occurs initially near the substrate surface, producing desired material as it condenses on the substrate forming a layer of thin film. Commercial techniques often use very low pressures of precursor gas.

3.2 Typical nanomaterials used in biosensors

3.2.1 ZnO

Among nanomaterials, ZnO has attracted much attention due to wide range of applications. ZnO as a wide band gap (3.37 eV) semiconductor plays an important role in optics, optoelectronics, sensors, and actuators due to its semiconducting, piezoelectric, and pyroelectric properties. Nanostructured ZnO not only possesses high surface area, nontoxicity, good biocompatibility and chemical stability, but also shows biomimetic and high electron communication features, making it great potential applications in biosensors. More importantly, as a biocompatible material, it has a high isoelectric point (IEP) of about 9.5. This makes it suitable for absorption of proteins with low IEPs, as the protein immobilization is primarily driven by electrostatic interaction. ZnO with various nanostructures by same or different fabrication techniques has been widely used for enzyme immobilization in recent years. Fig. 1 gives some examples to show various ZnO nanostructures in different shapes by several various synthesis techniques.

Wet chemical route is quite a popular method to fabricate various ZnO nanostructures, such as nanoparticles, nanorods and nanosheets. It had been proposed to use these ZnO naonostructures as platform for cholesterol oxidase (ChOx) immobilization via physical adsorption. For example, using ZnO nanoparticles for enzyme immobilization, the prepared biosensor had a high and reproducible sensitivity of 23.7 $\mu A/cm^2.mM$, detection limit of 0.37 nA and linear dynamic range from 1 to 500 nA (Umar et al., 2009). Recently, an ultra-sensitive cholesterol biosensor was developed using flowerlike ZnO nanostructure, in which ChOx was immobilized to the surface of modified electrode via physical adsorption followed by the covering of Nafion solution. Such biosensor exhibited a very high and reproducible sensitivity of 61.7 $\mu A/cm^2.mM$ with a Michaelis-Menten constant (K_M) of 2.57 mM and fast response time of 5 s (Umar et al., 2009). A H_2O_2 biosensor was prepared using waxberry-like ZnO microstructures consisting of nanorods (8-10 nm) by wet chemical method (Cao et al., 2008). Such kind of ZnO microstructures with high surface area could provide the platform for the reduction of H_2O_2 by contributing excess electroactive sites and enhanced electrocatalytic activity. The transport characteristics of the electrode were controlled by diffusion process, and the prepared biosensor had a much wider linear range from 0.l5 to 15 mM.

Gluose biosensors were also reported using ZnO nanocombs as platform by vapor-phase transport (Wang et al., 2006). For enzyme immobilization, glucose oxidase (GOD) were physically adsorpted to the nanocomb modified Au electrode, followed by Nafion solution covered on the surface of the modified electrode. The prepared biosensor had a diffusion-controlled electrochemical behavior. The covered linear range was from 0.02 to 4.5 mM and the reported sensitivity was 15.33 $\mu A/cm^2.mM$. The value of K_M was as low as 2.19 mM. Using a similar technique, Weber et al. obtained ZnO nanowires with a typical length of 0.5-2 μm and a diameter of 40-120 nm, which were grown on the substrate with an array of ZnO nanowires (Weber et al., 2008). Physical adsorption was also adopted to immobilize GOD onto the electrode. This kind of biosensor had a linear trend (0.1-10 mM). A reagentless

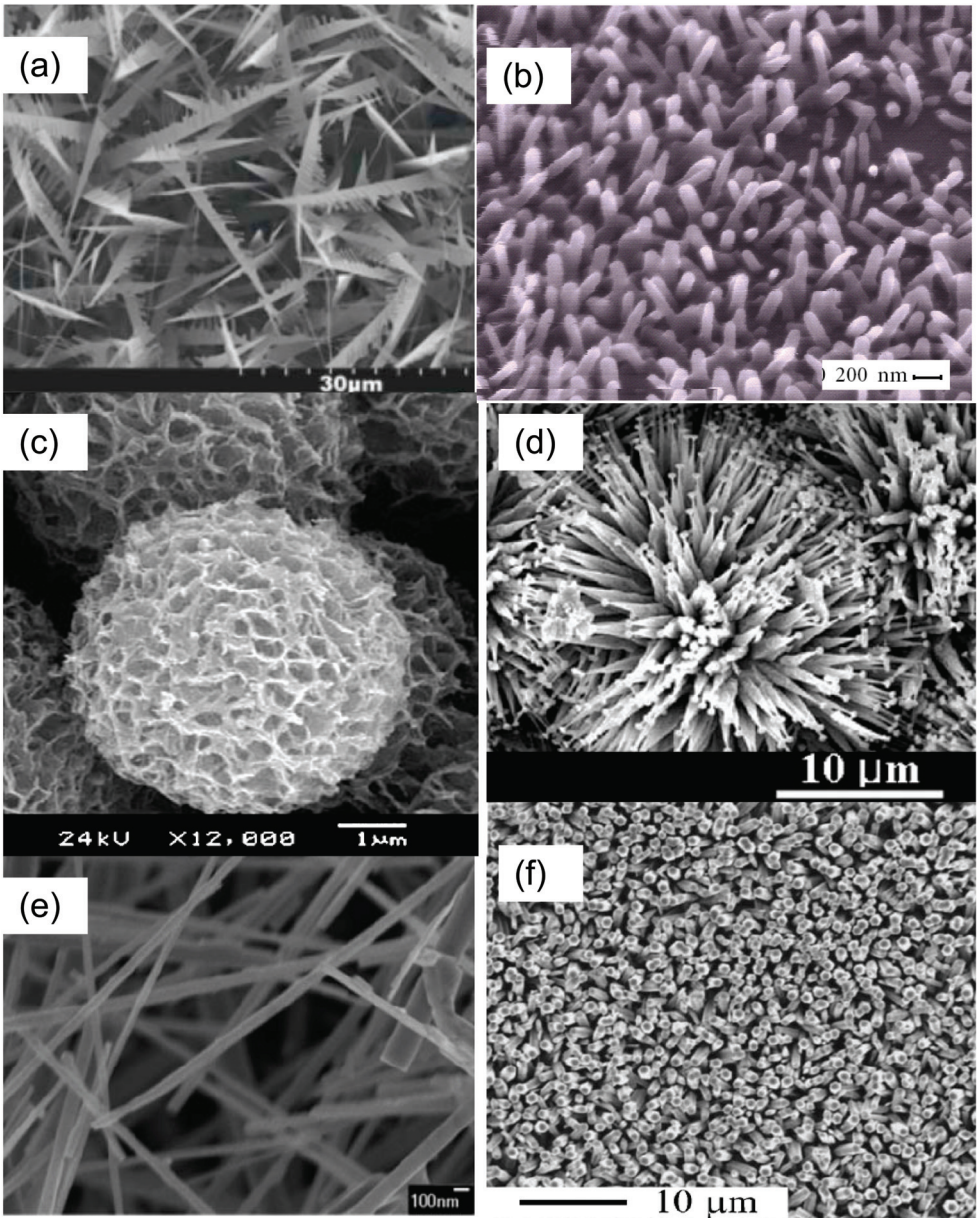

Fig. 1. ZnO nanostructure materials with various shapes. (a) nanocombs by vapor-phase-transport (Wang et al., 2006); (b) nanowires by vapor-liquid-solid (Weber et al., 2008); (c) microspheres consisting of nanosheets by wet chemical route (Lu et al., 2008); (d) nanonails by thermal evaporation (Umar et al., 2008); (e) nanowires by thermal evaporation (Zang et al., 2007); (f) nanorods by hydrothermal decomposition (Wei et al., 2006).

phenol biosensor was prepared by immobilizing tyrosinase on ZnO nanorods through electrostatic attraction and then covered by Nafion, in which ZnO nanorods were also fabricated by vapor-phase transport technique (Chen et al., 2008). Tyrosinase was adsorbed on the ZnO nanorods and its bioactivity can be well remained. Such prepared biosensor had a fast response within 5 s. The linear range of concentration spanned from 0.02 to 0.18 mM, and K_M was calculated to be as low as 0.24 mM, reflecting a high affinity of tyrosinase to phenol on ZnO nanorods and a good bioactivity (Chen et al., 2008).

Gluose biosensors were also reported using ZnO nanocombs as platform by vapor-phase transport (Wang et al., 2006). For enzyme immobilization, glucose oxidase (GOD) were physically adsorpted to the nanocomb modified Au electrode, followed by Nafion solution covered on the surface of the modified electrode. The prepared biosensor had a diffusion-controlled electrochemical behavior. The covered linear range was from 0.02 to 4.5 mM and the reported sensitivity was 15.33 $\mu A/cm^2.mM$. The value of K_M was as low as 2.19 mM. Using a similar technique, Weber et al. obtained ZnO nanowires with a typical length of 0.5-2 μm and a diameter of 40-120 nm, which were grown on the substrate with an array of ZnO nanowires (Weber et al., 2008). Physical adsorption was also adopted to immobilize GOD onto the electrode. This kind of biosensor had a linear trend (0.1-10 mM). A reagentless phenol biosensor was prepared by immobilizing tyrosinase on ZnO nanorods through electrostatic attraction and then covered by Nafion, in which ZnO nanorods were also fabricated by vapor-phase transport technique (Chen et al., 2008). Tyrosinase was adsorbed on the ZnO nanorods and its bioactivity can be well remained. Such prepared biosensor had a fast response within 5 s. The linear range of concentration spanned from 0.02 to 0.18 mM, and K_M was calculated to be as low as 0.24 mM, reflecting a high affinity of tyrosinase to phenol on ZnO nanorods and a good bioactivity (Chen et al., 2008).

ZnO nanowires can also be obtained using thermal evaporation, in which ZnS powders were thermal evaporated under controlled conditions with Au thin film as a catalyst layer (Zang et al., 2007). GOD was immobilized onto ZnO nanowires by physical adsorption. K_M and sensitivity could be modulated in a wide range by the variation of the loading amount of ZnO/GOD onto the electrode. Umar et al. also using thermal evaporation to synthesize ZnO nanonails (Umar et al., 2008), where Zn powder was used as reaction source of Zn, and oxygen was introduced into the system. The constructed biosensor exhibited a diffusion-controlled electrochemical behavior with a linear calibration range from 0.1 to 7.1 mM. It showed a high sensitivity of 24.6 $\mu A/cm^2.mM$, while K_M was relatively higher around 15 mM. Uric acid biosensor was prepared based on ZnO nanorods also by thermal evaporation (Zhang et al., 2004). Uricase with a low IEP of 4.3, was immobilized on ZnO nanorods by electrostatic attraction. The prepared biosensor had a linear range from 5 μM to 1 mM and detection limit of 2 μM. Besides, it had a lower K_M of 0.24 mM and a good thermal stability (10 - 85^oC).

Among the various strategies followed, a useful and simple way for ZnO is to grown directly on electrode. This was realized in the work of Wei et al. (Wei et al., 2006), where ZnO nanorods with a hexagonal cross section were grown directly on the standard Au electrode by hydrothermal decomposition. Enzyme immobilization was done via the cover of GOD solution on the surface of the electrode. The prepared biosensor presented a quite fast response within 5 s and a high sensitivity of 23 $\mu A/cm^2.mM$. It also had a low K_M value of 2.9 mM and a low detection limit of 10 μM.

ZnO matrix by sol-gel procedure was developed for tyrosinase immobilization (Liu et al., 2005). The porous and positively charged ZnO sol-gel matrix provided a moderate

microenvironment for the tyrosianse to remain its bioactivity. The so prepared biosensor had a sensitivity of 168 μA/mM, and the linear range covered from 0.15 to 40 μM (Liu et al., 2005). Another kind of matrix of ZnO/chitosan was developed for tyrosinase immobilization by dispersion of ZnO nanoparticles into the chitosan solution (Li et al., 2006). The matrix could provide a favorable microenvironment in terms of its isoelectric point for tyrosinase loading, and the immobilized tyrosinase could retain its bioactivity to a large extent. The biosensor using ZnO/chitosan matrix had a better performance than that using ZnO sol-gel matrix. K_M was calculated to be 23 μM and the detection limit was lower to be 0.05 μM (Li et al., 2006).

Different from above mentioned ZnO nanostructures, a new kind of nanostructure, nanoclusters, was proposed for a novel biosensor construction (Zhao et al., 2007). These ZnO nanoclusters doped by Co (2%) were obtained by nanocluster-beam deposition (Zhao et al., 2005; Zhao et al., 2007). Home-made electrode based on PET plate was used for enzyme immobilization instead of traditional standard electrode. Briefly, Ti ions from the plasma were implanted into PET plate, followed by a thin Au layer deposited on Ti-implanted PET substrate by magnetron sputtering. After that ZnO-based nanoclusters were directly grown on the modified PET plate. Cross-linking was used via glutaraldehyde for enzyme immobilization. The prepared biosensor had a response time within 10 s and the sensitivity was over 13 μA/ cm^2.mM. ZnO porous thin films by RF magnetron sputtering was also proposed for ChOx immobilization by physical adsorption. The film was grown under high pressure (50 mTorr) so as to creat native defects and therefore porous film formed. The prepared biosesnor had a K_M of 2.1 mM. The wide linear range spanned from 0.65 to 10.34 mM.

In recent years, nanostructured inorganic-organic hybrid materials have emerged to fabricate biosensors by entrapping enzymes, which combine the physicochemical attributes of components to improves their features. Organic components (e.g. Nafion, chitosan) benefit the formation of defect-free inorganic membranes and make these membranes less brittle, and organic membranes can have their chemical and thermal stability improved by an inorganic phase. A H_2O_2 biosensor with good stability was developed with horseradish peroxidase (HRP) entrapped in the nanoporous ZnO/chitosan composite (Yang et al., 2005). The sensor exhibited a sensitivity of 43.8 μA/cm^2.mM, and it retained 80% of its initial current response after 40 days. It is expected that the numerous nanoscaled cavities on the surface of the microspheres are highly advantageous for the entrapment of enzymes by sequestering in the cavities or binding on the surface of the microspheres. Using this approach, Lu et al. synthesized the porous ZnO microspheres consisting of nanosheets using wet chemical route (Lu et al., 2008). Hemoglobin (Hb) was entrapped in the composite film of Hb, ZnO and Nafion. Besides the good reproducibility and long-term stability, the prepared biosensor had a sensitivity of 137 μA/cm^2.mM and a low K_M of 0.143 mM. Other nanocomposite consisting of ZnO nanoparticles and chitosan was also reported to immobilize ChOx by physical adsorption (Khan et al., 2008).

More complex inorganic-organic composites are also commonly prepared in biosensor development by introducing other inorganic materials (e.g gold and multi-walled carbon nanotubes (MWCNTs)). It's well known that gold and MWCNTs have been already used for enzyme immobilization to realize direct electron transfer between active sites and electrode. Besides, the presence of biocompatible Nafion in the biocomposite film not only makes the film uniform, but also could lead to the increased activity of enzyme. Recently, a biosensor

under these approches was prepared using the platform consisting of ZnO, MWCNTs and Nafion, which showed a very high sensitivity of 1310 μA/cm².mM and a very low of K_M of 82.8 μM (Ma et al., 2009). The composites consisting of ZnO, Nafion and gold nanoparticles were also developed to entrap HRP for H_2O_2 biosensors (Xiang et al., 2009). The biosensor had a Km of 1.76 mM and a low detection limit of 9 μM. It showed reproducibility and good stability after one month. Other composites are also proposed consisting of ZnO crystals, gold nanoparticles and chitoson (Zhang et al., 2009). The principle of enzyme immobilization differed from the methods mentioned above. It is known that ZnO crystals with high IEP are suitable for the electrostatic adsorption of proteins with lower IEP. The positively-charged ZnO crystals and amine-derivatized chitosan could facilitate higher capability of assembling negatively charged nanogold through strong electrostatic adsorption and the covalent bonds between amine groups and gold (Zhang et al., 2009). Biocompatible nanogold could further allow HRP to be immobilized with well-remained bioactivity in addition to increased loading amount. The prepared biosensor can achieve sensitive electrochemical response to H_2O_2 at a potential of - 0.2 V. Similar composites for enzyme immobilization was reported by Duan et al. (Duan et al., 2008), but the composites were mixed by the solutions of ZnO/chitosan, Hb and gold. The as-prepared biosensor has a fast response to H_2O_2 within 4 s and a detection limit of 0.097 μM.

Recent advances in phenol biosensors witness the use of modern process in semiconductor industry, such as photolithograph for designed patterns. A new tyrosinase biosensor was constructed based on the covalent immobilization of tyrosinase by glutaraldehyde on the biofunctional ZnO nanorod microarrays via photolithograph (Zhao et al., 2009). The as-prepared biosensor had a ultrahigh sensitivity of 287 μA/cm².mM and a detection limit of 0.25 μM. The linearity covered a wide range from 1-150 μM.

In the development of uric acid biosensor, multilayer structure was introduced toward a highly sensitive and stable uric acid biosensor. Using ZnO nanoparticles and MWCNTs, multilayer structure was realized firstly by negatively charged MWNTs cast on pyrolytic wafers, followed by decoration of ZnO nanoparticles (Wang et al., 2009). Uricase was immobilized onto ZnO nanoparticles also by electrostatic attraction, and finally PDDA layer was coated on the surface of uricase. The as-prepared biosensor had a wide linear response range of 1mM to 5 M, a high sensitivity of 393 μA/cm².mM. It also exhibited a long-term stability after 160 days.

3.2.2 Gold

Gold nanoparticles could provide a stable immobilization for biomolecules retaining their bioactivity. Moreover, electron transfer between redox proteins and electron surfaces is facilitated, which is induced by many factors, such as the high surface-to-volume ratio, high surface energy, decreased proteins-metal particles distance and the functioning as electron-conducting pathways between prosthetic groups and the electrode surface from the gold nanoparticles. Pingarron et al. recently reported a review on gold nanoparticle-based electrochemical biosensors, in which gold-based enzyme biosensor are summarized (Pingarron et al., 2008). Gold nanoparticles are normally synthesized by chemical route and electrodeposition.

The electrodes are usually modified by gold in different ways to improve the performance of the biosensor. The electrode surface could be roughened by gold nanoparticles to enhance the interaction of enzyme with the electrode. An example is the construction of

acetylcholinesterase biosensor in which electrode was modified by electrodeposited gold nanoparticles at the electrode surface after hydrolysis of acethlthiocholine by the immobilization enzyme (Shulga & Kirchhoff, 2007). This method is valuable for the development of new devices for the sensitive detection of potentially dangerous and deadly neurotoxins. Carbon paste electrode could be modified by the colloidal gold consisting of pretreated graphite power with colloid gold solution and paraffin oil (Liu & Ju, 2003). GOD was immobilized onto the modified electrode via physical adsorption. Such kind of GOD biosensor can efficiently exclude the interference of commonly coexisted uric and ascorbic acid (Liu & Ju, 2003). The similar methodology is also favored for other substrate detection, such as phenol and hydrogen peroxide (Liu & Ju, 2002; Liu et al., 2003). Gold electrode can be modified by attachement of gold nanoparticles via covalent bond. These gold nanoparticles by chemical route were self-assembled on gold electrode by dithiol via Au-S bond, where dithiol was physically absorbed on the electrode surface by putting gold electrode immersed into a dithiol ethanol solution (Zhang et al., 2005). A cystamine monolayer was then chemisorbed onto those gold nanoparticles and exposed to an array of amino groups, after that GOD was immobilized by covalently attached to the cystamine modified electrode (Zhang et al., 2005). The scheme diagram in Fig. 2 shows the steps for above procedure. The so prepared biosensor provided a linear response to glucose from 20 μM - 5.7 mM with a sensitivity of 88 $\mu A/cm^2.mM$. The sensor had a good reproducibility and remained stable over 30 days.

A wide variety of matrices, including inorganic materials, organic polymers, and other commercially available solid supports, have been used for enzyme immobilization. Chitosan, as mentioned in pervious part, is one of the most promising immobilization matrices due to its excellent properties. Colloidal gold nanoparticles have been also used as the matrix for the enzyme immobilization to retain the macromolecules' bioactivity. The adsorption of colloidal gold nanoparticles on the chitosan membrane could provide an assembly of gold nanoparticle mulilayers and a suitable microenvironment similar to the native environment of biomolecules. Based on this approach, a disposal biosensor was fabricated for the rapid detection of H_2O_2 by entrapping HRP in colloidal gold nanoparticle-modified chitosan membrane (Liu & Ju, 2003). The biosensor was characterized with good detection precision and storage stability. Based on a similar methodology, glucose (Luo et al., 2004) and HRP (Luo et al., 2005) biosensors were prepared by self-assembling gold bnanoparticles on chitosan hydrogel modified Au electrodes.

Nanocomposites by combination of gold nanoparticles with inorganic or organic nanomaterials have shown to possess interesting properties, which can be profited for the development of electrochemical biosensors. An example of such nanocomposites is a colloidal gold-CNT composite electrode using Teflon as the non-conducting binding material (Manso et al., 2007). The constructed biosensor showeded significantly improved responses to H_2O_2, and the incorporation of GOD into the new composite matrix allowed the preparation of a mediatorless glucose biosensor with a remarkably higher sensitivity than that from other GOD-CNT bioelectrodes (Manso et al., 2007). Hybrid nanocomposites of gold nanoparticles and organic materials are proposed, in which gold and PPy are fabricated by wet chemical route using $HAuCl_4$ and pyrrole as the reaction reagents (Njagi & Andreescu, 2007). The reaction occurs in mild aqueous conditions and doesn't involve application of an electrical potential, surfactants or solvents that could affect the biological activity. A stable nanocomposite strongly adhered to the surface of GCE electrode and

enzyme was entrapped into the matrix. The fabricated biosensor showed high sensitivity for phenol detection, fast response time, good operational stability and reproducibility (Njagi & Andreescu, 2007).

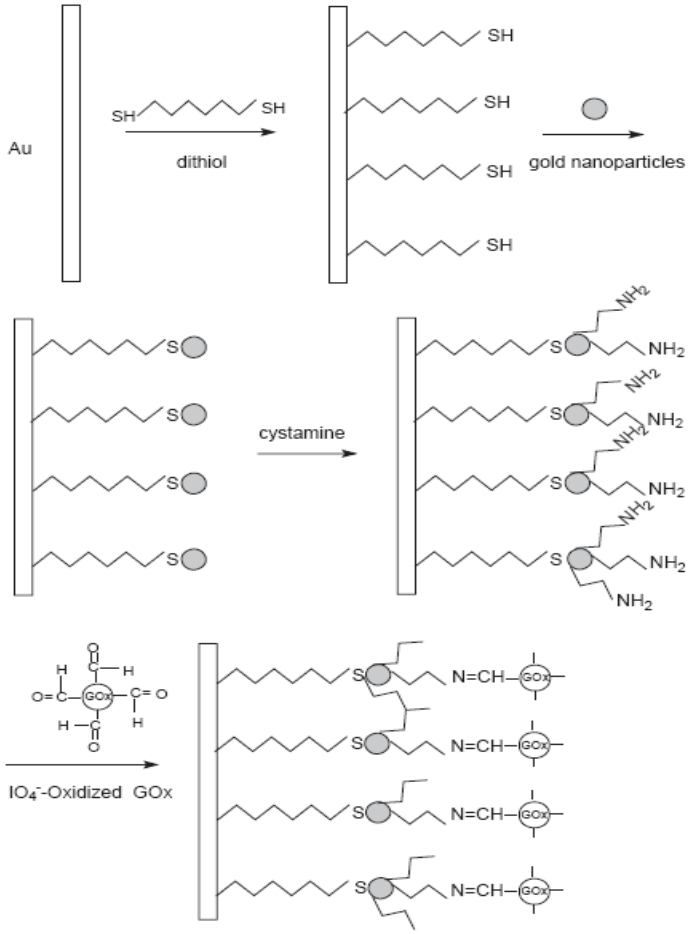

Fig. 2. Stepwise assembly of dithiol, gold, cystamine, IO_4^- oxidized GOD on a gold electrode, from paper (Zhang et al., 2005)

Enzymes deposited in ordered monolayer or multilayer systems have an important significance for fabrication of biosensors and bioelectronic devices. Layer-by-layer self-assembly technique based on electrostatic interaction attracts extensive interest due to its simplicity of the procedure, wide choice of the composition and thickness of the layer on the molecular level (Yang et al., 2006). This technique was originally developed by Decher and coworkers (Decher et al., 1992; Lvov et al., 1993) for linear polyelectrolytes and later extended to proteins, enzymes, nanoparticles, and so on (Feldheim et al., 1996; Caruso et al., 1997; He et al., 1998). Using this technique, a glucose biosensor was constructed, in which PMMA dendrimers with modified gold nanoparticles were alternated with

poly(vinylsulfonic acid) layers on ITO electrodes (Crespilho et al., 2006). The method of cross-linking was chosen for enzyme immobilization (Crespilho et al., 2006). Other glucose biosensor by layer-by-layer self-assembled technique could also be realized consisting of different multilayer films with chitosan, gold nanoparticles and GOD (Wu et al., 2007). A method of layer-by-layer covalent attachment of enzyme molecules was proposed to overcome the unstability occurring in the layer-by-layer self-assembly technique casued by the driving force of electrostatic interaction. Such kind of biosensor was prepared by construction of multilayer films consisting of glucose oxidase and gold nanoparticles using cysteamine as a cross-linker based on two covalent reactions: Schiff bases reaction between aldehyde-group of IO_4-oxidized GOD and amino-group of cysteamine, and covalent bond between gold nanoparticles (GNPs) and sulphydryl of cysteamine (Yang et al., 2006). Layer-by-layer construction of GOD/GNPs multilayer film on an Au electrode were shown in Fig. 3. The constructed biosensor exhibited a good stability and long lifetime up to 4 weeks.

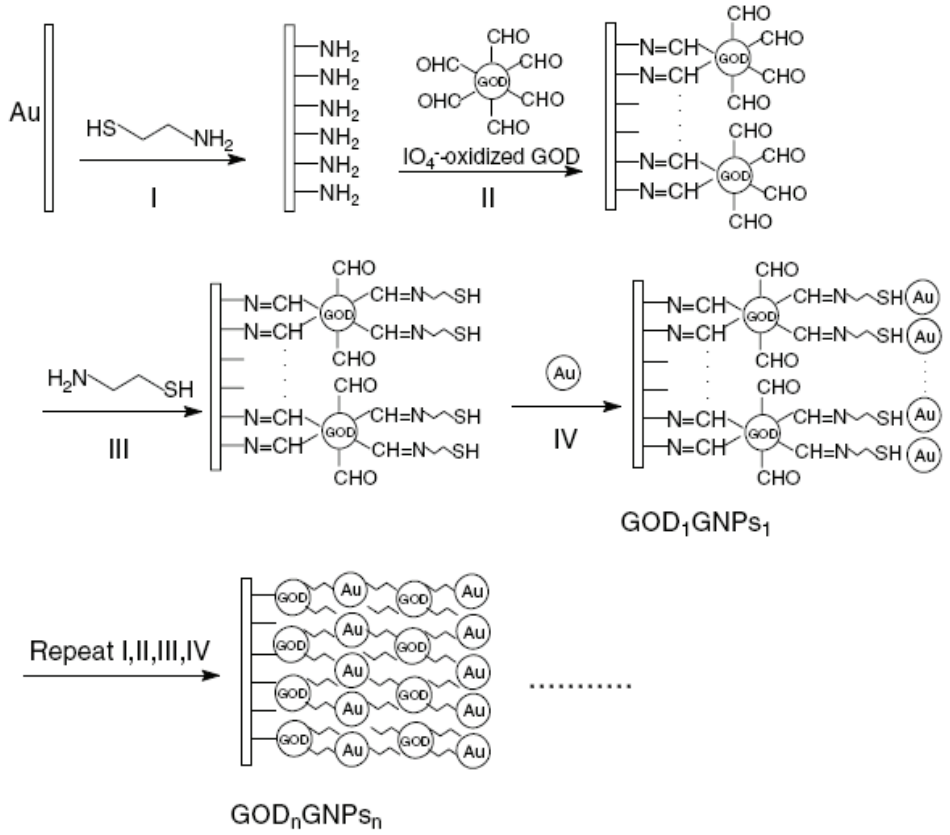

Fig. 3. Layer-by-layer construction of the GOD/gold nanoparticles multilayer films on an Au electrode (Yang et al., 2006).

Sol-gel technology provides unique means to prepare there-dimensional networks suited for the encapsulation of biomolecules. Sol-gel hybrid materials prepared by physically

encapsulating gold nanoparticles into porous sol-gel networks have been used for the fabrication of biosensors. For instance, an acetylcholinesterase biosensor was constructed, where the sol-gel derived silicate network assembling gold nanoparticles provided a biocompatible microenvironment around the enzyme molecule to stabilize its biological activity and prevent them from leaking out of the interface (Du et al., 2008).

3.2.3 CNT

CNTs are unique one-dimensional materials with unique properties such as good electrical conductivity, strong adsorptive ability and excellent bioconsistency. CNTs have led to development of many new techniques, and the applications in the biosensors have shown that CNTs have an electrocatalytic effect and fast electron-transfer rate between the electroactive species and the electrode.

A biosensor could be simply fabricated using multi-walled CNTs (MWCNTs) as immobilization platform with direct electron transfer and enhanced catalytic effect. For example, bilirubin oxidase could be immobilized directly onto MWCNTs modified glassy carbon electrods (Weigel et al., 2007). Direct electron transfer reactions of bilirubin oxidase occur and the incorporation of MWCNTs enhances the catalytic bilirubin oxidase reaction up to a factor of 26 (Weigel et al., 2007).

An extremely robust, sensitive and selective galactose biosensor was proposed by the dispersion of single-wallled CNTs (SWCNTs) into a chitosan matrix to form a stable dispersion, followed by the chemical cross-linking with glutaraldehyde and free aldehyde groups produced a substrate for covalent immobilization of galactose oxidase (Tkac et al., 2007). The detection of oxygen uptaken by galactose oxidase on chitosan/SWCNTs layer at -0.4 V was robust with a low detection limit of 25 μM.

Activating CNT surfaces is an essential prerequisite in order to effectively improve the performance of the prepared biosensors. In practical, CNT solubilization in aqueous media is essential for CNTs as supporting matrix for the immobilization of proteins. This can be achieved by the surface functionalization of CNTs with ionic or hydrophilic groups or the functionalization of CNTs with water-soluable polymers. Based on this approach, MWCNTs are modified by redox polymer, poly(vinylimidazole) complexed with $Os(4,4'dimethylbpy)_2Cl$(PVI-demeOs), resulting in the turning of MWCNT surface from hydrophobic to hydrophilic without changes of surface morporlogy (Cui et al., 2009). The prepared biosensor showed the enhanced sensing sensitivities induced by the redox polymer film, where the enzyme molecules was wired through the redox centers tethered on the mobile redox polymer backbones to the MWCNTs electrodes. MWCNTs could be modified by the coating of polyethylene imine (PEI) or poly(acrylic acid) (PAA) to obtain water-soluble MWCNTs (Yan et al., 2008). Recent development on the modified MWCNTs was to use O_2 plasma to treat MWCNTs, and thus oxygen contained functional groups were introduced onto their surface without influencing their bulk properties (Lee et al., 2009). Attaching metal nanoparticles to CNT and to CNT sidewalls is of interest to obtain nanotube/nanoparticle hybrid materials with useful properties. By electrostatic interaction, CNTs could be coated with gold nanoparticles and further filled with gold nanocluster after heat treatment in NH_3 (Jiang & Gao, 2003). Such heat treatment with NH_3 could make CNTs open-ended and generate functional basic groups on the inner wall of the nanotubes.

The composite of CNTs with other organic/inorganic materials has an important role in CNT-based enzyme biosensors. For instance, MWCNTs/PVP/Prussian blue (PB) composite

film were synthesized by casting films of MWCNTs wrapped with PB on Au electrodes followed by electrochemical deposition of PB on the matrix (Li et al., 2007). The modified electrode thus shows prominent electrocatalytic activity towards the reduction of hydrogen peroxidase, due to the remarkablely synergistic effect of the MWCNTs and PB. Hydrogen peroxide biosensor could be also prepared by entrapping HRP in a new ormosil composite doped with ferrocene monocarboxylic acid-bovine serum albumin conjugate and MWCNTs (Tripathi et al., 2006), which exhibited a very low mass transport barrier to the substrate. Nafion and chitosan as organic materials are quite popular in the CNTs-based nanocomposites. In addition, sol-gel matrix, like titania and silica, were applied for effective enzyme immobilization (Lee et al., 2007; Tiwari & Gong, 2008). Meanwhile, metal nanoparticles of platinum were also incorporated into the composites of chitosan and MWCNTs to improve the performance of the prepared biosensor (Tsai et al., 2008).

Lactate detection is of great importance for the clinical analysis, fermentation as well as for food analysis. Enzyme-based electrochemical techniques for lactate detection is inexpensive, rapid and reliable compared to other methods, such as chromatographic and spectrometric analysis (Posner et al., 1996; Wulkan et al., 2001; Bariskaner et al., 2003; Fernandes et al., 2003). One kind of lactate biosensor was proposed by co-immobilization of lactate dehydrogenase (LDH) and Meldola's Blue on MWCNTs through cross-linking with glutaraldehyde and agglutination with mineral oil (Pereira et al., 2007). The biosensor shows a good stability after 300 times of determinations within a wide linear response range (0.1-10 mM). A MWCNT-CHIT-LDH nanobiocomposite film as a lactate biosensor was developed (Tsai et al., 2007), where MWCNT, chitosan, and LDH were mixed by a simple solvent-evaporation process. The enzyme in this kind of biosensor was entrapped in the biocomposite and the prepared biosensor showed a much fast response around 3s. In addition to MWCNT and chitosan as immobilization materials, polyvinylimidazole-Os (PVI-Os), can be also introduced into the biocomposite to form network structure (Cui et al., 2007). In the nanocomposite of chitosan/PVI-Os/MWCNT/LOD(lactate oxidase), negatively charged LOD was entrapped by a positively charged chitosan. PVI-Os was used as a leachables electron mediator due to its polymeric redox form and its positive charge could also enhance the entrapment for LOD. Negatively charged CNT was designed as a cross-linker to network chitosan and PVI-Os for the nanocomposite. The prepared biosensor showed significantly improved conductivity, stability and electroactivity for lactate detection. The sensitivity could reach 19.7 $\mu A/cm^2.mM$, and the low limit of detection of 5 μM. Recently, a new kind of hybrid composite for lactat biosensor was developed by introducing double-walled CNTs (DWCNTs) into alginate gel (Ma et al., 2008). DWCNTs with two concentric grapheme cylinders have attracted great interests in recent years because of their unique coaxial structure and promising mechanical, electrical, optical and thermal properties over SWCNTs and MWCNTs. LDH was prepared by pre-adsorbed on DWCNTs and then they were incorporated into alginate gel followed by Ca^+ cross-linking. The prepared lactate biosensor could greatly reduce the water loss and LDH leakage.

Recent advances in CNT-based enzyme biosensors have shown to design a biocomposite biosensor so as to detect more than one substrate. An good example was given by a bienzyme biosensor with a bienzyme-channelling configuration, where toluidine blue functionalized MWCNTs were used for enzyme immobilization (Jeykumari & Narayanan, 2009). The constructed biosensor shows a short response time (< 2s), good stability and anti-interferant ability. Many efforts have been made to detect the biomolecules at very low

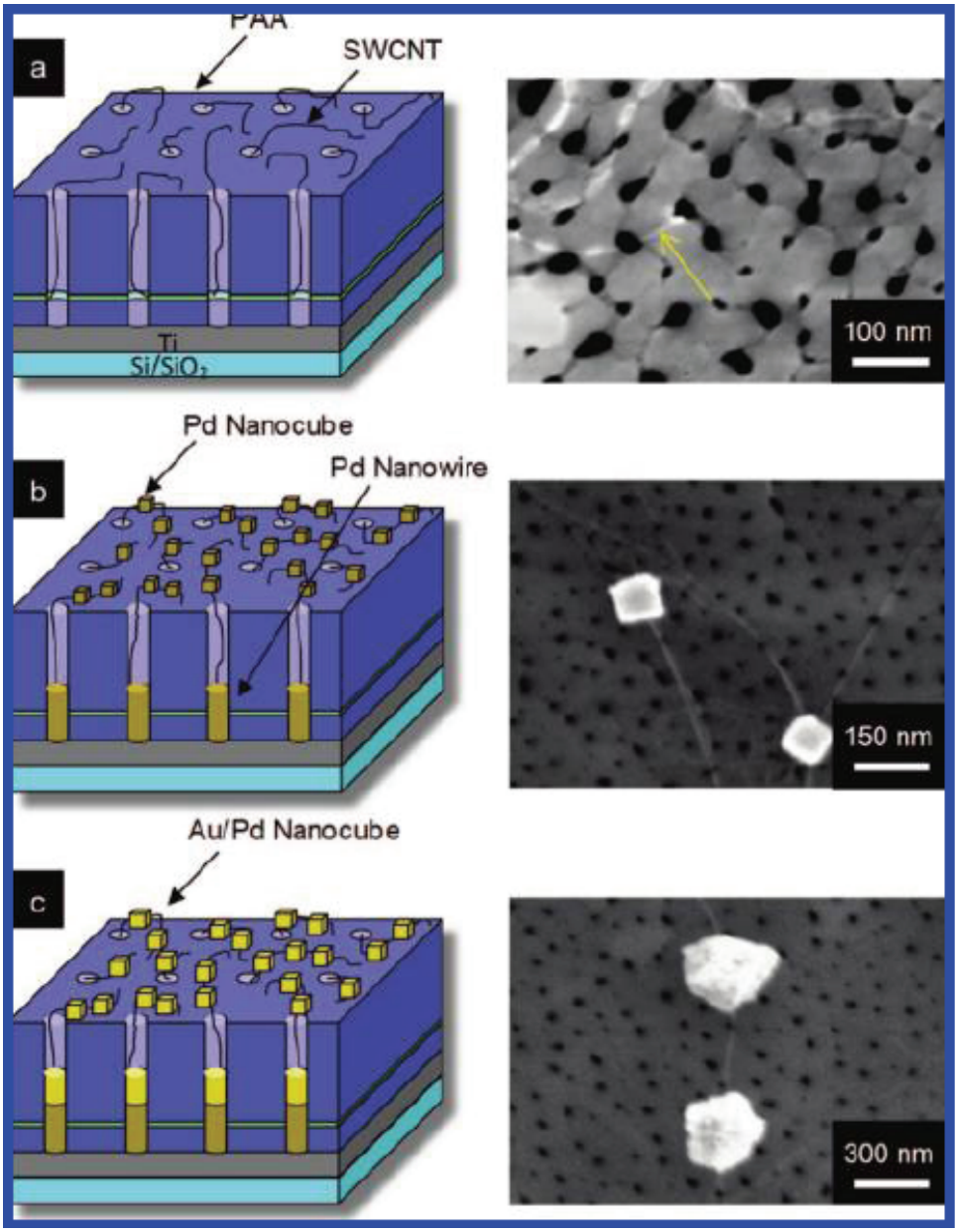

Fig. 4. Tilted cross-sectional schematics with corresponding SEM images portraying sequential fabrication process steps: (a) SWCNTs grown from the pores of the PAA via MPCVD, (b) electrodeposition of Pd to form Pd nanowires in pores and Pd nanocubes on SWCNTs and (c) electrodeposition to coat the existing Pd nanocubes with a thin layer of Au (Claussen et al., 2009).

concentrations. Networks of SWCNTs decorated with Au-coated Pd nanocubes are employed as electrochemical biosensors showing a limit of detection as low as 2.3 nM for H_2O_2, in which Au-coated Pd nanocubes were grown at the defect sites of template SWCNT networks through a simple electrodeposition process (Claussen et al., 2009). Fig. 4 shows the schematic fabrication process steps with corresponding SEM images.

3.2.4 Polypyrrole

Among various conducting polymers, polypyrrole (PPy) as an intelligent material plays an important role in the electrochemical biosensors for the purpose of increased electrochemical activity and sensitivity, owing to its good biocompatibility, conductivity, stability, and efficient polymerization at neutral pH as well as easy synthesis. PPy films can be easily formed from aqueous solutions by chemical or electrochemical routes, and have a high degree of selectivity due to the inherent size-exclusion property. A recently good review on the applications of polymers in electrochemical biosensors could be found in the literature (Teles & Fonseca, 2008), in which polypyrrole was highlighted.

In biosensor construction, PPy is often used as a conducting matrix and thus other organic/inorganic materials could be introduced into the matrix to further improve the performance of the biosensor. For example, stable and homogenous hybrid films consisting of PPy and copper hexacyanoferrate by electrochemical method were synthesized, aiming to obtain an electrocatalyst for H_2O_2 reduction in the presence of either Na^+ or K^+ ions (Fiorito et al., 2006). The constructed biosensor shows excellent catalytic properties towards H_2O_2 detection, with a performance higher than those observed for Prussian Blue and other analogues due to the electronic conductivity of the polymeric matrix (Fiorito et al., 2006).

In practical, it is important to find ways to obtain PPy polymers with desirable properties for biosensor applications by introducing various dopants. For instance, electrical conductivity can be achieved in polymer films by doping or inserting anionic or cationic species during the process of polymerization. Besides, the incorporation of a large size dopant anion, such as polyvinyl sulphonate (PVS), *p*-toluene sulphonate (*p*TS), and dodecylbenzene sulphonate (DBS) into PPy films during electropolymerization makes PPy film more porous, which is very important for the facile immobilization of enzyme (Tsai et al., 1988). According to this strategy, by using electrochemical method, PPy-PVS(polyvinyl sulphonate) nanocomposite film could be easily fabricated onto ITO electrode, and the enzyme is immobilized by cross-linking via glutaraldehyde on the hybrid film. A good performance of the biosensor was exhibited in terms of dynamic range of detection, short response time, long lifetime and stability. PPy can also be doped with alginate. Alginate hydrogel supports are usually made by cross-linking the carboxyl group of the guluronic acid residue with a solution of cationic crosslinkers such as calcium choloride, barium chloride, strontium, etc., and thus enzyme could retain their activity in alginate hydrogels (Martinsen et al., 1989). By taking advantages of both of alginate and PPy, a novel composite was synthesized through providing a gel by Ca^+ cross-linking (Ionescu et al., 2005), which exhibitis a greater enzyme retention as well as increased alginate stability towards the destructive effect of phosphate anions compared to the natural alginate gel. Recently, protonated sodium alginate (pSA) was also reported to be a dopant for electrogeneration of Ppy/pSA functionalized films for GOD immobilization. This was achieved via covalent bonding of carboxyl groups of the main chain of alginate with amino groups of the enzyme (Chen et al., 2008).

Layer-by-layer assembled technology has been also used in PPy-based biosensors. An example is that layer-by-layer assembled PPy and CNTs multilayer films were fabricated on Pt coated Polyvinylidene fluoride membrane, where PPy film was prepared by electrochemical polymerization and CNTs layers were coated by a vacuum filtration technique (Shirsat et al., 2008). Such multilayer structure provided an excellent matrix for the immobilization of enzyme, which possessed the favorable features of both PPy and CNTs. Cross-linking was chosen for GOD immobilization, and such prepared biosensor showed enhanced linear range, response time and sensitivity (Gade et al., 2006).
Interestingly, soluble PPy synthesized by the incorporation of sulfonate dopant anion could be well incorporated into microscopic polyacrylamide particles for glucose biosensing by concentrated emulsion polymerization method (Retama et al., 2005). The novelty of this method over conventional emulsion polymerization lies in the large volume of the aqueous dispersed phase used. The PPy/polyacrylamide microparticles showed the semi-conductivity, and GOD was immobilized in the microparticles by incorporating the enzyme into the aqueous phase of the concentrated emulsion before starting polymerization. To construct the biosensor, the obtained microparticles layer was covered and flattened around the platinum electrode surface using a dialysis membrane (Retama et al., 2005), and it showed the great interest for the application in glucose detection.
Other types of PPy nanostructures, like PPy nanotubes have been also proposed for enhanced adsorption of glucose oxidase in glucose biosensors (Ekanayake et al., 2007), where PPy nanotube array was synthesized using a solution of pyrrole and $NaPF_6$ at a fixed current density for 90 s. GOD was immobilized onto the electrode through physical adsorption. With this new approach, the constructed biosensor had exhibited remarkable improvement in the sensitivity, response time and linear range values.

4. Outlook

This chapter mainly presents intelligent nanomaterials (e.g ZnO, gold, CNT and polyrrole) for construction of enzyme-based electrochemical biosensors to show the development in this area. To construct a biosensor with promising applications, it should be carefully considered to modify electrode in an effective way. The immobilization of enzyme onto the electrodes should be considered as another key step due to the important roles of the amount and bioactivity of immobilized enzyme on the performance of biosensors.
There are many challenges currently faced towards practical applications of biosensors. For example, the construction of a biosensor with a low cost is still essential when considering the commercial devices. The major application field of biosensors is medical diagnostics with commercial devices. The biosensors in other areas, such as food industry and ecology, needed to be explored deeply for more applications. Challenges also exist to find ways to improve the performance criteria including high sensitivity, wider linear range, low limit of detection, fast response and repetitive ability. Research work now still keeps continuing to investigate more effective ways to construct enzyme-based electrochemical biosensors with more perfect performance.
In the future development of electrochemical biosensors, the demands for portable and cheap biosensors with multifunctions (e.g. to detect several target analytes) will keep increasing for practical applications. Many thanks to the emergence of nanotechnology, many researchers could incorporate this technology into the biosensor construction to obtain novel structures. Miniaturization will play an important role in the trend of biosensor

development in the future. However, it may result in low current because of the decreased amount of immobilized enzyme onto the available active area. This can be overcom by the nanostructures, which enhance the sensitivity of a biosensor by one to two orders of magnitude, due to the large surface area per unit volume ration, which allows the immobilization of a larger amount of the enzyme. Overall, electrochemical biosensors with perfect performance towards commercial systems keep a main thrust in future research.

5. Acknowledgements

This work was supported financially by National Natural Science Foundation of China (Grant No. 40971279) and Nature Science Foundation of Jiangsu province (Grant No. BK2009264).

6. References

Bariskaner, H.; Ustun, M. E.; Yosunkaya, A. A. A.; Dogan, N. & Gurbilek, M. (2003). Effects of deferoxamine on tissue lactate and malondialdehyde levels in cerebral ischemia. *Methods & Findings in Experimental & Clinical Pharmacology* 25, 371-376

Buerk, D. G. (1993). *Biosensors: Theory and applications*, Technomic, Pennsylvania Lancaster.

Cao, X.; Ning, W.; Li, L. D. & Guo, L. (2008). Synthesis and characterization of waxberry-like microstructures ZnO for biosensors. *Sensors and Actuators B-Chemical* 129, 268-273

Caruso, F.; Niikura, K.; Furlong, D. N. & Okahata, Y. (1997). Assembly of alternating polyelectrolyte and protein multilayer films for immunosensing. *Langmuir* 13, 3427-3433

Chen, L. Y.; Gu, B. X.; Zhu, G. P.; Wu, Y. F.; Liu, S. Q. & Xu, C. X. (2008). Electron transfer properties and electrocatalytic behavior of tyrosinase on ZnO nanorod. J*ournal of Electroanalytical Chemistry* 617, 7-13

Chen, S. J.; Chen, W. & Xue, G. (2008). Electrogeneration of polypyrrole/alginate films for immobilization of glucose oxidase. *Macromolecular Bioscience* 8, 478-483

Claussen, J. C.; Franklin, A. D.; Haque, A. U.; Porterfield, D. M. & Fisher, T. S. (2009). Electrochemical biosensor of nanocube-augmented carbon nanotube networks. *ACS Nano* 3, 37-44

Crespilho, F. N.; Ghica, M. E.; Florescu, M.; Nart, F. C.; Oliveira, O. N. & Brett, C. M. A. (2006). A strategy for enzyme immobilization on layer-by-layer dendrimer-gold nanoparticle electrocatalytic membrane incorporating redox mediator. *Electrochemistry Communications* 8, 1665-1670

Cui, H. F.; Ye, J. S.; Zhang, W. D. & Sheu, F. S. (2009). Modification of carbon nanotubes with redox hydrogel: Improvement of amperometric sensing sensitivity for redox enzymes. *Biosensors and Bioelectronics* 24, 1723-1729

Cui, X. Q.; Li, C. M.; Zang, J. F. & Yu, S. C. (2007). Highly sensitive lactate biosensor by engineering chitosan/PVI-Os/CNT/LOD network nanocomposite. *Biosensors and Bioelectronics* 22, 3288-3292

Decher, G.; Hong, J. D. & Schmitt, J. (1992). Buildup of ultrathin multilayer films by a self-assembly process: III. Consecutively alternating adsorption of anionic and cationic polyelectrolytes on charged surfaces. *Thin Solid Films* 210-211, 831-835

Du, D.; Chen, S. Z.; Cai, J. & Zhang, A. D. (2008). Electrochemical pesticide sensitivity test using acetylcholinesterase biosensor based on colloidal gold nanoparticle modified sol-gel interface. *Talanta* 74, 766-772, 0039-9140.

Duan, G. P.; Li, Y. F.; Wen, Y.; Ma, X. L.; Wang, Y.; Ji, J. H.; Wu, P.; Zhang, Z. R. & Yang, H. F. (2008). Direct Electrochemistry and Electrocatalysis of Hemoglobin/ZnO-Chitosan/nano-Au Modified Glassy Carbon Electrode. *Electroanalysis* 20, 2454-2459

Dzyadevych, S. V.; Arkhypova, V. N.; Soldatkin, A. P.; El'skaya, A. V.; Martelet, C. & Jaffrezic-Renault, N. (2008). Amperometric enzyme biosensors: Past, present and future. *Irbm* 29, 171-180

Eggins, B. R. (1996). *Biosensors: an introduction*, Wiley.

Ekanayake, E.; Preethichandra, D. M. G. & Kaneto, K. (2007). Polypyrrole nanotube array sensor for enhanced adsorption of glucose oxidase in glucose biosensors. *Biosensors and Bioelectronics* 23, 107-113

Feldheim, D. L.; Grabar, K. C.; Natan, M. J. & Mallouk, T. E. (1996). Electron transfer in self-assembled inorganic polyelectrolyte/metal nanoparticle Heterostructures. *Journal of the American chemical Society* 118, 7640-7641

Fernandes, L.; Relva, A. M.; da Silva, M. D. R. G. & Freitas, A. M. C. (2003). Different multidimensional chromatographic approaches applied to the study of wine malolactic fermentation. *Journal of Chromatography A* 995, 161-169

Fiorito, P. A.;Brett, C. M. A.&de Torresi, S. I. C. (2006). Polypyrrole/copper hexacyanoferrate hybrid as redox mediator for glucose biosensors. *Talanta* 69, 403-408

Gade, V. K.; Shirale, D. J.; Gaikwad, P. D.; Savale, P. A.; Kakde, K. P.; Kharat, H. J. & Shirsat, M. D. (2006). Immobilization of GOD on electrochemically synthesized Ppy-PVS composite film by cross-linking via glutaraldehyde for determination of glucose. *Reactive & Functional Polymers* 66, 1420-1426

He, J. A.; Samuelson, L.; Li, L.; Kumar, J. & Tripathi, S. K. (1998). Oriented bacteriorhodopsin/polycation multilayers by electrostatic layer-by-layer assembly. *Langmuir* 14, 1674-1679

Ionescu, R. E.; Abu-Rabeah, K.; Cosnier, S. & Marks, R. S. (2005). Improved enzyme retention from an electropolymerized polypyrrole-alginate matrix in the development of biosensors. *Electrochemistry Communications* 7, 1277-1282

Jeykumari, D. R. S. & Narayanan, S. S. (2009). Functionalized carbon nanotube-bienzyme biocomposite for amperometric sensing. *Carbon* 47, 957-966

Jiang, L. Q. & Gao, L. (2003). Modified carbon nanotubes: an effective way to selective attachment of gold nanoparticles. *Carbon* 41, 2923-2929

Khan, R.; Kaushik, A.; Solanki, P. R.; Ansari, A. A.; Pandey, M. K. & Malhotra, B. D. (2008). Zinc oxide nanoparticles-chitosan composite film for cholesterol biosensor. *Analytica Chimica Acta* 616, 207-213

Lee, J. Y.; Park, E. J.; Lee, C. J.; Kim, S. W.; Pak, J. J. & Min, N. K. (2009). Flexible electrochemical biosensors based on O-2 plasma functionalized MWCNT. *Thin Solid Films* 517, 3883-3887

Lee, Y. J.; Lyu, Y. K.; Choi, H. N. & Lee, W. Y. (2007). Amperometric tyrosinase biosensor based on carbon nanotube-Titania-Nafion composite film. *Electroanalysis,* 19, 1048-1054

Li, J.; Qiu, J. D.; Xu, J. J.; Chen, H. Y. & Xia, X. H. (2007). The synergistic effect of Prussian-Blue-grafted carbon nanotube/poly(4-vinylpyridine) composites for amperometric sensing. *Advanced Functional Materials,* 17, 1574-1580

Li, Y. F.; Liu, Z. M.; Liu, Y. L.; Yang, Y. H.; Shen, G. L. & Yu, R. Q. (2006). A mediator-free phenol biosensor based on immobilizing tyrosinase to ZnO nanoparticles. *Analytical Biochemistry,* 349, 33-40

Liu, S. Q. & Ju, H. X. (2002). Renewable reagentless hydrogen peroxide sensor based on direct electron transfer of horseradish peroxidase immobilized on colloidal gold-modified electrode. *Analytical Biochemistry,* 307, 110-116,0003-2697.

Liu, S. Q. & Ju, H. X. (2003). Reagentless glucose biosensor based on direct electron transfer of glucose oxidase immobilized on colloidal gold modified carbon paste electrode. *Biosensors and Bioelectronics* 19, 177-183,0956-5663.

Liu, S. Q.; Yu, J. H. & Ju, H. X. (2003). Renewable phenol biosensor based on a tyrosinase-colloidal gold modified carbon paste electrode. *Journal of Electroanalytical Chemistry,* 540, 61-67,0022-0728.

Liu, Z. M.; Liu, Y. L.; Yang, H. F.; Yang, Y.; Shen, G. L. & Yu, R. Q. (2005). A mediator-free tyrosinase biosensor based on ZnO sol-gel matrix. *Electroanalysis*, 17, 1065-1070

Lu, X. B.; Zhang, H. J.; Ni, Y. W.; Zhang, Q. & Chen, J. P. (2008). Porous nanosheet-based ZnO microspheres for the construction of direct electrochemical biosensors. *Biosensors and Bioelectronics,* 24, 93-98

Luo, X. L.; Xu, J. J.; Du, Y. & Chen, H. Y. (2004). A glucose biosensor based on chitosan-glucose oxidase-gold nanoparticles biocomposite formed by one-step electrodeposition. *Analytical Biochemistry,* 334, 284-289,0003-2697.

Luo, X. L.; Xu, J. J.; Zhang, Q.; Yang, G. J. & Chen, H. Y. (2005). Electrochemically deposited chitosan hydrogel for horseradish peroxidase immobilization through gold nanoparticles self-assembly. *Biosensors and Bioelectronics,* 21, 190-196,0956-5663.

Lvov, Y.; Decher, G. & Moehwald, H. (1993). Assembly, structural characterization, and thermal behavior of layer-by-layer deposited ultrathin films of poly(vinyl sulfate) and poly(allylamine). *Langmuir,* 9, 481-486

Ma, L. J.; Wen, J. P.; Lu, W. Y.; Caiyin, Q. G. & Liang, Y. (2008). Efficient immobilization of lactate dehydrogenase in biocomposites of double-walled carbon nanotube-doped alginate gel. *Enzyme and Microbial Technology,* 42, 235-241

Ma, W.; Song, W. & Tian, D. B. (2009). ZnO-MWCNTs/Nafion inorganic-organic composite film: Preparation and application in bioelectrochemistry of hemoglobin. *Chinese Chemical Letters,* 20, 358-361

Manso, J.; Mena, M. L.; Yanez-Sedeno, P. & Pingarron, J. M. (2007). Electrochemical biosensors based on colloidal gold-carbon nanotubes composite electrodes. *Journal of Electroanalytical Chemistry,* 603, 1-7

Martinsen, A.; Skjak-Brak, G. & Smidsrod, O. (1989). Alginate as immobilization materials: I. correlation between chemical and physical properties of alginate gel beads. *Biotechnology and bioengineering*, 33, 79-89

Njagi, J. & Andreescu, S. (2007). Stable enzyme biosensors based on chemically synthesized Au-polypyrrole nanocomposites. *Biosensors and Bioelectronics* 23, 168-175

Nunes, G. S. & Marty, J. L. (2006). Chapter 21 Immobilization of Enzymes on Electrodes *Immobilization of Enzymes and Cells* (Methods in Biotechnology). J. M. Guisan. Totowa, NJ, Humana Press Inc. : 239.

Pereira, A. C.; Aguiar, M. R.; Kisner, A.; Macedo, D. V. & Kubota, L. T. (2007). Amperometric biosensor for lactate based on lactate dehydrogenase and Meldola Blue coimmobilized on multi-wall carbon-nanotube. *Sensors and Actuators B-Chemical,* 124, 269-276

Pingarron, J. M. ; Yanez-Sedeno, P. & Gonzalez-Cortes, A. (2008). Gold nanoparticle-based electrochemical biosensors. *Electrochimica Acta*, 53, 5848-5866

Posner, B. A.; Li, L. Y.; Bethell, R.; Tsuji, T. & Benkovic, S. J. (1996). Engineering specificity for folate into dihydrofolate reductase from Escherichia coli. *Biochemisty*, 35, 1653-1663

Retama, J. R.; Mecerreyes, D.; Lopez-Ruiz, B. & Lopez-Cabarcos, E. (2005). Synthesis and characterization of semiconducting polypyrrole/polyacrylamide microparticles with GOx for biosensor applications. *Colloids and Surfaces a-Physicochemical and Engineering Aspects*, 270, 239-244

Shirsat, M. D.; Too, C. O. & Wallace, G. G. (2008). Amperometric glucose biosensor on layer by layer assembled carbon nanotube and polypyrrole multilayer film. *Electroanalysis*, 20, 150-156

Shulga, O. & Kirchhoff, J. R. (2007). An acetylcholinesterase enzyme electrode stabilized by an electrodeposited gold nanoparticle layer. *Electrochemistry Communications*, 9, 935-940,1388-2481.

Singh, M.; Verma, N.; Garg, A. K. & Redhu, N. (2008). Urea biosensors. *Sensors and Actuators B-Chemical*, 134, 345-351

Teles, F. R. R.&Fonseca, L. P. (2008). Applications of polymers for biomolecule immobilization in electrochemical biosensors. *Materials Science & Engineering C-Biomimetic and Supramolecular Systems*, 28, 1530-1543

Tiwari, A. & Gong, S. Q. (2008). Electrochemical Study of Chitosan-SiO2-MWNT Composite Electrodes for the Fabrication of Cholesterol Biosensors. *Electroanalysis*, 20, 2119-2126

Tkac, J.; Whittaker, J. W. & Ruzgas, T. (2007). The use of single walled carbon nanotubes dispersed in a chitosan matrix for preparation of a galactose biosensor. *Biosensors and Bioelectronics,* 22, 1820-1824

Tripathi, V. S.; Kandimalla, V. B. &J u, H. X. (2006). Amperometric biosensor for hydrogen peroxide based on ferrocene-bovine serum albumin and multiwall carbon nanotube modified ormosil composite. *Biosensors and Bioelectronics*, 21, 1529-1535

Tsai, E. W.; Pajkossy, T.; Rajeshwar, K. & Reynolds, J. R. (1988). Anion-exchange behavior of polypyrrole membranes. *Journal of Physical Chemistry*, 92, 3560-3565

Tsai, Y. C.; Chen, S. Y. & Lee, C. A. (2008). Amperometric cholesterol biosensors based on carbon nanotube-chitosan-platinum-cholesterol oxidase nanobiocomposite. *Sensors and Actuators B-Chemical,* 135, 96-101

Tsai, Y. C.; Chen, S. Y. & Liaw, H. W. (2007). Immobilization of lactate dehydrogenase within multiwalled carbon nanotube-chitos anhanocompo site for application to lactate biosensors. *Sensors and Actuators B-Chemical,* 125, 474-481

Umar, A.; Rahman, M. M.; Al-Hajry, A. & Hahn, Y. B. (2009). Highly-sensitive cholesterol biosensor based on well-crystallized flower-shaped ZnO nanostructures. *Talanta*, 78, 284-289

Umar, A.; Rahman, M. M.; Kim, S. H. & Hahn, Y. B. (2008). ZnO nanonails: Synthesis and their application as glucose biosensor. *Journal of Nanoscience and Nanotechnology*, 8, 3216-3221

Umar, A.; Rahman, M. M.; Vaseem, M. & Hahn, Y. B. (2009). Ultra-sensitive cholesterol biosensor based on low-temperature grown ZnO nanoparticles. *Electrochemistry Communications,* 11, 118-121

Wang, J. X.; Sun, X. W.; Wei, A.; Lei, Y.; Cai, X. P.; Li, C. M. & Dong, Z. L. (2006). Zinc oxide nanocomb biosensor for glucose detection. *Applied Physics Letters*, 88, 233106

Wang, Y. T.; Yu, L.; Zhu, Z. Q.; Zhang, J. & Zhu, J. Z. (2009). Novel Uric Acid Sensor Based on Enzyme Electrode Modified by ZnO Nanoparticles and Multiwall Carbon Nanotubes. *Analytical Letters,* 42, 775-789

Weber, J.; Jeedigunta, S. & Kumar, A. (2008). Fabrication and Characterization of ZnO Nanowire Arrays with an Investigation into Electrochemical Sensing Capabilities. *Journal of Nanomaterials,*2008, 638523

Wei, A.;S un, X. W.; Wang, J. X.; Lei, Y.; Cai, X. P.; Li, C. M.; Dong, Z. L. & Huang, W. (2006). Enzymatic glucose biosensor based on ZnO nanorod array grown by hydrothermal decomposition. *Applied Physics Letters,* 89, 123902

Weigel, M. C.; Tritscher, E. & Lisdat, F. (2007). Direct electrochemical conversion of bilirubin oxidase at carbon nanotube-modified glassy carbon electrodes. *Electrochemistry Communications*, 9, 689-693

Wu, B. Y.; Hou, S. H.; Yin, F.; Li, J.; Zhao, Z. X.; Huang, J. D. & Chen, Q. (2007). Amperometric glucose biosensor based on layer-by-layer assembly of multilayer films composed of chitosan, gold nanoparticles and glucose oxidase modified Pt electrode. *Biosensors and Bioelectronics,* 22, 838-844, 0956-5663.

Wulkan, R. W.; Verwers, R.; Neele, M. & Mantel, M. J. (2001). Measurement of pyruvate in blood by high-performance liquid chromatography with fluorescence detection. *Annals of Clinical Biochemistry,* 38, 554-558

Xiang, C.; Zou, Y.; Sun, L. X. & Xu, F. (2009). Direct electrochemistry and enhanced electrocatalysis of horseradish peroxidase based on flowerlike ZnO-gold nanoparticle-Nafion nanocomposite. *Sensors and Actuators B-Chemical*, 136, 158-162

Yan, Y. M.; Baravik, I.; Yehezkeli, O. & Willner, I. (2008). Integrated Electrically Contacted Glucose Oxidase/Carbon Nanotube Electrodes for the Bioelectrocatalyzed Detection of Glucose. *Journal of Physical Chemistry C,* 112, 17883-17888

Yang, W. W.; Wang, J. X.; Zhao, S.; Sun, Y. Y. & Sun, C. Q. (2006). Multilayered construction of glucose oxidase and gold nanoparticles on Au electrodes based on layer-by-layer covalent attachment. *Electrochemistry Communications,* 8, 665-672.

Yang, Y. H.; Yang, M. H.; Jiang, J. H.; Shen, G. L. & Yu, R. Q. (2005). A novel biomolecular immobilization matrix based on nanoporous ZnO/Chitosan composite film for amperometric hydrogen peroxide biosensor. *Chinese Chemical Letters,* 16, 951-954

Zang, J. F.; Li, C. M.; Cui, X. Q.; Wang, J. X.; Sun, X. W.; Dong, H. & Sun, C. Q. (2007). Tailoring zinc oxide nanowires for high performance amperometric glucose sensor. *Electroanalysis*, 19, 1008-1014

Zhang, F. F.; Wang, X. L.; Ai, S. Y.; Sun, Z. D.; Wan, Q.; Zhu, Z. Q.; Xian, Y. Z.; Jin, L. T. & Yamamoto, K. (2004). Immobilization of uricase on ZnO nanorods for a reagentless uric acid biosensor. *Analytica Chimica Acta,* 519, 155-160

Zhang, S. X.; Wang, N.; Yu, H. J.; Niu, Y. M. & Sun, C. Q. (2005). Covalent attachment of glucose oxidase to an Au electrode modified with gold nanoparticles for use as glucose biosensor. *Bioelectrochemistry*, 67, 15-22

Zhang, Y. W.; Zhang, Y.; Wang, H.; Yan, B.; Shen, G. L. & Yu, R. Q. (2009). An enzyme immobilization platform for biosensor designs of direct electrochemistry using flower-like ZnO crystals and nano-sized gold particles. *Journal of Electroanalytical Chemistry,* 627, 9-14

Zhao, J. W.; Wu, D. H. & Zhi, J. F. (2009). A novel tyrosinase biosensor based on biofunctional ZnO nanorod microarrays on the nanocrystalline diamond electrode for detection of phenolic compounds. *Bioelectrochemistry,* 75, 44-49

Zhao, Z. W.; Chen, X. J.; Tay, B. K.; Chen, J. S.; Han, Z. J. & Khor, K. A. (2007). A novel amperometric biosensor based on ZnO: Co nanoclusters for biosensing glucose. *Biosensors and Bioelectronics*, 23, 135-139,0956-5663.

Zhao, Z. W.; Tay, B. K.; Chen, J. S.; Hu, J. F.; Lim, B. C. & Li, G. P. (2007). Large magnetic moment observed in Co-doped ZnO nanocluster-assembled thin films at room temperature. *Applied Physics Letters*, 90, 152502, 0003-6951.

Zhao, Z. W.; Tay, B. K.; Chen, J. S.; Hu, J. F.; Sun, X. W. & Tan, S. T. (2005). Optical properties of nanocluster-assembled ZnO thin films by nanocluster-beam deposition. *Applied Physics Letters,* 87, 251912,0003-6951.

2

Nanostructured Metal Oxides Based Enzymatic Electrochemical Biosensors

Anees A. Ansari, M.Alhoshan, M.S. Alsalhi and A.S. Aldwayyan
King Abdullah Institute for Nanotechnology, King Saud University, Riyadh-11451 Saudi Arabia

1. Introduction

Studies of nanobiosensors based on semiconductor nanostructured metal oxides are of practical and theoretical importance in biological science, environmental science and analytical chemistry (Wang et al., 2005; Luo et al., 2006; Valentini & Palleschi (2008); Chopra et al., 2007). These one-dimensional nanostructured metal oxides have profound applications in optics, optoelectronics, sensors, and actuators duo to their semiconducting, piezoelectric, and pyroelectric properties (Wang et al., 2005; Chopra et al., 2007; Kerman et al., 2008; Chow et al., 2005). Nanostructured metal oxides not only possesses high surface area, nontoxicity, good biocompatibility and chemical stability, but also shows fast electron communication features made the materials to be able to function as biomimetic membrane material to fix and modify proteins (Wang et al., 2005; Chopra et al., 2007; Valentini & Palleschi (2008)). These biomimetic and high electron communication features, high surface to volume ratio and electro-catalytic activity of the nanosized materials make them ideal as immobilization matrices, as transduction platform and/or mediators. Stability, sensitivity, selectivity and other analytical characteristics of biosensors are essential features to design desirable microenviroment for the direct electron transfer between the enzyme's active sites and the electrode. To improve these characteristics various conventional materials matrices have been proposed. Among them nanostructured metal oxides matrices not only retain the bioactivity of the immobilized enzyme but also enhanced the sensing characteristics such as sensitivity, selectivity and low detection limit of the fabricated amperomatric enzymatic biosensors. Morphology of the nanosized material is one of the most ideally suited important factor to determine the properties for biosensor applications since they are conductive, biocompatible, easily functionalized while they have very large surface area. Nanosized metal oxides based electrochemical enzymatic biosensors have active surfaces that can easily be modified for immobilization of biomolecules. However, this advantage may not apply to many non-oxide semiconductor nanomaterials because their surfaces are not stable in an air environment, which leads to formation of an insulating native oxide layer and may degrade device reliability and sensitivity.

Whereas, nanostructured metal oxides based electrochemical transducer surfaces promote the direct electron transfer reactions, amplify and orient the analytic signal of the biorecognition events. When a redox protein is immobilized on a biocompatible metal oxide electrode surface, it will exhibit reasonably fast electron transfer kinetic and permit the

electrochemical measurement of its substrate without addition of a mediator to the analyzed solution. Since the direct contact of redox protein with metal oxide surfaces usually leads to significant changes in protein structure, function and increased the bioactivity of the electrochemical enzymatic transducer. These electrochemical transducers are regarded as particularly suitable for direct and fast biosensing since they can convert the biological recognition event into a direct electrical signal. This means, that there is no need for complex signal transduction equipment and the detection can be accomplished with an inexpensive electrochemical analyzer. Electrochemical biosensing approaches include the intrinsic electroactivity of redox enzyme, electrochemistry of nanoparticles and metal oxide nanoparticles. Recently electrochemical enzymatic transducers have received considerable popularity in connection to the simple detection of analytes (proteins and enzymes), because of their rapid, high sensitivity, portability, low cost (disposability), simpler and minimal power requirements make them excellent candidate for analyte detection.The high sensitivity and wide linear range of such devices have opened new door in widespread biomedical applications such as clinical diagnosis (for cancer diagnostics and detection of infectious organisms), in environmental monitoring (for pesticide detection, heavy metal–trace pollutant quantification, and genotoxic molecules), and finally in food quality control (for genetically modified organisms-GMOs-and several food toxins). In this article, we describe the importance of nano-structured metal oxides for fabrication of amperomatric of amperometric and voltammetric electrochemical enzymatic biosensors.

2. Synthesis and properties of nanostructured metal oxides

For the synthesis of nanostructured metal oxides various physical and chemical routes have been developed to determine their morphological properties and possible applications in biosensors (see in Table 1). Physical methods, which often involve vapor deposition, or ball milling process require subdivision of bulk precursors to nanoparticles. Chemical procedures start from reduction of metal ions to metal atoms, followed by controlled aggregation and separation of atoms from the bulk. The chemical methods or solution based chemistry methods are quit more suitable to obtaining small, uniform nanoparticles such as nanorods, nanowires, nanofibers, nanobelt, nanocomb, nanotubes and porous materials than the former for the particular biosensor applications of the nanomaterials.

The properties of the nanoparticles generally depend on size, shape and stabilizing agents, which are controlled by the preparation conditions. Moreover, the size and the uniformity of the nanoparticles depend on the kind and the amount of reducing agent employed in synthesis. Recently, the use of MnO_2 nanoparticles to construct an interface for direct electron transfer of redox proteins and retention of bioactivity is being extensively reported. One dimensional (1D) nanostructures (including rods, wires, belts, and tubes) provide a better model system for investigating the dependence of electronic transport, optical and mechanical properties on size confinement and dimensionality. They are also expected to play an important role as both interconnects and functional units in fabricating electronic, optoelectronic, electrochemical, and electromechanical devices with nanoscale dimensions. Considering the importance of metal oxides in catalysis, electrochemistry, functional ceramics, and sensors, their fabrication in nanostructured form with anisotropic morphology appears to be a particularly attractive goal and has been pursued in a number

Nanostructured Processing methods			
SN	**Physical vapour deposition Methods**	**Chemical vapor deposition methods**	**Solution based chemistry methods**
1	Pulse laser deposition	Thermal and Low Pressure Chemical Vapor Deposition	Sonochemical method
2	Thermal Evaporation	Plasma-Enhanced Chemical Vapor Deposition	Sol-gel technique
3	Rf magnetron sputtering	Metal-Organic Chemical Vapor Deposition	Microemulsion process
4	Flame pyrolysis	Molecular Beam Epitaxy	Hydrothermal/solvothermal methods
5	Laser ablation	Atomic Layer Deposition	Supercritical fluid precipitation process
7	Mechanical alloying techniques		Homogeneous/heterogeneous precipitation
8	Mechanical milling		Electrochemical deposition process

Table 1. General applied synthesis methods of nanostructured materials

of laboratories. Much effort has been devoted to synthesized, characterized the novel properties and application of metal oxides such as nanofibers, nanorods, nanowires, and nanotubes. When developing a synthetic method for generating nanostructures, the most important issue that one need to address is the simultaneous control over dimensions, morphology (or shape), and mono-dispersbility (or uniformity).

3. Electrocatalytic behavior of nanostructured metal oxides in the development of biosensor

Numerous papers have been published in the literature indicating nanostructured metal oxides as a convenient component, forming an appropriate environment for the immobilization of enzyme at the electrode surface and its interaction with metallic or conducting electrode surface. Stable immobilization of macromolecular biomolecules on semiconducting metal oxide nano-surface with complete retention of their biological recognition properties is a crucial problem for the commercial development of miniaturized biosensor. Owing to large specific surface area and high surface free energy of nanoparticles can absorb enzymes strongly and play an important role in the immobilization of enzymes in construction of biosensor devices. Generally, the adsorption of enzymes directly onto naked surfaces of bulk materials may frequently result in their denaturation and loss of bioactivity. However, the adsorption of such enzymes onto the surfaces of nanoparticles can retain their bioactivity because of biocompatibile nature of metal oxides nanoparticles. Since most of the metal oxide nanoparticles carry high isoelectric point (>IEP), they can

electrostatically adsorb enzymes with different charges with the low isoelectric point enzymes or protiens. Wang et al., (2006) have applied ZnO nanocomb as a glucose sensing matrix that is most frequently used nanomaterial because they have high isoelectric point (IEP~9.5). Therefore, low isoelectric point enzymes and protein strongly adsorbed on the nanostructured metal oxide surface and provides direct electron communication between the enzymes and conducting electrode. For example, it is reported that ZnO nanorods (Wei et al., 2006) have high isoelectric point (IEP~9.5), it is suitable for immobilization of low isoelectric point enzymes such as glucose oxidase (GOx) or (IEP~4.2), cholesterol oxidase etc. The positively charged ZnO nanorods matrix not only provides a friendly microenvironment for immobilization of negatively charged GOx and retain its bioactivity, but also promotes electron transfer between GOx and the electrode to a large extent. Ansari et al., (2008) have immobilized GOx and cholesterol on sol-gel derived nanostructured CeO_2 film deposited on indium-tin-oxide (ITO) glass plate for fabrication of glucose and cholesterol biosensors, respectively. Topoglidis et al.,(2000) firstly employed titanium nanoparticles for successfully immobilization of horseradish peroxidase to construct the H_2O_2 biosensor. Several investigators have studied the influence of nanoparticle size on the performance of the prepared biosensors and nanoparticles with smaller size were found to be more suitable for enzyme immobilization. Many similar studies have been reported for the construction of biosensors based on the immobilization of different enzymes with nanostructured metal oxides, such as glucose oxidase, cholesterol oxidase, urease, HRP, myoglobin, hemoglobin, cytochrome C, and tyrosinase etc. Other nanostructured metal oxides, such as CeO_2, SnO_2, Fe_3O_4, MnO_2, Pr_6O_{11}, Sb_2O_3, TiO_2, ZnO and ZrO_2 nanoparticles have been used for the immobilization of enzymes for sensitive bioelectronic device development.

Electrical contacting of redox-enzymes with electrodes is a key process in the construction of third-generation enzyme electrodes. While enzymes usually lack direct electrical communication with electrodes due to the fact that the active centers of enzymes are surrounded by considerably thick insulating protein shells, and the electron transfer between electrodes and the active centers are blocked, the electro-catalytic properties of nanoparticles, mostly metal oxide nanoparticles at nanoscale dimensions made them suitable for enhancing the electron transfer between the active centers of enzymes and electrodes acting as electron transfer "mediators" or "electrical wires". The conductance of metal oxides nanoparticles depend on their crystalline structure. It has been reported that the conductances of nanowires, nanotubes, nanoribbons, nanorods and nanofibers was superior in respect to other morphological nanomaterials. Due to the high electrical conductivity of the resulting dimension nanostructured metal oxides, these materials constructed sensors amplify the signal-to-noise ratio and the sensitivity by more than one order of magnitude compared to that observed at bulk materials electrodes. This improved analytic performance was due to both factors, such as the high enzyme loading and a better electrical communication ability of the nano-morphological structure and the active center of the biomolecules. This is known as the direct electron transfer ability of nanowires, nanotubes, nanorodes and nanofibers demonstrated that both flavin adenine dinucleotide(FAD) and glucose oxidase (GOx) were found to spontaneously adsorb (physical adsorption) to metal oxides nanoparticles (deposited on the conducting glass

electrodes by different casting process) and to display quasi-reversible one electron transfer reaction.

Several electroanalytical techniques such as cyclic voltammetry, pulse and square-wave voltammetry and electrochemical impedance spectroscopy have been employed to analyze the electron transport phenomena such as charge transfer, diffusional mass transport, adsorption, chemisorption, chemical reaction, and convection. Electroanalytical techniques can provide information on chemical, biochemical, and physical systems, which can supplement spectroscopic characterization and perhaps theoretical calculations. Since last decade, it was interesting to find that direct electron transfer of some redox proteins can also take place with the help of metal oxides nanoparticles without need for additional mediators. Modification of electrode surfaces with nanoparticles provides a microenvironment similar to that of the redox proteins in native systems and gives the protein molecules more freedom in orientation, thereby reducing the insulating effect of the protein shell for direct electron transfer through the conducting tunnels of metal oxide nanoparticles.

4. Performance of nanostructured metal oxide based enzymatic electrochemical biosensors

Because of novel electrocatalytic behavior of nanostructured metal oxide, which combines characteristics of electrochemistry (e.g., simplicity, fast, high sensitivity & selectivity and low detection limit). Metal oxide nanoparticles exhibit higher ratios of surface area to volume than their bulk counterparts, so metal oxide nanoparticle modified electrochemical interfaces will provide larger electrochemically active areas and therefore probably lead to higher detection sensitivity for target molecules. Some novel nanoparticles, particularly manganese oxide (MnO_2) nanoparticles, can easily act as enhancing agents for effective acceleration of electron transfer between electrode and detection molecules, so leading to more rapid current response for target molecules. Superparamagnetic iron oxide nanoparticles act as a supramolecular assembling unit with advanced functional properties for constructing a variety of architectures on the surface of electrodes and further tailoring of an electrochemical-sensing interface. These metal oxide nanoparticles conjugate with some important biomolecules (e.g., redox enzyme) and act as nano-connectors that activate redox enzymes or electrical labels for biorecognition events. Furthermore, metal oxide nanoparticles modified electrochemical interfaces behave as nanoelectrode ensembles; in principle, the electroanalytical limit of detection at a nanoelectrode ensemble can be much lower than that at an analogous macrosized electrode because, there is a bigger ratio between Faradaic and capacitive currents. Inspired by the important features of nanostructured metal oxide has been in full flourish recently and a great deal of literature has reported that metal oxide-modified interfaces have enhanced electrochemical signaling. Nanostructured metal oxide based enzymatic biosensors have excellent prospects for interfacing biological recognition events with electronic signal transduction so as to design a new generation of bioelectronic devices with high sensitivity. Indeed, there has been substantial progress in the past decade on enzymatic electrochemical biosensors. In this article, we have collected the recent research activities on nanostructured metal oxide based enzymatic electrochemical biosensors.

4.1 Glucose biosensors

For determination of glucose, the reaction with glucose oxidase (GOX) enzyme electrode is shown with the following equations:

$$\beta\text{-glucose} + O_2 \rightarrow \beta\text{-gluconic acid} + H_2O_2 \quad (1)$$

$$H_2O_2 \rightarrow O_2 + 2H+ + 2e^- \quad (2)$$

The amount of H_2O_2 produced in equation (1) is usually determined by amperometric method by oxidation at the working electrode according to equation (2). This is referred as an amperometric biosensor. Equation (2) shows that protons are produced in the follow-up oxidation reaction. The production amount of H_2O_2 is usually detected by measuring the current during the oxidation reaction in equation (2). GOx carried a negative charge normally immobilized by physically onto nanostructured metal oxide films fabricated by solution based chemistry or physical methods. These metal oxides with nanostructure could provide large surface to volume ratio and increased surface activity, making their unique advantages over other conventional materials for enzym immobilization and signal transduction. They could keep activity of enzyme due to the desirable microenvironment and enhance the direct electron transfer between the enzyme's active sites and the electrode. It has been reported that the glucose biosensor based on nanostructured metal oxides has a high sensitivity, selectivity and fast response with low detection limit for hydrogen peroxide as compared to the other conventional materials, as discussed in the following reports. Kumar et al., (2008) have collected the applications of nanostructured ZnO for construction of electrochemical glucose biosensors, which are successfully applied in the development of a new glucose sensing platform for electrochemical glucose detection. As discussed earlier, nanostructured metal oxide platform possess several unique advantages such as high specific surface area, nontoxicity, chemical stability, electrocatalytic activity, and high electron communication features. The large specific surface energy and high electron communication features of the nanosized ZnO enhanced the electrochemical sensitivity of biomolecular reaction and rapid response with low detection limit. Nanosize metal oxide enhanced electrochemical sensitivity is based on the discovery that immobilized metal membranes either as a continuous film, particles, colloid or monolayer significantly amplifies the electrochemical signals following molecular recognition at enzyme electrodes. Wang and his co-workers (2006) synthesized ZnO nanocomb by vapor phase transport method to immobilization of GOx for sensitive detection of glucose. The electron transfer pathways between immobilized enzyme (GOx) molecules which are integrated with nanocomb ZnO. They suggetsted that, electrons are directly transferring from electrode to redox enzyme *via* nanosized ZnO nanocomb. The nanozied nanocomb provides a channel to communicate the electrons from enzyme to electrode surface. To understand of these pathways are very important to construct the nanostructured metal oxide based electrochemical enzymatic biosensors. The developed ZnO nanocomb glucose biosensor shows high sensitivity (15.33 $\mu A/cm_2$ mM) for glucose detection and high affinity of GOx to glucose (the apparent Michaelis-Menten constant Km^{app} = 2.19 mM) with low detection limit measured upto 0.02 mM. In another report, Wei et al., (2006) grows ZnO nanorods on standard gold electrode for use as an electrochemical biosensing interface at low potential

(+0.8V). Electrochemical characterization of the ZnO nanorod-GOx-modified system retains its bioactivity and can specifically catalyze the oxidation of glucose. Interestingly, it was found that the ZnO nanorods have high affinity with enzyme (GOx, the apparent Michaelis-Menten constant *Km* = 2.9 mM) for higher loading of enzyme. This biosensor was highly reproducible sensitive (23.1 μA cm^{-2} mM^{-1}), selective and shows rapid response (5 s) toward glucose with a linear range covered from 0.01 to 3.45 mM of glucose and an experiment limit of detection of 0.01 mM. Zang et al., (2007) have immobilized GOx by physically and chemically onto ZnO nanowires for construction of high performance glucose sensor. The extended bioaffinity of enzyme with ZnO nanowires could be achieved by selecting the right metal oxide film thickness on the electrode surface, because in the presence of a thicker metallic layer, a diffusion barrier toward the glucose oxidation was observed. This effect produces the ease bioaffinity of glucose for the low loading of enzyme and avoiding the high detection limit of analyte. Moreover, this glucose sensor showed long term stability with the incorporation of the inorganic zinc oxide nanowire. Zhao et al., (2007) proposed new strategy for co-adsoprtion of GOx onto porous Co doped ZnO nanoclusters with an averaged particle size of 5 nm to construct a novel amperometric glucose sensing. Electrochemical characterization of the developed ZnO-based nanoclusters electrode shows nanoporous network structure, making them differ from undoped ZnO nanostructures and other low dimensional nanostructures. ZnO:Co nanoclusters-GOx system exhibited high electrocatalytic activity to impart high sensitivity(13.3 μA/mA cm^2), selectivity and low detection limit (20 μM).

Based on these electrocatalytic properties of the metal oxides, Li et al., (2001) applied porous nanocrystalline TiO_2 for immobilization of GOx to electrochemically detection of glucose. Transmission electron microscopy, Infrared and Raman spectroscopy were employed to analyze the morphology of the material and interaction of the enzyme with nanocrystalline TiO_2. The resulting biosensor shows rapid, stable and linear response in the concentration range of 0±3mM with apparent Michaelis-Menten constant *Km* of 6.08 mM.

Umar et al., (2009) synthesized flower-shaped copper oxide nanostructured by simple low-temperature hydrothermal process and used to fabricate highly sensitive amperometric glucose biosensor. They found the linear dynamic range from 0.01 to 10.0 mM with detection limit upto 1.37 μM. The proposed glucose sensor exhibits reproducible sensitivity (47.19 μAmM^{-1} cm^{-2}) and fast response time less than 5 s.

Ansari et al., (2008) have developed a simple, highly reproducible sensitive and selective method for electrochemical detection of glucose using by sol-gel derived nanostructured CeO_2 film deposited onto gold electrode surface. The fabricated biosensor show linear amperomatric response (50–400 mg/dL) with low detection limit (12.0 μM). Nanoporous sol-gel film provides higher loading and strong bioaffinity (*Km* = 13.55 μM) of the enzyme to enhance the detection limit as well as shelf-life (12 weeks) of the bioelectrode. In another approach (Saha et al., 2009), similar group has developed nanoporous CeO_2 film onto platinum electrode by pulse laser deposition method for immobilization of GOx to sensitive detection of glucose. Atomic force microscopy images were used to investigate the surface texture of the electrode surface before and after enzyme immobilization, which is porous in nature. The biosensor has linearity within the concentration range from 25–300 mg/dl.

In order to explore applications of nanosized metal oxides for construction of electrochemical biosensors Yang et al., (2004) employed ZrO_2/Chitosan nanoporous matrix

for adsorption of GOx to detect the glucose concentration. Electrochemical characterization demonstrated that chitosan membrane enhanced the adhesive ability to the electrode, which is increasing the enzyme affinity to the biometallic surface. The linearity of this biosensor was within the concentration range from 1.25×10^{-5} to 9.5×10^{-3}M. This novel biosensor exhibited quite high response sensitivity (0.028 μAmM^{-1}) and low detection limit (1.0×10^{-5}M) useful for potential applications. In order to overcome the insolubility of the nonconducting biopolymer chitosan Kim et al., (2006) had employed Nafion to improve the adhesive ability as well higher enzyme loading. This bioelectrode show better stability for enzyme immobilization and detect the glucose concentration within the range of 0.03-15.08 mM with a sensitivity of 3.40 μA/mM and the detection limit of 0.037 mM**.**

Ansari et al., (2009) prepared sol–gel derived nanostructured tin oxide film onto indium-tin-oxide (ITO) for glucose sensing. High bioaffinity of the enzyme (GOx) was observed to the sol-gel derived nanostructured tin oxide electrode which can be attributed to favorable conformation of GOx and higher GOx loading due to microenvironment of nanoporous sol–gel derived Nano-SnO_2 film. The proposed sensor was highly sensitive (2.687 $\mu Amg/dLcm^2$) and selective toward glucose sensing, which exhibits wide linearity concentration rage (10–300 mg/dL) and low detection limit (0.169 mg/dL).

Another strategy was proposed to employed nanomaterials for construction of enzymatic biosensors for rapid, selective and highly reproducible sensitive detection of glucose concentrations from serum samples. Chen et al., (2008) have coupled the MnO_2 nanoparticles with MWCNTs resulted in remarkable improvement of the electrocatalytic activity of the nanocomposite materials toward the electrode surface through synergistic effect. The proposed biosensor permits effective low potential amperometric detection. The biosensor exhibits excellent response performance to glucose with the linear range upto 28 mM with a sensitivity of 33.19 μAmM^{-1}. In addition, chitosan was introduced into the MnO_2 nanoparticles and electrochemically deposited on the electrod to immobilization of GOx for sensing glucose (Xu et al., 2004). Furthermore, the biosensor shows rapid response, high sensitivity, good reproducibility, long-term stability, and freedom of interference from other coexisting electroactive species.

Another approach in the electrochemical sensor field concerns the assembling of a sensing platform based on the magnetic loading of ferrocene modified $Fe_3O_4@SiO_2$ nanocomposite on electrode surface. The resulting magnetic nanocomposite brings new capabilities for electrochemical devices by combining the advantages of ferrocene and $Fe_3O_4@SiO_2$ nanocomposite provides an alternative way for loading ferrocene on electrodes. Electrochemical measurements Indicated that ferrocene incorporated electrod exhibited higher electrocatalytic activity toward the redox processes of H_2O_2. The response for glucose was improve because of the presence of ferrocene in the nanocomposite electrode, higher sensitivity and extended linear range of response from 1.0×10^{-5} to 4.0×10^{-3} M with a detection limit of 3.2 μM observed. Other glucose sensing applications of superparamagnetic iron oxide nanoparticles have been reported in literature (Wang et al., 2006), such biosensor based on carbon nanotube (CNT)/Fe_3O_4 dispersed into chitosan, successfully used to detect glucose (Qu et al., 2007). It has been found that, CNTs enhanced the electroactive surface area for higher enzyme loading. Another report this group proposed polyaniline coated CNT/Fe_3O_4 nanocomposite for glucose sensing (Liu et al., 2008). Due to the ability of carbon nanotubes to promote electron-transfer reactions, the high

conducting properties of polyaniline and the sensitivity of presented electrochemical glucose biosensors were remarkably improved. It was found that CNTs can promote the electroactive surface area and can accelerate the rate of electron transfer between the redox-active enzyme and the electrode.

A novel approach have introduced for glucose sensing by Salimi et al., (2007). They found the excellent electrochemical performance of electrochemically co-deposited nickel oxide nanoparticles and GOx onto the glassy carbon electrode surface. The resulting biosensor showed strong adsorption of GOx to the nickel nanoparticles (the apparent Michaelis–Menten constant of 2.7 mM), which improved the enzyme loading and detect the glucose concentration with wide concentration range from 30 μM to 5 mM. Nickel nanoparticles facilitating the direct electron transfer between the active site of enzymes and surface of the electrodes. The corresponding detection sensitivity was 446.2 nA/mM.

4.2 Cholesterol biosensors

Cholesterol oxidase (ChOx) is most commonly used enzyme in the construction of cholesterol biosensor. Cholesterol oxidase is a flavin-enzyme (flavin-adenine-dinucleotide) that produces hydrogen peroxide according to the reaction.

$$\text{Cholesterol} + O_2 \rightarrow \text{4-Cholesten-3-one} + H_2O_2 \quad (3)$$

The structure of cholesterol oxidase reveals deeply buried active sites occupied by water molecules in the absence of its substrate steroids. Cholesterol oxidase is industrially and commercially important for application in bioconversions for clinical determination of total or free serum cholesterol in the serum samples. More recently, cholesterol biosensor based on physically cholesterol oxidase onto metallic oxide nanoparticle have been applied to determine the cholesterol concentration from the serum samples some of them are summarized here. Singh et al., (2007) revealed the effective applications of nanoporous ZnO film fabricated by rf sputtering method on gold electrode for cholesterol detection. The biosensor showed excellent linear sensing response to cholesterol with in concentration range from 25–400 mg/dl. In another report nanostructured ZnO film deposited onto ITO electrode via sol-gel chemical rout represented reproducible, highly linear response in a wide concentration range (5–400 mg/dl) and fast response time (10 s) to cholesterol(Solanki et al., 2009). The high sensitivity (0.059 μA/mg dl^{-1} cm^{-2}) and moderate detection potential (+0.8 V) led to cholesterol low detection limit of 0.5 mg/dl. In another approach (Khan et al., 2008) these authors dispersed ZnO nanoparticles in chitosan matrix for film fabrication onto conducting electrode by selective immobilization of cholesterol oxidase to construct the cholesterol biosensor. ZnO-chitosan nanocomposite films deposited on ITO electrode surface were mechanically stable due to excellent film forming ability of chitosan. The resulting biocompatible nanocomposite of ZnO/chitosan has been applied as matrix to covalently immobilize cholesterol oxidase, considering that chitosan has abundant amino groups, exhibits excellent film-forming ability for the solubility in slightly acidic solution due to the protonation and insolubility in solution with pH above pKa 6.3. High sensitivity (1.41×10^{-4} $Amgdl^{-1}$) with a wide linear concentration range from 5-300 $mgdl^{-1}$ of cholesterol with a detection limit as 5mg dl^{-1} was achieved. This cholesterol biosensor can be used to estimate cholesterol in serum samples. An attractive electrochemical protocol for measuring cholesterol based on ZnO nanoparticles grow at low temperature has been proposed by Umar et al., (2009). The novelty of this work concerns the observed electro-catalytic activity

of the ZnO-ChOx based nanocomposite bioelectrode demonstrating the ultra sensitivity for cholesterol sensing at a low potential and at higher current values. These optimized nanocomposite electrodes showed significantly better performance than those obtainable from flower shaped ZnO nanostructured (used here for comparison) in terms of linear range of concentration (0.001–0.5 μM), low detection limit (0.00037μM), higher sensitivity (23.7 μA μM cm^{-2})) and response time of 5 s. Finally, an excellent amperomatric response was measured at low temperature synthesized ZnO nanoparticles bioelectrode might be due to synthesized procedure as well as particle size effect on the matrix performance.
Sol-gel derived nanostructured CeO_2 film had been applied to immobilization ChOx for cholesterol sensing. Electrochemical signal of cholesterol concentration was linear in a wide range from 10–400 mg/dL and high sensitivity 2.08 mA ($mgdL^{-1}$ cm^{-2}). A low value of Michaelis–Menten constant (*Km*) was achieved 2.08 mM indicates strong ChOx affinity to cholesterol and no interference was found in the presence of cholesterol (Ansari et al., 2008).
Chitosan as a biocompatible, nontoxic and nonconducting natural biopolymer applied in biosensor. Chitosan has strong adhesive ability to the substrate to improve the enzyme adsorption on the substrate surface. Tin oxide nanoparticles introduced into the chitosan matrix enhanced the electrocatalytic activity of the biopolymer for sensitive cholesterol detection. High linear response was measured over the concentration range of 10 – 400 mg/dL with low detection limit of 5 mg/dL. Good stability and reproducibile sensitivity (34.7 μA/mg dL^{-1} cm^{-2}) to cholesterol detection within response time 5 s (Ansari et al., 2009).
Kouassi et al.,(2005) have studied the activity of cholesterol oxidase immobilized on magnetic nanoparticles via carbodiimde chemistry. The enzyme activity was well preserved upon binding onto the nanoparticle when subjected to thermal and various pH conditions. Kinetic studies showed a significant improvement in magnetic nanoparticles bound cholesterol oxidase owing to the large surface area and high chemical and thermal stability of magnetic nanoparticles, which enhanced the electrocatalytic activity of the nanocomposite.

4.3 Hydrogen peroxide biosensors

Sensitive and accurate determination of a small quantity of H_2O_2 is of great importance, because H_2O_2 is not only a byproduct of several highly selective oxidases, but also an essential mediator in biology, medicine, industry, and many other fields. Different configurations for the design of the H_2O_2 biosensors have been reviewed. In fabrication of H_2O_2 biosensor, there are two major issues to realize the application of electrochemical technique. First, the key process is to retain the biologic activity of the redox protiens (HRP, myoglobin, hemoglobin, cytochrom C etc.) immobilized on the electrode surface in its native status. Another key factor is to electrically connect redox protiens with the electrode surface, which can provide a pathway of electron transfer between the redox center of protienes and the electrode surface. The simplest method is direct adsorption of native enzyme on the electrode surface for direct transferring of electron to the electrode. In order to fabricate sensitive and selective biosensor a variety of materials have been employed to modify the electrodes as a bridge of electron transfer between the redox center of enzymes and the electrode surface.
Some metal oxide nanoparticles have been extensively used in bioaffinity sensors for immobilized heme proteins to detect the H_2O_2. Because, nanometer size materials gives rise

to high reactivity and other beneficial physical properties (electrical, electrochemical, optical and magnetic). Furthermore, direct electron transfer ability of the nanosized metal oxide made them able to function as biomimic membrane material to fix and modify proteins. The direct electrochemical responses of heme-protien have been achieved on the nanostructured metal oxide film. Many proteins have been employed to construct the potential H_2O_2 biosensors, such as HRP, cytochrome c, myoglobin, and hemoglobin, are capable of reducing H_2O_2 electrocatalytically. (Zhu et al., 2007; Liu et al., 2005; Zhao et al., 2006; Lu et al., 2008; Duan et al., 2008; Xiang et al., 2009). The improved electro-catalytic ability of the microperoxidase/ZnO nanoparticles co-modified electrode was measured, which greatly promote the direct electron transfer between the protein and electrode. The fast electron transfer between them beneficial to developing more sensitive H_2O_2 biosensors. Zhao et al., (2006) have employed nanoporous ZnO film deposited on graphite electrode to measured the electrocatalytic response of NO_2^- and H_2O_2 by immobilization of myoglobin.The entrapped myoglobin realized fast direct electron transfer with the electrode and displayed an elegant catalytic activity toward the reduction of hydrogen peroxide, nitrite, and trichloroacetic acid. This mediator-free biosensor showed linear response within the concentration range from 1.0 $x10^{-5}$ to 1.8 x 10^{-4} mol L^{-1} and 4.8 x 10^{-6} to 2.0 x 10^{-4} mol L^{-1} and detection limit 4.0 x 10^{-6} mol L^{-1}, 2.0 x 10^{-6} mol L^{-1} for NO_2^- and H_2O_2, respectively. Liu et al., (2005) used hydroquinone as a mediator for covalent immobilization of HRP enzyme for sensing of H_2O_2. The linearity of this fabricated biosensor was achieved of1.0 $x10^{-5}$ to 1.8 x 10^{-3}M with a low detection limit 2.0 μM. Good reproducibility sensitivity and stability was found retained about 78% upto 40 days. An enhanced sensitivity and selectivity of the Nafion mixed flower like ZnO-gold nanocomposite was measured, due to negatively charged gold nanoparticles provides a tunnel to transfer the electron from surface to electrode. On the other hand Nafion is a proton-conductive and biocompatible perfluorosulfonate linear polymer that exhibits excellent film-forming ability, which improves the proteins loading as well as communication of the electron on the matrix. Therefore, the immobilized protein on the substrate represented strong affinity (the apparent Michaelis–Menten constant K_m =1.76mM). The biosensor have linear response in a wide concentration rang 1.5×10^{-5} to 1.1×10^{-3} M and detection limit is 9.0×10^{-6}M (Xiang et al., 2009). Lu et al., (2008) have developed porous nanosheet-based ZnO microspheres for the construction of direct electrochemical H_2O_2 biosensor. In this context, porous ZnO nanosheet permit a direct electron transfer between redox proteins and bulk electrode materials, allowing electrochemical sensing to be performed without using electron-transfer mediator. ZnO nanosheet efficiently improved the electron transfer rate between the analyte and the electrode surface with an apparent Michaelis-Menten constant (K_m) of 143 μM for the peroxide sensing. The developed biosensor displayed good performance for the detection of H_2O_2 and $NaNO_2$ with a wide linear range of 1–410 and 10–2700 μM, respectively. Duan et al., (2008) prepared complex film containing of hemoglobin, nano ZnO, chitosan and nano Au to immobilized onto glassy carbon electrode for H_2O_2 sensing. Chitosan improved the film forming ability to the substrate and presence of gold nanoparticles enhanced electrocatalytic performance such as reproducible high sensitivity, linearity (1.94 x 10^{-7} - 1.73 x 10^{-3} mol L^{-1}) and detection limit (9.7x 10^{-8} mol L^{-1}) of the fabricated bioelectrode.

To fabricate a highly reproducible sensitive and selective biosensor based on direct electron transfer from enzymes to the electrode surface. Recently, research activities have been directed toward combining the advantageous feature of sol-gel derived nanostructured TiO_2

film and the glassy carbon electrode fabrication. So-gel network is helpful to retain the biological activity on the matrix. These matrixes preserve the native stabilities and reactivities of biological macromolecules for sensing. Amperomatric biosensor provid a wide linear calibration range from 4.0×10^{-6} M to 1.0×10^{-3} M, with a detection limit of 8.0×10^{-7} M (Xu et al., 2002; Yu & Ju et al., 2002). A similar strategy has been followed by Yu and Ju (2002) to immobilize HRP onto sol-gel modified porous titania matrix. Sol-gel network provide long term stability of enzyme in storage and showed strong bioaffinity to the substrate (Km = 1.89 ± 0.21 mM). The biosensor provided a wide linear calibration range (0.08 to 0.56 mM) with a detection limit of 1.5 μM and high sensitivity (61.5 μAmM^{-1}) for monitoring of H_2O_2. The biosensor retained 80% of its original activity after two months of operation. The developed sol-gel TiO_2 films represent good sensitivity and long term stability for enzymes immobilization, owing to its high surface area for enzyme loading and good biocompatibility. Some investigators have been fabricated titania nanoparticles to immobilize heme protein for H_2O_2 detection (Kumar et al., 2008; Zhao et al., 2008; Lo et al., 2008; Curulli et al., 2007). They suggested that the nanoparticles promote the electron transfer rate efficiently from enzyme to the electrode surface. Titania nanotubes exhibited superior biosensing capabilities towards H_2O_2. Owing to their large surface area, titania nanotubes provides friendly microenvironment for enzyme loading and improve the stability of the entrapped enzymes (the apparent Michaelis-Menten constant Km = 140 μM). Heme proteins (myoglobin) in these films facilitated relatively faster electron transfer (k_{ET} = 86 ± 7 s^{-1}) and catalytic activity than that between myoglobin in the solution and bare electrodes ((Liu et al., 2005). Most studies reported (Topoglidis et al., 2000) in literature are based on immobilization of protein which were focused on layered or mesopore structured materials due to their higher specific surface area. They found that titania nanotubes based biosensor exhibited high sensitivity to H_2O_2 and low detection limit (0.6 μM). Xiao et al., (2007) have analyzed the electrocatalytic ability of HRP-TiO_2 nanotube arrays, they possessed appreciably different sensitivities to H_2O_2 due to their different conductivity. They suggested that TiO_2 nanotube arrays demonstrated the best sensitivity for H_2O_2 in the range of 10^{-5}–$3x10^{-3}$ M at pH 6.7 and at a potential of -600 mV. Titania nanotubes containing thionine were electrochemically deposited on Ti substrate to immobilization of HRP for H_2O_2 sensing. The constructed biosensor has linear response to the H_2O_2 concentration from $1.1x\ 10^{-5}$ to $1.1\ x\ 10^{-3}$ M and detection limit was optimized as $1.2\ x\ 10^{-6}$ M (Liu et al., 2005). The sensor was fabricated by electrochemical deposition of nanotubular TiO_2 and platinum nanoparticles at very low potential (+ 0.3 V) for amperomatrically detection of H_2O_2. They found amperomatric signals were linear that is proportional to hydrogen peroxide concentration in the range $4\ x\ 10^{-6}$ to $1.25\ x\ 10^{-3}$ M and detection limit of the sensor was 4.0 μM (Cui et al., 2008). Zhang et al., (2004) have presented that TiO_2 nanoparticles exhibited better biosensing capabilities towards H_2O_2. The sensor was fabricated by casting the mixture of HRP solution and aqueous titanium oxide nanoparticles dispersed onto pyrolytic graphite electrode. They found that the constructed biosensor presented a better amperomatric response at 0 V with a larger sensitivity and a wider linear range. Viticoli and his co-workers (2006) have developed third-generation biosensors based on TiO_2 nano-structured films. They found that, functionalised TiO_2 thin films deposited on Si substrates exhibited high sensitivity, low detection limit (~10^{-6} M) and fast response time to H_2O_2.

Liu et al., (2003) have reported amperomatric biosensor based on sol-gel derived nanoporous ZrO_2 for H_2O_2 sensing. The resulting biosensor exhibited high sensitivity (111 μAmM^{-1}) for H_2O_2 over a wide concentration range from 2.5×10^{-7} to 1.5×10^{-4} mol l^{-1}, fast

response (10 s). This biosensor was stabile over 3 months. Liu et al., (2004) measured the direct electrochemistry and thermal stability of hemoglobin immobilized onto nanometer-sized ZrO_2 modified pyrolytic graphite electrode. They suggested that nanometer-sized ZrO_2 and dimethyl sulfoxide accelerate the electron transfer rate between hemoglobin and the electrode. The modified electrode showed a high thermal stability up to 74°C. The response was linear for H_2O_2 over the concentration ranging from 1.5 to 30.2 μM with a detection limit of 0.14 μM. Zong et al., (2007) reported reagent less biosensor based on hemoglobin modified zirconia nanoparticles for H_2O_2 detection. They examined the enzymatic activity with the zirconia nanoparticles that is strongly co-adsorbed to the surface nanoparticles and showed an excellent electrocatalytic activity to the reduction of H_2O_2. They found fast electron transfer (electron transfer rate constant = 6.46 s^{-1}) between the surfaces adsorbed enzyme (hemoglobin) and electrode. A wide linear concentration range for H_2O_2 was achieved 0.8 to 132 μM and low detection limit 0.12 μM. This research group proposed another strategy for H_2O_2 sensing by co-adsorption of myoglobin on zirconia nanoparticles enhanced grafted collagen hybrid composite (Zong et al., 2007). Grafted collagen provided a good matrix for protein immobilization and biosensing preparation. This method was useful for monitoring H_2O_2 in practical samples with the satisfactory results. They examined that ZrO_2- grafted collagen matrix accelerate the electron transfer between Mb and the electrode with a surface-controlled process and an electron transfer rate constant of 3.58±0.35 s^{-1} at 10–500mVs^{-1}. The linearity of the biosensor to H_2O_2 concentration was from 1.0 to 85.0 μMwith the limit of detection of 0.63 μM. Tong et al., (2007) applied HRP-ZrO_2 nanocomposite deposited by electrochemical method on gold electrode for fabrication of sensitive electrochemical biosensor. Under optimized conditions such as pH and potential, biosensor exhibited linear amperomatric response for H_2O_2 in a wide concentration range from 0.02 - 9.45mM with a detection limit of 2 μM. In another approach HRP was covalently immobilized on DNA/electrodeposited ZrO_2/modified, gold electrode. They suggetsted that sandwich DNA provides a microenvironment for the immobilization of enzyme or protiens and promotes electron transfer between HRP and the electrode surface. The resulting biosensor (HRP–ZrO_2/Au electrode) showed a linear response to H_2O_2 over a concentration range from 3.5 μM -10 mM with a detection limit 0.8 μM. The optimized bioelectrode represent excellent electrochemical performance such as sensitivity, reproducibility and response time for sensitive and selective detection of H_2O_2 in clinical samples (Tong et al., 2007).

Magnetic nanoparticles are promising materials in fabrication of biosensors and bioreactors. Among magnetic nanoparticles, Fe_3O_4 nanoparticles are the most commonly used magnetic materials because of their good biocompatibility, strong superparamagnetic property, low toxicity and easy preparation. Iron oxide nanocomposites matrices have applied for covalent immobilization of heme proteins for sensitive biosensor device development. The sensitivity of the fabricated biosensors depends on the proteins immobilization procedure on the conducting electrode. Several immobilization procedures have been used for the enzyme immobilization on the nanomaterials electrode surface, through them can examine the electron transfer features of bioelectrode (Cao et al., 2006; Cao et al., 2003; Zhao et al., 2006; Zhang et al., 2007). The direct immobilization of redox protein or enzyme without mediator onto nanomaterials electrode surface has an advantageous procedure among them due to sensitive and selective detection of analyte. Studies of direct electrochemistry of protein or enzymes at electrodes serve as a basis for building electrochemical biosensors, enzymatic

bioreactors, and biomedical devices. Cao et al., (2006) investigated the direct electrochemistry of heme protein immobilized on Fe_3O_4 nanoparticles for highly reproducible sensitive H_2O_2 sensing. This approach simplified such devices without using mediators and is of particular significance for fabrication the third generation biosensors. Direct electrochemical study can also establish a model for mechanistic studies of electron transfer between enzymes in biological systems. The direct electron transfer of haemoglobin by immobilizing it on Fe_3O_4 nanoparticle multilayer films was investigated (Zhao et al., 2006). The good sensitivity and long-term stability of the biosensor was measured indicating that the direct immobilization of heme proteins on Fe_3O_4 matrix is a promising substrate for hydrogen peroxide sensing. These films were constructed on several conductive bases (glassy carbon electrode, ITO glass, and Al foil) by first electrodeposition of chitosan/Fe_3O_4 thin films and then a layer-by-layer assembly using phytic acid and chitosan/Fe_3O_4. To enhance the sensitivity of the biosensor and minimize the problems of mediators, Zhao et al., (2005) fabricated a H_2O_2 biosensor based on Prussian blue modified magnetic nanoparticles. The synthesized nanoparticles catalyze the reduction of H_2O_2 without mediator. Crosslinked glutaraldehyde chemistry have used to covalent immobilization of hemoglobin onto carbon-coated iron nanoparticles for sensitive amperomatric hydrogen peroxide sensing. The resulting nanocomposite provides a shelter for the enzyme to retain its bioactivity under considerably extreme conditions, and the iron nanoparticles in the biocomposite offer excellent affinity to enzyme. The electrocatalytic response exhibited a linear dependence on H_2O_2 concentration in a wide range from 3.1 mM to 4.0 mM with a detection limit of 1.2 mM (Zhang et al., 2007). Hrbac et al., (2007) have reported amperomatrically H_2O_2 detection by adsorption of heme protein on iron oxide nanoparticles (hematite, maghemite, amorphous Fe_2O_3, β-Fe_2O_3 and ferrihydrite) deposited carbon past electrode. Prussian blue modified iron oxide nanopartilces based electrode exhibited excellent amperomatric response towards detection of hydrogen peroxide such as linearity (8.5 mM) and reproducible sensitivity, response time (<3 s) with detection limit was 2×10^{-5} M. HRP was immobilized on gold modified nanoporous silica based magnetic microparticles matrix for H_2O_2 sensing. The analytical performance of the resulting biosensor was characterized by electrochemical techniques. The resulting bioelectrode provided a linear response to H_2O_2 over a concentration range comprised between 5×10^{-7}-1.3×10^{-4} M with a detection limit of 4×10^{-7} M (Elyacoubia et al., 2006). Lin et al., (2005) have fabricated a CH-Fe_3O_4 nanocomposite modified glassy carbon electrode for determination of H_2O_2. The linearity range was obtained as 4-5 mM with detection limit 7.6 and 7.4 μmol/L and biosensor was stable up to 9 months.

Attempts have been made to applied sol-gel tin oxide matrix to heme proteins immobilization for rapid detection of H_2O_2 (Jia et al., 2005a&b; Topoglidis et al., 2003). Sol-gel derived bioelectrodes showed better analytical performance in respect to other conventional method prepared bioelectrodes, such as faster response, wider detection range, lower detection limit, better affinity, higher enzyme loading, simpler operation and better storage stability for electrochemical detection of hydrogen peroxide due to the introduction of the collagen to form well-distributed porous three-dimensional structure. The linear concentration range of the biosensor was from 0.01-0.25 mM. (Jia et al., 2005a). The smaller *Km* (the apparent Michaelis-Menten constant value *Km* = 0.345 mM) value was measured means that the immobilized HRP onto SnO_2 film possesses higher enzymatic activity, and exhibits higher affinity to H_2O_2. (Jia et al., 2005b)

Ansari et al., (2009) have applied nanostructured CeO_2 film deposited onto indium-tin-oxide (ITO) glass substrate by solution casting process to immobilization of HRP via physiosorption technique for H_2O_2 reduction. The designed biosensor exhibited acceptable stability (5 weeks), wide linearity range (1.0–170 μM) for H_2O_2 concentration, long-term shelf life and good reproducibility. A similar approach has been used to fabricate an amperometric hydrogen peroxide biosensor based on electrochemically deposited PANI/CeO_2 nanocomposite films onto ITO electrode (Ansari et al., 2009). Polyaniline is used to modify the electrocatalytic activity of the CeO_2. Polyaniline CeO_2 nanoparticles served as a linker for rapid detection of H_2O_2. This property results in an electrocatalytic activity of the immobilized HRP to the reduction of H_2O_2, used for preparation of H_2O_2 sensors. The proposed biosensor showed excellent performance for H_2O_2 sensing such as sensitivity (159.6 nA/mM), detection limit (50 mM), long time stability (8 weeks) and fast response time.

MnO_2 nanoparticles and dihexadecyl hydrogen phosphate composite film have been used as an enzyme (HRP) immobilization matrix with enhanced activity and stability (Yao et al., 2006). Manganese dioxide (MnO_2) nanoparticles have been proved to be a catalytic substance to promote the decomposition of H_2O_2 to O_2. The MnO_2nanoparticles can retain the bioactivity of proteins to a large extent and accelerate the electron transfer between proteins and electrodes. The biosensor was optimized under optimal conditions which showed high sensitivity ($2.66\times105\ \mu AM^{-1}cm^{-2}$) wide linear concentration range of 1.2×10^{-7}–2.0×10^{-3} M with a substantially low detection limit of 8.0×10^{-8} M.

Antimony oxide bromide (AOB) nanorods dispersed in chitosan have been applied for H_2O_2 biosensor (Lu et al., 2006). Chitosan is a biopolymer has an excellent film-forming ability and biocompatibility. The solubility of antimony oxide bromide nanorods in these biopolymers facilitates the construction of electrochemical biosensing platform. AOB nanorods mixed with chitosan were placed on the surface of a glassy carbon electrode results in a robust AOB-chitosan film, which facilitates the electrooxidation of NADH. The fabricated biosensor has a linear response from 1–121 μM with a correlation coefficient of 0.993. They found the bioelectrode displayed good sensitivity ($1.44mAcm^{-2}M^{-1}$) and reproducibility, wide linear range, low detection limit, fast response and excellent long-term stability.

4.4 Urea biosensor

Zinc oxide nanoparticles have been introduced into the chitosan solution to immobilization of urease enzyme for urea sensing. Chitosan film containing ZnO have been deposited onto ITO electrode for covalent immobilization of urease. The possibility to combine both properties, such as the higher surface area and electrocatalytic effect exhibited from ZnO, with the surface adhesive properties of chitosan can be used to manipulate and control the analytic signal in the presence of a specific substrate. The marked electrocatalytic activity toward urea permits effective low-potential amperometric biosensing. The optimum configuration for biosensors has allowed highly sensitive ($0.13\ \mu A/mM\ cm^{-2}$), fast response time (10 s), and highly selective (0% interference of at glucose (5 mM), ascorbic acid (0.05 mM), uric acid (0.1 mM), cholesterol (5 mM), and lactic acid (5 mM) at maximum physiological levels) analytes quantification with lower detection limit (3 mg/dl), higher reproducibility and long shelf life upto 3 month (Pratima et al., 2009). Hubalek et al., (2007)

have developed nickel nanoelectrode to determined the urease by electrochemical and votammetry methods. Ansari el al. (2009) prepared sol-gel-derived titanium oxide–cerium oxide (TiO_2–CeO_2) nanocomposite film deposited onto ITO-coated glass substrate for urea sensing. A biosensor was fabricated by casting the mixture of enzymes (urease and glutamate dehydrogenase) on nanobiocomposite for determination of urea concentration. The performance of the sensor showed sensitive determination of urea with a linear range from10–700 mg/dL, response time of 10 s, sensitivity as 0.9165 $\mu Acm^{-2}mM^{-1}$, detection limit of 0.166 mM with negligible interference from physiological levels of uric acid, cholesterol, glucose, and ascorbic acid **(**Ansari et al., 2009). Recently, Zhang et al., (2004) reported the use of uricase immobilized ZnO nanorods dispersed into Nafion placed onto glassy carbon electrodes (GCE) as a new platform for developing enzymatic biosensors. They found that, ZnO nanorods derived electrode retained the enzyme bioactivity and enhance the electron transfer between the enzyme and the electrode. In the presence of an electron mediator electrode showed high affinity (*Km* = 0.238 mM) to the electrode and excellent electrocatalytic response such as linearity dependence on the uric acid concentration ranging from 5.0×10^{-6} to 1.0×10^{-3} mol L^{-1} with a detection limit of 2.0×10^{-6} mol L^{-1}. Functionalized multiwalled carbon nanotubes (MWCNTs) mixed with tin oxide has applied for the fabrication of reagentless amperomatric uric acid biosensor. MWCNTs have used as an electron promoter which efficiently enhanced the electron transfer rate between the enzyme and electrode surface. This biosensor exhibited a linear dependence on the uric acid concentration over the range from 1.0 x 10^{-7} to 5.0 x 10^{-4} mol L^{-1} with little ascorbic acid interference in physiological level (Zhang et al., 2005). In a novel strategy based on titanate nanotubes have developed by Liu et al., (2006) for measuring the biosensing properties amperomatrically. Titania nanotubes have deposited onto glassy carbon electrode for selective detection of dopamine in the presence of ascorbic acid and uric acid. The linear calibration curve for dopamine was observed over the concentration range 0.1–30 lM in a physiological solution that contains 0.1 mM AA and 0.3 mM uric acid.

4.5 Choline biosensor

Choline is also an important component of phospholipids (lecithin and sphingomyelin), which is required for the synthesis of the neurotransmitter acetylcholine precursor. Choline found in central and peripheral nervous systems of mammals. Therefor, direct monitoring of choline from the serum samples by enzyme-based biosensors have emerged as most promising field. A number of enzyme electrodes, with immobilized ChOx, were reported for choline determination based on the detection of liberated H_2O_2. Amperometric biosensors based on the immobilization of bi-enzymes HRP and ChOx for the determination of choline were also reported. In the single enzyme system as following Eq.,

$$\text{choline} + O_2 \rightarrow \text{betaine aldehyde} + H_2O_2 \quad (4)$$

In the presence of oxygen, choline is converted by ChOx, producing H_2O_2. Then H_2O_2 can be subsequently detected with the help of conducting materials electrodes. Bai et al., (2007) have used MnO_2 nanoparticles based electrod for sensitive determination of choline concentration. MnO_2 nanoparticles modified electrode in the presence of H_2O_2 exhibited bi-direction electrocatalytic ability toward the reduction/oxidation of H_2O_2. The amperomatric signal was linear of choline chloride in the concentration range 1.0 x 10^{-5} – 2.1 x 10^{-3} M and

no obvious interference from ascorbic acid and uric acid was observed in physiological level (Bai et al., 2007). Similar nanocomposite material–based on electrochemical H_2O_2/choline biosensors have been developed by modifying a glassy carbon electrode with chitosan and three different dimensionality (amorphous MnO_2 nanoparticles, α-MnO_2 nanoparticles, and β-MnO_2 nanowires)/GCE film **(**Bai et al., 2008**)**. They found the biocatalytic activity of the three different nanostructures for the determination of choline amperomatrically in the following order: amorphous MnO_2 > α-MnO_2 > β-MnO_2. Due to the different specific surface areas of the nanomaterials, the amount of enzyme entrapped on MnO_2 electrode surface is different that is depend on crystalline structures, and dimensionality of the materials. Therefor, the biosensors based on α-MnO_2 nanoparticles and β-MnO_2 nanowires represent excellent electrochemical response for amperometric detections of choline chloride in the linear ranges of 2.0×10^{-6}-5.8×10^{-4} M and 1.0×10^{-6}-7.9×10^{-4} M with the detection limits of 1.0 and 0.3 μM, respectively. For sensitive determination of choline and acetylcholine, bovine serum albumin and choline oxidase co-adsorbed electropolymerized poly (*N*-acetylaniline) film/sol–gel ZnO membrane prepared onto Pt electrode. They suggested that BSA improved the stability and activity of the enzymes on sol-gel derived electrode. The resulting biosensors at an applied potential of +0.6V exhibited fast response, expanded linear response in the concentration range of 1.0×10^{-6} to 1.5×10^{-3}M to acetylcholine with a detection limit of 6.0×10^{-7} M and a linear response range up to 1.6×10^{-3} M to choline with a detection limit of 5.0×10^{-7} M (Yang et al., 2005**)**.

4.6 Phenol biosensors

Phenolic compounds are very toxic, showing adverse effects on animal and plants which are often exist in the wastewaters of many industries. Therefore, the identification and quantification of such compounds are very important for environment monitoring. Li et al., have developed phenolic biosensor based on ZnO nanoparticles. ZnO nanoparticles dispersed chitosan nanocomposite provid an advantageous microenvironment in terms of its favorable isoelectric point for tyrosinase loading and the immobilization of tyrosinase enzyme. They suggested that nanocomposite electrode retained its activity to a large extent and facilitated the electron communication on the electrode surface at a large extent.The resulting biosensor has 95% of steady-state current within 10 s, and the sensitivity was 182 μA $mmol^{-1}L$. The linear range for phenol was determined from 1.5 x 10^{-7} to 6.5 x 10^{-5} mol L^{-1} with a detection limit of 5.0 x 10^{-8} mol L^{-1}**(**Li et al.,). Another approach mediator free sol-gel derived ZnO matrix has used for phenol sensing. The performance of the developed biosensor was such as linearity (1.5 x 10^{-7} to 4.0 x 10^{-5} mol L^{-1}), sensitivity (168 μAmmol L^{-1}), detection limit (8.0 x 10^{-8} mol L^{-1}) fast response time long term stability (2 weeks) (Liu et al., 2005**)**. Zhang et al., (2003) have applied hybrid sol-gel titania matrix for the construction of sensitive mediator free tyrosinase biosensor. Under optimum pH titania retained the tyrosinase activity and stability attached on to the surface of a glassy carbon electrode. The reproducible high sensitivity $15.78\mu A\mu M^{-1}cm^{-2}$ and low detection limit 1×10^{-8} M was achieved for monitoring phenols.

To determination of pesticides in vegetable samples Yang et al., (2005) have proposed an acetylcholinesterase biosensor based on nanoparticles ZrO_2/chitosan. Acetylcholinesterase was covalently immobilized onto ZrO_2/chitosan nanocomposite matrix. The experimental conditions were optimized showed that pesticides inhibit the activity of enzyme with an effect of decreasing of oxidation current. The linear response was achieved from 9.90 x 10^{-6}

to 2.03 x 10^{-3} M, 6.6 x 10^{-6} to 4.4 x 10^{-4} M, 1.0 x 10^{-8} to 5.9 x 10^{-7} M and 8.6 x 10^{-6} to 5.2 x 10^{-4} M acetylcholinesterase, phoxim, malathion and dimethoate, respectively with the detection limit of 1.3 x 10^{-6} M for phoxim. The proposed samples have used to determine pesticides in real vegetable samples.

A chitosan film containing MnO_2 nanoparticles was electrodeposited on glassy carbon electrode to covalent immobilization of lactate oxidase for the determination of lactate concentrations. Due to their excellent film-forming ability and strong adsorbability of enzyme on the nanocomposite electrode surface. They found linear response to lactate in the range of 0.020–4.0 mM, with reproducibile high sensitivity (3.98 μAcm^{-2} mM^{-1}) and long-term stability **(**Wang et al., 2006**)**.

Umar et al., (2009) have employed ZnO nanowires coated onto gold electrode for ultra-sensitive determination of hydrazine by amperometrically. The proposed biosensor has reproducible high sensitivity 12.76 μAcm^{-2} nM^{-1}, low detection limit, 84.7 nM, fast response time less than 5 s, good linear range from 500 - 1200nM with correlation coefficient of R = 0.9989.

Magnetic core–shell (Fe_3O_4–SiO_2) nanoparticles modified film onto the surface of carbon past electrode for covalently immobilization of Laccase enzyme, done by chemical cross-linking with glutaraldehyde and free aldehyde groups to determined the hydroquinone concentration. Magnetic core–shell nanoparticles provide microenvironment for retaining the bioactivity of laccase. The linear range for hydroquinone was determination as 1×10^{-7} to 1.375×10^{-4} M, with a detection limit of 1.5×10^{-8} M and 95% steady-state current was reached within 60 s (Zhang et al., 2007).

5. Conclusions

The unique electrocatalytic properties of the metal oxides and the ease of metal oxide nanostructured fabrication make them extremely interesting materials for electrochemical enzymatic biosensor applications. The application of nanostructured metal oxides in such sensing devices has taken off rapidly and will surely continue to expand. This article provides a review on current research status of electrochemical enzymatic biosensors based on various new types of nanostructured metal oxides such as nanotubes, nanorods, nanobelts, and nanowires. These nanostructured-based amperomatric biosensors represent a powerful detection platform for electrochemical enzymatic biosensors. It is a crucial requirement of consumers to design simple, affordable, reliable and portable electrochemical biosensors, which provides novel key features, including high sensitivity, selectivity, fast response, low detection limit, fast response with minimum intereferences from bulk species and could operate at low potential. Such electrochemical biosensors could be useful for diagnosing and monitoring infectious disease, monitoring the pharmokinetics of drugs, detecting cancer, and disease biomarkers, analyzing breath, urine and blood for drugs of abuse. It is only a matter of time before such protocols are used for routine diagnostic applications.

6. References

Ansari, A.A.; Kaushik, A.; Solanki, P.R.; Malhotra, B.D. (2008), Sol–gel derived nanoporous cerium oxide film for application to cholesterol biosensor. *Electrochem. Commun.* 10: 1246-1249.

Ansari, A.A.; Kaushik, A.; Solanki, P.R.; Malhotra, B.D. (2009), Electrochemical cholesterol sensor based on tin oxide-chitosan nanobiocomposite film. *Electroanalysis*, 21: 965-972.

Ansari, A.A.; Solanki, P.R.; Malhotra, B. D. (2009), Sol-gel derived nanostructured tin oxide film for glucose. *Sensor Letter* 7:64-71.

Ansari, A.A.; Solanki, P.R.; Malhotra, B.D. (2008), Sol-gel derived nanostructured cerium oxide film for glucose sensor.*Appl. Phys. Lett.* 92: 263901-3.

Ansari,A.A.; Sumana,G.; Khan R.; Malhotra, B.D.(2009), Polyaniline-cerium oxide nanocomposite for hydrogen peroxide sensor. *J.of Nanosc. and Nanotechnology* 9: 1–7.

Ansari,A.A.; Solanki,P.R.; Malhotra, B.D. (2009), Hydrogen peroxide sensor based on HRPimmobilized nanostructured cerium oxide film. *J. Biotechnology* 142:179–184

Ansari,A.A.; Sumana, G.; Pandey, M.K.; Malhotra, B.D. (2009), Sol-gel derived titanium oxide-cerium oxide biocompatible nanocomposite film for urea sensor; *J. Material Research* 24(5): 1667-1673.

Bai, Y.H.; Du, Y.; Xu, J.J.; Chen, H.Y. (2007), Choline biosensors based on a bi-electrocatalytic property of MnO_2 nanoparticles modified electrodes to H_2O_2. *Electrochem. Commun.*, 9: 2611–2616.

Bai, Y.H.; Zhang, H.; Xu, J.J.; Chen, H.Y. (2008), Relationship between nanostructure and electrochemical/biosensing properties of MnO_2 nanomaterials for H_2O_2/choline. *J. Phys. Chem. C* 112: 18984–18990.

Cao, D. F.; He, P.L.; Hu, N.F. (2003), Electrochemical biosensors utilising electron transfer in heme proteins immobilised on Fe_3O_4 nanoparticles.*Analyst* 128: 1268-1274.

Cao, D.; Hu, N. (2006), Direct electron transfer between hemoglobin and pyrolytic graphite electrodes enhanced by Fe_3O_4 nanoparticles in their layer-by-layer self-assembly films.*Biophys. Chem.*, 121: 209-217.

Chen, J.; Zhang, W.D.; Ye, J.S. (2008), Nonenzymatic electrochemical glucose sensor based on MnO_2/MWNTs nanocomposite. *Electrochem. Commun.* 10: 1268-1271.

Chopra, N.; Gavalas, V.G.; Bachas, L.G.; Hinds, B.J.; Bachas, L.G. (2007), Functional one-dimensional nanomaterials: applications in nanoscale biosensors. *Analytical Letters* 40(11): 2067-2096.

Chow, D.C.; Johannes, M.S.; Lee, W.K.; Clark, R.L.; Zauscher, S.; Chilkoti, A. (2005), Nanofabrication with biomolecules, *Materials Today*, 8: 30-39.

Cui, X.; Li, Z.; Yang, Y.; Zhang, W.; Wang, Q. (2008), Low-potential sensitive hydrogen peroxide detection based on nanotubular TiO_2 and platinum composite electrode. *Electroanalysis* 20: 970- 975.

Curulli, A.; Valentini, F.; Padeletti, G.; Viticoli, M.; Caschera, D.; Palleschi, G. (2005), Smart (Nano) materials: TiO_2 nanostructured films to modify electrodes for assembling of new electrochemical probes. *Sens. and Actuat. B* 111–112: 441–449.

Duan, G.; Li, Y.; Wen, Y.; Ma, X.; Wang, Y.; Ji, J.; Wu, P.; Zhang, Z.; Yang, H. (2008), Direct electrochemistry and electrocatalysis of hemoglobin/ZnO-chitosan/nano-Au modified glassy carbon electrode. *Electroanal.* 20(22):2454- 2459

Elyacoubia, A.; Zayeda, S.I.M.; Blankert, B.; Kauffmann, J.M. (2006), Development of an amperometric enzymatic biosensor based on gold modified magnetic nanoporous microparticles. *Electroanalysis* 18(4): 345-350

Hrbac, J.; Halouzka, V.; Zboril, R.; Papadopoulos, K.; Triantis, T. (2007), Carbon electrodes modified by nanoscopic iron(III) oxides to assemble chemical sensors for the hydrogen peroxide amperometric detection. *Electroanalysis* 19(17): 1850-1854.

Hubalek, J.; Hradecky, J.; Adam, V.; Krystofova, O.; Huska, D.; Masarik, M.; Trnkova, L.; Horna, A.; Klosova, K.; Adamek, M.; Zehnalek, J.; Kizek, R. (2007), Spectrometric and voltammetric analysis of urease–nickel nanoelectrode as an electrochemical sensor. *Sensors*, 7: 1238-1255.

Jia, N.; Zhou, Q.; Liu, L.; Yan, M.; Jiang, Z. (2005), Direct electrochemistry and electrocatalysis of HRPimmobilized in sol–gel-derived tin oxide/gelatin composite films. *J. Electroanal. Chem*. 580: 213–221

Jia, N.-Q.; Xu, J.; Sun, M.-H.; Jiang, Z.-Y.(2005), A mediatorless hydrogen peroxide biosensor based on HRPimmobilized in tin oxide sol-gel film. *Anal. Lett*. 38(8):1237-1248.

Kerman, K.; Saito, M.; Yamamura, S.; Takamura, Y.; Tamiya, E. (2008), Nanomaterial-based electrochemical biosensors for medical applications. *Trends in Anal. Chem.*,27: 585-592.

Khan, R.; Kaushik, A.; Solanki, P. R.; Ansari, A. A.; Pandey, M. K.; Malhotra, B.D. (2008), Zinc oxide nanoparticles-chitosan composite film for cholesterol biosensor. *Anal. Chim. Acta* 616: 207-213.

Kim, H. J.; Yoon, S. H.; Choi, H. N.; Lyu, Y. K.; Lee, W. Y. (2006), Amperometric glucose biosensor based on sol-gel-derived zirconia/Nafion composite film as encapsulation matrix. *Bull. Korean Chem. Soc.* 27(1): 65-70.

Kouassi, G.K.; Irudayaraj, J.; McCarty, G. (2005), Examination of cholesterol oxidase attachment to magnetic nanoparticles. *J. of Nanobiotechnology*, 3(1):1-9.

Kumar, S.A.; Chen, S.M. (2008), Nanostructured zinc oxide particles in chemically modified electrodes for biosensor applications. *Anal. Lett.*, 41(2): 141-158.

Kumar, S.A.; Lo P.H.; Chen, S.M. (2008), Electrochemical synthesis and characterization of TiO_2 nanoparticles and their use as a platform for flavin adenine dinucleotide immobilization and efficient electrocatalysis. *Nanotechnology* 19:255501-7

Li, Q.; Luo, G.; Feng, J.; Zhou, Q.; Zhang, L.; Zhu, Y. (2001), Amperometric detection of glucose with glucose oxidase absorbed on porous nanocrystalline TiO_2 film. *Electroanalysis*, 13(5): 413-416.

Li, Y.F.; Liu, Z.M.; Liu, Y.L.; Yang, Y.H.; Shen, G.L.; Yu, R.Q. (2006), A mediator-free phenol biosensor based on immobilizing tyrosinase to ZnO nanoparticles. *Anal. Biochem.*, 349: 33–40.

Lin, M.S.; Leu, H.J. (2005), A Fe_3O_4-based chemical sensor for cathodic determination of hydrogen peroxide.*Electroanalysis*, 17(22): 2068-2073.

Liu S.; Chen, A. (2005), Coadsorption of HRPwith thionine on TiO_2 nanotubes for biosensing. *Langmuir* 21: 8409-8413.

Liu, A.; Wei, M.; Honma, I.; Zhou, H. (2005), Direct electrochemistry of myoglobin in titanate nanotubes film. *Anal. Chem*., 77:, 8068-8074

Liu, A.; Wei, M.; Honma, I.; Zhou, H. (2006), Biosensing properties of titanate-nanotube films: selective detection of dopamine in the presence of ascorbate and uric acid. *Adv. Funct. Mater*., 16: 371–376

Liu, B.; Cao, Y.; Chen, D.; Kong, J.; Deng, J. (2003), Amperometric biosensor based on a nanoporous ZrO_2 matrix. *Anal. Chim. Acta* 478: 59-66.

Liu, S.; Dai, Z.; Chen, H.; Ju, H.(2004), Immobilization of hemoglobin on zirconium dioxide nanoparticles for preparation of a novel hydrogen peroxide biosensor. *Biosens. Bioelectron.* 19: 963-969.

Liu, Y. L.; Yang, Y. H.; Yang, H. F.; Liu, Z. M.; Shen, G. L.; Yu, R. Q. (2005), Nanosized flower-like ZnO synthesized by a simple hydrothermal method and applied as matrix for horseradish peroxidase immobilization for electro-biosensing. *J. Inorg. Biochem.* 99: 2046-2053.

Liu, Z.; Liu, Y.; Yang, H.; Yang, Y.; Shen, G.; Yu, R. (2005), A mediator-free tyrosinase biosensor based on ZnO sol-gel matrix. *Electroanalysis*, 17(12):1065-1070

Liu, Z.; Wang, J.; Xie, D.; Chen, G. (2008), Polyaniline-coated Fe_3O_4 nanoparticle–carbon-nanotube composite and its application in electrochemical biosensing. *Small*, 4(4): 462–466.

Lo, P.H.; Kumar, S.A.; Chen, S.M. (2008), Amperometric determination of H_2O_2 at nano-TiO_2/DNA/thionin nanocomposite modified electrode. *Colloids and Surfaces B: Biointerf.* 66:266–273.

Lu, X.; Wen, Z.; Li, J.(2006), Hydroxyl-containing antimony oxide bromide nanorods combined with chitosan for biosensors. *Biomaterials* 27: 5740–5747

Lu, X.; Zhang, H.; Ni, Y.; Zhang, Q.; Chen, J. (2008),Porous nanosheet-based ZnO microspheres for the construction of direct electrochemical biosensors. *Biosensors and Bioelectronics* 24:93–98

Luo, X.; Morrin, A.; Killard, A.J.; Smyth, M.R. (2006), Application of nanoparticles in electrochemical sensors and biosensors, *Electroanalysis* 18: 319-326.

Qu, S.; Wang, J.; Kong, J.; Yang, P.; Chen, G. (2007),Magnetic loading of carbon nanotube/nano-Fe_3O_4 composite for electrochemical sensing.*Talanta* 71: 1096–1102

Saha, S.; Arya, S.K.; Singh, S.P.; Sreenivas, K.; Malhotra, B.D.; Gupta, V. (2009), Nanoporous cerium oxide thin film for glucose biosensor. *Biosensors and Bioelectronics* 24:2040–2045

Salimi, A.; Sharifi, E.; Noorbakhsh, A.; Soltanian, S. (2007), Immobilization of glucose oxidase on electrodeposited nickel oxide nanoparticles: Direct electron transfer and electrocatalytic activity. *Biosens. Bioelectron.* 22: 3146-3153.

Singh, S.P.; Arya, S.K.; Pandey, P.; Malhotra, B.D.; Saha, S.; Sreenivas, K.; Gupta, V. (2007), Cholesterol biosensor based on rf sputtered zinc oxide nanoporous thin film. *Appl. Phys. Lett.*, 91: 063901-3.

Solanki, P. R.; Kaushik, A.; Ansari, A. A.; Malhotra, B. D. (2009), Nanostructured zinc oxide platform for cholesterol sensor.*Appl. Phys. Lett.* 94, 163903-3.

Solanki,P.R.; Kaushik,A.; Ansari,A.A.; Malhotra, B.D. (2008), Zinc oxide-chitosan nanobiocomposite for urea sensor, *Appl. Phys. Lett.*, 93:163903-3

Tong, Z.; Yuan, R. ; Chai, Y.; Xie, Y.; Chen, S. (2007), A novel and simple biomolecules immobilization method: electro-deposition ZrO_2 doped with HRP for fabrication of hydrogen peroxide biosensor. *J. Biotechnology* 128: 567-575.

Tong, Z.; Yuan, R.; Chai, Y.; Chen, S.; Xie, Y. (2007), Direct electrochemistry of horseradish peroxidase immobilized on DNA/electrodeposited zirconium dioxide modified, gold disk electrode. *Biotechn. Lett.*, 29: 791-795.

Topoglidis, E.; Astuti, Y.; Duriaux, F.; Gratzel, M.; Durrant, J. R. (2003), Direct electrochemistry and nitric oxide interaction of heme proteins adsorbed on nanocrystalline tin oxide electrodes.*Langmuir*, 19: 6894-6900.

Topoglidis, E.; Lutz, T.; Willis, R.L.; Barnett, C.J.; Cass, A.E.G.; Durrant, J.R. (2000), Protein adsorption on nanoporous TiO2 films: a novel approach to studying photoinduced protein/electrode transfer reactions. *Faraday Discuss*., 116, 35-46

Umar, A.; Rahman, M.M., Al-Hajry, A.; Hahn, Y.B.; (2009), Enzymatic glucose biosensor based on flower-shaped copper oxide nanostructures composed of thin nanosheets. *Electrochem. Commun*. 11:278–281

Umar, A.; Rahman, M.M.; Hahn, Y.B.(2009),Ultra-sensitive hydrazine chemical sensor based on high-aspect-ratio ZnO nanowires. *Talanta* 77: 1376–1380.

Umar, A.; Rahman, M.M.; Vaseem, M.; Hahn, Y.B. (2009), Ultra-sensitive cholesterol biosensor based on low-temperature grown ZnO nanoparticles. *Electrochem. Commun.,* 11:118–121

Valentini, F.; Palleschi, G.(2008), Nanomaterials and analytical chemistry, *Analytical Letters*, 41: 479–520.

Viticoli, M.; Curulli, A.; Cusma, A.; Kaciulis, S.; Nunziante, S.; Pandolfi, L.; Valentini, F.; Padeletti, G. (2006), Third-generation biosensors based on TiO_2 nanostructured films. *Mater. Sci. Engin. C*, 26: 947-951.

Wang, J. (2005), Nanomaterial-based electrochemical biosensors. *Analyst*, 130: 421–426.

Wang, J. X.; Sun, X. W.; Wei, A.; Lei, Y.; Cai, X. P.; Li, C. M.; Dong, Z. L. (2006), Zinc oxide nanocomb biosensor for glucose detection. *Appl. Phys. Lett.*,88, 233106-3.

Wang, J.; Snchez, A. A. (2006), Biocatalytically induced formation of cupric ferrocyanide nanoparticles and their application for electrochemical and optical biosensing of glucose. *Small*, 2(1):129–134

Wang, K.; Xu, J.J.; Chen, H.Y. (2006), Biocomposite of cobalt phthalocyanine and lactate oxidase for lactate biosensing with MnO_2 nanoparticles as an eliminator of ascorbic acid interference. *Sens. and Actuat. B* 114:1052–1058.

Wei, A.; Sun, X.W.; Wang, J.X.; Lei, Y.; Cai, X.P.; Li, C.M.; Dong, Z.L.; Huang, W. (2006), Enzymatic glucose biosensor based on ZnO nanorod array grown by hydrothermal decomposition. *Appl. Phys. Lett*, 89, 123902-3.

Xiang, C.; Zou, Y.; Sun, L.X.; Xu, F. (2009), Direct electrochemistry and enhanced electrocatalysis of horseradish peroxidase based on flowerlike ZnO–gold nanoparticle–Nafion nanocomposite. *Sens.and Actuat. B* 136: 158–162

Xiao, P.; Garcia, B.B.; Guo, Q.; Liu, D.; Cao, G. (2007), TiO_2 nanotube arrays fabricated by anodization in different electrolytes for biosensing. *Electrochem. Commun.* 9:2441–2447

Xu, J.J.; Luo, X.L.; Du, Y.; Chen, H.Y. (2004), Application of MnO_2 nanoparticles as an eliminator of ascorbate interference to amperometric glucose biosensors. *Electrochem. Commun.,* 6:1169–1173

Xu, X.; Zhao, J.; Jiang, D.; Kong, J.; Liu, B.; Deng, J. (2002), TiO_2 sol-gel derived amperometric biosensor for H_2O_2 on the electropolymerized phenazine methosulfate modified electrode, *Anal. Bioanal. Chem.* 374:1261–1266

Yang, M.; Yang, Y.; Yang, Y.; Shen, G.; Yu, R. (2005), Microbiosensor for acetylcholine and choline based on electropolymerization/sol–gel derived composite membrane.*Anal. Chim. Acta,* 530: 205-211.

Yang, Y.; Guo, M.; Yang, M.; Wang, Z.; Shen, G.; Yu, R. (2005), Determination of pesticides in vegetable samples using an acetylcholinesterase biosensor based on

nanoparticles ZrO_2/chitosan composite film. *Intern. J. Environ. and Anal.Chem.* 85(3) 163–175.

Yang, Y.; Yang, H.; Yang, M.; Liu, Y.; Shen, G.; Yu, R. (2004), Amperometric glucose biosensor based on a surface treated nanoporous ZrO_2/Chitosan composite film as immobilization matrix. *Anal. Chim. Acta*, 525: 213-220.

Yao, S.; Xu, J.; Wang, Y.; Chen, X.; Xu, Y.; Hu, S. (2006), A highly sensitive hydrogen peroxide amperometric sensor based on MnO_2 nanoparticles and dihexadecyl hydrogen phosphate composite film. *Anal. Chim. Acta*, 557: 78-84.

Yu, J.; Ju, H. (2002), Preparation of porous titania sol-gel matrix for immobilization of horseradish peroxidase by a vapor deposition method. *Anal. Chem.,* 74: 3579-3583.

Zang, J.; Li, C.M.; Cui, X.; Wang, J.; Sun, X.; Dong, H.; Sun, C.Q. (2007), Tailoring zinc oxide nanowires for high performance amperometric glucose sensor. *Electroanalysis* 19(9): 1008-1014.

Zhang, F.; Wang, X.; Ai, S.; Sun, Z.; Wan, Q.; Zhu, Z.; Xian, Y.; Yamamoto, K. (2004), Immobilization of uricase on ZnO nanorods for a reagentless uric acid biosensor. *Anal. Chim. Acta*, 519: 155-160.

Zhang, F.F.; Wang, X.L.; Li, C.X.; Li, X.H.; Wan, Q.; Xian, Y.Z.; Jin, L.T.; Yamamoto, K. (2005), Assay for uric acid level in rat striatum by a reagentless biosensor based on functionalized multi-wall carbon nanotubes with tin oxide. *Anal. Bioanal. Chem.*, 382: 1368-1373.

Zhang, H. L.; Zou, X. Z.; Lai, G. S.; Han, D. Y.; Wanga, F.; (2007), Direct electrochemistry of hemoglobin immobilized on carbon-coated iron nanoparticles for amperometric detection of hydrogen peroxide. *Electroanalysis* 19(18): 1869-1874.

Zhang, T.; Tian, B.; Kong, J.; Yang, P.; Liu, B. (2003) A sensitive mediator-free tyrosinase biosensor based on an inorganic–organic hybrid titania sol–gel matrix. *Analytica Chimica Acta* 489: 199–206

Zhang, Y.; He, P.; Hu, N. (2004), Horseradish peroxidase immobilized in TiO_2 nanoparticle films on pyrolytic graphite electrodes: direct electrochemistry and bioelectrocatalysis. *Electrochimica Acta* 49:1981–1988

Zhang, Y.; Zeng, G.M.; Tang, L.; Huang, D.L.; Jiang, X.Y.; Chen, Y.N. (2007), A hydroquinone biosensor using modified core–shell magneticnanoparticles supported on carbon paste electrode. *Biosen. and Bioelectron.* 22:2121–2126.

Zhao, G.; Lei, Y.; Zhang, Y.; Li, H.; Liu, M. (2008), Growth and favorable bioelectrocatalysis of multishaped nanocrystal Au in vertically aligned TiO_2 nanotubes for hemoprotein. *J. Phys. Chem. C*, 112:14786–14795

Zhao, G.; Xu, J. J.; Chen, H. Y. (2006), Fabrication, characterization of Fe_3O_4 multilayer film and its application in promoting direct electron transfer of hemoglobin.*Electrochem. Commun.* 8:148-154.

Zhao, G.; Xu, J.J.; Chen, H.Y. (2006), Interfacing myoglobin to graphite electrode with an electrodeposited nanoporous ZnO film. *Anal. Biochem.,* 350():145–150

Zhao, Z.W.; Chen, X.J.; Tay, B.K.; Chen, J.S.; Han, Z.J.; Khor, K.A. (2007), A novel amperometric biosensor based on ZnO:Co nanoclusters for biosensing glucose. *Biosens. Bioelectron.*, 23: 135-139.

Zhao, G.; Feng, J.J.; Zhang, Q.L.; Li, S.P.; Chen, H.Y. (2005), Synthesis and characterization of prussian blue modified magnetite nanoparticles and its application to the electrocatalytic reduction of H_2O_2. *Chem. Mater.*, 17: 3154–3159

Zhu, X.; Yuri, I.; Gan, X.; Suzuki, I.; Li, G. (2007), Electrochemical study of the effect of nano-zinc oxide on microperoxidase and its application to more sensitive hydrogen peroxide biosensor preparation. *Biosens. and Bioelectron.* 22: 1600-1604.

Zong, S.; Cao, Y.; Zhou, Y.; Ju, H. (2007), Hydrogen peroxide biosensor based on hemoglobin modified zirconia nanoparticles-grafted collagen matrix. *Anal. Chim. Acta*, 582: 361-366.

Zong, S.; Cao, Y.; Zhou, Y.; Ju, H. (2007), Reagentless biosensor for hydrogen peroxide based on immobilization of protein in zirconia nanoparticles enhanced grafted collagen matrix. *Biosens. Bioelectron.*, 22: 1776-1782.

3

Amperimetric Biosensor Based on Carbon Nanotube and Plasma Polymer

Hitoshi Muguruma
Shibaura Institute of Technology
Japan

1. Introduction

Carbon nanotubes (CNTs) have been the focus of considerable studies since their discovery by Iijima (Iijima, 1991). CNTs are considered to be formed by the folding of graphene layers into carbon cylinders. They are of two distinct structural types: single-walled carbon nanotubes (SWCNTs) and multi-walled carbon nanotubes (MWCNTs). A SWCNT is a single shell extending from end to end with 1.3-2 nm tube diameter. A MWCNT is composed of several coaxial shells, each formed with rolled graphite sheets, with diameters varying from 2 to 50 nm and the distance between sheets being about 0.34 nm. CNTs have many new applications to electronic devices, such as field-effect transistors (Maki et al., 2006; Ohnaka et al., 2006) and gas sensors (Ueda et al., 2006; Wongwiriyapan et al., 2005), because of their unique electronic properties, unique geometric structure, high mechanical strength, and high chemical stability.

Recently, amperometric biosensors using CNTs have been increasingly reported. The typical structure of a CNT-based amperometric biosensor is the combination of biomacromolecules (e.g., enzymes) and CNTs in the vicinity of the electrode. Because of the well-defined nanostructure of CNTs, a good connection between CNTs and enzymes can be obtained. CNTs also enhance the electron transfer from reaction center of enzyme to electrode. Therefore, high performance of biosensor characteristics can be realized. Many strategies has been reported: the treatment of CNTs with nitric or sulfonic acid in order to introduce the chemically active functional groups (Liu et al., 2005a; Gooding et al., 2003; Azamian et al., 2002; Kim et al., 2006; Li et al., 2005; Liu et al., 2006), which enables subsequent modification. Another strategy is the dispersion of CNTs with a binder such as Nafion (Tang et al., 2004; Tsai et al., 2005; Hrapovic et al., 2004; Lee et al., 2007), Teflon (Wang & Musameh, 2003), sol-gel (Gavalas et al., 2004; Salimi et al., 2004; Yang et al., 2006; Kandimalla et al., 2006), poly(methyl methacrylate) (PMMA) (Rege et al., 2003), redox hydrogel (Joshi et al., 2005; Wang et al., 2006), poly(dimethyldiallylammonium chloride) (Zhao & Ju, 2006; Yan et al., 2007), chitosan (Liu et al., 2005b; Rivas et al., 2007), and electropolymerized film (Tsai et al., 2006; Pan et al., 2005). However, these methods require that enzymes and other biomolecules receive careful treatment in order to retain their tertiary structure. Moreover, when using such wet processes, it is difficult to control the nanoscale fabrication. A method where the CNTs are directly treated by plasma has recently been reported (Khare et al., 2005; Khare et al., 2004; Khare et al., 2002; Plank et al., 2005). The

advantage of this modification is that chemically active functional groups, such as amino and carboxyl groups can be easily introduced on the side wall and/or edge of the CNTs without contamination. Also, our group proposed an amperometric biosensor based on a plasma polymer (Muguruma & Karube, 1999; Muguruma et al., 2000; Muguruma et al., 2005; Muguruma & Kase, 2006; Muguruma et al., 2006).
With this in mind, the combination of the PP and/or plasma modification has been explored with a CNT-based amperometric biosensor application. Here we choose a glucose oxidase as a model of enzyme family because of the most popular amperometric biosensor. The proposed strategy not only simplifies the configuration of the CNT-based biosensor composed of plasma polymer (PP) and the enzyme, but also provides high performance biosensor characteristics, such as high sensitivity, high selectivity toward targets, and reliability.

2. Plasma polymerization for biosensor design

In this section, the methods of preparation and the properties of plasma polymer are briefly described (Yasuda, 1985). The plasma polymer (PP) is achieved in a glow discharge or plasma in the vapor phase. The resulting polymer was directly deposited onto the substrate as a thin film. The typical apparatus for plasma polymerization is shown in Figure 1. The monomers are vaporized and filled into the chamber. Gas monomers and liquid monomers can be supplied by bombs and reservoirs, respectively. The starting monomer gases may not contain the type of functional groups (e.g. double bond) normally associated with conventional polymerization. The pressure and flow rate are appropriately controlled. The electromagnetic power is supplied to generate active species for polymerization and glow discharge occurs. Inductive coils or capacitance are used for the power supply and a radio frequency (RF) of 13.56 MHz is industrially available. The thin film is deposited onto the surface of substrate with a typical deposition rate of 10-100 nm/min. The parameters for polymerization are discharge power and frequency, monomer structure, reactor type, flow rate of monomer, plasma pressure, substrate temperature and substrate position (Yasuda, 1985). The properties of the film are attributed to the fact that the polymerization occurs with the participation of many active species in the plasma state. The structure of the ethylene plasma-polymerized films is, for example, different from that of polyethylene films. The latter consists of chains with a regular repeat unit whereas the former tends to form an irregular three-dimensional crosslinked network.
Introduction of surface amino groups with plasma polymer is a common step in biosensor fabrication processes. The surface amino group has dual characteristics; one is hydrophilicity, which allows for dense loading of biological components onto the film surface, and the other is its behavior as a seed for subsequent chemical grafting, such as changing the surface properties and covalent bond immobilization to prevent leaching of immobilized biomaterials. Allylamine is the most popular monomer for providing surface amino groups. Allylamine PP has been used as a porous membrane modification for reverse osmosis applications, due to the hydrophilic nature of the polymer backbone (Bell et al., 1975). Biomedical applications of allylamine PP were first reported by Muratsugu et al. (Muratsugu et al., 1991) in which the $F(ab')_2$ fragments of antibody proteins were densely immobilized on the surface of allylamine PP. Allylamine PPs were subsequently widely used in biomedical applications (Mahoney et al., 2004; Kurosawa et al., 2002; Basarir et al., 2007; Zhang et al., 2003; Zhang et al., 2005). The PP surfaces of ethylenediamine (EDA) and

alkylamines have amino groups and have also been used in biomedical applications (Jung et al., 2006; Nakanishi et al., 1996; Wang et al., 2003). The resulting film is sometimes different from that of the original monomer structure, because the plasma polymerization process involves fragmentation and reorganization in the presence of highly energetic active species. Therefore, plasma control during the production of biomedical PPs is the central issue; for example, the acetonitrile PP surface (Hiratsuka et al., 2000) and surfaces prepared by plasma treatment of nitrogen (Everhart & Reilley, 1981), ammonia (Hollahan et al., 1969), and a mixture of N_2/H_2 (Meyer-Plath et al., 2003) gas have amino groups, despite the original monomers having no amino groups. Chemical derivative X-ray electron spectroscopy (XPS) surface analysis and infrared (IR) spectroscopy of acetonitrile have shown that surface nitrogen is present not only as amino groups, but also as other nitrogen-based functional groups, such as C–NH-C, C-N=N-C, –C=N-, and –CN (Hiratsuka et al., 2000; Muguruma, 2008). The structure of the PP is characterized by highly branched and incompletely crosslinked aliphatic hydrocarbon backbone chains containing nitrogen atoms, and double bonds (C=C) are interspersed along the chains.

In summary, characteristics of PP include (i) easily control of the thickness range from several ten nanometer to micrometer, (ii) processing that facilitates the wetness and charge control of the surface properties, (iii) good adhesion to the substrate, (iv) ability to protect against interferant agents, and (v) an affinity with biological components. Therefore, PPs are suitable for the interfacial design between a biological component (enzyme) and an electrode.

3. Optimization for device fabrication

3.1 Device fabrication procedure

The preparation scheme is shown in Fig. 2. The device was formed on a 0.15-mm-thick glass substrate, with planar dimensions of approximately 50 × 50 mm^2. All the metal layers were sputter-deposited and patterned by a masking process. The glass slides used to make the thin film electrodes were boiled in a hydrogen peroxide/ammonia/water solution (approximately 1:1:8 by volume) for 1 h, and then rinsed with water and acetone. Au thin films were deposited using sputtering apparatus (VEP-1000, Ulvac Inc., Tokyo, Japan). A 40-nm-thick Cr intermediate layer was used to promote the adhesion of the Au layer. The dimension of the opening for the working electrode was 5×5 mm2.

A plasma generator (VEP-1000, Ulvac Inc., Tokyo, Japan) was used to deposit a 6-nm-thick acetonitrile-PP (AN-PP) (first/lower PP) onto the sputtered Au electrode at 150 W and under a pressure of 0.6 Pa for a deposition time of 60 s. The CNTs were dispersed in a 1:1 mixed solution of ethanol and phosphate buffer solution (20 mM, pH 7.4) in which the optimized CNT concentration was 0.75 mg mL^{-1}. The CNT suspension was deposited dropwise onto the PP surface, and then dried in a vacuum oven. Subsequently, the CNT-adsorbed surface was treated with nitrogen plasma under the following parameters: power, 100 W (optimized); flow rate, 15 mL min^{-1}; pressure, 3 Pa; exposure time, 60 s. The enzyme was then added by dropping an aliquot of GOx (10 mg mL^{-1}) in phosphate buffer (20 mM, pH 7.4) onto the film. One hour later, the device was washed with water. Finally, the enzyme-adsorbed surface was overcoated with a second AN-PP (6 nm thickness), using the same deposition parameters as that for the first PP. The devices were stored in a refrigerator at 4 °C until use.

Cyclic voltammetry was performed using an electrochemical analyzer (Model 701A, ALS Instruments, West Lafayette, IN), with a three-electrode configuration. A reference electrode (Ag/AgCl, RE-1C) and a counter electrode (platinum wire) were purchased from Bioanalytical Systems Inc. Electrochemical measurements were carried out in a 10 mL vessel at ambient temperature (20±1 °C). A phosphate buffer (20 mM, pH 7.4) was used as the supporting electrolyte. The measurement was carried out at least four times.
The fabricated amperometric biosensor based on CNT and PP has a unique sandwich-like structure of PP/GOx/CNT/PP/Au. The device was fabricated with a dry-chemistry basis of the layer-by-layer process. Figure 3 showed the SEM image of the device surface. In Fig 3a, the distinct CNT was not observed probably because surface concentration of CNT was small. Nevertheless, the large current response was obtained (discuss below). Therefore, the electrochemical contact is completed in this process. Fig. 3b supports the fact that the flat and homogeneous surface for enzyme immobilization is obtained. The each step of the fabrication processes was optimized.

3.2 Effectiveness of CNT

The effectiveness of using CNTs was examined and the results are given in Fig. 4. The amperometric response of the device with CNTs (PP/GOx/CNT/PP/Au, Fig. 4d) was 16-fold larger than that without CNTs (PP/GOx/PP/Au, Fig. 4a). The current response to the enzymatic reaction given by the CNT-PP electrode was the largest, and more than any other PP-based enzyme electrode, such as electron transfer mediators (Muguruma & Kase, 2006) and platinum electrodes (Muguruma et al., 2000). The obtained maximum current density of ca. 0.4 mA cm-2 was comparable with that of other CNT-based biosensors (Tang et al., 2004; Joshi et al., 2005; Pan et al., 2005; Patolsky et al., 2004).
Two mechanisms can be considered for the large current response; the direct electron transfer via the CNTs, and the catalytic ability of the CNTs (Merkoçi et al, 2005; Wang and Musameh, 2003; Salimi et al, 2004; Liu et al., 2005) toward hydrogen peroxide generated by the enzymatic reaction. The latter is supported by the fact that oxidation currents with CNT-based electrodes start at around +0.2 V. The electrode with sputtered platinum (Pt), which also has catalytic ability (PP/GOx/PP/Pt, Fig. 4b), displays an oxidation peak at >+0.2 V. The current at >+0.6 V for PP/GOx/CNT/PP/Au (Fig. 4d) was much larger than that for PP/GOx/PP/Pt, which suggests that the CNTs provide enhancement of electron transfer as an electron conductive component of the electrode. (a) The manuscript must be written in English, (b) use common technical terms, (c) avoid abbreviations, don't try to create new English words, (d) spelling: Follow Merriam Webster´s Collegiate Dictionary, Longman or Oxford Dictionaries.

3.3 Effectiveness of the first PP layer between the Au electrode and CNTs

he current observed for the electrode with the first PP layer (PP/GOx/CNT/PP/Au, Fig. 4d) after glucose addition was much larger than that for the electrode without the PP layer (PP/GOx/CNT/Au, Fig. 4c), which indicates that the first PP layer acts as an interface between the Au electrode and the GOx-CNT complex. In fact, a densely packed array of GOx molecules can be formed on the hydrophilic and positively charged surface of acetonitrile PP than on a bare Au electrode. Because the enzyme layer on the PP surface is two dimensional, this process does not depend on the thickness or the loading amount of the enzyme (Muguruma et al., 2000; Muguruma et al., 2006).

The background current of the electrode with the first PP layer (Fig. 4c) was smaller than that for the device without the PP layer (Fig, 4d). Two reasons are considered for this. One reason is that the nano-sandwich structure does not enlarge the effective geometric area (i.e. very flat surface) of the electrode, and the other is that the PP layer appears to present a diffusion barrier to the supporting electrolyte, causing a partitioning between the electrode and the bulk solution (Muguruma et al., 2000).
From atomic force microscopic measurements of the surface, the dimension of a GOx molecule is observed as a compact ellipsoid with an approximate dimension of 12.2×8.3 nm^2 (Muguruma et al., 2006). One dimension of a single-walled CNT (1.2-2.0 nm) is smaller than that of a GOx molecule; therefore, an effective electrochemical contact of the GOx-CNT-Au electrode can be achieved.

3.4 Optimization for GOx-CNT mixture

Since the CNTs are chemically inert and insoluble in most solvents, solution casting of the CNT layer was achieved by temporal dispersion of the CNTs in solution. The cyclic voltammetry (CV) response of the PP/GOx/PP/Au biosensor with a CNT layer cast using a 1:1 mixture of buffer and ethanol displayed a response higher than that of CNT layers cast using only buffer or only ethanol, as shown in Fig. 5. This confirms that the 1:1 buffer/ethanol mixture provides a more stable CNT suspension, as shown by the photograph of vial suspensions in Fig. 5. However, this suspension is less stable than that obtained by other processes using binder such as Nafion, polypyrrole, and surfactants (Hrapovic et al., 2004; Joshi et al., 2005; Wang et al., 2006; Gavalas et al., 2004; Merkoçi et al., 2005). Therefore, it is probable that the CNT layer is mechanically and electrically loose (probably slack packing). Combined with the subsequent plasma treatment, a high sensor response was obtained (Fig. 5c). This method for the formation and modification of a CNT layer is a very simple and clean process.

3.5 Optimization of CNT concentration in solution for CNT layer casting formation

Optimization of the CNT concentration in the suspension solution for casting was carried out. Figure 6 shows CVs obtained in the presence and absence of glucose as a function of the CNT concentration. Comparing Figs. 6a and 6b, it can be seen that the current due to glucose addition to the device with CNTs at 0.75 mg mL^{-1} was larger than that with 0.3 mg mL-1. From the CV with the largest concentration of 15 mg mL^{-1} (Fig. 6), both the oxidation and background currents increased. The CNT acts as the catalyst or direct electron transfer via CNT (discussed next section). From these mechanisms, in spite of higher concentration of CNT, the output current in higher CNT concentration of 15 mg/ml decreased than that of 0.75 mg mL^{-1}. This is because the amount of CNT is so large compared with enzyme GOx that generation of hydrogen peroxide and electron due the enzymatic reaction toward glucose reduced. This shows that the design for enzyme-CNT electrode need to consider the balance between the amount of enzyme and CNT. Therefore, the optimized concentration of CNTs was determined as 0.75 mg mL^{-1}, due to the largest increment in current with glucose addition.

3.6 Optimization of plasma power for treatment of CNT layer

A subsequent CNT modification on the first PP layer is a key step. The CNT is directly treated by oxygen or nitrogen plasma instead of a wet-chemical treatment for CNTs. The

effectiveness of plasma treatment on the CNT was investigated. The fabricated amperometric biosensor has a unique sandwich-like structure denoted as the basic structure of PP/GOD/PT/CNT/PP/Au. Figure 8 show cyclic voltammograms obtained in the absence and presence of glucose. First, the effectiveness of CNTs and oxygen plasma treatment (PT) for CNTs was investigated. The current responses of the devices without CNTs (PP/GOx/PP/Au, Fig. 8a) and oxygen plasma treatment (PP/GOx/CNT/PP/Au, Fig. 7b) were much smaller than that of the optimized device (PP/GOx/PT-70W/CNT/PP/Au, Fig. 7f). The higher the power of oxygen plasma for modifying CNTs, the larger the increase in current for sensor response. In PP/GOx/PT-60W/SWCNT/PP/Au (Fig. 7e) and PP/GOx/PT-70W/SWCNT/PP/Au (Fig. 7f), upon the addition of glucose, the observed current changed markedly with a large increase in oxidation current. Additionally, we confirmed that the current observed for the electrode with the first PP layer (PP/GOx/PT/CNT/PP/Au) after glucose addition was 4-5-fold larger than that for the electrode without the PP layer (PP/GOx/PT/CNT/Au), which indicates that the first PP layer acts as an interface between the Au electrode and the GOx-CNT complex.

Figure 8 summarizes the current of the PP/GOx/CNT/PP/Au device as a function of plasma power for the treatment of CNTs on the first PP layer (CV data were shown in Fig. 7). It was concluded that the optimal plasma power for CNT-treatment was 70-100 W. The oxidation current response to 48 mM glucose initially increases, plateaus, and then decreases with increasing plasma power treatment of the CNTs. At less than 70 W, the CNT modification is insufficient for suitable contact with the GOx. At more than 150 W, the current decreases, because the higher energy of the plasma species has etched the mechanical structure of CNTs and a detrimental effect on the electronic properties of the CNTs. However, the electronic properties of CNTs were almost retained less than 100-W of the plasma power because the large current sensor response was comparable with the other CNT-base biosensor (Azaman et al., 2002; Hrapovic et al., 2004; Tsai et al., 2005).

These results indicate that both PP and nitrogen (or oxygen) plasma modification is an effective strategy for fabrication of an enzyme-friendly platform in CNT-based amperometric biosensors. The effectiveness of the nitrogen or oxygen plasma treatment is probably due to the introduction of carboxyl or amino groups to the side wall surface of the CNTs. This experimental evidence of introduction of functional groups is experimentally reported by Khare's group (Khare et al., 2005; Khare et al., 2004; Khare et al., 2002).

As a result, the hydrophobic surface of the CNTs is changed to a stable hydrophilic environment that facilitates contact with GOx. Additionally, when comparing between nitrogen and oxygen plasma treatment, the current response with nitrogen plasma was slightly larger than that with oxygen plasma. This is attributed to difference of functional groups. Nitrogen plasma treatment can introduce positive charge (amino) groups, whereas oxygen plasma treatment can introduce nagetive charge (carboxyl) groups (Everhart and Reilly, 1981). Therefore, the negatively charged GOx (p*I* = 4.2) is densely loaded onto positively charged surfaces than onto negatively charged surfaces (Muguruma et al., 2006).

3.7 Comparison between single- and multi-walled CNT

Figure 9 shows the responses of several glucose sensors, each of which was prepared using different types of CNT: single-walled CNT and multi-walled CNT (SWCNTs, 20-30-nm-diameter MWCNTs, and 40-70-nm-diameter MWCNTs). When comparing these CNTs, the increment in current is SWCNTs > 20-30-nm-diameter MWCNTs > 40-70-nm-diameter MWCNTs. SWCNTs are the most suitable materials among CNTs. However, the

relationship between current due to glucose and plasma power for the treatment of MWCNT is unclear. The possible explanation for this is that the GOx molecule is a compact ellipsoid with approximate dimensions of 12.2 × 8.3 nm2 (measured by atomic force microscopy) (Muguruma et al., 2005). Then, the redox center exists at the smaller pocket in the larger (10 nm) three-dimensional structure of GOx. The dimension of SWCNTs (1.2-2 nm) is smaller than that of GOx, whereas that of MWCNTs (> 20 nm) is larger than that of GOx. Therefore, almost all of the reaction centers of GOx were intact and connected to SWCNTs.

3.8 Effectiveness of the second PP layer over the immobilized enzyme

The final step was the overcoating of acetonitrile PP (denoted as the second PP layer) onto the immobilized GOx and CNTs. Our group has already reported that the GOx adsorbed on the surface was more deeply embedded, immobilized within the second acetonitrile PP layer (Muguruma & Kase, 2006). Two thicknesses were investigated for the second PP coating; 10 nm and 20 nm. The 10-nm-thick PP layer probably provides a coating to completely cover the adsorbed enzyme because the height of the GOx monolayer was 6-7 nm (Muguruma & Kase, 2006). In spite of the fact that GOx was treated by high-energy plasma, the response to 2.5 mM glucose with the second PP coating film is almost the same as that with no second PP layer on the device; that is, the initial enzymatic activity of GOx is retained. This means that under milder exposure to organic plasma, the enzyme does not become seriously dysfunctional, as previously demonstrated (Muguruma et al., 2005; Muguruma and Kase, 2006). The fact that the glucose response of the devices with and without the second PP layer were similar shows that the coating is not a barrier toward access by glucose.

Figure 10 shows a comparison of the amperometric response due to an interferant (ascorbic acid) and glucose. The maximum level of ascorbic acid under physiological conditions is 0.5 mM. From our previous report, the first acetonitrile PP layer reduces the effect of interference. This was attributed to the first PP layer serving a role as an anti-fouling coating against oxidizing interference (Muguruma et al., 2000). The first PP layer can incompletely eliminate the current due to interference. In fact, the device without a second acetonitrile PP layer (GOx/CNT/PP/Au) shows a current of 2 μA due to 0.5 mM ascorbic acid in which this is similar with the current due to the response of 0.14 mM glucose (Fig. 10a). If the coating film is thicker, then the oxidation current due to ascorbic acid is smaller. The effect of addition of ascorbic acid to the response of the device with a 20-nm-thick PP coating (PP/GOx/CNT/PP/Au) was negligible (almost similar with background, Fig. 10c), because the access of ascorbic acid to the CNTs is blocked by the second PP coating. Therefore, the second PP layer completely eliminates interference and enables the selective detection of glucose.

The other advantage of the second PP layer is also demonstrated in Fig.11. The operational stability under continuous polarization at +0.8 V in the presence of 48 mM glucose was investigated. For the device without the second PP coating, the current decreased to 25% of the initial current after 24 h, due to leaching of the physically adsorbed GOx and CNTs onto the first PP layer. In contrast, the electrochemical response of the device with the second PP layer retained a current response of more than 90%. This suggests that the overcoating with a second acetonitrile PP layer prevents leaching and contamination of the GOx and CNTs.

3.9 Mechanism of sensor response

Two mechanisms can be considered for the large current response. One is the catalytic activity of the CNTs (Kim et al., 2006; Tang et al., 2004; Hrapovic et al., 2004) toward hydrogen peroxide generated by the enzymatic reaction. GOx specifically catalyzes the oxidation of glucose as follows:

$$\beta\text{-D-glucose} + O_2 \rightarrow (\text{Gox})\ \text{D-gluconic acid} + H_2O_2, \quad (1)$$

and the CNT catalyzes the reaction of hydrogen peroxide as follows:

$$H_2O_2 \rightarrow 2H^+ + O_2 + 2e^-. \quad (2)$$

The Au electrode receives the electron, and as a result, the current increases.
The other mechanism is the direct electron transfer via the CNTs, and a possible mechanism is

$$\beta\text{-D-glucose} + \text{GOx(FAD)} \rightarrow \delta\text{-gluconolactone} + \text{GOx}(FADH_2) \quad (3)$$

$$\text{GOx}(FADH_2) + 2M_{ox} \rightarrow \text{GOx(FAD)} + 2M_{red} + 2H^+ \quad (4)$$

$$2M_{red} \rightarrow 2M_{ox} + 2e^- \quad (5)$$

where FAD locates in the vicinity of the reaction center of GOx, and M represents an electron transfer mediator.

4. Sensor performance

The previous sections have presented the optimization of the sensor fabrication process based on CNTs and PP. Here, the sensor performance of the optimized device is demonstrated. In Fig. 12, a steady state amperometric response at +0.8 V vs. Ag/AgCl was demonstrated for a wide range of glucose concentration (0.025-14 mM). The remarkable characteristic is the small background current (0.35 ± 0.013 μA) compared with the glucose response, indicating there is no need to calibrate the baseline for the glucose measurement. This is because the nano-sandwich structure and the permiselective coating of the first PP layer on the Au electrode provide effective electrochemical communication.
The nanometer size sandwich-like configuration provides a suitable distance for electrochemical communication between the electrode and the reaction center of the enzyme. As a result, a short response time (<4 s, 95% to maximum response) was obtained. The detection limit (signal/noise ratio: 3) of 6 μM is much lower than that of GOx/PP/Pt electrode (0.25 mM) (Muguruma et al., 2000). Since the devices were fabricated in the same batch, reasonable reproducibility (relative standard deviation: 3%, n=4) from sample-to-sample was obtained.
Figure 13 show the current vs. glucose concentration based on the data from Fig. 12. The characteristics of this device display good linearity (r=0.993) in the low concentration region (0.025-2.2 mM) and the sensitivity was 42 μA mM^{-1} cm^{-2}. Deviation from linearity is observed at higher (>5 mM) glucose concentration, representing a typical characteristic of the Michaelis-Menten model. The apparent Michaelis-Menten activity (K_M^{app}) of the immobilized enzyme was calculated according to the Lineweaver-Burk plot shown in the upper inset of Fig. 13. According to this, the K_M^{app} is calculated to be 11 mM. This value is similar to that of other CNT-based glucose biosensor (Tang et al., 2004; Liu et al., 2005) and is smaller than that of GOx in solution (33 mM) (Liu et al., 2005).

5. Conclusion

A new simple and reliable method for the fabrication of a CNT-based amperometric biosensor was demonstrated. CNTs and GOx enzyme were sandwiched between 6-nm-thick PPs on a sputtered gold electrode. Optimization of the casting formation of a CNT layer onto the lower PP was stressed. An organic plasma polymer coating method and a semiconductor-technology-compatible layer-by-layer process provided a well-defined nanocomposite of enzyme, CNTs, and PPs. This highly efficient electron transfer system was able to detect a relevant bioelectrochemical signal equal to 0.44 mA cm^{-2}. This also suggests that the PP and/or plasma process is a suitable interface design for electrochemical communication from the reaction center of GOx to an electrode via CNTs. The method presented here can be easily extended to other biosensor devices using other enzymes and proteins. As a simple dry process intended for mass production, this might be of benefit to the development of microscale and/or arrayed sensors.

6. References

Azamian, B.R.; Davis, J.J.; Colemann, K.S.; Bagshaw, C.B. & Green, M.L.H. (2002). Bioelectrochemical single-walled carbon nanotubes, J. Am. Chem. Soc., 124., 12664-12665.

Basarir, F.; Cuong, N.; Song, W.–K. & Yoon, T.–H. (2007). Surface modification via plasma polymerization of allylamine for antibody immobilization, Macromol. Symp., 249-250., 61-66.

Bell, A.T.; Wydeven, T. & Johnson, C.C. (1975). A study of the performance and chemical characteristics of composite reverse osmosis membranes prepared by plasma polymerization of allylamine, J. Appl. Polym. Sci., 19., 1911-1930.

Cai, C. & Chen, J. (2004). Direct electron transfer of glucose oxidase promoted by carbon nanotunes, Anal. Biochem., 332., 75-83.

Everhart, D.S. & Reilley, C.N. (1981). Chemical derivatization in electron spectroscopy for chemical analysis of surface functional group introduced on low-density polyethylene film, Anal. Chem., 53., 665-676.

Gavalas, V.G.; Law, S.A.; Ball, J.C.; Andrews, R. & Bachas, L.G. (2004). Carbon nanotube aqueous sol-gel composites: enzyme-friendly platforms for the development of stable biosensors, Anal. Biochem., 329., 247-252.

Gooding, J.J.; Wibowo, R.; Liu, J.; Yang, W.; Losic, D.; Orbons, S.; Mearns, F.J.; Shapter, J.G. & Hibbert, D.B. (2003). Protein electrochemistry using aligned carbon nanotube arrays, J. Am. Chem. Soc., 125., 9006-9007.

Guldi, D.M.; Rahman, G.M.A.; Zerbetto, F. & Prato, M. (2005). Carbon Nanotubes in Electron Donor−Acceptor Nanocomposites, Acc. Chem. Res., 38., 871-878.

Hiratsuka, A.; Muguruma, H.; Nagata, R.; Nakamura, R.; Sato, K.; Uchiyama, S. & Karube, I. (2000). Mass transport behavior of electrochemical species through plasma-polymerized thin film on platinum electrode, J. Membr. Sci., 175., 25-34.

Hollahan, J.R.; Stafford, B.B.; Falb, R.D. & Payne, S.T. (1969). Attachment of amino group to polymer surface by radiofrequency plasmas, J. Appl. Polym. Sci., 13., 807-816.

Hrapovic, S.; Liu, Y.; Male, K.B. & Luong, J.H.T. (2004). Electrochemical biosensing platforms using platinum nanoparticles and carbon nanotubes, Anal. Chem., 76., 1083-1088.

Iijima, S. (1991). Helical microtubules of graphitic carbon, Nature, 354., 56-58.

Joshi, P.P.; Merchant, S.A.; Wang, Y. & Schmidtke, D.W. (2005). Amperometric biosensors based on redox polymer-carbon nanotube-enzyme composites, Anal. Chem., 77., 3183-3188.

Jung, D.; Yeo, S.; Kim, J.; Kim, B.; Jin, B. & Ryu, D. Formation of amine groups by plasma enhanced chemical vapor deposition and its application to DNA array technology, Surf. Coatings Tech., 200., 2886-2891.

Kandimalla, V.B.; Tripathi, V.S. & Ju, H. (2006). A conductive ormosil encapsulated with ferrocene conjugate and multiwall carbon nanotubes for biosensing application, Biomaterials, 27., 1167-1174.

Khare, B.; Wilhite, P.; Tran, B.; Teixeira, E.; Fresquez, K.; Mvondo, D.N.; Bauschlicher, Jr.,C. & Meyyappam, M. (2005). Functionalization of carbon nanotubes via nitrogen glow discharge, J. Phys. Chem. B, 109., 23466-23472.

Khare, B.; Wilhite, P.; Quinn, R.C.; Chen, B.; Schingler, R.H.; Tran, B.; Imanaka, H.; So, C.R.; Bauschlicher, Jr.,C. & Meyyappam, M. (2004). Functionalization of carbon nanotubes by ammonia glow-discharge: experiments and modeling, J. Phys. Chem. B, 108., 8166-8172.

Khare, B.; Meyyappam, M.; Cassell, A.M.; Nguyen, C.V. & Han, J. (2002). Functionalization of carbon nanotubes using atomic hydrogen from a glow discharge, Nano Lett., 2., 73-77.

Kim, J.-Y.; Baek, J.Y.; Kim, H.H.; Lee, K.A. & Lee, S.H. (2006) Integration of enzyme immobilized single-walled carbon nanotubes mass into the microfluidic platform and its application for the glucose-detection, Sens. Actuators A, 128., 7-13.

Kurosawa, S.; Hirokawa, T.; Kashima, K.; Aizawa, H.; Park, J.-W.; Tozuka, M.; Yoshimi, Y. & Hirano, K. (2002). Adsorption of anti-C-reactive protein monoclonal antibody and its $F(ab')_2$ fragment on Plasma-Polymerized Styrene, allylamine and acrylic acid coated with quartz crystal microbalance, J. Photopolym. Sci. Tech., 15., 328-330.

Lee, C.–H.; Wang, S.–C.; Yuan, C.–J.; Wen, M.–F. & Chang, K.–S. (2007). Comparison of amperometric biosensors fabricated by palladium sputtering, palladium electrodepsition and Nafion/carbon nanotube casting on screen-printed carbon electrodes, Biosen. Bioelectron., 22., 877-884.

Li, J.; Wang, Y.–B.; Qiu, J.–D.; Sun, D.–C. & Xia, X.–H. (2005). Biocomposites of covalently linked glucose oxidase on carbon nanotubes for glucose biosensor, Anal. Bioanal. Chem., 383., 918-922.

Liu, G. & Lin, Y. (2006). Amperometric glucose biosensor based on self-assembling glucose oxidase on carbon nanotubes, Electrochem. Commun., 8., 251-256.

Liu, J.; Chou, A.; Rahmat, W.; Paddon-Row, M.N. & Gooding, J.J. (2005a). Achieving direct electrical connection to glucose oxidase using aligned single walled carbon nanotube arrays, Electroanalysis, 17., 38-46.

Liu, Y.; Wang, M.; Zhao, F.; Xu, Z. & Dong, S. (2005b). The direct electron transfer of glucose oxidase and glucose biosensor based on carbon nanotubes/chitosan matrix, Biosen. Bioelectron., 21., 984-988.

Mahoney, D.J.; Whittle, J.D.; Milner, C.M.; Clark, S.J.; Mulloy, B.; Buttle, D.J.; Jones, G.C.; Day, A.J. & Short, R.D. (2004). Amethod for the non-covalent immobilization of heparin to surfaces, Anal. Biochem., 330., 123-129.

Maki, H.; Sato, T. & Ishibashi, K. (2006). Transport characteristic control of field-effect transistors with single-walled carbon nanotube films using electrode metals with low and high work functions, Jpn. J. Appl. Phys., 45., 7234-7236.

Merkoçi, A.; Pumera, M.; Llopis, X.; Pérez, B.; Valle, M. & Alegret, S. (2005). New materials for electrochemical sensing vi: carbon nanotubes, Trend. Anal. Chem., 24., 826-838.

Meyer-Plath, A.A.; Schröder, K.; Finke, B. & Ohl, A. (2003). Current trends in biomaterial surface functionalization−nitrogen-containing plasma assisted processes with enhanced selectivity, Vacuum, 71., 391-406.

Muguruma, H.; Hiratsuka, A. & Karube, I. (2000). Thin film glucose biosensor based on plasma-polymerized film: simple design for mass production, Anal. Chem., 72., 2671-2675.

Muguruma, H. & Karube, I. (1999). Plasma-polymerized films for Biosensors, Trend. Anal. Chem., 18., 62-68.

Muguruma, H.; Kase, Y. & Uehara, H. (2005). Nanothin ferrocene film plasma polymerized over physisorbed glucose oxidase: toward high throughput fabrication of bioelectronic devices without chemical modifications, Anal. Chem., 77., 6557-6562.

Muguruma, H. & Kase, Y. (2006). Structure and biosensor characteristics of complex between glucose oxidase and plasma-polymerized nanothin film, Biosens. Bioelectron., 22., 737-743.

Muguruma, H.; Kase, Y.; Murata, N. & Matsumura, K. (2006). Adsorption of glucose oxidase onto plasma-polymerized film characterized by atomic force microscopy, quartz crystal microbalance, and electrochemical measurement, J. Phys. Chem. B, 110., 26033-26039.

Muguruma, H. (2008). Quantitative characterization of surface amino groups of plasma-polymerized films prepared from nitrogen-containing monomers for bioelectronic applications, IEICE Trans. Electron., E91-C., 963-967.

Muratsugu, M.; Kurosawa, S. & Kamo, N. (1991). Adsorption and desorption of F(ab')2anti-hIgG on plasma-polymerized allylamine thin film: the application of the film to immunoassay, J. Colloid Interf. Sci., 147, 378-386.

Nakanishi, K.; Muguruma, H. & Karube, I. (1996). A novel method of immobilizing antibodies on a quartz crystal microbalance using plasma-polymerized films for immunosensors, Anal. Chem., 68., 1695-1700.

Ohnaka, H.; Kojima, Y.; Kishimoto, S.; Ohno, Y. & Mizutani, T. (2006). Fabrication of carbon nanotube field effect transistors using plasma-enhanced chemical vapor deposition grown nanotubes, Jpn. J. Appl. Phys., 45., 5485-5489.

Pan, D.; Chen, J.; Yao, S.; Tao, W. & Nie, L. (2005). An amperometric glucose biosensor based on glucose oxidase immobilized in electropolymerized poly(*o*-aminophenol) and carbon nanotube composite film on a gold electrode, Anal. Sci., 21., 367-371.

Patolsky, F.; Weizmann, Y. & Willner, I. (2004). Long-range electrical contacting of redox enzyme by SWCNT connectors, Angew. Chem. Int. Ed., 43., 2113-2117.

Plank, N.O.V.; Forrest, G.A.; Cheung, R. & Alexander, A.J. (2005). Electronic properties of n-type carbon nanotubes prepared by CF_4 plasma fluorination and amino functionalization, J. Phys. Chem. B, 109., 22096-22101.

Rege, K.; Raravikar, N.R.; Kim, D.–Y.; Schadler, L.S.; Ajayan, P.M. & Dordick, J.S. (2003). Enzyme-polymer-single walled carbon nanotube composites as biocatalytic films, Nano Lett., 3., 829-832.

Rivas, G.A.; Miscoria, S.A.; Desbrieres, J. & Barrera, G.D. (2007). New biosensing platforms based on the layer-by-layer self-assembling of polyelectrolytes on Nafion/carbon nanotubes-coated glassy carbon electrodes, Talanta, 71., 270-275.

Salimi, A.; Compton, R.G. & Hallaj, R. (2004). Glucose biosensor prepared by glucose oxidase encapsulated sol-gel and carbon-nanotube-modified basal plane pyrolytic graphite electrode, Anal. Biochem., 333., 49-56.

Tasis, D.; Tagmatarchis, N.; Bianco, A. & Prato, M. (2006). Chemistry of carbon nanotubes, Chem. Rev., 106., 1105-1136.

Tang, H.; Chen, J.; Yao, S.; Nie, L.; Deng, G. & Kuang, Y. (2004). Amperometric glucose biosensor based on adsorption of glucose oxidase at platinum nanoparticle-modified carbon nanotube electrode, Anal. Biochem., 331., 89-97.

Tsai, Y.–C.; Li, S.–C. & Liao, S.–W. (2006). Electrodeposition of polypyrrole-multiwalled carbon nanotube-glucose oxidase nanobiocomposite film for the detection of glucose, Biosen. Bioelectron., 22., 495-500.

Tsai, Y.–C., Li, S.–C. & Chen, J.–M. (2005). Cast thin film biosensor design based on a Nafion backbone, a multiwalled carbon nanotube conduit, and a glucose oxidase function, Langmuir, 21., 3653-3658.

Ueda, T.; Norimatsu, H.; Hossain Bhuiyan, Md.M.; Ikegami, T. & Ebihara, K. (2006). NO sensing property of carbon nanotube based thin film gas sensors prepared by chemical vapor deposition techniques, Jpn. J. Appl. Phys., 45., 8393-8397.

Wang, H.; Wang, C.; Lei, C.; Wu, Z.; Shen, G. & Yu, R. (2003). A novel biosensing interfacial design produced by assembling nano-Au particles on amine-terminated plasma-polymerized films, Anal. Bioanal. Chem., 377., 632-638.

Wang, J. & Musameh, M. (2003). Carbon nanotube/Teflon composite electrochemical sensors and biosensors, Anal. Chem., 75., 2075-2079.

Wang, J.; Musameh, M. & Lin, Y. (2003). Solubilization of carbon nanotubes by Nafion toward the preparation of amperometric biosensors, J. Am. Chem. Soc., 125., 2408-2409.

Wang, Y.; Joshi, P.P.; Hobbs, K.L.; Johnson, M.B. & Schmidtke, D.W. (2006). Nanostructured biosensors built by layer-by-layer electrostatic assembly of enzyme-coated single-walled carbon nanotubes and redox polymers, Langmuir, 22., 9776-9783.

Wongwiriyapan, W.; Honda, S.; Konishi, H.; Mizuta, T.; Ikuno, T.; Ito, T.; Maekawa, T.; Suzuki, K.; Ishikawa, H.; Oura, K. & Katayama, M. (2005). Single-walled carbon nanotube thin-film sensor for ultrasensitive gas detection, Jpn. J. Appl. Phys., 44., L482-L484.

Yan, X.B.; Chen, X.J.; Tay, B.K. & Khor, K.A. (2007). Transparent and flexible glucose biosensor via layer-by-layer assembly of multi-wall carbon nanotubes and glucose oxidase, Electrochem. Commun., 9., 1269-1275.

Yang, M.; Yang, Y.; Liu, Y.; Shen, G. & Yu, R. (2006). Platinum nanoparticles-doped sol-gel/carbon nanotubes composite electrochemical sensors and biosensors, Biosen. Bioelectron., 21., 1125-1131

Yasuda, H. (1985). Plasma Polymerization, Academic Press, Inc. ISBN 0-12-768760-2, Orland, Florida.

Zhang, Z.; Chen, Q.; Knoll, W.; Foerch, R.; Holcomb, R. & Roitman, D. (2003). Plasma polymer film structure and DNA probe immobilization, Macromolecules, 36., 7689-7694.

Zhang, Z.; Knoll, W.; Foerch, R.; Holcomb, R. & Roitman, D. (2005). DNA hybridization on plasma-polymerized allylamine, Macromolecules, 38., 1271-1276.

Zhao, H. & Ju, H. (2006). Multilayer membranes for glucose biosensing via layer-by-layer assembly of multiwall carbon nanotubes and glucose oxidase, Anal. Biochem., 350., 138-144.

7. Figures

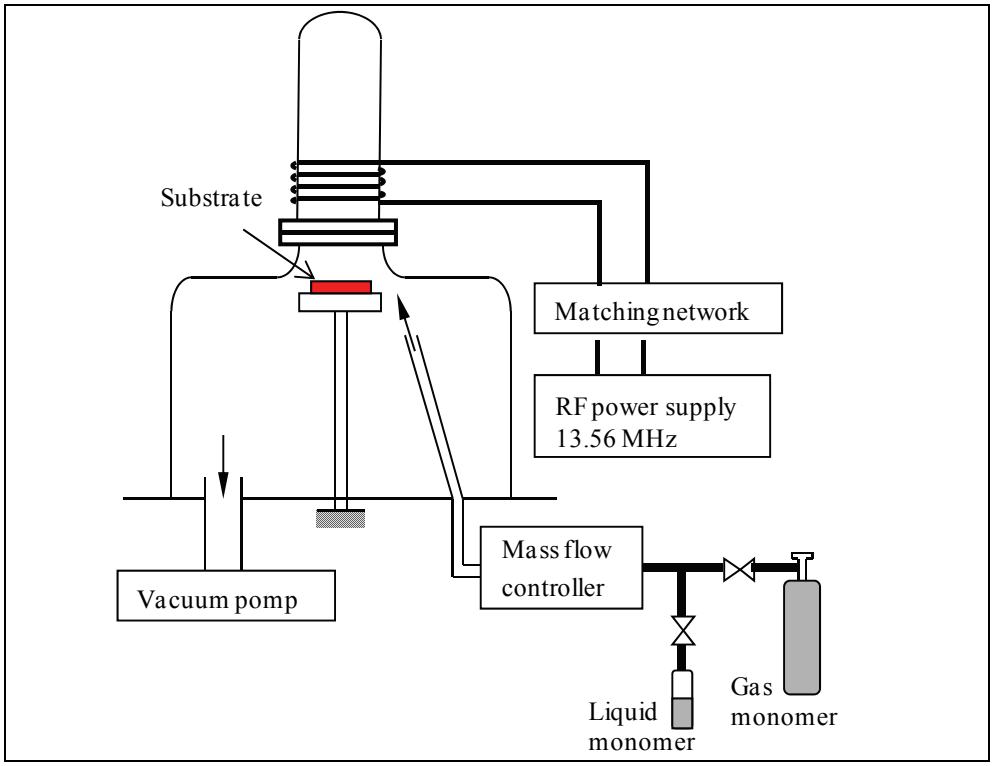

Fig. 1. Schematic representation of typical apparatus for plasma polymer.

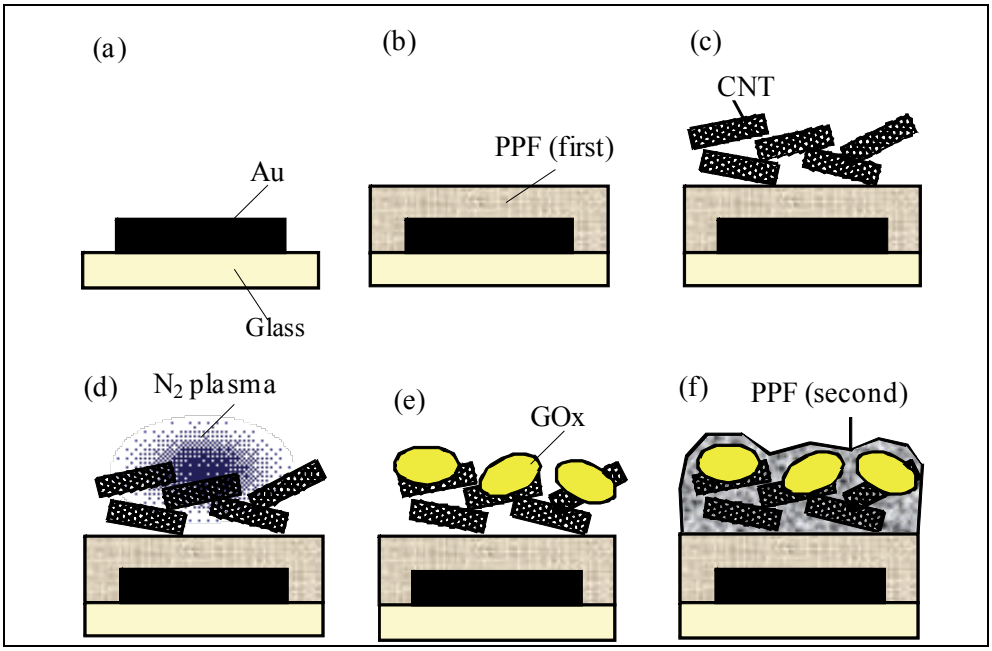

Fig. 2. Schematic representation of the fabrication of an amperometric biosensor based on CNT and PPs. (a) Au electrodes are sputtered onto a glass substrate through a metal mask. (b) A 6-nm-thick acetonitrile plasma-polymerized film (first PP) was deposited. (c) Solution casting is used to form the CNT layer. (d) Nitrogen plasma treatment of the CNT layer. (e) Solution casting of the enzyme layer onto the CNT layer. (f) Immobilized GOx is overcoated by a second PP.

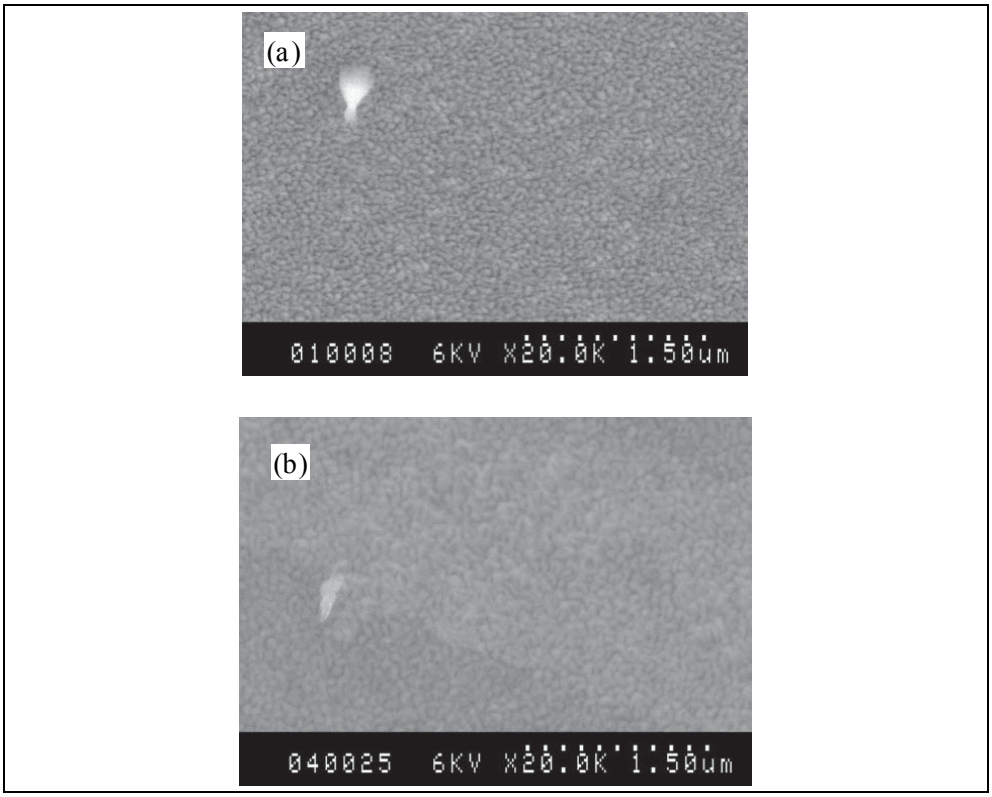

Fig. 3. Scanning electron microscopic image of (a) casting CNTs on the first PP and (b) the completed device.

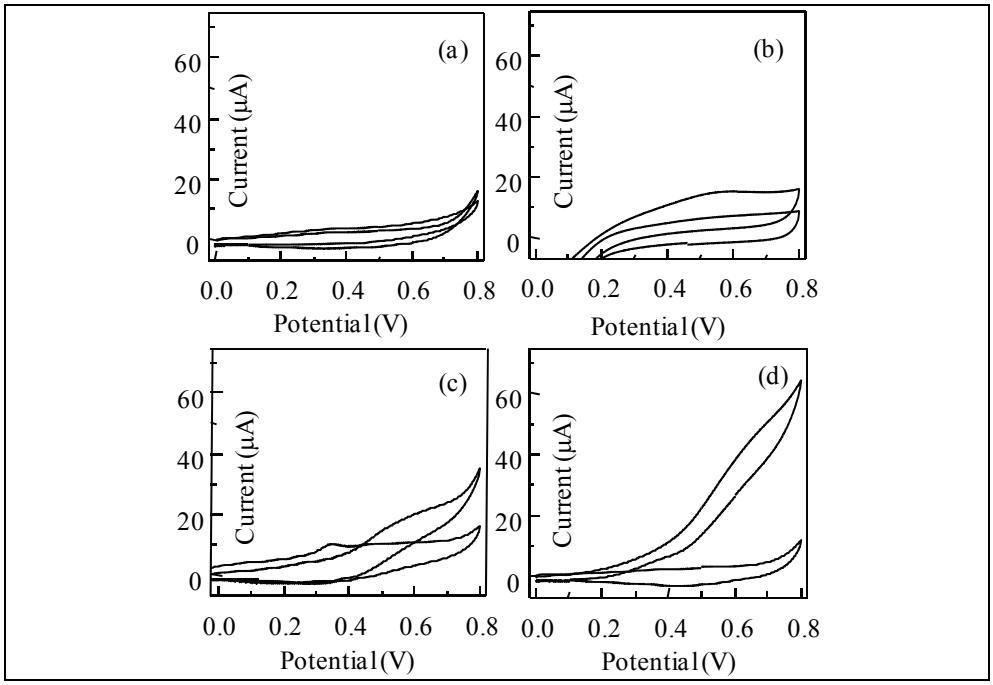

Fig. 4. Glucose response by cyclic voltammetry in the absence and the presence of glucose. The sweep rate was 50 mV s^{-1}, the glucose concentration 48 mM, and the electrolyte used was a pH 7.4, 20 mM phosphate buffer solution. The structures of the devices are
(a) PP/GOx/PP/Au
(b) PP/GOx/PP/Pt
(c) PP/GOx/CNT/Au, and
(d) PP/GOx/CNT/PP/Au.

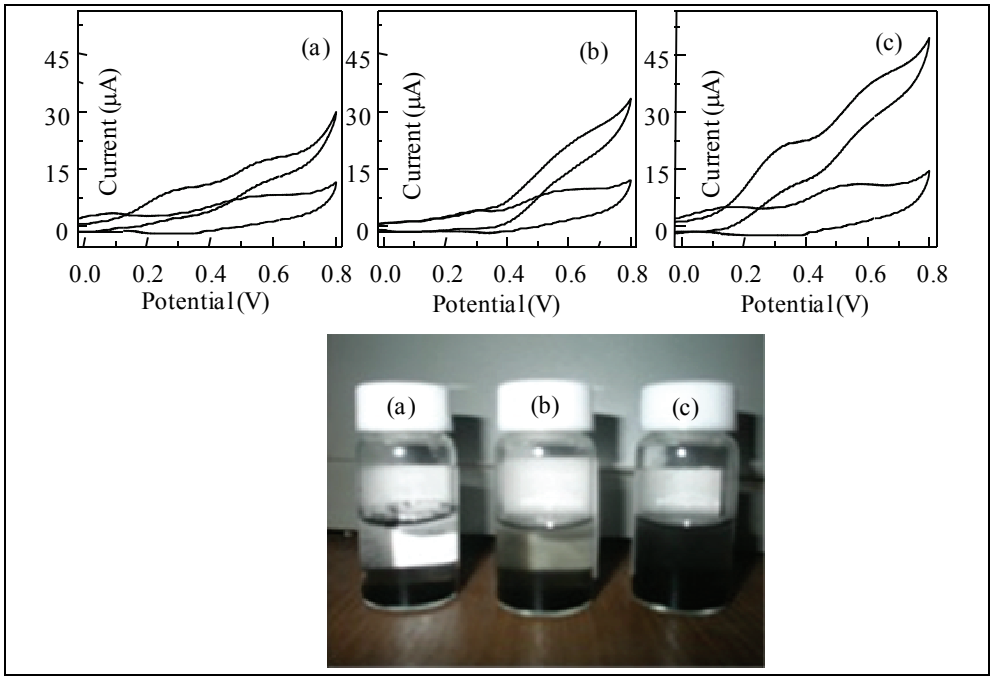

Fig. 5. Cyclic voltammetry of the biosensor response in the presence or absence of glucose. Sweep rate: 50 mV s^{-1}. Glucose concentration: 48 mM; pH 7.4; 20 mM phosphate buffer solution. Carbon nanotubes were dispersed in (a) buffer solution, (b) ethanol, and (c) 1:1 mixture of buffer solution and ethanol. Photograph: Vials of CNT dispersions after 4 h.

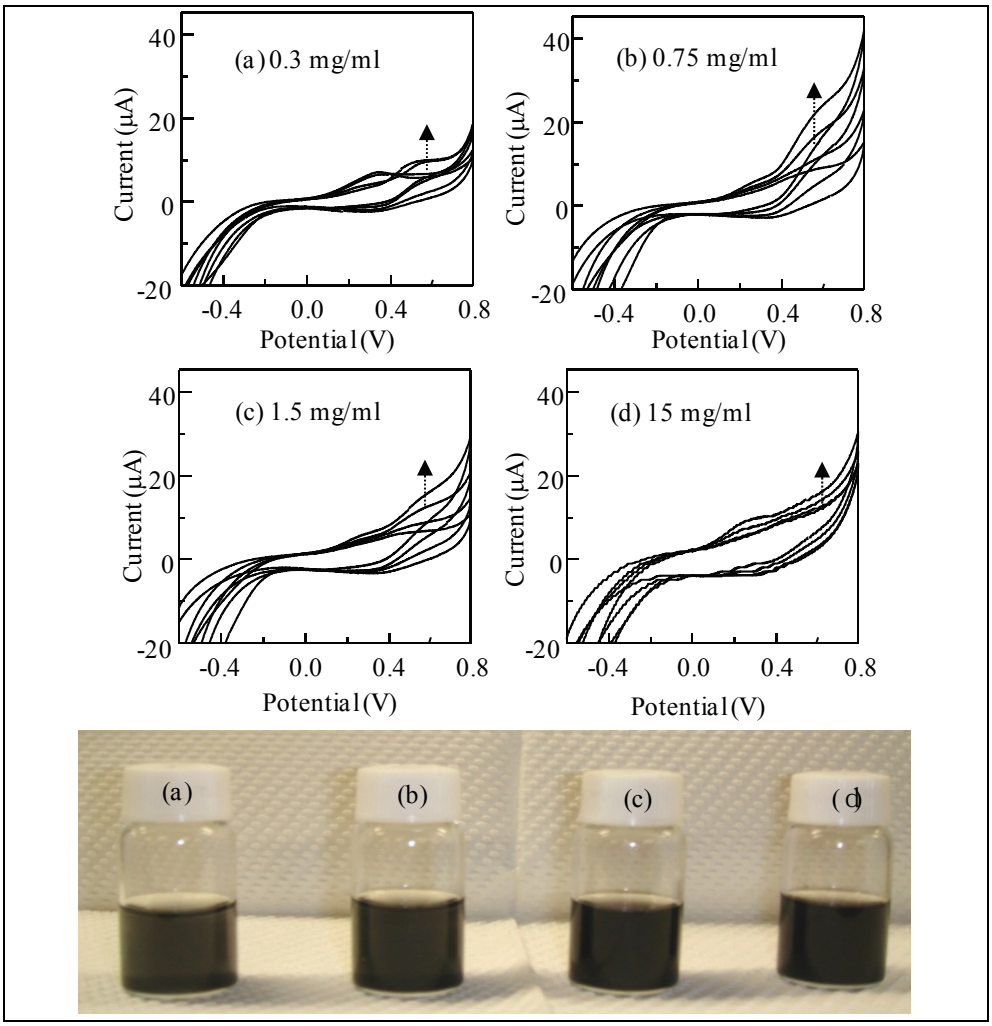

Fig. 6. Cyclic voltammograms of the fabricated amperometric glucose sensor using GOx, CNTs, and PP (PP/GOx/CNT/PP/Au) as a function of the CNT concentration used for casting the CNT layer. CNT concentrations: (a) 0.3, (b) 0.75, (c) 1.5, and (d) 15 mg mL^{-1}. Arrow directions indicate the glucose concentration increments at 0, 2.5, 14, and 48 mM. Conditions: 20 mM phosphate buffer; pH=7.4; 20 °C; scan rate, 50 mV s^{-1}; electrode area (geometric), 25 mm^2. . Photograph: Vials of CNT dispersions after 4 h.

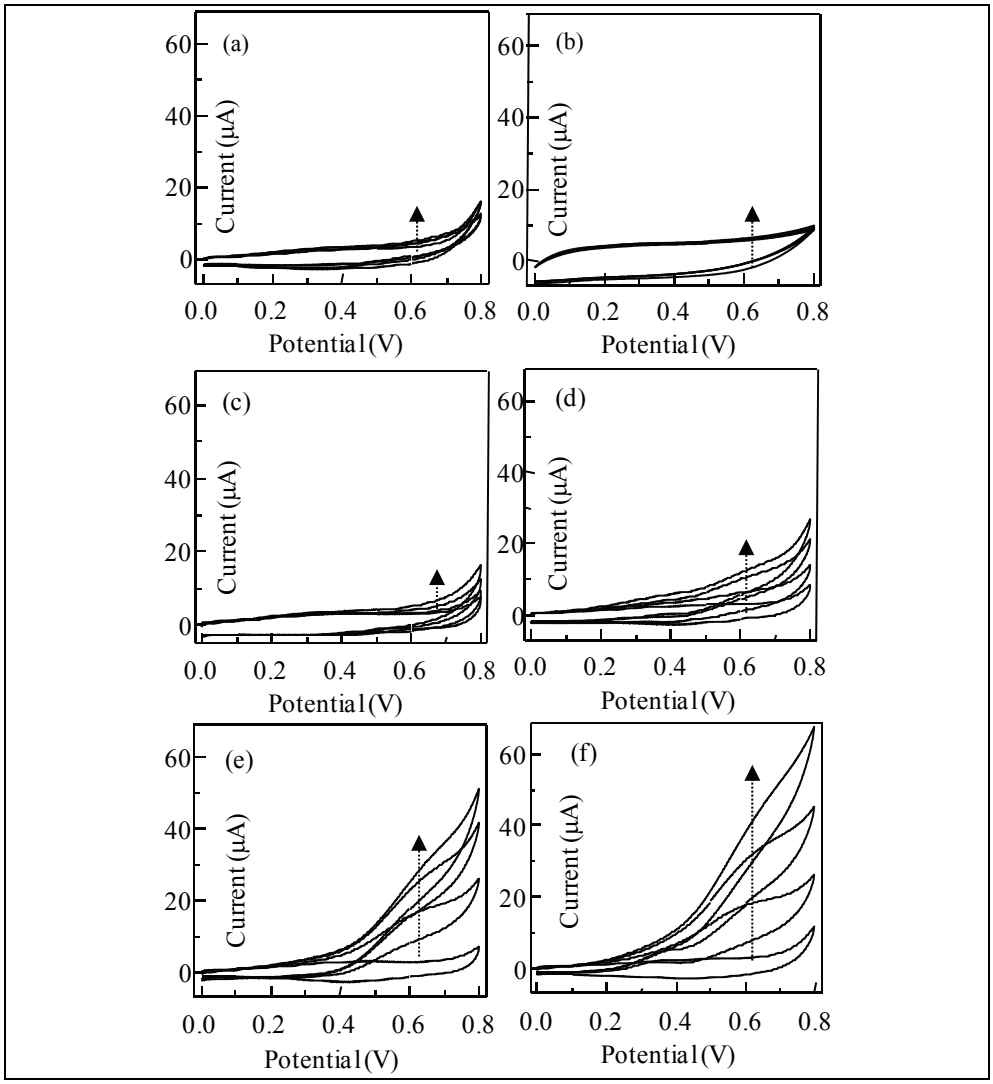

Fig. 7. Cyclic voltammograms of the fabricated amperometric biosensor using SWCNTs and PP in the absence and presence of glucose. Arrow direction represents the glucose concentration increments at 0, 2.5, 14, 35, and 48 mM. Conditions: 20 mM phosphate buffer; pH=7.4; 20 °C; scan rate, 50 mV s^{-1}; electrode geometrical area, 25 mm^2. (a) PP/GOD/PP/Au. (b) PP/GOD/CNT/PP/Au. (c) PP/GOD/PT-30W/CNT/PP/Au. (d) PP/GOD/PT-50W/CNT/ PP/Au. (e) PP/GOD/PT-60W/CNT/ PPF/Au. (f) PP/GOD/PT-70W/CNT/ PP/Au.Title of figure, left justified

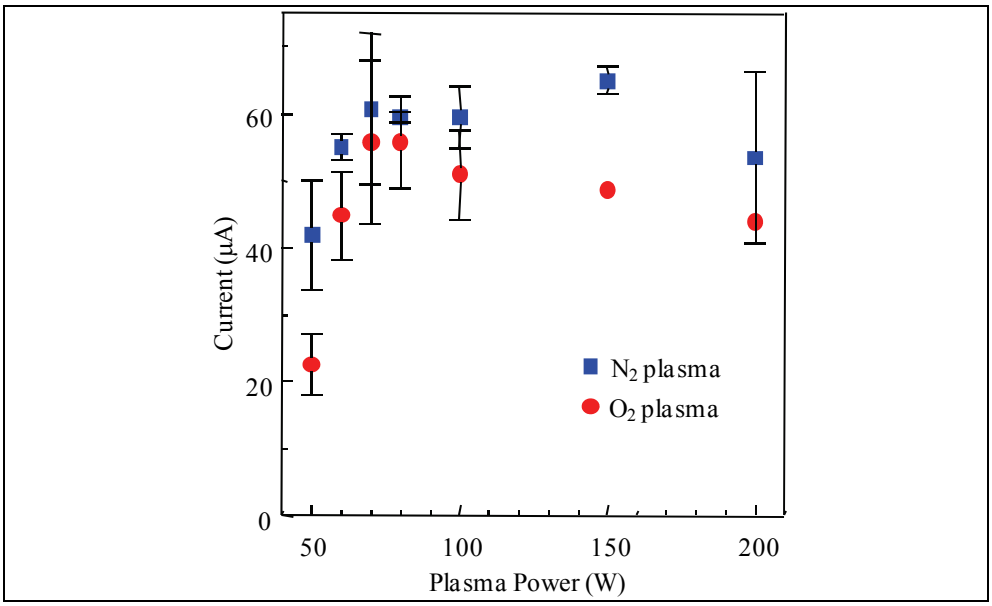

Fig. 8. Dependence of the current response on the plasma power for treatment of the CNT layer on the first PP. Cyclic voltammetry was performed at +0.8 V in the presence of 48 mM glucose, with a sweep rate of 50 mV s-1 in an electrolyte of pH 7.4 20 mM phosphate buffer solution.

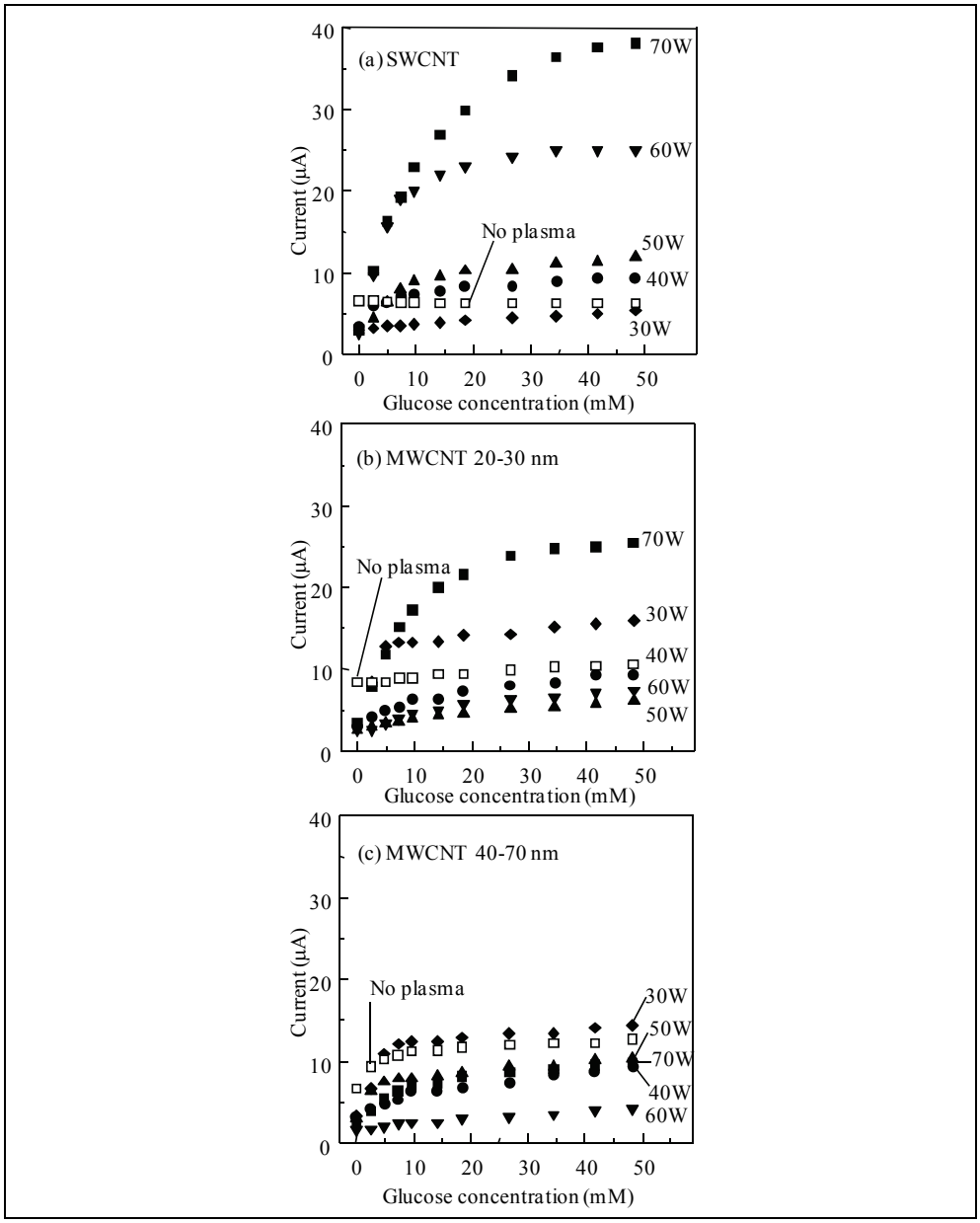

Fig. 9. Calibration of devices in 20 mM phosphate buffer (pH 7.4) with different types of CNTs, (a) SWCNTs, (b) 20-30-nm-diameter MWCNTs, and (c) 40-70-nm-diameter MWCNTs nm as a function of oxygen plasma power for treatment of CNTs: rhombus, 30 W; circle, 40 W; triangle, 50 W; inverse triangle, 60 W; closed square, 70 W; open square, no plasma. The oxidation current at +0.6 V vs. Ag/AgCl under cyclic voltammetry was used.

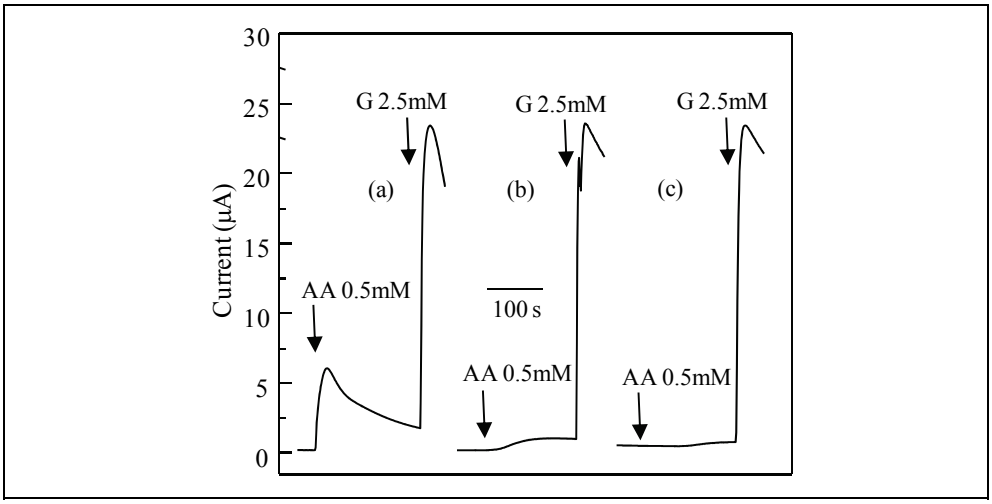

Fig. 10. Amperometric response to 0.5 mM ascorbic acid (AA) and 2.5 mM glucose (G). Acetonitrile plasma polymer coating on the immobilized enzyme: (a) no PP overcoating (GOx/CNT/PP/Au), (b) 10 nm PP overcoat, (10 nm PP/GOx/CNT/PP/Au), and (c) 20 nm PP overcoat (20 nm PP/GOx/CNT/PP/Au). The polarized potential was +0.8 V vs. Ag/AgCl. The electrolyte was a pH 7.4 20 mM phosphate buffer solution.

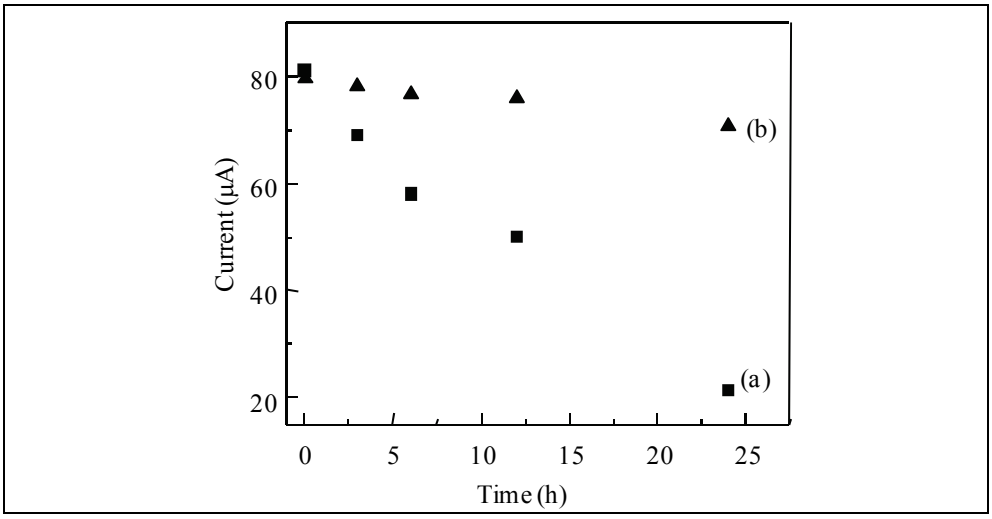

Fig. 11. Operational stability of the biosensor under continuous operation. The polarization potential was +0.8 V vs. Ag/AgCl at a glucose concentration of 48 mM, with an electrolyte of pH 7.4; 20 mM phosphate buffer solution. Working electrodes are (a) GOx/CNT/PP/Au (no overcoating) and (b) PP/GOx/CNT/PP/Au.

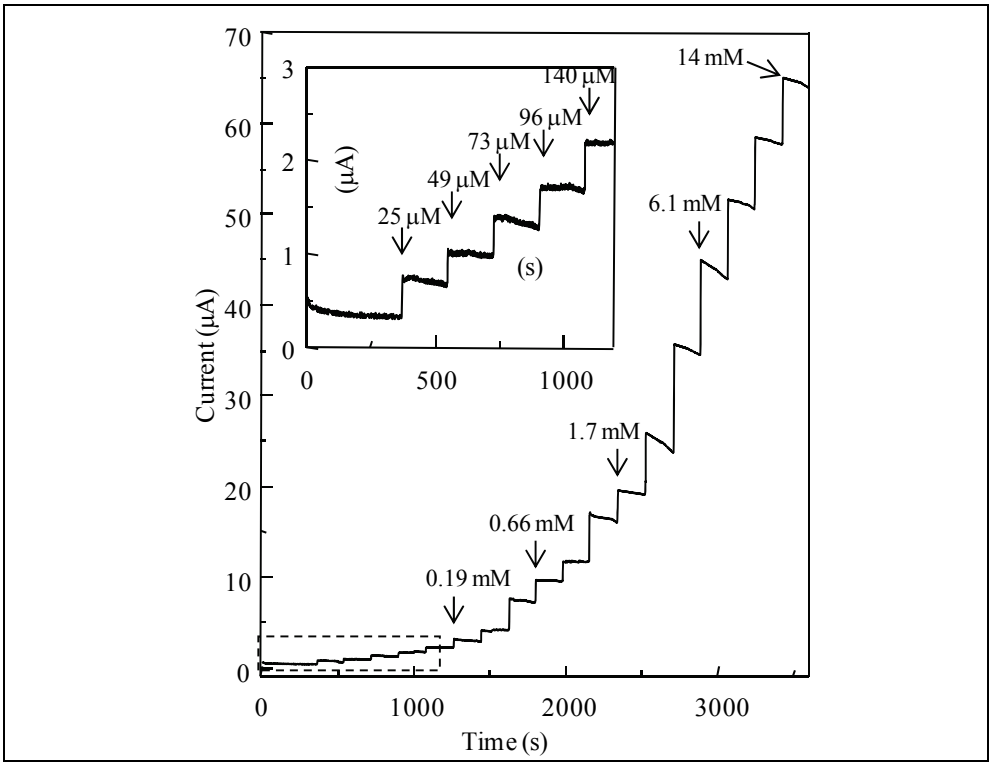

Fig. 12. Time-current response to sequential glucose addition at concentrations of 0.025, 0.049, 0.073, 0.096, 0.14, 0.19, 0.25, 0.45, 0.66, 0.88, 1.3, 1.7, 2.3, 4.2, 6.1, 8.1, 12, and 14 mM. The electrode was 20 nm PP/GOx/CNT/PP/Au, the polarized potential was +0.8 V vs. Ag/AgCl, with an electrolyte of pH 7.4 20 mM phosphate buffer solution. Inset: Enlargement of the region of lower glucose concentration.

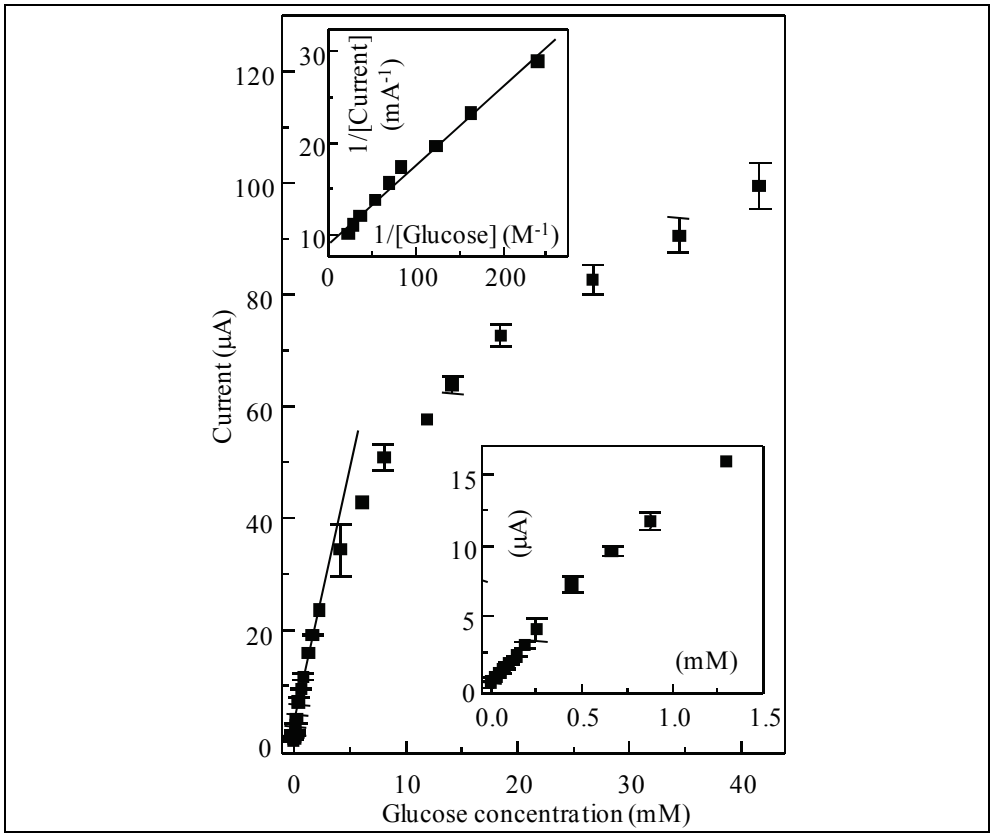

Fig. 13. Calibration plot for glucose response using the data in Fig. 12. Correlation line at low glucose concentration range (0-2.2 mM); sensitivity of 42 mA mM^{-1} cm^{-2} (r = 0.993). Lower inset: Enlargement of the low concentration range. Upper inset: Lineweaver-Burk plot. I_{max}, 0.44 mA cm^{-2}; K_M^{app}, 11 mM.

4

Design and Fabrication of Nanowire-Based Conductance Biosensor using Spacer Patterning Technique

U. Hashim, S. Fatimah Abd Rahman and M. E. A. Shohini
Nano Biochip Research Group
Institute of Nano Electronics Engineering (INEE)
Universiti Malaysia Perlis,01000 Kangar, Perlis,
Malaysia

1. Introduction

A biosensor can be generally defined as a device that consists of a biological recognition system, often called a bioreceptor, and a transducer [1]. The combination of nanotechnology and biosensor has leaded a new discovery called Nano-biosensor [2]. Advances in this field potentially created useful approaches to new detection methods and revolutionize the way in of biosensing. Nano-biosensor, although still an emerging technology, promise fast, accurate, and inexpensive ways to measure an extremely wide variety of analytes produced or consumed in biological and biochemical processes, as well as ways to measure more directly the activity of biological systems or their components [3].

One feature of DNA sensors that could make both goals attainable is the utilization of a transduction mechanism that is nano-scale and can be easily integrated with CMOS technology. The ultimate goal of researchers is to develop a suitable base requires a base that can interact individually, requiring a detector of a similar size [2]. Molecular electronic properties have usually been examined using electrodes with nanoscale wires (nanowires) as small as the molecular sizes, fabricated by electron-beam lithography (EBL), photolithography or electromigration methods [3-6]. However, these techniques are very expensive due to its low throughput. In this study we present parallel processes for nanometer pattern generation on a wafer scale with resolution comparable to the best electron beam lithography.

The focus of this work is the fabrication of nanowire based on spacer patterning lithography (SPL); a type of size reduction technique. The design and fabrication of nanowire using SPL require the proper selection and integration of material and methodology. Up to this point, we describe the design of specifying the process flow and material that is appropriate to fabricate the device using conventional CMOS process. The process flow involves every step in SPL including the deposition of a sacrificial layer, the definition of vertical step by means of lithography and etch-back process, the deposition of a conformal layer, final anisotropic etching and formation of gold pad by Physical Vapor Deposition (PVD).

Fig. 1. Step Requirement for fabricating Nanowire using SPL

1.1 Operation principle

The operation principle of the sensor is as follows. Any tiny size sample like DNA should be bound ligand with an absorbed receptor on the Si nanowires. When molecules are fixed between them, it can change the charge carrier density of the wires. This change of charge carrier density results in an effective change of conductance by time that can be monitored electronically. The sensor structure allows for direct conversion of molecular recognition and binding events to electronic signals. [3]

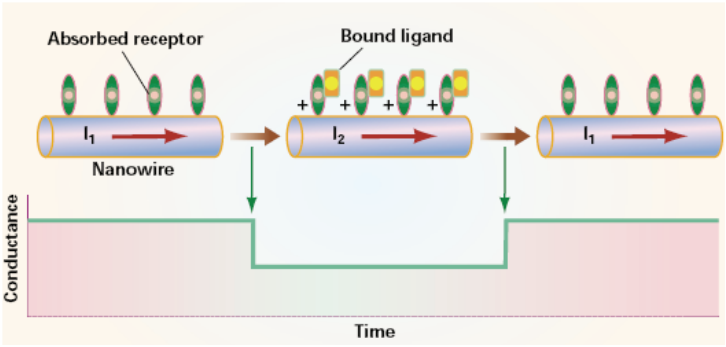

Fig. 2. Operation principle of nanowire filled with DNA [7].

2. Experimental details

In this research, the following flow is used to conduct the research starting from material used until the detection of DNA hybridization.

2.1 Starting material

The 4 inch silicon-on-insulator (SOI) wafers is used as starting material with a BOX thickness of 160 nm, a top Si layer of 160 nm thickness and boron doped 9–23 Ωcm. Reported benefits of SOI technology relative to conventional silicon (bulk CMOS) processing include:

- Lower parasitic capacitance due to isolation from the bulk silicon, which improves power consumption at matched performance.
- Resistance to latchup due to complete isolation of the n- and p- well structures.

Silicon on insulator (SOI) wafer is used to reduce parasitic device capacitance and thus improve the final device performance. Prior to fabrication process, the first step is to check the wafer type from its specification, measure wafer thickness (Si thickness), measure the sheet resistance and check the dopant type. After doing this, lightly scribe the backside of each wafer, protect the top surface, using the sribe tool provided. Mark gently but make it

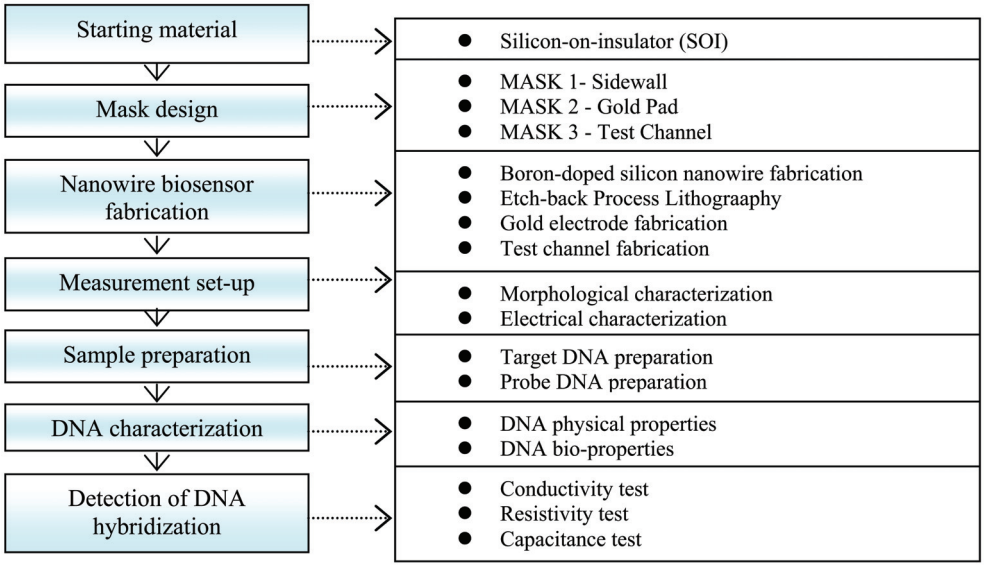

Fig. 3. Research methodology flow

visible and place scribed wafer in container. Wafer is cleaned before each process. Then, the SOI wafer is doped with boron on the silicon layer using spin on dopant technique. Concentration and sheet resistance is checked again to make sure the doping process gives effect to the structure.

2.2 Mask specification and layout design

As for the lithography process, three photomask are employed to fabricate the nanowire using conventional photolithography technique. Commercial Chrome mask is expected to be used in this research for better photomasking process. Mask 1 is used to develop the sidewall, Mask 2 is used for the gold pad and Mask 3 is for the test channel. The photomask is designed using AutoCAD and then printed onto a chrome glass surface.

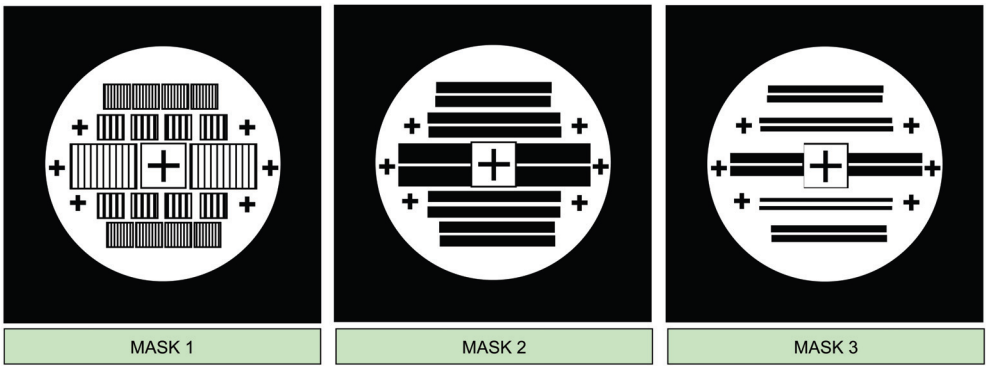

Fig. 4. Mask design for Nanowire fabrication

3. Process fabrication development

The fabrication of nanowire in this research uses the Spacer Patterning Lithography (SPL) method which is low-cost and compatible to standard CMOS fabrication process. Spacer patterning lithography coupled with anisotropic etching using ICP-RIE is the two main processes used in this experiment to fabricate this silicon nanowire. Electrical properties of silicon nanowire are then controlled by choosing a silicon substrate with an intended dopant type and concentration.

3.1 Spacer patterning lithography

The process begins with the deposition of the 200-500 nm layer layer of silicon oxide (SiO_2) as the sacrificial layer on a clean highly doped SOI wafer following by the first mask pattern on top of it. This SiO_2 and Si_3N_4 are deposited by Plasmalab 80 plus Compact Plasma System by Oxford Instruments, plasma enhance will deposit the SiO_2 layer before making the proper mask alignment on top of it. The conditions are 700 sccm N_2O, 150 sccm Ar, 1000 mT pressure, 30 Watt power and 150^{o}C temperature for SiO_2. After deposition, photo resist (PR) solution will be loaded onto the SiO_2 layer before making the proper mask alignment on top of the PR. By using MIDAS exposure system (by applying UV light through a mask), pattern from the first mask is transferred on the PR. Buffered Oxide Etch (BOE) can be used to remove the silicon oxide layer but in this case, vertical profile is needed, so dry etch is the choice to etch the silicon oxide layer. Prior to this, development and etching process using SAMCO ICP-RIE inductive coupled plasma – reactive ion etching at 2.5nm s^{-1}, the pattern layer is finally moved onto the SiO_2 layers. The conditions are 50 sccm CF_4, 30 sccm Ar, 250V bias, 800Watt ICP power and 5 Pa pressure. This recipe etched produced vertical sidewall profile with an angle 82^o-88^o. The residue PR is then removed using the Plasma-PreenII-862 system by Plasmatic Systems Inc. Then, a thin layer about 100nm-200nm of Silicon Nitride (Si_3N_4) is deposited on top of it. The conditions are 60 sccm Ar, 285 sccm N2, 600mT pressure, 25 Watt power and 150^{o}C temperature.

This thin layer of Silicon Nitride (Si_3N_4) is deposited uniformly onto the SOI to create the layer for spacer formation (the main process of the SPL technique). The spacer is then defined using ICP-RIE etching by removing the silicon oxide. The spacer formed will be the next mask for the highly doped crystalline silicon substrate. The nanowire is then defined using ICP-RIE etching by removing the silicon. This process is the critical step on fabrication process, since it determines the nanowire size and dimension as can see in Figure 5.

3.2 Gold pad contact formation

Prior characterization and electrical testing, contact point is formed by deposition of aurum (gold) material prior to the fabricated nanowire. Gold is used to have a good reliability via contact and it has a very good conductivity. This is to ensure the device has a good electron flow and no bias effect to the sensing nanowire.

A layer of 500nm thick of Aurum is deposited using E-beam Evaporator onto the surface of the fabricated nanowire. The layer is then coated and patterned using photolithography process to form the contact point. Aqua Regia is used for etching. Finally, the photoresist layer is removed to expose the gold pad for contact.

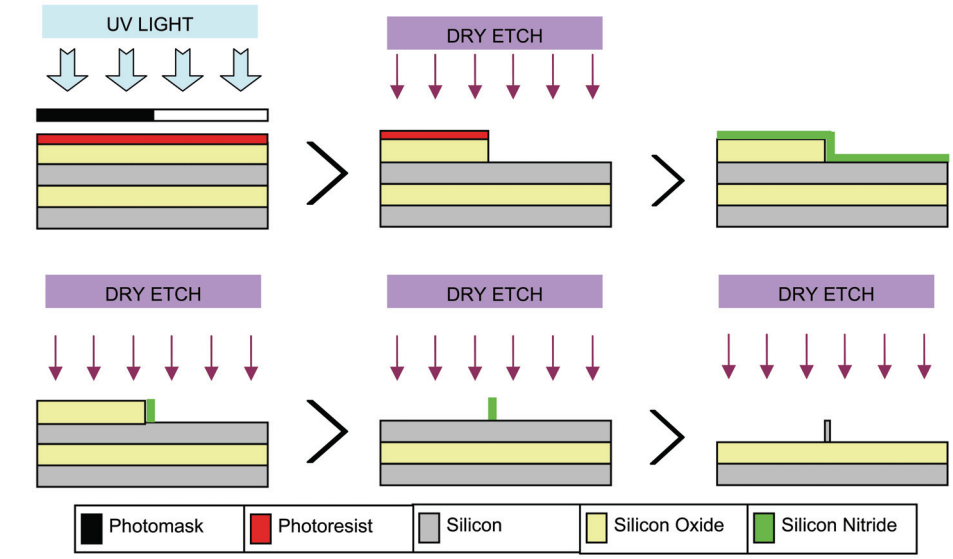

Fig. 5. Layer by layer alignment and patterning method.

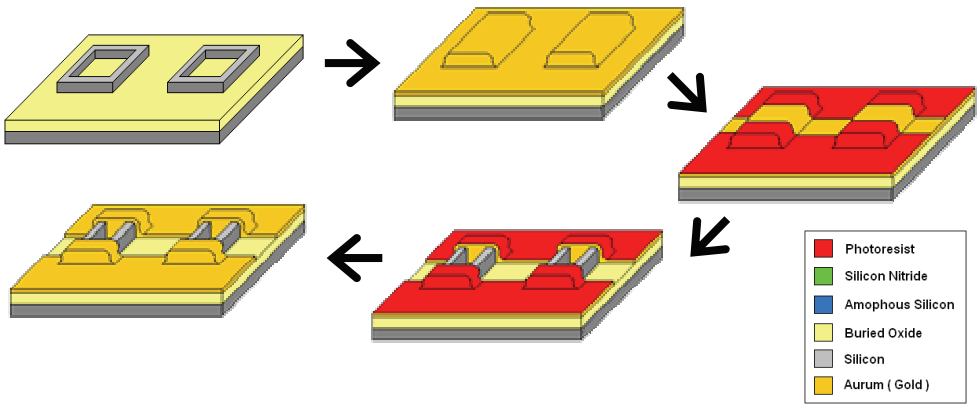

Fig. 6. Process flow of gold pad.

3.3 Test channel formation

Figure 7 shows the fabrication of the Si_3N_4 passivation layer which uses the Si_3N_4 to isolate the testing area and the electrical contact point. Starting with the deposition of the Si_3N_4 using Plasma Enhanced Chemical Vapor Deposition (PECVD), a layer of Si_3N_4 is deposited on the surface of the nanowire and the gold pad. Then, a photoresist is coated and patterned using photolithography process. Inductively Coupled Plasma Reactive-Ion-Etching (ICP-RIE) is used to etch the Si_3N_4 between the patterns and exposed the nanowire area for DNA sample drop and contact point. Finally, the photoresist layer is removed to form the Si_3N_4 passivation layer.

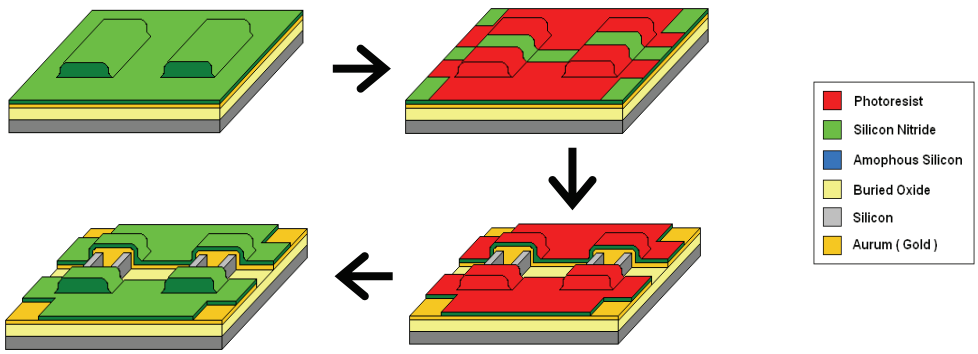

Fig. 7. Si_3N_4 passivation layer process flow

4. Detection of DNA hybridization

There are two types of sample needs to be prepared and tested in this experiment.

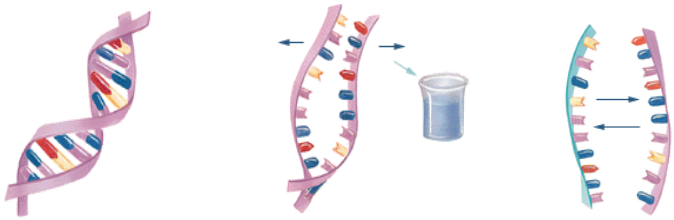

Fig. 8. DNA sample

Preparation of 2 sample known as separate ds-DNA (Probe DNA) and various unknown ss-DNA (Target DNA). The Probe DNA is a known reference sample DNA for testing the unidentified Target DNA. The mixture of these 2 DNA will hybridize or not is known earlier for testing purpose.

The process of identification starts with the Probe DNA is denatured by heat or chemical denaturant and placed in solution or on a solid substrate, forming a reference segment. Then, a various unknown ss-DNA (Target DNA) is prepared. Unknown DNA sample is introduced to the reference segment. The complement of the reference segment will hybridize to it. This concentration must be suitable to the size of nanowire area. Identification of electrical form is counter measured to test the sample and conclude the result. The semiconductor parameter analyzer (SPA) system is used to characterize the conductivity of the nanowire. Spectrum analyzer (SA) is used to manipulate the output signal and easier identification process.

A DNA molecule is positioned on the nanowires by electrostatic trapping from a dilute aqueous buffer. This technique was developed for the trapping of single molecules, and has been shown to be successful for a variety of nanoparticles.

In this procedure, the reference plane of the first-tier calibration was placed in the first pad, as described above. The reference plane of the second-tier calibration was located at the second contact pads fabricated on the silicon substrate. The signal line of this nanowire

fabricated in the second level of metal (metal 2), and its ground plane was fabricated in the first level of metal (metal 1). This allowed us to directly measure the scattering parameters of the contact pads we had fabricated on the silicon wafer.

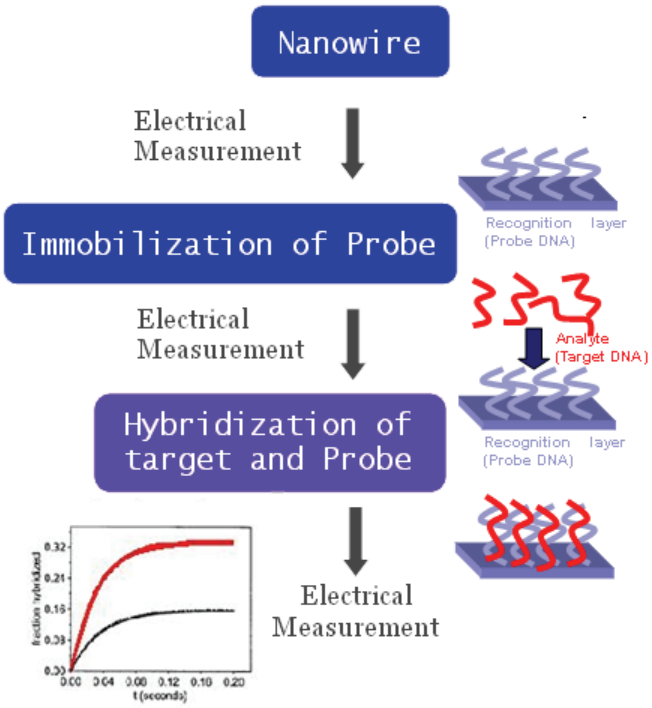

Fig. 9. Signal identification

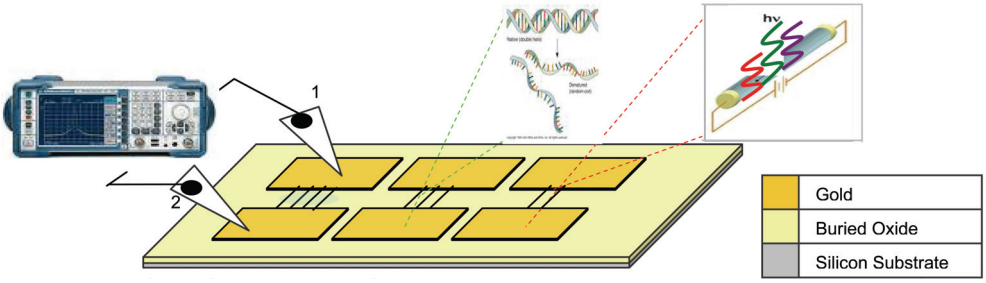

Fig. 10. Pad to pad measurement of different nanowire pattern using spectrum analyzer / semiconductor parameter analyzer

5. Results and discussions

A 1µm thick hard mask oxide is depositedon a SOI wafer and followed by 100nm thickness of Si_3N_4 conformal layer is deposited on the hard mask oxide by LPCVD. This Si_3N_4 layer

serves as a sacrificial support for the sidewall spacers patterning. The pattern transfer is carried out using MIDAS MDA400M UV with light source of 350 Watt intensity system through the photomask glass with chrome pattern to the 1 μm positive photoresist layer. After resist development, etching process is conducted by plasma reactive ion etching (RIE). The Si_3N_4 is removed by CHF_3/Ar based plasma etch, which provide high etch selectivity of Si_3N_4 to oxide layer. Based on Figure 11, after removing the oxide layer, the sidewall Si_3N_4 spacer is left and it serves as a hard mask to etch the underlying silicon layer to form as silicon nanowire. The resulting pattern sidewall profile was observed by scanning electron microscope. The pattern is not ideally vertical, showing some broadening feature from top to bottom layer but this condition is still acceptable for forming spacer using SPL technique. The SiO_2 etched produced vertical sidewall profile with an angle 82^o-88^o as can see in Figure 7. The length of nanowire totally depends on width of spacer. This certain restriction of nanowire length as long as the uniformity of anisotropic etching could cover up the whole wafer size.

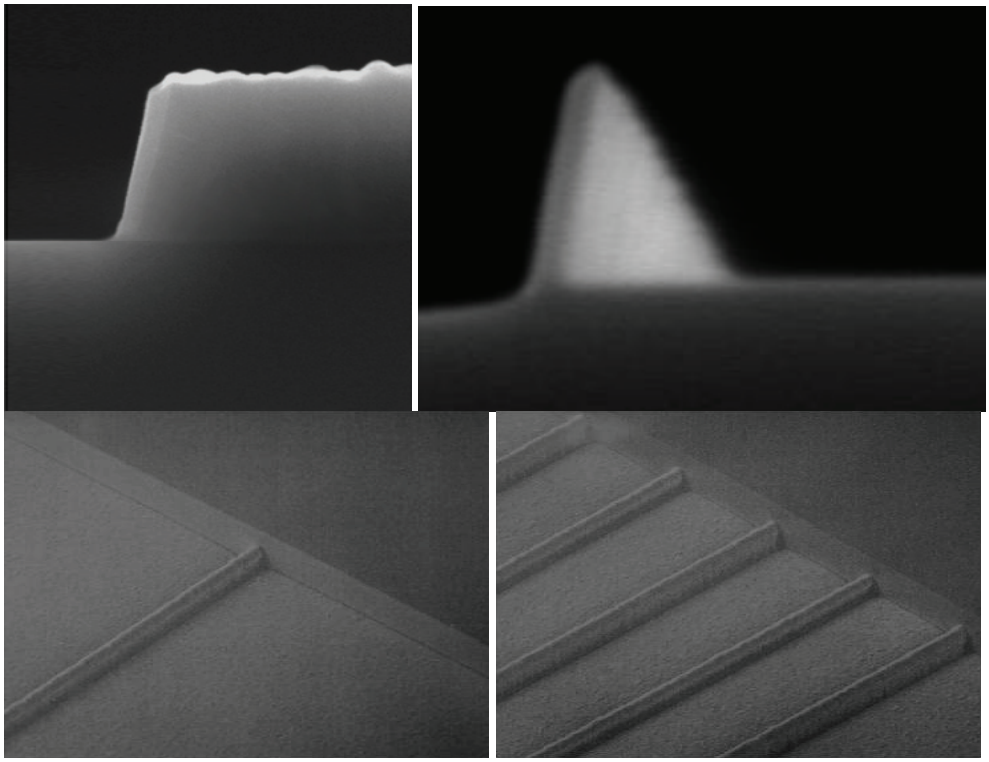

Fig. 11. Image of sidewall and spacer formation under SEM

The height of the spacer were not perfectly the same because of the Si layer is over etched during etch back process and it is not easy to confirm the height of two separating layer while etching.

Subsequently, the silicon layer is then anisotropically etched by CF_4/O_2 based plasma ion etch. This nanowire is formed on a top of 90 nm silicon layer with underlying of 150 nm

oxide layer and boron-doped of 9-23 ohm-cm. The hard mask oxide is removed by the same recipe from before. Figure 12 shows SEM photographs of the nanowire.

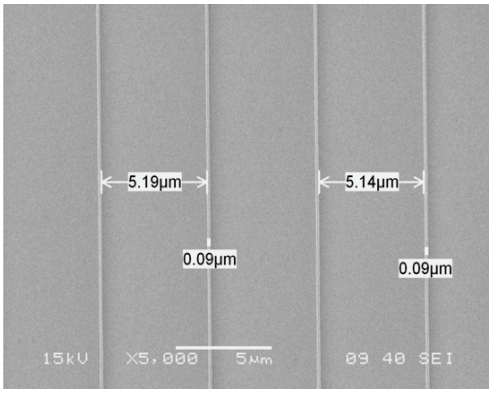

Fig. 12. The SEM image of the silicon nanowires.

Then, the two metal electrodes which are designated as source (S) and drain (D) are fabricated on top of individual nanowire using photolithography process. A 10 nm of Ti and followed by 50 nm of Au layer is evaporated on the silicon nanowire surface. Aqua regia was used to etch the Au layer and Ti layer in room temperature. Au is used as probing point because of good conductivity and low interconnection resistance.

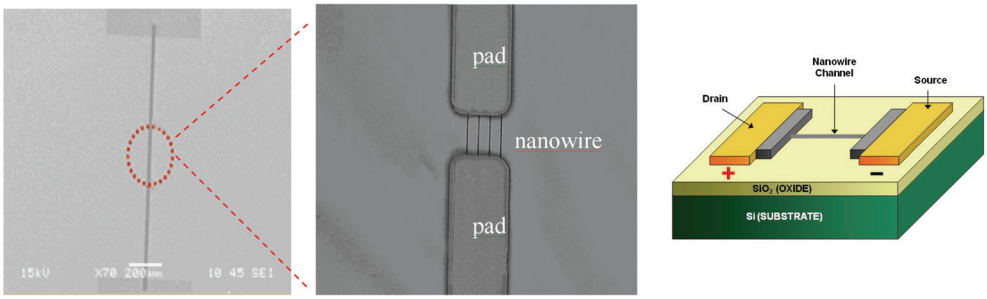

Fig. 13. HPM image observed the connected nanowire between the two electrode pads and the 3-D model of overall pattern fabricated on the sample.

Characterization and optimization of the fabricated nanowire is the crucial steps in the development of this biosensor. It's extremely important to produce the perfect nanowire at the nano-scale resolution [9].

6. Summary

The sublithographic nanowire was fabricated by the spacer lithography. We have shown an example application of these techniques. Experiments show the nanowire conductive conductor can be fabricated by spacer lithography and used for the detection of DNA hybridization without labeling. DNA hybridization was detected by conductance measurements, and the conductance was found to decrease as input frequency decreases when hybridization occurs. Due to the full compatibility with silicon microfabrication

technology, DNA chips without any requirement of labeling process are thus practical which can be capable of cost reduction and dramatically speed up evaluation of DNA hybridization.

7. Acknowledgement

The authors wish to thank Universiti Malaysia Perlis (UniMAP), Ministry of Science, Technology & Innovation (MOSTI) and Ministry of Higher Education for giving the opportunities to do this research in the Micro & Nano Fabrication Cleanroom. The appreciation also goes to all the team members in the Institute of Nanoelectronics Engineering especially in the Nano Biochip Research Group.

Biographical notes:

Uda Hashim received his PhD in Microelectronic from Universiti Kebangsaan Malaysia (UKM) in 2000. He is a Professor and Director of the Institute of Nano Electronic Engineering in Universiti Malaysia Perlis (UniMAP), Malaysia. He is the core researcher of microelectronics & nanotechnology cluster and also the team leader in the UniMAP Nano-Biochip Research Group. His current research interest includes Research Managements, Nanoelectronics, Biochips, E-Beam Lithography, Photolithography, Nano-structure formation, Semiconductor processing, CMOS process and devices. He has produced more than 100 academic papers in journals as well as conference proceedings worldwide in nanotechnology especially in nanoelectronics related field of research.

8. References

[1] Arnoldus Jan Storm, *Delft University Press*, pp. 1-2, 2004.

[2] Y. Okahata, T. Kobayashi, K. Tanaka, and M. Shimomura, *American Chemical Society, 120*, pp. 6165, 1998.

[3] http://en.wikipedia.org/wiki/Biosensor

[4] International Union of Pure and Applied Chemistry. "biosensor". *Compendium of Chemical Terminology* Internet edition.

[5] Umasankar Yogeswaran and Shen-Ming Chen, 21 January 2008, *A Review on the Electrochemical Sensors and Biosensors Composed of Nanowires as Sensing Material*

[6] Muhamad Emi Azri Shohini and Uda Hashim. *Nanogap Gold Electrodes by Spacer Lithography for DNA Hybridization Detection.* Proceeding Malaysian Technical Universities Conferences on Engineering and Technology. Vol. 2. pp. 292-295. March 8-10 2008, Kangar, Perlis.

[7] James F. Klemic, Eric Stern and Mark A. Reed. *Hotwiring Biosensor*. Nature Biotechnology, Vol. 19, 2001.

[8] Uda Hashim, S.Fatimah Abd Rahman, M. Nuzaihan Md Nor and S. Salleh. *Design and Process Development of Silicon Nanowire Based DNA Biosensor using Electron Beam Lithography*. IEEE proceeding of International Conference on Electronic Design, pp. 1-6, 2008, Penang, Malaysia.

5

Complementary use of Label-Free Real-Time Biosensors in Drug Discovery of Monoclonal Antibodies

Yasmina Noubia Abdiche
Pfizer, Inc
United States of America

1. Introduction

Biosensors measure the real-time reversible interactions between biologically-relevant molecules independent of labels. Typically, they harness an optical phenomenon to detect the binding of a solution molecule (analyte) to its immobilized partner (ligand) on a sensor and record the output as a "sensorgram", which tracks the binding signal in arbitrary units proportional to mass sensed at the surface of the biosensor as a function of time. These cutting-edge biophysical tools are revolutionizing our understanding of molecular-level processes because they reveal an entire binding profile between unlabeled reactants and dissect it into kinetic components from which an affinity can be deduced. By definition, the affinity or equilibrium dissociation constant (K_D, in units of molar concentration, M) is the ratio of the kinetic rate constants (k_d/k_a) where k_d is the dissociation rate constant in units of reciprocal seconds (1/s) and k_a is the association rate constant in units of 1/Ms. Knowing the affinity of an interaction is important to drug discovery because it affects the dose at which a drug is efficacious; drugs that bind their targets tightly can be administered at lower levels than those that bind weakly and thus are less likely to exhibit undesirable side-effects and are more cost-effective. End-point analyses, like ELISA, are less informative and rely upon labeling the reactants and adsorbing one of them, which can spoil their native activity, give high non-specific background signals, and limit the scope of an assay. Biosensors are commonplace in industrial and academic research laboratories worldwide and the Biacore technology has dominated the commercial sector for almost two decades. Recently, other manufacturers have innovated on the concept of a flow cell and how samples are handled to increase the number of interactions that can be studied simultaneously in an automated mode, enable longer measurements, and consume less sample (Rich & Myszka, 2007).

1.1 Diverse biosensor configurations

Fig. 1 depicts the way in which three different biosensor platforms address samples. The Octet is a fairly new technology that uses bio-layer interferometry by employing fiber-optic sensors incorporated on disposable tips. Another emerging technology, the ProteOn, uses surface plasmon resonance (SPR) and gold sensor chips, as does the Biacore. For more information about the principles upon which these detectors are based, the reader is referred to the manufacturers' websites; www.fortebio.com, www.bio-rad.com, and

www.biacore.com. By reversing the configuration where now the sensors move to the samples, the Octet renders the microfluidics that delivers samples to a stationary sensor chip in the ProteOn and Biacore systems, unnecessary. The Octet adopts a well-based dip-and-read format in which a column of up to eight sensor tips immerses into samples held in an open shaking microplate (Fig. 1A). Binding steps are defined by moving these sensors along the rows in the plate and the tips are discarded at the end of the assay. Dipping into samples rather than injecting them allows the Octet to measure longer association times and re-use samples within an assay or recover them for other uses. The ProteOn also processes samples in parallel, delivering them via six injections that flow perpendicularly to create a unique six-by-six interaction array (Fig. 1B). This generates 36 "reaction spots" (shown by the red squares in Fig. 1B) where flowpaths intersect and 42 "interspots" (in each direction), which provide a local-referencing option as an alternative to traditional whole-channel referencing. In contrast, the Biacore 3000 injects one sample at a time over up to four serially-addressed flow cells, one of which typically serves as a reference channel (Fig. 1C).

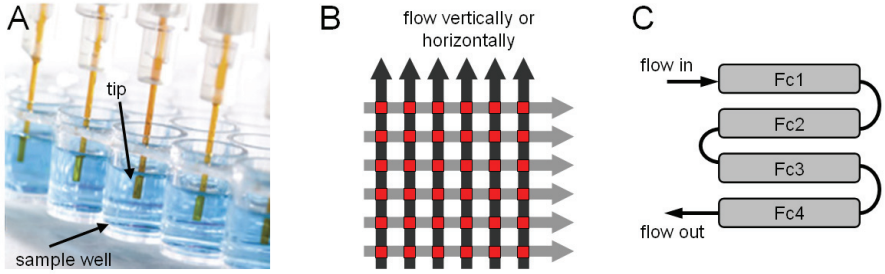

Fig. 1. Sample addressing in (A) Octet QK, (B) ProteOn XPR36, and (C) Biacore 3000 biosensors. The sample plate used in A is black.

The above-named SPR platforms support a limited number of immobilized ligands per experiment and rely upon being able to regenerate them. In contrast, the Octet can analyze up to 96 ligands per experiment on inexpensive single-use sensors that can be regenerated to make an assay more cost-effective. The throughput offered by the ProteOn may make regeneration unnecessary if the 36 interactions that can be addressed in a single binding cycle cover all the desired permutations. An unique advantage of the Octet's configuration is that ligands can be loaded *offline* onto batches of sensors, which increases the number of ligands that can be studied in a single run and speeds up the assay because fewer steps need to be performed online.

1.2 The importance of benchmark studies

It is important to assess the performances of emerging technologies relative to well-establish ones since biosensors are now routinely multiplexed to meet the demands of drug discovery for higher throughput. Determining whether there is consensus across different biosensor platforms operated by independent users has been a theme of several benchmark studies (Rich et al., 2009; Navratilova et al., 2007; Katsamba et al., 2006; Papalia et al., 2006; Cannon et al., 2004; Myszka et al., 2003). The largest and most recent of these engaged 150 participants from 20 countries who used instruments from ten different manufacturers. These collaborations enhance the biosensor community's ability to design experiments and provide insights into the variability of biosensor data where it can become difficult to

discriminate between sub-optimal instrument quality and an unskilled user. Inspired by these studies and the continuing evolution of biosensors, we compared the performances of two parallel-processing platforms, namely the Octet QK and the ProteOn XPR36 interaction array, head-to-head with the serial flow Biacore 3000 unit that represents the current "workhorse" of the biosensor research community as judged from it being the most frequently cited platform in the literature (Rich & Myszka, 2008). First, we addressed binding kinetics which is perceived as the signature role of biosensors based upon the abundance of literature on the topic. Then we explored competitive binding which, despite its relevance to drug discovery, is scarcely reported on in the literature.

2. Comparing binding kinetics from different biosensors

2.1 Model interaction system

For the purpose of comparing instruments side by side and to enable other investigators to reproduce our work, we adopted a commercially available antigen/antibody pair as a model system. The murine monoclonal antibody 4901 (Wong et al., 1993) was chosen because it binds various forms of calcitonin gene-related peptide (CGRP) with affinities that fall within a measurable range (high picomolar to mid-nanomolar) and allows for facile regeneration in all assay orientations. CGRP is implicated in migraine and other types of pain and thus interfering with its biological activity is relevant to drug discovery (Geppetti et al., 2005). We studied wild-type (1-37) rat-CGRP-alpha (rCGRPα) and 1-37, 26-37, and 32-37 forms of human-CGRPα (hCGRPα), which spanned molecular masses of 609Da to 3806Da and bound antibody 4901 with affinities ranging from 0.5nM to about 500nM. We oriented the assay in three different ways. First, we presented naked peptides to antibody-coupled sensors. Secondly we presented Fab fragments to N-biotinylated peptides that were captured via streptavidin sensors. Lastly, we deduced an affinity of the CGRP/4901 interactions indirectly via solution competition. The following sections describe each assay orientation as published elsewhere (Abdiche et al., 2008).

2.2 Binding solution antigen to sensors coupled with antibody

When the goal is to generate binding kinetics, it is prudent to present a monomeric partner in solution so that its binding can be modeled easily without interference of avidity (Myszka, 1999). Therefore, one way to study the CGRP/4901 interaction was to allow the solution peptides to bind amine-coupled antibody. None of the peptides could be detected directly on the Octet due to their binding signals being within instrument noise, but all were clearly visible on the SPR platforms; small molecule analysis is routine on the Biacore 3000 (Navratilova et al., 2007; Papalia et al., 2006; Cannon et al., 2004; Myszka et al., 2003) and was first described on the ProteOn by Bravman et al., 2006. These authors introduced a method called "one-shot kinetics" that exploits the parallel injection mode of the ProteOn to deliver in a single step a six-membered dilution series of the analyte over six surfaces of immobilized ligand with varying binding capacities. This generates a robust data set because a large number of binding curves are fit simultaneously to converge upon an unique pair of kinetic rate constants, whose ratio gives a global affinity for the interaction. Using this method, we analyzed four peptides binding to multiple levels of coupled 4901 by regenerating the immobilized antibody after each "one-shot" series and duplicating every injection. The kinetic analysis of one of these peptides, namely hCGRPα 32-37, is shown in Fig. 2A. This interaction was also amenable to an equilibrium analysis (Frostell-Karlsson et

al., 2000) as a non-kinetic route to the affinity owing to all the binding responses reaching plateau values within the association phase (Fig. 2B).

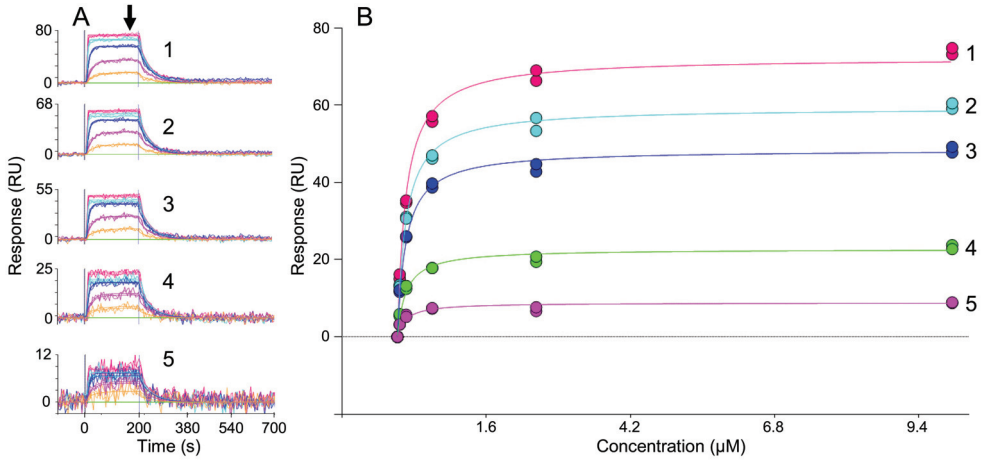

Fig. 2. One-shot kinetics on the ProteOn. (A) Primary data (noisy lines) for hCGRPα 32-37 binding five levels of coupled antibody 4901 (where 1-5 depict the high to low surface capacities) and their simultaneous fit to a simple kinetic model (solid lines) that gave a K_D of 147nM ±1% standard error for the fit. (B) Alternate analysis of the same data set by plotting the equilibrium binding responses (arrowed in panel A) from all five surfaces as a function of injected peptide concentration and fitting them simultaneously to a global K_D of 149nM ±3% standard error for the fit.

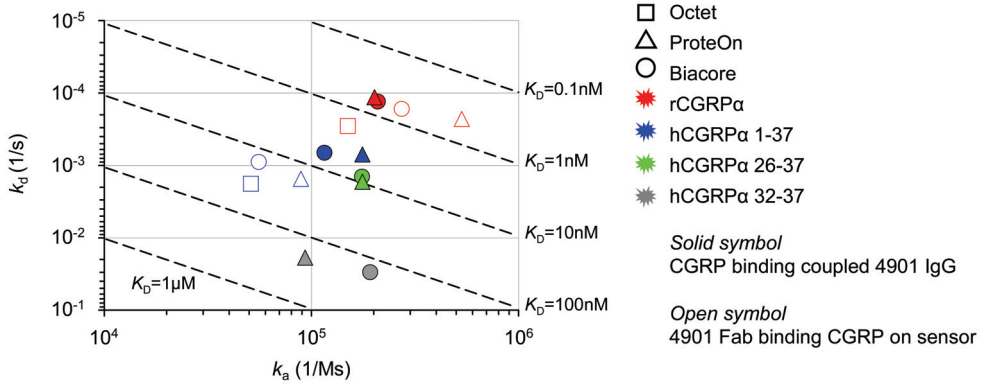

Fig. 3. Kinetic rate constants determined in two assay orientations. Not all permutations of biosensor, peptide, and assay orientation were investigated (see Table 1). Diagonal dotted lines trace the isoaffinities.

The ProteOn and Biacore platforms returned remarkably similar kinetic rate constants for an array of CGRPs binding coupled 4901 IgG (Fig. 3, solid symbols) and the affinity ranking was consistent with 4901's known species-selectivity and its epitope that incorporates the ten most C-terminal residues of CGRP.

2.3 Binding solution Fab to sensors coated with peptide

Another assay orientation that we explored was the direct binding of Fab to N-biotinylated full-length peptides on streptavidin or neutravidin sensors. This method was less convenient than the one described above because the reagents had to be modified. While the Fab was easily detectable on the Octet, it rebound the CGRP-saturated tips, to different extents depending upon the CGRP used, as evidenced by the deviation of the dissociation phase from a single exponential decay (black lines in Fig. 4A and 4B). While rebinding is a drawback of the Octet's well-based format, it was rectified by spiking the dissociation buffer with high concentrations of a tight-binding competing antigen (100μM rCGRPα) (red lines in Fig. 4A and 4B).

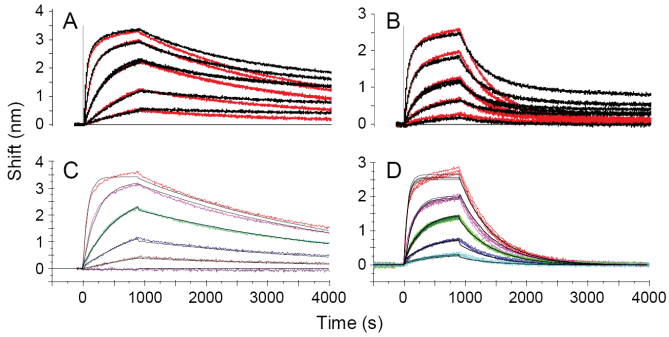

Fig. 4. Primary Octet data for "one-shot" kinetics of 4901 Fab binding streptavidin tips coated with (A) rCGRPα or (B) hCGRPα, dissociating them into buffer (black) or a sink (red). (C) and (D) show the kinetic fits (in black) of the "sinked" data (in color) in panels A and B, respectively. The global fit in D is for quadruplicate analyses on one column of tips.

Not only did the fitted kinetic rate constants and affinities (Table 1) describe the Octet data very well (Fig. 4C and 4D), but they agreed closely with those obtained for similar analyses on ProteOn and Biacore platforms (Fig. 5) and previously published values (Zeller et al., 2008). The Octet and ProteOn data were performed in a parallel "one-shot" kinetic mode whereas the Biacore data were collected in a serial multi-cycle mode by regenerating the surfaces after each injection.

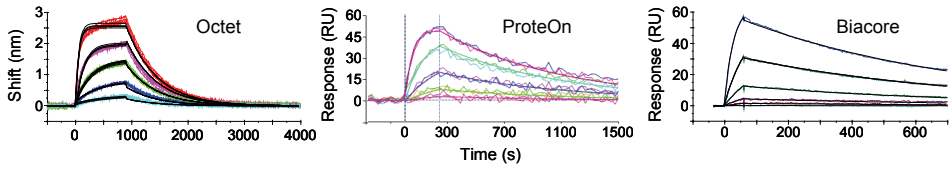

Fig. 5. Direct comparison of 4901 Fab interacting with hCGRPα surfaces on different biosensors. The measured data and their global fits are overlaid. The timing of the binding steps varied according to the biosensor used.

2.4 Determining affinity via solution competition

While the Octet cannot detect small molecules directly, it can access affinities indirectly via solution competition. An advantage of deducing a solution affinity is that it is unbiased by the

assay orientation and unaffected by the immobilization process. In this type of experiment, two binding partners are mixed in solution at various concentrations and the free concentration of one of them is probed by an immobilized molecule whose affinity is not being measured. An appealing feature of our model system was that the sensors could be coated with the tight-binding rCGRPα to probe the weaker affinities of the other peptides (Fig. 6).

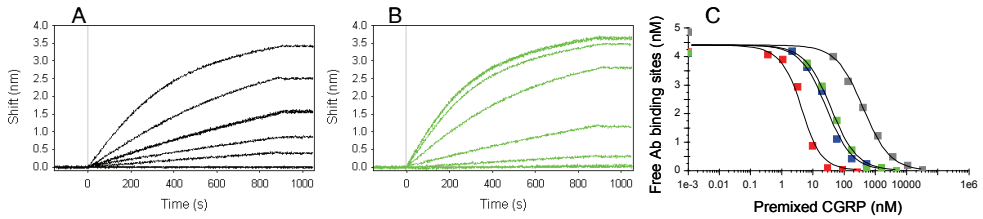

Fig. 6. Solution competition on the Octet using rCGRPα-saturated tips to probe for free antibody binding sites in (A) standard curve (twofold serial dilution of 4901) and (B) inhibition curve (fivefold serial dilution of hCGRPα 26-37 into a fixed concentration of 4901). (C) Overlay plot of the inhibition by rCGRPα (red) and 1-37 (blue), 26-37 (green), and 32-37 (grey) hCGRPα with fits in black.

Similar results were obtained on all three biosensors (Table 1), but only the Biacore was sensitive enough to work at the sub-nanomolar concentrations of fixed antibody binding sites needed to estimate the tight affinity of the rat peptide. Ideally, the concentration of the partner being detected at the sensor (in this case, the antibody) should be fixed (at or) far below the anticipated affinity of the solution interaction being measured in order for binding to be driven by affinity. If it is fixed far above the anticipated affinity of the solution interaction, then binding will be driven mainly by concentration and thus will instead determine the antibody's "active concentration" by titrating out CGRP in a stoichiometric manner.

2.5 Comparing assay orientations in affinity measurements

The ProteOn and Biacore returned virtually identical kinetics (Fig. 3) regardless of the assay orientation used, while those determined on the Octet were typically within twofold of them with direct binding of small molecules beyond its detection limit (Table 1). The affinity of the rCGRPα/4901 interaction was consistently around 0.5nM by SPR by all three methods, suggesting that neither binding partner had been adversely affected upon immobilization or modification. In contrast, the wild-type hCGRPα discriminated between the Fab and intact

CGRPα	CGRP binding coupled 4901			4901 Fab binding CGRP on sensor			Solution competition with IgG (or Fab)		
	Octet	ProteOn	Biacore	Octet	ProteOn	Biacore	Octet	ProteOn	Biacore
Rat 1-37	ND	0.565	0.569	2	0.612	0.432	ND	ND	0.54 (0.45)
Hu 1-37	ND	5.78	4	36	16.2	17.3	28 (22)	7 (20.3)	5.8 (18.2)
Hu 26-37	ND	8.13	9.55	NT	NT	NT	38 (27)	34 (23.6)	44 (23.1)
Hu 32-37	ND	147	202	NT	NT	NT	500 (280)	370 (224)	460 (239)

Table 1. Affinities (K_D, nM) of CGRPα/4901 interactions determined in various assay orientations on different biosensors. ND=not determined due to lack of sensitivity. NT=not tested. Values are the mean of replicate experiments (with typical standard deviation <20%) or the global fit of a single measurement (with typical standard error <1%)

IgG; the Fab bound hCGRPα on chip with a threefold weaker affinity than its IgG counterpart with the trend being corroborated by solution competition measurements. In a separate experiment, we confirmed that the naked and N-biotinylated peptides bound with identical kinetics when flowed over coupled IgG. Our results demonstrate that the assay orientation can affect the results as much or more than the biosensor used.

3. Exploring blocking assays on biosensors

The next application we explored was competitive binding because of its relevance to drug discovery. Most drugs functioning as antagonists are aimed at blocking a natural interaction such as that between a ligand and its receptor. Monoclonal antibodies (Abs) are becoming increasingly utilized as therapeutic entities in blocking these ligand-receptor interactions. An epitope is defined as the three-dimensional region on an antigen (Ag) where an antibody binds. Discriminating Abs based on their epitope rather than their apparent affinity for the target Ag is often more important because of established protocols for affinity maturation by protein engineering, while changing an epitope to a desired one is not typically possible. We decided to illustrate the use of biosensor blocking assays in the context of epitope binning (Abdiche et al., 2009).

3.1 Sandwiching assays in the context of epitope binning

Biosensors are essentially mass-based detectors. Therefore, determining whether an Ab blocks another's ability to bind Ag is simply a yes/no read-out, regardless of the assay orientation used. Under conditions that favor complete blocking, i.e. overlapping epitopes, no binding response will be detected at the sensor for any of the arrowed interactions in Fig. 7. In contrast, a binding signal at each of these interactions identifies a pair of Abs that can coexist on the Ag at distinct, non-overlapping epitopes and thus form a sandwich complex. Using this yes/no detection of the arrowed interactions, we assign Abs to epitope bins according to their blocking profiles relative to one another.

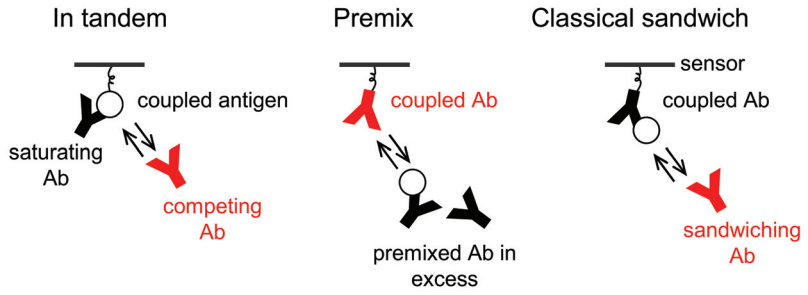

Fig. 7. Three assay orientations that can be used in epitope binning. In each case, the antigen binds the black Ab before the red Ab.

In order for two Abs to belong to the same bin, they must block one another and exhibit similar blocking profiles when each is paired with the other Abs in the test panel. Thus, the observation that two Abs block one another is necessary but not sufficient to conclude that they belong to the same bin. Once two Abs have been assigned to the same bin it is possible that another Ab will be discovered in the future that blocks one and not the other, thus

resolving them into different bins. We used six Abs (1-6) against a dimeric Ag to illustrate "in tandem" and "premix" methods and six different Abs (A-F) against an unrelated monomeric Ag to illustrate the "classical sandwich" method. We performed each assay on the three above-mentioned biosensors and since all biosensors gave similar results we only show data from the ProteOn because its two-dimensional interaction array makes it particularly well-suited to pairwise and combinatorial approaches to binning. The following sections describe each assay orientation in turn.

3.2 In tandem binning

In tandem blocking is probably the simplest conceptually. It involves coating the sensors with Ag and presenting two Abs one after another, namely a "saturating Ab" followed by a "competing Ab" (Fig. 7A). Fig. 8 shows how we performed an in tandem binning on the ProteOn and addressed 36 pairs of Abs in a single binding cycle with a complete set of six "self-blocking" controls along the diagonal of the interaction array. Consolidating the results into a matrix that can be read horizontally or vertically (Table 2) revealed three blocking patterns or "bins", namely Ab1 and 3; Ab2 and 4; and Ab5 and 6. Thus, Ab1 and 3 each sandwiched with Ab5 and 6, whereas Ab2 and 4 blocked all six.

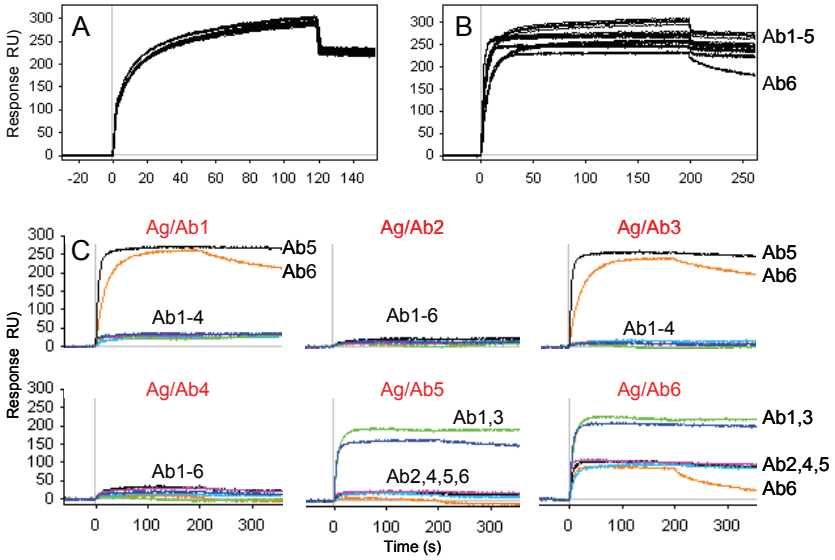

Fig. 8. In tandem binning. (A) Immobilizing Ag on all vertical channels. (B) Saturating with six Abs (1-6) on separate vertical channels. (C) Competing with the same Abs (1-green, 2-pink, 3-blue, 4-cyan, 5-black, and 6-orange) in the horizontal direction, where the plots are grouped and named (in red) by the "saturating" Ab that was prebound to the immobilized Ag.

3.3 Premix binning

We used the same set of reagents, namely Abs1-6 raised against a dimeric Ag, to illustrate the premix approach, which involved premixing the Ag separately with a large molar excess of each Ab, and then presenting these preformed complexes to an array of Abs coupled to

Saturating Ab	Competing Ab					
	1	2	3	4	5	6
1	SB	B	B	B	NB	NB
2	B	SB	B	B	B	B
3	B	B	SB	B	NB	NB
4	B	B	B	SB	B	B
5	NB	B	NB	B	SB	B
6	NB	?	NB	?	?	SB (?)

Table 2. Blocking matrix for in tandem binning. Y = blocks, N = does not block, SS=self-sandwich control, ? = intermediate.

the chip (Fig. 7B). Three controls are needed to validate the assay. First, the premixed Abs themselves in the absence of Ag should be presented to the naked coupled Abs to confirm that they do not bind one another non-specifically; indeed, one should confirm empirically that all three assay orientations depicted in Fig. 7 are free of non-specific Ab/Ab interactions. Second, the Ag is premixed with buffer to establish the Ag-binding response expected to each of the coupled Abs. Third, the Ag should be premixed with a solution counterpart of each coupled Ab on the chip to demonstrate that the premixed Abs are at high enough concentrations to self-block.

On the ProteOn, a premix binning experiment involves coupling an array of Abs along the vertical channels and then injecting Ag premixed with an array of Abs along the horizontal channels. Ag premixed with buffer is used as the sixth sample. Thus, in a single binding cycle, we addressed 36 interactions that incorporated six Ag-only controls, five self-blocking controls, and 25 sandwiching pairs. Relative to the Ag-only response, a premixed Ab either abolished or augmented binding, consistent with it respectively blocking or sandwiching with the coupled Ab (Fig. 9). Of the six Abs tested, only Ab6 (orange curve) did not fully block Ag binding at the concentration tested, even against itself when coupled on chip, consistent with this Ab's weak affinity for the Ag. The premix binnings agreed with those determined by tandem binning.

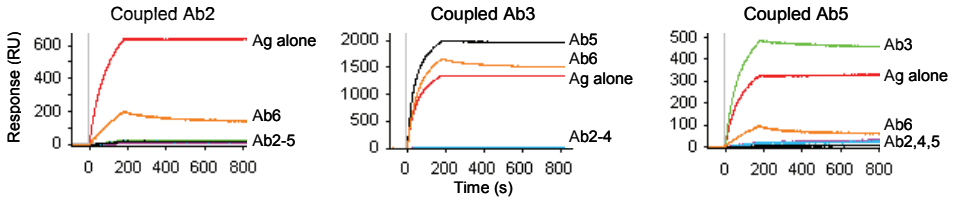

Fig. 9. Premix binning. One example of each blocking pattern is shown, grouped by coupled Ab. Premixed Abs are distinguished by color (2-pink, 3-green, 4-blue, 5-black, 6-orange, and none-red). The different response values of the three panels reflect the different coupled levels of Abs 2, 3, and 5.

3.4 Classical sandwich binning

The classical sandwich assay involves coupling an Ab onto the sensor, binding Ag, and then binding another Ab (Fig. 7C). Only monomeric Ags can be binned in this way because multivalent Ags could potentially bind the coupled Ab with one subunit and the solution

Ab with another subunit, even if the two Abs in question bound overlapping epitopes. On the ProteOn, this assay involves coupling six Abs in the vertical direction and then rotating to the horizontal direction to inject Ag followed by an array of Abs. By matching the sandwiching Abs to the coupled ones, a complete set of "self-sandwich" controls are generated along the diagonal of the interaction array. Based on the patterns of blocking activity shown for the six Abs in Fig. 10 when paired against one another, B and F binned together, D and E binned together, and A and C were unique because they each sandwiched with the other five Abs.

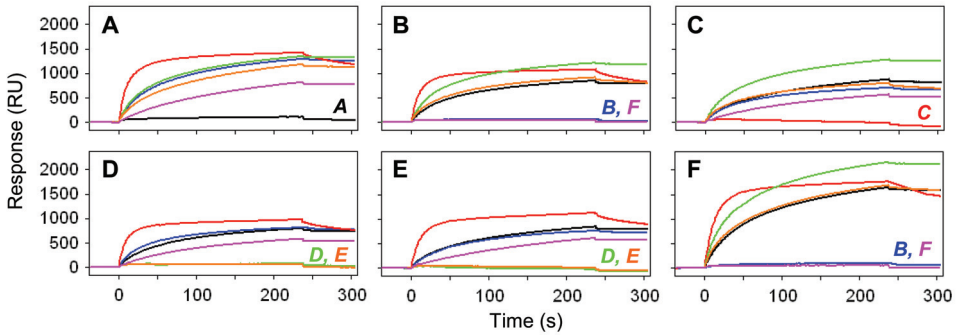

Fig. 10. Classical sandwich binning. Panels are grouped and labeled by the coupled Ab (A-F) and colored by the sandwiching Ab (A-black, B-blue, C-red, D-green, E-orange, and F-pink).

3.5 Intermediate responses

Although it is obvious in most of our examples when Abs did and did not bind, some Abs bound with intermediate responses that introduced uncertainty into whether they blocked or sandwiched. For example, the panel marked Ag/Ab6 in Fig. 8C shows an in tandem binning result where the competing array was exposed to "free" and "Ab-bound" Ag because Ab6 dissociated rapidly from the Ag (arrowed in Fig. 8B) rather than "saturating" it, as desired. However, when Ab6 was used in the "competing" step (orange curves in Fig. 8C) it clearly binned with Ab5 (black curves). Similarly, premixing Ab6 gave an intermediate binding response (orange curves, Fig. 9) because it was at a concentration below its affinity for the Ag (which was unknown at that time). In general, weak binders like Ab6 should be assigned the role of "competing" Ab when studied in tandem or "on chip" in the premix or classical sandwich methods. However, Abs that dissociate rapidly from their Ag may be inappropriate candidates for coupling in classical sandwich assays because there may be insufficient Ag bound when a sandwiching Ab is presented subsequently. Since weak binders can often give ambiguous results when studied in some assay orientations, it is prudent to switch the roles of the two Abs in question and/or explore other orientations to verify a result.

Ag heterogeneity is another possible source of ambiguity in interpreting biosensor blocking data because consensus across all three assay orientations assumes that the Ag is a uniform population. If it is not, the assay orientations may give conflicting outcomes.

4. Future directions

Recently, a number of next-generation Octet units have been released that provide solutions to some of the shortcomings of the QK platform. One improvement is a better signal-to-

noise that may now make the direct detection of small molecules possible and allow for lower surface capacities that may be preferred for kinetic runs. Moreover, their 384-well plate formats enable higher throughputs by addressing 16 interactions at once and trays of sensor tips can be re-racked to extend their lifetime.

5. Conclusion

Assay orientation can affect the results as much or more than the biosensor used. While the ProteOn XPR36 and Biacore 3000 platforms returned virtually identical affinities within each assay orientation tested, the Octet QK's lower sensitivity made it amenable to fewer uses and required a sink to abolish rebinding artifacts. Despite these limitations, the Octet's affinities were within twofold of those determined by SPR. Binning results were comparable across the three biosensors, but differed in throughput due to each platform's unique configuration that could be exploited in creative assay design. Biosensors are versatile and reliable tools that continue to evolve and provide valuable information on diverse molecules in a research, diagnostic, and drug discovery setting above and beyond binding kinetics.

6. Acknowledgement

I gratefully acknowledge Arvind Rajpal and Pavel Strop for their useful comments.

7. References

Abdiche, Y., Malashock, D., Pinkerton, A., Pons, J. (2008). Determining kinetics and affinities of protein interactions using a parallel real-time label-free biosensor, the Octet. *Anal. Biochem.,* 377., 2., (Jun) 209-217.

Abdiche, Y., Malashock, D., Pinkerton, A., Pons, J. (2009). Exploring blocking assays using Octet, ProteOn, and Biacore biosensors. *Anal. Biochem.,* 386., 2., (Mar) 172-180.

Bravman, T., Bronner, V., Lavie, K., Notcovich, A., Papalia, G., Myszka, D. (2006). Exploring "one-shot" kinetics and small molecule analysis using the ProteOn XPR36 array biosensor. *Anal. Biochem.*, 358., 281-288.

Cannon, M. et al. (2004). Comparative analyses of a small molecule/enzyme interaction by multiple users of Biacore technology. *Anal. Biochem.,* 330., 1., (Jul) 98-113.

Frostell-Karlsson, A., Remaeus, A., Roos, H., Andersson, K., Borg, P., Hämäläinen, M., Karlsson, R. (2000). Biosensor analysis of the interaction between immobilized human serum albumin and drug compounds for prediction of human serum albumin binding levels. *J. Med. Chem.* 43., 10., (May) 1986-1992.

Geppetti, P. Capone, J., Trevisani, M., Nicoletti, P., Zagli, G., Tola, M. (2005). CGRP and migraine: neurogenic inflammation revisited. *J. Headache. Pain*., 6., 2., (Apr) 61-70.

Katsamba., P. et al. (2006). Kinetic analysis of a high-affinity antibody/antigen interaction performed by multiple Biacore users. *Anal. Biochem*., 352., 208–221.

Myszka, D. (1999). Improving biosensor analysis. *J. Mol. Recognit.,* 12., 279–284.

Myszka, D. et al. (2003). The ABRF-MIRG'02 study: assembly state, thermodynamic, and kinetic analysis of an enzyme/inhibitor interaction. *J. Biomol. Tech.,* 14., 4., (Dec) 247-269.

Navratilova, I. et al. (2007). Thermodynamic benchmark study using Biacore technology. *Anal. Biochem.,* 364., 1., (May) 67-77.

Papalia, G. et al. (2006). Comparative analysis of 10 small molecules binding to carbonic anhydrase II by different investigators using Biacore technology. *Anal. Biochem.,* 359., 1., (Dec) 94-105.

Rich, R. & Myszka, D. (2007). Higher-throughput, label-free, real-time molecular interaction analysis. *Anal. Biochem*., 361., 1-6.

Rich, R. & Myszka, D. (2008). Survey of the year 2007 commercial optical biosensor literature. *J. Mol. Recognit.*, 21., 6., (Nov-Dec) 355-400.

Rich, R. et al. (2009). A global benchmark study using affinity-based biosensors. *Anal. Biochem*., 386., 2., (Mar) 194-216.

Wong, H., Taché, Y., Lloyd, K., Yang, H., Sternini, C., Holzer, P., Walsh, J. (1993). Monoclonal antibody to rat alpha-CGRP: production, characterization, and *in vivo* immunoneutralization activity. *Hybridoma,* 12., 93-106.

Zeller, J., Poulsen, K., Sutton, J., Abdiche, Y., Collier, S., Chopra, R., Garcia, C., Pons, J., Rosenthal, A., Shelton, D. (2008). CGRP function-blocking antibodies inhibit neurogenic vasodilatation without affecting heart rate or arterial blood pressure in the rat. *Br. J. Pharmacol*. 155., 7., (Dec) 1093-1103.

6

Urea Biosensor based on Conducting Polymer Transducers

Bhavana Gupta, Shakti Singh, Swati Mohan and Rajiv Prakash
School of Materials Science and Technology,
Institute of Technology, Banaras Hindu University, Varanasi -221005,
India

1. Introduction:

Urea is one of the final products of protein metabolism. In clinical analysis and dairy industry urea is a very significant parameter as excess in blood serum from its permissible range causes dysfunction of the kidney. Hence, its analysis is significant and is carried out frequently in various laboratories [1, 2]. Urea is an omnipresent compound present in blood and various organic fluids. It passes directly into milk through diffusion. Therefore, milk is the second major biological sample for the study of urea concentration [3]. A periodic monitoring of urea in milk can be used to predict the state of animal's health and predict the protein requirement in its diet [4]. Besides milk, presence of urea in agricultural land as a pollutant due to excessive use fertilizers is also widely known. Various methods used for the determination of urea (without use of biocatalyst) are gas chromatography, calorimetric and flourimetric analysis etc [5]. However, these methods need sample pretreatment which stands as a major disadvantage in their versatility of applications. Alongside, these methods can not used for field monitoring. Therefore, devices developed based on biocatalyst "urease" to analyze urea also known as urea biosensors are of vital importance. The first urea biosensor was developed by Guilbault et al. [6] followed by many clinical and biochemical analysts. For the fabrication of the urea biosensor, urease is immobilized over a substrate. The immobilized urease there after catalyzes the urea conversion in to ammonium and bicarbonate ions based on enzyme substrate reaction. Many biosensors have been developed for the determination of urea in the biological samples namely spectrometry [7-9], potentiometry with application of pH sensitive electrode or an ion selective electrode or an ion sensitive field effective transistor [10-13], conductometry [14-16], coulometry [17], amperometry [18] and inductometry [19]. Amongst these methods, detection through electrochemical mode is highly adopted and versatile. This method involves the use of electrochemical urea biosensor. In the development of electrochemical urea biosensors, immobilization of urease over electrodes is the key parameter which decides the sensitivity and reproducibility of the sensor.

Urea biosensors are collectively formed by biorecognition layer - biocatalyst i.e. urease, a biotransducer – to read change in physical environment and convert into electronic signal. The complete working principle of the biotransducer component of urea biosensor is shown in Scheme 1. For making biotransducer and choice of substrate, conducting polymers are

most widely being researched. These materials have a key advantage in facilitating the conversion of physiochemical change into an electronic signal. A close harmony between the selective biorecognition system and physiochemical transducer also helps in overall performance of the biosensor.

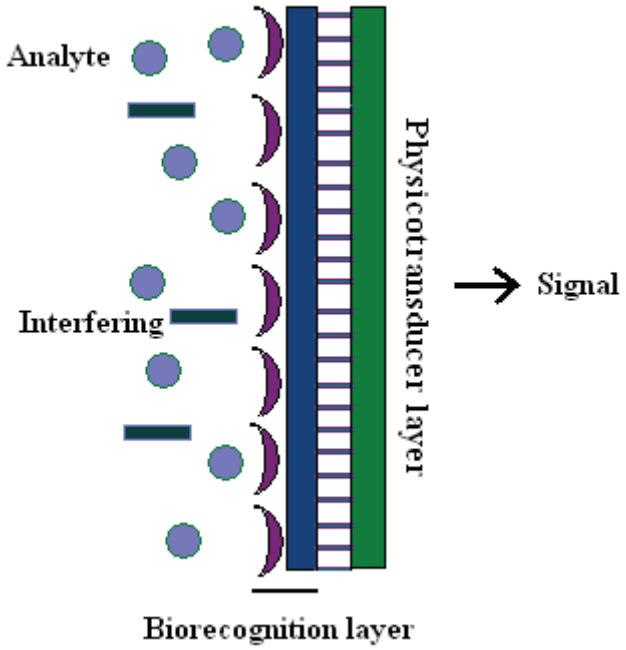

Scheme 1. The biotransducer components of a urea biosensor composed of biorecognition layer having an intimate contact with transducer.

2. Various electrochemical techniques of urea sensing based on conducting polymers:

The electrode configuration of the conducting polymer based biosensor varies according to the sensing mechanism. A potentiometric and amperometric signals can be read through a single electrode [20]. Conductometric sensor devices, on the other hand, are most easily monitored by passing charge between two electrodes. Further low cost biosensors can be obtained using screen printed electrodes and reducing its size that is called miniaturized screen printed biosensors. Eggenstein et al [2] described urea sensitive biosensor electrode in the shape of test strips. Further, Trivedi et al [21] developed a miniaturized low cost screen printed disposable NH_4^+ ion sensitive electrode with double matrix membrane. Detection and estimation of urea in milk sample in this sensor is based on potentiometric changes occurring at the interface.

As mentioned before, in urea biosensors the enzyme immobilized to the electrode surface catalyzes the hydrolysis of the urea, in an overall reaction leading to the formation of ammonium, bicarbonate and hydroxide ions as shown below:

$$\text{Urea} + 3H_2O \xrightarrow{\text{Urease}} 2NH_4^+ + HCO_3^- + OH^-$$

The ionic products of the above reaction change the electronic properties of the biosensor electrode (modified with conducting polymers), which can be observed by various electrochemical techniques as follows:

2.1 Conductometric technique

There are many processes taking place in the vicinity of the polymer film which may lead to change in mobility and density of the carriers which thereby lead to a change in conductivity of these polymers. Conducting polymers are most suitable for conductimetric biosensor fabrication as their conductivity is sensitive to surrounding ions and their mobility. In case of conductimetric biosensor film conductivity can be calculated by four probe or two probe DC interrogation. In two probe interrogation, resistance of the polymer film is measured at a fixed potential with an increasing concentration of analyte. However, in case of four probe interrogations current is measured by sweeping the potential with the polymer fixed between a pair of interdigited microelectrode [22]. Current developed due to the potential drop is related to the film conductivity. The reason of potential drop is the interaction of analyte gaseous or ionic product cause the degree of doping of the polymer directly affects the conductivity. Sometimes analyte interactions cause a conformational transition of the polymer chain from "compact coil" to an "expanded coil" through the process of secondary doping, which might be accompanied by concomitant change in conductivity [23, 24]. Both types of interrogation have been applied for urea biosensors as the products of enzymatic reaction in both the methods are able to change the electronic property of the polymer.

These biosensors can be fabricated by putting enzyme layer over the polymeric transducer. Jha et. al. [25] used electropolymerized polyaniline-polystyrene (PANI-PSS) with brevibacterium ammoginase as a biocatalyst for urea biosensor. The immobilized cell works as a source of unpurified urease to develop conductometrc urea biosensor. The pH dependent change in resistivity of the polymer was also used as a basis for sensing. The response was linear over a range of 0-75mM urea with a sensitivity of 0.125 mM^{-1}. Ortega et. al. [26] reported a urea biosensor based on NH_3 gas interaction by two probe method with DBSA-doped polyaniline-poly(styrene-co-potassium acrylate in a poly(n-butyl methacrylate) matrix. He also estimated urea concentration normal to pathological level.

2.2 Impedimetric technique:

Impedimetric transducer measures the effect of sinusoidal varying, nonperturbing voltage relative to a suitable reference electrode in term of impedance. The current originate allows the transfer function to real (Z″) and imaginary (Z′) component of impedance that changes as a function of the concentration of the analyte after each exposure. The impedimetric response can be measured either at one frequency (electrochemical impedance EI) or in a frequency range (electrochemical impedance spectroscopy EIS) [27]. The response might be direct or indirect depending on the interactions of the analyte with the recognition layer embedded in the conducting polymer or the analyte convert into some reaction product

after reacting with recognition layer and affects the carrier density (doping) or mobility (swelling) of the conducting polymer. Enzymatic biosensor based on conducting polymer comes in the category of the indirect and genosensors in the direct impedimetric biotransducer either by EI or EIS. There is still a debate whether impedimetric biosensor is truly or signal comes from the conformational change of the polymer. Ho et. al. [19] formed an impedimetric urea biosensor based on poly(methyl vinyl ether)/maleic anhydride which transformed rapidly in response to alkaline pH which was a link to enzyme reaction between urea and urease. The polymer was screen printed onto the interdigited screen printed carbon electrode and the electrode was overlaid with absorbent pad containing the associated enzyme. This type of electrode design was used for simple integrated and disposable sensor for clinical use.

2.3 Amperometric technique:

Amperometry is most commonly used technique for biosensors based on conducting polymers. Devices based on amperometry measure the change in current as a consequence of specific chemical reactions which take place at biotransducer electrode surface under non-equilibrium condition. The principal of the amperometry is based on the efficiency of the electron transfer between the biomolecule and underlying electrode surface in presence of electron mediator or conducting polymer. Moreover, amperometric biosensors are not only limited to the redox enzyme but also related to the biocatalyst reaction and interaction of the reaction product with conducting polymer to induce change in current [28]. Urea biosensor is the typical example of biocatalytic amperometric biosensor where ammonium ion which is a product of biocatalytic reaction interacts with polymer to induce a change in conductivity of the polymer. Adeloju et al [18] developed an amperometric urea biosensor based on flow injection analysis (FIA) to get linear responses between 3-15mg/l at the optimum condition of pH and potential of buffer and electrode respectively. The presence of interfering ions (KCl and KNO_3) at the concentration upto 0.01 M did not interfere with the estimation of the urea in blood and urine samples without any pretreatment. Rajesh et al [29] reported an amperometric urea biosensor with urease covalently immobilized with conducting copolymer poly (N-3 aminopropyl pyrrole-co-pyrrole) film. Amperometric response was measured as a function of concentration of urea, at a fixed bias voltage of 0.0 V vs. Ag/AgCl in a phosphate buffer (pH=7.0). The electrode gave a linear response range of 0.16-5.02 mM. W. J. Cho [30] described a new procedure for the urea determination through polyaniline-Nefion composite electrode which effectively sensed ammonium ion by amperometric technique. The sensor showed a detection limit as low as 0.5 μM (very less) with short response time. Nefion shortened the diffusion path and thus increased the sensitivity of the biosensor.

2.4 Potentiometric technique:

Electrochemical estimation of the urea is mainly carried out using potentiometric techniques because of a simpler mode of construction of the sensor electrode, detection and general availability of the instrumentation required for their utilization. On the other hand, for fully exploiting this technique, more durable and maintenance-free ion-selective electrodes (ISEs) which can be easily miniaturized are needed. Conducting polymers are widely studied for estimation of the urea by pH sensitive potentiometric technique. These polymers not only act as good transducers but also unique support to the immobilization of the enzyme due to

having capability for direct electron transfer between enzyme and polymer through the π electron (hydrophilic and hydrophobic interaction). In the following, we shall discuss about the critical parameters of solid state potentiometric urea biosensor based on conducting polymer pH transducer.

2.4.1 Conducting polymer based pH transducers:

pH sensor is widely known amongst all types of chemical sensors. A unique property possessed by conducting polymers is their low resistivity and conjugation. In addition, conducting polymers are known for better electronic communication through pi electrons. They also enhance ion to electron transduction performance of sensors and thereby increase the linear dynamic sensitivity, response time and stability of the sensor [31-40]. pH sensor is a type of chemical sensor extensively studied for the identification of the hydrogen ion concentration of the medium depending on the interaction and ion exchange between polymer and hydrogen ion in the bulk. Conducting polymer found in various oxidation states depends on pH and potential change affects conductivity, thus the change in the electronic parameter (change in electronic structure) measured by different type of electrochemical techniques for the identification of the pH. The mechanism of the potentiometric pH sensor based on conducting polymer is directly related to protonic interaction of the monomers. Amino group containing polymers have high affinity to the proton due to their behavior as protonation/deprotonation nitrogen i.e. Lewis base site [41]. The second mechanism based on the reaction of H^+ onto amino groups because of polarization creates local charge density excess at the electrode surface in comparison to the bulk concentration. The pH response mechanism of membrane may be represented by the following equation [42]:

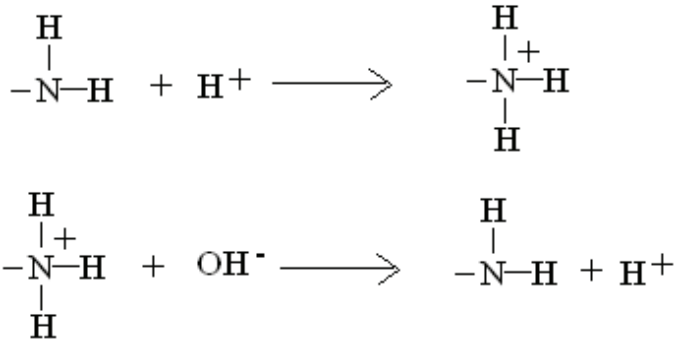

The build up of charges on the inside of the conducting polymer membrane is proportional to the amount of hydrogen ions in the external solution as shown in figure 1.

The potential difference across the membrane in the potentiometric mode of detection is proportional to the logarithm of the ionic concentration in the external solution. Undissociated acidic groups (not participating in the doping) also participate in the H^+ sensitivity [43]. Various conducting polymers having some weak acidic groups over their backbone (self doped polymers) can explored for the pH sensor application, structures of some of them have been shown below in figure 2.

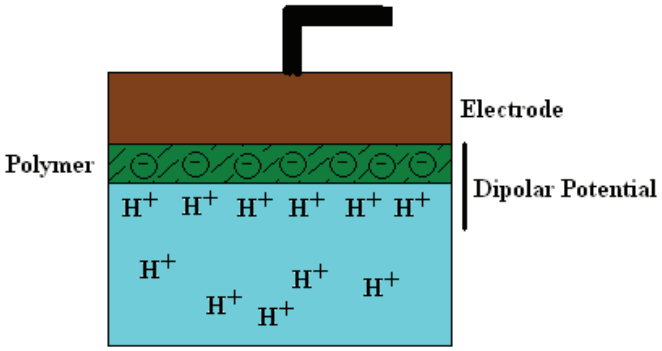

Fig. 1. Dipolar layer formation over the surface of conducting polymer modified electrode

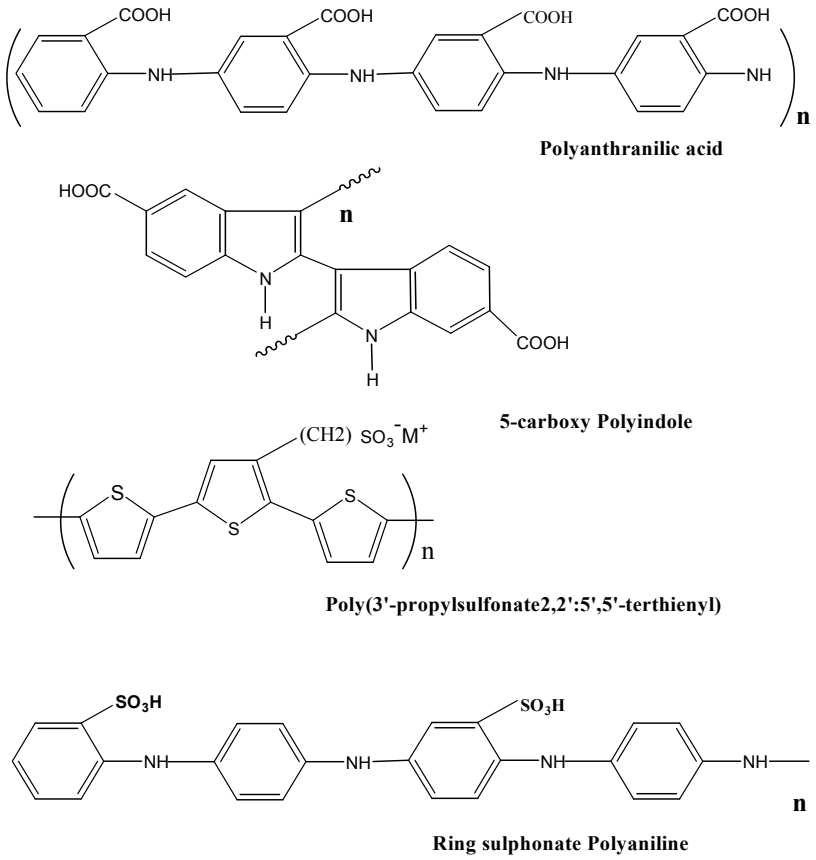

Fig. 2. Electronic structure of self doped conducting polymers

Amongst the various conducting polymers, polyaniline has been found most suitable for pH sensing in aqueous medium. Pandey et. al. [44] found that hydrophobic ion exchanger used as a dopant for the polyaniline synthesis in acetonitrile facilitates pH estimation in the both aqueous and non-aqueous medium. Potentiometric chemical sensors relate open circuit potential to the concentration of analyte (with the generation of constant dipolar potential essentially required for baseline recovery after each addition of the electrolyte) by using an ion-selective or conducting polymer based electrode as a physical transducer.
These are selective, have large dynamic ranges and are nondestructive. They are frequently used for pH sensing. During the last decade, enormous efforts have been made on developments of potentiometric pH transducer based on polymer modified electrode. Charge over the polymer (oxidation state) is compensated by the counter i.e. dopants, thereby giving the ion exchanging opportunity to the polymer [45]. Thus the performance of the sensor is affected by oxidation state and structure of the polymers. Responses of various conducting polymers for pH are mentioned in table1.

Conducting Polymer	**Dynamic Linear Range (M)**	**Slope (mV decade $^{-1}$)**	**Detection Limit (M)**	**Reference**
Polyaniline (PANI)	pH 2-9	52.7	1×10^{-9}	T. Lindfors et. al. [48]
Polypyrrole	N.M	58	N.M	H. Kaden et. al. [49]
Polyaniline ultrathin films	pH 3-9	55-59	1.0×10^{-9}	C. H. Ge et. al. [50]
Polyaniline and poly (o-ethoxyaniline)	3 < pH < 9–10	~60 or 50	1.0×10^{-9}	C Slim et. al. [51]
Polypyrrole (PPy)	2-11	48	1.0×10^{-11}	B. Lakard et. al [42]
Polydiethylenetriamine (PPPD)	2-11	34	1.0×10^{-11}	B. Lakard et. al [42]
Polyethyleneimine (PEI)	2-11	46	1.0×10^{-10}	B. Lakard et. al [42]
Polypropyleneimine (PPI)	2-11	43	1.0×10^{-10}	B. Lakard et. al [42]
Orthomethoxyaniline and ortho-methylaniline	2-11	63.6	NM	C. A. Lindino et. al. [52]
Polyaniline and its substituted derivatives	2-9	62.9±0.9	1×10^{-9}	T. Lindfors et. al. [53]

Table 1. pH sensing parameter of a number of reported conducting polymers.

2.4.1.1 Effect of polymer composites on pH responses:

It is reported that conducting polymers having some more ion exchanging moieties viz functional group, dopant and other polymer modifier to form composites or blends not only affect total pH sensitivity but give stable immobilization matrix also. Different insulation polymer has been tried as a matrix for sensing membrane. PVC derivatives with carboxylate

groups (~1.8 %) got much more attention by the researchers. The reason is the COOH groups which principally remain undissociated. The weak acidic PVC or similar polymers are partly protonated upon contact with the aqueous solution and are being used to fabricate so-called ionophore-free H^+-selective liquid membrane electrodes.

Prissanaroon-Ouajai et al. [46] developed pH sensor based on polypyrrole (PPy) with hydroquinone monosulphate and oxalate co-doping. Co-doped PPy showed the response slope of -54.67±7 mV/pH and a non-Nernstian slope of -35.0±7 mV/pH.

In our work for the first time we used 5-carboxy polyindole (5-carboxy PIn) and 5-carboxy PIn-Polyvinyl chloride carboxylated (PVC carboxylated) composite for the development of pH transducers. Incorporation of the functional group over polyindole and PVC (carboxylated) in polyindole matrix not only increases the sensitivity of the sensor but also provided stability to the sensing membrane. Besides, it also facilitated post synthetic processing. We measured the pH dependence of our electrodes by recording the open circuit potential in various buffer solutions ranging from pH 10 to 1 in 5ml buffer solution of 0.1mM using standard addition or batch method at the constant stirring of 100 rpm. Before each measurement, the sensor was immersed into pure water in order to ensure the same starting conditions (for batch method). Results are presented in figure 3 for 5-carboxy PIn and 5-carboxy PIn-carboxylated PVC composites based sensors. Both the electrodes demonstrated very good linearity. For 5-carboxy Pin and 5-carboxy PIn-Polyvinyl chloride carboxylated composite, we found a slope of 38.5 and 47.5 mV/pH respectively, which showed semi Nernstian behavior indicating that less than one proton per electron is involved in changing the stationary potential.

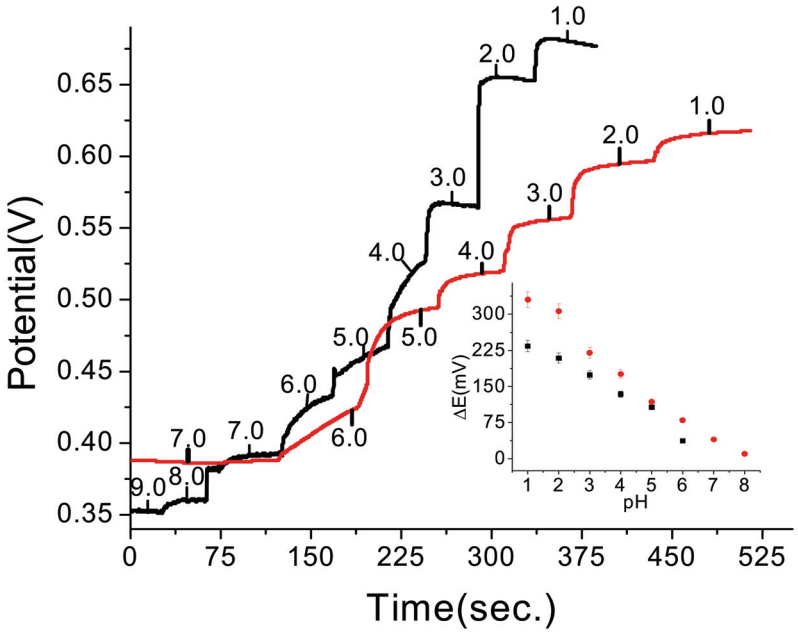

Fig. 3. Potentiometric pH sensing behavior of 5-carboxy PIn (Red) and 5-carboxy PIn-carboxylated PVC composite (Black)

2.4.1.2 Effect of Multiwall carbon nanotube (MWCNT)-Carboxylated on pH responses:

CNTs are well known as suitable materials for chemical sensing in which electron exchange is the basis of the mechanism. CNTs networks form an electrical contact to an outer device; whereas the sensitive coating acts as a transducer and converts physical phenomenon into electrical signals. Carbon is also known to give a pH response. In addition, it was found that thin carbon nanotube networks work as a conductive and transparent backbone structures for conducting polymer coating thereby increasing the electronic conductivity of the system. Use of carboxylated CNTs increases pH sensitivity with polymer not only due to the undissociated carboxylic group but also due to its reduced size which increases effective surface area. Kaempgen et. al [47] found that in polyaniline coated over CNT, pH response falls in the range of super Nernstian and linearity in response increases with increase in the amount of polyaniline. MWNTs helps in the total pH sensitivity of the electrode. Similarly our synthesized nanocomposite showed an increase in slope up to 69mV/pH for wide range of pH 10-1.0 as shown in figure 4.

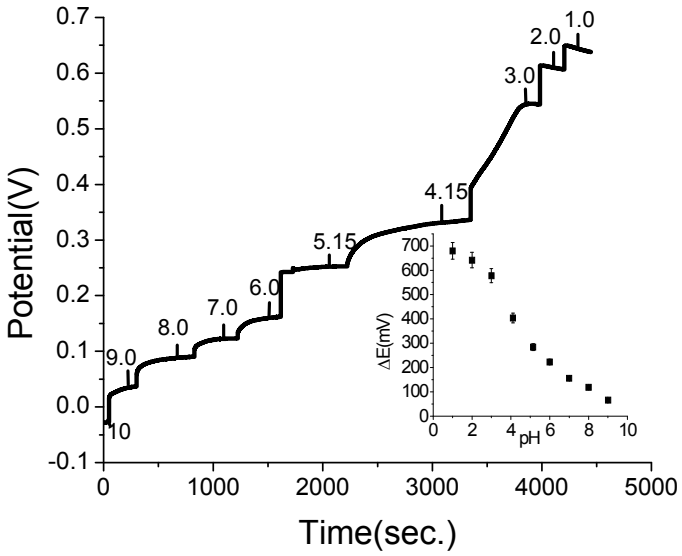

Fig. 4. Potentiometric pH sensing behavior of 5-carboxy PIn-carboxylated PVC-Carboxylated MWNTs nanocomposite.

2.4.2 Importance of conducting polymers for biosensors:

Biosensor is an electroanalytical device which transduces a physicochemical change in the presence of biological or biologically derived molecule such as enzymes, tissues, bacteria, yeast, antibodies/antigens, liposomes, organelles and DNA etc. Biosensors represent a new trend emerging in the diagnostic technology. Various types of matrices have been proposed for the immobilization of enzymes such as membranes, gels, carbon, graphite, silica, polymeric films etc. Conducting polymers are attractive materials for electron transfer over

the surface of the electrode as well for immobilization [54, 55]. The overall performance of electrochemical biosensor is characterized by metal substrate, biocatalyst immobilization and electronic and morphological properties of the conducting polymer. There are some advantages of using conducting polymers as transducing materials. Firstly, they are easy to synthesize through chemical and electrochemical polymerization techniques. Secondly, the ease of fabrication of sensors from these materials on substrate either by spin coating and/or drop casting from solution or directly by anodic electrochemical polymerization from an electrolyte solution [56, 57]. These polymers can be synthesized over the electrodes by electropolymerization also. The biosensor development by two different ways of polymer thin film formation is shown in Scheme 2.

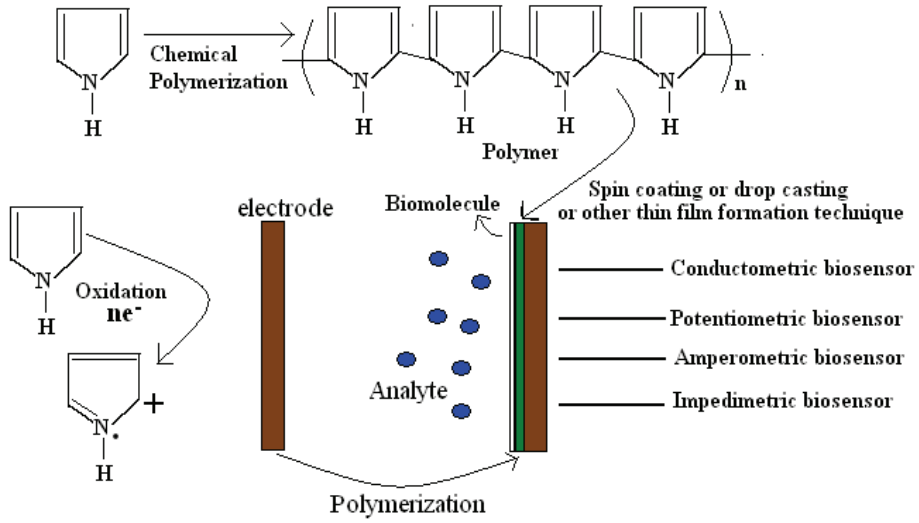

Scheme 2. Schematic representation of conducting-polymer based biosensors fabrication technique by different methods of polymer film formation on solid and conducting substrate.

Biomolecules can be directly immobilized with the electropolymerization process to get these molecules in a specific arrangement or orientation. It is a widely adopted method for biosensor development. Beside, chemically synthesized polymers have their own advantages in post synthesis modification to desired mechanical and electrical properties. Moreover, these polymers can be molded by other materials which are more suitable for biomolecules immobilization which helps in enhancement of various properties. Conducting polymer is being researched as a material to enhance various analytical transduction properties of biosensors such as speed, sensitivity and versatility because of availability of various stable electronic states. Electrical (electronic state) and mechanical properties of conducting polymers can also be tailored by applying electrical stimuli thus affect the biochemical transduction performance. In the biosensor application conducting polymers can perform various roles viz. as a catalyst, a redox mediator, an ON/OFF switch,

ion sensitive membrane and as chemiresistor which shows change in the resistivity because of biochemical reaction. Due to biochemical reaction between the analyte and biomolecule various products are formed viz. proton, different ion and gases etc. These products related to a specific type of analyte which modulates the electronic and optical properties of the conducting polymer [58-61, 45], and thereby becomes a source of typical analytical signal which can be monitor at the electrode surface by various electrochemical techniques either in the change in impedance, change in open circuit potential (dipolar potential) change in current at fixed applied potential and conductivity etc. The sensitivity of the biosensor depends upon the electron relay between conducting polymer and solid electrode support over which polymer is fabricated. Here, we chemically synthesized 5-carboxy polyindole (5-carboxy PIn) by using two miscible solvents (water and ethanol) and prepared polymer used for the composite formation by solution casting method [62]. Carboxylated PVC and MWNTs used as a conventional and nanofiller (20 and 10wt. % respectively). Use of the filler not only modifies mechanical, morphological and electrical properties of the polymer but also helps to improve the chemical and biosensor performance of the polymers.

2.4.3 Immobilization of urease over the polymer membrane for urea biosensor:

Solid state biosensors are adopted more as compared to liquid state as the stability of the enzyme is very less in the liquid state. The immobilization of the biological component should be at the environmental conditions otherwise it results in decreased enzyme activity. Thus research is going on in the field of solid state biosensor based on polymer [63]. The activity of immobilized molecules depends upon various parameters such as surface area, porosity, hydrophilic character of immobilizing matrix, reaction conditions and the methodology chosen for immobilization [64, 65]. The popularity of using conducting polymers in biotransducer application is mainly due to various reasons such as availability of a spectrum of immobilization techniques for bioreceptor (even molecule through cell) location, each of which is compatible with maintaining bioactivity, faithful presentation of the bioreceptor to the analyte, and controlled thickness of the biorecognition layer. All these parameters are related to polymer suitable for immobilization due to rough, porous and hydrophilic nature. The incorporation of large size dopants, dodecylbenzene sulphonate (DBS) into polypyrrole film during electropolymerization makes PPy more porous [66, 67]. Moreover the incorporation of the nanoparticle in the conducting polymer not only increases the surface area and nanofabrication but also changes various properties viz morphological and electrical which help in the immobilization of the biomolecules and better performance of the biosensor by proper diffusion of the analyte specific product [68]. Enzyme over the immobilization matrix must be in the form of a thin layer with efficient loading. The immobilization of the suitable enzyme on the surface of the sensing electrode is a critical step in fabricating the biosensor of required choice. Additionally, the method used for enzyme immobilization should not affect the quality of the urea biosensor in terms of cost per use; it's easiness in carrying and its effectiveness in the transducer performance [69]. Immobilization of urease in conducting polymer can be achieved by several techniques.

These include physical adsorption, electrochemical entrapment, chemical cross linking and covalent coupling. These methods have their own advantages and disadvantage as mentioned in table2.

The steps involving in different type of immobilization method are shown in Scheme 3.

Way of immobilization	Advantage	Disadvantage	Reference
Physical adsorption	No structural change of biocatalyst and cheap, fast immobilization	Physical interaction easily braked by change in environment condition cause leaching	M. J. Syu et. al. [75]
Entrapment	One step biosensor fabrication, low cost	Unsymmetrical distribution of biocalatyst cause diffusion barrier	S. B. Adelojo et. al. [18]
Cross linking	Stable interaction, moderate cost	Side effect of chemical used for immobilization, it take time, difficult enzyme recovery	W. J. Cho [30]
Covalent bonding	Stable interaction with high enzyme loading	Side effect of chemical used for immobilization, it take time, difficult enzyme recovery	Rajesh et. al. [29]

Table 2. Different method of biomolecule immobilization

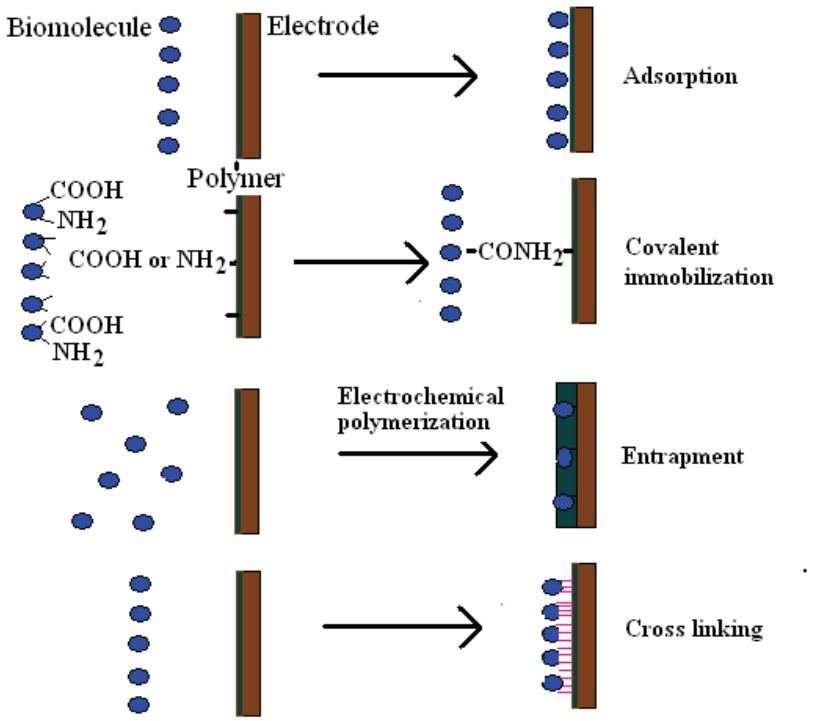

Scheme 2. Schematic representation of process in different immobilization methods.

Amongst all the immobilization methods covalent immobilization is the most advanced one. In this method biomolecule is incorporated in the conducting polymer matrix through complementary functional group chemistry. This way of immobilization confers strong interaction between polymer and biomolecule that can be achieved by amide or ester linkage in the presence of some coupling agent. Covalent immobilization not achieved in polymer only can be participate with other moieties (having functional group) present with conducting polymer after modification viz plasticizer or fillers. Covalent immobilization not only inhibits leaching of the enzyme but also provides thin coating of the enzyme which facilitates fast ionic movement thereby increasing sensitivity and long life stability of the biosensor. Rajesh et. al [29] immobilized urease in the copolymer poly-(N-3 aminopropylpyrrole-co-pyrrole) in the presence of 1-ethyl -3-(3-dimethylaminopropyl) carbodiimide hydrochloride (EDC) and N-hydroxysuccinimide (NHS) as coupling agent in aqueous medium. 95% baseline recovery in 40 second was thereafter observed. Thus it can be concluded that carbodiimide coupling reaction has a feature of strong covalent bonding with the enzyme with the matrix, which in turn is responsible for high enzyme loading at the surface of polymeric modified electrode.
We used 5-carboxy PIn, 5-carboxy PIn-carboxylated PVC and 5-carboxy PIn-carboxylated PVC-MWNT composites for immobilization of urease and studied morphological properties. After composite formation film became porous with carboxylated PVC. Due to MWNT surface area increased which is good for immobilization of urease. This matrix was further applied for covalent immobilization in the presence of coupling agent DCC and NHS. Treatment of DCC and NHS was carried out in cyclohexane; immobilization was carried out in aqueous solution of the enzyme in distilled water.

2.4.4 Mechanism of potentiometric urea biosensors based on conducting polymer:

Potentiometric measurements are based on monitoring potential values under a zero current flow regime (under equilibrium), in order to determine the analytical concentration of desired components after catalytic reaction between biomolecule and analyte in the sample solution [43, 70-72]. Source of potential may be a physical phenomena not involving explicit redox reactions but having non-zero free energy initial conditions because of enzymatic reaction and ionic gradient. For instance ion concentration gradient over the surface of sensing membrane is one of such phenomena and ionic potential similar to dipolar potential. Potentiometric sensor either symmetric or asymmetric depends on the homogeneous and heterogeneous interface between the dipolar layers of charges. Conducting polymer or solid state ion selective electrodes (ISEs) based potentiometric sensor falls in the asymmetric type because ionic dipolar layer is generated at the interface of liquid and solid phases [73]. Since the biochemical reaction between analyte and urease change pH due to the formation of ammonia and carbondioxide, it can be analysed using pH sensitive or H+ exchanger moieties through potentiometric mode of detection [74]. In addition, potentiometric sensor for detection of ammonia, and ammonium ion generated by enzymatic reaction, using ISE are being studied [75]. The major problem for pH sensitive electrode is that the sensor response is strongly dependent on the buffer capacity of the sample. This is because the pH change produced in the course of the enzymatic reaction is suppressed by the buffer used. The general problem of ammonium sensitive electrode is

interference by Na+, K+ and Ca+ ion, which are present in the serum and other biological derive fluid. Potentiometric response is affected by various parameters viz. concentration of the buffer, pH of the buffer, loading of the enzyme, temperature, stirring rate etc. Sensor gives best response at an optimum condition of these parameters [1, 76]. Polymers both intrinsically conducting and non conducting, have played a prominent role in pH sensitive potentiometric sensor as well for urea biosensor. Some of the ureabiosensor based on pH sensitive conducting polymer using potentiometric technique is shown in table 3.

Electrode	Sensitivity	Mode of sensing	Lower detection limit	Linear Dynamic range	Reference
Polypyrrole (Ppy)-Bovine serum albumin	~25mV	pH, Chronapotentiometry	6.6×10^{-6}M	6.6×10^{-6}-7.5×10^{-4}	T. Ahuja et. al. [82]
Poly(N-vinyl carbazole)/stearic acid	~50mV	pH Potentiometry	1mM	10-68mM	R. Singhal et. al. [64]
Polyaniline-Tetraphenyl borate doped-PVA	~26.6mV	pH Potentiometry	20µM	~60µM-to mM	P. C. Pandey et. al. [44]
Electroactive polypyrrole/poly anion complex	110mV/decade	pH Potentiometry	0.02mM	0.3-30mM	Osaka et. al. [77]

Table 3. pH transducer based urea biosensor with different conducting polymers

We developed potentiometric urea biosensor fabricated using 5-carboxy PIn-Carboxylated PVC composite based on solid state pH transducer. A classical two electrode cell required for the estimation of urea by potentiometric technique having one H^+ ion sensitive electrode coated with enzyme urease and reference electrode. Total response of Urease/PIn-PVC/Pt biosensor electrode gave 130±10mV/ change in urea concentration of 10^{-6}-10^{-1} M (24.6 mV/decade) as shown in figure 6. The linearity obtained for the above biosensor in the range of 10^{-5}-10^{-1}M. Lower detection limit of the biosensor was 10^{-5} M concentration of urea. The apparent Michaelis-Menten constant K_m is an indicator of the enzyme-substrate reaction kinetics and used to evaluate the biological activity of the immobilized enzyme. Two linear ranges were obtained viz., 10^{-6}-10^{-4} M and 10^{-3} to 10^{-1}M. The reciprocal of apparent Michaelis-Menten constant (lower concentration region) in the present study was found to be -$1/K_{mapp}$=-5.276882x10^{-6} for Urease/5-carboxy polyindole-carboxylated PVC electrode in the lower concentration range (when the enzyme was 20µl, optimum loading of enzyme), which is lower than any other urea sensor reported in literature so far.

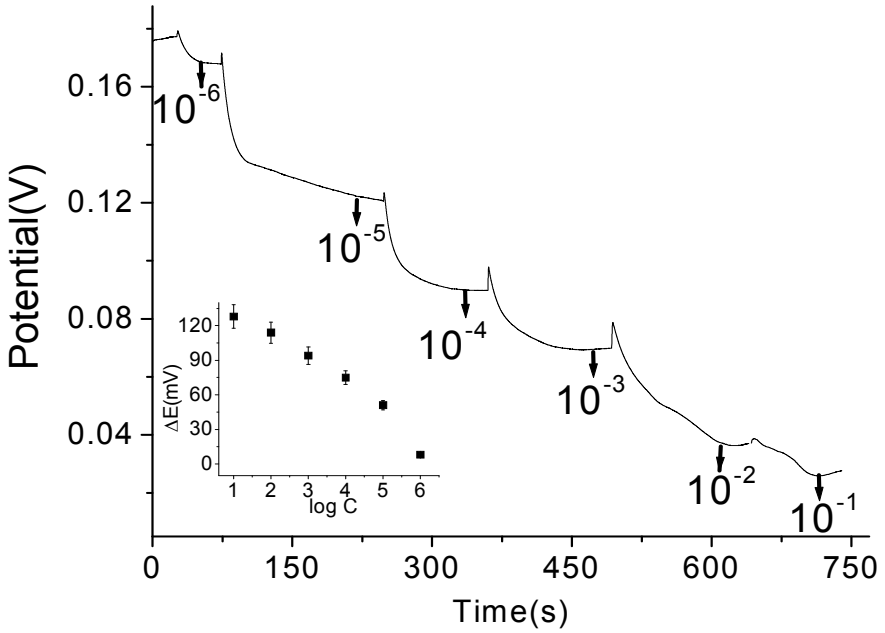

Fig. 6. Potentiometric response of the biosensor (Urease (20µl) /PIn-PVC/Pt) to increasing urea concentration (10^{-6}-10^{-1})M. 1 mM Tris–HCl buffer (pH 7.0) calibration curve (Inset)

2.4.4.1 Carboxylated-MWCNTs-Conducting polymer composite based urea biosensor:

CNTs are used to increase the biosensor sensitivity because for their electron relay properties and at times due to interaction with analyte products. 5-carboxy PIn-carboxylated PVC- carboxylated MWNT composite was used for urea biosensor. The response for the urea increased up to 152±10mV for urea concentration in the range of 10^{-6}-10^{-1} M. In the presence of MWCNTs biosensor showed slope of 28.4 mV/decade of urea concentration (for 10^{-6}-10^{-1} M concentration of urea) in well accordance with its super Nerstien pH response of the same composite as shown in figure 7.

3. Effect of enzyme loading on urea biosensor response:

The amount of urease over the transducing membrane affects activity, response time and linear dynamic range due to thickness of sensing membrane and amount of enzyme. Activity of the biosensor was used to estimate the minimum enzyme unit required for the construction of the biosensor. In our biosensor we found that the lower and higher urea concentration responses of the biosensor can be altered by changing the loading of the urease over the electrode. When the loading was less (5-10 µl) biosensor was more sensitive in the lower concentration (10^{-6}-10^{-3}M) range and vise versa.

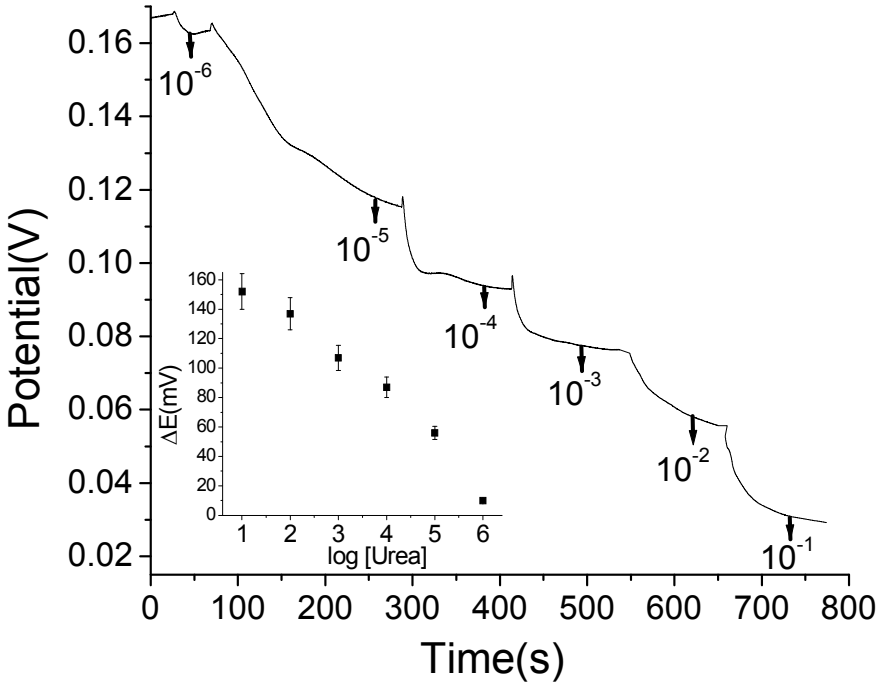

Fig. 7. Potentiometric response of the biosensor (Urs(20µl) /PIn-PVC-MWCNT/Pt) to increasing urea concentration (10^{-6}-10^{-1})M. 1 mM Tris–HCl buffer (pH 7.0) calibration cure (Inset)

4. Stability of the urea biosensor:

Stability of the conducting polymer based biosensor depends on the chemical stability (for long term usage) and electrochemical stability (for short term usage) of the conducting polymer layer over the solid substrate and enzyme layer immobilized with the polymer matrix. Stability of both of the components over the conducting electrode directly or indirectly affects the overall performance of the biosensor. Stability of the conducting polymer is measured by two parameters, firstly their inherent stability of the conductive and electroactive material (related to it functioning) and secondly their stable deposition over the electrically conducting substrate (physical stability) [28]. The ion exchange into and out of the conducting polymer creates concomitant dynamic change in the polymer (due to expansion and contraction) and causes interfacial shear stress there by causing leaching of the polymer from the surface. The interaction between polymer film and underlying

electronic conducting substrate is primarily hydrophobic in nature and is supported by some weak forces. Several attempts have been made to improve the adhesion of conducting polymer onto the conducting substrate for long term applications by using rough surface electrode, giving thiol modified polymer and by providing functional group over the substrate with the help of some chemical [78-82]. Through functional group chemistry, a stable deposition of the polymer has been achieved. Long term stability of the enzyme over the matrix is an important factor for consideration in the construction of the biosensor, since this is not only beneficial for the biosensor transport but it also reduces measurement cost. In addition due to the efficient coupling it is easy to achieve monolayer (thin and regular) deposition of the enzyme over the polymer which is good for the biosensor sensitivity. This could be achieved only; there would be strong and efficient bonding between enzyme and immobilizing material [69]. Biosensor developed here is highly stable and sensitive when enzyme immobilization is processed and stored at 5^0C. When the biosensor developed at room temperature sensitivity of the biosensor was in the range of 10^{-4}-10^{-1} M and at 5^0C it was responsive in broader range (10^{-6} - 10^{-1}M). The stability experiment was carried out in 0.1M urea concentration for two months, keeping biosensor electrode at 5^0C. It was found that the biosensor was stable for ~2 months with 75% degradation of the enzyme, similar to the recently reported urea biosensor having immobilization through carbodiimide coupling reaction.

5. Estimation of urea in biological sample

Urea is an important parameter which is frequently analyzed in biological samples such blood serum, urine and milk. Urea concentration in the above constituents above an optimum quantity directly affects the human health. The normal range of urea in blood is between 1.7- 8.3 mmol/l and levels increased up to 100 mM/l under pathophysiological condition affect the normal functioning of kidney [75]. The proposed urea biosensor was performed in human serum after 50 times dilution using standard addition method. The 5-carboxy polyindole/PVC electrode immobilized with 20 ul urease enzyme was used for the estimation of blood urea in the blood serum of healthy volunteers using three point calibration methods. The concentration of the urea in the blood was found to be $9.5x10^{-5}$ M (in 50 times diluted) or $4.75x10^{-3}$ M (in real sample) using standard addition method as shown in figure 8.

In this chapter potentiometric pH sensors and urea biosensors using conducting polymer composite and nanocomposite materials are discussed especially based on carboxyl functionalized polyindole conducting polymer. We have tried to identify the role of various materials and there capability to influence the performance of a sensing device based on pH transducer. We have also considered the effect of the different materials, processing, immobilization and morphology of the conducting polymer composite systems on sensing property. Finally we close our discussion along with work done by our group. The sensors and biosensors developed are compared with earlier known sensors and found to be more sensitive and stable over the others. We not only reported improved pH solid state sensor and urea biosensors based on such pH transducers but also showed the importance and potential of the novel carboxyl functionalized polyindole conducting polymer composites and nanocomposites for future direction for sensor and biosensor technology.

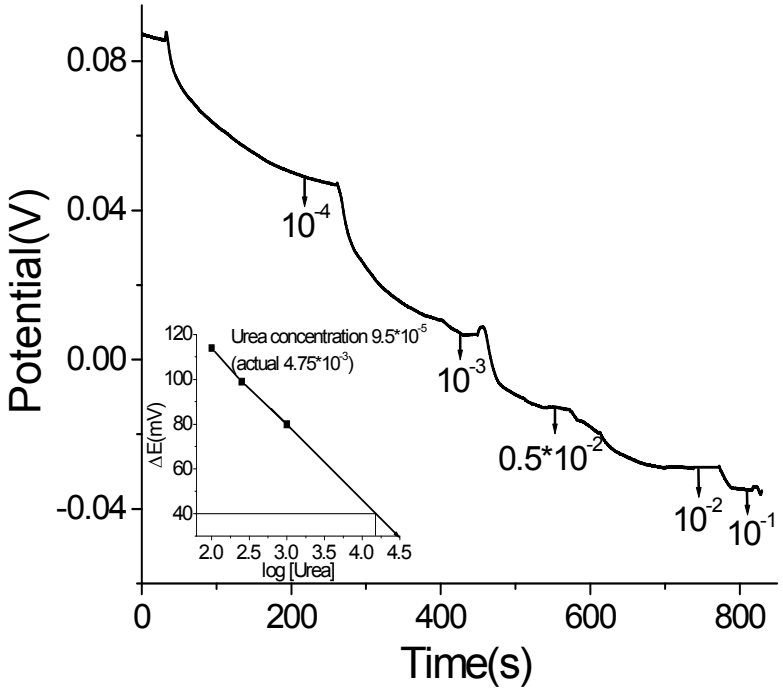

Fig. 8. Potentiometric response in blood serum. Three point calibration curve of this response to estimate urea concentration (Inset)

6. Reference:

[1] E. Karakus, S. Pekyardımc, E. Kılıc, Urea biosensor based on PVC membrane containing palmitic acid, Blood Substitutes, and Biotechnology. 33 (2005) 329

[2] C. Eggenstein, M. Borchardt, C. Diekmann, B. Grundig, C. Dumschat, K. Cammann, M. Knoll, F. Spener, A disposable biosensor for urea determination in blood based on an ammonium-sensitive transducer. Bioelectron. 14 (1999) 33.

[3] M. J. R. Leema, S. M. V. Fernandes, A. O. S. S. Rangel, Enzymatic determination of Urea in milk by sequential injection with spectrophotometric and conductometric detection. J. Agric Food Chem 52 (2004) 6887

[4] G. Hof, M. D. Vervoorn, J. Lenaers, S. Tamminga, Milk Urea Nitrogen as a Tool to Monitor the Protein Nutrition of Dairy Cows. J. Dairy Sci. 80 (1997) 3333

[5] A. V. Rebriiev, N. F. Starodub Enzymatic Biosensor Based on the ISFET and Photopolymeric Membrane for the Determinaion of Urea Electroanalysis 16 (2004)1891

[6] G. G. Guilbault, R. K. Smith, J. G. Montalvo, Use of ion selective electrodes in enzymic analysis. Cation electrodes for deaminase enzyme systems. Anal. Chem. 41 (1969) 600

[7] D.Liu, K. Ge, K. Cheng, L. Nie, S.Yao, Clinical analysis of urea in human blood by coupling a surface acoustic wave sensor with urease extracted from pumpkin seeds. Anal. Chim. Acta 307 (1995) 61.

[8] M. Mascini, Enzyme-based optical-fibre biosensors. Sens. Actuators B 29 (1995)121.

[9] X. Xie, A. A. Suleiman, G. G. Guilbault, Determination of urea in serum by a fiber-optic fluorescence biosensor. Talanta 38 (1991) 1197.

[10] S. B. Adeloju, S. J. Shaw, G. G. Wallace, Polypyrrole-based potentiometric biosensor for urea part 1. Incorporation of urease Anal. Chim. Acta 281 (1993) 611.

[11] S. B. Adeloju, S. J. Shaw; G. G. Wallace, Polypyrrole-based potentiometric biosensor for urea: Part 2. Analytical optimisation. Anal. Chim. Acta 281 (1993) 621.

[12] M. F. Esteve, S. Alegret, The Modern Student Laboratory: A Practical Approach to Chemical Sensors through Potentiometric Transducers: Determination of Urea in Serum by Means of a Biosensor. J. Chem. Educ. 71 (1994) A67.

[13] D. Liu, M. E. Meyerhoff, H. D. Goldberg, R. B.Brown, Potentiometric ion- and bioselective electrodes based on asymmetric polyurethane membranes. Anal. Chim. Acta, 274 (1993) 37.

[14] K. Chen, D. Liu, L.Nie, S. Yao, Determination of urea in urine using a conductivity cell with surface acoustic wave resonator-based measurement circuit. Talanta 41 (1994) 2195.

[15] A. S. Jdanova, S. Poyard, A. P. Soldatkin, N. Jaffrezic-Renault, C. Martelet, Conductometric urea sensor. Use of additional membranes for the improvement of its analytical characteristics. Anal. Chim. Acta 321 (1996) 35.

[16] H. Sangodkar,S. Sukeerthi, R. S. Srinivasa, R. Lal, A. Q. Contractor, A Biosensor Array Based on Polyaniline. Anal. Chem. 68 (1996) 779.

[17] R. E. Adams, P. W. Carr, Coulometric flow analyzer for use with immobilized enzyme reactors. Anal. Chem. 50 (1978) 944.

[18] S. B. Adelju, S. J. Shaw, G. G. Wallace, Polypyrrole-based amperometric flow injection biosensor for urea. Analytica Chimica Acta, 323 (1996) 107

[19] W. O. Ho, S. Krause, C. J. McNeil, J. A. Pritchard, R. D. Armstrong, D. Athey, K. Rawson, Electrochemical Sensor for Measurement of Urea and Creatinine in Serum Based on ac Impedance Measurement of Enzyme-Catalyzed Polymer Transformation. Anal. Chem. 71 (1999) 1940

[20] K. Sugiyasu, T. M. Swager, Conducting-polymer-based chemical sensor: transduction mechanism. Bull. Chem. Soc. Jpn., 11 (2007) 2074

[21] U. B. Trivedi, D. Lakshminarayana, I. L. Kothari, N. G. Patel, H. N. Kapse, K. K. Makhija, P. B. Patel, C. J. Panchal, Potentiometric biosensor for urea determination in milk. Sensors and Actuators 140 (2009) 260

[22] M. K. Malmros, A. Guiseppi-Elli, Sensor application of electroactive polymer MIT summer sesson programe, Cambrige, Massachusettes, 1987, July 1987

[23] A. G. MacDiarmid, A. J. Epstein, secondary doping in polyaniline. Synth. Met. 69 (1995) 85

[24] A. G. MacDiarmid, Polyaniline and polypyrrole: Where are we headed? Synth. Met. 84 (1997) 27

[25] S. K. Jha, M. Kanungo, A. Nath, S. F. D'Souza, Entrapment of microbial cells in electropolymerized polyaniline and their use as urea biosensor, Biosensor and Bioelectronics 14 (2009) 2637

[26] M.M. Castillo-Ortega, T. D. Castillo-Castro, V.J. Ibarra-Bracamontes, S.M. Nuño-Donlucas, J.E. Puig, P.J. Herrera-Franco, Urea sensing film prepared by extrusion from DBSA-doped polyaniline-poly(styrene-co-potassium acrylate) in a poly(n-butyl methacrylate) matrix Sensors and Actuators B: Chemical, 125 (2007) 538

[27] A. G. Elie, L. Lingerfelt. 2005, In current topic in chemistry, Ed. Chritine Withmann. Germany, Springer Verlag

[28] A. G. Elie, S. Brahim, A. M. Wilson, Biosensor based on conducting electroactive polymer, Handbook of conducting polymer, Third addition CRC Press, Taylor and Francis

[29] Rajesh, V. Bisht, W. Takashima, K. Kaneto, An amperometric ureabiosensor based on covalent immobilization of urease onto an electrochemically prepared copolymer (N-3-amino propyl-co-pyrrole) film Biomaterials 26 (2005) 3683

[30] W. J. Cho, H. J. Huang, An amperometric urea biosensor based on a polyaniline – perflourosulphonate ionomer composite electrode. Anal. Chem. 70 (1998) 3946

[31] A. Hellar, electrical wire of redox enzyme. ACC. Chem. Res. 23 (1990) 128

[32] T. W. Lewis, G. G. Wallace, M. R. Smith, Electrofunctional polymer : There role in the development of new analytical system Analyst, 124 (1999) 213

[33] K. S. V. Santhanam, Conducting polymer for biosensor: Rationale based on model. Pure Appl. Chem. 70 (1998)1259

[34] C. Kranz, H. Wohlschlager, H. L. Schmidt, W. Schuhmann, Controlled electrochemical preparation of amperometric biosensor based on conducting polymer multilayer Electroanalysis 10 (1998) 546

[35] S. B. Adelju, G. G. Wallace, Conducting polymer and the bioanalytical science. Analyst 121 (1996) 699

[36] W. Schuhmann, Conducting polymer and their application in amperometric biosensors. Mikrochim Acta 121(1995) 1

[37] M. Trajanowicz, T. K. vel Krawczyk, Electrochemical biosensor based on enzyme immobilized in electropolymerized film. Microchim Acta 121 (1995) 167

[38] A. Q. Contractor, T. N. Sureshkumar, R. Narayanan, S. Sukeerti, R. Lal, R. S. Srinivasa, Conducting polymer based biosensor, Electrochimica Acta, 39 (1994) 1321

[39] V. Singh, S. Mohan, G. Singh, P.C. Pandey, R. Prakash Synthesis and characterization of polyaniline–carboxylated PVC composites: Application in development of ammonia sensor Sensors and Actuators B: Chemical, 132(2008) 99

[40] R. Prakash, R. Srivastava, P. Pandey Copper(II) ion sensor based on electropolymerized undoped conducting polymers J. Solid State Electrochem 6 (2002) 203

[41] M. Yuqing, C. Jianrong, F. Keming, New technology for the detection of pH. J. Biochem. Biophys. Methods 63 (2005) 1

[42] B. Lakard, G. Herlem, S. Lakard, R. Guyetant, B. Fahys. Potentiometric pH sensors based on electrodeposited polymers. Polymer 46 (2005) 12233

[43] F. Faridbod, M. R. Ganjali, R. Dinarvand, P. Norouzi. Developments in the Field of Conducting and Non-conducting Polymer Based Potentiometric Membrane Sensors for Ions Over the Past Decade. Sensors 8 (2008) 2331

[44] P. C. Pandey, G. Singh, Tetraphenylborate doped polyaniline based novel pH sensor and solid-state urea biosensor. Talanta 55 (2001) 773

[45] A. Chaubey, K. K. Pandey, V. S. Singh, B. D. Malhotra, Co-immobilization of lactate oxidase and lactate dehydrogenase on conducting polyaniline film. Anal. Chimi. Acta 407 (2001) 97
[46] W. Prissanaroon-Ouajai, P. J. Pigram, R. Jones, A. Sirivat, A sensitive and highly stable polypyrrole-based pH sensor with hydroquinone monosulfonate and oxalate co-doping Sensors and Actuators B 138 (2009) 504
[47] M. Kaempgen, S. Roth, Transparent and flexible carbon nanotube/polyaniline pH sensors Journal of Electroanalytical Chemistry 586 (2006) 72
[48] T. Lindfors, S. Ervela, A. Ivaska, Polyaniline as pH-sensitive component in plasticized PVC membranes. J. Electroanal. Chem. 560 (2003) 69
[49] H. Kaden, H. Jahn, M. Berthold, Study of the glass/polypyrrole interface in an all-solid-state pH sensor. Solid State Ionics, 169 (2004) 129
[50] C. H. Ge, N. R. Armstrong, S. S. Saavedra, PH-sensing properties of poly(aniline) ultrathin films self-assembled on indium-tin oxide. Anal. Chem. 79 (2007) 1401
[51] C. Slim, N. Ktari, D. Cakara, F. Kanoufi, C. Combellas Polyaniline films based ultramicroelectrodes sensitive to pH. Journal of Electroanalytical Chemistry, 612 (2008) 53
[52] C. A. Lindino, L. O. S. Bulhoes, The potentiometric response of chemically modified electrodes. Anal. Chim. Acta, 334 (1996) 317
[53] T. Lindfors, A. Ivaska, pH sensitivity of polyaniline and its substituted derivatives. *J.* Electroanal. Chem. 531 (2002) 43.
[54] K. Kaneto, M. Kaneko. 2002. Handbook of polymer in electronics, Ed. B. D. Malhotra, 255. Shawbury, UK:Rapra Technology Ltd.,chap. 8
[55] A. L. Sharma, M. Garard, R. Singhal, S. Annaporni, B. D. Malhotra, Synthesis and charactreization of flourosubstituted polyaniline Appl. Biochem. Biotecnol. 96 (2001) 155
[56] R. Prakash , R. C. Srivastava, P. K. Seth, Polycarbazole Modified; Nitric Oxide Sensor Polymer Bulletin, 46(2001)487
[57] B. Gupta, R. Prakash Synthesis of Processible Doped Polyaniline-Polyacrylic Acid Composites. Journal of Applied Polymer Science114 (2009) 874
[58] E. W. Paul, A. J. Ricco, M. S. Wrington, Resistance of Polyaniline film as a function of electrochemical potential and the fabrication of polyaniline based microelectronics devices. J. Phys Chem 89 (1985)1441
[59] M.S. Wrighton,. Surface functionalization of electrodes with molecular reagents. Science 231 (1986) 32.
[60] G. P. Kittlesen, H.S. White, M.S. Wrighton, Chemical derivatization of microelectrode arrays by oxidation of pyrrole and N-methyl pyrrole. Fabrication of molecule-based electronic devices. J. Am. Chem. Soc. 106 (1984) 7389
[61] E.W. Paul, A.J. Ricco, M.S. Wrighton, Resistance of polyaniline films as a function of electrochemical potential and the fabrication of polyaniline-based microelectronic devices. J. Phys. Chem. 89 (1985) 1441
[62] M. Gerard, A. Chaubey, B.D. Malhotra, Application of conducting polymers to biosensors. Biosensors & Bioelectronics 17 (2002) 345
[63] B. Gupta, R. Prakash, Processible polyacid doped polyaniline composites: Application for charge storage devices. Materials Science and Engineering: C 29 (2009)1746
[64] R. Singhal, A. Gambhir, M. K. Pandey, S. Annapoorni, B. D. Malhotra, Immobilization of urease on poly(N-vinyl carbazole)/stearic acid Langmuir-Blodgett film for the application to urea biosensor. Biosensor and Bioelectronics 17 (2002) 697

[65] S. Xu, M. Wen, J. Li, S. Guo, M. Wang, Q. Du, J. Shen, Y. Zhang, S. Jiang, Structure and properties of electrically conducting composites consisting of alternating layers of pure polypropylene and polypropylene with a carbon black filler, Polymer 49 (2008) 4861

[66] H. H. Kuhn, W. C. Kimbrell, J. E. Fowler, C. N. Barry, Properties and applications of conductive textiles Synth. Met. 55 (1993) 3707.

[67] R. V. Gregory, W. C. Kimbrell, H. H. Kuhn, Conductive textiles. Synth. Met. 28 (1989) 823.

[68] J. Huang, B. Kaner, A General Chemical Route to Polyaniline Nanofibers. J. Am. Chem. Soc. 126 (2004) 851-855

[69] Rajesh, V. Bisht, W. Takashima, K. Kaneto, Development of of a potentiometric urea biosensor based on copolymer poly(N-3-aminopropyl pyrrole-co-pyrrole) film. Reactive and functional polymer 62(2005) 51

[70] J. Bobacka, A. Ivaska, A. Lewenstam, Potentiometric ion sensor based on conducting polymers. Electroanalysis 15(5-6) (2003) 366

[71] S. Komaba, M. Seyama, T. Momma, T. Osaka, Potentiometric biosensor for urea based on electropolymerized electroinactive polypyrrole. Electrochim Acta, 42(3)(1996) 383

[72] N. H. Chou, J. C. Chou, T. P. Sun, S. K. Hsiung, Measurment and comparison on potentiometric sensitivity coefficient of urea biosensor based on Ammonium ion selective electrode. IEEE Sensor Journal 5 (2005) 1362

[73] N. Gupta, S. Sharma, I. A. Mir, D. Kumar, Advances in sensor based on conducting polymer Journal of scientific and Industrial research 65 (2006) 549

[74] P.C. Pandey, S. Upadhyay, G. Singh and Rajiv Prakash, R.C. Srivastava and P.K. Seth, A New Solid-State pH Sensor and its Application in the Construction of All Solid-State Urea Biosensor, Electroanalysis, 12, 7, 517-521 (2000).

[75] M. J. Syu, Y. S. Chang, Ionic effect investigation of a potentiometric sensor for urea and surface morphology observation of entrapped urease/polypyrrole matrix. Biosensors and Bioelectronics 24 (2009) 2671.

[76] I. Walcerz, R. Konchi, E. Leszczynska, B. Salamonowicz, S. Glab. Ureabiosensor based on PVC Membrane ion-selective electrode. Analytical Leter, 29(11) (1996) 1939

[77] T. Osaka, S. Komaba, M. Seyama, K. Tanabe, High-sensitivity urea sensor based on the composite film of electroinactive polypyrrole with polyion complex. Sens.Actuators B 35–36 (1996). 463

[78] E. Smela, G. Zuccarello, H. Hariis, B. Liedburg, Thiol modified pyrrole monomer part 1: synthesis, characterization and polymerization of 1-(2-thioethyl)pyrrole and 3-(2-thioethyl)-pyrrole. Langmuir 14(11) (1998) 2970

[79] E. Smela, H. Hariis, Z. P. Yang, K. Uvdal, G. Zuccarello, B. Liedburg, Thiol modified pyrrole monomer part 2: Electrochemistry of 1-(2-thioethyl)pyrrole and 3-(2-thioethyl)-pyrrole. Langmuir 14(11) (1998) 2976

[80] E. Smela, H. Hariis, Z. P. Yang, M. Mecklenburg, B. Liedburg, Thiol modified pyrrole monomer part 2: Electrochemistry of 1-(2-thioethyl)pyrrole and 3-(2-thioethyl)-pyrrole monomer layer in propylene carbonate. Langmuir 14(11) (1998) 2984

[81] K. Idla, O. Inganas, M. Strandberg, Good adhesion between chemically oxidized titanium and electrochemically deposit polypyrrole. Electrochim Acta 45 (13) (2000) 2121

[82] T. Ahuja, I. A. Mir, D. Kumar, Rajesh, Potentiometric urebiosensor based on BSA embedded surface modified polypyrrole film. Sensors and Actuators 134 (2008) 140

7

Biosensors for Detection of *Francisella Tularensis* and Diagnosis of Tularemia

Petr Skládal, Miroslav Pohanka, Eva Kupská and Bohuslav Šafář
Masaryk University, Brno; Military Technical Institute of Protection, Brno; Military Academy, Hradec Králové
Czech Republic

1. Introduction

The detection of various types of microbial agents with harmful effects on human population is required in different situations including civil rescue and security units, homeland security, military operations in field, protection of public buildings and transportation systems including airports, metro and railway stations. Such situations need quickly responding, but sufficiently specific detection systems which could be satisfied by portable, rapid and simple instrumentation based on the bioanalytical detection principles (Lim et al., 2005; Gooding, 2006). For bioagents as microbes, viruses and toxins, various types of immunochemical devices seem to be preferred for the early response, good sensitivity and continuous monitoring capabilities. The detection occurs on the phenotype level, thus no extraction of the genetic material from the agent is required, which is the case for methods based on the polymerase chain reaction PCR (Paddle, 1996; Iqbal et al., 2000).

Our efforts in the biodection area started few years ago; the research on the electrochemical immunosensors for bioagents developed from the previous projects focused on the enzyme-based detection of chemical agents (Krejčí et al., 2008). The principle was amperometric biosensor with immobilized cholinesterase, its inhibition was indication of the presence of target compounds (organophosphate nerve agents) in the surrounding air. From the technological point of view, the biosensor employed thick film based sensors produced by screen-printing; the bioanalytical module was easily exchangable. The whole device BioNA was small enough (~ 0.5 kg) for hand-held use and it allowed for several hours of continuous operation. The acquired experience was further directed to the development of electrochemical immunosensors for bioagents detection.

The detection of bioagents was originally purely military-oriented task due to the long-lasting historical development of biological warfare agents (BWA). The common classification of bioagents comes from the Centers for Disease Control and Prevention (CDC, www.cdc.gov). BWA are classified in categories A, B and C. The category A contains the most danger agents suitable for easy dissemination and rapid transmition among persons resulting in high mortality; the following microbes are on this list: *Bacillus anthracis*, *Clostridium botulinum* toxin, *Yersinia pestis*, *Variola major*, *Francisella tularensis* and several viruses causing hemorrhagic fevers - Ebola, Marburg and Machupo. The category B includes lower mortality agents moderately easily disseminating, and the category C consists of pathogens that could potentially be engineered for mass dissemination. Overall, some 1400

infectious organisms are pathogenic to humans, including some 200 viral and 500 bacterial species (Taylor et al., 2001). *F. tularensis* was chosen as a model category A microorganism for development and verification of performance of the immunosensor device in our case; this was because this microbe has traditionally been investigated in the Department of Immunology of Military Academy in Hradec Králové for many years (Janovská et al., 2007).

2. Tularemia and Francisella tularensis

2.1 Description of the bacterium and the disease

Tularemia belongs to diseases of wild animals as hares, rabbits and rodents; it can be spread by ticks, flies and mosquitoes. The infection can also be obtained from contaminated food, water supply and soil. Occasionally, humans become infected, too. The most frequent disease manifestations are ulceroglandular, glanular, oculoglanular, oropharyngeal, pneumonic, typhoidal and septic, the onset of tularemia is quite fast and symptoms as high fever 38-40 °C, body aches and dry cough can be observed. For disease treatment, antibiotics as streptomycin and gentamicin are widely recommended and tetracycline and chloramphenicol are alternatives (Enderlin et al., 1994).

Francisella tularensis is small and nonmotile gram-negative coccobacillus. As the causative agent of tularemia, it is highly infective and only few microbes aspirated from the surrounding air are able to initiate the disease. For this reason, it was included in the category A of potential biological weapons. *F. tularensis* used to be divided into subtypes A and B. At present, four subspecies are described; the most virulent is the subsp. *tularensis* (subt. A; sometimes also named as *nearctica*, it occurres in the North America and was reported in Europe), *holartica* (subt. B; also referred as *palaeartica*, it is found in the North America as well as in Eurasia), *mediaasiatica* (central Asia) and *novicida* (it was isolated from water supplies in Utah).

2.2 Assay methods

Significant efforts exist towards rapid detection of *Francisella* in various types of samples including air, soil and food. For effective detection in the case of its bioterroristic missuse or for any preventive monitoring, very high sensitivity needs to be achieved, as only few microbes must trigger the positive result. Otherwise, the assay would become inefficient. When cultivation tests are used, the best growth is observed in cysteine-enriched broths and blood or chocolate-supplemented agars. The characteristically opalescent colonies are formed after 24 to 48 hours of incubation at 37 ^{o}C in wet atmosphere. A wide range of immunoassays was described including microagglutination (Özcürümez et al., 2004) and ELISA (Schmitt et al., 2005). The PCR is typically focused on the tul4 and fopA genes encoding 17 and 43 kDa outer membrane proteins, respectively (Emanuel et al., 2003). In the case of soil samples, the lowest limit of detection reached only 20 CFU per 1 g of soil (Whitehouse & Hottel, 2006). The real-time PCR based on SYBR Green I and tul4 gene for *F. tularensis* LVS achieved limit of detection of 0.69 fg of genomic DNA (Sellek et al., 2008). An extensive review of detection methods was published recently (Pohanka et al., 2008).

3. Immunosensing of *Francisella*

For bioanalytical detection of *Francisella*, various types of immunosensors were developed and tested. Generally, immunosensors for microbes employ specific capture of the target

cells in the sensitive area of a suitable transducer followed by formation of an immunocomplex (Fig. 1A). The specific antibodies are mostly prepared against microbial antigens exposed at the cellular surface. Antibodies become immobilized at the sensing surface, and binding of the microbes is followed either directly in real time using piezoelectric and optical devices (Fig. 1A), or indirectly using suitable enzyme labeled secondary antibody and an electrochemical measuring system (Fig. 1B).

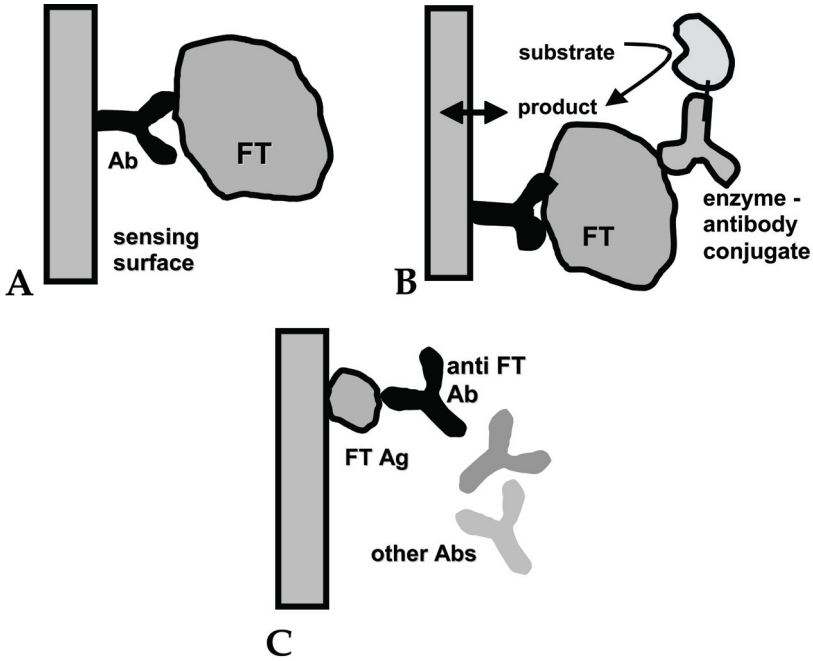

Fig. 1. Schematic view of direct (A) and indirect (B) immunosensors for detection of microbial cells and the direct detection of anti FT antibodies (C). The variants (A, B) employ immobilized capture anti FT antibody, which is specifically binding the target microbe. Alternatively (C), the immobilized FT antigen binds antibodies specific against it. The signal becomes generated in real time for the direct formats (A, C). For the indirect case (B), the captured microbial cell is labeled with the secondary antibody conjugated to a suitable enzyme label. After washing, the bound enzyme converts the added substrate into a measurable product and signal is generated as the last step of the assay.

Properties of the existing immunosensors for detection of *Francisella* are summarized in the following Table 1.

The direct measurement seems very attractive as signal is generated in real time - immediately after addition of the sample, and no additional reagents are required. However, as shown in Table 1, most direct devices provide detection capabilities only for microbial contents above 10^5 CFU/ml; a better sensitivity of assays was demonstrated for some of the indirect devices, where the use of sandwich assay formats with enzyme- or fluorophore-labelled secondary antibodies provides higher specificity and improved detection limits around 10^4 and even 10^3 CFU/ml. On the other hand, these formats employ

additional immunoreagents (Fig. 1B) and also more complex manipulation. The limits of detection required for sufficiently sensitive assay of microbial agents in the form of bioaerosols in air are hard to achieve; a partial improvement can be expected due to the collection systems capturing microbes from the air to the liquid phase (cyclones), though this was not yet demonstrated for *Francisell tularensis*.

Principle / Assay details	LOD (CFU/ml)	Length (min)	Reference
optical bidiffractive grating biosensor / D ID M R	$3 \cdot 10^4$	50	O'Brien et al., 2000
RAPTOR, fiber optic biosensor / ID M R	$1 \cdot 10^5$	10	Anderson et al., 2000
fluorescence immunosensor / ID M R	$5 \cdot 10^5$	15	Taitt et al., 2002
piezoelectric immunosensor / D (IgM clusters)	$5 \cdot 10^6$	35	Pohanka & Skládal, 2005
optial protein chip, sandwich / ID M	$2 \cdot 10^6$	60	Huelseweh et al., 2006
magnetic biosensor, sandwich, freq. mixing / ID, R	$1 \cdot 10^4$	> 60	Meyer et al., 2007
piezoelectric immunosensor / D	$1 \cdot 10^5$	5	Pohanka & Skládal, 2007
electrochemical immunosensor / ID, M	1000	25	Skládal et al., 2006

Table 1. Immunosensors proposed for detection of *Francisella tularensis*. Abbreviations: format D direct, ID indirect (with label), R repeated use, M multianalyte. LOD, limit of detection

4. Immunosensor for detection of tularemia

As it was mentioned above, the detection of cells of *Francisella* is currently not satisfactory compared to the high infectivity, when only few aspirated microbes start the disease. However, the progress of the disease after infection takes few days before clinical symptoms become manifested. Thus, as an alternative to the rather complicated detection of few microbes, an early identification of preclinical symptoms in infected individuals should be considered. In fact, tularemia can be treated with antibiotics effectively if detected shortly after infection. An early detection of the infection in the pre-clinical phase thus can be very valuable for the cases when the detection of microbes fails due to low contents under LOD of the assay. This task should employ measurement of anti-*Francisella* antibodies in serum where these appear during immunological defence of human body against infection.
The immunosensors developed for this purpose in our group will be described in the following text. Again, the formats of such assys can be direct (shown in Fig. 1C) and indirect where the captured anti-*Francisella* antibodies from serum are labeled similarly as in Fig. 1B. For testing of this approach, the mouse model was used (no human samples from individuals suffering with tularemia were available in our country) and the safe live vaccination strain of *Francisella tularensis* LVS was used. As direct and indirect assay formats, piezoelectric and electrochemical immunosensors were developed and tested, respectively.

4.1 Immunization of mice

As an animal model for tularemia, a group of female mice BALB/c was used (specific pathogen free, supplied by BioTest Konárovice, Czech Rep.). Mice were immunized by *F.*

tularensis in order to obtain the immunized mouse serum (IMS); another control group was immunized with *Escherichia coli* to obtain control (CMS) and the last group provided normal serum (NMS) to serve as a blank.
F. tularensis was applied subcutaneously with 10% of the lethal dose LD_{50} (0.1 ml of solution containing 10^5 CFU/ml. A similar amount of *E. coli* was inoculated as a negative control. On the days 1, 2, 4, 5, 6, 7, 10, 14 and 21 after immunization, three mice per each group were bled under anesthesia and the collected blood sample was incubated at 37.0 °C for 30 min, the clot was separated and serum was obtained as supernatant after two centrifugations at 3000g for 3 min. Serum samples were stored frozen at -20 °C in aliquots and thawed before measurements. All experiments on animals were realized strictly according to local legislation.

4.2 Direct piezoelectric immunosensor

The piezoelectric quartz crystals with gold electrodes (10 MHz, International Crystal Manufacturing) were modified with a monolayer of cystamine, to which the *F. tularensis* antigen was covalently linked using glutaraldehyde (Pohanka et al., 2007a). The crystal was fixed in a flow-through cell and all assay steps were performed in a flow-through set-up, the solutions at the input were exchanged manually. After stabilization of the initial background frequency (signal) in buffer for 2 to 5 min, the sample was introduced for 5 min to measure its association with the immobilized antigen. Afterwards, a zone of buffer followed and finally, the surface was regenerated for repeated use with 50 mM NaOH with 0.1% Triton X-100. The typical real-time signals for both blank serum and sera from infected mice are shown in Fig. 2, left part, regeneration phase is not shown. The experimental system for measurements with piezoelectric biosensors is presented in Fig. 3.

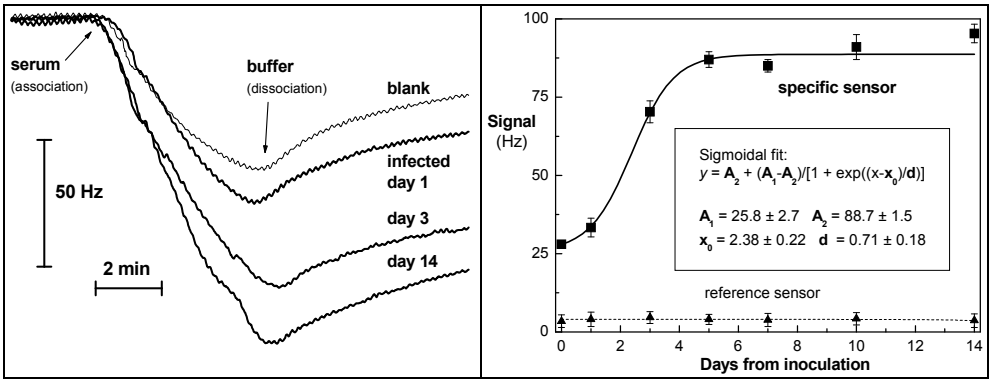

Fig. 2. Progress of infection with *Francisella* in mouse followed using the piezoelectric immunosensor. Levels of anti-*Francisella* antibodies were measured in mouse sera taken in the indicated days after innoculation. Response traces (left) and plot of responses (decrease of frequency as signal) vs. time (right). Specific sensor contained FT antigen covalently linked to the sensing surface, the reference sensor was modified with bovine serum albumin.

The crude non-purified (only diluted 10-times) sera collected from the infected mice on days 1, 3, 5, 7, 10 and 14 after inoculation were measured. NMS from healthy mice and CMS from

mice immunized by *E. coli* served as negative controls. Each sample was diluted ten times. The overall progress of antibody production is presented in Fig. 2, right part. The infection process was obvious even on the 1st day after innoculation; the signal of 33 Hz resulted for IMS while NMS provided only 28 Hz. The rapid increase of response continued to the 5th day (87 Hz) and the further increase was slower achieving maximum at 95 Hz on the 14th day. This behaviour corresponds with the first manifested symptoms of disease around the 5th day from infection (Ohara et al., 1991). No relevant difference between signal of NMS and CMS was observed. The control sensor containing immobilized bovine serum albumin as sensing element provided signals below 5 Hz with all the tested sera – CMS, NMS as well as IMS; this proves specifity of the immunosensor assay.
The obtained results were evaluated using the t-test (IMS vs. NMS, both measured on the specific immunosensor with immobilized LVS antigen, n = 3). The results measured on the 1st day after inoculation can be classified as positive with the probability level of 0.95, results from the following days (3rd and higher) were always detected with the probability level of 0.99. The RSD values for the NMS and IMS (day 14) samples were 2.3% and 2.4% for intra-day measurements (n = 5).

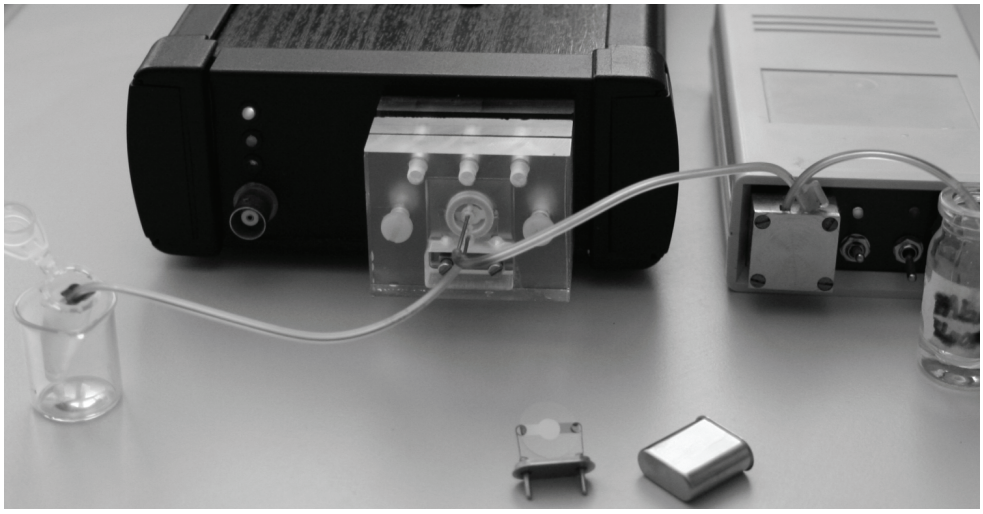

Fig. 3. The compact piezoelectric immunosensor (left) with integrated flow-through cell. The flow of solutions is realized using the miniperistaltic pump (right). The exchangable piezoelectric quartz crystal is shown in front.

4.3 Indirect amperometric immunosensor

The amperometric immunosensor was based on the gold screen-printed 4-channel electrode array (AC8, BVT Technologies), *F. tularensis* antigen was covalently immobilized on the self-assembled monolayer of cysteamine (Pohanka & Skládal, 2007b). The serum sample was measured in duplicate together with control and blank; 2.5 μl of diluted serum was directly dropped on the working electrode and incubated for 5 min. After washing, the anti-mouse peroxidase-labeled tracer Ab (SwAmPx, Sevapharma) was added and incubated for 5 min. Finally, the surface-bound peroxidase was measured amperometrically in a flow-through system:

$$H_2O_2 + 2I^- + 2H^+ \xrightarrow{\text{peroxidase}} I_2 + 2H_2O$$

$$I_2 \xrightarrow{\text{electrode, } -50\text{ mV}} 2I^-$$

Thus generated signal traces are shown in Fig. 4, left part, for the blank serum (non-infected mouse) and from sera obtained from infected mice taken in the indicated days after infection. The responses of sera (decrease of current) from individual days are shown in the right part together for both *F. tularensis* (immunized) and *E. coli* (control) groups.
The blank signal for NMS varied near around 21 nA without exhibiting any pronounced trend; similar but slightly higher response was observed for the control serum; CMS provided a higher signal (22 to 25 nA) in comparison with NMS. The IMS samples taken one day after immunization demonstrated a signal above 23 nA which was continuously increasing in the following days and resulted in the maximal response of 41 nA 21 days after immunization.

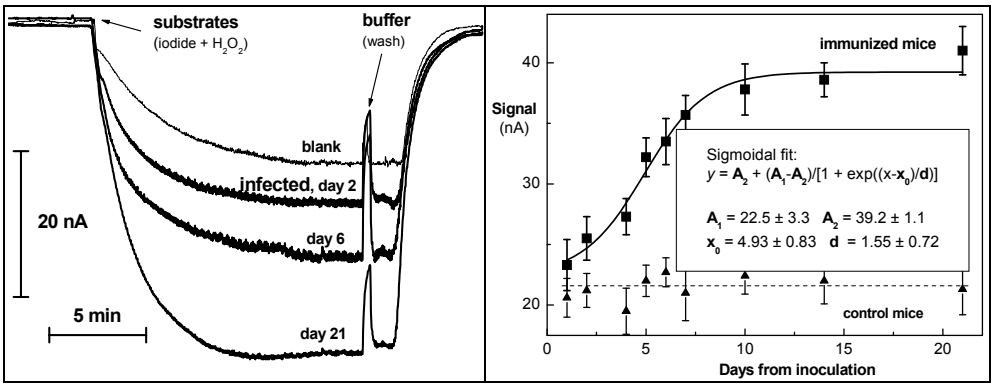

Fig. 4. Progress of infection with *Francisella* in mouse followed using the amperometric immunosensor. Response traces (left) and plot of responses (decrease of current as signal) vs. time (right). Specific sensor contained FT antigen covalently linked to the sensing surface, sera from non-imunized mice served as control.

Significantly higher signals from IMS were measured on the 5th day after immunization (32.2 ± 1.6 nA) in comparison with CMS (25.0 ± 1.9 nA). Statistically, distinguishing IMS and CMS in one day after immunization was questionable; the probability of difference was on the level 0.60 (t-test). In the following sampling on days 2 and 4, the probability grew up to the levels 0.75 and 0.89, respectively, and starting on the 5th day, the probability level was above 0.99.
The developed amperometric immunosensor provided good reliability and sensitivity of assays. A small amount of 2.5 µl sample was based on appropriately diluted 0.1 µl of original sera. Consequently, this technique can be applied in field laboratories. The instrumentation used for measurements (Fig. 5) is fully portable and battery operated (> 10 hours after full charge). After insertion of the strip sensor to the cell, the measuring sequence is fully automated using a script-based programming. The flow-through format was adopted due to better precision of assays; if the measurement will be based on a drop of substrate mixture, further miniaturization can be feasible. An important parameter of the assay is the speed of measurement. Here, the limiting step was measurement of the output signal (5 min). The other assay steps such as preincubation with sample and regeneration

can be parallelized and include unlimited number of biosensors. Thus, considering four measuring spots per the strip, up to ten measuring cycles corresponding to 40 assays can be realized within one hour.

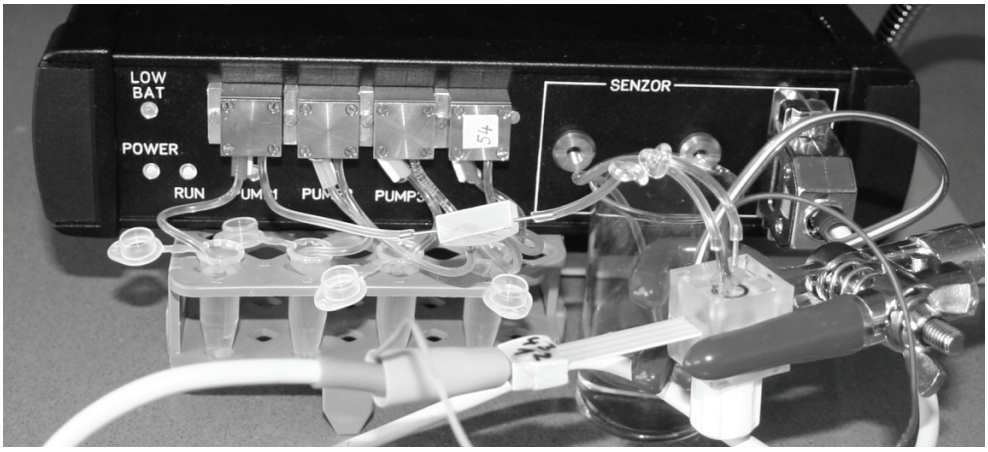

Fig. 5. The amperometric immunosensor detector ImmunoSMART. In the left part of the front pannel, four miniature peristaltic pumps are connected to minitubes with bioreagents. The flow-through cell fixed in the holder contains the exchangable screen-printed immunosensor.

4.4 Correlation of results from piezoelectric and amperometric immunosensors

To compare evaluation of sera originated from infected mice, the results obtained from both piezoelectric and amperometric immunosensors were plotted in Fig. 6. For a straightforward

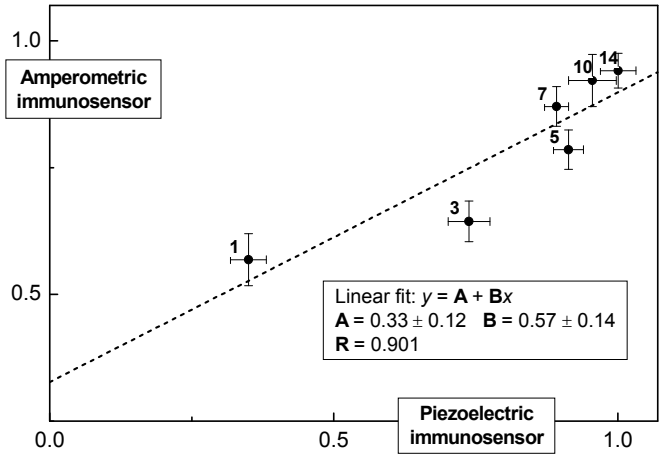

Fig. 6. Correlation of results for detection of anti FT antibodies in immunized mouse sera between piezoelectric and amperometric immunosensor; normalized data were used for correlation.

comparison, data from both systems were normalized; the results were divided by the maximal observed response to be within the 0 to 1 range. A linear correlation was obtained (R = 0.901), however, the slope of the linear regression was not equal to 1 as well as the intercept value was significantly different from 0. Obviously, this is due to the higher proportion of the binding fraction of serum immunoglobulins able to recognize a wider group of microbial antigens even before the infection with *F. tularensis* took place; this was affecting response of the amperometric immunosensor significantly more than the piezoelectric one. In fact, the simplified assay procedure for the latter one seems advantageous, as there can not be any influence of the tracer binding. In addition, based on the statistical t-test data, the direct piezoelectric system allowed earlier to resolve the sera originating from control and infected mice.

5. Future trends

Despite the promising results allowing rather fast identification of infection with tularemia, the straightforward detection and identification of bioagents remains challenging.

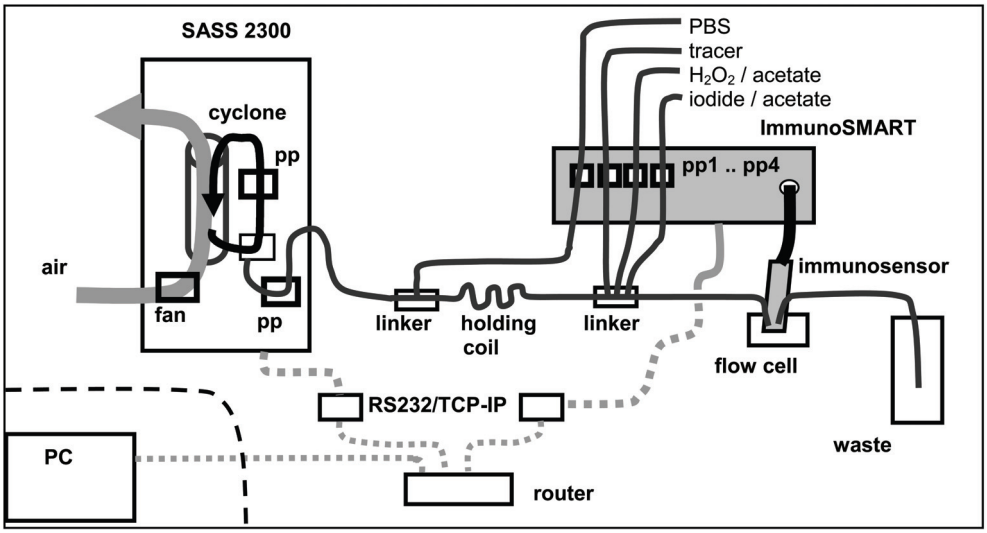

Fig. 7. Schematic representation of an amperometric immunosensor linked to the cyclone device for detection of bioaerosols.

In real situations, the monitoring of air for presence of danger bioagents should be carried out with sufficiently low limits of detection. For this reason, sampling of the monitored air should be realized with the help of a cyclone system, which captures particles from air and concetrates them in a small volume of solution. Thus obtained sample can be subsequently analyzed with either direct or indirect immunosensor (Fig. 7). For detection of bioagents, the amperometric detector should be preferred, as the use of enzyme labels provides significantly enhanced sensitivity compared to direct protocols (Table 1). The system based on the developed immunosensor detector ImmunoSMART and a commercially available cyclone SASS 2300 (Research International) is shown in Fig. 8. A program controlling both subsystems was developed in order to allow synchronized operation.

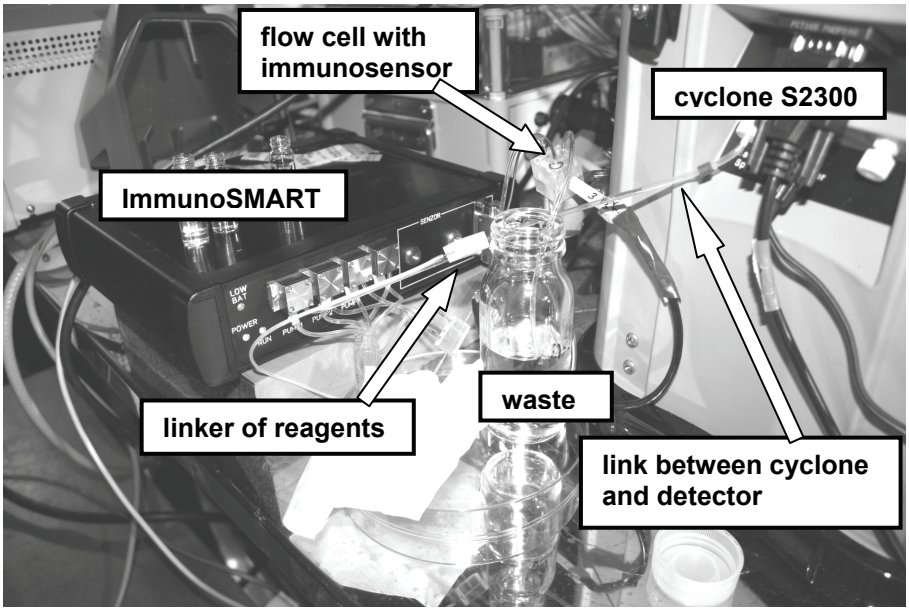

Fig. 8. Set-up for analysis of bioaerosols consisting of the detector ImmunoSMART and cyclone SASS 2300 (Research International).

For model detection of microbes in bioaerosols, the completely safe strain of *Escherichia coli* DH5α was used as *Francisella* must not be disseminated in air. In this case, sampling of air was carried out using a cyclone device for 10 min and the accumulated sample was transferred to the ImmunoSMART device. Preliminary unpublished results indicate feasibility of detection of 100 CFU/l in air, the total time of analysis being around 20 min.

6. Conclusion

The amperometric and piezoelectric immunosensors suitable for assay of *Francisella tularensis* and the associated disease tularamia are developed. A novel method for the indirect detection was based on the measurement of anti tularemic antibodies in serum samples of infected mice as a model microorganism. The direct piezoelectric biosensor was able to detect the onset of the infection process very early, even one day after injection of the bioagent. The advantage of this method is a simple direct arrangement with low cost of analysis. The proposed concept of the immunosensor seems to be suitable also for screening of human sera. The current efforts are mainly focused on the direct detection of harmful bioagents as bacteria, viruses, toxins and other pathogen and biosensors play quite important role. However, for the highly toxic bioagents causing infection in only a very small dose (low concentration, few microorganisms only), the primary detection could potentially fail and the bioagents will remain undetected. In this case, the highly sensitive complementary detection of the infection becomes extremely important. In adddition, a novel method for the indirect detection of *Francisella tularensis* was based on the screen-printed electrochemical sensing array with four measuring spots. The advantage of this multichannel sensor is the option for simultaneous measurement of the tested sample and

the control negative blank. In this way, the acquired responses will allow compensation of fluctuations in assay conditions (temperature, flow rate stability, decrease of the binding capacity, etc.). This becomes quite important when the developed immunosensor becomes utilized in field conditions.

7. References

Anderson, G.P.; King, K.D.; Gaffney, K.L. & Johnson, L.H. (2000) Multi-analyte interrogation using the fiber optic biosensor. *Biosens. Bioelectron.* 14, 10-11 (Nov. 2000) 771-777, 0956-5663

Emanuel, P.A.; Dang, J.; Gebhardt, J.S.; Aldrich, J.; Garber, E.A.E.; Henrieta, K.; Stopa, P.; Valdes, J.J. & Schultz, A.D. (2000). Recombinant antibodies: a new reagent for biological agent detection. *Biosens. Bioelectron.* 14, 10-11, (Nov. 2000) 761-770, 0956-5663

Enderlin, G.; Morales, L.; Jacobs, R.F. & Cross, J.T. (1994). Streptomycin and alternative agents for the treatment of tularemia: review of the literature. *Clin. Infect. Dis.* 19, 1 (July 1994) 42–47, 1058-4838

Gooding, J.J. (2006). Biosensor technology for detecting biological warfare agents: Recent progress and future trends. *Anal. Chim. Acta* 559, 2 (Feb. 2006) 137-151, 0003-2670

Huelseweh, B.; Ehricht, R. & Marschall, H.J. (2006) A simple and rapid protein array based method for the simultaneous detection of biowarfare agents. *Proteomics* 6, 10 (May 2006) 2972-2981, 1615-9853

Iqbal, S.S.; Mayo, M.W.; Bruno, J.G.; Bronk, B.V.; Batt, C.A. & Chambers, J.P. (2000). A review of molecular recognition technologies for detection of biological threat agents, *Biosens. Bioelectron.* 15, 11 (Dec. 2000), 549-578, 0956-5663

Janovská, S.; Pávková, I.; Hubálek, M.; Lenco, J.; Macela, A. & Stulík, J. (2007). Identification of immunoreactive antigens in membrane proteins enriched fraction from *Francisella tularensis* LVS. *Immunol. Lett.* 108, 2 (Feb. 2007) 151-159, 0165-2478

Krejčí, J.; Grosmanová, Z; Krejčová, D.; Skládal, P. & Šafář, B. (2008). Biosensor Detection of Organophosphorous Gases, In: *Commercial and Pre-Commercial Cell Detection Technologies for Defence against Bioterror - Technology, Market and Society, NATO Science for Peace and Security Series - E: Human and Societal Dynamics, Vol. 39*, Lechuga, L.M.; Milanovich, F.P.; Skládal, P.; Ignatov, O. & Austin, T.R. (Ed.) 155-165, IOS Press, 978-1-58603-858-8, Amsterdam, The Netherlands

Lim, D.V.; Simpson, J.M.; Kearns, E.A. & Kramer, M.F. (2005). Current and developing technologies for monitoring agents of bioterrorism and biowarfare. *Clin. Microbiol. Revs.* 18, 4 (Oct. 2005) 583-607, 0893-8512

Meyer, M.H.F.; Krause, H.J.; Hartmann, M.; Miethe, P.; Oster, J. & Keusgen, M. (2007) *Francisella tularensis* detection using magnetic labels and a magnetic biosensor based on frequency mixing. *J. Magnetism Magnet. Mat.* 311, 1 (Apr. 2007) 259-263, 0304-8853

O'Brien, T.; Johnson, L.H.; Aldrich, J.L.; Allen, S.G.; Liang, L.T.; Plummer, A.L.; Krak, S.J. & Boiarski, A.A. (2000) The development of immunoassays to four biological threat agents in a bidiffractive grating biosensor. *Biosens. Bioelectron.* 14, 10-11 (Nov. 2000) 815-828, 0956-5663

Ohara, T.; Sato, H.; Fujita, T.; Ueno, M. & Homma, M. (1991) Clinical manifestation of tularemia in Japan – analysis of 1355 cases observed between 1924 and 1987. *Infection* 19, 1 (Jan. 1991) 14-17, 0300-8126

Özcürümez, M.P.; Kischel, N.; Priebe, H.; Splettstöster, W.; Finke, E.J. & Grunow, R. (2004). Comparison of enzyme-linked immunosorbent assay, western blotting, microagglutination, indirect immunofluorescence assay, and flow cytometry for serological diagnosis of tularemia. *Clin. Diagn. Lab. Immunol.* 11, 6 (Nov. 2004) 1008-1015, 1098-6588

Paddle, B.M. (1996). Biosensors for chemical and biological agents of defence interest. *Biosens. Bioelectron.* 11, 11 (Nov. 1996), 1079-1113, 0956-5663

Pohanka, M. & Skládal, P. (2005) Piezoelectric immunosensor for *Francisella tularensis* detection using immunoglobulin M in a limiting dilution. *Anal. Lett.* 38, 3 (March 2005) 411-422, 0003-2719

Pohanka, M. & Skládal, P. (2007a) Piezoelectric immunosensor for the direct and rapid detection of *Francisella tularensis*. *Folia Microbiol.* 52,4 (Feb. 2007) 325-330, 0015-5632

Pohanka, M. & Skládal, P. (2007b) Serological diagnosis of tularemia in mice using the amperometric immunosensor. *Electroanalysis* 19,24 (Dec. 2007) 2507-2512, 1040-03971040-0397

Pohanka, M.; Pavliš, O. & Skládal, P. (2007) Diagnosis of tularemia using piezoelectric biosensor technology. *Talanta* 71,2 (Feb. 2007) 981-985, 0039-9140

Pohanka, M; Hubálek, M.; Neubauerová, V., Macela, A.; Faldyna, M.; Bandouchová, H. & Pikula, J. (2008). Current and emerging assays for Francisella tularensis detection: a review. *Veterinarni Medicina* 53, 11 (Nov. 2008) 585-594, 0375-8427

Schmitt, P.; Splettstösser, W.; Özcürümez, M.P.; Finke, E.J. & Grunow, R. (2005). A novel screening ELISA and a confirmatory western blot useful for diagnosis and epidemiological studies of tularemia. *Epidemiol. Infect.* 133, 4 (Aug. 2005) 759-766, 1469-4409

Sellek, R., Jimenez, O.; Aizpurua, C.; Fernandez-Frutos, B.; De Leon, B.; Camanacho, M.; Fernandez-Moreira, D.; Ybarra, C. & Carlos Cabria, J. (2008). Recovery of Francisella tularensis from soil samples by filtration and detection by real-time PCR and cELISA. J. Environ. Monit. 10, 3 (Mar. 2008) 362-369, 1464-0325

Skládal, P.; Symerská, Y.; Pohanka, M.; Šafář, B. & Macela, M. (2005) Electrochemical immunosensor for detection of Francisella tularensis, In: Defence against Bioterror: Detection Technologies, Implementation, Strategies and Commercial Opportunities, NATO Security through Science Ser. B – Physics and Biophysics, Morrison, D; Milanovich, F.; Ivnitski, D. & Austin, T.R. (Ed.) 221-232, Springer, 1-4020-3386-9, Dordrecht, The Netherlands

Taitt, C.R.; Anderson, G.P.; Lingerfelt, B.M.; Feldstein, M.J. & Ligler, F.S. (2002) Nine-analyte detection using an array-based biosensor. Biosens. Bioelectron. 74, 23 (Dec. 2002) 6114-6120, 0956-5663

Taylor, L.H.; Latham, S.M. & Woolhouse, M.E.J. (2001). Risk factors for human disease emergence. *Phil. Trans. R. Soc. Lond. B* 356, 1411 (July 2001) 983-989 1471-2970

Whitehouse, C.A. & Hottelm H.E. (2006). Comparison of five commercial DNA extraction kits for the recovery of *Francisella tularensis* DNA from spiked soil samples. Mol. Cell Probes 21, 2 (Apr. 2006) 92-96, 1096-1194

8

New Ideas for *in vivo* Detection of RNA

Irina V. Novikova, Kirill A. Afonin and Neocles B. Leontis
Bowling Green State University
USA

1. Introduction

The parallel discovery of the catalytic potential of RNA by Tom Cech and Sydney Altman at the beginning of the 1980s completely changed our view of the capabilities of RNA molecules and won them the Nobel prize in 1989 (Kruger et al., 1982; Guerrier-Takada et al., 1983). Since then, many new roles have been discovered and assigned to RNA, including the ability to form complex multitasking, supramolecular machines, such as ribosomes or spliceosomes, in which RNAs play leading roles. While only about 1.5 % of the human genome codes directly for protein sequences, a large fraction of it is nonetheless transcribed to produce many noncoding RNAs (ncRNA) that carry out important cellular functions (International Human Genome Sequencing Consortium, 2004). The structures and functions of some ncRNA have been extensively characterized, for example, ribosomal RNAs (rRNA), transfer RNAs (tRNA), small nuclear and nucleolar RNAs (snRNA and snoRNA). Moreover, applications of recent technological advances are revealing new classes of ncRNA molecules with novel or yet unknown functions, ranging in size from very small (20-30 nts) to thousands of nucleotides long. Small ncRNA (~20-30nts in length) include microRNA (miRNA), Piwi-interacting RNA (piRNA), small interfering RNA (siRNA), trans-acting siRNA (ta-siRNA), natural antisense transcript siRNA (nat-siRNA) and small scan RNA (scnRNA) all of which help regulate various stages of gene expression (Choudhuri, 2009). The functions of "long noncoding RNA" are still not understood, but they seem to be involved in transcriptional and epigenetic gene regulation (Ponting et al., 2009).

Many ncRNAs form distinct yet very diverse three-dimensional structures to carry out their functions (Noller, 2005; Staple & Butcher, 2005; Montange & Batey, 2008). These functions include fundamental roles at all stages of gene expression including chromosome remodeling, transcriptional and translation regulation, mRNA processing, transport, and localization, protein translocation and posttranslational modification. RNA molecules use various mechanisms to participate in these processes. For example, miRNA, siRNA and piRNA inhibit gene expression by hybridizing to complementary sequences of target mRNAs in association with RISC ribonucleoprotein complexes and either temporarily block translation or target the mRNA for destruction (Carthew, 2006; Bushati & Cohen, 2007; Boyd, 2008). Riboswitches, usually located in the 5' untranslated region (5'-UTR) of mRNA, also inhibit translation, but do so by forming specific three-dimensional structures, that respond to small molecule metabolites that are products of the pathway to which the gene belongs. Upon binding cognate metabolites, riboswitches undergo conformational changes in their secondary and tertiary structures which usually result in suppression of

transcription or translation. Some riboswitches actually function as ribozymes, resulting in self-cleavage of the mRNA and complete inactivation of the mRNA (Montange & Batey, 2008; Winkler et al., 2004).

Defects in RNA expression or processing due to mutations and misregulation can lead to serious diseases (Cooper et al., 2009). Recent studies of miRNA suggest their important role in cancer biology (Lee & Dutta, 2009). The expression levels of specific miRNA are highly correlated with tumor, tissue type or disease stage. Aberrant miRNA levels are also involved in other diseases, including Tourette's syndrome, fragile X syndrome, myotonic dystrophy, and schizophrenia (Abelson, 2005; Caudy et al., 2002; Bilen et al., 2006; Perkins et al., 2007).

All RNAs are produced by transcription in the nucleus, where most processing also takes place. Processing may require transport of RNA between specific locations in the nucleus (Vargas et al., 2005). Once mature, most RNAs are exported to the cytoplasm through the nuclear pores (Stewart, 2007; Kelly & Corbett, 2009), where some may be shuttled back to the nucleus (Hwang et al., 2007; Takano et al., 2005). Once in the cytoplasm, RNAs maybe further transported to specific sites to carry out their functions, depending on the cell type, its developmental stage, environmental signals or perturbations.

2. Review of RNA detection/visualization methods

Several general methods for *in situ* or *in vivo* visualization of RNA processing and transport are currently being used. However, none are as powerful and versatile as methods developed to visualize proteins *in vivo* that employ autofluorescent proteins such as green fluorescent protein (GFP) and its relatives. Autofluorescent ptotein (AFP) technology was made possible by a series of advances beginning with the isolation of GFP from jellyfish in 1962 by Osamu Shimomura. It was not until much later, however, that GFP was cloned by Douglas Prasher (1992) and expressed in different microorganisms by Martie Chalfie (Shimomura, 2009; Chalfie, 2009; Shimomura et al., 1962; Prasher et al., 1992; Chalfie et al.; 1994). Later, Roger Tsien contributed to this field by engineering a whole library of GFP color mutants with increased photostabilities and a wide range of absorption and emission frequencies (Tsien, 2009; Shaner et al., 2004; Wang et al., 2004; Heim et al., 1995). In conjunction with advances in fluorescence microscopy and new spectroscopic tools, AFP technology enabled the development of general purpose methods for intra-cellular genetic tagging to monitor the motions and interactions of two or more proteins simultaneously. This methodology involves genetic fusion of an autofluorescent protein to the protein of interest and its localization at the subcellular level by fluorescence microscopy *in vivo* (Bertrand et al., 1998). Unfortunately, no autofluorescent RNA molecules have been discovered to date that can be used to both detect and monitor RNA *in vivo.* Given the important and diverse roles RNA molecules play in living cells, developing new tools for *in vivo* monitoring of RNA dynamics is crucial for better understanding RNA transport, localization, and functional interactions.

2.1 FISH and molecular beacons probes

Traditional methods for determining which RNAs are produced by a given cell population involve cell disruption and total RNA extraction and its analysis *in vitro* using various tools to identify and quantify specific RNAs. Currently available methods include polymerase chain reaction (PCR), to amplify low copy RNA, Northern Blotting, to separate cellular RNA

by size, microarrays and serial analysis of gene expression (SAGE) for high throughput detection of many RNAs at once. Most techniques require the extraction of RNA from cell populations although some have been adapted for single-cell analysis. The ability to study RNA in a single live cell offers new capabilities for investigating gene expression to better understand RNA function in living cells. This chapter focuses exclusively on fluorescence-based methods, which at this time seem to be the best adapted for *in vivo* real-time RNA visualization to yield subcellular spatial information.

Fluorescence-based techniques have gained popularity for several reasons. While radioactive labeling and autoradiography are potentially more sensitive, fluorescent-based methods have the advantages of 1) using labels with long shelf lives, 2) low toxicity and ease of handling, and 3) high resolution imaging at the single cell level. Moreover, a variety of fluorophores and quenchers, which differ in excitation and emission wavelength, fluorescence lifetime, and anisotropy, are commercially available. This makes fluorescent-based methods excellent candidates for high-throughput screening and real-time *in vivo* detection.

Several recent reviews provide a critical evaluation of fluorescent methods that are currently available for live-cell RNA imaging (Bao et al., 2009; Rodriguez et al., 2007; Tyagi, 2009; Schifferer & Griesbeck, 2009, Raj & van Oudenaarden, 2009). Modern fluorescent visualization approaches can be subdivided into the two main groups with respect to how the fluorescent probe is delivered (Figure 1). The traditional and still most widely used method is fluorescent *in situ* hybridization (FISH) (Moter & Gobel, 2000; Amann et al., 2001), which makes use of short exogenous oligonucleotide probes (about 15-30 nts in length) that carry a fluorophore tag and are complementary to a selected sequence in the target cellular RNA molecule. The main limitation of FISH is that the emission signal of bound and unbound probes is about the same, so cells must be fixed prior to hybridization and then extensively washed to remove unbound probes, which otherwise interferes with the desired signal. Newer "quenched probe" methods for *in vivo* RNA visualization employ fluorophore-labeled hybridization probes to which quencher molecules are also attached to quench the emission of the fluorophore when the probe is not bound to the target RNA (Figure 1A). This approach eliminates the need for washing unbound probes and allows direct imaging of RNA in intact cells. A variety of probe designs have been implemented to position the quencher close to the fluorophore in the unbound state while separating them when the probe binds to its target. "Molecular beacons" (MBs) are the best-known examples of this class of probes (Tyagi and Kramer, 1996; Tyagi et al.; 1998). In the simplest design, the quenched probe forms a hairpin stem-loop structure in which the loop sequence is complementary to the target RNA and the fluorophore and quencher molecules are attached to the 5' and 3' ends of the probe. The terminal four to six bases of the 5′ and 3′ ends are complementary, so that in the absence of the target they form a short double helical stem that brings the quencher close to the fluorophore, thus quenching its fluorescence. Upon recognition of the target sequence, the hairpin stem of the probe unfolds. This separates the fluorophore from the quencher and restores fluorophore emission. For more information about the design and use of molecular beacons as probes for *in situ* hybridization the reader is referred to the recent publications on the subject (Silverman & Kool, 2005; Tsourkas et al., 2003; Wang et al., 2009; Bao et al., 2009). Numerous variations of quenched probes, which aim to improve the signal-to-background ratio, increase *in vivo* stability or target specificity, have been introduced (Bao et al., 2009). A major concern is to balance specificity and binding kinetic on- and off-rates. Increasing the length of the probe sequence complementary

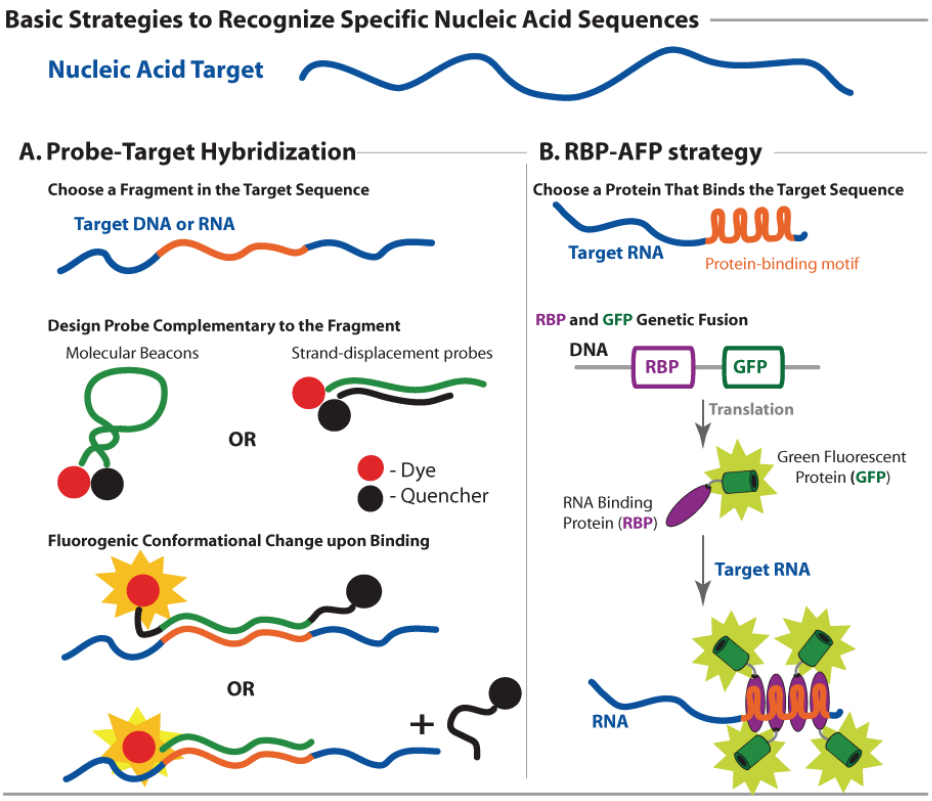

Fig. 1. Schematic representation of several strategies for *in vivo* RNA visualization. The target RNA is represented as a blue strand containing an orange probe hybridization site or protein-binding motifs. A. Probe-target hybridization using "quenched" probes (green strands with attached fluorophore (red) and quencher (black). "Quenched" probes are optically silent in the absence of target. Molecular beacons (on the left) form helical stem that brings quencher close to chromophore. Upon target binding, the terminal stem is disrupted, separating the fluorophore-quencher pair and restoring fluorescence. Strand-displacement probes (on the right) are the pairs of complementary sequences. Upon target recognition, green strand forms more stable probe-target hybridization complex leading to the black strand displacement and yielding emission signal. B. RBP-AFP strategy. Multiple binding motifs for a specific RBP are genetically encoded into the 3'-UTR region of the target RNA (orange region of the sequence). RNA-binding protein (shown in pink) is than fused with GFP (green color) that serves as a fluorescent reporter. When both modified target RNA and RBP-GFP construct are co-expressed in the cell, RBP-GFP constructs interact with target RNA resulting in high localization of fluorescent signal.

to the target increases specificity so long as (i) the melting temperature for exactly matching sequences is greater than physiological temperature and (ii) the melting temperature for single-base mismatches remains below this temperature. If the hybridization sequence is too short, unintended targets may also be bound thus decreasing specificity. If it is too long, one

or more mismatches may be tolerated, decreasing specificity and reducing off-rates from correct targets and thus decreasing the biosensor's responsiveness to decreases in levels of the target RNA.

To increase *in vivo* stability and prevent Rnase H degradation of the probe, oligonucleotides with modified backbone have been introduced, including 2'-O-methyl modified MBs, locked nucleic acid MBs (LNA-MBs) and peptide nucleic acid MBs (PNA-MBs). For further information regarding these modifications, the following publications should be consulted (Tsourkas et al., 2002; Wang et al., 2005, Kuhn et al., 2002).

A number of innovations have been proposed to improve the signal-to-noise ratio of molecular beacons such as dual fluorescence resonance energy transfer (FRET) MBs and quenched autoligation (QUAL) probes (Santangelo et al., 2004; Santangelo et al., 2006; Satterfield et al., 2007). Dual FRET MBs involve a pair of quenched probes that bind to adjacent sites on the target RNA. One probe contains a FRET donor, and the other a FRET acceptor. When both are bound to the target, the donor can transfer its excitation energy to the acceptor, producing FRET emission. A further improvement to dual probes is the use of quenched autoligation (QUAL) probes which bind to adjacent sites and autoligate forming a single long probe that binds to the target with high specificity (Silverman and Kool, 2005). However QUAL probes have the disadvantage of binding essentially irreversibly to targets and hence cannot be used to monitor decreases in target RNAs dynamically.

Quantum dots, gold or silver nanoparticles and photoluminescent polymers were recently introduced as alternatives to organic fluorescent dyes for labeling hybridization probes (Algar et al., 2009; Kim et al., 2008). Quantum dots are brighter and have better resistance to photobleaching than organic fluorophores. Moreover, quantum dots possess broad absorption bands and narrow tunable emission bands that are desirable for optical multiplexing. In comparison with conventionally labeled probes, that have a tendency to accumulate rapidly in nuclei when microinjected, probes conjugated to quantum dots remain in the cytoplasm (Chen et al., 2007). Photoluminescent polymers and gold nanoparticles have better quenching efficiencies as compared to organic dyes (Kim et al., 2008).

Disadvantages of FISH and "quenched probe" techniques include the requirements for time-consuming and expensive chemical modifications of probe sequences to covalently attach fluorophore and quencher molecules. Moreover, these conjugates are not able to diffuse directly into cells and require perturbation or disruption of the membranes.

2.2 RNA labelling with AFP conjugates

2.2.1 General GFP-based strategy

GFP and related autofluorescent proteins, proven immensely useful in visualizing proteins *in vivo*, have also been adapted for detection of RNA molecules *in vivo* (Bertrand et al., 1998; Valencia-Burton et al., 2007). The basic approach involves the genetic fusion of an RNA-binding protein domain (RBP) to an auto-fluorescent protein such as GFP (Figure 1B). The simultaneous genetic modification of the gene for the cellular RNA of interest incorporates an RNA sequence that is recognized by the RBP domain in the target RNA at a location, that does not interfere with its function. This approach was demonstrated by Bertrand and coworkers, who genetically fused the coat protein from the bacterial phage MS2 to GFP to track *in vivo* mRNA encoded from a gene into which multiple MS2 coat protein-binding sites were inserted (Bertrand et al., 1998). When the RBP-GFP fusion and the modified target

RNA are co-expressed in the same cells, multiple copies of RBP-GFP bind to the target RNA, producing a strong fluorescent signal. However, RBP-GFP constructs also emit in their unbound forms and contribute to the background signal. Thus, the need to bind multiple copies of RBP-GFP to the target RNA is to achieve adequate signal-to-background ratio. The disadvantage is the relatively large size of the fluorescent probe complex, which can potentially interfere with RNA transport and localization.

2.2.2 "Split-GFP"

To reduce the background signal from unbound RBP-GFP, the "protein fragment complementation" (PFC) or "split-GFP" methodology was introduced (Valencia-Burton et al., 2007). This method involves the application of rational protein design to separate the autofluorescent protein sequence into two parts that do not fluoresce individually and can be expressed separately. Each part is fused to a different RBP domain. In the presence of a target RNA that is engineered to contain adjacent binding motifs specific to the two RBPs, the two protein fragments are brought together to reconstitute an intact fluorescent protein. In addition to reduced background signal, this method has the virtue that it does not require introducing exogenous RNA fluorescent probes, and can therefore be considered a label-free method. The main disadvantage of this method is the fact that signal generation is essentially irreversible, limiting its use for real-time dynamics of RNA expression levels. An additional limitation of AFP-based methods is the relatively large size of the protein tag (~270 kDa for multiple copies), which raises concerns that transport and localization of the target RNA may be perturbed (Bao et al, 2009; Tyagi, 2009).

We compare the features and advantages/disadvantages of the latter-mentioned methods for *in vivo* imaging of RNA in Table 1. Rows specify probe and target parameters or additional limitations/advantages. Hybridization probes are subdivided into FISH probes (column 2) and "quenched probes", including MBs (Column 3); autofluorescent probes (AFP), including GFP, are subdivided into fused (Column 4) and split formats (Column 5). An alternative imaging strategy involves fluorogen-binding aptamers (column 6,7) and will be discussed in the next section, starting with a brief overview of aptamer selection technology and extending to a detailed discussion of how aptamers have been adapted for use as biosensors. These methods are not as developed as RBP-AFP and hybization methods but show potential for further development for *in vivo* use.

3. Aptamer-based RNA detection

3.1 Overview of aptamer technology

Aptamers are functional, single-stranded RNA or DNA oligonucleotides, usually 30 to 100 nts in length, artificially selected from combinatorial libraries for high binding affinities to specific molecular targets. Combinatorial libraries of oligonucleotides, randomized at desired sequence positions and comprising up to 10^{16} different sequences, can be easily generated by modern nucleic acid synthesizers. The process of screening a randomized oligonucleotide pool to identify and amplify sequences that perform a specific function is called "Systematic Evolution of Ligands by Exponential Enrichment" (SELEX) and was introduced almost 20 years ago (Tuerk & Gold, 1990; Ellington & Szostak, 1990). SELEX has been used to obtain high affinity aptamers to almost any conceivable target and has even been adapted to obtain catalytic nucleic acids (ribozymes and DNAzymes) by selecting for

Column 1	Column 2	Column 3	Column 4	Column 5	Column 6	Column 7
Method	Hybridization probes		AFP-based		Fluorogen-binding aptamers	
	Fluorescent in situ hybridization (FISH)	Quenched probes	General	split-AFP	Gnetic fusion of aptamer into target RNA	Allosteric aptamer-based approach
Suitable for in vivo study	No (cells must fixed)	YES	YES	YES	YES	YES
Average probe size	15-30 nts (5-10 kDa)*	< 50 nts (16.5 kDa)	Multiple probes (about 270kDa)	Single probe (< 100 kDa)	< 60 nts (20 kDa)	
Unbound probe	Fluorescent	Notfluorescent or low fluorescent	Fluorescent	Nonfluorescent	Nonfluorescent	Nonfluorescent
Delivery of the probe	Exogenous		Transfection or genetic fusion		Genetic fusion	Exogenous
Target RNA	Unmodified or modified		Genetically modified		Genetically modified	Unmodified
Additional advantages	Well-adapted	1) High potential for optical multiplexing; 2) better specificity compare to FISH; 3) low background; 4) easy adapted for FRET	1) No perturbation of the cell; 2) not as sensitive to target secondary structure.	1) Low background; 2) the tag size is reduced.	no need for additional co-expressed constructs and to balance the AFP probe levels with the target RNA	no chemical attachments of fluorophores and quenchers - label free
	Real-time in vivo RNA imaging is not possible.			GFP reconstitution is irreversible (not possible to monitor the gene downregulation).	1) free dyes penetrate cells better than hybridization probes; 2) signal generation is reversible	
Additional drawbacks and limitations	1) Unmodified probes are subject to degradation- leading to false positives; 2) Hybridization site selection is difficult due to target secondary structure and multiple protein binding sites; 3) probes tend to accumulate in the nucleus .		1) Genetic manipulation of RNA may not always achievable; 2) Large probe size may interfere with RNA transport; 3) AFPs are phototoxic to the cells.		1) the number of suitable fluorogenic dyes is rather limited; 2) low number of fluorophore-binding aptamers with light-up properties are available; 3) not adequately tested in living cells.	
Challenges and opportunities	New bioinformatic methods to achieve better hybridization site selection.		1) Infrared emission proteins for tissue and organism studies; 2) new bioinformatic methods for positioning of protein binding motifs.		1)Expanding the number of available fluorogenic dyes; 2) Expanding light-up pairs to fully cover the visible-near-IR spectrum; 3) adapt for *in vivo* use; 4) improving bioinformatic tools to identify aptamer insertion or hybridization sites.	

* calculate 330Da per nucleotide

Table 1. Comparative analysis of in vivo RNA visualization methods. *-calculations based on 330 Da per nucleotide.

transition-state analogues (Weigand et al., 2006; Schlosser et al., 2006). This technology has therefore revolutionized the field of sensing chemistry by enabling researchers to systematically generate numerous aptamers targeting a diverse range of analytes. Large numbers of RNA and DNA aptamers have been obtained by this method in the past 20 years, targeting a broad range of small molecules including organic dyes, amino acids, cofactors, carbohydrates and nucleotides, as well as proteins and nucleic acids (Klussmann, 2006). Aptamers against different classes of antibiotics, proteins and even whole cells have already found wide applications in biosensing, diagnostics, drug development and nanomedicine, as recently reviewed by other authors (Liu et al., 2009; Cho et al., 2009).

Aptamers provide a nucleic acid-based alternative technology to monoclonal antibodies for specific recognition of diverse molecular targets. Aptamer selection exhibits a number of advantages over monoclonal antibody technology including: 1) versatility in designing selection strategies; 2) lower cost; and 3) easy scale-up and production as no cell or animal culture is needed. Other advantages of using nucleic acid aptamers in biosensors include their relatively small sizes, high analyte specificities and high affinities (K_ds down to pM range), low toxicities and immunogenicities, and amenability to chemical modification to suit the desired application. Finally, they are small enough that their 2D structures can be reliably predicted and their 3D structures solved by NMR solution methods, which facilitates "tuning up" their chemical and biological properties.

SELEX begins with chemical synthesis of a randomized DNA pool. If selection of an RNA aptamer is the goal, the DNA pool is transcribed prior to the selection procedure. Next, the pool is incubated with the target molecule to achieve efficient binding. This is followed by a carefully designed selection step to sequester those DNA or RNA oligonucleotides in the pool exhibiting the desired functional properties - this selection process being the most crucial step. Finally, the amplification step enriches the pool, and the entire cycle is repeated for a sufficient number of times to obtain a pool comprising only molecules with a desired functional property. The original SELEX procedure has been modified to achieve higher affinity and specificity of aptamer products (e.g. Negative SELEX, Counter SELEX), to improve selection towards more complex targets (e.g. Genomic SELEX, Deconvolution-SELEX, Tissue-SELEX) or to select aptamers with novel functional properties (e.g.Covalent SELEX, Photo-SELEX) (Stoltenburg et al., 2007).

The Ellington group established a database of aptamers that is current as of 2006 and provides aptamer targets, sequences, details regarding selection procedures and references to original publications. It can be accessed at http://aptamer.icmb.utexas.edu/site (Lee et al., 2004).

3.2 Fluorogen-binding aptamer-based systems with light-up properties

Organic dyes were the first targets used to develop the SELEX methodology for RNA and DNA (Ellington & Szostak, 1990; Ellington & Szostak., 1992). Recent work has been directed to obtain aptamers that target fluorogenic dyes, with the aim of developing new *in vivo* tagging systems for cellular RNA molecules as alternatives to RBP-GFP fusion constructs. However, initial selections of fluorophore-binding aptamers were actually intended for other purposes. For example, Malachite Green (MG) dye has long been known to generate hydroxyl free radicals when irradiated with visible light. Liao *et al* exploited this property in 1994 by conjugating MG to antibodies to target proteins *in vivo,* a technique called "Chromophore-assisted laser inactivation" (Liao et al., 1994). This inspired Grate and

Wilson to select an RNA aptamer to bind MG and selectively target specific RNA molecules for inactivation *in vivo (*Grate & Wilson, 1999). An RNA aptamer to Hoechst dye 33258 was also selected to study gene regulation while RNA aptamers for Sulforhodamine B and Fluorescein were selected for potential *in vivo* RNA labeling (Werstuck & Green, 1998; Holeman et al, 1998). Werstuck and Green showed that they could regulate a gene *in vivo* which had been modified by the insertion of the Hoechst dye by adding the dye to the medium (Werstuck & Green, 1998).

This earlier work was subsequently adapted to obtain high-affinity aptamers that specifically bind to fluorogenic dyes, defined as molecules which exhibit minimal emission when free in solution, but which fluoresce intensely when tightly bound. Any strategy where an increase in emission signal occurs upon specific binding to a target is called a "light-up" methodology, and fluorogen-aptamer complexes are often referred to as “fluoromodules” or “light-up pairs”. The performance of sensing systems is usually quantified in terms of “fluorescence enhancement” and so it is important to define what is meant by this term. For classic molecular beacons or FRET probes, fluorescence enhancement is defined as the ratio of the emission of the probe bound to its cognate target divided by the emission of free probe in the absence of the target. For light-up dye/aptamer pairs, fluorescent enhancement is defined as the ratio of the emission of the light-up dye bound to its aptamer divided by the emission of the free dye in solution. For biosensors employing light-up dye/aptamer pairs allosterically linked to target recognition domains, fluorescence enhancement is defined as the ratio of the emission of the dye in the presence of both biosensor and target divided by the emission of the dye in the presence of the biosensor alone. In genetic fusions of dye-binding aptamers with target RNAs, fluorescence enhancement is the ratio of the emission of the dye bound to the aptamer fused with the target RNA divided by the emission of the dye in the presence of the target lacking aptamer modules.

We focus the rest of this section on efforts to design light-up pairs and to adapt them for use as biosensors to detect and image specific molecules *in vitro* and *in vivo*. We begin with the MG aptamer light-up pair, which exhibits the most dramatic increase in fluorescence (Figure 2). Triphenylmethane dyes such as MG exhibit low fluorescence when free in solution due to deactivation channels associated with torsional motion of phenyl groups. When placed in environments that restrict these motions, these dyes become strongly fluorescent. Babendure et al were the first to observe that MG fluorescence increased dramatically when the dye is bound to the aptamer selected by Grate and Wilson, and thus subsequent works focused on adapting this light-up pair for biosensing (Babendure *et al*., 2003; Grate & Wilson, 1999). Crystal structure analysis of the MG aptamer bound to tetramethylrosamine (TMR), a MG analog, revealed that it comprises an RNA helix containing a large and asymmetrical internal loop (Baugh et al., 2000). The nucleotides of the internal loop form a series of stacking and non-Watson-Crick basepairing interactions to create a unique binding pocket that restricts the flexibility of the dye and keeps it in a highly fluorescent state (Figure 2A, 2B). The high affinity of this aptamer for MG (K_d=117 nM) and the high fluorescence enhancement that results from binding (2360-fold) have encouraged several groups to apply it to create programmable nucleic acid biosensing platforms (Babendure et al., 2003; Stojanovic & Kolpashchikov, 2004; Hirabayashi et al., 2006; Afonin et al., 2008). These will be described in more detail in the next section after we cover other efforts to develop new light-up pairs.

3.3 Novel approaches for "light-up" dye/aptamer pairs selection

Sando and coworkers suggested a new route for generating specific light-up pairs starting with a conventional fluorescent DNA-staining dye that exhibits a number of favorable characteristics, including cell permeability, solubility, and stability in cellular environments (Sando et al., 2007; Sando et al., 2008). The key idea to this approach was demonstrated using Hoechst dye 33258, a widely used fluorescent stain for dsDNA molecules that fluoresces upon binding to the minor groove of dsDNA. To adapt this dye for more specific light-up applications, a variety of chemical modifications of the dye were employed to reduce or completely suppress its nonspecific affinity for dsDNA. The most effective modification of the dye for this purpose was the addition of two t-Butyl groups to its terminal phenol ring (The resulting "Hoechst 33258 derivative" is shown in Figure 2C). Next, SELEX was used to obtain a DNA aptamer that bound Hoechst 33258 derivative with K_d = 878 nM and enhanced fluorescence emission by 191-fold (Sando et al., 2007). Further work obtained an improved RNA aptamer showing higher affinity for the dye (K_d=35 nM) but somewhat reduced emission enhancement (56-fold).

A similar strategy was adapted by Constantin and coworkers to design a novel fluorogenic cyanine dye, Dimethyl Indole Red (DIR) (Constantin et al., 2008). Cyanine dyes such as thiazole orange (TO) and its derivatives are fluorogenic intercalation dyes that comprise two heterocycles separated by a methine group. Substitution in TO of a bulky dimethylindole heterocycle in place of the thiazole ring sterically hindered intercalation. Addition of an anionic propylsulfonate group further minimized nonspecific interactions with nucleic acids by increasing electrostatic repulsion (DIR is shown in Figure 2C). An RNA aptamer was obtained for DIR by SELEX that binds with K_d=87 nM and 60-fold emission enhancement. An advantage of the cyanine dyes is that they have relatively narrow emission bands, their emission wavelength maxima easily varied by chemical modification. As a group, their emission maxima cover much of the visible spectrum and extend into the near infrared.

Another recently developed approach for creating light-up dyes is to start with a dye that emits when free in solution and to covalently attach electron donor groups that quench its emission by a photo-induced electron transfer (PET) process (Sparano & Koide, 2005; Sparano & Koide, 2007). Aptamers that bind exclusively to the quencher moieties are then selected. The idea is to obtain aptamers that can block electron transfer and thereby restore emission of the fluorophore moiety. The PET approach was demonstrated in principle using 2',7'-dichlorofluorescein (DCF) as a fluorophore and N-(p-methoxyphenyl)-piperazine (MPP) as a quencher (Figure 2D). An RNA aptamer for the MPP quencher moiety was obtained by SELEX and was indeed found to enhance DCF fluorescence in the DCF/MPP conjugate in a concentration-dependent manner. As the authors pointed out, however, this particular DCF-MPP/aptamer system is unsuitable for *in vivo* applications because the fluorescence enhancement is only about 13-fold at 100 μM aptamer concentration (Sparano & Koide, 2007).

A novel class of light-up probes for RNA detection was developed by Stojanovic's group by conjugating nonspecific fluorogenic intercalating dyes such as thiazole orange (TO) to small molecules such as GMP and AMP, for which RNA aptamers have previously been obtained (Pei et al., 2009). The GMP aptamer binds the GMP-TO conjugate with K_d=60 nM and a 500-fold fluorescence enhancement (Figure 3). Similar results were obtained with an AMP aptamer and AMP-TO conjugate. To adapt this approach for *in vivo* use, multiple copies of the appropriate aptamer would have to be inserted into the gene encoding the cellular RNA to

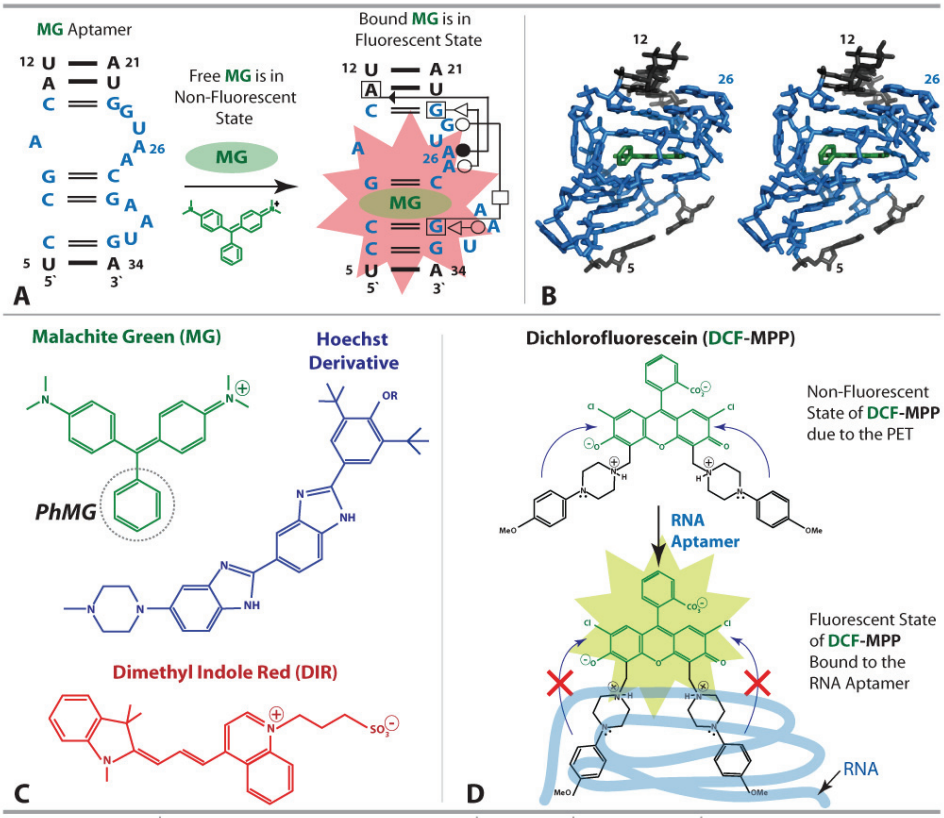

Aptamer Type	Binding Dye	K_d, nM	Fluorescence enhancement	Ref
RNA aptamer	Malachite Green (MG)	117	2360x	Babendure et al., **2003**
DNA aptamer	Hoechst (33258) Derivative	878	191x	Sando et al., **2007**
RNA aptamer	Hoechst (33258) Derivative	35	56.2x	Sando et al., **2008**
RNA aptamer	Dimethyl Indole Red (DIR)	87	60x	Constantin et al., **2008**
RNA aptamer	Dichlorofluorescein (DCF-MPP)	N/R	C/D	Sparano and Koide, **2005**
				Sparano and Koide, **2007**

N/R - Not Reported; C/D - Concentration-Dependent

Fig. 2. Light-up dye/aptamer pairs and their properties. A. Malachite Green (MG) aptamer 3D structure with basepairs annotated with Leontis-Westhof nomenclature. Watson-Crick Edges are shown in circles, Hoogsteen Edges in squares, and the Sugar Edges in triangles (Leontis & Westhof, 2001). Hollow symbols indicate trans basepairs and filled symbols, cis basepairs. Boxes indicate nucleotides pairing with more then one base. B. 3D stereo view of the X-ray structure of the MG aptamer binding to tetramethylrosamine (PDB file: 1f1t). Nucleotides are colored to match the annotated 3D structure. C. Several examples of fluorogenic dyes for which nucleic acid aptamers have been obtained to create "light-up" pairs. In case of MG, phenyl ring (PhMG) mentioned in text is circled. D. Schematic

representation of a strategy use to obtain a new "light-up" pair (Sparano & Koide, 2005). Dichlorofluorescein (DCF, shown in green) is attached to two quencher molecules (shown in black). Photoinduced electron transfer (PET, blue arrows) quenches fluorescence. Binding of an aptamer selected to bind exclusively to the quencher moieties blocks PET, leading to the recovery of emission. Lower panel. Binding affinities and fluorescence enhancements of the light-up pairs described in this chapter.

be visualized, and the small-molecule dye conjugate would have to be delivered into the cell by an appropriate mechanism (for a review of cellular delivery systems, see Bao et al., 2009). The main drawback of this approach is competition for aptamer binding by endogenous molecules (for example, cellular GMP or AMP). Nevertheless, this approach has great potential, as the number of small molecules that can be used here is almost limitless.

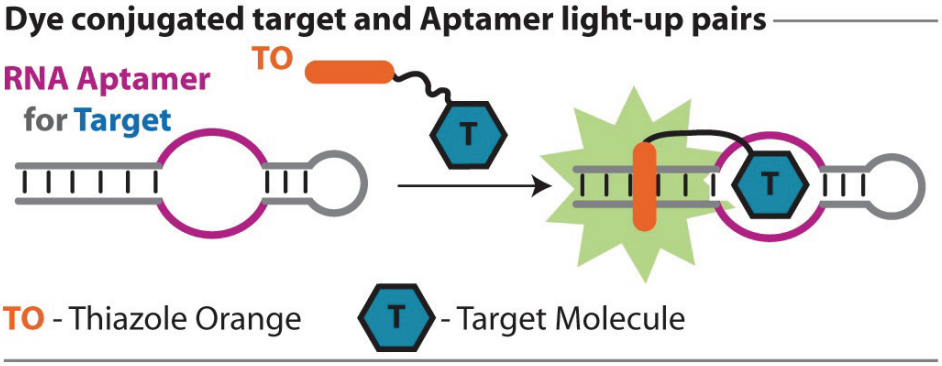

Fig. 3. Stojanovic's strategy for RNA detection. Thiazole Orange (TO), a fluorescent intercalator, is conjugated to a small molecule (blue hexagon). RNA aptamer (pink region) specific for its target binds the small molecule and forces TO binding to double-stranded region at the specific location.

3.4 Fluorogen-binding aptamers as signalling elements for label-free, specific nucleic acid detection

Some of the disadvantages of other RNA imaging methods (described above in section 2.1 and 2.2) may potentially be overcome using label-free approaches based on fluorogen-binding aptamers. First, aptamers can be entirely composed of unmodified RNA, allowing genetic fusion to genes coding for cellular RNAs of interest (Figure 4B). This has the advantage of endogenous synthesis of the targeting sequence. Moreover, these aptamers, even when used in multiple copies, do not significantly increase the size of the cellular RNA, and only the imaging dye needs to be introduced exogenously, as most organic dyes are able to diffuse into cells. Finally, dyes with suitable light-up characteristics and low affinity for cellular targets can be expected to give low background signals.

However, selecting appropriate sites for aptamer insertion remains a critical issue. To obtain valid imaging results one must ensure that the insertion of the aptamer molecules does not disrupt functionally important target RNA secondary or tertiary structure or protein-binding sites. In cases where the organism of interest is difficult to genetically modify, these aptamers can be coupled to a specific target recognition domain and introduced exogenously using a variety of delivery methods (Figure 4A).

3.4.1 Allosteric aptamer-based sensors

Aptamers have been conjugated to other aptamers forming "allosteric aptamers" or to ribozymes forming "aptazymes" (Soukup, 2004; Silverman, 2003). Stojanovic and Kolpashchikov first reported the design of novel allosteric sensing systems produced by coupling the MG-binding RNA aptamer through a "communication module" to each of a series of specific aptamers for ATP, FMN (flavin monomucleotide), and theophylline. These "allosteric aptamers" are capable of transducting binding information between the two aptamers (Stojanovic & Kolpaschikov, 2004). They showed that binding of the target molecule to its respective aptamer domain caused a significant conformational change in the RNA sensor that was relayed through the communication module to the MG aptamer module so as to enable it to bind MG and produce a fluorescent signal.

Within a year, Kolpashchikov adapted this concept to create an allosteric RNA aptamer probe system to sense specific nucleic acid targets (Kolpashchikov, 2005). The MG aptamer domain of the probe was divided into two fragments, each of which also contained half of the sequence complementary to the target DNA (see Figure 5). In the presence of the target, the complementary "binding arms" of the binary probe hybridize cooperatively to the target, forming a three-way junction structure and reconstituting the MG aptamer by stabilizing the helix containing it. The probe-target complex then binds MG and renders it

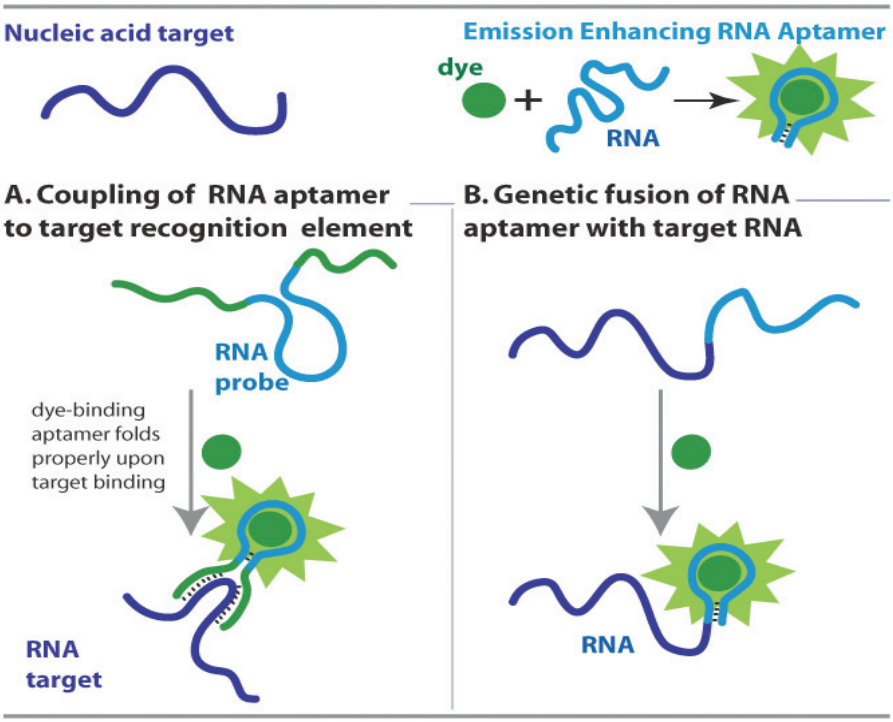

Fig. 4. Label-free approaches for in vivo RNA imaging. A. Allosteric coupling of fluorogen-binding aptamer to another target recognition element. B. Genetic fusion of the fluorogen-binding aptamer to target RNA sequence.

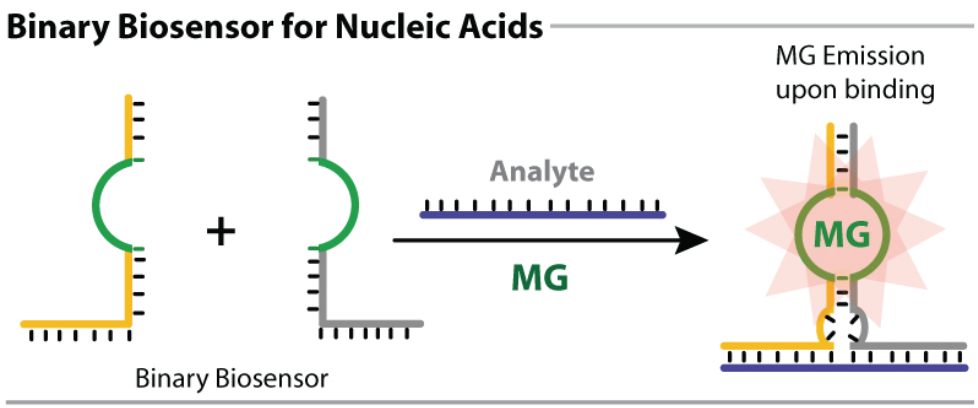

Fig. 5. Binary MG-aptamer based sensor (Kolpashchikov, 2005). Analyte-promoted assembly and stabilization of binary biosensor to form MG aptamer (shown in green color).

fluorescent, signaling the presence of the analyte. A 20-fold fluorescence enhancement was reported for this biosensor in the presence of 2 μM concentration of the target, with discrimination factors greater than 20-fold for half of the sequences differing from the intended analyte by single nucleotide substitutions. Sando and coworkers tested the applicability of Kolpashchikov's strategy to design a binary probe using their novel light-up Hoechst derivative/DNA aptamer light-up pair (see section 2.2 above) (Sando et al., 2007). The same design principle was used: the DNA aptamer for the Hoechst dye was split into two molecules, each of which contains half of the sequence complementary to the target. When the target DNA binds to the complementary regions of the binary probe, a three-way junction forms which restores the DNA aptamer structure and allows it to bind to the Hoechst dye. These binary DNA probes showed 70-fold fluorescence enhancement; correct analyte was discriminated from single-mismatches by a factor of 15.

A major hurdle in designing probes for specifically detecting or imaging biological RNAs in complex environmental or whole cell samples is the presence of secondary structure in the target RNA, which may compete with probe binding, thus reducing the binding affinity of the biosensor. Paranemic binding between two pre-formed nucleic acid structures was originally developed for DNA nanotechnology by Seeman and coworkers (Shen et al., 2004) and subsequently demonstrated in RNA (Afonin et al., 2008). Paranemic binding provides the means to design probes targeting internal loop structures in the RNA analyte in a programmable, sequence-specific manner that obviates the need to unfold the target to expose extended single-stranded regions. Paranemic binding can be applied for recognition of symmetrical internal loops ranging in size from 4 to 8 nucleotides (Afonin et al., 2008), as well as asymmetrical loops which have different numbers of bases in each strand (Novikova et al, unpublished observations). Afonin *et al* coupled the MG aptamer to an RNA paranemic binding motif to establish proof-of-principle for programmable sensing of pre-folded RNA secondary structures using paranemic binding (Afonin et al., 2008). To make MG binding contingent upon binding of the target RNA, the position and orientation of the aptamer motif was optimized relative to the paranemic binding motif. In the resulting constructs, crucial non-WC basepairs that "zip-up" the MG binding site and fix MG in its

fluorescent state only form in the presence of the target RNA, as shown in Figure 6. Using several different probe and target sequences, the generality of this approach was demonstrated. Target sequences were bound with low nM affinity and fluorescence enhancements ranged from 6 to 15-fold. Furthermore, it was shown that single-base mismatches could be discriminated by about a factor of 13.
The key principle of the sensing strategies described above involves the incorporation of a fluorogen-binding aptamer within the probe structure in such a way that fluorogen binding depends upon the specific recognition and binding to the target.

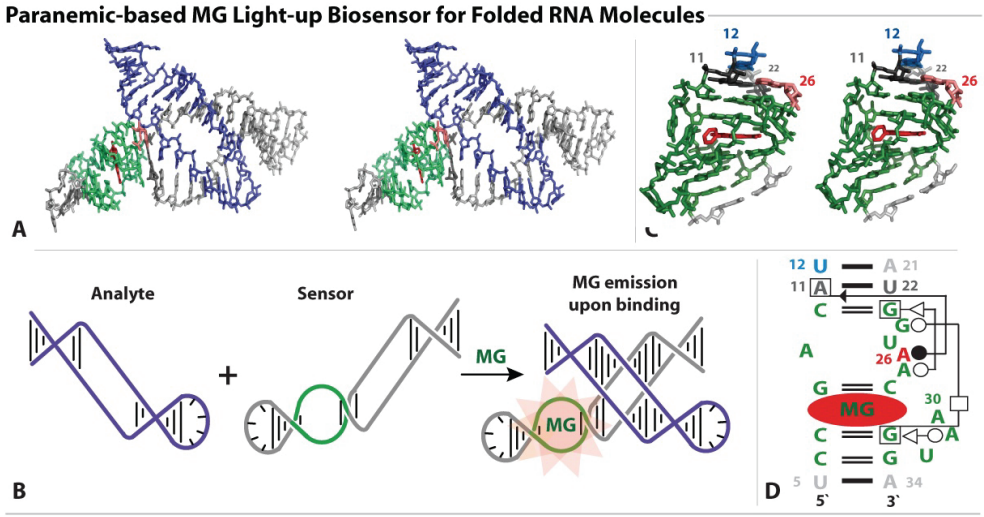

Fig. 6. Paranemic RNA biosensor for folded RNA molecules (Afonin et al., 2008) **A.** 3D model of the biosensor-target complex. **B.** Schematic representation of the paranemic assembly of the MG-aptamer containing biosensor (grey)with the pre-folded analyte RNA (in blue). Formation of the recognition complex stabilizes the Malachite Green (MG) aptamer structure (in green). **C.** 3D stereo view of the MG aptamer (Baugh et al., 2000; PDB file 1f1t). **D.** Corresponding annotation of the 3D structure using Leontis-Westhof basepair annotations (Leontis and Westhof, 2001). Bases are numbered as in X-ray (1f1t). U12 (blue) of target RNA interacts with A21 of biosensor probe RNA (in grey), stabilizing the flanking A11/U22 (grey) basepair of the biosensor, which interacts with A26 (red) in the aptamer to "zip-up" the MG binding site.

3.4.2 Genetic fusion of fluorogen- or fluorophore-binding aptamers and target RNA sequences

In the previous section, we described strategies for RNA detection and visualization using hybridization probes allosterically coupled to fluorogen-binding aptamers. A related approach is to genetically encode the fluorogen- or fluorophore-binding aptamer directly into the gene sequence of a cellular RNA of interest. Sando *et al.* recently reported the selection of an effective RNA aptamer for Hoechst 33258 derivative and the insertion of five tandem repeats of this aptamer sequence on the 3′ side of the stop codon of the luciferase gene (Sando et al., 2008). They showed that transcription of the mRNA containing the

tandem aptamers could be monitored *in vitro* by fluorescence in the presence of the dye, and observed a 5-fold enhancement compared to parallel transcription of the same mRNA lacking the aptamer sequences. The authors call this method "blue fluorescent RNA" and reported K_d=35 nM for binding of the dye to the isolated aptamer, but did not report apparent K_d's in the context of the mRNA construct.

Eydeler *et al.* reported detailed measurements of the Sulforhodamine B-binding aptamer (SRB2m), selected by Holeman et al (1998), fused to a variety of genetic constructs, including intact EGFP-mRNA produced *in vivo* and assayed *in vitro* in the presence of other cellular RNAs (Eydeler et al., 2009). They used fluorescence correlation spectroscopy (FCS), a method that allows one to obtain diffusion constants and other kinetic parameters from fluorescence fluctuations generated by molecules diffusing in and out of the focal volume. They reported K_d's ranging between 120 nM and 1130 nM for different constructs containing single aptamer modules compared to K_d~238 nM for the isolated aptamer. Tandem repeats of the aptamer sequence in these constructs showed a significant increase in binding affinities, with K_d values of 60-70 nM. The lowest apparent binding affinity of Sulforhodamine B was observed for aptamer embedded into EGFP-coding mRNA (k_d~1.13 μM), which was attributed to improper RNA folding. Even though the binding of Sulforhodamine B to its aptamer SRB2m does not cause a significant emission change (this is not a "light-up" pair), this work shows the value of using multiple tandem copies of aptamers and points out the need for careful consideration of target secondary structure to obtain optimal *in vivo* results.

Zhang and co-workers inserted the MG aptamer sequence into the cloned gene of *V. proteolyticus* 5S rRNA so that the aptamer motif replaced Helix 5 and Loop C of the 5S molecule (Zhang et al., 2009). They transcribed the 5S/ MG aptamer chimera *in vitro* and showed that it binds to MG and enhances its fluorescence to a comparable extent as free aptamer (Kd ~ 900 nM for 5S/MG chimera vs. Kd ~ 800 nM for isolated aptamer, Baugh et al., 2000; cf. Kd ~ 117 nM, Babendure et al., 2003). They also expressed the 5S/MG chimera from a plasmid in *E. coli* cells and observed fluorescence enhancement of MG dye added to the medium, although they did not report detailed *in vivo* measurements.

Applications of light-up dye/aptamer pairs are not solely limited to sensing nucleic acids. Other applications for these technologies have been proposed and are under development. For example, MG dye was conjugated to kinesin-driven microtubules to develop mobile bioprobes that can capture MG aptamer-tagged mRNAs from a transcription mixture and sequester them in a microfluidic device for high-throughput screening (Hirabayashi et al., 2006).

4. Conclusions

To date, remarkable progress has been made to visualize specific RNA molecules with high spatial and temporal resolution in living cells. These studies have begun to reveal detailed mechanisms of RNA trafficking, localization and turnover (Bratu et al., 2003, Lange et al., 2008; Zimyanin et al., 2008). However, significant challenges remain to render these methods more generally applicable and to overcome shortcomings of currently used methods. The ideal RNA biosensing system should be easy to deliver to living cells, non-toxic and non-perturbing to cellular functions. It should penetrate all parts of the cell homogeneously and be chemically stable in different cellular environments. The fluorescent

reporter of the biosensor should have high absorptivity and quantum yield (brightness) as well as good photostability and low phototoxicity. The sensor system should be easy to implement, so that different RNA targets can be studied without extensive optimization. It should allow optical multiplexing so that interactions between two or more cellular RNAs (or RNA and protein) can be monitored. It should only fluoresce when bound to the intended target and otherwise produce low background fluorescence. It should bind specifically to the intended target with minimal binding to targets having similar sequence and should exhibit fast binding kinetics to monitor rapid changes in RNA concentration. Finally, it should allow for studying specific RNAs in whole tissues or organs. Of course, no current method possesses all these desired characteristics.

Currently, hybridization probes offer the greatest variety and versatility in choice of fluorescent reporters as they can be conjugated to semiconductor quantum dots, in addition to a wide variety of organic dyes. However, they still require exogenous delivery which can perturb cell functions. Hybridization methods suffer from signal sensitivity issues for two reasons. Unmodified targets generally bind only one hybridization probe and degraded probes release fluorescent reporters. To minimize degradation, hybridization probes are usually synthesized with resistant, modified backbones (see above). To increase sensitivity, multiple copies of the complementary binding sequence can be introduced in the target gene (van den Bogaard & Tyagi, 2009). Whether or not the target is genetically engineered, the use of hybridization probes raises several concerns related to choosing appropriate binding sites on the target RNAs. First the target sites should have relatively weak secondary structures to allow the probe to bind with high affinity with minimal competition. Second the selected binding sites should not participate in crucial functions, especially related to the processing, localization, or regulation of the target RNA. Hybridization probes targeting RNA sequences that bind other cellular factors can potentially interfere with these processes and produce spurious imaging results.

Autofluorescent protein (AFP) probes are synthesized intra-cellularly from gene fusions directly encoded in cell lines or from plasmids that can be introduced by transfection. These methods are less perturbing than those used to deliver hybridization probes. Moreover, AFP probes can be directed to desired cellular compartments with appropriate peptide targeting sequences. However, the use of AFP probes requires insertion of RNA binding protein (RBP) recognition sites into target RNA sequences, which also requires attention to target RNA sequence to avoid interfering with RNA function, but is potentially less sensitive to RNA secondary structure. One disadvantage of the general AFP strategy is that unbound probes are also fluorescent. This has been largely solved by the "split-AFP" approach, but this method has the disadvantage that signal generation is irreversible upon reconstitution of the fluorescent protein. Contrary to common perceptions, autofluorescent proteins also have phototoxicity issues, as under irradiation, they produce reactive oxygen species that can damage cells (Remington et al., 2006).

New methods, employing fluorogen-binding aptamers, hold promise of addressing many of the shortcomings of the two currenty used methods. First, aptamer-based methods are generally simpler and potentially more flexible and can be readily adapted to the particular application. Like AFP probes and unlike hybridization probes, the aptamers themselves can be produced endogenously. They can be either genetically encoded in the target RNA or produced from plasmids. Of course, they can also be introduced exogenously like

hybridization probes if that is required. Like hybridization probes and unlike AFP probes, there is no need for co-expressing additional fusion constructs that require additional time to mature and that need to be balanced in their expression to target RNA expression levels– a significant simplification of the procedure. Additionally, because fluorogen-binding aptamers can be genetically integrated in their targets, signal generation is rapidly and completely eliminated upon RNA degradation, thus reducing background and false-positive rates providing further improvement over both AFP and hybridization methods. Finally, the aptamer size is quite insignificant compared to protein-based probes. However, it is not yet well established how many tandem aptamers are required to achieve adequate sensitivity for single-molecule detection *in vivo*. Based on recent studies, it appears that tandem repeats of aptamers domains in target RNA are preferred to achieve proper aptamer folding and significant increase in binding affinities. Unlike hybridization probes, only free fluorogenic dyes need to penetrate cells when genetically encoded aptamers are used and there is no need to covalently attach the fluorescent reporters and quenchers to the probe. However, a number of challenges must be met for fluorogen-binding aptamers to become practical alternatives to the currently used methods. First of all, the number of available fluorogenic dyes is still quite limited and they have not been adequately tested for suitability *in vivo*. Further work is needed to identify which fluorogenic dyes have low *in vivo* toxicity and phototoxicity, low background fluorescence, and produce sufficient signal when bound specifically to their target aptamers to make single-molecules detection possible *in vivo* with modern imaging methods. For example, MG, while exhibiting low background fluorescence, has substantial phototoxicity issues. Cyanine dyes appear promising. In addition to DIR, a number of cyanine dyes with reduced affinity to nonspecific nucleic acids and substantial light-up signal have been synthesized by Armitage's group and tuned to emit across the visible spectrum and even into the near-infrared (Ozhalici-Unal et al., 2008; Shank et al., 2009). Second, a challenge for future work is to expand the available choices of light-up pairs by selection of new aptamers that specifically bind new improved fluorogenic dyes, including near-IR emitters. Just as new AFPs emitting in the NIR have recently been reported (Shu et al., 2009), new aptamer/NIR dye light-up pairs will make it possible to detect signals from specific molecules located deep inside tissues (Amiot et al., 2008). While, a number of innovative approaches for aptamer/dye pair selection have been developed *in vitro*, most of them have been tested only *in vitro*. Thus, more *in vivo* testing is a high priority to determine which fluorogenic dyes and aptamer-based biosensing platforms are suitable for *in vivo* use. Finally, improved bioinformatic methods are needed to identify optimal sites for aptamer insertion or hybridization into target RNAs.

5. References

Abelson, J. F., Kwan, K. Y., O'Roak, B. J., Baek, D. Y., Stillman, A. A., Morgan, T. M., et al. (2005). Sequence variants in SLITRK1 are associated with tourette's syndrome. *Science, 310*(5746), 317-320.

Afonin, K. A., Cieply, D. J., & Leontis, N. B. (2008). Specific RNA self-assembly with minimal paranemic motifs. *Journal of the American Chemical Society, 130*(1), 93-102.

Afonin, K. A., Danilov, E. O., Novikova, I. V., & Leontis, N. B. (2008). TokenRNA: A new type of sequence-specific, label-free fluorescent biosensor for folded RNA molecules. *Chembiochem : A European Journal of Chemical Biology, 9*(12), 1902-1905.

Algar, R., Massey, M., & Krull, U. (2009). The application of quantum dots, gold nanoparticles and molecular switches to optical nucleic-acid diagnostics. *Trends in Analytical Chemistry, 28*(3), 292-306.

Amann, R., Fuchs, B. M., & Behrens, S. (2001). The identification of microorganisms by fluorescence in situ hybridisation. *Current Opinion in Biotechnology, 12*(3), 231-236.

Amiot, C., Xu, S., Liang, S., Pan, L., & Zhao, J. (2008). Near-infrared fluorescent materials for sensing of biological targets. *Sensors, 8*(5), 3082-3105.

Babendure, J. R., Adams, S. R., & Tsien, R. Y. (2003). Aptamers switch on fluorescence of triphenylmethane dyes. *Journal of the American Chemical Society, 125*(48), 14716-14717.

Bao, G., Rhee, W. J., & Tsourkas, A. (2009). Fluorescent probes for live-cell RNA detection. *Annual Review of Biomedical Engineering, 11*, 25-47.

Baugh, C., Grate, D., & Wilson, C. (2000). 2.8 A crystal structure of the malachite green aptamer. *Journal of Molecular Biology, 301*(1), 117-128.

Bertrand, E., Chartrand, P., Schaefer, M., Shenoy, S. M., Singer, R. H., & Long, R. M. (1998). Localization of ASH1 mRNA particles in living yeast. *Molecular Cell, 2*(4), 437-445.

Bilen, J., Liu, N., & Bonini, N. M. (2006). A new role for microRNA pathways: Modulation of degeneration induced by pathogenic human disease proteins. *Cell Cycle (Georgetown, Tex.), 5*(24), 2835-2838.

Boyd, S. D. (2008). Everything you wanted to know about small RNA but were afraid to ask. *Laboratory Investigation; a Journal of Technical Methods and Pathology, 88*(6), 569-578.

Bratu, D. P., Cha, B. J., Mhlanga, M. M., Kramer, F. R., & Tyagi, S. (2003). Visualizing the distribution and transport of mRNAs in living cells. *Proceedings of the National Academy of Sciences of the United States of America, 100*(23), 13308-13313.

Bushati, N., & Cohen, S. M. (2007). microRNA functions. *Annual Review of Cell and Developmental Biology, 23*, 175-205.

Carthew, R. W. (2006). Molecular biology. A new RNA dimension to genome control. *Science (New York, N.Y.), 313*(5785), 305-306.

Caudy, A. A., Myers, M., Hannon, G. J., & Hammond, S. M. (2002). Fragile X-related protein and VIG associate with the RNA interference machinery. *Genes & Development, 16*(19), 2491-2496.

Chalfie, M. (2009). GFP: Lighting up life (nobel lecture). *Angewandte Chemie (International Ed.in English), 48*(31), 5603-5611.

Chalfie, M., Tu, Y., Euskirchen, G., Ward, W. W., & Prasher, D. C. (1994). Green fluorescent protein as a marker for gene expression. *Science, 263*(5148), 802-805.

Chen, A. K., Behlke, M. A., & Tsourkas, A. (2007). Avoiding false-positive signals with nuclease-vulnerable molecular beacons in single living cells. *Nucleic Acids Research, 35*(16), e105.

Cho, E., Lee, J., & Ellington, A. (2009). Application of aptamers as sensors. *Annu. Rev. Anal. Chem., 1*, 241.

Choudhuri, S. (2009). Lesser known relatives of miRNA. *Biochemical and Biophysical Research Communications, 388*(2), 177-180.

Constantin, T. P., Silva, G. L., Robertson, K. L., Hamilton, T. P., Fague, K., Waggoner, A. S., et al. (2008). Synthesis of new fluorogenic cyanine dyes and incorporation into RNA fluoromodules. *Organic Letters, 10*(8), 1561-1564.

Cooper, T. A., Wan, L., & Dreyfuss, G. (2009). RNA and disease. *Cell, 136*(4), 777-793.

Ellington, A. D., & Szostak, J. W. (1990). In vitro selection of RNA molecules that bind specific ligands. *Nature, 346*(6287), 818-822.

Ellington, A. D., & Szostak, J. W. (1992). Selection in vitro of single-stranded DNA molecules that fold into specific ligand-binding structures. *Nature, 355*(6363), 850-852.

Eydeler, K., Magbanua, E., Werner, A., Ziegelmuller, P., & Hahn, U. (2009). Fluorophore binding aptamers as a tool for RNA visualization. *Biophysical Journal, 96*(9), 3703-3707.

Grate, D., & Wilson, C. (1999). Laser-mediated, site-specific inactivation of RNA transcripts. *Proceedings of the National Academy of Sciences of the United States of America, 96*(11), 6131-6136.

Guerrier-Takada, C., Gardiner, K., Marsh, T., Pace, N., & Altman, S. (1983). The RNA moiety of ribonuclease P is the catalytic subunit of the enzyme. *Cell, 35*(3 Pt 2), 849-857.

Heim, R., Cubitt, A. B., & Tsien, R. Y. (1995). Improved green fluorescence. *Nature, 373*(6516), 663-664.

Hirabayashi, M., Taira, S., Kobayashi, S., Konishi, K., Katoh, K., Hiratsuka, Y., et al. (2006). Malachite green-conjugated microtubules as mobile bioprobes selective for malachite green aptamers with capturing/releasing ability. *Biotechnology and Bioengineering,*

Holeman, L. A., Robinson, S. L., Szostak, J. W., & Wilson, C. (1998). Isolation and characterization of fluorophore-binding RNA aptamers. *Folding & Design, 3*(6), 423-431.

Hwang, H. W., Wentzel, E. A., & Mendell, J. T. (2007). A hexanucleotide element directs microRNA nuclear import. *Science, 315*(5808), 97-100.

International Human Genome Sequencing Consortium. (2004). Finishing the euchromatic sequence of the human genome. *Nature, 431*(7011), 931-945.

Kelly, S. M., & Corbett, A. H. (2009). Messenger RNA export from the nucleus: A series of molecular wardrobe changes. *Traffic (Copenhagen, Denmark), 10*(9), 1199-1208.

Kim, Y., Sohn, D., & Tan, W. (2008). Molecular beacons in biomedical detection and clinical diagnosis. *International Journal of Clinical and Experimental Pathology, 1*(2), 105-116.

Klussman, S. (Ed.). (2006). *The aptamer handbook: Functional oligonucleotides and their applications.* WILEY-VCH Verlag GmbH & Co. KGaA, Weinheim.

Kolpashchikov, D. M. (2005). Binary malachite green aptamer for fluorescent detection of nucleic acids. *Journal of the American Chemical Society, 127*(36), 12442-12443.

Kruger, K., Grabowski, P. J., Zaug, A. J., Sands, J., Gottschling, D. E., & Cech, T. R. (1982). Self-splicing RNA: Autoexcision and autocyclization of the ribosomal RNA intervening sequence of tetrahymena. *Cell, 31*(1), 147-157.

Kuhn, H., Demidov, V. V., Coull, J. M., Fiandaca, M. J., Gildea, B. D., & Frank-Kamenetskii, M. D. (2002). Hybridization of DNA and PNA molecular beacons to single-

stranded and double-stranded DNA targets. *Journal of the American Chemical Society, 124*(6), 1097-1103.

Lange, S., Katayama, Y., Schmid, M., Burkacky, O., Brauchle, C., Lamb, D. C., et al. (2008). Simultaneous transport of different localized mRNA species revealed by live-cell imaging. *Traffic (Copenhagen, Denmark), 9*(8), 1256-1267.

Lee, J. F., Hesselberth, J. R., Meyers, L. A., & Ellington, A. D. (2004). Aptamer database. *Nucleic Acids Research, 32*(Database issue), D95-100.

Lee, Y. S., & Dutta, A. (2009). MicroRNAs in cancer. *Annual Review of Pathology, 4*, 199-227.

Leontis, N. B., & Westhof, E. (2001). Geometric nomenclature and classification of RNA base pairs. *RNA, 7*(4), 499-512.

Liao, J. C., Roider, J., & Jay, D. G. (1994). Chromophore-assisted laser inactivation of proteins is mediated by the photogeneration of free radicals. *Proceedings of the National Academy of Sciences of the United States of America, 91*(7), 2659-2663.

Liu, J., Cao, Z., & Lu, Y. (2009). Functional nucleic acid sensors. *Chemical Reviews, 109*(5), 1948-1998.

Montange, R. K., & Batey, R. T. (2008). Riboswitches: Emerging themes in RNA structure and function. *Annual Review of Biophysics, 37*, 117-133.

Moter, A., & Gobel, U. B. (2000). Fluorescence in situ hybridization (FISH) for direct visualization of microorganisms. *Journal of Microbiological Methods, 41*(2), 85-112.

Noller, H. F. (2005). RNA structure: Reading the ribosome. *Science, 309*(5740), 1508-1514.

Ozhalici-Unal, H., Pow, C. L., Marks, S. A., Jesper, L. D., Silva, G. L., Shank, N. I., et al. (2008). A rainbow of fluoromodules: A promiscuous scFv protein binds to and activates a diverse set of fluorogenic cyanine dyes. *Journal of the American Chemical Society, 130*(38), 12620-12621.

Pei, R., Rothman, J., Xie, Y., & Stojanovic, M. N. (2009). Light-up properties of complexes between thiazole orange-small molecule conjugates and aptamers. *Nucleic Acids Research, 37*(8), e59.

Perkins, D. O., Jeffries, C. D., Jarskog, L. F., Thomson, J. M., Woods, K., Newman, M. A., et al. (2007). microRNA expression in the prefrontal cortex of individuals with schizophrenia and schizoaffective disorder. *Genome Biology, 8*(2), R27.

Ponting, C. P., Oliver, P. L., & Reik, W. (2009). Evolution and functions of long noncoding RNAs. *Cell, 136*(4), 629-641.

Prasher, D. C., Eckenrode, V. K., Ward, W. W., Prendergast, F. G., & Cormier, M. J. (1992). Primary structure of the aequorea victoria green-fluorescent protein. *Gene, 111*(2), 229-233.

Raj, A., & van Oudenaarden, A. (2009). Single-molecule approaches to stochastic gene expression. *Annual Review of Biophysics, 38*, 255-270.

Remington, S.J. (2006). Fluorescent proteins: maturation, photochemistry and photophysics. *Current Opinion in Structural Biology, 16,* 714-721.

Rodriguez, A. J., Condeelis, J., Singer, R. H., & Dictenberg, J. B. (2007). Imaging mRNA movement from transcription sites to translation sites. *Seminars in Cell & Developmental Biology, 18*(2), 202-208.

Sando, S., Narita, A., & Aoyama, Y. (2007). Light-up hoechst-DNA aptamer pair: Generation of an aptamer-selective fluorophore from a conventional DNA-staining dye. *Chembiochem : A European Journal of Chemical Biology, 8*(15), 1795-1803.

Sando, S., Narita, A., Hayami, M., & Aoyama, Y. (2008). Transcription monitoring using fused RNA with a dye-binding light-up aptamer as a tag: A blue fluorescent RNA. *Chemical Communications, (33)*(33), 3858-3860.

Santangelo, P., Nitin, N., & Bao, G. (2006). Nanostructured probes for RNA detection in living cells. *Annals of Biomedical Engineering, 34*(1), 39-50.

Santangelo, P. J., Nix, B., Tsourkas, A., & Bao, G. (2004). Dual FRET molecular beacons for mRNA detection in living cells. *Nucleic Acids Research, 32*(6), e57.

Satterfield, B. C., West, J. A., & Caplan, M. R. (2007). Tentacle probes: Eliminating false positives without sacrificing sensitivity. *Nucleic Acids Research, 35*(10), e76.

Schifferer, M., & Griesbeck, O. (2009). Application of aptamers and autofluorescent proteins for RNA visualization. *Integrative Biology, 1*, 499-505.

Schlosser, K., McManus, S., & Li, Y. (2006). Deoxyribozymes: Catalytically active DNA molecules. *The aptamer handbook: Functional oligonucleotides and their applications* (pp. 228-264) WILEY-VCH Verlag GmbH & Co. KGaA, Weinheim.

Shaner, N. C., Campbell, R. E., Steinbach, P. A., Giepmans, B. N., Palmer, A. E., & Tsien, R. Y. (2004). Improved monomeric red, orange and yellow fluorescent proteins derived from discosoma sp. red fluorescent protein. *Nature Biotechnology, 22*(12), 1567-1572.

Shank, N. I., Zanotti, K. J., Lanni, F., Berget, P. B., & Armitage, B. A. (2009). Enhanced photostability of genetically encodable fluoromodules based on fluorogenic cyanine dyes and a promiscuous protein partner. Journal of the American Chemical Society, 131(36), 12960-12969.

Shen, Z., Yan, H., Wang, T., & Seeman, N. C. (2004). Paranemic crossover DNA: A generalized holliday structure with applications in nanotechnology. *Journal of the American Chemical Society, 126*(6), 1666-1674.

Shimomura, O. (2009). Discovery of green fluorescent protein (GFP) (nobel lecture). *Angewandte Chemie (International Ed.in English), 48*(31), 5590-5602.

Shimomura, O., Johnson, F. H., & Saiga, Y. (1962). Extraction, purification and properties of aequorin, a bioluminescent protein from the luminous hydromedusan, aequorea. *Journal of Cellular and Comparative Physiology, 59*, 223-239.

Shu, X., Royant, A., Lin, M. Z., Aguilera, T. A., Lev-Ram, V., Steinbach, P. A., et al. (2009). Mammalian expression of infrared fluorescent proteins engineered from a bacterial phytochrome. *Science, 324*(5928), 804-807.

Silverman, A. P., & Kool, E. T. (2005). Quenched probes for highly specific detection of cellular RNAs. *Trends in Biotechnology, 23*(5), 225-230.

Silverman, S. K. (2003). Rube goldberg goes (ribo)nuclear? molecular switches and sensors made from RNA. *RNA (New York, N.Y.), 9*(4), 377-383.

Soukup, G. A. (2004). Aptamers meet allostery. *Chemistry & Biology, 11*(8), 1031-1032.

Sparano, B. A., & Koide, K. (2005). A strategy for the development of small-molecule-based sensors that strongly fluoresce when bound to a specific RNA. *Journal of the American Chemical Society, 127*(43), 14954-14955.

Sparano, B. A., & Koide, K. (2007). Fluorescent sensors for specific RNA: A general paradigm using chemistry and combinatorial biology. *Journal of the American Chemical Society, 129*(15), 4785-4794.

Staple, D. W., & Butcher, S. E. (2005). Pseudoknots: RNA structures with diverse functions. *PLoS Biology, 3*(6), e213.

Stewart, M. (2007). Ratcheting mRNA out of the nucleus. *Molecular Cell, 25*(3), 327-330.

Stojanovic, M. N., & Kolpashchikov, D. M. (2004). Modular aptameric sensors. *Journal of the American Chemical Society, 126*(30), 9266-9270.

Stoltenburg, R., Reinemann, C., & Strehlitz, B. (2007). SELEX--a (r)evolutionary method to generate high-affinity nucleic acid ligands. *Biomolecular Engineering, 24*(4), 381-403.

Takano, A., Endo, T., & Yoshihisa, T. (2005). tRNA actively shuttles between the nucleus and cytosol in yeast. *Science (New York, N.Y.), 309*(5731), 140-142.

Tsien, R. Y. (2009). Constructing and exploiting the fluorescent protein paintbox (nobel lecture). *Angewandte Chemie (International Ed.in English), 48*(31), 5612-5626.

Tsourkas, A., Behlke, M. A., & Bao, G. (2002). Hybridization of 2'-O-methyl and 2'-deoxy molecular beacons to RNA and DNA targets. *Nucleic Acids Research, 30*(23), 5168-5174.

Tsourkas, A., Behlke, M. A., Rose, S. D., & Bao, G. (2003). Hybridization kinetics and thermodynamics of molecular beacons. *Nucleic Acids Research, 31*(4), 1319-1330.

Tuerk, C., & Gold, L. (1990). Systematic evolution of ligands by exponential enrichment: RNA ligands to bacteriophage T4 DNA polymerase. *Science, 249*(4968), 505-510.

Tyagi, S. (2009). Imaging intracellular RNA distribution and dynamics in living cells. *Nature Methods, 6*(5), 331-338.

Tyagi, S., Bratu, D. P., & Kramer, F. R. (1998). Multicolor molecular beacons for allele discrimination. *Nature Biotechnology, 16*(1), 49-53.

Tyagi, S., & Kramer, F. R. (1996). Molecular beacons: Probes that fluoresce upon hybridization. *Nature Biotechnology, 14*(3), 303-308.

Valencia-Burton, M., McCullough, R. M., Cantor, C. R., & Broude, N. E. (2007). RNA visualization in live bacterial cells using fluorescent protein complementation. *Nature Methods, 4*(5), 421-427.

van den Bogaard, P. T., & Tyagi, S. (2009). Using molecular beacons to study dispersal of mRNPs from the gene locus. *Methods in Molecular Biology (Clifton, N.J.), 464,* 91-103.

Vargas, D. Y., Raj, A., Marras, S. A., Kramer, F. R., & Tyagi, S. (2005). Mechanism of mRNA transport in the nucleus. *Proceedings of the National Academy of Sciences of the United States of America, 102*(47), 17008-17013.

Wang, K., Tang, Z., Yang, C. J., Kim, Y., Fang, X., Li, W., et al. (2009). Molecular engineering of DNA: Molecular beacons. *Angewandte Chemie (International Ed.in English), 48*(5), 856-870.

Wang, L., Jackson, W. C., Steinbach, P. A., & Tsien, R. Y. (2004). Evolution of new nonantibody proteins via iterative somatic hypermutation. *Proceedings of the National Academy of Sciences of the United States of America, 101*(48), 16745-16749.

Wang, L., Yang, C. J., Medley, C. D., Benner, S. A., & Tan, W. (2005). Locked nucleic acid molecular beacons. *Journal of the American Chemical Society, 127*(45), 15664-15665.

Weigand, B., Zerressen, A., Schlatterer, J., Helm, M., & Jaschke, A. (2006). Catalytically active RNA molecules: Tools in organic chemistry. *The aptamer handbook: Functional oligonucleotides and their applications* (pp. 211-227) WILEY-VCH Verlag GmbH & Co. KGaA, Weinheim.

Werstuck, G., & Green, M. R. (1998). Controlling gene expression in living cells through small molecule-RNA interactions. *Science (New York, N.Y.), 282*(5387), 296-298.

Winkler, W. C., Nahvi, A., Roth, A., Collins, J. A., & Breaker, R. R. (2004). Control of gene expression by a natural metabolite-responsive ribozyme. *Nature, 428*(6980), 281-286.

Zhang, X., Potty, A. S., Jackson, G. W., Stepanov, V., Tang, A., Liu, Y., et al. (2009). Engineered 5S ribosomal RNAs displaying aptamers recognizing vascular endothelial growth factor and malachite green. *Journal of Molecular Recognition : JMR, 22*(2), 154-161.

Zimyanin, V. L., Belaya, K., Pecreaux, J., Gilchrist, M. J., Clark, A., Davis, I., et al. (2008). In vivo imaging of oskar mRNA transport reveals the mechanism of posterior localization. *Cell, 134*(5), 843-853.

9

Surface Plasmon Resonance Biosensors for Highly Sensitive Detection of Small Biomolecules

John S. Mitchell and Yinqiu Wu
The New Zealand Institute for Plant and Food Research Ltd
New Zealand

1. Introduction

Small biomolecules (< 2 kDa) are crucial to a wide range of biochemical processes in the human body. Their diverse functions can include acting as hormones, neurotransmitters and pheromones. Small molecules are typically found in the blood stream and their concentrations can often be indicative of the biochemical functioning of the organism. This is particularly true of the steroids, a major class of small molecule hormone.

Measurement of steroid concentrations is commonly performed to track the progression of the fertile cycle, to detect pregnancy and to help diagnose hormonal diseases (Clark et al., 1998). Immunoassay techniques dominate the market for hormonal assays. These assay kits utilise the highly selective binding of an antibody to its target antigen to detect small molecule analytes in highly complex matrices. Typically, for small molecules, the assay will consist of a plate or tube onto which the antibody is immobilised and the sample is passed over the plate surface along with an aliquot of labelled antigen. The label used is either radiochemical (radioimmunoassay (RIA)) or enzyme-based (enzyme-linked immunosorbent assay (ELISA)). The labelled antigen occupies the un-bound sites on the immunoassay plate and the signal obtained from the label by either measuring the resultant radiation, or through enzyme catalyzed colour changes, gives a standard curve from which the concentration of the free analyte can be determined.

Small molecule targets are typically found in complex matrices such as blood and saliva where high molecular mass components predominate. These include proteins that can in some cases bind to the steroid hormone of interest. Their large size relative to the target antigen can also serve to sterically impede antibody binding to the steroid. Furthermore, large molecule contaminants can also bind to immunoassay surfaces causing biofouling that can further interfere with assay results.

Despite their widespread application, RIA and ELISA are practically limited to use in centralised laboratory environments where careful control of the experimental conditions can be exercised. They typically involve multiple steps that require trained operators and in the case of RIA they involve the use of radioisotopic labels that require specialised handling and represent a significant health hazard. Analysis is also very labour intensive and consequently quite expensive. Samples therefore must be transported to a laboratory and

testing and processing of results typically takes several hours-days. This arrangement is inadequate for a wide range of applications that need results in much shorter timeframes.
To help address these issues, there has been much research devoted to the development of immunochromatographic test strip technology (Weller, 2000). This technology has been utilised for detection of drug residues (Chen et al., 2009) and drugs of abuse by transferring the immunoassay process onto a single-use test strip that generates a colour response after the sample has flowed over the immobilised protein conjugate. Such tests however, are largely semi-quantitative and so can be of limited use when a concentration result is required rather than a simple yes/no answer.
Biosensors offer a very promising means of achieving more versatile determination of small molecule concentrations in diverse matrices. A biosensor is an instrument that utilises a biomolecule/s, such as an enzyme or antibody, to interact with the target molecule being measured. From this interaction an electrical signal is then generated which can be used to determine the concentration of the target compound. Biosensors are typically classified according to the biochemical interaction used and the method of transduction. For detection of small molecules, antibody based biosensors are a logical choice as they retain the excellent specificity of antibodies allowing for detection in complex matrices, including those with a number of structurally similar compounds present in the same sample, as is the case with the steroid hormones. Furthermore, their relatively high binding affinities allow efficient uptake of the analyte from the sample and thus maximise the number of binding events and the biosensor signal. High quality antibodies are widely available for a broad range of small molecule analytes, including most of the physiologically significant steroid hormones.
When we examined the range of transduction technologies available for small molecule biosensing, we decided to investigate the use of the quantum optical-electrical phenomenon known as surface plasmon resonance (SPR). When a photon of light is incident on a noble metal surface (typically gold or silver) it can couple with the electrons in the metal, exciting the electrons and causing them to move as a single electrical entity known as a plasmon which propagates parallel to the metal surface. As the plasmon oscillates it generates an electric field that extends about 300 nm out from the metal surface (Homola et al., 1999). At a particular angle where the energy transfer from the photon to the plasmon is well matched a resonance occurs, significantly increasing energy transfer from the photon to the plasmon and causing a corresponding decrease in reflectance. If mass is bound to the surface within this 300 nm range then it perturbs the plasmon and, for a photon of fixed wavelength, shifts the resonance angle. If the plane of the metal surface is fixed, then the resonance wavelength can be identified by scanning through a range of angles of incidence for the photon and determining the resonance angle (Mullet et al., 1998). An SPR biosensor effectively measures minute changes in refractive index corresponding to binding events on the sensor surface (Homola, 2008). SPR biosensors can typically achieve resolutions down to 1 resonance unit (RU) which is 1×10^{-6} refractive index units (Stenberg et al., 1991). SPR biosensors can effectively detect binding by molecules as small as about 2 kDa, but smaller molecules generate insufficient changes in bound mass and so cannot be directly measured adequately. This poses particular challenges for detecting small molecules. In this case it is necessary to detect the binding of an antibody to an analyte conjugated sensor surface or to tag the small molecule with a large molecular mass tag and use this to bind to un-bound antibody sites on the sensor surface. Once the binding event/s have taken place, then the sensing surface can be returned to its original state by application of a suitable regeneration cocktail, allowing some re-use of the surface.

BIAcore SPR instruments have been widely used for years for the analysis of biomolecular interactions. It is extensively applied as a research tool to examine antibody / antigen (McCormick et al., 2004; Kubitschko et al., 1997), oligonucleotide / complementary oligonucleotide (Kai et al., 1999), receptor / target (Zhang et al., 2004) and host / guest (Chen et al., 2002) interactions. These instruments contain sophisticated microfluidics and temperature control units and range from the conventional four channel versions such as BIAcore 3000, to the more recent array format in the BIAcore Flexchip. The instruments use chips which contain the gold sensing surface and can be docked and un-docked from the main instrument as required. The work discussed in this chapter uses either a BIAcore 2000 or 3000 in the 4-channel format with a carboxymethylated (CM) dextran coating.

SPR biosensor assays have the advantages that binding data can be collected in real-time as the sensorgram (plot of response vs. time) is generated and so there is no need to wait for the signal development of an entire immunoassay plate to obtain results. This makes the technology particularly amenable to use in applications where data is required to inform decisions in near-real-time, such as in the diagnosis of disease or in the study of human hormonal responses. Furthermore, SPR assays are semi-automated. Once the samples are loaded into an instrument such as a BIAcore, then a wizard program can run the assay automatically and feed results to your desktop. With pre-prepared standards very little pipetting is required and this significantly reduces costs. SPR assays also do not use any radioactive labels. Increasingly, SPR biosensor technology is improving to the extent that a number of more compact and affordable options are now appearing on the market thus beginning a wider dissemination of the technology beyond large, well-funded centralised laboratories.

Potentially SPR is a very sensitive transduction technique where only small changes in refractive index are required to generate signal. This means that provided the immunoassay format and surface coating chemistries are well-designed, very sensitive assays can be achieved. However, in the case of small molecule immunoassay, the lack of mass in the analyte means that specialised enhancement technologies need to be applied to achieve the very low detection limits needed for measurement at the physiologically relevant concentrations found in certain biological fluids, including saliva.

It is very easy for steric hindrance to occur between the small molecule and the large antibodies used or between the small molecule and the sensing surface. If the analyte is sterically impeded from binding to the antbody this reduces the sensor signals that can be obtained and worsens the sensitivity of the immunoassay. Given that an SPR sensor detects bound mass on the sensor surface, if large molecules bind non-specifically to the surface then they will generate an SPR signal which can obscure the signal results from specific immunoassay binding of the analyte. This risk is particularly high if the sample matrix contains high concentrations of high molecular mass species, such as in the case of saliva which is rich in mucins. For a given assay it is very beneficial to be able to use the same biosensor surface over and again many times. This approach means that the need for calibrating different sensor surfaces is minimised, cost of consumables is reduced and risk of failure of the sensing surface during crucial analyses is mitigated. Most SPR sensor surfaces rely upon self-assembled monolayers (SAMs) to conjugate small molecules or antibodies to the sensor surface. This method of attachment lacks longer-term stability as do most direct immobilisations of proteins onto sensor surfaces. Typically such SAM surfaces only last about 100-400 binding and regeneration cycles (Yuan et al., 2007).

Given these significant challenges faced by small molecule SPR immunosensing it is very important to consider how such assays can be rationally designed to overcome problems of steric hindrance, biofouling, sensor surface stability and signal enhancement for greater sensitivity. In this chapter we examine the strategies taken in our laboratories to overcome these challenges and to help make SPR immunosensing a more practical technique for sensitive detection of small molecules, even in complex matrices.

2. Rational design of steroid conjugates

To optimise the sensitivity of SPR immunoassays of the steroid hormones, it is necessary to achieve maximum specific antibody binding to the antigen-conjugated sensor surface. The first step in ensuring this is to allow free access by the antibody to the specific parts of the steroid molecule that the antibody recognises, that is the epitopes. To do this one must conjugate the steroid through a position distant from these critical functional groups and not conjugate through an existing functional group. For the steroids, this can be done by conjugating to the A-ring 4-position using the formation of a thioether linkage (Fig. 1). This technique was selected after SPR analysis revealed much stronger binding to the 4-position for progesterone than was obtained through the more conventional 7-position (Wu et al., 2002) (Fig. 2).

In the case of estradiol, another conjugation technique utilising a Mannich reaction to conjugate at the 2-position of the A-ring was found to be equally useful in retaining strong binding responses. This was in contrast to hemisuccinate conjugation through the hydroxyl group at the 3-position, which gave only 2% as much binding (Mitchell et al., 2006).

The next factor to consider is the length of the intermediate linker that spaces the antigen from the sensing surface (Bieniarz et al., 1996). The linker should project the antigen into the flow of fluid that passes through the biosensor flow cell and so allow optimal presentation of the immobilized antigen to the antibody thus ensuring maximum sensor signal. We have considered the effects of incremental changes in linker length for progesterone – protein conjugates, examining linkers of 4-, 11- and 18-atoms in length (Wu et al., 2002). The linker length was found to be crucial to the amount of antibody binding in the SPR flow-through biosensor format with binding responses increasing up to 18-atoms in linker length (Wu et al., 2002). Based on these observations, an oligoethylene glycol linker was attached to the steroid at the 4-position through a thioether bridge. This produced a 19-atom linker chain (Mitchell et al., 2005). Oligoethylene glycol is well known as being non-immunogenic

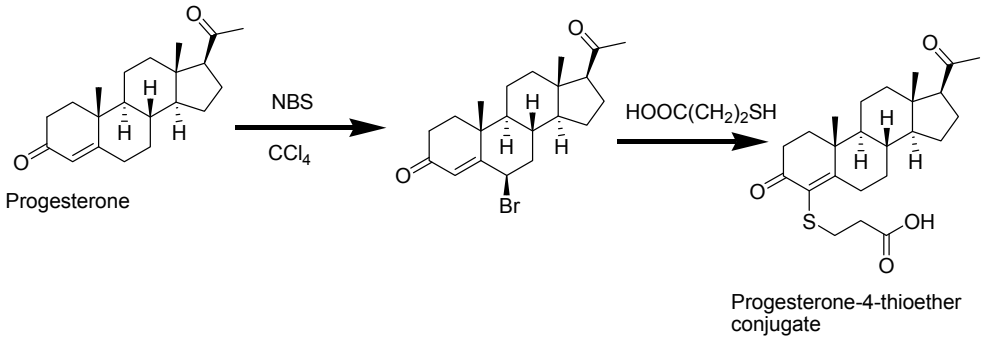

Fig. 1. Synthesis of progesterone-4-thioether conjugate for attachment of linkers

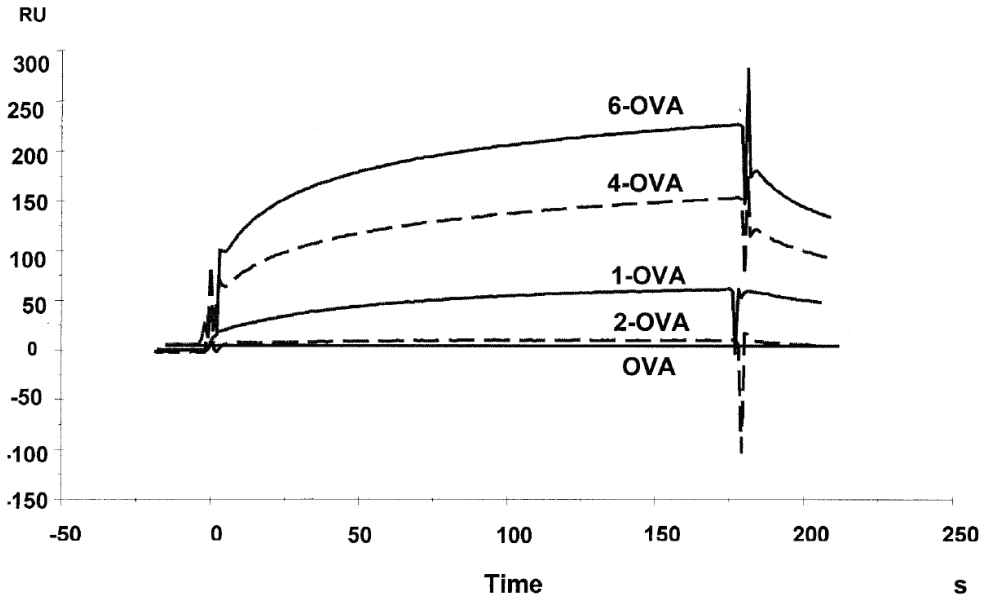

Fig. 2. SPR sensorgrams showing the binding of progesterone – protein conjugates to a progesterone monoclonal antibody (mAb) functionalised surface. OVA: ovalbumin, 2-OVA: conjugate through the 7-position, 1-OVA: conjugate through the 4-position, 4-OVA: 4-position conjugate with 11-atom linker, 6-OVA: 4-position conjugate with 18-atom linker. Reprinted from Steroids, 67, Mitchell, J. S.; Wu, Y.; Cook, C. J.; Main, L. (2002) Evaluation of progesterone-ovalbumin conjugates with different length linkers in enzyme-linked immunosorbent assay and surface plasmon resonance-based immunoassay. 565-572, 2002, with permission from Elsevier.

(Kurusu et al., 2003) and biocompatible (Otsuka et al., 2003) thus minimising non-specific binding to the linker. It is hydrophilic and thus allows good projection of the antigen into the aqueous mobile phase. Furthermore, it has high chemical stability and the length can be incremented as required by addition of more ethylene glycol units. Attachment to one end of the chain is achieved by protecting the amine at the opposite end by attachment of a *t*-butoxy carbonyl group which can be conveniently removed at the time of immobilisation.

3. Covalent linker conjugation technology

3.1 Immobilization

High immobilization stability can be achieved by use of a totally covalent immobilisation of the steroid antigen to the sensor surface. In these studies, the most effective means of achieving this was to utilize a carboxymethylated (CM) dextran polymer coating applied to the gold surface. This dextran hydrogel extends for about 100 nm from the gold surface and is highly porous, giving a very high surface area. The polymer is studded with carboxylic acid groups which can be conveniently used as anchor or immobilisation points for covalent attachment of steroid-linker conjugates. This attachment is achieved by the formation of an

amide linkage between the carboxylic acid groups and the primary amines at the end of the oligoethylene glycol linkers. This can be further facilitated by use of *N*-hydroxysuccinimide (NHS) activation of the carboxylic acids.
Immobilization was achieved by simply flowing a mixture of NHS and *N*-ethyl-*N*-(3-dimethylaminopropyl)-carbodiimide (EDC) over the CM dextran surface to activate it and then flowing the steroid linker conjugate. This is ideally performed at low flow rates (5 μL/min) to ensure maximum conjugation to the sensor surface. This technique provides high binding capacity surfaces without the need to disassemble the chip. Finally, ethanolamine solution (pH 8) can be passed over the surfaces to cap any un-conjugated carboxylic acid groups and so prevent them from reacting with proteins in the samples.

3.2 Surface stability and regeneration

To achieve a high throughput of samples and standards over a single surface, it is necessary to have very high sensor surface stability as the surface must be able to withstand multiple binding and regeneration cycles. The regeneration process involves exposing the surface to harsh regeneration "cocktails" which chemically remove the bound antibodies. The cocktails used in this work are typically 50 mM NaOH with 20%v/v acetonitrile, providing a combination of high pH and a chaotrophic reagent. Despite exposure to such a harsh mixture, progesterone conjugated surfaces are able to withstand more than 1100 binding and regeneration cycles without appreciable loss of binding capacity (Mitchell et al., 2005). This greatly extends the lifetime of a single sensor surface and allows extensive re-use without the need for immobilization of a fresh surface and in so doing, significantly reduces the costs per assay cycle.

4. Assay format and gold nanoparticle signal enhancement

The assay format adopted was a competitive inhibition assay. In this format, the small molecule analyte was covalently immobilised on the surface. The sample containing the small molecule was then mixed with a primary antibody raised against the analyte and the mixture injected over the sensor surface. Primary antibody that had not bound the "free" sample antigen, bound the surface immobilized antigen thus producing a refractive index change on the surface (Fig. 3). This SPR signal is inversely related to the concentration of the "free" antigen and a standard curve can be produced that takes the form of an S-curve.
The sensitivity of the assay can be assessed as the amount of signal change achieved per unit of analyte concentration change and the limit of detection as the minimum concentration that can be statistically distinguished from the blank. Lower concentrations of the analyte can be detected by reducing the concentration of the primary antibody as less free antigen would be required to inhibit antibody binding to the antigen-immobilized surface. The problem with this approach in SPR, is that this will also reduce the signal by reducing the bound mass on the surface. To achieve a highly sensitive assay, it is therefore crucial to minimise the primary antibody concentration whilst retaining high signal.
When the above assay design was applied to the SPR biosensor as described, it gave assays with a LOD of approximately 1 ng/mL in the case of progesterone. Whilst this LOD is suitable for measurement of steroids in human blood serum, it is far too high to measure steroids in other matrices such as saliva, where concentrations are typically 1% of those found in blood. To shift the assay curve to lower concentrations, it was necessary to further reduce the primary antibody concentration. To retain sensor signal, strategies for labelling

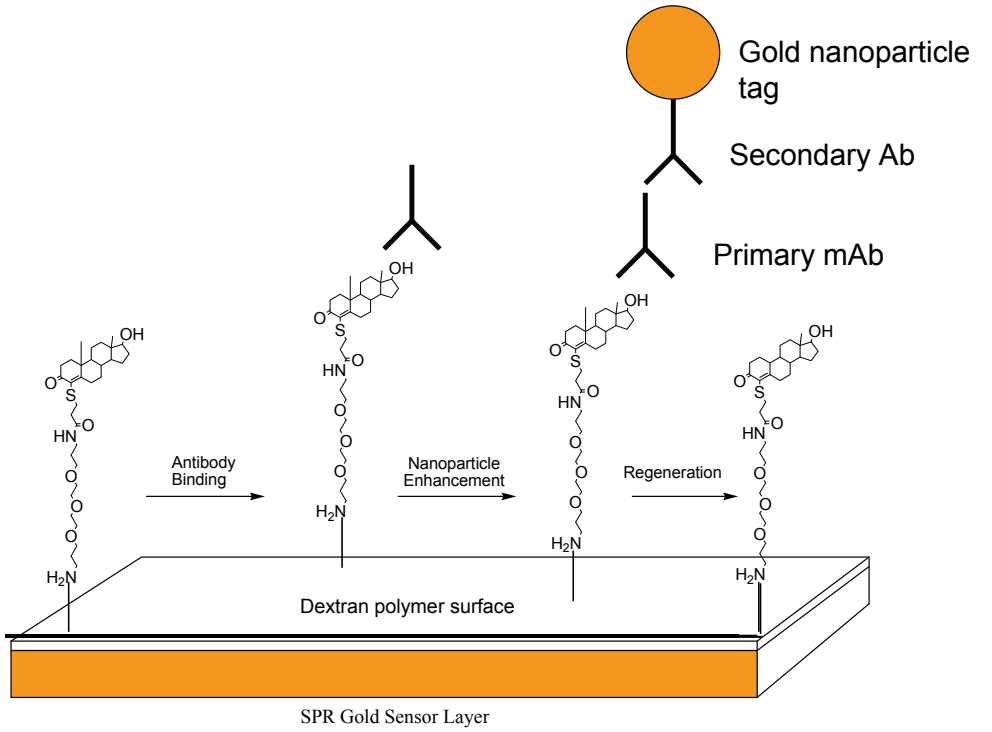

Fig. 3. Schematic showing the steroid immobilised SPR sensor surface, binding of primary antibody and labelling with secondary antibody – gold nanoparticle conjugate.

the binding interaction were applied. First, a secondary antibody that recognises the primary antibody, was bound in a separate binding step to add signal to the binding interaction and allow significant reductions in the concentration of the primary antibody (Fig 3.). LOD of 20.1 pg/mL could now be obtained for progesterone and signal was enhanced 8.1-fold (Mitchell et al., 2005) (Fig. 4).

As well as using secondary antibody there are other means of adding high mass tags to the binding interaction. Gold nanoparticles have a high mass contained in nanospheres the diameter of which can be altered as required between about 1 nm – 100 nm by altering the conditions of their synthesis. This size range is ideal for tagging antibodies and furthermore, gold nanoparticles can be readily conjugated to proteins such as antibodies through charge interactions. Gold nanoparticle enhancement has been applied to large molecule immunoassays (Gu et al., 1998; Lyon et al., 1998; White & Rosi, 2008) but significant steric challenges exist for its use with small molecules. Gold nanoparticles of 25, 45, 55 and 70 nm diameters were examined as tags for secondary antibodies for signal enhancement in small molecule SPR immunosensing. 25 nm nanoparticles were found to give the highest signal enhancement and were applied in a progesterone assay. Signal enhancement further increased to 13-fold and the LOD could be reduced to 8.6 pg/mL for progesterone (Fig. 5) (Mitchell et al., 2005). By application of gold-secondary antibody signal enhancement, the LOD could thus be reduced by more than two orders of magnitude (Mitchell et al., 2005),

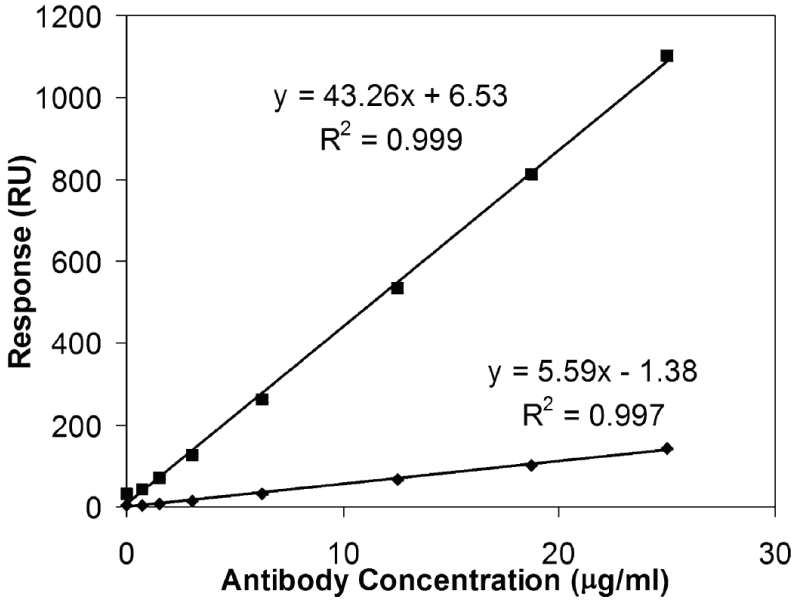

Fig. 4. Plots of SPR response (RU) vs. antibody concentration (µg/mL) for unenhanced mAb only assay (◆) and secondary antibody enhanced assay (■). Reprinted from Analytical Biochemistry, 343, Mitchell, J. S.; Wu, Y.; Cook, C. J.; Main, L. Sensitivity enhancement of surface plasmon resonance biosensing of small molecules. 125-135, 2005, with permission from Elsevier.

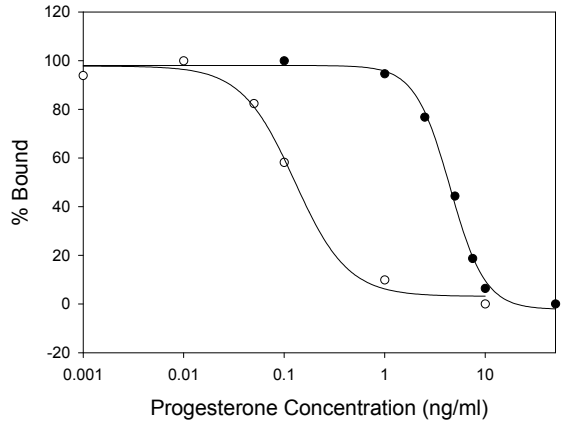

Fig. 5. Progesterone SPR immunoassay standard curves for assay without signal enhancement (●) and with gold nanoparticle signal enhancement (○), showing improvements in LOD. Reprinted from Analytical Biochemistry, 343, Mitchell, J. S.; Wu, Y.; Cook, C. J.; Main, L. Sensitivity enhancement of surface plasmon resonance biosensing of small molecules. 125-135, 2005, with permission from Elsevier. (RSC) (www.rsc.org)

allowing sensitive detection of steroid hormones at the concentrations typically found in human saliva. The signal enhancement arising from the gold labelling could result not only from the added mass but also from cooperative plasmon coupling between the gold nanoparticles and the underlying gold sensor surface. This effect has been suggested before with large molecule binding targets (Lyon et al., 1999).

Using bulky nanoparticles to enhance SPR signal strength, adds to the potential for steric hindrance in immunoassays of small molecules. These assays were constructed around a "double spacer" system whereby spacers or linkers project the antigen out from the sensor surface and hold the primary antibody out from the gold surface, thus allowing space for the antigen / antibody interactions and ensuring optimal sensor signal. Non-specific binding from the conjugated gold nanoparticles could be reduced significantly by the addition of polyethylene glycol (PEG)-400 or PEG-4000 (Mitchell et al., 2005). By using a 25 nm gold nanoparticle, the risk of the colloid settling or aggregating over the course of the assay is minimised. Bovine serum albumin (BSA) could also be used to further reduce non-specific binding (Mitchell et al., 2005).

5. Small molecule analytes

The immunobiosensor format outlined in the previous sections is quite generic and can be applied to a wide range of small molecules provided they have a suitable site for conjugation and have high affinity monoclonal antibodies available (Fig. 6). The SPR immunobiosensor approach outlined was first tried with progesterone as a model compound. Progesterone has well developed monoclonal antibodies and its measurement is of significant interest in the monitoring of oestrous cycles in animals and in the early

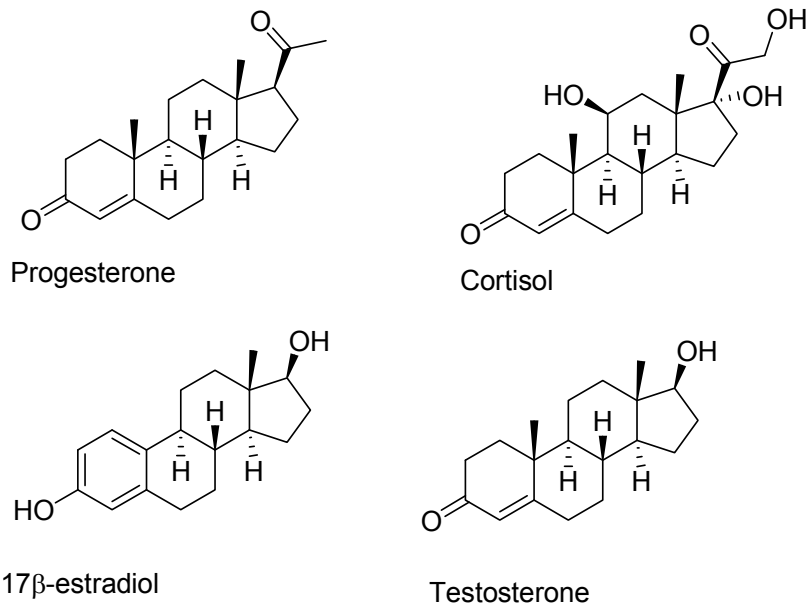

Fig. 6. Structures of steroid analytes covalently conjugated to SPR sensor surface through the 4-position

identification of pregnancy. The assay concept was later extended to 17β-estradiol which has an aromatic A-ring and so required a slightly different approach to the attachment of the thioether unit. Assays using secondary antibody enhancement gave an LOD of 25 pg/mL for 17β-estradiol (Mitchell et al., 2006). Other steroid hormones measured using this technique include cortisol (Mitchell et al., 2009) and testosterone (Mitchell & Lowe, 2009). Cortisol detection can be used in the diagnosis and management of conditions such as Addison's disease (Lovas & Husebye, 2003) and as an indicator of stress (Riad et al., 2002). Testosterone is the principal male sex hormone and its concentrations are of interest in sports physiology (Crewther et al., 2006). For cortisol, an LOD of 13 pg/mL was obtained in buffer with secondary antibody enhancement (Mitchell et al., 2009) and for testosterone it was 35 pg/mL (Mitchell & Lowe, 2009). Both cortisol and testosterone used analogous conjugation techniques to that of progesterone. When the testosterone assay utilised gold nanoparticle enhancement, the LOD dropped further to 23 pg/mL (Mitchell & Lowe, 2009).
Another positive feature of these assays is that the primary monoclonal antibody concentrations used are minimised to improve assay LOD. This also serves to lower the costs per assay and so individual determinations can usually be done for <NZ$2 in materials cost. The volumes of sample required are also very low (typically 50 μL) making these techniques amenable to applications where samples are very precious.
Extending the range of compounds beyond the steroids, the catecholamine dopamine was also conjugated to an SPR surface using an OEG linker attached to a mercaptothioether moiety conjugated *ortho* to a phenol group (Mitchell et al., 2007) (Fig. 7). This allowed conjugation at a point distant from characteristic functional groups and without compromising existing functional groups. Antibody binding interactions were then studied in this flow-through biosensor format and various conjugation techniques compared and contrasted (Mitchell et al., 2007).

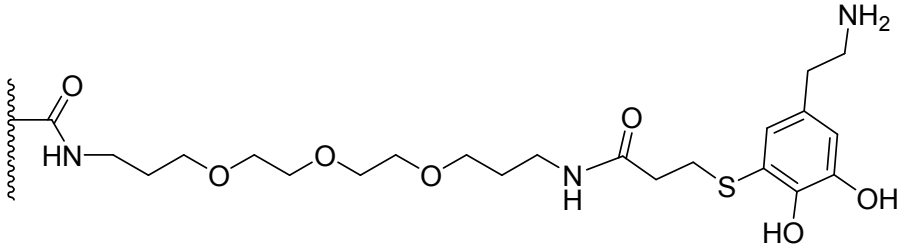

Fig. 7. Covalent conjugation of dopamine to the SPR biosensor surface utilising a CM-dextran polymer

As well as examining SPR using a continuous gold underlayer as the sensor surface, the use of gold nanohole array substrates for biosensors are attracting attention (Brolo et al., 2004; Gao et al., 2007). They are of interest for use in biosensors as they have a lower functionalisation area giving rise to increased sensitivity, a simple optical set-up with transmission measurement of well-defined spectral features and they allow for optical field concentration giving interesting enhancement effects. As a precursor to their use in immunobiosensors, immunochemical interactions were studied using a gold nanohole array where the signal response is expressed as a movement in the plasmon transmission peak of the array which can be simply measured using a UV-visible spectrophotometer (Sharpe et al., 2008). In this case, monoclonal antibody binding to immobilised cortisol could be clearly

detected as could enhancement with gold-nanoparticle labelled secondary antibody (Fig. 8). The system could also be regenerated and had low non-specific binding from the gold nanoparticles (Sharpe et al., 2008).

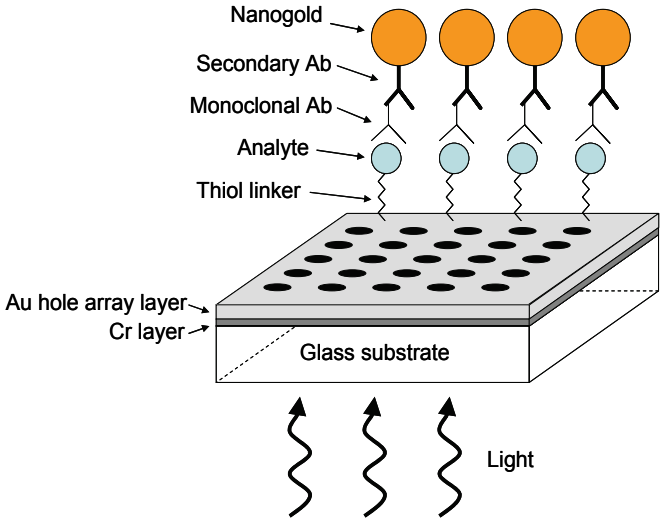

Fig. 8. Schematic showing a gold nanohole array functionalised with analyte (cortisol) conjugated to a thiol linker. The analyte is bound by a primary monoclonal antibody and then labelled with a secondary antibody-nanogold conjugate. Reprinted with permission from Sharpe, J. C.; Mitchell, J. S.; Lin, L.; Sedoglavich, N.; Blaikie, R. J. (2008) *Anal Chem*, 80, 6, 2244-2249. 2008 American Chemical Society.

6. Measurement in saliva

Human saliva contains very high concentrations of high molecular mass components such as mucins. These compounds can bind to SPR sensor surfaces and generate erroneous responses. This problem is particularly acute for small molecules, such as the steroid hormones, present at very low concentrations. Cortisol is present typically at 0.1 – 10 ng/mL in human saliva and testosterone at 29-290 pg/mL (Ellison et al., 2002). Measurement in saliva is particularly advantageous as it allows non-invasive detection of small molecules and regular sampling. Samples ideally need to be analyzed rapidly in near real-time, so chemical extraction and extensive pre-treatment of samples are not options.

Standards of cortisol and testosterone spiked into stripped human saliva could be used for the measurement of salivary hormonal concentrations. These standards could be passed through a BIAcore SPR instrument without clogging of the microfluidics (Mitchell et al., 2009). In the case of cortisol, saliva samples from human subjects were analyzed in the BIAcore without extensive pre-treatment through the addition of sodium dodecyl sulphate (SDS) to the antibody diluent at carefully controlled concentrations. The SDS is thought to minimise adhesion of salivary mucins to the sensor surface through charge repulsion, but at the concentrations used it did not affect the antibody or compromise the assay sensitivity greatly (Mitchell et al., 2009). The non-specific binding was reduced to a consistent and low

level enabling an assay curve to be formed without significant interference from high-molecular mass species (Mitchell et al., 2009). An LOD of 49 pg/mL was obtained for salivary cortisol, well below that required for analysis of saliva samples. Additionally, a strong signal sensitivity of 162 RU.mL/ng was attained allowing accurate discrimination of concentrations ranging to below 1 ng/mL (Mitchell et al., 2009). Despite the use of SDS, interassay CVs of 13.5% were achieved, comparable to many ELISA (Mitchell et al., 2009; Mitchell et al. 2004). No clogging of the microfluidics was observed despite the high viscosity of saliva. To ensure the accuracy of the salivary cortisol measurements, samples from 40 healthy male volunteers were compared to results from RIA. The slope of the correlation line was close to 1 with an r = 0.94, showing good agreement between the two techniques (Mitchell et al., 2009) (Fig. 9). Binding and regeneration steps could be completed in 10 min per sample thus allowing for a fast throughput of samples. Another advantage of this method is that pre-concentration of samples is avoided as the technique has sufficient sensitivity to measure samples without complex pre-treatment (Mitchell et al., 2009). Furthermore, measurement can be made in small sample volumes (50 μL of sample is sufficient).

This SPR technique for measurement of salivary cortisol provides a useful means of monitoring hormone concentrations non-invasively in near-real-time and can be applied to both diagnostic and stress monitoring applications. As the technique is largely generic, it can be extended to other target small molecules found in human saliva. A later cortisol SPR study using a different sensor surface approach has failed to achieve comparably low LOD (Frasconi et al., 2009).

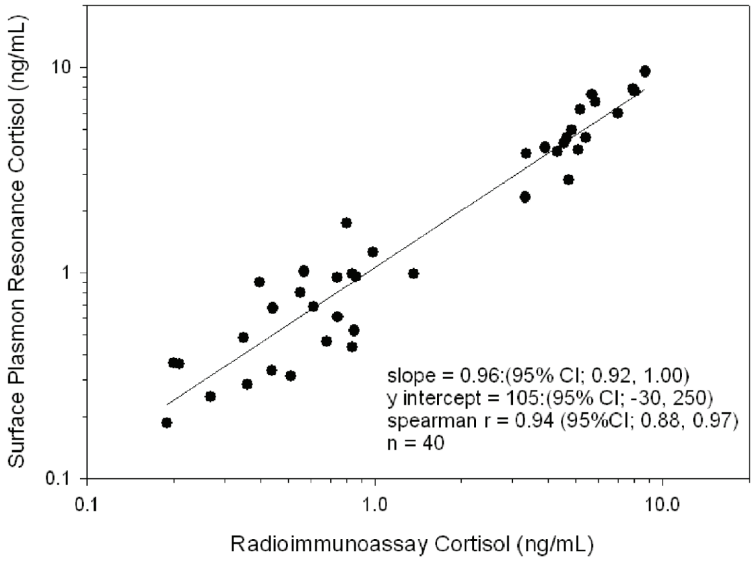

Fig. 9. Correlation plot comparing concentration determinations made by the SPR cortisol immunoassay and salivary cortisol radioimmunoassay. Rapid ultrasensitive measurement of salivary cortisol using nano-linker chemistry coupled with surface plasmon resonance detection. *Analyst*, 134, 2, 380-386 – Reproduced by permission of The Royal Society of Chemistry

7. Context in wider plasmonic biosensor research

The ever widening field of plasmonic biosensor research largely falls into three main areas. 1. The use of SPR to study biomolecular interactions. This includes antibody, oligonucleotide, receptor and enzyme research and involves using SPR as a tool to probe biological systems. 2. The study of plasmon fields and their relationship to the noble metal surfaces from which they emanate (Lyon et al., 1999). This typically involves using quantum, electrical and optical physics to systematically investigate the plasmon resonance phenomenon at a fundamental level. 3. The use of SPR biosensors to detect large molecule targets, including proteins and DNA (Huang et al., 2008). The use of SPR for the sensitive measurement of low concentrations of small molecules has not received as much attention as assays for proteins and oligoneucloetides. There is now growing research interest in improving small molecule SPR immunoassay through design of the sensor interface (Mitchell et al., 2005; Miura et al., 2008; Shankaran et al., 2007). Recent studies have examined the use of SAM layers combined with protein conjugates to fabricate sensor layers for a herbicide (2,4-D, LOD of 10 pg/mL) (Kim et al., 2006), benzaldehyde (Gobi et al., 2007 b) and a steroid hormone (progesterone, LOD of 4.9 pg/mL) (Yuan et al., 2007) either with or without protein or nanogold enhancement. This approach has also been applied to measurement of the antimicrobial chloramphenicol (Yuan et al., 2008). Further work using direct covalent immobilisation to SAMs for TNT analysis has also been combined with secondary antibody signal enhancement (LOD of 50 pg/mL) (Mizuta et al., 2008) and a similar strategy developed for detection of benzaldehyde using PEG linker chains (Gobi et al, 2007 a). Immobilisation of histamine through a SAM layer without enhancement has yielded poorer LOD (3 ng/mL) (Li et al., 2006). Gold nanoparticle enhancement has also been used to improve LOD in the immunoassay of the metabolite estriol-16-glucuronide (LOD of 14 pg/mL) (Jiang et al., 2009) using protein conjugate immobilized on CM dextran. A protein conjugate to a small molecule dye has also been used as the high mass labelled antigen in a competitive SPR immunoassay with immobilised antibody (Aizawa et al., 2007) and biotin-BSA has been used as a high mass label for 2,4-D immunoassay (Kim et al., 2007). With gold nanoparticle enhancement of small molecule SPR immunoassays now well established, it is hoped that it will be successfully applied to an even broader range of compounds. The issue of biofouling in small molecule SPR is also receiving attention but often the techniques used involve total removal of the background matrix by time-consuming methods such as flow filtering where blockages can occur and LOD are too high (Stevens et al., 2008) or else extensive dilution of samples (Gillis et al., 2002) which worsens the practical LOD.

By combining surface and conjugation chemistry with immunology and optics, it is possible to create new sensor interfaces that offer significantly improved detection of small molecules, not only in buffer but also in real biological samples. The research detailed in this chapter represents several advances in the use of SPR to detect small molecules of biological significance at very low concentrations and particularly in a complex biological matrix.

8. Conclusions and future research

The sensitive measurement of very low concentrations of small molecule analytes is of great value in the diagnosis of disease, study of human and animal physiology and the monitoring of product quality and environmental integrity. Many small molecules are

routinely measured by traditional RIA or ELISA in expensive, time-consuming and centralised processes. In this chapter we have examined how SPR immunobiosensors can be used to measure very low small molecule concentrations accurately, quickly, affordably, with low labour requirements and even in complex biological matrices on highly re-usable sensor surfaces. The use of chemical linkers to covalently immobilise steroid antigens to the sensor surface allows the surface to be re-used many times even under harsh regeneration conditions. By selecting a conjugation position and linker length that optimises antigen presentation in the flow-through assay format, antibody binding can be maximised and high signal sensitivities obtained. The use of hydrophilic and non-immunogenic linkers also improves specific binding response. Secondary antibody labelling of the primary monoclonal antibody binding interaction is a convenient means of enhancing the sensor signal and further reducing LOD. Enhancement is further increased by the use of gold nanoparticles which add further mass and cooperatively enhance the plasmon shift. As the technology is generic, it can be applied to a wide range of small molecule targets. The application of this technology to the sensitive measurement of salivary cortisol has been demonstrated with the addition of SDS surfactant to minimise non-specific binding and allow measurement without chemical extraction or extensive pre-treatment of samples.

To achieve the next generation of SPR biosensors for small molecules, future research will likely focus on expanding the types of small molecule analyte conjugated to the sensor surface and on examining alternative gold substrate designs to further improve sensitivity. The covalent nanolinker approach described in this chapter has been applied to a range of steroid hormones but it is also amenable to use with other small molecules such as pesticides, pharmaceutical residues and human and animal metabolites. Given that new regulations increasingly require sensitive measurement of many of these compounds, there is a very real role for SPR biosensors to play in semi-automated, high-throughput analysis of environmental and food samples. Biomedical testing laboratories may increasingly look to semi-automated alternatives to traditional plate-based assay formats as their sample loads increase for diagnosis and monitoring of medical conditions. Accessing new classes of analytes is limited only by the conjugation technique used to attach the linker to a point distant from existing functional groups. Alternative gold substrates that are attracting much attention include the use of “nano-islands” of deposited noble metal. These islands can generate localised surface plasmons (LSPs) particularly around their vertices and can generate very steep plasmon field gradients which could potentially result in greater sensitivity. Another emerging technique is the use of gold nanohole arrays as described above. Here, optical field concentration around the nanoholes offers the potential for further improvements in sensitivity.

When developing biosensor technologies for highly sensitive detection of small molecules, it is crucial to consider the chemistry of the sensor / sample interface, as it is here that the critical binding interactions needed for measurement take place. By rationally designing this interface, one can greatly improve the performance of the biosensor by maximising specific binding interactions, minimising non-specific binding and biofouling and creating chemically stable and highly re-usable sensor interfaces. This approach combined with the rapid advances in plasmonic transduction technology, particularly plasmonic substrate design, offer great promise for even more sensitive and reliable small molecule biosensors.

9. Acknowledgments

The authors would like to thank Associate Professor Lyndsay Main, Dr Christian Cook, Dr Tim Lowe and Dr John Ingram for their advice and encouragement. Our research was funded by the New Zealand Foundation for Research Science and Technology.

10. References

Aizawa, H.; Tozuka, M.; Kurosawa, S.; Kobayashi, K.; Reddy, S. M.; Higuchi, M. (2007) Surface plasmon resonance-based trace detection of small molecules by competitive and signal enhancement immunoreaction. *Anal Chim Acta*, 591,2, 191-4

Bieniarz, C.; Husain, M.; Barnes, G.; King, C. A.; Welch, C. J. (1996) Extended length heterobifunctional coupling agents for protein conjugations. *Bioconjugate Chem*, 7, 1, 88-95

Brolo, A. G.; Gordon, R.; Leathem, B.; Kavanagh, K. L. (2004) Surface plasmon sensor based on the enhanced light transmission through arrays of nanoholes in gold films. *Langmuir*, 20, 12, 4813-4815

Chen, L. B.; Wang, Z. F.; Ferreri, M.; Su, J. L.; Han, B. (2009) Cephalexin residue detection in milk and beef by ELISA and colloidal gold-based one-step strip assay. *J Agric Food Chem*, 57, 11, 4674-4679

Chen, S.; Yu, Q.; Li, L.; Boozer, C. L.; Homola, J.; Yee, S. S.; Jiang, S. (2002) Detecting the adsorption of dye molecules in homogeneous poly(propylene imine) dendrimer monolayers by surface plasmon resonance sensor. *J Am Chem Soc*, 124, 13, 3395-401

Clark, P. M.; Neylon, I.; Raggatt, P. R.; Sheppard, M. C.; Stewart, P. M. (1998) Defining the normal cortisol response to the short Synacthen test: implications for the investigation of hypothalamic-pituitary disorders. *Clin Endcrinol*, 49, 3, 287-292

Crewther, B; Keogh, J.; Cronin, J.; Cook, C. (2006) Possible stimuli for strength and power adaptation – acute hormonal responses. *Sports Med*, 36, 3, 215-238

Ellison, P. T.; Bribiescas, R. G.; Bently, G. R.; Campbell, B. C.; Lipson, S. F.; Panter-Brick, C.; Hill, K. (2002) Population variation in age-related decline in male salivary testosterone. *Hum Reprod*, 17, 12, 3251-3253

Frasconi, M.; Mazzarino, M.; Botre, F.; Mazzei, F. (2009) Surface plasmon resonance immunosensor for cortisol and cortisone determination. *Anal Bioanal Chem*, 394, 8, 2151-2159

Gao, D.; Chen, W.; Mulchandani, A.; Schultz, J. S. (2007) Detection of tumor markers based on extinction spectra of visible light passing through gold nanoholes. *Appl Phys Lett*, 90, 7, 073901

Gillis, E. H.; Gosling, J. P.; Sreenan, J. M.; Kane, M. (2002) Development and validation of a biosensor-based immunoassay for progesterone in bovine milk. *J Immunol Methods*, 267, 2, 131-138

Gobi, K. V.; Matsumoto, L.; Toko, K.; Ikezaki, H.; Miura, N. (2007) Development of polyethyleneglycol monolayer-based SPR immunosensor for detection of low-molecular-weight fragrants. *6th IEEE Sensors Conference*, pp. 686-689, Atlanta GA, Oct 2007, IEEE, New York

Gobi, K. V.; Matsumoto, L.; Toko, K.; Ikezaki, H.; Miura, N. (2007) Enhanced sensitivity of self-assembled-monolayer-based SPR immunosensor for detection of benzaldehyde using a single-step multi-sandwich immunoassay. *Anal Bioanal Chem*, 387, 8, 2727-2735

Gu, J. H.; Lu, H.; Chen, Y. W.; Liu, L. Y.; Wang, P.; Ma, J. M.; Lu, Z. H. (1998) Enhancement of the sensitivity of surface plasmon resonance biosensor with colloidal gold labelling technique. *Supramol Sci*, 5, 5-6, 695-698

Homola, J.; Yee, S. S.; Gauglitz, G. (1999) Surface plasmon resonance sensors: review. *Sensor Actuat B-Chem*, 54, 1-2, 3-15

Homola, J. (2008) Surface plasmon resonance sensors for detection of chemical and biological species. *Chem Rev*, 108, 2, 462-493

Huang, H. Z.; Ran, P. X.; Liu, Z. G. (2008) Signal enhancement of surface plasmon resonance-based immunoassays for the allergen detection. *Sensor Actuat B-Chem*, 131, 2, 417-423

Jiang, X. Q.; Waterland, M.; Blackwell, L.; Wu, Y.; Jayasundera, K. P.; Partridge, A. (2009) Sensitive determination of estriol-16-glucuronide using surface plasmon resonance sensing. *Steroids*, 74, 10-11, 819-824

Kai, E.; Sawata, S.; Ikebukuro, K.; Iiida, T.; Honda, T.; Karube, I. (1999) Detection of PCR products in solution using surface plasmon resonance. *Anal Chem*, 71, 4, 796-800

Kim, S. J.; Gobi, K. V.; Tanaka, H.; Shoyama, Y.; Miura, N. (2006) Enhanced sensitivity of a surface-plasmon-resonance (SPR) sensor for 2,4-D by controlled functionalization of self-assembled monolayer-based immunosensor chip. *Chem Lett* , 35, 10, 1132-3.

Kim, S. J.; Gobi, K. V.; Iwasaka, H.; Tanaka, H.; Miura, N. (2007) Novel miniature SPR immunosensor equipped with all-in-one multi-microchannel sensor chip for detecting low-molecular-weight analytes. *Biosens Bioeletron*, 23, 5, 701-707

Kubitschko, S.; Spinke, J.; Bruckner, T.; Pohl, S.; Oranth, N. (1997) Sensitivity enhancement of optical immunosensors with nanoparticles. *Anal Biochem*, 253, 112-122

Kurusu, F.; Ohno, H.; Kaneko, M.; Nagasaki, Y.; Kataoka, K. (2003) Functionalisation of gold electrode surface with heterobifunctional poly(ethylene oxide)s having both mercapto and aldehyde groups. *Polym Advan Technol*, 14, 1, 27-34

Li, Y.; Kobayashi, M.; Furui, K.; Soh, N.; Nakano, K.; Imato, T. (2006) Surface plasmon resonance immunosensor for histamine based on an indirect competitive immunoreaction. *Anal Chim Acta*, 576, 1, 77-83

Lovas, K.; Husebye, E. S. (2003) Replacement therapy in Addison's disease. *Expert Opin Pharmacother*, 4, 12, 2145-2149

Lyon, L. A.; Musick, M. D.; Natan, M. J. (1998) Colloidal Au-enhanced surface plasmon resonance immunosensing. *Anal Chem*, 70, 24, 5177-5183

Lyon, L. A.; Pena, D. J.; Natan, M. J. (1999) Surface plasmon resonance of Au colloid-modified Au films: particle size dependence. *J Phys Chem B*, 103, 28, 5826-5831

McCormick, A. N.; Leach, M. E.; Savidge, G.; Alhaq, A. (2004) Validation of a quantitative SPR assay for recombinant FVIII. *Clin Lab Haematol*, 26, 1, 57-64

Mitchell, J. S.; Wu, Y.; Cook, C. J.; Main, L. (2004) Technical note: protein conjugate-based immunoassay of whole milk progesterone. *J Dairy Sci*, 87, 9, 2864-2867

Mitchell, J. S.; Wu, Y.; Cook, C. J.; Main, L. (2005) Sensitivity enhancement of surface plasmon resonance biosensing of small molecules. *Anal Biochem*, 343, 1, 125-135

Mitchell, J. S.; Wu, Y.; Cook, C. J.; Main, L. (2006) Estrogen conjugation and antibody binding interactions in surface plasmon resonance biosensing. *Steroids*, 71,7, 618-31

Mitchell, J. S.; Wu, Y.; Cook, C. J.; Main, L. (2007) Direct ring conjugation of catecholamines and their immunological interactions. *Bioconjugate Chem*, 18, 1, 268-274

Mitchell, J. S.; Lowe, T. E. (2009) Rapid ultrasensitive measurement of salivary cortisol using nano-linker chemistry coupled with surface plasmon resonance detection. *Analyst*, 134, 2, 380-386

Mitchell, J. S.; Lowe, T. E. (2009) Ultrasensitive detection of testosterone using conjugate linker technology in a nanoparticle-enhanced surface plasmon resonance biosensor. *Biosens Bioeletron*, 24, 7, 2177-2183

Miura, N.; Shankaran, D. R.; Gobi, K. V.; Kawaguchi, T.; Kim, S. J. (2008) An overview of the Development and application of surface plasmon resonance based immunosensors for detection of small molecules. *Sens Lett*, 6, 6, 891-902

Mizuta, Y.; Onodera, T.; Singh P.; Matsumoto, K.; Miura, N.; Toko, K. (2008) Development of an oligo(ethylene glycol)-based SPR immunosensor for TNT detection. *Biosens Bioeletron*, 24, 2, 191-197

Mullett, W.; Lai, E. P. C.; Yeung, J. M. (1998) Immunoassay of fumonisins by a surface plasmon resonance biosensor. *Anal Biochem*, 258, 2, 161-167

Otsuka, H.; Nagasaki, Y.; Kataoka, K. (2003) PEGylated nanoparticles for biological and pharmaceutical applications. *Adv Drug Deliv Rev*, 55, 3, 403-419

Riad, M.; Mogos, M.; Thangathurai, D.; Lumb, P. D. (2002) Steroids. *Curr Opin Crit Care*, 8, 4, 281-284

Shankaran, D. R.; Gobi, K. V. A.; Miura, N. (2007) Recent advancements in surface plasmon resonance immunosensors for detection of small molecules of biomedical, food and environmental interest. *Sensor Actuat B-Chem*, 121, 1, 158-177

Sharpe, J. C.; Mitchell, J. S.; Lin, L.; Sedoglavich, N.; Blaikie, R. J. (2008) Gold nanohole array substrates as immunobiosensors. *Anal Chem*, 80, 6, 2244-2249.

Stenberg, E.; Persson, B.; Roos, H.; Urbaniczky, C. (1991) Quantitative determination of surface concentration of protein with surface plasmon resonance using radiolabelled proteins. *J Colloid Interface Sci*, 143, 2, 513-526

Stevens, R. C.; Soelberg, S. D.; Near, S.; Furlong, C. E. (2008) Detection of cortisol in saliva with a flow-filtered, portable surface plasmon resonance biosensor system. *Anal Chem*, 80, 17, 6747-6751

Weller, M. G. (2000) Immunochromatographic techniques – a critical review. *Fresen J Anal Chem*, 366, 6-7, 635-645

White, K. A.; Rosi, N. L. (2008) Gold nanoparticle-based assays for the detection of biologically relevant molecules. *Nanomedicine*, 3, 4, 543-553

Wu, Y.; Mitchell, J. S.; Cook, C. J.; Main, L. (2002) Evaluation of progesterone-ovalbumin conjugates with different length linkers in enzyme-linked immunosorbent assay and surface plasmon resonance-based immunoassay. *Steroids*, 67, 7, 565-572

Yuan, J.; Oliver, R.; Li, J.; Lee, J.; Aguilar, M.; Wu, Y. (2007) Sensitivity enhancement of SPR Assay of progesterone based on mixed self-assembled monolayers using nanogold particles. *Biosens Bioeletron*, 23, 1, 144-148.

Yuan, J.; Oliver, R.; Aguilar, M. I.; Wu, Y. (2008) Surface plasmon resonance assay for chloramphenicol. *Anal Chem*, 80, 21, 8329-8333

Zhang, Q.; Pan, R. M.; Ge, Y. C.; Xu, P. (2004) Expression of the soluble extracellular domain of human thrombopoietin receptor using a maltose-binding protein-affinity fusion system. *Biol Pharm Bull*, 27, 2, 219-221

10

Detection of SARS-CoV Antigen via SPR Analytical Systems with Reference

Dafu Cui, Xing Chen and Yujie Wang
State Key Lab. of Transducer Tech., Institute of Electronics, Chinese Academy of Sciences
Beijing 100190,
P. R. China

1. Introduction

Surface Plasmon Resonance (SPR) is an extremely sensitive optical technique to detect the changes in refractive index occurring at the metal interface, which can monitor the processes in real time without labelling requirements (Lee et al., 2006; Kanda et al., 2004; Homola, 2003). Since 1989, our group have been focusing on SPR technology development. Several generations of SPR analytical platforms, including Reference SPR Analysis System, Electrochemical-SPR Analysis System, Portable SPR Analysis System, and High-Throughput, Multi-analyte Imaging SPR Analysis System, have been designed, fabricated and tested for various applications.

SARS (Sever Acute Respiratory Syndrome) is a kind of serious infection, which caused tremendous loss in China at 2003. It is caused by the infection with SARS-associated coronavirus (SARS-CoV) (Rota et al, 2003) and early diagnosis of SARS is very important for better control of future SARS epidemics (Drosten et al, 2003). There have been several diagnostic methods currently used in hospital, but none of them can be used for early detection with low cost. For example, ELISA cannot detect antibodies that were produced in the infected patients within the first two-week's infections..

In this chapter, a novel detection method of the SARS-CoV antigens was reported by using a home-developed Reference SPR Instrument, which can monitor reaction spots with control in a single flow cell. Monoclonal antibodies to SARS-CoV were immobilized only on the reaction spots via selective chemical modification, with no immobilization on the reference spots. Then a higher version of reference SPR analytical system: high-throughput, multi-analyte imaging SPR (HMI-SPR) analytical system, was developed and tested successfully

2. Theory

Surface plasma resonance (SPR) is a physical phenomenon which occurs when a polarized light beam is projected through a prism onto a thin metal film (gold or silver). At a specific angle of the projected light, resonance coupling between light photons and surface plasmons of the gold can occur when their frequencies match. Because the resonance leads to an energy transfer, the reflected light shows a sharp intensity drop at the angle where SPR takes place. Resonance coupling of the plasmons generates an evanescent wave that extends 100 nm above and below the metal surface. As an analytical tool it is important that a

change in the refractive index within the environment of the evanescent wave causes a change of the resonant angle, when the sharp intensity drop can be observed. Binding of single target biomolecue to immobilize single molecule on top of the metal (gold) surface of the sensor leads to a change of refractive index and could be recorded as a change of intensity in the reflected light by a detector. This setup enables real-time measurement of biomolecular interactions, with refractive index changes proportional to mass changes.
Generally the Kretschmann configuration and resonance angle modulation are used in SPR. Kretschmann configuration (Kretschmann & Reather, 1968) is the most-common geometry setup of SPR platforms, in which the incident light comes from the high refractive index medium (prism) and reflects at the gold surface without travelling through the liquid. The resonance angle is defined according to the resonance peak of SPR, which is further defined based on the SPR curve, obtained by recording the change of light intensity of the reflective light along with the change of angle of the incident light. The resonance peak of SPR is at the lowest point of the SPR curve, where light absorption is the maximum and the light intensity of the reflective light is the minimum under a specific angle of the SPR curve.
SPR is a well established technique for observing biomolecular binding reactions. In a usual setup, light traveling through a high refractive index (RI) substrate reflects from the substrate surface, which is coated with a thin layer of gold (50 nm). Certain biomolecules have been immobilized on the gold surface, which bind the targeted biomolecules in aqueous samples. As targeted biomolecules bind to the gold surface, the surface RI increases roughly proportional to the quantity of the molecules immobilized. The change of the surface RI results in the shift of the resonance peak of SPR and detection of the shift of the resonance peak of SPR monitors the reaction between biomolecules quantitatively such as the concentration of targeted molecules. Since the shift of the resonance peak of SPR could also be brought by other disturbances (e.g. temperature changes), it is necessary to use control signals to distinguish the shifts caused by the reactions from the shifts by other interferential factors.

3. Experimental

3.1 Reagents and materials

Protein A (from *Staphylococcus aureus*), EDC, NHS, HEPES and ethanolamine were purchased from SIGMA company. Human Immunoglobulin G (IgG), rabbit IgG, goat anti human IgG, and goat anti rabbit IgG were purchased from Beijing Xinjingke Biotechnology Company.
Sterilized SARS-CoV (PUMC-01 strain, TCID50 is 10^6puf/ml) and monoclonal antibodies (11G9, 2F1, 13D10, 11H12) to this virus were supplied by the Institute of Laboratory Animal Science, CAMS & PUMC.
The others were purchased from Beijing Chemical Reagents Company.

3.2 Bare gold slide patterning

The patterns of bare gold slides with reaction areas and reference areas were designed in L-edit and transferred to a photolithograph mask of chromium. The fabrication was as follows. The glass slides were spin coated with positive photoresist (AZ 1500) and patterned by an MA4 optical stepper (Karlsuss, Germany). The exposed photoresist was developed and the glass slides were coated with 2 nm of chromium plus 50 nm of gold in a JGP560B3 type magnetron sputtering instrument (SDY Technology Development Co., LTD, Chinese

Academy of Sciences, China). After removing photoresist in acetone, the bare gold slides with patterned areas were finally obtained (Fig.1). Prior to each experiment, bare gold slides were washed in ethanol to remove fingerprints, oily residues and dust particles.

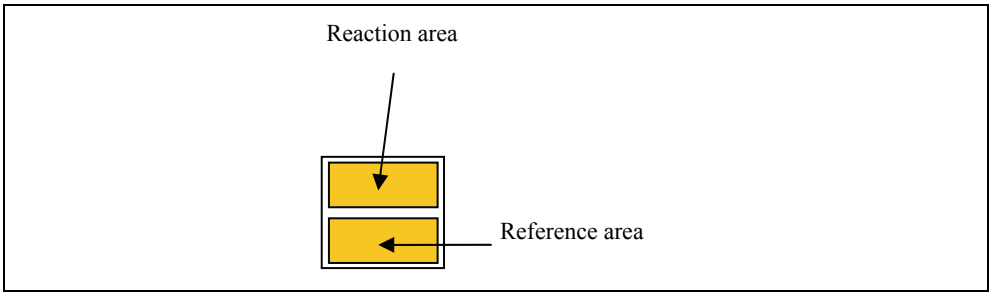

Fig. 1. Schematic of a SPR biochip with a reference area and a reaction area

3.3 SPR chip preparation

The sensor chips were prepared in the following procedure. Firstly bare gold slides were treated in piranha solution ((H_2O_2 35%): (H_2SO_4 96%) = 3:7) at 90°C for an hour. After the slides were washed by deionized water and ethanol, they were soaked in the 16-mercapto-hexadecan-1-ol solution (5×10^{-3}mol/L 16-mercapto-hexadecan-1-ol in 80% ethanol and 20% water) to obtain a hydrophilic surface. Then the slides were soaked in the solution including 0.4mol/L sodium hydroxide, diglyme and 0.6mol/L epichlorophdrin at 25°C for 4h. After the slides were thoroughly washed by deionized water, ethanol and deionized water sequentially, they were soaked in the dextran solution (3.0g dextran T500 in10ml 0.1mol/L NaOH) at 25°C for 20h. Finally, a bromoacetic acid solution was only dropped on the detection gold areas of the slides at 25°C for 16h. A thin layer of carboxymethyl dextran was formed only on the detection gold areas of the slides, while nothing was immobilized on the reference gold areas.

3.4 Protein immobilization online

After a SPR chip was mounted in the home-developed Reference SPR Analytical System, the angle scanning was conducted to choose a proper position for the fixing angle detection. HBS buffer (HEPES, 0.01mol/L; NaCl, 0.15mol/L; Tween 20, 0.05%, pH7.4) was firstly introduced to wash the chip. Then the mixed solution of EDC and NHS (final concentrations were 0.2mol/L and 0.05mol/L, respectively) was used to activate the SPR chip.

After activation, the chip was washed with HBS buffer. Then a protein solution (pH of the solution is less than PI of the protein) was introduced into the chip to react with the activated area for protein immobilization.

In order to eliminate the activated sites without immobilizing proteins, the chip was deactivated by flushing in Ethanolamine (1M) to remove molecules adsorbed loosely on the chip (Johnsson et al, 1991).

3.5 SPR instrument setup

As shown in Fig. 2, a Reference SPR Instrument System, with the function of qualitative and quantitative measurements, was manufactured by our group. The reaction area and the

control area of the system could be simultaneously detected in one flow channel by using this new Reference SPR Instrument System, resulting in recording two signals at one run in which one signal shows the curve of the reaction, and the other shows the curve of reference simultaneously. The range of the angle adjustment is 40°~70°, which makes it feasible for both the gas sample and liquid sample measurements. The detetion resolution of the resonance angle is 0.001°. And the detective range of refractive index is from 1.04 to 1.43 with a sensitivity better than 1×10^{-5}RIU.

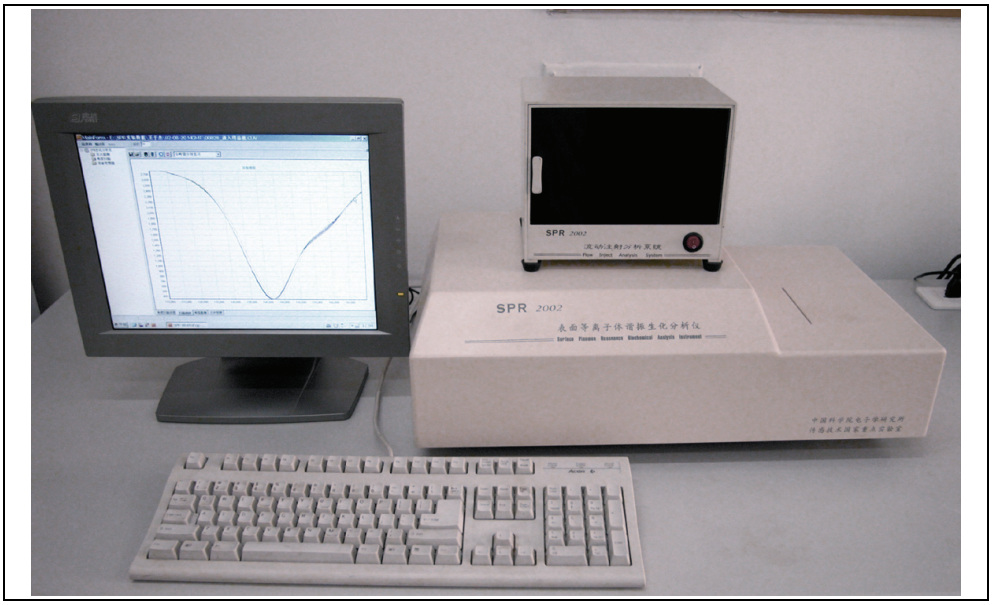

Fig. 2. Photograph of the home-developed Reference SPR Instrument System

4. Results and discussion

4.1 Design of home-developed reference SPR analytical system

As shown in Fig. 3, the reference SPR analytical system consists of a semiconductor laser (1), a system of a polarizing filter and lens (2), a prism (3), a high resolution detector (4), a computer (5), a sampling system (6), a SPR chip with reference (7) and a microfluidic devive with a microchannel (8). The laser and the optical system were installed on a circumrotated arm, while the high-resolution detector was installed on another circumrotated arm. The prism, the SPR chip and the microfluidic device were installed on an anti-floating surface between the two circumrotated arms. Both circumrotated arms were controlled by the stepper motor with the coding system. During experiments, a beam of the light from the semiconductor laser with the wavelength of 650nm through the optical system shined in the prism and reached the SPR chip. Then the beam of the light reflected into the detector. Finally, the intensity of the reflected light was recorded and exported to the computer. The sampling system controlled two peristaltic pumps and different solutions were introduced to the SPR chip by using the microfluidic device.

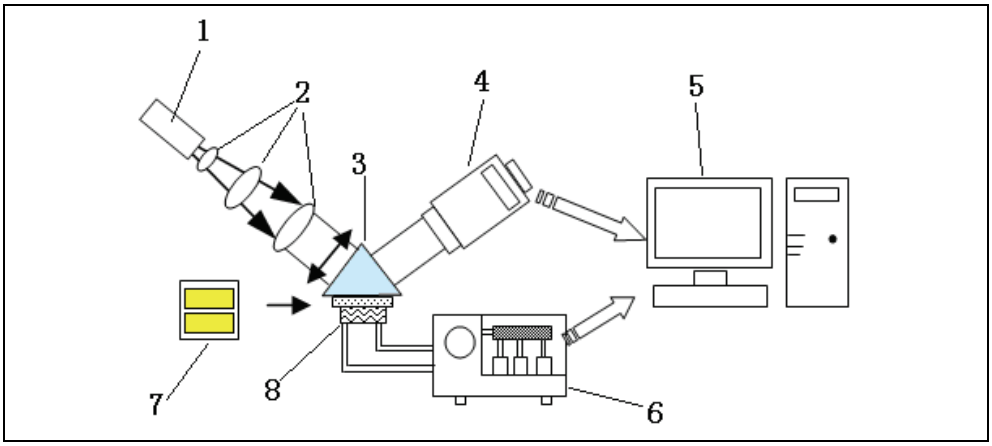

Fig. 3. Schematic of the home-developed Reference SPR Instrument System

4.2 Detection of SARS-CoV by immobilizing antibodies directly

In the type I design, the antibodies to SARS-CoV were immobilized directly on the experiment area after the chip was activated. The solution of the monoclonal antibodies to SARS-CoV (pH 4.6) was pumped into the microfluidic device for 2000s. Then ethanolamine (1M, pH 8.5) was pumped in to deactivate the chip for 10 min. Finally HBS buffer was pumped in to wash the SPR chip. The signal recording of the immobilization step is shown in Fig. 4. When introducing the monoclonal antibodies to SARS-CoV, the reaction line increased significantly and the light intensity of the reaction line after the deactivation was still higher than the intensity before the antibody immobilization. This light intensity increase of the reaction line with reference line unchanged demonstrated that the monoclonal antibodies to SARS-CoV were successfully immobilized on the reactive area.

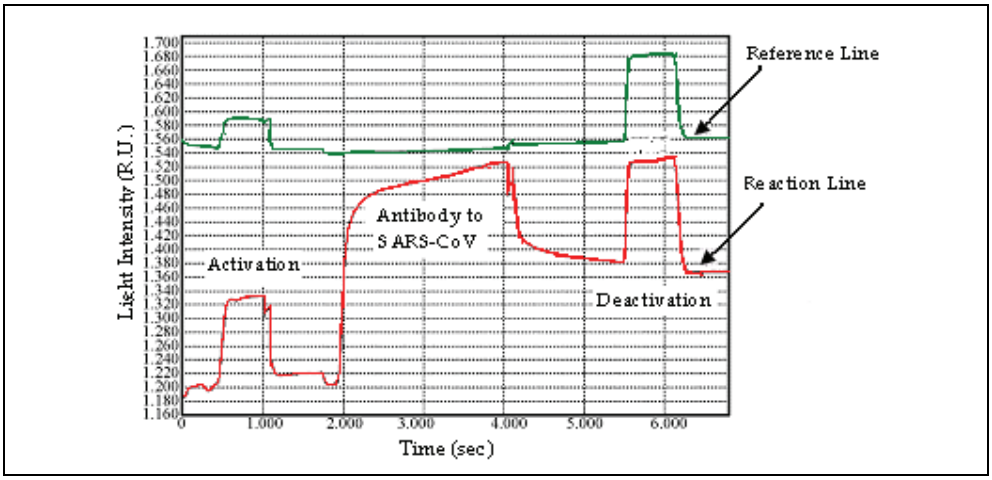

Fig. 4. Signal recording of immobilizing antibodies directly
The green line is a reference curve. The red line is a reaction curve.

After the antibodies were fixed on the SPR chip, sterilized SARS-CoV (1:5 diluted with acetic acid buffer, pH 4.4) was pumped into the microfluidic device and the reaction between the antibodies and SARS-CoV was recorded in Fig.5. However, from the Fig. 5, there was no obvious light intensity increase of the reaction line, which may be caused by spatial obstacles which keep antibodies from contacting SARS-CoV.

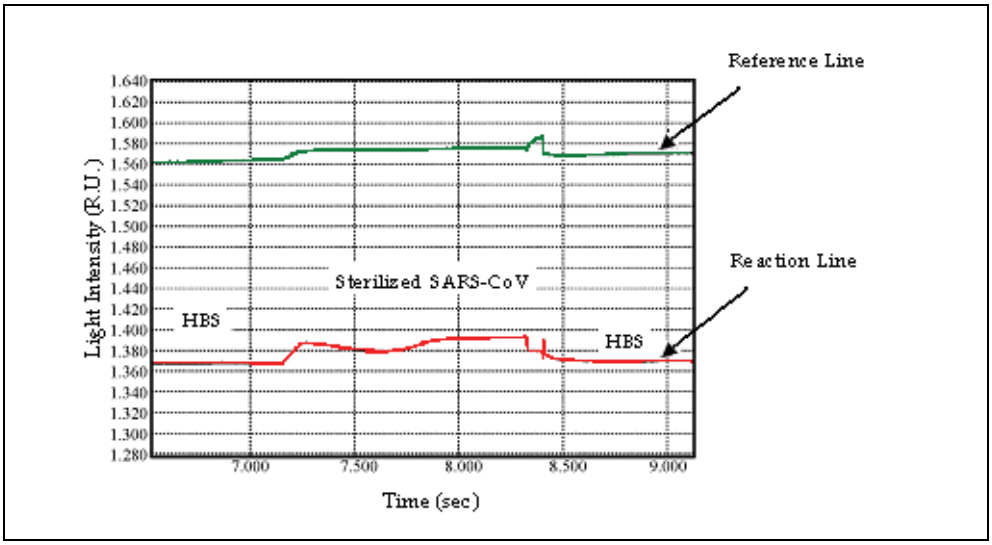

Fig. 5. Detection of sterilized SARS-CoV by immobilizing antibodies directly
The green line is a reference curve. The red line is a reaction curve.

4.3 Detection of SARS-CoV by using Protein A

In the type II design, 0.5mg/ml Protein A solution was pumped in after the activation step. The solution of the monoclonal antibodies to SARS-CoV (pH 4.6) was flushed in after the deactivation step, aiming to bind with immobilized protein A. Then the chip was washed with PBS buffer until the base-line signal was stable. After that, the same sterilized SARS-CoV solution (1:5 diluted with acetic acid buffer, pH 4.4) was pumped into the microfluidic device to react with immobilized antibody. The entire procedure was recorded, shown in Fig. 6, which demonstrates that the antibody to SARS-CoV was immobilized efficiently onto the reaction area of the SPR chip with the detection signal of SARS-Cov increasing to 60 units. It is 55 units higher than the reference signal with the binding rate about 1.4unit/min.
Protein A has pseudoimmune interaction with the Fc fragments of immunoglobulins (Cedergreen et al, 1993) that could extend the distance between the antibodies and the surface so that the free degree of the antibodies could be increased. At the same time Fab fragments which react with antigens could face the solution side due to Protein A. Protein A seems to be a useful agent for antibody immobilization by increasing the binding efficiencies between antigens and antibodies.
Reference area was used to detect absorption of impurity in analyte, in order to eliminate the disturbance of non-specific absorption. The sensitivity of SARS-CoV detection reached 1. 66 $\times 10^4$ PFU/mL.

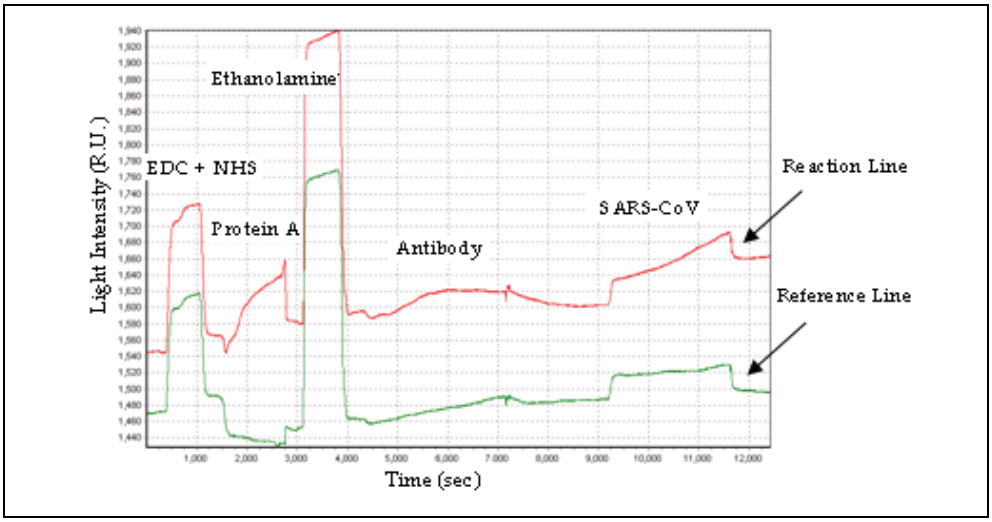

Fig. 6. Detection of sterilized SARS-CoV using Protein A
The green line is a reference curve. The red line is a reaction curve.

4.4 Detection of IgG by using an improved reference SPR system

This Reference SPR Analytical System used to detect SARS-CoV is an analytical instrument with one channel and two parameters in which only two analytes in one sample would be detected. The next generation of the reference SPR system: the high throughput, multi-analyte imaging SPR (HMI-SPR) analytical system, has been designed, fabricated and tested, shown in Fig. 7.

Fig. 7. Photograph of the high throughput, multi-analyte imaging SPR analytical system.

A 5-spots sensor chip was used as an example to briefly demonstrate the functions of HMI-SPR instrument. Firstly the 5-spots rare gold slides were modified by means of chemical methods. A thin layer of carboxymethyl dextran was immobilized on the gold spots of the slides to form a carboxyl-terminated surface. Then the mixed solution of EDC and NHS

(final concentrations are 0.2mol/L and 0.05mol/L) was used to activate the surface. 0.5μL solutions containing 1mg/mL rabbit IgG were dotted on the left two gold spots, while 0.5μL solutions containing 1mg/mL human IgG were dotted on the right two gold spots with the middle gold spot unmodified.

After the solutions were dotted on the gold areas, rabbit IgG and human IgG reacting with the dextran on the rare gold areas for 10min were fully immobilized on the chip. Then the sensor chip was deactivated by dipping in the ethanolamine solution of 1mol/L. During this process, the proteins which didn't bind to the sensor chip firmly were removed. After that, the sensor chip was put into the deionised water to wash away the remained salt solution. Finally, the modified sensor chip was mounted in the HMI-SPR system for different immunoassay tests.

The process of detection was conducted with the results of 5 real-time curves for 5-spots chip, shown in Fig. 8a. At first, HBS buffer was introduced for getting the base lines for 400s and then a solution containing 1.2mg/mL goat anti rabbit IgG was injected and stopped for reaction for 300s. Secondly, HBS buffer was introduced again for recovering the base lines for 400s and then a solution containing 0.5mg/mL goat anti human IgG was injected and stopped for reaction for 300s. Finally HBS buffer, HCl buffer and HBS buffer were introduced sequentially in which HCl buffer was used to bring the sensor chip back to the original setup. As shown in Fig. 8a, when goat anti rabbit IgG was injected, the immunoreaction occurred at rabbit IgG binding areas (curves 1 and 2). When goat anti human IgG was injected, the immunoreaction occurred at human IgG binding spots (curves 4 and 5). After HCl buffer was injected, all the gold areas of the sensor chip restored to base lines.

The linear calibration method of signal curves was performed to move base lines to zero and subtract the reference curve, shown in Fig. 8b.

Until now, we have designed, fabricated and tested 15-spot, 27-spot, 45-spot, 96-spot and 144-spot sensor chips.

5. Conclusion

In this chapter, a home-developed Reference SPR Analytical System has been demonstrated, in which the successful detection of the SARS-CoV antigens has been recorded by the measurement mode of fixed angle in which Protein A has been used to obtain a higher sensitivity. Then an improved reference SPR system, high throughput, multi-analyte imaging SPR (HMI-SPR) analytical system, was briefly illuminated by using a 5-spot sensor chip to detect two kinds of Immunoglobulin G. By using a reference area, the performance of the SPR system has been improved to avoid the refractivity inference of different solutions, different temperatures, and even to eliminate the disturbances due to non-specific absorptions. Therefore, the home-developed Reference SPR Analytical System is promising to implement clinic diagnosis by directly detecting the crude patients' samples without pretreatment procedures.

6. Acknowledgements

The authors greatly acknowledge the financial support from the National Science Foundation of China (Grant number No. 60427001 and 60701019), and National High Technology Research and Development Program of China (Grant No. 2006AA04Z355).

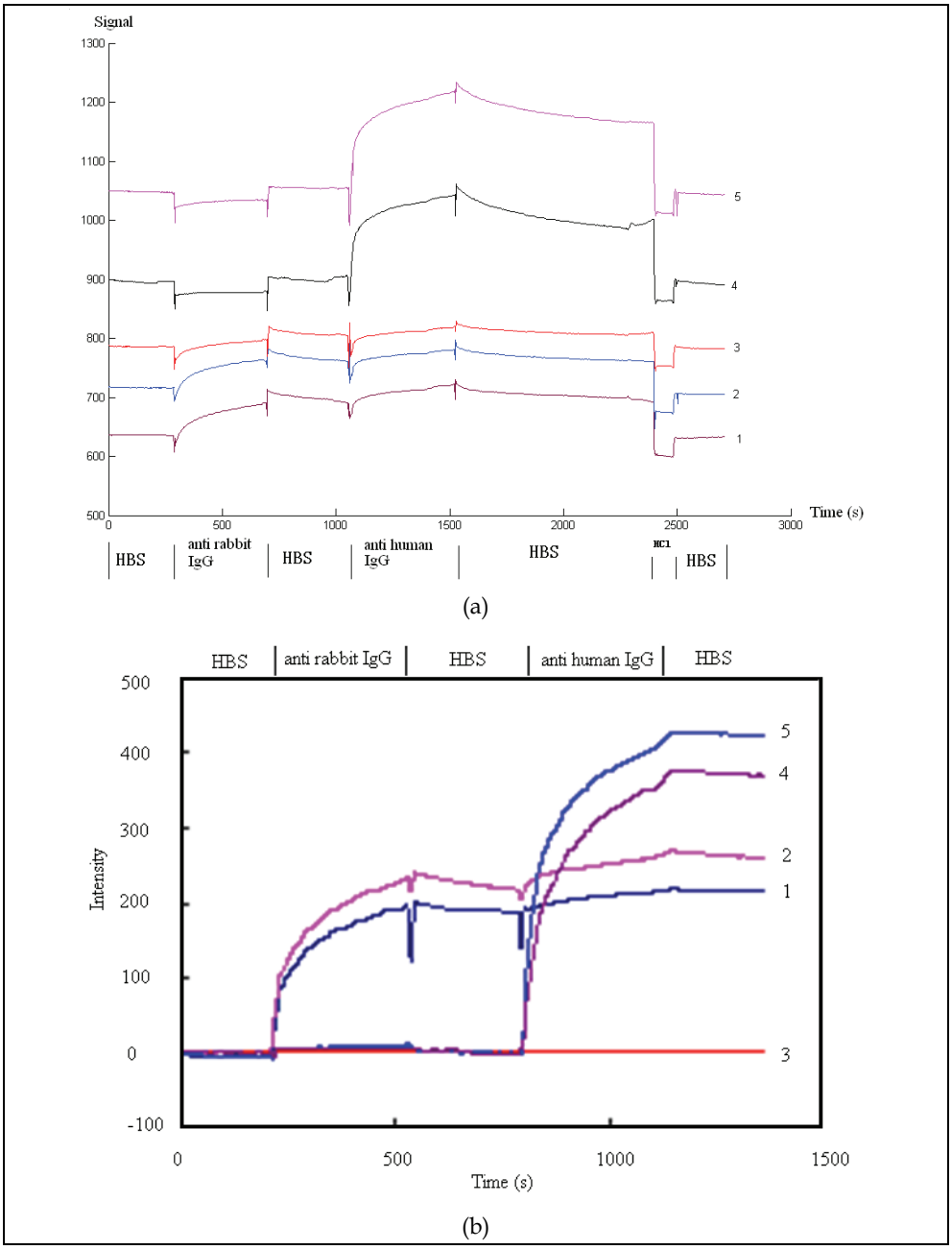

Fig. 8. SPR response curves for qualitative detections (a) before and (b) after data processed. Curves 1 and 2 for immobilization of rabbit IgG, Curves 4 and 5 for immobilization of human IgG, Curve 3 for reference.

7. References

Lee, H.J., Wark, A.W., Corn, R.M. (2006) Langmuir 22, 5241-5250.
Kanda, V., Kariuki, J.K., Harrison, D.J., McDermott, M.T. (2004) Anal. Chem. 76, 7257-7262.
Homola, J. (2003) Anal. Bioanal. Chem. 377, 528-539.
Rota, P.A., Oberste, M.S., Monroe, S.S., et al. (2003) Science, 300, 1394–9
Drosten, C., Gunther, S., Preiser, W., et al. (2003) N Engl J Med; 348, 1967–76
Kretschmann, E., Raether, H. (1968) Z. Naturforsch. A: Phys. Sci. 23A, 2135-2136
Johnsson, B., Löfås S., Lindquist G. (1991) Analytical Biochemistry, 198, 268-277
Cedergreen L., Anderson R., Jansson B., Uhlen M., Nilsson B. (1993) Protein Engineery engineering, 6, 441-448

11

Bacterial Bioluminescent Biosensor Characterisation for On-line Monitoring of Heavy Metals Pollutions in Waste Water Treatment Plant Effluents

Thomas Charrier, Marie José Durand, Mahmoud Affi, Sulivan Jouanneau, Hélène Gezekel and Gérald Thouand
University of Nantes, UMR CNRS 6144 GEPEA, CBAC Laboratory, Campus de la Courtaisière-IUT, Département Génie Biologique, 18 Bd Gaston Defferre, 85035 La Roche-sur-Yon cedex, France

1. Introduction

The detection of pollutants in the environment is becoming a health and economic issues. The sector of water realises more than 700.000 analyses per year with an average price of approximately 15 euros/analysis. In 2001, the European Community published in the official journal a list of priority substances to be detected within the water framework (Decision N° 2455/2001/EC). Heavy metals like cadmium, lead and mercury belong to this list. The current measurement techniques are not applicable to the on line analysis of these pollutants because they are too expensive and complex to be applied in the field.
Our laboratory develops since ten years alternative measurement methods of chemical pollutants in water and pathogenic bacteria in the food industry either as bioassay or biosensor.

2. Generalities about bioluminescence, heavy metals and biosensors

2.1 Bacterial bioluminescence

The mechanism of the bacterial bioluminescence is studied since 1944 (McElroy & Ballentine, 1944). Today eleven bioluminescent bacterial species classified in four genus are listed. Three genus are coming from marine origin: *Vibrio*, *Photobacterium* and *Alteromonas*. The fourth, more recently discovered is of terrestrial origin: *Photorhabdus* (ex *Xenorhabdus*) (Meighen & Szittner, 1992).
From the biological and ecological point of view, the interest of the bioluminescence is related to the symbiotic character of the bacteria. It was suggested that the metabolic function of the bacterial luciferase was connected to its capacity to the electrons transfer to oxygen rather than to its light output. Thus, it would be an alternative pathway for the electrons transport under low oxygen pressure like in fish organs (Hastings et al., 1985; Meighen, 1993) and the hosts would draw advantage from the light emitted by using it for communication or defence (Nealson & Hastings, 1979; Meighen, 1994; Visick et al., 2000).

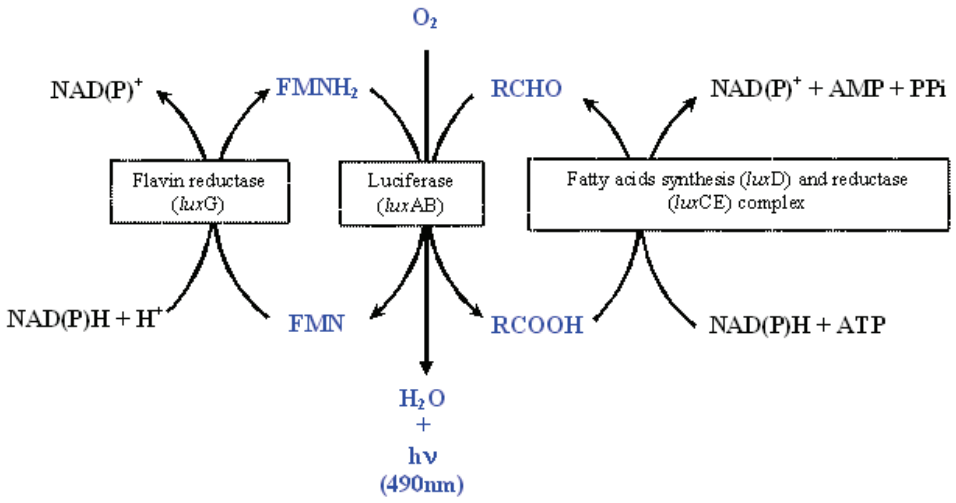

Fig. 1. Bioluminescence reaction (adapted from Sung & Lee, 2004 and Tu & Mager, 1995)

The reaction of bioluminescence is catalyzed by the luciferase enzyme coded by the *lux*AB genes (Figure 1) (Blum, 1997). Three key substrates modulate the light reaction: the dissolved oxygen provided by the surrounding environment, the reduced flavine mononucleotide coming from the bacterial metabolism and a long chain aldehyde such as decanal coded by the *lux*CDE genes (Meighen, 1991). When spectral emission from the whole bacteria was recorded from 400 to 750 nm with a highly sensitive spectrometer initially devoted to Raman scattering, two peaks were clearly identified, one at 491-500 nm (±5 nm) and a second peak at 585-595 (±5 nm) with the Raman CCD (Thouand et al., 2003).

2.2 Heavy metals and bacterial resistance

a. Heavy metals

Among metals it is necessary to separate metals and metalloids essential to the biological life (for example copper, zinc, iron, selenium…), from non essential metals such as for example cadmium, mercury. However all metals according to their concentration have a toxicity with respect to living organisms.

Heavy metals are naturally present both in the environment and in water at trace levels (5ng. L^{-1} Cd in water, INERIS, France), but the anthropogenic activity increases metals concentration found in the natural environments (Audry et al., 2004). Because of their great solubility in water heavy metals are easily absorbed by the living organisms and are found accumulated in human at the end of the food chain (Kurniawan et al., 2006). In fact the industrial wastes are mainly responsible for the current pollution of the rivers by heavy metals that are normally collected and treated by waste water treatment plants (WWTP). However, Karvelas et al, 2003, pointed out that even a fraction is adsorbed in the activated sludges, between 37 to 77% (depending to the metal) are rejected into the river. The WWTP can thus be a considerable source of pollution in spite of the existing standards of rejections and the treatments carried out.

b. Bacterial heavy metals resistance mechanisms

Basically, heavy metals action in the bacterial cytoplasm leads to important oxydative stresses (Nies, 1999). The minimal inhibition concentrations of heavy metals/metal for *Escherichia coli* are reported in table 1.

MIC (mM)	Heavy metals
0.01	Hg^{2+}
0.02	Ag^{2+}, Au^{3+}
0.2	CrO_4^{2-}, Pd^{2+}
0.5	Pt^{4+}, Cd^{2+}
1.0	Co^{2+}, Ni^{2+}, Cu^{2+}, Zn^{2+}
2.0	Tl^{+}, UO_2^{2-}, La^{3+}, Y^{3+}, Sc^{3+}, Ru^{3+}, Al^{3+}
5.0	Pb^{2+}, Ir^{3+}, Os^{3+}, Sb^{3+}, Sn^{2+}, In^{3+}, Rh^{2+}, Ga^{3+}, Cr^{3+}, V^{3+}, Ti^{3+}, Be^{2+}
10.0	Cr^{2+}
20.0	Mn^{2+}

Table 1. Minimal inhibition concentrations (MIC) of heavy metals to *Escherichia coli* (Nies, 1999)

The entry of heavy metals into the bacterial cell is done by the regulation systems of the divalent cations or oxyanions. Indeed, heavy metals are not distinguishable for these transmembrane proteins, from the other divalent cations or oxyanions (for example: SO_4^{2-}, HPO_4^{2-}, Fe^{2+}, Mg^{2+}, Mn^{2+}, etc…). Bacteria have developed two kinds of resistance mechanisms to cure this passive entry. The first of them is fast, non specific and is based on the gradient of concentration or on proto-motive force. The second mechanism is more specific, inducible and is activated in the presence of a metal and generally requires ATP hydrolysis.

This second inducible mechanism of resistance is subdivided in three types.

- The first of them is a more or less specific system of cation/oxyanion efflux by ATPases pumps (ATPase CPx-type).
- The second system is based on the complexation capacity of some divalent heavy metals with the -SH group of the gluthation or the metallothionines for cyanobacteria (Cavet et al., 2002).

Lastly, the third mechanism, more specific for oxyanions, allows a reduction of them in a less toxic form. These reduced forms are then evacuated from the cytoplasm with a specific ATPases pumps (Nies, 1995; Nies, 1999; Nies, 2003).

The bacterial mechanisms of regulation and resistance to heavy metals are summarised in figure 2. The efflux systems using ATPases pumps are preferred in the bacteria because their energy cost per cell is lower than the complexation of metals by the glutathion or the metallothioneins. Indeed one ATP molecule is enough to evacuate a divalent metal with an ATPase pump belonging to the family of the ATPases CPx-type, whereas 16 ATP are necessary to complex only one divalent metal (Nies, 1999).

It is important to note that the mechanisms of inducible resistances, known to be specific, are thus not activated by only one metal even if their name seems to make it believe (Nies, 2003). In the same way, only one metal can activate several systems of resistance (Moore et al., 2005; Wang & Crowley, 2005).

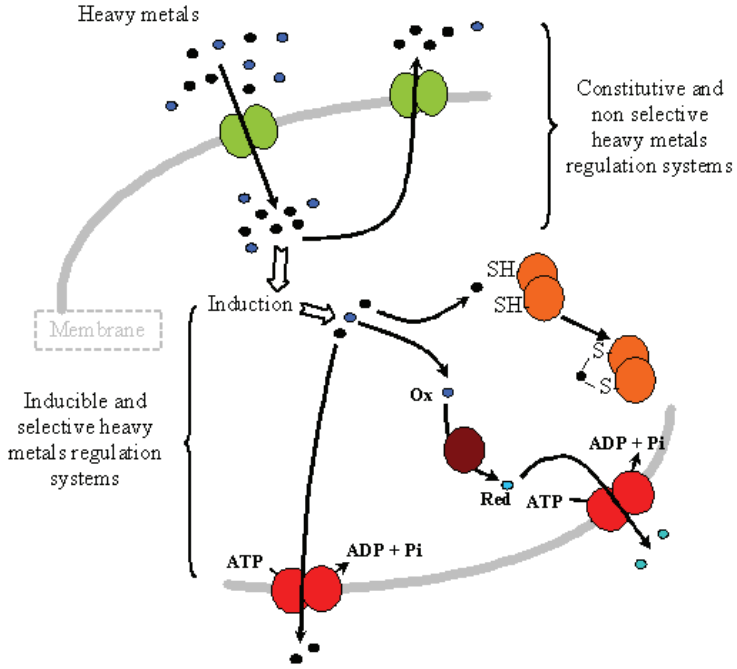

Fig. 2. Main heavy metals regulation and resistance mechanisms in bacteria.

c. Molecular basis of the ZntA/ZntR system of Escherichia coli

The action of the MerR regulators consists first of all to the repression of the target promoter in the absence of the metal. This inactivation is due to a distortion of the DNA double helix on the RNA polymerase fixation site. The regulator, having fixed the metal pollutant, changes its conformation allowing the RNA polymerase to fix to the promoter. The regulation of the *pzntA* promoter, by the ZntR protein is an example of the mechanisms of regulation of the MerR type (Brocklehurst et al., 1999; Outten et al., 1999; Binet & Poole, 2000) (Figure 3).

The regulators of the MerR type are activators/repressors. This family of proteins has at its N-terminal part a site for DNA fixation and the ligands are fixed to the C-terminal.

2.3 Detection of heavy metals with bioluminescent bacteria: choice of a heavy metal-bacterial resistance mechanism.

The inducible bioluminecent bacteria are used to detect specifically a pollutant or a family of pollutants or even the toxic effects. The action of the pollutants on the cells induces in this case the synthesis of the genes of bioluminescence and thus the emission of light. Thus, the choice of an inducible resistance system to build a sensitive strain is foremost justified by its sensitivity to metals *in vivo*. The sensitivity depends on the origin of the genetic system and the host strain.

To obtain an interesting sensitivity, the resistance systems coming from less resistant bacteria such as *Escherichia coli* should be preferred. Indeed, the strain *Ralstonia metallidurans* CH34 (Mergeay et al., 2003) which harbors a great number of resistance systems from the

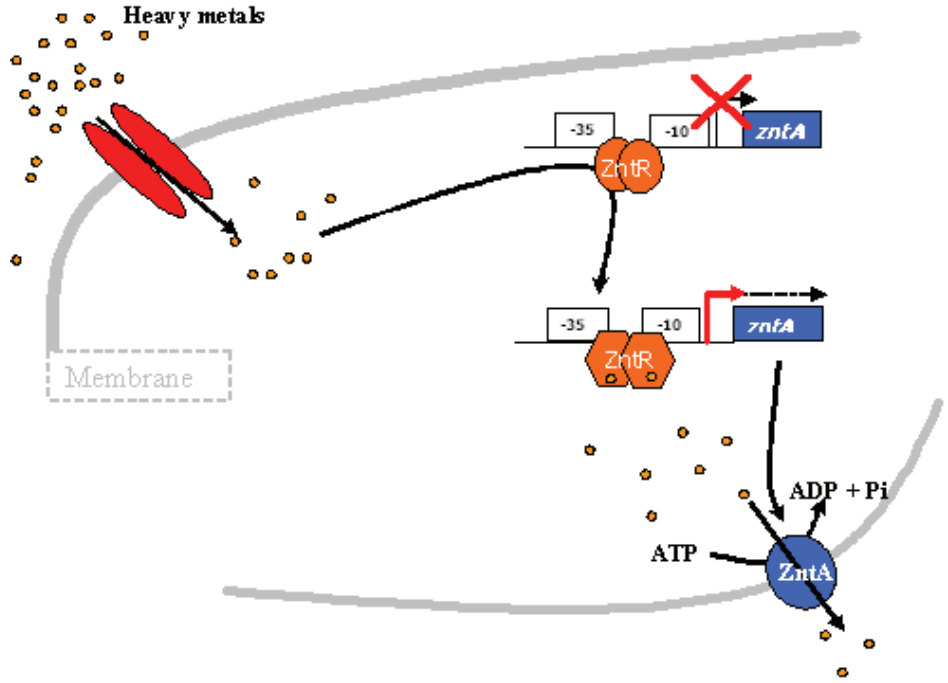

Fig. 3. Regulation of the *pzntA* promoter by the ZntR protein

pMOL28 and pMOL30 plasmids was the object of an insertion of the transposon Tn4431 containing the *lux*AB genes (Corbisier et al., 1993; Tauriainen et al., 1998). The detection limit of the strain obtained was 1mM of Pb^{2+} against 30nM of Pb^{2+} for mechanisms resulting from the less resistant bacteria such as *Escherichia coli* and *Staphylococcus aureus*.

Table 2 reports the detection limits of three bioluminescent strains for heavy metals detection using various mechanisms of resistance from *Escherichia coli*: ZntA/ZntR, CopA/CueR and the *ars* operon. The three plasmidic constructions based on these resistance systems make it possible to detect a range of eleven heavy metals with detection limits sometimes lower than the standards for water. However, it should be noted that the ranges of detection of the CopA/CueR system and the *ars* operon are not studied completely in comparison with the ZntA/ZntR system. Indeed, the *ars* operon is also activated by bismuth (Bi) and antimony (Sb) and the CopA/CueR system is also activated by gold (Au) (Wu & Rosen, 1993).

Various developments are proposed or were proposed on the market such as: the BIOMET® kit developed from transcriptional fusions between the *luxCDABE* operon and various resistance systems to heavy metals of the *Ralstonia metallidurans* strain (Vito, Belgium, http://www.vito.be/). One other kit using the inducible bioluminescent strains for arsenic or mercury (Biologically Heavy metal Assay kit) is distributed by Aboatox company following the works of Tauriainen et al. (1997, 1998).

The team of S.Daunert (Lexinton, Irvine, the USA) developed an original microfluidic and analysis system integrated in a compact disc allowing arsenic detection with the arsenic-sensitive *E.coli* pSD10 (*parsR:: arsR:: gfpuv*) (Rothert et al., 2005). Ivask et al. (2009) proposed

a set of 13 inducibles strains (Gram - and Gram +) covering a broad range of sensitivity. Lastly, Hakkila et al. (2004) described a bioassay with 8 inducible bioluminescent strains to heavy metals encapsulated to disposable fiber optics.

Metals tested	***E.coli* heavy metals resistance mechanisms**			**European standards for water***
	ZntA/ZntR	**CopA/CueR**	***Ars* operon**	
	DL *E.coli* MG1655 pzntlux (Riether et al., 2001)	DL *E.coli* MG1655 pcoplux (Riether, Dollard et al., 2001)	DL *E.coli* pJAMA-arsR (Stocker et al., 2003)	
Cd	0.010µM	/	/	0.045µM
Hg	0.3µM	/	/	0.005µM
Pb	0.03µM	/	/	0.005µM
Sb	10µM	/	/	/
As(V)	/	/	0.4µM	0.135µM
A(III)	/	/	0.2µM	0.135µM
Zn	1µM	/	/	nc
Ni	10µM	/	/	0.34µM
Co	10µM	/	/	nc
Cr(VI)	30µM	/	/	1µM
Cr(III)	30µM	/	/	1µM
Ag	/	0.3µM	/	/
Cu	/	3µM	/	30µM

Table 2. Detection Limits (DL) of the genetic constructions based on heavy metals resistance mechanisms of *E.coli*. *: Values obtained from INERIS (Institut National de l'Environnement Industriel et des Risques); /: unavailable data; nc: metal not concerned by a standard.

2.4 Bioluminescent bacterial biosensors

A biosensor is an integrated and autonomous device able to provide a quantitative or semi-quantitative analytical information by using a biological element of recognition (the bioelement) retained to transducer (Figure 4) (Thévenot, 2001). The biosensors are distinguished from bioassay that are disposable kits. The microbial biosensors can be classified according to whether the bioelement is in liquid phase or immobilised phase.

The liquid phase biosensors remains on the principle of reactor cultures in batch or continuous modes.

In the reactors culture, sets of probes ensure the traditional control of the temperature, oxygenation and the pH. In many systems, measurements of bioluminescence and sometimes optical density are done in a second reactor for the pollutant measurement. Thus, if the sample injected is toxic, the bacteria in culture are not affected and the analyses can continue (Gu et al., 1999; Gu et al., 2002). Only one apparatus allows the simultaneous measurement of the bioluminescence and optical density in the same reactor (Thouand et al., 2003; Horry et al., 2004; Picart, 2004).

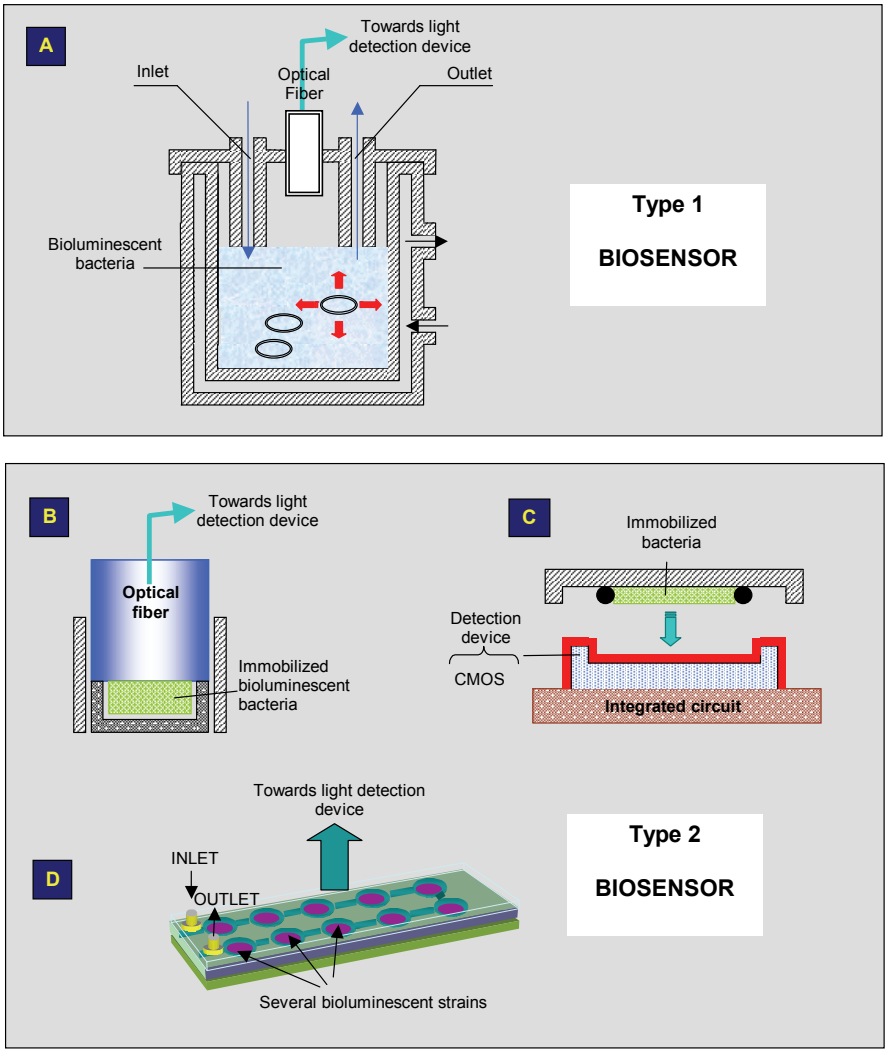

Fig. 4. Figures showing the two kinds of biosensors (type 1 and 2). CMOS = complementary metal oxyde semiconductor

These biosensors often can use only one bioelement at the same time that limits the number of analyses, excepted a multi-reactors platform developed by (Lee & Gu, 2005). Another drawback of these systems is the dilution of the analysed sample after injection into the culture volume inside the reactor.

Contrary to the biosensors in liquid phase, the biosensors in immobilised phase allow a direct contact between the micro-organisms, the transducer but also with the sample. The photomultipliers, associated with a beam of fiberoptics are mainly used as physical transducer (Polyak et al., 2001; Horry et al., 2006) but also the CCD camera (Charrier, Thesis, 2006) or the CMOS (Complementary Metal Oxide Semi-conductor (Simpson et al., 1998).

Few bioluminescent bacterial biosensors multichannel match with the strict definition provided by the IUPAC were developed excepted for example Charrier (Thesis, 2006) and the systems approaching the biosensor but of single use, therefore being able to be regarded as bioassay (Kamidate et al., 2001; Philp et al., 2003; Tani et al., 2004; Lee & Gu, 2005; Maehana et al., 2006; Rabner et al., 2006).

3. Experimental procedures

3.1 Molecular biology

V.fischeri luxCDABE operon was amplified from plasmid pRL1114 (*luxCDABE V.fischeri,* Kn^R) (Fernandez-Pinas & Wolk, 1994) with Dynazime polymerase (Finzyme) and the following selected primers: 5′ACG TGA ATT CAT GAA TAA ATG TAT TCC AAT GA3′, 5′ACG TCT GCA GTT AAT CCT TTA TAT TCT TTT GTA TG3′. The PCR fragment was purified (QIAquick), digested by NruI and EcoRI restriction enzyme (NEB) and introduced (T4 DNA ligase, NEB) in pBtac2 (Roche) vector under the control of the p*tac* promoter to obtain the plasmid pBfiluxCDABE. This plasmid transformed in *E.coli* DH1 allowed a constitutive expression of bioluminescence.

The p*znt*A promoter was amplified on a boiled preparation of *E.coli* DH1 by PCR using Deep Vent polymerase (NEB) and the following primers : 5′CAC TTC CTG ATC GTC CGC TCG CTG CT 3′, 5′AGC ATG AAT TCG GCA TCC TCC GGT TAA GTT T3′. Plasmid pBfiluxCDABE was digested by NruI and EcoRI, purified and cloned into the linearized vector to obtain plasmid pBzntlux (Ap^R, p*znt*A :: *luxCDABE*).

3.2 Bacterial strains and media

E.coli DH1 strain (C.I.P. 104745, [F-, *rec*A1, *end*A1, *gyr*A96, *thi*-1, *hsd*R17, *sup*E44 *rel*A1]) was used for all the experimentations of this study.

LB medium supplemented with ampicillin (100µg.mL^{-1}, Sigma) or kanamicyn (20µg.mL^{-1}, Sigma) was used for molecular biology. Solid LB was supplemented with 15g.L^{-1} of bacteriologic agar (Biokar Diagnostics).

An acetate medium with a C/N/P ratio of 100/10/1 was used for the growth of *E.coli* DH1 pBzntlux for biosensor applications. 1L of tap water was filtered through a 0.45 µm filter (Sartorius) and supplemented with 2.835g acetate (panreac), 1.1919 g NH_4Cl (Merck), 0.028 g K_2HPO_4 (Merck), 5 g NaCl, 0.5 g yeast extract (Merck) and 0.1 g tryptone (Biokar Diagnotics). The pH was adjusted to 7 and the medium was sterilized by autoclaving at 100°C for 30 min. For biosensors application, the feeding media was acetate medium diluted ten times (1/10X) supplemented with ampicillin (final concentration 50µg.mL^{-1}), in order to limit cell division in agarose matrix.

Batch cultures were prepared at 30°C and shaken at 250rpm in 100ml Erlen flasks. Bacterial growth was monitored using a spectrophotometer (Unicam) and optical density measurement was reached at 620nm (OD_{620nm}).

3.3 Cell immobilization procedure

Agarose hydrogel matrix was used for cells immobilization in the biosensor chip according to previous published results (Pernetti, 2003; Horry et al., 2006).

In a first step, *E.coli* DH1 pBzntlux was cultivated 14 hours in acetate medium at 30°C. The next morning, OD_{620nm} of the culture was measured and cells were diluted with fresh

medium to OD_{620nm}=0.2. At the same time a 4% agarose solution was prepared by dissolving at 90°C, 0,4g agarose LGT (Agarose Type VII-A Low Gelling Temperature of 26°C; Sigma, reference A0701) in 10mL of acetate medium on a warming magnetic stirrer. 5mL of this solution was preserved at 37°C in a water bath with a constant agitation. Then 5ml of bacterial solution diluted to OD_{620nm}=0,2 then added to the 5mL 4% agarose solution preserved at 37°C. After homogenisation, the final solution obtained was at an OD_{620nm}=0.1 for a final agarose concentration of 2%. In a final step, this solution was pulled in the Lumisens2 biosensor chip (Horry et al., 2006). Agarose immobilized cells were used immediately in Lumisens2 biosensor for samples analysis without any conservation time.

3.4 Chemicals

Metals used were: $CdCl_2$ (Panreac), $HgCl_2$ (Prolabo France), $PbCH_3CH_2O$ (Panreac), $SnCl_2$ (Merck), $ZnCl_2$ (Merck), $NiSO_4$ (Labosi), $CoCl_2$ (Labosi), $K_2Cr_2O_7$ (Labosi), $CrCl_3$ (Acros), $AgNO_3$ (Prolabo France), $CuSO_4$ (Labosi), $FeSO_4$ (Labosi), $MnCl_2$ (Panreac) and As_2O_3 (Sigma). The purity of the metals was greater than 95%. Metal stock solutions were prepared at a high concentration (1M or 0.5M) in acidified distilled water (pH≈5-6) and conserved at +4°C in brown bottles. Working dilutions of metals were made daily in distilled water acidified to pH≈5-6.

3.5 Bioassay

Measurements of bioluminescence were made at controlled temperatures (30°C or 37°C) using a microtiter plate luminometer (Microlumate L96V, EGG Berthold). Heavy metal detection with *E.coli* DH1 pBzntlux, after an overnight culture at 30°C, bacteria were diluted to an OD_{620nm}=0.05 in fresh media. One hundred microliters of the dilution were added to a 96-well microtiter plate. Bacterial bioluminescence was induced after the addition of 25µL of a 5X metal solution.

3.6 Environmental samples treatment and analysis

Environmental water samples were all coming from the city waste water treatment plant of La Roche sur Yon (Moulin Grimaud, capacity of 83000 population equivalent). The samplings were carried out at the exit of the station, before the effluent rejection in the Yon river.

In laboratory, samples were first filtered on 0.45µM membrane (Pall Corporation) and preserved at 4°C during one or two days. Filtration was necessary to withdraw the largest particles which would clog the fluidic biosensors system.

Before their injection in the biosensor, samples were all supplemented with acetate media at 1/10X final concentration and, for cadmium detection control, with 0.5µM of $CdCl_2$.

DOC (Dissolved Organic Carbon) was measured in environmental samples with a TOCmeter : (COT-5000A Shimadzu). Total sulphate was measured with Hach Lange kit Sulfaver and total phosphate with the Briggs method.

3.7 Description and operation of Lumisens2 biosensor

Lumisens 2 (Horry et al, 2006) features three distinct parts: the fluidic layout, the disposable card and the optoelectronic equipment (Figure 5). The latter is composed of the power supply, the temperature regulation and the bioluminescence measurement device. The temperature, measured with a J thermocouple (TC Online), is regulated via a threshold

value given by the controller (Chauvin-Arnoult), connected to a heater (Radiospares), inserted close to the disposable card. The bioluminescence is monitored with a photon-counting photomultiplier (Hammamatsu) connected to the disposable card with a fiber optic (Oriel). The light measurements are automatically recorded with a dedicated LabView® interface throughout all of the experiments.

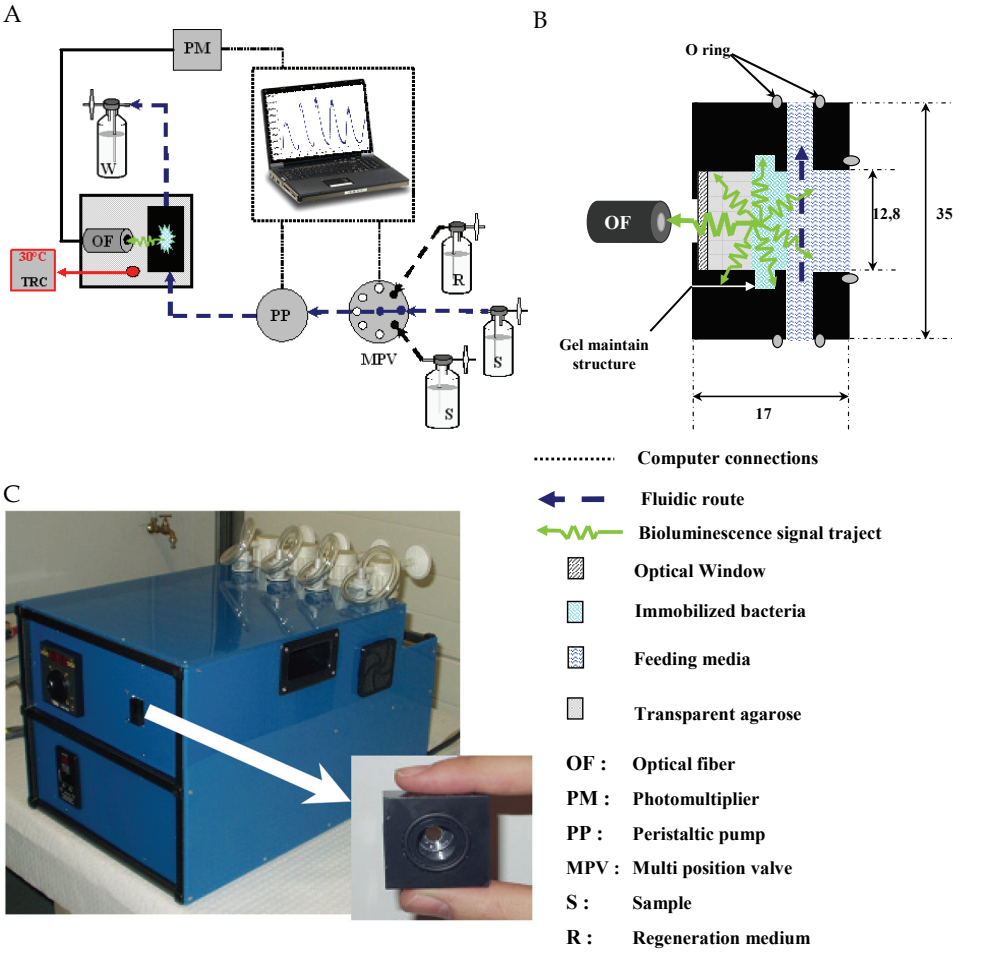

Fig. 5. Diagrams of Lumisens2 biosensor (A), its measurement chip (B) and Photo (C) modified according to Horry et al. (2006). (dimensions are in millimetres)

The bacteria are immobilized in a 35 x 35 x 17 mm disposable parallelepipedic card designed in Ertacetal® plastic. The card is bored through the center to let the fluids come in contact with the bacteria. A 13 mm diameter enclosure has been placed at the depth in which the bacteria are immobilized and includes a measuring chamber of 1.32 cm^3. An optical window (Edmund Optics) is hermetically stuck to the bottom of the measuring chamber on which the membrane of the bacteria is coated and maintained because of a 1 mm groove.

Inserted into its fixed pad, the disposable card closes the hydraulic layout, and the immobilized bacteria are in contact with the fluid diffusing into the immobilization agarose matrix.
Three independent samples are linked to a remote controlled 10 channel multiposition valve (Valco AG) that allows their specific selection. Each channel can be periodically selected throughout the experiments with a Windows® Hyperterminal® protocol, allowing the design of sequences of liquid exposures. The liquids are drawn out of the disposable card with a peristaltic pump (Meredos, Germany) located between two anti-return valves to avoid the reflux of the liquids into the card.
Measurement cycles were programmed with a soft specially dedicated to Lumisens2. Experimentations were all realised with a flow rate of 5mL.min^{-1}. Induction medium was first injected in the biosensor during 100 minutes to induce bioluminescence. Then the biosensor switched automatically to the regeneration medium during 140 minutes to let the bioluminescence signal back to ground. Bioluminescence was measured each six seconds during all the experimentation and results were directly shown on the computer screen.
Constant oxygenation of the feeding medium was realised by a continuous bubbling of sterile filtered air (0.22µM filters, Sartorius) among the measurement cell.

4. Results

The aim of this study was to demonstrate the applicability of a bioluminescent bacteria for the on line cadmium detection in waste water treatment plant. The strain *E.coli* DH1 pBzntlux was immobilized in an agarose matrix and then used in the Lumisens 2 biosensor once described by Horry et al. (2006) for TBT detection. In our present study, every parameters describing the biosensor were carefully calculated before to applied the biosensor to environmental samples.

4.1 Specificity and detection limits of *E.coli* DH1 pBzntlux

The range of detected metals and their associated detection limits are listed in Table 3. Of the fourteen heavy metals used, eight were detected by *E.coli* DH1 pBzntlux. Detection limits for cadmium and mercury were under or equivalent to the recommended E.U. standards for water. Other heavy metals like lead, zinc, tin, cobalt, nickel and chromium (VI) were detected at levels above their E.U. limits. Chromium(III), silver, copper, iron, manganese and arsenic were not detected by *E.coli* DH1 pBzntlux. *E.coli* DH1 pBzntlux detects a large number of heavy metals and as a consequence it cannot be used as a specific sensor, rather it should still be considered as a general warning system for heavy metal water pollution.

4.2 Flow rate effect on the bioluminescence measurement

A first study was undertaken in order to evaluate the effect of various flow rates on the bacterial bioluminescence rate (Figure 6). The light production rates were comparable whatever the flow tested according to a statistical analysis (Test of Levene, α =0,01).
The fluids circulation rates inside the Lumisens2 biosensor thus do not influence significantly the detection efficiency by the immobilized bacteria in the range of the flows tested. However one can note a lower variability for 5mL.min^{-1}, that was selected in all our following experiments.

Metal tested	Specificity	Detection Limit	EU Pollution Standards*
$CdCl_2$	+	0.005µM	0.045µM
$HgCl_2$	+	0.005µM	0.005µM
$PbCH_3CH_2O$	+	5µM	0.005µM
$SnCl_2$	+	5µM	?
$ZnCl_2$	+	5µM	NC
$NiSO_4$	+	50µM	0.34µM
$CoCl_2$	+	50µM	NC
$K_2Cr_2O_7$	+	50µM	1µM
$CrCl_3$	-	-	1µM
AgNo3	-	-	?
$CuSO_4$	-	-	30µM
$FeSO_4$	-	-	NC
$MnCl_2$	-	-	?
As_2O_3	-	-	0.135µM

Table 3. Specificity and detection limits of *E.coli* DH1 pBzntlux in bioassay.
+ = Heavy metal detected, - = Heavy metal not detected, NC = Not concerned by legislation
* Obtained from INERIS (Institut National de l'Environnement Industriel et des Risques)

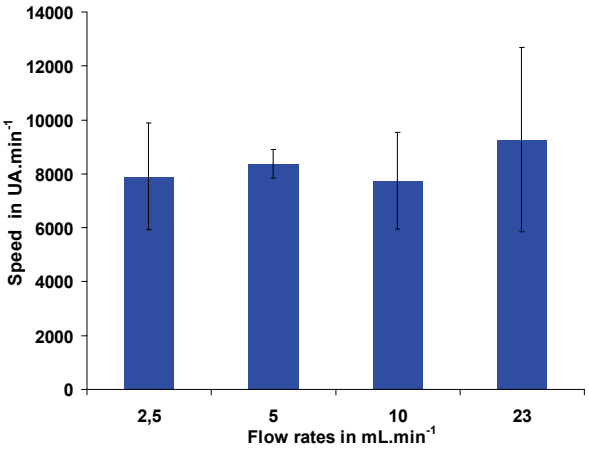

Fig. 6. Variation speed of the luminous intensity of *E.coli* DH1 pBzntlux according to the flow rate. (N=3 for each tested flow rate).
Experimental conditions: *E.coli* DH1 pBzntlux was immobilized in agarose 2% (OD_{620nm}≈0,1). Tested flow rates were 2.5mL.min^{-1}, 5 mL.min^{-1}, 10 mL.min^{-1} and 23 mL.min^{-1} at 30°C with acetate medium 1/10X supplemented with ampicilline (50µg.mL^{-1}) and 0.5µM $CdCl_2$

4.3 Reproducibility of the measurement

The phases of induction and regeneration have a low signal variability (lower than 10%). The maximum of variation (17.1%) of the signal is observed at the peak of bioluminescence (Figure 7).

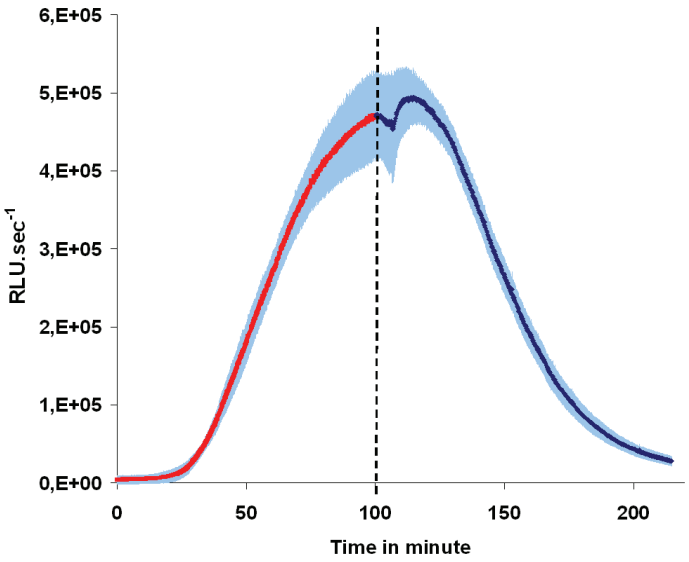

Fig. 7. Reproductibility of cadmium measurement by Lumisens 2 biosensor using *E.coli* DH1 pBzntlux. Results are the average of 5 independent experiments.
Experimental conditions : *E.coli* DH1 pBzntlux was immobilized in agarose 2% (OD_{620nm}≈0,1). Used flow rate was 5mL.min-1. Induction medium (–) containing acetate medium 1/10X supplemented with 50µg.mL^{-1} ampicilline and 0.5 µM $CdCl_2$ was first injected during 100 minutes. Then regeneration medium (–) containing acetate medium 1/10X supplemented with 50µg.mL^{-1} ampicilline was injected. Skye blue bands represent standard deviation (–).

One can note a significant reproducible light decrease signal with the switch from induction to regeneration medium linked to a variation of oxygen in the bottle. The total time of the measurement cycle is 220 minutes, including 100 minutes of induction with the medium of test and then 120 minutes of regeneration. It should be noted that the time of arrival to the peak of bioluminescence is lengthened compared to the bioassay (45 minutes in liquid phase against 60 minutes in immobilized phase)

4.4 Repeatability of the measurement

In an application point of view, it is necessary to know the repeatability of the measurement for one single agarose membrane. The cycle of measurement 100 minutes of induction then 120 minutes of regeneration was thus repeated on the same membrane until extinction of the bioluminescence signal (Figure 8).
The intensity of the detection peaks decreased in an important way during time. However, 5 analyzes producing a significant peak of bioluminescence were monitored in less than 20 H. This signal decrease affecting the repeatability could be attributed to:

- parameters related to the environment of the bacteria:
  - Toxicity of cadmium by accumulation in the membrane
  - Availability of oxygen in the measuring chamber

- parameters related to the bacteria:
  - Growth of the bacteria in the membrane
  - Lack of aldehyde for the bioluminescence reaction
  - Adaptation of the microorganisms to cadmium

These parameters were successively studied during various experiments in order to quantify their role in the signal.

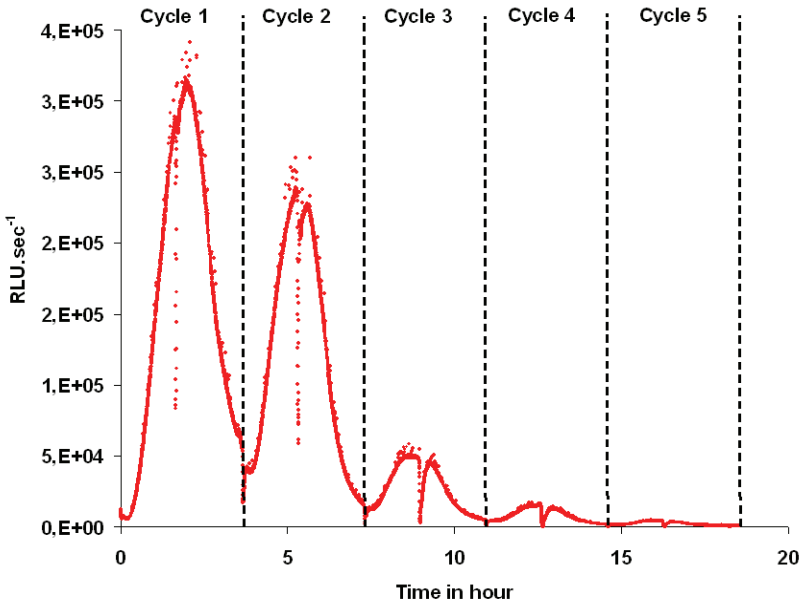

Fig. 8. Cadmium measurement repeatability. Experimental conditions were as described in Fig 7.

4.5 Influence of several parameters on the repeatability

a. Cadmium concentration monitoring inside the membrane

The accumulation of cadmium inside the membrane could cause an increasing toxicity for the bacteria. The cadmium concentration was measured by ICP-MS (Inductively Coupled Plasma - Mass Spectrometry) at different time in the membrane (without bacterium) having undergoes several cycle- metal addition/washing (Figure 9).

The agarose membrane contains an initial quantity of residual cadmium (51.6 nM), ten times higher than the detection limit of *E.coli* DH1 pBzntlux (5nM). This can partly explain the flush of bioluminescence at the beginning of the metal addition.

As expected, the assay medium contains a cadmium concentration close to 500 nM (470 nM) that was never reached inside the membrane (305.1 nM and 356.7nM instead of 470 nM). Moreover, after regenerations, the metal concentration does not go down to the initial Cd concentration (51.6nM) but remains at concentrations from 83 nM to149 nM (Figure 9).

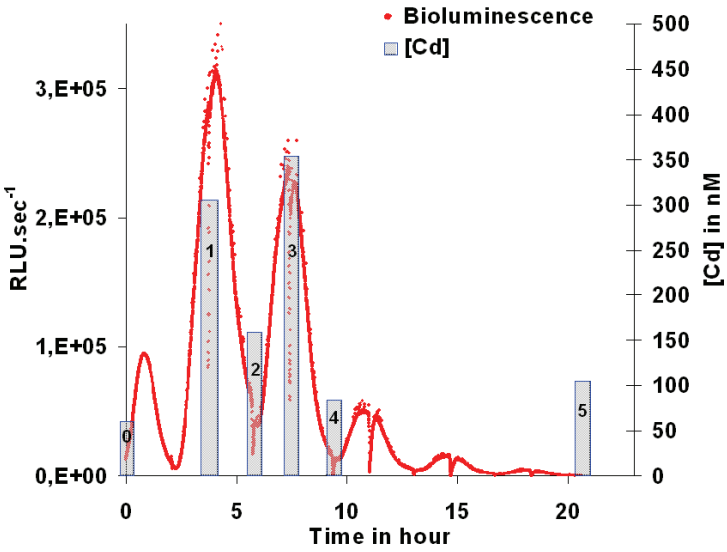

Fig. 9. Concentrations in cadmium in membranes without bacteria during several cycles of measure. (The bioluminescence curve of bioluminescence, with the initial peak is presented only for indication).
Experimental conditions: Cadmium titrations were realized on membranes without bacteria by ICPMS in the departmental laboratory of analysis of Vendée (LDA85). For each measure, the membrane to be analyzed underwent the deliberate number of cycles and was then taken off for analysis.

Hence, cadmium was not accumulated during all the cycles, but a fraction remained blocked in the agarose, while this material is not considered as an adsorbant according to Pernetti et al. (2004).

b. Oxygen effect

Oxygen is necessary both for the catabolism of the bacteria and the reaction of bioluminescence. The oxygen brought to the bacteria comes only from the assay and the regeneration media and dropped during the biosensor measurement (Figure 10).
During the first induction, the oxygen concentration at the biosensor output decreased significantly (from 5.8 to 5.2mg.L^{-1}) whereas it remained stable during the following regeneration (5.4mg. L^{-1}). The oxygen fall was confirmed with the following cycle and can be at the origin of the decrease of bioluminesence.
To address this steady lack of oxygen inside the card, a permanent bubbling device was designed to bring air inside the card. Figure 11 compares the results obtained with and without air bubbling.
These results show a very significant improvement of the living time of the card with a constant air feeding allowing eleven cycles of measurement instead of five without air bubbling. However the bioluminescence signal disappeared after more than forty operating hours. Oxygen even in excess in the measuring cell did not seem to be the only limiting factor of the living time of the membrane.

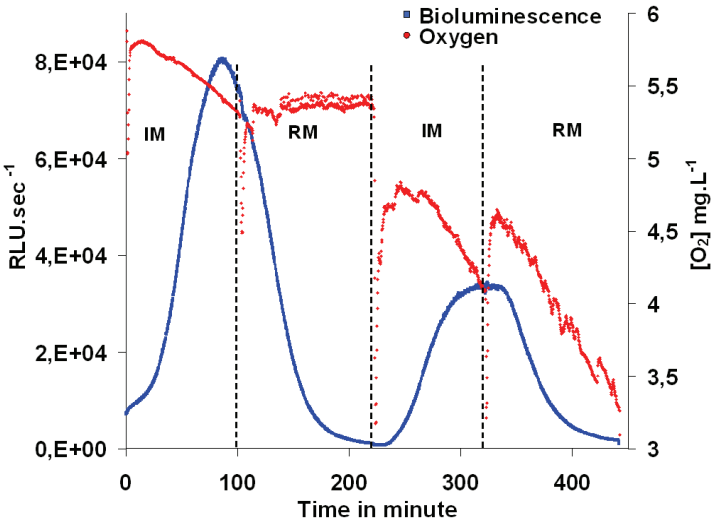

Fig. 10. Evolution of oxygen concentration at the exit of the Lumisens2 biosensor measurement cell.
Experimental conditions were as described in Fig 7. Oxygen measurements were realized by a O_2 probe (SCHOTT 9009/2) connected with an IT interface Reacell 1.11 (Jeulin).

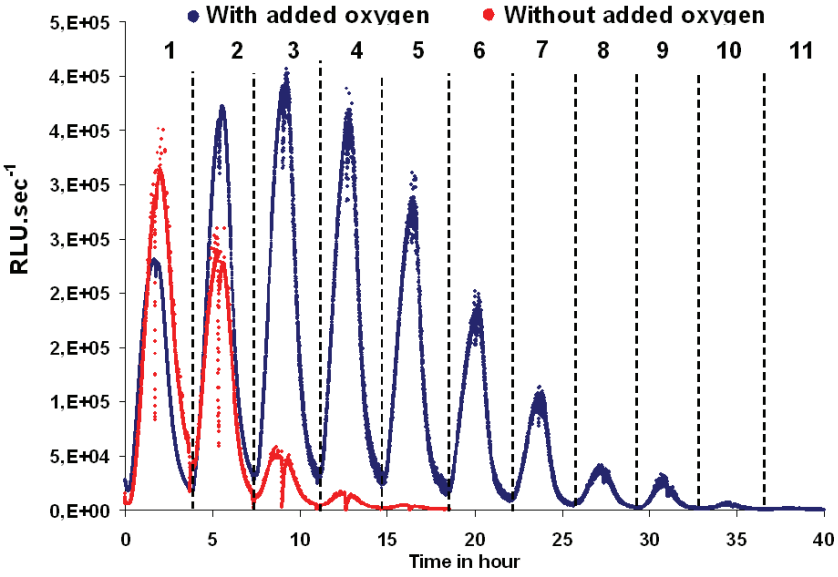

Fig. 11. Repetability of cadmium detection by Lumisens 2 biosensor and *E.coli* DH1 pBzntlux with and without oxygenation of the feeding medium.
Experimental conditions were as described in Fig 7.

c. Bacterial growth inside the agarose matrix

The carbon provided by the circulating medium (acetate medium 1/10X: DCO=148mg.L^{-1}) is low, but could allow the cellular division. In order to check this hypothesis, the absorbance (OD 620nm) was measured in situ during a whole experiment after each medium substitution (Figure 12).

As supposed the bacteria divided in the membrane and the optical density doubled in 24 hours (from 0.068 to 0.127) with a low growth rate (μ=0.081h^{-1}). As a consequence the opaqueness of the resulting agarose membrane led to a quenching of photon and caused a fall of the quantity of light collected by the fiber optic beam. Other consequences are possible, like a more important adsorption of cadmium onto the bacteria.

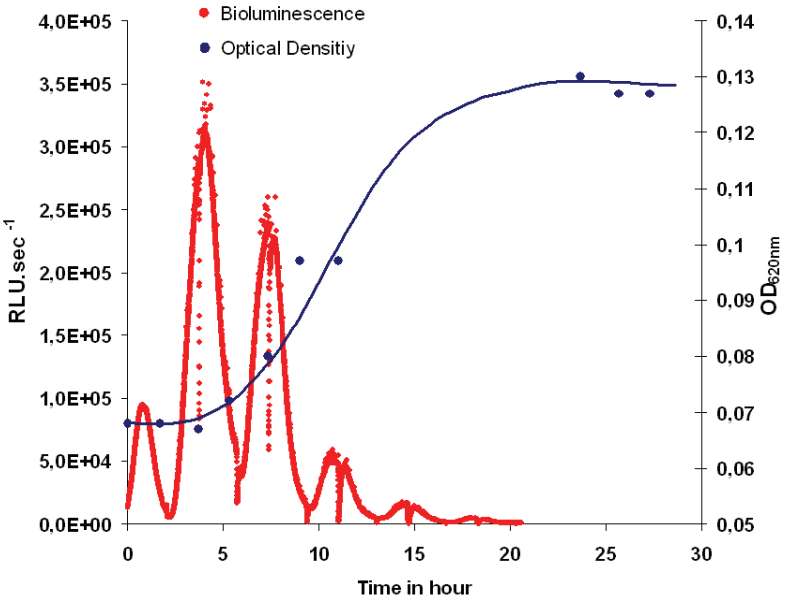

Fig. 12. Evolution of OD_{620nm} in the agarose membrane of bacteria during a repeatability experiment without added oxygen (The bioluminescence curve is presented only for indication).

Experimental conditions were as described in Fig7. OD620nm was monitored at each switch between induction and regeneration medium.

d. Other parameters influencing the repeatability

Three other parameters were tested due to their possible effects on bioluminescence :

- A lack of oxygen already addressed above but increased to avoid any limitation.
- A lack of tetradecanal (resulting from the *luxC,D* et *E* genes activities*)* involved in the bioluminescence reaction. The tetradecanal is not produced at saturated concentration in the *Vibrio* genus and could be limited in *E.coli* DH1 pBzntlux too (Meighen, 1999).

- An adaptation to the Cadmium concentration. Another fundamental parameter, which can affect the answer of the bacteria during long and repeated exposures to the same cadmium concentration, is their adaptation to the toxic. Indeed, the ZntA/ZntR system that we used for the detection of heavy metals belongs to systems induced naturally to evacuate the cadmium from the cytoplasm of the cell.

These different hypothesis were tested and the results are presented in the Figure 13.

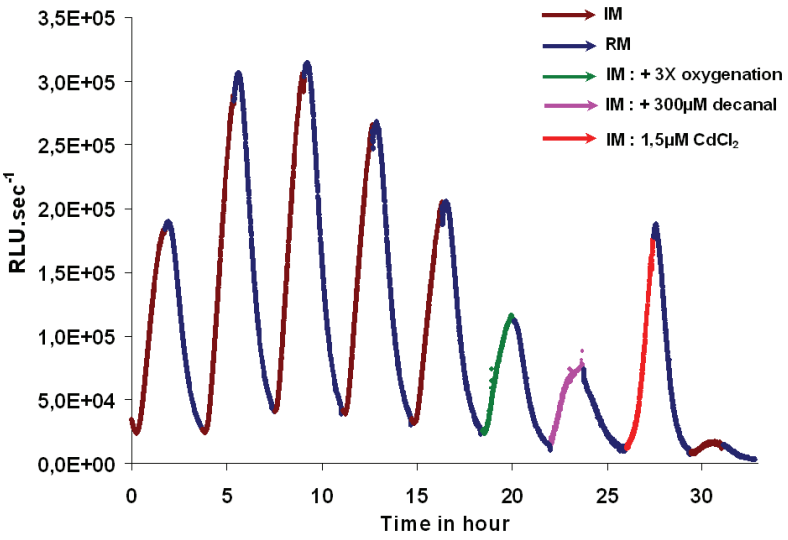

Fig. 13. Parameters influencing the repeatability of the cadmium detection by Lumisens2 biosensor using *E.coli* DH1 pBzntlux. IM: Induction Medium; RM: Regeneration Medium. Experimental conditions were as described in Fig 7 with constant oxygenation of the feeding media.

The induction with more oxygen or the addition of decanal did not improve the signal. On the other hand, an induction carried out with more cadmium (1.5 µM instead of 500 nM) made it possible to obtain the same signal as the first cycles of analysis. This result would consolidate the assumption according to which the bacteria adapt to the metal concentration tested (500nM CdCl2).

4.6 Detection limit

The period of 15 to 20 hours, where the signal of the bacteria is stable, was used to determine the limit of detection of Lumisens2 for cadmium. For that, 5 cadmium concentrations were successively used on the same membrane and the experiment was repeated three times to determine the limit of detection when metal was added either in distilled water or in the waste water treatment plant of la Roche sur Yon (France) effluent (Figure 14). The detection limit of the biosensor for cadmium was 50 nM with or without environmental matrix. This value was close to the European standard for water (45 nM) but was ten times more important than the limit of detection observed for cadmium in bioassays in liquid or immobilised phase (5nM).

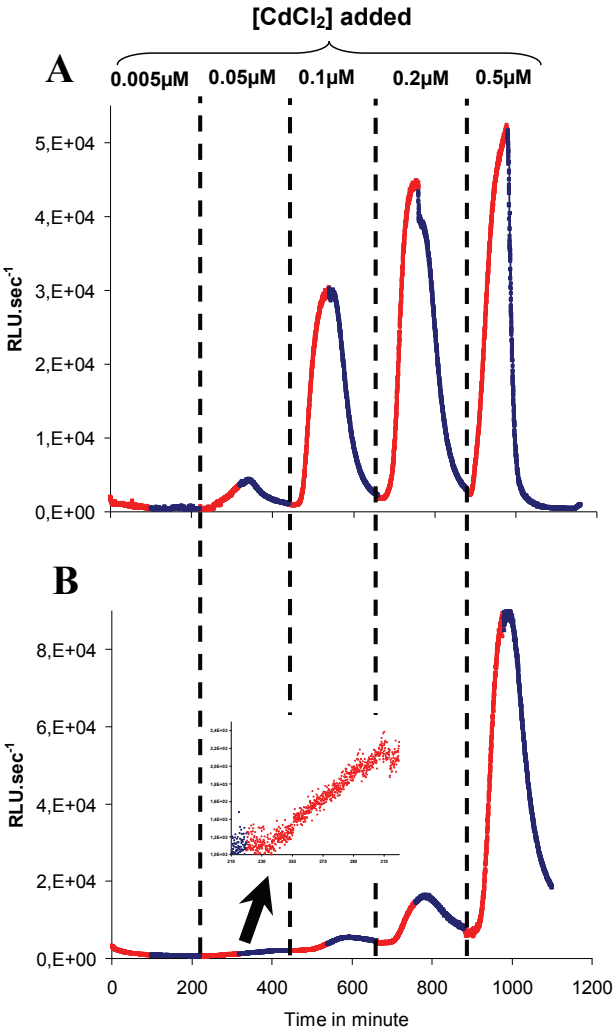

Fig. 14. Detection limit of Lumisens2 biosensor for cadmium detection either in distilled water (A) or in waste water from waste water treatment plant (B) using strain *E.coli* DH1 pBzntlux.

4.7 Application to the detection of cadmium in a waste water treatement plant output.

In a last stage, we wished to associate the biosensor for the detection of cadmium in an effluent from the urban waste water treatment plant (WWTP) of la Roche sur Yon (France). Since technically it was not possible to bring the biosensor on site, the samples of the WWTP were collected twice a day (morning and evening) during 4 days and tested in the laboratory. For each day, a card containing the *E.coli* DH1 pBzntlux bacteria was introduced into the Lumisens 2 biosensor and was used all the day without exceeding 5 cycles of

measurements to avoid the bioluminescence decrease. During these cycles, the two samples were introduced directly to check the presence of Cd in the effluent and after addition of 500 nM of $CdCl_2$ in order to confirm the response of the bacteria.
The figure 15 shows that the bacteria of the biosensor did not detect metals because of a cadmium-free effluent or a concentration lower than the detection limit (50nM). On the other hand, the bioluminescence was monitored when metal was added in the effluent (for example Day 1) that confirmed the measurement's capacity of the bacteria.

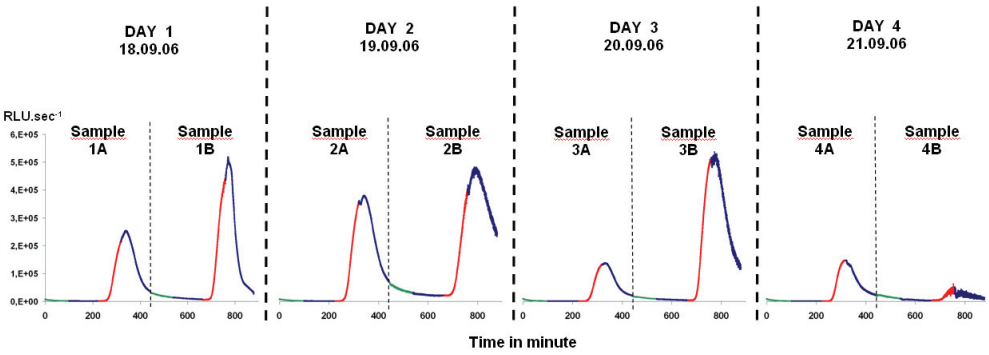

Fig. 15. Detection of heavy metals in waste water treatment plant samples from city of La Roche sur Yon with Lumisens 2 biosensor and *E.coli* DH1 pBzntlux.

It also appears that the produced bioluminescence ranged between 100,000 and 500,000 $RLU.s^{-1}$ according to the samples which received the same metal concentration. The 4B sample was positive while bioluminescence was weak but remained significant compared to the other samples.
Experimental conditions: Each day tow samples of water were taken at the exit of the waste water treatment plant of La Roche sur Yon. For each day, samples were analysed with one chip of Lumisens 2 biosensor. Analysis cycles first start with the injection of the raw sample, in order to determine the presence of heavy metals, during 100 minutes (green curve). In a second step, regeneration medium was introduced to wash the membrane during 120 minutes. In a third step, the same sample, supplemented with 0.5µM of CdCl2, was introduced in the biosensor during 100 minutes and in a final step the membrane was washed during 120 minutes. Flow rate was $5mL.min^{-1}$ with constant oxygenation and the temperature was 30°C.

	1A	1B	2A	2B	3A	3B	4A	4B
DOC ($mg.L^{-1}$)	9.115	6.839	7.828	8.990	8.468	8.589	7.566	14.020
Sulfate ($mg.L^{-1}$)	34	43	74	38	34	60	60	25
Phosphate ($mg.L^{-1}$)	0.425	0.625	0.421	0.365	0.563	0.587	0.374	0.447

Table 4. Chemical analysis results of all samples taken from waste water treatment plant of La Roche sur Yon. DOC analyses were realized with TOCmeter (COT-5000A Shimadzu), sulfate analyses with Hach Lange kit and phosphate analysis with the Briggs method.

The average bioluminescence was 312,000 RLU.sec^{-1} with a variability of 64%, exceeding the variability between membranes (see figure 7). We sought to identify external factors able to influence the signal of bioluminescence such as the dissolved carbon, the sulphates and phosphates, all three chelators of metals (Table 4). No correlation was identified between the fall of the optical signal and a strong content of one of the three measured elements. No explanation could be given and it is finally possible to conclude that measurement is currently of all-or-nothing basis. In other word, if a metal is present at a concentration ranging from the limit of detection and the limit of toxicity, the biosensor is able to measure it without to quantify the concentration by the means of the luminous intensity.

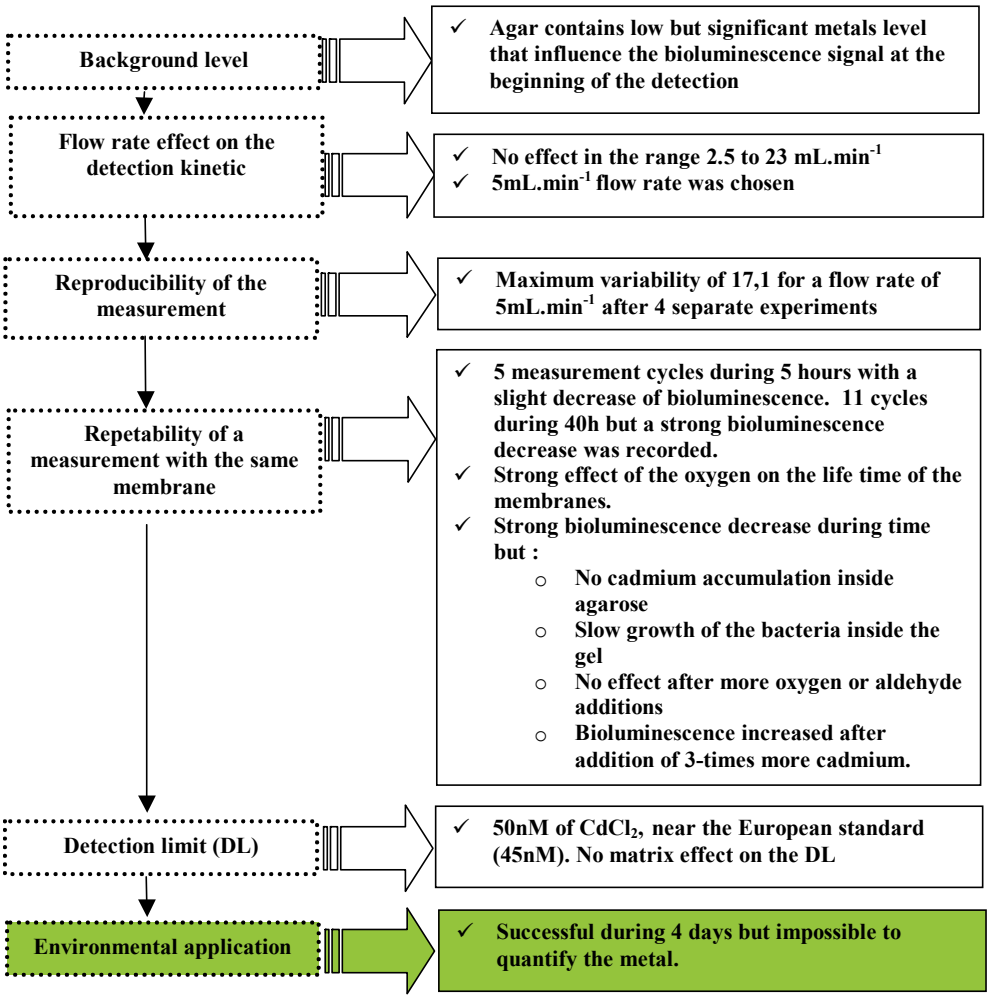

Fig. 16. Summary of the main results obtained in this study with the *E.coli* DH1 pBzntlux immobilized in the Lumisens 2 biosensor.

5. Discussion

The study carried out with Lumisens2 made it possible to better understand and characterise the on line detection of a metal with an immobilised inducible bioluminescent strain: *E.coli* DH1 pBzntlux. The main results are summarised in figure 16.
The reproducibility of the measurement of cadmium at the selected flow rate is acceptable. The lifetime of the same membrane in a continuous mode is forty hours and during this period, eleven analyses are possible. Lee et al., (2004) bring back a life time of 60 hours with their biosensor with only six possible analyses. Heitzer et al., (1994) describe a lifetime of 14 days but they shown only 3 possible analyses in twenty hours. Our results in comparison with the above data, are thus satisfactory. However, as we noted, a progressive fall of the signal of bioluminescence was observed after a prolonged use of the same membrane, that could be attributed to two parameters (combined or not) discussed below.

5.1 Bacterial growth effect

The growth of the bacteria inside the membrane caused a fall of the bioluminescence while acting on three factors: the "quenching" of the light by the bacteria, the increase in the consumption of nutrient and oxygen (Figure 17).

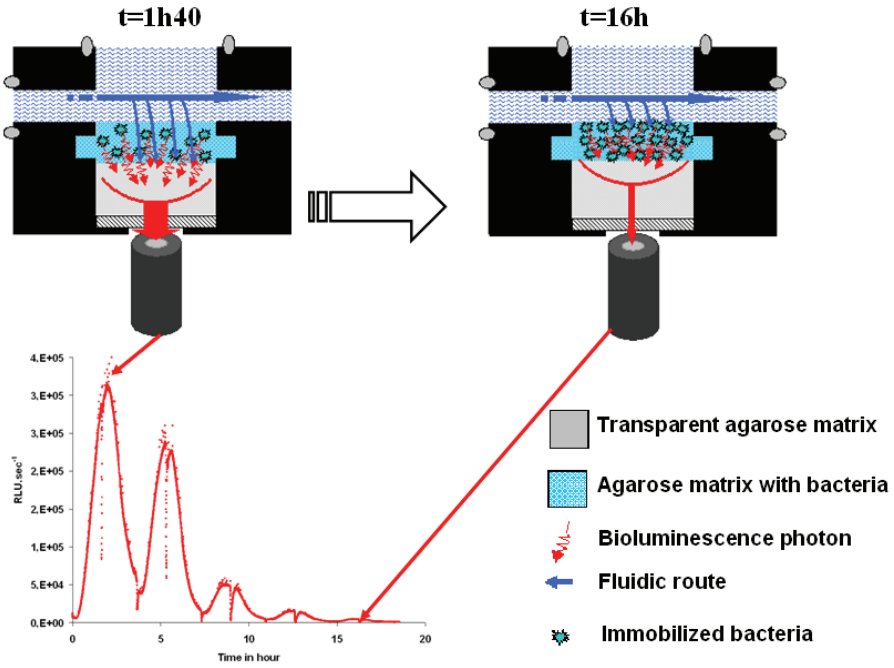

Fig. 17. Possible effects on cadmium detection of the bacterial growth in Lumisens2 Biosensor chip.

At the beginning of the experimentation, the immobilised bacteria are in low number in the membrane. The nutrient, oxygen and metal would be sufficient so that each bacterium emits a strong and detectable bioluminescence. However, after 16 hours of use, the growth of the

bacteria in the membrane of agarose limits the diffusion of the nutrients and metal. Affi et al. (2009) demonstrated that oxygen is the limiting factor since oxygen concentration moving from 100% saturation at the surface to 10% at the bottom off the gel.
The calculation of instantaneous S0/X0 ratio (ratio between the mass of carbon, S0 versus the mass of bacteria, X0) in the measuring cell is 309 at the beginning of an experiment and 265 at the end of the analysis. Those ratios allow the growth of the bacteria and a solution would be to limit the growth by decreasing the quantity of carbon available but certainly at the expense of the bioluminescence.

5.2 Effect of the adaptation to the metal

The adaptation of the bacteria to cadmium is a believable hypothesis because after addition of higher cadmium concentration (Figure 13), the levels of induction were restored. As shown in the figure 18, the presence of cadmium induces both the bioluminescence production and also the synthesis of the resistance mechanism to heavy metals ZntA/ZntR (Binet & Poole, 2000). The repeated exposure to metal would cause an important synthesis of the ZntA protein into *E.coli* DH1 pBzntlux cytoplasm. According to our assumption, the quantity of transmembrane ATPases pumps would become sufficient so that the cadmium once entered in the cytoplasm would be immediately evacuated outside the bacteria. This phenomenon would prevent the fixation of metal by the ZntR protein and the activation of the synthesis of the *luxCDABE* operon. The strain would thus be adapted to the presence of the same cadmium concentration. Moreover, the resistance system ZntA/ZntR is not alone and other systems of efflux or complexation of heavy metals can amplify this phenomenon of adaptation and thus take part in the progressive fall of the signal of bioluminescence (Nies, 1992; Ferianc et al., 1998; Nies, 1999; Spain, 2003; Wang & Crowley, 2005).

6. Conclusions

The Lumisens2 biosensor designed with the *E.coli* DH1 pBzntlux bacteria made it possible to better understand the on line detection of a metal. In spite of the signal bioluminescence decrease attributed to adaptation and growth effect, we showed that lifetime for the same membrane is 40 hours (eleven analyses), that the reproducibility of measurements was satisfactory with a reproducibility of 17% and finally that the limit of detection of cadmium was 50nM. A card can be used with a stable signal during one day and it is possible to monitor the pollution of an effluent of a WWTP during 4 days.

7. Aknowledgments

We would like to thank Professor C.P. Wolk (MSU-DOE Seedling Research Laboratory, Michigan State University) for sending us the *V.fischeri* bioluminescence operon.
The research has been funded through the CER 2000-2006 Action 15 Grant (section 1), Research Programme n°18035: Ville de La Roche-sur-Yon, Conseil Général de Vendée, Conseil Régional des Pays de la Loire, Ministère Français chargé de la Recherche (DRRT Pays de la Loire).
T. Charrier would like to warmly acknowledge the support from the town of La Roche sur Yon, the University of Nantes and the IUT de la Roche sur Yon.

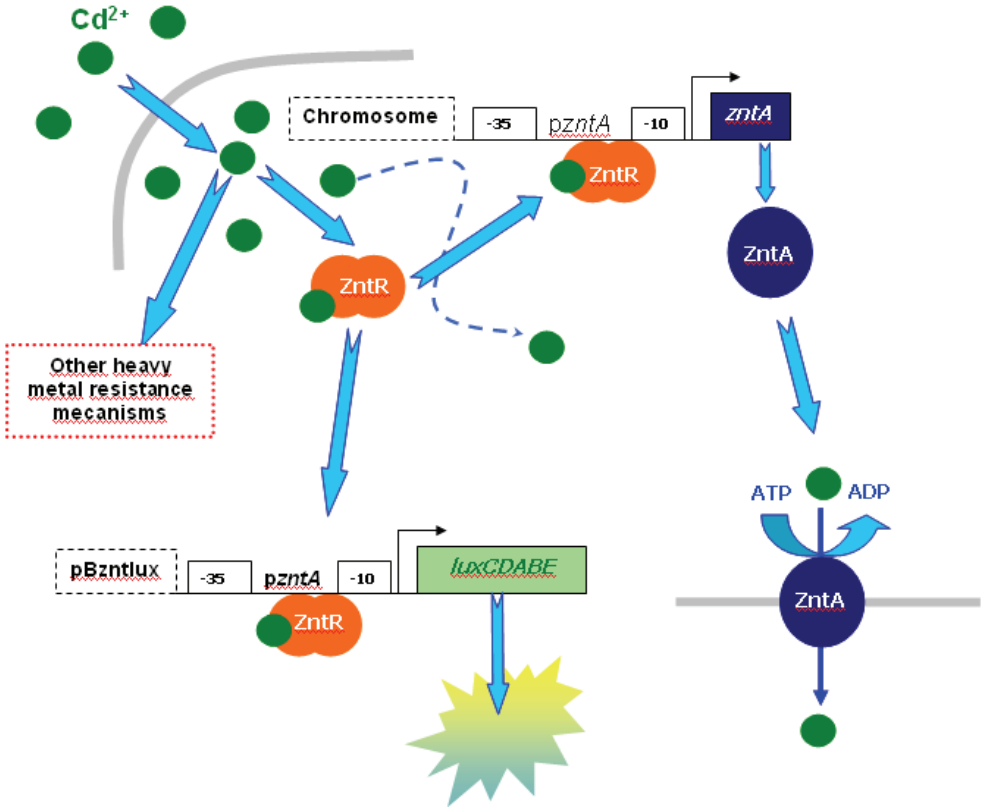

Fig. 18. Synthetic plan of cadmium activated mechanisms in *E.coli* DH1 pBzntlux.

8. References

Audry, S., Schafer, J., Blanc, G. & Jouanneau, J.M. (2004). Fifty-year sedimentary record of heavy metal pollution (Cd, Zn, Cu, Pb) in the Lot River reservoirs (France). *Environ Pollut*, Vol.132, Nb.3, pp.413-26

Binet, M.R.B. & Poole, R.K. (2000). Cd(II), Pb(II) and Zn(II) ions regulate expression of the metal-transporting P-type ATPase ZntA in Escherichia coli. *FEBS Letters*, Vol.473, Nb.1, pp.67-70

Blum, L.J. (1997). Bio- and chemi-luminescent sensors. Singapur, World Scientific Publishing.

Brocklehurst, K.R., Hobman, J.L., Lawley, B., Blank, L., Marshall, S.J., Brown, N.L. & Morby, A.P. (1999). ZntR is a Zn(II)-responsive MerR-like transcriptional regulator of zntA in Escherichia coli. *Mol Microbiol*, Vol.31, Nb.3, pp.893-902

Cavet, J.S., Meng, W., Pennella, M.A., Appelhoff, R.J., Giedroc, D.P. & Robinson, N.J. (2002). A nickel-cobalt-sensing ArsR-SmtB family repressor. Contributions of cytosol and effector binding sites to metal selectivity. *J Biol Chem*, Vol.277, Nb.41, pp.38441-8

Charrier, T. (2006), Development of a multi-channel bioluminescent bacterial biosensor for the detection of pollutants in the environment, *Thesis*

Corbisier, P., Ji, G., Nuyts, G., Mergeay, M. & Silver, S. (1993). luxAB gene fusions with the arsenic and cadmium resistance operons of Staphylococcus aureus plasmid pI258. *FEMS Microbiol Lett*, Vol.110, Nb.SV, pp.231-8

Ferianc, P., Farewell, A. & Nystrom, T. (1998). The cadmium-stress stimulon of Escherichia coli K-12. *Microbiology*, Vol.144 (Pt 4), pp.1045-50

Fernandez-Pinas, F. & Wolk, C.P. (1994). Expression of luxCD-E in Anabaena sp. can replace the use of exogenous aldehyde for in vivo localization of transcription by luxAB. *Gene*, Vol.150, Nb.1, pp.169-74

Gu, M.B., Gil, G.C. & Kim, J.H. (1999). A two-stage minibioreactor system for continuous toxicity monitoring. *Biosens Bioelectron*, Vol.14, Nb.4, pp.355-61

Gu, M.B., Gil, G.C. & Kim, J.H. (2002). Enhancing the sensitivity of a two-stage continuous toxicity monitoring system through the manipulation of the dilution rate. *Journal of Biotechnology*, Vol.93, Nb.3, pp.283-288

Hakkila, K., Green, T., Leskinen, P., Ivask, A., Marks, R. & Virta, M. (2004). Detection of bioavailable heavy metals in EILATox-Oregon samples using whole-cell luminescent bacterial sensors in suspension or immobilized onto fibre-optic tips. *J Appl Toxicol*, Vol.24, Nb.5, pp.333-42

Hastings, J.W., Potrikus, C.J., Gupta, S.C., Kurfurst, M. & Makemson, J.C. (1985). Biochemistry and physiology of bioluminescent bacteria. *Adv Microb Physiol*, Vol.26, pp.235-91

Heitzer, A., Malachowsky, K., Thonnard, J.E., Bienkowski, P.R., White, D.C. & Sayler, G.S. (1994). Optical biosensor for environmental on-line monitoring of naphthalene and salicylate bioavailability with an immobilized bioluminescent catabolic reporter bacterium. *Appl Environ Microbiol*, Vol.60, Nb.5, pp.1487-94

Horry, H., Charrier, T., Durand, M.-J., Vrignaud, B., Picart, P., Daniel, P. & Thouand, G. (2006). Technological conception of an optical biosensor with a disposable card for use with bioluminescent bacteria. *Sensors and Actuators B: Chemical*, Vol.122, Nb.2, pp.527-534

Horry, H., Durand, M.J., Picart, P., Bendriaa, L., Daniel, P. & Thouand, G. (2004). Development of a biosensor for the detection of tributyltin. *Environ Toxicol*, Vol.19, Nb.4, pp.342-5

Ivask, A., Rolova, T. & Kahru, A. (2009). A suite of recombinant luminescent bacterial strains for the quantification of bioavailable heavy metals and toxicity testing. *BMC Biotechnol*, Vol.9, pp.41

Kamidate, T., Kaide, T., Tani, H., Makino, E. & Shibata, T. (2001). Effect of mixing modes on chemiluminescent detection of epinephrine with lucigenin by an FIA system fabricated on a microchip. *Anal Sci*, Vol.17, Nb.8, pp.951-5

Kurniawan, T.A., Chan, G.Y.S., Lo, W.-H. & Babel, S. (2006). Physico-chemical treatment techniques for wastewater laden with heavy metals. *Chemical Engineering Journal*, Vol.118, Nb.1-2, pp.83-98

Lee, J.H. & Gu, M.B. (2005). An integrated mini biosensor system for continuous water toxicity monitoring. *Biosens Bioelectron*, Vol.20, Nb.9, pp.1744-9

Lee, J.H., Mitchell, R.J. & Gu, M.B. (2004). Enhancement of the multi-channel continuous monitoring system through the use of Xenorhabdus luminescens lux fusions. *Biosens Bioelectron*, Vol.20, Nb.3, pp.475-81

Maehana, K., Tani, H. & Kamidate, T. (2006). On-chip genotoxic bioassay based on bioluminescence reporter system using three-dimensional microfluidic network. *Analytica Chimica Acta*, Vol.560, Nb.1-2, pp.24-29

McElroy, W.D. & Ballentine, R. (1944). The Mechanics of Bioluminescence. *Proc Natl Acad Sci U S A*, Vol.30, Nb.12, pp.377-82

Meighen, A.E. (1999). Autoinduction of light emission in different species of bioluminescent bacteria. *Luminescence*, Vol.14, Nb.1, pp.3-9

Meighen, E.A. (1991). Molecular biology of bacterial bioluminescence. *Microbiol Rev*, Vol.55, Nb.1, pp.123-42

Meighen, E.A. (1993). Bacterial bioluminescence: organization, regulation, and application of the lux genes. *Faseb J*, Vol.7, Nb.11, pp.1016-22

Meighen, E.A. (1994). Genetics of bacterial bioluminescence. *Annu Rev Genet*, Vol.28, pp.117-39

Meighen, E.A. & Szittner, R.B. (1992). Multiple repetitive elements and organization of the lux operons of luminescent terrestrial bacteria. *J Bacteriol*, Vol.174, Nb.16, pp.5371-81

Mergeay, M., Monchy, S., Vallaeys, T., Auquier, V., Benotmane, A., Bertin, P., Taghavi, S., Dunn, J., van der Lelie, D. & Wattiez, R. (2003). Ralstonia metallidurans, a bacterium specifically adapted to toxic metals: towards a catalogue of metal-responsive genes. *FEMS Microbiol Rev*, Vol.27, Nb.2-3, pp.385-410

Moore, C.M., Gaballa, A., Hui, M., Ye, R.W. & Helmann, J.D. (2005). Genetic and physiological responses of Bacillus subtilis to metal ion stress. *Mol Microbiol*, Vol.57, Nb.1, pp.27-40

Nealson, K.H. & Hastings, J.W. (1979). Bacterial bioluminescence: its control and ecological significance. *Microbiol Rev*, Vol.43, Nb.4, pp.496-518

Nies, D.H. (1992). Resistance to cadmium, cobalt, zinc, and nickel in microbes. *Plasmid*, Vol.27, Nb.1, pp.17-28

Nies, D.H. (1995). The cobalt, zinc, and cadmium efflux system CzcABC from Alcaligenes eutrophus functions as a cation-proton antiporter in Escherichia coli. *J Bacteriol*, Vol.177, Nb.10, pp.2707-12

Nies, D.H. (1999). Microbial heavy-metal resistance. *Appl Microbiol Biotechnol*, Vol.51, Nb.6, pp.730-50

Nies, D.H. (2003). Efflux-mediated heavy metal resistance in prokaryotes. *FEMS Microbiol Rev*, Vol.27, Nb.2-3, pp.313-39

Outten, C.E., Outten, F.W. & O'Halloran, T.V. (1999). DNA distortion mechanism for transcriptional activation by ZntR, a Zn(II)-responsive MerR homologue in Escherichia coli. *J Biol Chem*, Vol.274, Nb.53, pp.37517-24

Pernetti, M., Poncelet, D., Thouand, G., Annesini, M.C., Merli, C. (2003). Characterisation of agarose as immobilization matrix model for a microbial biosensor. *Chem. Ind.*, Vol.57, Nb.12, pp.600-604

Philp, J.C., Balmand, S., Hajto, E., Bailey, M.J., Wiles, S., Whiteley, A.S., Lilley, A.K., Hajto, J. & Dunbar, S.A. (2003). Whole cell immobilised biosensors for toxicity assessment of

a wastewater treatment plant treating phenolics-containing waste. *Analytica Chimica Acta*, Vol.487, Nb.1, pp.61-74

Picart, P., Bendriaa, L., Daniel, P., Horry, H., Durand, M.J.,Jouvanneau, L., Thouand, G. (2004). New bioreactor for in situ simultaneous measurement of bioluminescence and cell density. *Review of Scientific Instruments*, Vol.75, Nb.3, pp.747-755

Polyak, B., Bassis, E., Novodvorets, A., Belkin, S. & Marks, R.S. (2001). Bioluminescent whole cell optical fiber sensor to genotoxicants: system optimization. *Sensors and Actuators B: Chemical*, Vol.74, Nb.1-3, pp.18-26

Rabner, A., Belkin, S., Rozen, R. & Shacham, Y. (2006). Whole-cell luminescence biosensor-based lab-on-chip integrated system for water toxicity analysis. Microfluidics, BioMEMS, and Medical Microsystems IV, San Jose, CA, USA, SPIE.

Riether, K.B., Dollard, M.A. & Billard, P. (2001). Assessment of heavy metal bioavailability using Escherichia coli zntAp:lux and copAp:lux-based biosensors. *Appl Microbiol Biotechnol*, Vol.57, Nb.5-6, pp.712-6

Rothert, A., Deo, S.K., Millner, L., Puckett, L.G., Madou, M.J. & Daunert, S. (2005). Whole-cell-reporter-gene-based biosensing systems on a compact disk microfluidics platform. *Anal Biochem*, Vol.342, Nb.1, pp.11-9

Simpson, M.L., Sayler, G.S., Applegate, B.M., Ripp, S., Nivens, D.E., Paulus, M.J. & Jellison Jr, G.E. (1998). Bioluminescent-bioreporter integrated circuits form novel whole-cell biosensors. *Trends in Biotechnology*, Vol.16, Nb.8, pp.332-338

Spain, A. (2003). Implications of Microbial Heavy Metal Tolerance in the Environment. *Reviews in Undergraduate Research*, Vol.2, pp.1-6

Stocker, J., Balluch, D., Gsell, M., Harms, H., Feliciano, J., Daunert, S., Malik, K.A. & van der Meer, J.R. (2003). Development of a set of simple bacterial biosensors for quantitative and rapid measurements of arsenite and arsenate in potable water. *Environ Sci Technol*, Vol.37, Nb.20, pp.4743-50

Sung, N.D. & Lee, C.Y. (2004). Coregulation of lux genes and riboflavin genes in bioluminescent bacteria of Photobacterium phosphoreum. *J Microbiol*, Vol.42, Nb.3, pp.194-9

Tani, H., Maehana, K. & Kamidate, T. (2004). Chip-based bioassay using bacterial sensor strains immobilized in three-dimensional microfluidic network. *Anal Chem*, Vol.76, Nb.22, pp.6693-7

Tauriainen, S., Karp, M., Chang, W. & Virta, M. (1997). Recombinant luminescent bacteria for measuring bioavailable arsenite and antimonite. *Appl Environ Microbiol*, Vol.63, Nb.11, pp.4456-61

Tauriainen, S., Karp, M., Chang, W. & Virta, M. (1998). Luminescent bacterial sensor for cadmium and lead. *Biosensors and Bioelectronics*, Vol.13, Nb.9, pp.931-938

Thévenot, D.R., Tothb, K., Durstc, R.A., Wilsond, G.S. (2001). Electrochemical biosensors:next term recommended previous termdefinitionsnext term and classification. *Biosensors and Bioelectronics*, Vol.16, Nb.1-2, pp.121-131

Thouand, G., Daniel, P., Horry, H., Picart, P., Durand, M.J., Killham, K., Knox, O.G., DuBow, M.S. & Rousseau, M. (2003). Comparison of the spectral emission of lux recombinant and bioluminescent marine bacteria. *Luminescence*, Vol.18, Nb.3, pp.145-55

Thouand, G., Horry, H., Durand, M.J., Picart, P., Bendriaa, L., Daniel, P. & DuBow, M.S. (2003). Development of a biosensor for on-line detection of tributyltin with a

recombinant bioluminescent Escherichia coli strain. *Appl Microbiol Biotechnol*, Vol.62, Nb.2-3, pp.218-25

Tu, S.C. & Mager, H.I. (1995). Biochemistry of bacterial bioluminescence. *Photochem Photobiol*, Vol.62, Nb.4, pp.615-24

Visick, K.L., Foster, J., Doino, J., McFall-Ngai, M. & Ruby, E.G. (2000). Vibrio fischeri lux genes play an important role in colonization and development of the host light organ. *J Bacteriol*, Vol.182, Nb.16, pp.4578-86

Wang, A. & Crowley, D.E. (2005). Global gene expression responses to cadmium toxicity in Escherichia coli. *J Bacteriol*, Vol.187, Nb.9, pp.3259-66

Wu, J. & Rosen, B.P. (1993). Metalloregulated expression of the ars operon. *J Biol Chem*, Vol.268, Nb.1, pp.52-8

12

Integrated Biosensor and Interfacing Circuits

Lei Zhang, Zhiping Yu and Xiangqing He
Institute of Microelectronics, Tsinghua University
Beijing, 100084,
China

1. Introduction

Driven by the demand of the bioelectronics market, many biosensors need to work in parallel or in a controllable way to achieve complicated biodetections, however the limited scale, speed, cost, complex signal processing, and bulky circuit routing problems prohibit the discrete biosensor solutions (Drummond et al., 2003). Nowaday biosensor are usually integrated on the same substrate to form biosensor array to improved the scale and efficiency, and solve the signal routing difficulties.

CMOS technology emerges since the mid-1960s, and rapidly captured the IC market. The aggressive scaling of CMOS technology following the famous Moore's Law enables the realization of high-speed digital circuits, analog and mixed-signal circuits, as well as radio-frequency (RF) communication circuits. A single chip monotonically integrating all components of a complex electronics systems or laboratory systems which contain digital, analog, mixed-signal, and RF communication, microelectromechanical systems (MEMS), and other experimental functions, i.e. lab-on-a-chip (LOC) is avidly to be implemented to possess the capabilities of high-efficiency characterization, high-speed complex signal processing and communication, mass production, large scale, low cost, and low power as well. Fortunately, most of the fabrication processes of biosensors are compatible with the standard CMOS technology either directly or via the post-CMOS processes, e.g. DNA sensors fabricated on Si-nanowire (Li et al., 2004) and gold surface (Cheng et al., 2005) etc, which makes it possible to integrate the biosneosr arrays and CMOS IC on a single chip as a CMOS integrated biosensing system (IBS) (Augustyniak et al., 2006; Prakash et al., 2006; Thewes et al., 2005; Han et al., 2007).

The CMOS IBS usually composes of four parts in its system circuitry: integrated biosensor array, interfacing circuits, analog-to-digital (A/D) conversion, and digital signal processor (DSP), as shown in Fig. 1(a). In some system requiring feedback controlling during the characterization, digital-to-analog (D/A) converters are also included depending on the applications, as shown in Fig. 1(b). In the system architecture of CMOS IBS, the overall performance such as noise, bandwidth, sensitivity etc are mainly governed by the performances of interfacing circuits which controls the electrolyte potential and directly acquires signals from the integrated biosensor array.

The three electrode system, as shown in Fig. 2, is the most popular electrode architecture of the integrated biosensor array in nowadays CMOS IBS. The system is composed of reference electrode, working electrode, and counter electrode (it is also called auxiliary electrode sometimes).

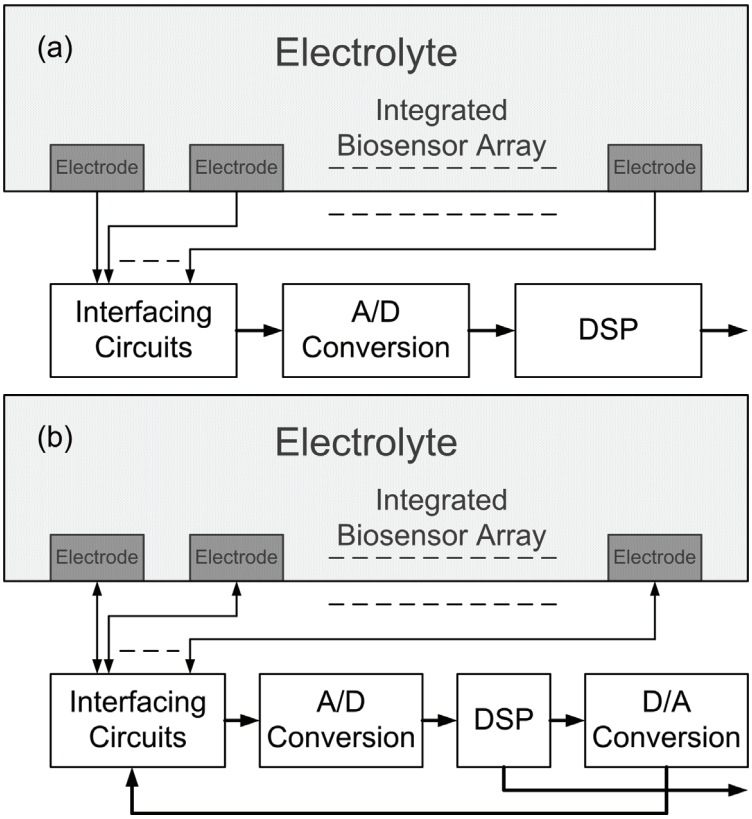

Fig. 1. System architectures of CMOS IBS. (a) Feedforward sensing. (b) Feedback controlled sensing.

Reference electrode is an electrode with a stable and well-known electrode potential. There are many types of reference electrode used in electrochemical systems, such as hydrogen electrode, copper-copper(II) sulphate electrode, silver chloride electrode etc, among which the silver chloride (Ag-AgCl) electrode is commonly employed in the IBS. In some systems with feedback stabilization, the reference electrode made from inert metals such as gold (Au), platinum (Pt) etc are also utilized to simplify the fabrication process.

Working electrode is an electrode in the IBS on which reaction of interest is occurring. Common working electrode is usually implemented in inert metals such as Au, Ag, Pt, etc. Most biosensors apply a control voltage on the working electrode in contact with the electrolyte while measuring the current by a signal acquisition circuit, as shown in Fig. 2.

Counter electrode is an electrode used in the IBS from which the sensing current is expected to flow and is also made from inert metals in most cases. The potential on this electrode is opposite in sign to that of the working electrode. Counter electrode is usually connected with the reference electrode by a potentiostat in a negative feedback loop to stabilize the electrolyte potential with respect to a reference during the biosensing process, as shown in Fig. 2. In some systems, acquisition circuit is combined into the potentiostat, but which is not against the architecture of the interfacing circuits we are discussing here.

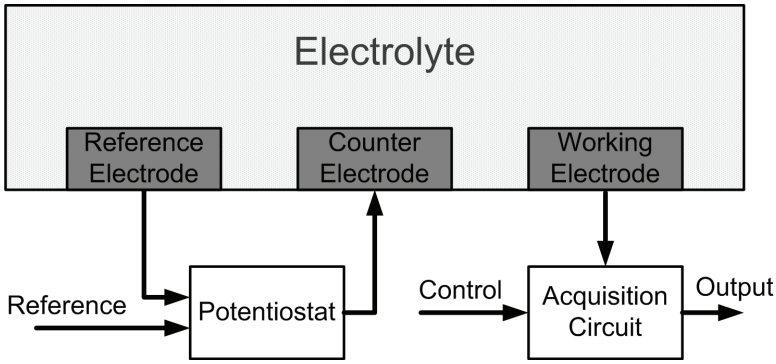

Fig. 2. Interfacing circuits in the CMOS IBS.

2. Potentiostat

The on-chip potentiostat circuit serving for stabilizations of electrolyte potential and accommodation of electrochemical current (Augustyniak et al., 2006; Prakash et al., 2006; Thewes et al., 2005) is one of the major components in the IBS, which is usually realized as an operational transconductance amplifier (OTA) (Zhang et al., 2009). Table 1 shows the specifications of the potentiostat OTA from a typical biosensor system based on nano-particle assembly.

Typical assembling voltage	1.8 ± 0.2 V
Min. assembling voltage	~1 V
Electrolyte potential range	0 to 1.8 V
Max. potential variation	5 mV
Assembling current range	~10 nA to ~100 μA
Max. signal bandwidth	< 100 kHz

Table 1. Sepcifications of potentiostat OTA from the experiment.

It can be seen that the assembling voltage range falls in the typical supply voltage range of standard CMOS technology, but due to the aggressive scaling of CMOS technology, typical supply voltage of mainstream CMOS process can barely satisfy the specifications in Table 1. For this reason, a potentiostat OTA with rail-to-rail input common-mode range is highly preferred in the CMOS IBS. On the other hand, considering the loading capability required by the assembling current range, a Class-AB output stage should also be incorporated for its bidirectional loading capability and high power efficiency.

The potentiostat OTA has been designed and illustrated in Fig. 3. The potentiostat OTA uses the complimentary folded-cascode input stage composed of transistor M_0 to M_{13} to achieve the rail-to-rail input common-mode range to enable the required assembling voltage, and reduce the input-referred noise to stabilize the potential as well, while incorporates the Class-AB output stage composed of transistor M_{29} to M_{32} to provide the maximized loading capability and accommodate the assembling current requirement. Transistors M_{14} to M_{21} function as the common-mode feedback circuit and provide biasing voltage for the folded-

cascode input stage. M_{25} to M_{28} are two source follower to match the DC voltage between stages, while the other biases are served by M_{22} to M_{24} from a current I_B. Simulation results show that biasing at a current of I_B=1 μA the circuit is capable of providing a rail-to-rail input and output dynamic range and a unit gain bandwidth up to 42.7 MHz, while the output current headroom, I_{max}, is over 450 μA, which meet the specifications in Table 1.

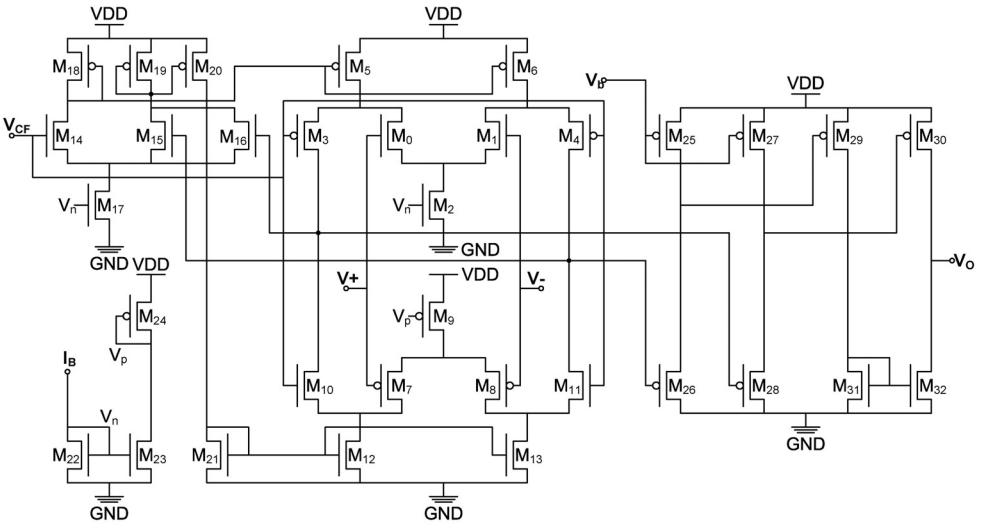

Fig. 3. Transistor level implementation of the potentiostat OTA with rail-to-rail input common-mode range and Class-AB output stage.

The potential variation is due to: (I) finite transconductance of the potentiostat OTA, (II) input referred noise, and (III) the input referred offset. If G_m^{DC} is the DC transconductance of the potentiostat OTA, the potential variation, V_{ft}, due to (I) can be expressed as

$$V_{ft} = \frac{I_{\max}}{G_m^{DC}} \tag{1}$$

According to the noise theory, transistors M_0, M_1, M_5, M_6, M_7, M_8, M_{12}, and M_{13} in the first stage contribute to the overall noise. The noise power spectral density, S_I, in a MOS transistor is given by (Linares-Barranco et al., 2003; Linares-Barranco et al., 2004)

$$S_I = \frac{4\gamma kTg_m + K_F I_{ds}^{A_F}}{f^{E_F} C_{ox} WL} \tag{2}$$

where γ is the thermal noise parameter, g_m is the transconductance, I_{ds} is the drain-source current, C_{ox}, W, and L are the gate capacitance per unit area, transistor width and length, respectively, and k, T, and f are the Boltzman constant, temperature, and frequency, respectively. K_F, A_F, and E_F are flicker noise parameters with the typical values of 2×10^{-25}, 2, and 1, respectively. Since the corner frequency f_c, where thermal noise and flicker noise exhibit the same power density, is calculated as 5.4 Hz by using parameters provided by the foundry, much smaller than the unit gain bandwidth, therefore, flicker noise is negligible in the proposed OTA, and the input referred noise voltage V_{irn} can be characterized by

$$\overline{V_{irn}^2} = \frac{8\gamma kT\left(g_{m0} + g_{m5} + g_{m7} + g_{m12}\right)}{\left(g_{m0} + g_{m7}\right)^2} \tag{3}$$

where g_{mj} is the transconductance of transistor M_j, j = 0, 1,…, 32.
V_{irn} can be diminished by increasing the biasing currents and aspect ratios of the input differential pairs, but trades off with the power consumption and the physical area. The spectral density input referred noise of proposed OTA on different common-mode input voltages are shown in Table 2.
Monte-Carlo simulation is also performed to characterize the input referred offset by utilizing the mismatch parameters provided by the foundry, and the results are also shown in Table 2. In the worst case with V_{CM} = 0 V, the overall potential variation due to the above three issues is 4.12 mV, which implies an 8 bit of potential resolution and satisfies the boundary condition in Table 1. The other circuit performances are summarized in Table 2.

Parameters	V_{CM} = 0 V	V_{CM} = 0.9 V	V_{CM} = 1.8 V
DC transconductance	2.22 S	5.43 S	3.90 S
3-dB bandwidth	1.97 kHz	2.07 kHz	1.94 kHz
Phase margin	>75°	>80°	>75°
Max. output pull current	451 μA	451 μA	–
Max. output push current	–	459 μA	459 μA
Input referred offset	3.51 mV	1.60 mV	2.75 mV
Input referred noise	61.8 nV/√Hz	38.2 nV/√Hz	57.7 nV/√Hz
Overall potential variation	4.12 mV	1.93 mV	3.24 mV
Potential resolution	8 bit	9 bit	9 bit
DC power dissipation	40.4 μW	50.3 μW	58.0 μW
Power supply	1.8 V	1.8 V	1.8 V

Table 2. Summary of performances of the potentiostat OTA

3. Acquisition circuits

The design of acquisition circuits in the IBS is circumscribed by the sensing mechanism of the biosensor. In the electrical biosensing, there are two major schemes in analyte detection: direct current (DC) sensing and alternative current (AC) sensing.
In the DC sensing, a DC voltage is usually applied to the working electrode in an IBS, and the current flowing from counter electrode to the working electrode is measured (Augustyniak et al., 2006; Thewes et al., 2005). This method suffers from the large background noise in the electrolyte seriously, which prevent it from the applications requiring high sensitivities of biosensing.
In the AC sensing, the acquisition circuit senses the AC modulation current by applying an AC voltage superimposed on a DC biasing on the working electrode (Huang & Chen, 2008).

Since only the background noise within the band-of-interest deteriorates the signal-to-noise ratio, the AC sensing has much better sensitivity than the DC sensing scheme.

DNA releasing voltage	0.9 V
DNA modulation voltage	±0.5 V
Current headroom	±100 nA
Current sensitivity	~100 pA
Max. signal bandwidth	10 kHz
Min. sensor impedance	~5 MΩ

Table 3. Specifications of a typical DNA IBS

A desirable acquisition circuit should usually accommodate both schemes of biosensing, however, as summarized in Table 3, the fastidious requirements, such as sensitivity, bandwidth, input range, etc., for the following circuits make great challenges to analog integrated circuit designers. There are various methods and circuits dealing with the ultralow current in biosensing applications, e.g., current integrator (sometimes it is called as potentiostat) (Ayers et al., 2007; Narula & Harris, 2006), transimpedance amplifiers (Rodriguez-Villegas, 2007; Basu et al., 2007), and ultralow current-mode amplifiers (ULCA) (Zhang et al., 2007; Ramirez-Angulo et al., 2004; Steadman et al., 2006; Zhang et al., 2009). The current integrator is capable of providing sub-picoampere sensitivity, however, the circuit bandwidth is typically below 1 kHz, which cannot fully accommodate the bandwidth of AC sensing. Transimpedance amplifiers possess wider bandwidth and good sensitivity, however, its dynamic range is limited by the supply voltage, which becomes a serious issue along with the scaling of supply voltage in today's CMOS technology. The ULCA turns out to be a favorable candidate with high sensitivity, sufficient bandwidth, and wide dynamic range for IBS with AC sensing capabilities.

3.1 Circuit design of ULCA

In ULCA design, conventional transistor-strong-inversion-based current-mode circuits are out of consideration due to the large noise background induced by the dc quiescent current, and weak-inversion-based (subthreshold) current-mode circuits emerge as the candidates. Since the subthreshold circuits suffer from supply voltage fluctuations and die-to-die process fluctuations (Mead, 1989), they are usually closely integrated with other adjacent stages on a single die and share the same supply voltage, along with careful considerations on the matching, symmetry, and biasing issues (Linares-Barranco et al., 2003; Linares-Barranco et al., 2004; O'Halloran & Sarpeshkar 2004).

Some ULCA topologies have been reported (Zhang et al., 2007; Ramirez-Angulo et al., 2004; Steadman et al., 2006), as shown in Fig. 4. The circuit in Fig. 4(a) is working in the Class A mode. It uses a regulated current mirror to achieve the current amplification. The quiescent currents are provided by current sources, whereas the bandwidth is limited by capacitor C_0. Although the circuit provides good linearity over the input range, since the quiescent current I_0 should be low enough to reduce the noise level and meet the requirement of sensitivity, the specified current headroom (in both positive and negative directions) can hardly be achieved. One can certainly introduce the Class B complementary topology in Fig.

4(b) to meet the headroom requirement and increase the sensitivity by removing the noise background induced by I_0; however, this comes at the cost of substantially losing bandwidth in the low-input cases.

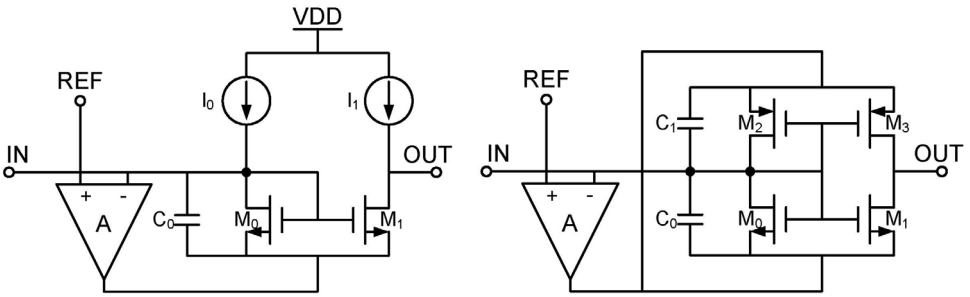

Fig. 4. Conventional current-mode amplifier topologies.

To meet the specifications in Table 3, a Class AB ULCA aiming at biosensing amplification has been designed and verified in SMIC 0.18-μm CMOS mixed-signal technology (Zhang et al., 2009). The design elaborately considered the issues and tradeoffs over gain, bandwidth, noise, and offset. The experimental results show that the ULCA can completely satisfy the requirements of typical DNA-based IBS and is eligible to serve for the preamplification of ultralow biosensor signals in the IBS.

The ULCA schematic is shown in Fig. 5. In this circuit, the current from DNA biosensors is input to a complementary regulated current mirror consisting of an N-type opamp A_{N0}, a P-type opamp A_{P0}, and transistors M_0, M_1, M_3, and M_4, where it is amplified by a factor of 10 (20 dB). The opamps A_{N1} and A_{P1} and the transistors M_6–M_{11} compose a voltage limiter.

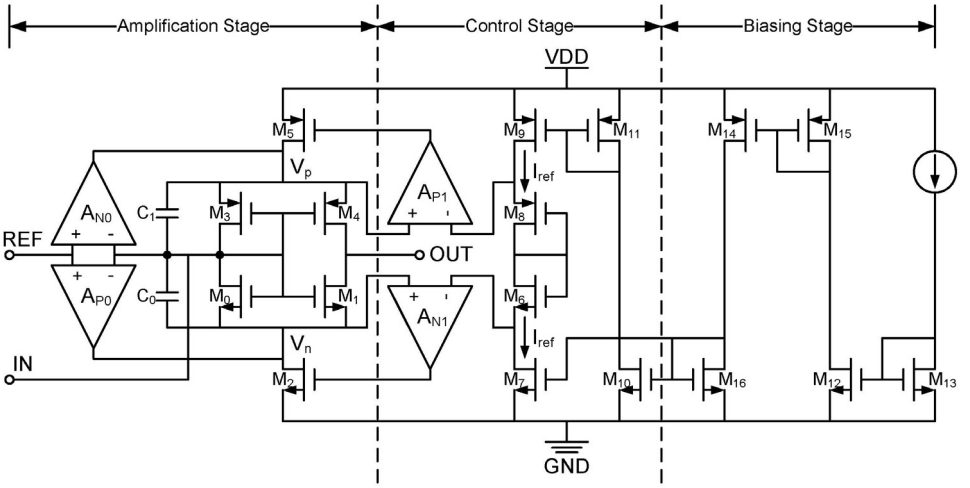

Fig. 5. Circuit schematic of the ULCA.

Due to the "virtual short" mechanism, "IN" is fixed at "REF" by A_{N0} and A_{P0}, and a quiescent current of I_{ref} is established in M_0 and M_3 by A_{N1} and A_{P1}. When a positive input is applied V_n, the output of the opamp A_{N1} reduces, thus turning off M_2. The current of M_0 and M_1 is sunk by A_{P0}. On the other hand, since V_p tends to drop down, the current provided by A_{N0} becomes smaller. However, M_5 is turned on by A_{P1} to compensate the current at node V_p, which limits V_p from dropping and maintains the quiescent current of M_0 and M_3 equal to the reference current I_{ref} provided by M_6−M_9, even if the input current I_{IN} is much larger than I_{ref} . A similar conclusion can also be made for the negative input cases.

It can be seen that M_2 and M_5 alternatively sustain the quiescent current for the current mirror, which in turn keeps a constant bandwidth as the input varies between positive and negative directions. Furthermore, I_{ref} can be designed small enough to achieve the required sensitivity and noise level without being restricted by the current headroom, since the current headroom no longer depends on the magnitude of the quiescent current in the ULCA. Therefore, the circuit can provide an extremely high sensitivity and a large current headroom at the required bandwidth. Due to the variation and pad leakage issues, I_{ref} is unpractical to be provided off-chip. Therefore, three steps of current mirroring are introduced by M_{12}−M_{16} in the biasing stage, where each step achieves a conversion factor of 0.1. A microampere-level off-chip current is downconverted 1000 times to relax these unwanted impacts. Capacitors C_0 and C_1 serve for frequency compensation and bandwidth limitation purposes in the circuit.

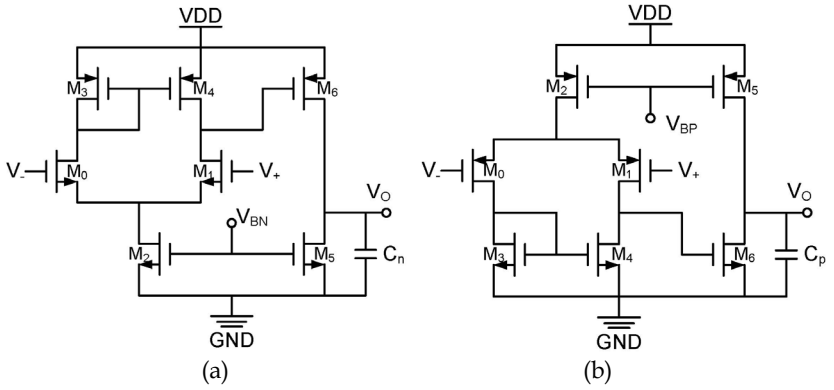

Fig. 6. Auxiliary N- and P-type opamps in the ULCA.

The auxiliary N- and P-type opamps are shown in Fig. 6(a) and (b). In the circuit, M_0, M_1, M_3, and M_4 consist of a differential input stage. M_0 and M_1 are biased in their subthreshold regions for the purpose of noise reduction; meanwhile, they are chosen as large dimensions to improve the matching and reduce the offset and flicker noise. Transistors M_5 and M_6 consist of a transconductance output stage that provides current for the following circuits. Capacitors C_n and C_p represent the load capacitances of the opamp.

As shown in Fig. 5, when a positive input is applied, the gain is provided by the regulated current mirror consisting of M_0, M_1, and opamp A_{P0}, whereas M_3−M_5 and opamp A_{P1} are serving as current sources providing the quiescent current for the stage, which can be simplified to the circuit shown in Fig. 7(a). A complementary discussion of the negative input case leads to the topology shown in Fig. 7(b).

3.2 Small signal AC analysis

The small-signal equivalent circuit for ac analysis is shown in Fig. 7(c). In this circuit, g_m, g_{mb}, g_o, and C_{gs} are the gate transconductance, body transconductance, output conductance, and gate capacitance of the MOSFET, and g_{oa}, C_{ia}, and C_{oa} are the output conductance, input capacitance, and output capacitance of the opamp, respectively. C_i is defined as $C_{gs0} + C_{gs1} + C_0$ (or C_1). The transconductance of the opamp is modeled as $g_{ma}(s)$, considering the delays introduced by the parasitic capacitances of its internal nodes. As suggested in (Linares-Barranco et al., 1992), $g_{ma}(s)$ can be written as

$$g_{ma}(s) = g_{ma}\left(1 - \frac{s}{\omega_a}\right) \tag{4}$$

where g_{ma} is the DC transconductance, and ωa models the delay.

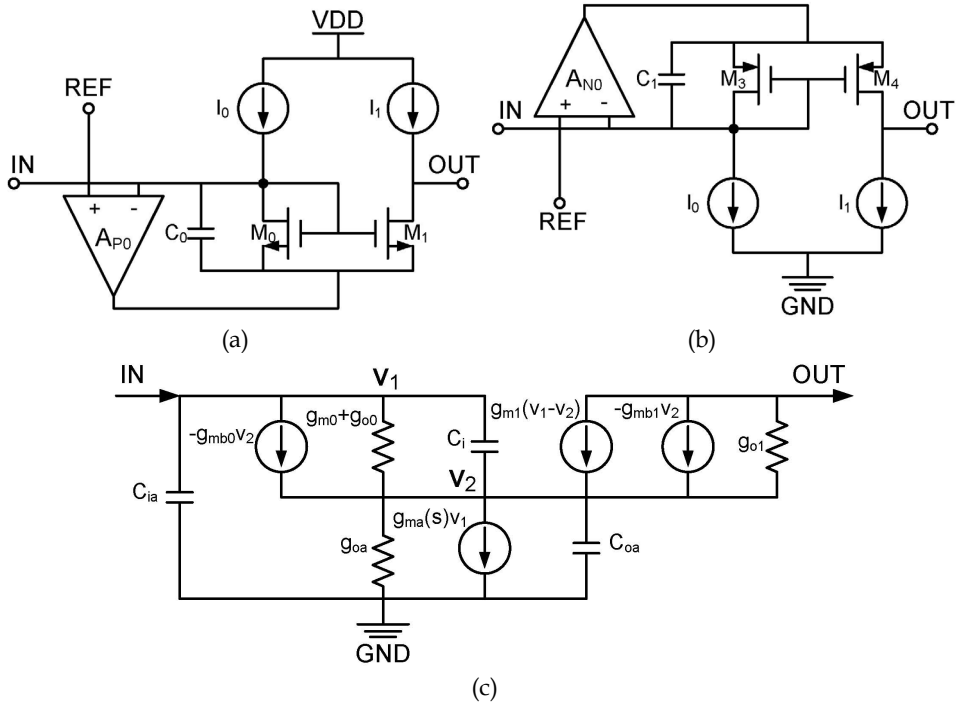

Fig. 7. (a) Simplified circuit of ULCA when a positive input is applied. (b) Simplified circuit of ULCA when a negative input is applied. (c) Small-signal equivalent circuit of a simplified ULCA.

Detailed analysis of the equivalent circuit results in the characterization function of $as^2+bs+\underline{c}=0$, where:

$$a = C_{ia}\left(C_i + C_{oa}\right)\omega_a + C_i\left(C_{oa} - \frac{g_{ma}}{\omega_a}\right)\omega_a \tag{5}$$

$$b \approx C_{ia}\left(g_{m0}+g_{m1}+g_{oa}\right)\omega_a+\left(g_{m0}+g_{o0}\right)\left(C_{oa}-\frac{g_{ma}}{\omega_a}\right)\omega_a \tag{6}$$

$$c \approx g_{mb0}\left(g_{ma}-g_{m1}\right)\omega_a+g_{m0}\left(g_{mb1}+g_{oa}+g_{ma}\right)\omega_a \tag{7}$$

and the parameters are defined as follows:

C_{ia}: Input capacitance of opamp.
C_{oa}: Output capacitance of opamp (C_n or C_p).
C_i: $C_{gs0}+C_{gs1}+C_0$ (or C_1).
g_m: Transconductance of MOSFET.
g_{mb}: Body transconductance of MOSFET.
g_o: Output conductance of MOSFET.
g_{oa}: Output conductance of opamp.

To maintain the ac stability, all the poles of the circuit transfer function must be placed in the left-hand side of the Laplace plane, i.e. $a>0$, $b>0$, $c>0$ must be satisfied, resulting in the conditions of g^N_{ma}, $g^P_{ma} > g_{m1}$, $C_0 > g^P_{ma}/\omega_a$, and $C_1 > g^N_{ma}/\omega_a$. Moreover, it can be found that provided the quiescent current I_{ref} , by adjusting C_0 and C_1, the bandwidth of the ULCA can be confined at the expected value.

3.3 Noise characterization

It is known that three kinds of noises are considered in the CMOS circuit: thermal noise and shot noise, which are white noise, and flicker noise or 1/*f* noise. According to the noise theory and the characterizations in (Linares-Barranco et al., 2003) and (Linares-Barranco et al., 2004), the subthreshold noises in the MOSFET are basically contributed by shot noise and flicker noise, and the noise power density S_{ID} is given by

$$S_{ID} = 2qI_D + \frac{KI_D^2}{WLC_{ox}^2}\frac{1}{f} \tag{8}$$

where I_D is the drain–source current of the MOSFET, W and L are the channel width and length, C_{ox} is the gate capacitance per unit area, and q, f, and K represent the unit charge, frequency, and a process-dependent parameter, respectively. In the 0.18-μm technology, the typical value of C_{ox} is about 1.08×10^{-2} F/m², and K is 2×10^{-24} F²/m² for nMOS and 4×10^{-26} F²/m² for pMOS.

By equaling the two terms in (8), one can derive the noise corner frequency as $f_c = KI_D/2qWLC^2_{ox}$. In a W = 10 μm and L = 1 μm sized nMOS, f_c is around 8 Hz when biased at I_D = 1.5 nA, which is no more than 0.1% of the required 10-kHz bandwidth, whereas for pMOS, f_c is two orders lower. In the DNA biosensor, the modulation signal is usually band limited with a typical bandwidth of 10 kHz and a lower frequency of 10 Hz; therefore, shot noise dominates over the whole signal band of interest from the above design.

The noise performance of the ULCA can be characterized by two noise sources v_n and i_n with the corresponding power densities of S_{vn} and S_{in}, which can be calculated as usual by evaluating the output noise current with the input open or shorted to the ground and dividing by the gain. The simplified expressions are reported as

$$S_{in} = 4qI_{\text{ref}}\left(1+\frac{1}{A}\right) \tag{9}$$

$$S_{vn} = \frac{4qAI_{\text{ref}}}{g_{ma}^2} + 2S_{va} \tag{10}$$

where A is the current gain of the ULCA, and S_{va} is the input referred noise power density of the opamp. From (9) and (10), S_{in} and S_{vn} can be reduced by decreasing the input-referred noise of the opamp and the quiescent current I_{ref}, however trading with the power consumption and the bandwidth of the ULCA.

3.4 Mismatch considerations

The performances of the practical circuit also suffer from process fluctuations due to transistor mismatches, e.g., variations of W, L, and threshold voltage V_T , which would induce the input-referred offset (IRO) I_{off}, gain error δA, and bandwidth variation δBW of the ULCA. More specifically, one can find that I_{off} is due to the IROs V_{off} of opamps A_{N0} and A_{P0} and the mismatches of M_0, M_1, M_3, and M_4; δA is caused by mismatches of M_0, M_1, M_3, and M_4; whereas δBW is mainly induced by V_{off} of opamps A_{N1} and A_{P1}. It is known that the variances of W, L, and V_T due to process fluctuations are inversely proportional to the area of the MOSFET; therefore, as a first-order approximation, I_{off}, δA, and δBW are inversely proportional to $\sqrt{WL}$, which can be reduced by increasing the sizes of M_0, M_1, M_3, and M_4 and the input differential pairs of opamps in the ULCA, provided that the bandwidth specification is satisfied.

Incorporating the above considerations on stability, noise, and mismatch, HSPICE simulations are made on the circuit to meet the circuit specification in Table 3, and the optimized quiescent current is designed as I_{ref} = 1.5 nA, whereas capacitors C_0 and C_1 are set to 1 pF. Monte Carlo simulation based on the design kit of SMIC 0.18-μm CMOS technology also shows that I_{off} and BW are within −30~120 pA and 12~16 kHz, whereas $\delta A/A$ is less than ±5%, when the channel length is chosen as L = 1 μm, and the aspect ratios (W/L) of N and P transistor units are 10 and 20, respectively.

3.5 Experiment and discussions

The ULCA is realized in the SMIC 0.18-μm CMOS mixed-signal technology, and Fig. 8 shows the die micrograph of the chip. The box encloses the ULCA circuitry, which occupies about 230 × 80 μm² of the chip area. The performance of the ULCA is measured in terms of gain, bandwidth, noise, offset, etc. The results are shown and discussed in this section.

To test the performance of the ULCA, very large resistors (from 1 to 10 GΩ) are used to convert the voltage into input currents down to the picoampere or sub-nanoampere range, which may further keep the input noise current small since the input noise current spectrum density due to the resistor is inversely proportional to the resistance. The whole circuit is placed in an aluminum box with Bayonet Neill-Concelman (BNC) connectors to shield from unwanted interferences. In the experiment, V_{REF} is biased at 0.9 V to provide maximized input range on both positive and negative directions while satisfying the voltage range specifications in Table 3. The input voltage varies between 1.9 and −0.1 V to provide the positive and negative input currents by replacing the resistors.

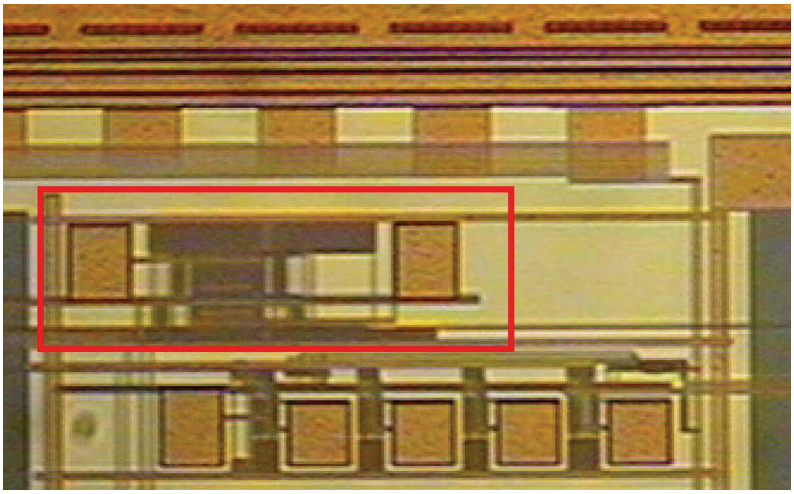

Fig. 8. Die micrograph of the ULCA circuit.

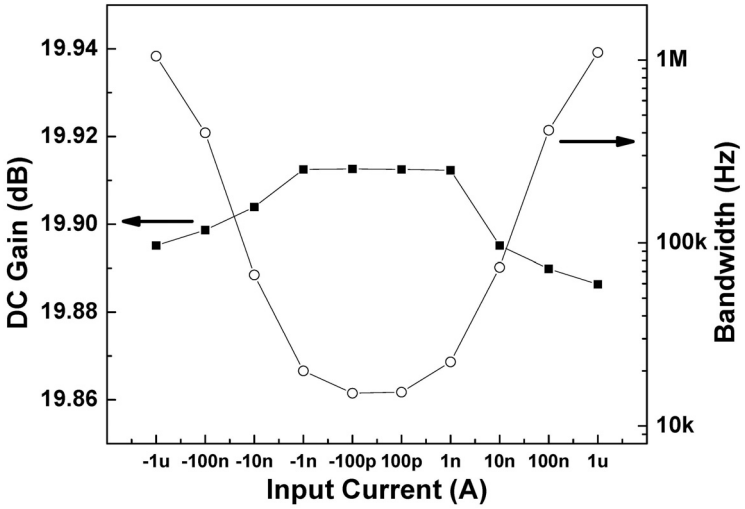

Fig. 9. DC gain and bandwidth as functions of input currents ranging from −1 to 1 μA. The black squares represent the dc gain, whereas the circles illustrate the bandwidth.

The DC gain as a function of input currents ranging from −1 to 1 μA is plotted in Fig. 9, which is 0.5% lower than the designed value of 20 dB and implies about 2% of the overall mismatch on transistors M_0, M_1, M_3, and M_4 due to fabrication variations. The gain error over the input range is less than 0.3%. One can certainly increase the transistor dimensions to further reduce the mismatch and achieve better linearity, however trading with the bandwidth performance.

The bandwidth has been characterized by analyzing the step response of the ULCA, which is cascaded by a commercial transimpedance amplifier, and the result as a function of input

currents is also illustrated in Fig. 9. It can be seen that the bandwidth basically linearly increases with the input current levels on both positive and negative directions from around 20 kHz to 1 MHz. The minimal bandwidth of 15 kHz occurs in the low-input cases, satisfying the 10 kHz requirement in the application. The overshoot of the bandwidth is because the offset of opamps A_{N1} and A_{P1} and the threshold mismatch shift the actual quiescent current of M_0 and M_3 up to around 2 nA (estimated value) from the designed value of 1.5 nA. A larger bandwidth may slightly degrade the noise performance and sensitivity, but it could be adjusted by somewhat tuning the biasing current I_{ref} down for compensation.

The IRO is analyzed by keeping the input open while measuring the mean current at the output and dividing by the gain, which is found to be 96.6 pA at V_{OUT} = 0.9 V. The IRO corresponds to the offsets of opamps and mismatches at the output node; however, it is not critical for the application. One can either slightly modify V_{OUT} for compensation or do the calibration after acquisition and analog-to-digital conversion in the digital domain by a simple subtraction.

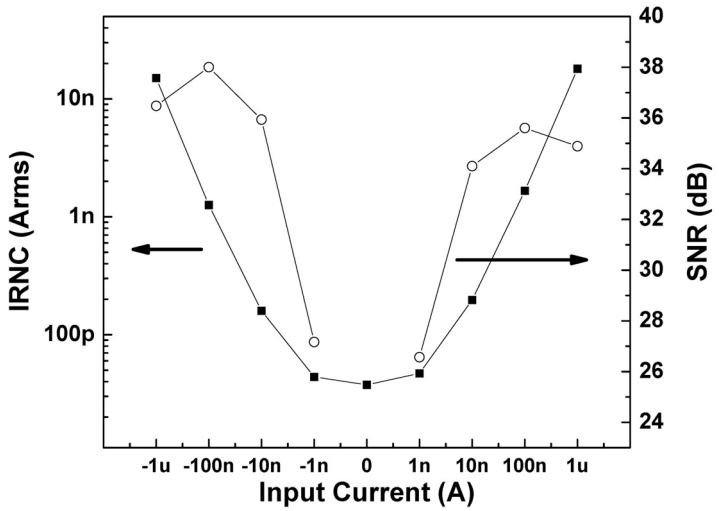

Fig. 10. IRNC and SNR as functions of input currents ranging from −1 to 1 μA. The black squares represent the IRNC, whereas the circles illustrate the SNR.

The noise performance of the ULCA is characterized in terms of the input-referred noise current (IRNC) by measuring the mean-square-root value of the output current fluctuation at each input current level and dividing by the gain. The result is shown in Fig. 10. It is noticed that the IRNC of the ULCA starts at 37.6 pArms at zero input and basically remains at the same level for $|I_{in}| < 1$ nA, whereas it linearly increases for larger input levels. The target current sensitivity of ~100 pA is satisfied. The signal-to-noise ratio (SNR) increases for $|I_{in}| < 10$ nA and gradually saturates at values around 36 dB for larger input levels. The SNR is smaller on the positive input side than on the negative side; this is due to the fact that nMOS exhibits a higher current noise than pMOS. It is worth mentioning that the minimal noise current is larger than the simulated value of 12 pArms but falls in the range provided by Monte Carlo simulation by utilizing parameters from the foundry, which can

be explained from two aspects: 1) the actual quiescent current of M_0 andM_3 is slightly larger than the designed value due to offsets of the opamp; and 2) the mismatches of M_0, M_1, M_3, and M_4 degrade the symmetry of the ULCA topology, thus increasing the noise level.

Linearity is presented by the gain versus input characteristic in Fig. 11. The gain approximately remains at 19.9 dB for the input range of −100 to 100 μA and degrades for larger input levels. The maximal input current is estimated to about ±0.4 mA as determined by the 1-dB (or 10% in the linear scale) degrading point of gain, which implies 141 dB of headroom-to-noise ratio or equivalent to 23 bit. Moreover, depending on the electric properties of the DNA sensor and the buffer solution, the minimal impedance from the biosensor electrode is around 5 MΩ. The input impedance of the ULCA is measured as 15.5 kΩ, which is much lower than the biosensor impedance in the application, satisfying the interface condition.

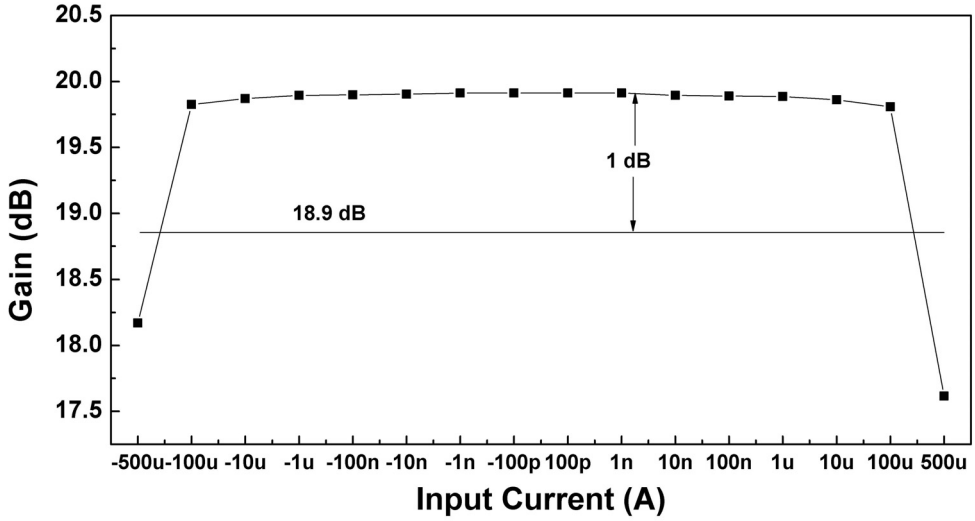

Fig. 11. Gain versus input current over the entire input range.

DC gain	19.9 dB
3-dB bandwidth	15 kHz
Current sensitivity	37.6 pArms
Potential variation	583 nVrms
Input-referred offset	96.6 pA
Input impedance	15.5 kΩ
Max. input current	±0.4 mA
Input dynamic range	141 dB
DC power consumption	35 μW
Power supply	1.8 V

Table 4. Summary of circuit parameter of the ULCA.

A novel subthreshold Class AB ULCA aiming at the application of signal preamplification in the IBS has been demonstrated in SMIC 0.18-μm CMOS technology. Experimental results show that the ULCA completely accommodates the application and can provide a current gain of 19.9 dB, 3-dB bandwidth of 15 kHz, and an input range of −0.4 to 0.4 mA, whereas the IRO and the noise current are less than 96.6 pA and 37.6 pArms, respectively. Table 4 shows the summarized parameters of the circuit. The ULCA can also be used for ultralow current amplification in other types of biosensor interfaces, nanoscale device sensing, and optical sensing in the future.

4. Discussion

4.1 A few trade-offs

In order to accurately acquire signals during the sensing process, CMOS IBS has to work on a stable electrolyte potential, which is precisely controlled by the potentiostat through the reference and counter electrodes from a negative feedback mechanism. The potential variation is mainly due to the offset and noise of the potentiostat OTA. Offset can be reduced by increasing the size of input differential pair of the OTA, or introducing a digital correction circuit via a D/A converter and logics, but trades with the circuit area. On the other hand, noise can be reduced by either increasing the size or biasing current of input differential pair, but trades with the area and power, respectively.

The sensitivity of CMOS IBS is mainly governed by the acquisition circuits, which translates to the IRNC of ULCA. One can reduce IRNC by reducing the DC quiescent current, but trading with the bandwidth required in the biosensing. In some biosening systems with low electrolyte impedance, noise voltage (potential variation on the working electrode) of ULCA also becomes a concern, which also trades with the power and area of the circuit.

In general, interfacing circuits is the bottle neck of the CMOS IBS design. A good design comes with various requirements of a specific biosensing system, which differs from one system to another. Various trade-offs must be considered in the circuit design according to the system specifications as well as power and area budgets.

4.2 Future research

Future research of CMOS IBS covers a number of directions to further improve the efficiency and performance of the system. One of the methods is to incorporate a preamplification step such as polymerase chain reaction (PCR) or rolling circle amplification (RCA) before the electrical sensing, which increases the analyte concentration in the electrolyte and biosensing current level, thus relaxing the sensitivity requirements of the interfacing circuit. Keeping the same sensitivity, one can further shrink the dimension of electrodes and increase the scale of IBS to improve the throughput and sensing efficiency.

As the scale of IBS growing up, asymmetry due to the electrode layout also becomes an issue, because the current density distributes from the counter electrode to all the working electrodes in the electrolyte, which could be quite different from each other depending on the positions. Some structures such as multiple counter electrodes, interlacing electrodes, partition, etc are being investigated. Further research also needs to be invested to characterize the current distribution in the electrolyte for a specific electrode layout when the number of electrode scales up.

From the circuit angle, the sensitivity can be further improved by using the lock-in filtering, which extracts the current only at the vicinity of frequency-of-interest therefore minimizing

the background noise contributions and maximizing the signal-to-noise ratio. The challenge part is that a high resolution A/D conversion is required to translate current signals into digital domain before the digital lock-in filtering. Logarithmic transimpedance amplification is another candidate to achieve high sensitivity and satisfying the bandwidth requirements, while ameliorating the dynamic range limitations by compressing output voltage range. The signal decompress can be realized by digital circuits after the voltage digitization.

5. Conclusion

The CMOS IBS research and production continue to offer a fertile ground for innovation. In this chapter, design considerations on the CMOS IBS interfacing circuits, including the integrated biosensor array, potentiostat, and acquisition circuits, have been introduced. A number of circuit design trade-offs between potential variation, sensitivity, speed, dynamic range, power, and physical area have also been discussed. Finally, future research directions to further improve the IBS performances in terms of efficiency and sensitivity are reviewed.

6. Acknowledgement

This work was supported by the National Science Foundation of China under Grant 60236020 and Grant 90307016, by a grant from Intel, and by a private research grant from Dr. D. Yang.

The authors would like to thank Prof. Y. Chen of the Mechanical and Aerospace Engineering Department, University of California, Los Angeles, for the collaboration with his research team.

7. References

Augustyniak, M.; Paulus, C.; Brederlow, R.; Persike, N.; Hartwich, G. & Schmitt-Landsiedel, D., et al. (2006). A 24×16 CMOS-based chronocoulometric DNA microarray. *ISSCC Digest of Technical Papers*, Feb 2006, (pp. 59–68).

Ayers, S.; Gillis, K. D.; Lindau, M. & Minch, B. A. (2007). Design of a CMOS potentiostat circuit for electrochemical detector arrays," *IEEE Trans. Circuits Syst. I, Reg. Papers*, vol. 54, no. 4, Apr. 2007, (pp. 736–744).

Basu, A.; Robucci, R. W. & Hasler, P. E. (2007). A low-power, compact, adaptive logarithmic transimpedance amplifier operating over seven decades of current, *IEEE Trans. Circuits Syst. I, Reg. Papers*, vol. 54, no. 10, Oct. 2007, (pp. 2167–2177).

Cheng, Y.T.; Pun, C.C.; Tsai, C.Y. & Chen, P.H. (2005). An array-based CMOS biochip for electrical detection of DNA with multilayer selfassembly gold nanoparticles, *Sens. Actuators B, Chem.*, vol. 109, no. 2, Sep. 2005, (pp. 249–255).

Drummond, T. G.; Hill, M. G. & Barton, J. K. (2003). Electrochemical DNA sensors, *Nat. Biotechnol.*, vol. 21, no. 10, Oct. 2003, (pp. 1192–1199).

Han, S.; Yu, H.; Murmann, B.; Pourmand, N. & Wang. S.X. (2007). A High-Density Magneto-resistive Biosensor Array with Drift-Compensation Mechanism, *ISSCC Digest of Technical Papers*, Feb. 2007, (pp. 168-169).

Huang, S.X. & Chen, Y. (2008). Ultrasensitive fluorescence detection of single protein molecules manipulated electrically on Au nanowire, Nano Lett. vol. 8, no. 9, Sep. 2008, (pp. 2829-2833).

Li, Z.; Chen, Y.; Li, X.; Kamins, T. I.; Nauka, K.; & Williams, R. S. Sequence-specific label-free DNA sensors based on silicon nanowires, *Nano Lett.*, vol. 4, no. 2, Feb. 2004, (pp. 245–247).

Linares-Barranco, B. & Serrano-Gotarredona, T. (2003). On the design and characterization of femto-ampere current-mode circuits, *IEEE J. Solid- State Circuits*, vol. 38, no. 8, Aug. 2003, (pp. 1353–1363).

Linares-Barranco, B.; Rodriguez-Vazquez, A.; Huertas, J. L. & Sanchez-Sinencio, E. (1992). Generation, design and tuning of OTA-C high frequency sinusoidal oscillators, *Proc. Inst. Elect. Eng.–G Circuits, Devices Syst.*, vol. 139, no. 5, Oct. 1992, (pp. 557–568).

Linares-Barranco, B.; Serrano-Gotarredona, T.; Serrano-Gotarredona, R. & Serrano-Gotarredona, C. (2004). Current mode techniques for sub-picoampere circuit design, *Analog Integr. Circuits Signal Process.*, vol. 38, no. 2/3, Feb./Mar. 2004, (pp. 103–119).

Mead, C. (1989). *Analog VLSI and Neural Systems*, Addison-Wesley, Boston, MA, U.S.A.

Narula, H. S. & Harris, J. G. (2006). A time-based VLSI potentiostat for ion current measurements, *IEEE Sensors J.*, vol. 6, no. 2, Apr. 2006, (pp. 239–247).

O'Halloran, M. & Sarpeshkar, R. (2004). A 10-nW 12-bit accurate analog storage cell with 10-aA leakage, *IEEE J. Solid-State Circuits*, vol. 39, no. 11, Nov. 2004, (pp. 1985–1996).

Prakash, S. B.; Abshire, P.; Urdaneta, M.; Christophersen, M. & Smela, E. (2006). A CMOS potentiostat for control of integrated MEMS actuators. *ISCAS 2006 Proceedings*, May 2006, (pp. 5555–5558).

Ramirez-Angulo, J.; Carvajal, R. G. & Torralba, A. (2004). Low supply voltage high-performance CMOS current mirror with low input and output voltage requirements, *IEEE Trans. Circuits Syst. II, Exp. Briefs*, vol. 51, no. 3, Mar. 2004, (pp. 124–129).

Rodriguez-Villegas, E. (2007). A low-power wide range transimpedance amplifier for biochemical sensing, *Proc. 29th Annu. Int. Conf. IEEE EMBS*, Aug. 2007, (pp. 2673–2676).

Steadman, R.; Vogtmeier, G.; Kemna, A.; Quossai, S. E. I. & Hosticka, B. J. (2006). A high dynamic range current-mode amplifier for computed tomography, *IEEE J. Solid-State Circuits*, vol. 41, no. 7, Jul. 2006, (pp. 1615–1619).

Thewes, R.; Paulus, C.; Schienle, M.; Hofmann, F.; Frey, A. & Schindler-Bauer, P., et al. (2005). A CMOS medium density DNA microarray with electronic readout. *Materials Research Society Symposia Proceedings*, 869, D3.4.1–D3.4.11.

Zhang, L.; Chang, Y.; Yu, Z.; He, X. & Chen, Y. (2009). Fully integrated CMOS nano-particle assembly circuit for biological detections, *Analog Integr. Circuits Signal Process.*, DOI: 10.1007/s10470-009-9342-6, in press.

Zhang, L.; He, X. & Yu, Z. (2007). Design and implementation of ultra low current sensing amplifier with pico-ampere sensitivity aiming at bio-sensor applications, *Chinese J. Electron.*, vol. 16, no. 2, Apr. 2007, (pp. 247–251).

Zhang, L.; Yu, Z. & He, X. (2009). Design and implementation of ultralow current-mode amplifier for biosensor applications, *IEEE Trans. Circuits Syst. II, Exp. Briefs*, vol. 56, no. 7, Jul. 2009, (pp. 540-544).

13

Intelligent Communication Module for Wireless Biosensor Networks

R. Naik, J. Singh and H. P. Le
La Trobe University
Australia

1. Introduction

Technological advancement, miniaturisation of electronic devices and progress in ad-hoc network routing protocols and embedded systems have facilitated developments in the field of biosensors and biosensor networks. Biosensor networks are a collection of biosensor units that collect information about biological responses and process it in order to make a decision for a desired outcome. In today's market there is a demand for ultra low power consumption, portability and wireless connectivity from the biosensors for information exchange. This chapter introduces a new paradigm of biosensors which have processing capability with an intelligent and adaptive wireless communication module. The adaptive communication module efficiently reconfigures its hardware components according to the changes in operating environment in order to reduce system power consumption and optimally utilise resources. Due to the intelligent wireless communication module, the biosensor unit becomes a state of the art independent system as well as part of a wireless biosensor network (WBSN).
The WBSNs find applications in areas such as medical parameter monitoring, environmental monitoring, chemical/biological detection, food and water analysis, soil monitoring, security and safety. These applications of the WBSNs potentially cover the current market trends and will significantly contribute to benefits of technological advancement for the community.
The chapter is structured as follows. Section 2 presents intelligent biosensor node, its functionality and design requirements. It also discusses the remote patient monitoring application and lists potential applications of WBSNs. Section 3 proposes to use Ultra Wideband (UWB) impulse radio as a communication module for biosensor nodes. It also discusses the potential problems and possible solutions for the use of UWB impulse radio architecture for biosensor node. Digital UWB impulse radio architecture suitable for biosensors is described in section 4. Section 5 discusses the parallelism requirement analysis, proposes real time reconfigurability algorithm (RTRA) and discusses its design requirements. Section 6 presents the design and implementation of the RTRA. Conclusions are drawn in section 7 followed by references in section 8.

2. Wireless biosensor network and applications

A wireless biosensor network consists of a number of biosensor nodes having the capability of communicating with each other in an adhoc network, collecting data, sending them to a

sink/base station (gateway) and receiving instructions from the sink/base station via a wireless network. The WBSN applications require low to medium data communication rates ranging from a few hundreds of Kbps to a few Mbps over a distance range of 10-30m and are categorized under IEEE 802.15.4a standard for wireless sensor networks (IEEE, 2009). A typical wireless biosensor network scenario is presented in Fig. 1 (a).

A modern biosensor node as presented in Fig. 1 (b) consists of a biosensor unit to sense the biological parameters and convert them into equivalent electric quantities. The low power digital signal processing unit analyses these signal and takes decisions according to the application and conditions. The radio block provides the wireless link for communication between the biosensor node and the central base station as well as other biosensor nodes. Information such as the current parameter measurement, the biosensor status and decisions taken are communicated between the biosensors and central base station. In the modern adhoc WBSNs, the decisions taken by a biosensor node are also dependent on this data communication and condition of the network as a whole. The actuator unit is commanded as per the decisions taken to take various actions.

With the above functionality requirements from the various components of the WBSN, ultra low power consumption is the most critical design requirement as the biosensor nodes are battery operated. Every component of the WBSN node has to be designed for low power consumption as it directly affects the system reliability, efficiency and life. In a typical intelligent biosensor node which comprises of a sensing element, signal conditioning circuits, a processing element and a transceiver for communication, more than 50% of power is consumed by the transceiver, of which 80% is consumed by the receiver section (Karl & Willig, 2003). This makes the design of the communication module and its receiver section very critical for WBSN applications.

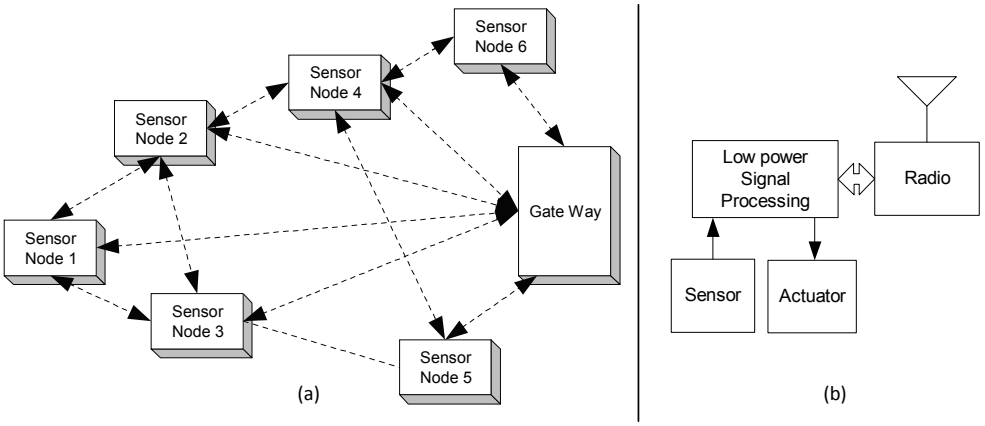

Fig. 1. (a) Typical wireless sensor network scenario (b) Sensor node block diagram

The potential of the biosensor node to sense, communicate, process and act in a WBSN represent a new paradigm for extracting data from the environment and enable reliable monitoring and networking for variety of applications. One of the promising areas of WBSN application is the remote patient monitoring and health care. In this application wearable or implanted miniature biosensors monitor different medical parameters such has heart beat, blood pressure, blood sugar level etc. The data from each body sensor is obtained and sent

over a low data rate wireless link to the central data collection unit at regular intervals of time. This data is then collectively sent for examination via internet or any other long range communication method to remotely placed hospital or medical practitioners. The data is analysed and suggestion can be made regarding medications or the actions to be taken by the medical practitioner. Fig. 2 presents a typical WBSN application scenario for remote patient monitoring.

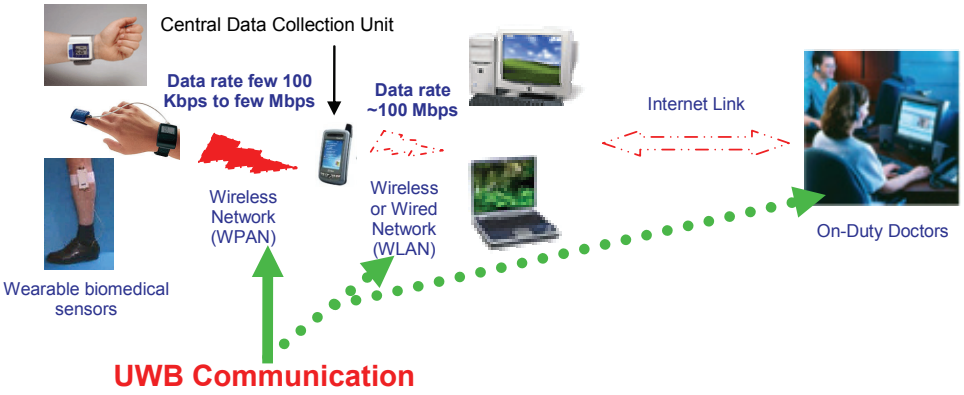

Fig. 2. WBSN application for remote patient monitoring

The remote patient monitoring system will result in a significant reduction in the medical costs, time and efforts, both for patient as well as the medical practitioner. It will improve the efficiency of the medical system and contribute to community wellbeing. Also, it has the potential of low cost implementation and reusability.

In this chapter we propose to use UWB radio for the communication module, as presented in Fig. 2, in the biosensor node due to its low power design and communication potentials which will be discussed in the next section. In addition to the remote patient monitoring system WBSNs with UWB connectivity find applications in a wide range of areas such as:

- Soil monitoring and smart irrigation, which will improve the efficiency of the agriculture industry and save large amounts of water;
- Real time data collection/monitoring for marine and coral research. These WBSNs can be extended to monitor changes in the marine activities and predict unusual weather patterns; and
- Safety of firemen and workers working in extreme conditions by installing bodily biosensors that sense different parameters and communicate to the central unit.

3. Ultra wideband radio as a communication module for WBSN

Low power design of a communication module in a WBSN is very critical due to battery operation. At the same time reliable communication, reusability of components and design flexibility are also important factors. UWB technology can be efficiently employed for the communication module in wireless biosensor nodes because of the following features:

- Capability to achieve data rates of few hundreds of Kbps to a few Mbps at 10-30m distance ranges;
- Wide bandwidth of over 8GHz; from 0 - 960MHz and 3.1 - 10.6GHz;
- Unlicensed communication with limited transmit power in above bands

- Potential for location tracking and precision ranging; and
- System-on-Chip implementation of radio facilitating ultra low power digital design, flexibility and scalability (Porcino & Hirt, 2003).

Digital UWB impulse radio proposed in (O'Donnell & Brodersen, 2005), is one of the most suitable architectures for achieving low data communication rates and potentially low power implementation for WBSNs as it is a carrierless communication scheme that reduces analog circuitry in the receiver. The possibility of digital implementation of the UWB impulse radio provides a potential to achieve low power design. However, due to the channel uncertainties, changes in the channel conditions, low transmit power and pulsed nature of UWB communication the digital UWB impulse receiver architectures use significant parallel hardware to ensure correct operation in these conditions. This parallelism results in high power consumption by the UWB receiver. This will deter the UWB receiver from being employed in WBSNs.

Also, as regulation and standardisation of commercial UWB operation is fairly new, different researchers and industries are attempting to propose various methods of making UWB communication work. Majority of the proposed transceiver architectures use parallel architectures as they concentrate on performance and data rates leading to high power consumption. Limited research attempts on power consumption reduction methodologies leads to a potential gap and provides an opportunity of thorough investigation and proposal of a possible solution for power saving. The research conducted for this chapter is carried out in order to fill those gaps and explore this potential. It presents the thorough investigation and analysis of parallelism requirements for different channel conditions and provides a solution for power consumption reduction by incorporating real time reconfigurability of the parallel blocks in the UWB impulse radio receiver. The reconfiguration of the parallel blocks will result in effective utilisation of the hardware, reduction in average power consumption and at the same time maintenance of data error rate performance as a normal receiver.

4. Digital UWB impulse radio

This section presents the design and functionality of the digital UWB impulse radio transceiver architecture. In the UWB impulse radio transceiver the transmitter uses short Gaussian derivative pulses spread over the 0-960MHz frequency band for communication. The receiver uses coherent detection to recover the data and performs three major operations viz. acquisition and synchronisation of transmitter/receiver, tracking and data detection (Chen, 2002), (O'Donnell & Brodersen, 2005).

4.1 UWB transmitter

The UWB transmitter block diagram is presented in Fig. 3. The binary data to be transmitted is spread using a pseudo random noise (PN) sequence in order to provide system processing gain. The length (N) of the PN code depends on the required processing gain. Any PN code can be used for spreading, but barker code is used in this design due to good cross-correlation with the side-lobe values and uniform distribution. One raw data bit is represented as 'N' bits of PN code individually known as a 'chip'. The entire spread data bit is termed as a 'symbol'. Each chip in the symbol modulates the Gaussian derivative pulse using binary phase shift keying (BPSK) modulation. These modulated pulses are repeated at a certain pulse repetition period (PRP) (PRP=128ns for this design). The transmit packet

consists of a preamble for receiver acquisition and synchronisation operation and data bits which is then sent over the wireless channel (Chen, 2002), (O'Donnell & Brodersen, 2005) (O'Donnell, 2006).

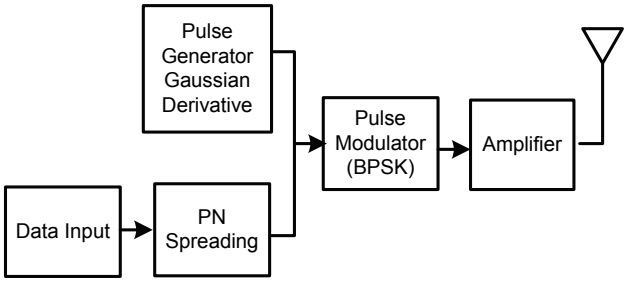

Fig. 3. UWB transmitter block diagram

4.2 UWB Receiver

The analog frontend of the receiver consists of an antenna and amplifier to receive and amplify the signal as presented in Fig. 4. Filtering follows the amplifier, which suppresses interferers in the mobile phone band around 900MHz, frequency modulation (FM) radios and most Very High Frequency (VHF) television signals below 110MHz. A bank of parallel, time-interleaved ADCs, sample the received signal at an effective sampling rate of 2 GHz. The ADC is brought as close as possible to the receiver antenna in order to utilise digital domain processing potential (O'Donnell, 2006).

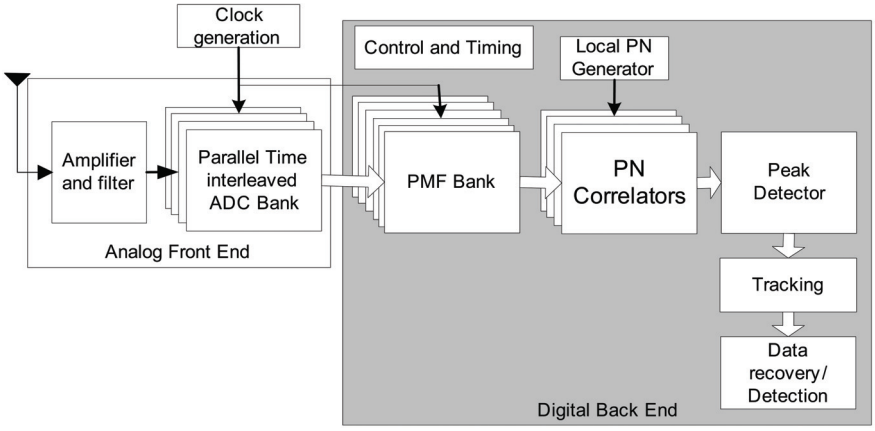

Fig. 4. UWB receiver block diagram

As the bandwidth of the UWB signal is 1GHz, minimum required ADC sampling frequency at the receiver is 2GHz. A single ADC working at 2GHz can be implemented to sample the entire PRP, but its power consumption will be very high. Therefore, a bank of parallel time interleaved 1-bit ADC's, each operating at a much lower frequency is used. This bank consists of 32 parallel ADCs, each sampling the received signal at 62.5MHz to provide an effective sampling rate of approximately 2GHz. As each of the ADC operates at low frequency, power consumption is low. The 1 bit sampling of a 128ns PRP signal at 2GHz

results in 256 bits of the received pulse which are parallel inputs to the digital backend (Chen, 2002), (O'Donnell & Brodersen, 2005) (O'Donnell, 2006).
Clock generation module, bank of parallel digital pulse matched filters (PMFs), bank of parallel pseudo noise correlators (PNCs), peak detector, local PN generator, data recovery and control block together constitute the digital-backend. The digital backend employs a bank of PMFs and PNC to perform acquisition and synchronisation operation followed by tracking and data detection.
Fig. 5 presents the block diagram of the digital backend (Chen, 2002), (O'Donnell & Brodersen, 2005). The banks of parallel PMF's and PNCs perform acquisition and synchronisation operation over the entire preamble. PMF's resolves the time delay in the received pulse to ensure maximum energy capture within the sampling window. Length of the PMF is 128ns corresponding to worst case delay spread of 64ns (O'Donnell & Brodersen, 2005). A single PMF for time delay resolution will need it to operate at sampling frequency of 2GHz which will consume significantly large amount of power and result in longer acquisition time. Therefore, 128 parallel PMF's process the 256 samples of the received pulse simultaneously. Each PMF now operates at pulse repetition frequency (1/PRP) instead of sampling frequency (1/Tsample) due to the parallel operation.

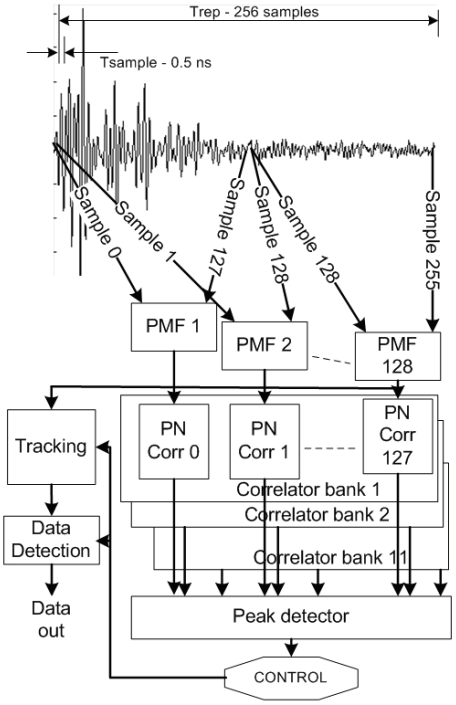

Fig. 5. UWB receiver digital backend (O'Donnell & Brodersen, 2005)

128 PNCs correlate 128 outputs of PMF's, to resolve the PN phase over symbol period. In order to further reduce the acquisition and synchronisation time, 11 such PNC banks operate simultaneously (Chen, 2002), (O'Donnell & Brodersen, 2005). Synchronization is declared once the PMF capturing maximum energy within the PRP and correct PN phase is

detected, by the peak detector. Data detection is then performed with a hard decision, depending on the sign of maximum correlation output.
In the acquisition and synchronisation mode all 128 PMF's and 128 x 11 PN correlators are in operation, where as in data detection, only the one capturing maximum energy is 'on'. Due to this the power consumption in the acquisition and synchronisation mode is high as compared to the data detection.

5. Real time reconfigurability algorithm

In order to meet the ultra low power requirement of WBSNs, it is required to reduce power consumption of the UWB receiver during the acquisition and synchronisation mode. In order to achieve this, the number of parallel PMF's and thus the successive PN correlators used in the acquisition mode needs to be reduced.

5.1 Parallelism requirement

The parallelism in the digital backend facilitates the receiver to cope with the worst case channel condition and different time delays in the received signal. However it is unlikely that always the channel condition will be worst and the receiver would not require all the parallel hardware for successful acquisition and synchronisation. In an indoor environment the received UWB signal is a collection of different paths reflected from different surfaces (walls, ceiling, floor, furniture etc) constituting multipaths and thus delay spread. The UWB indoor channel delay spread may vary from 20ns-60ns (O'Donnell & Brodersen, 2005) (Cassioli et al, 2002). Also in the non line of sight (NLOS) environment the direct path at the receiver may not be the strongest one. Due to the NLOS nature of the environment, different reflected multipaths and transmitter-receiver separation distance a time delay is observed in the received signal. This time delay is resolved by the PMF bank and is an important factor to be considered while collecting the energy from the received pulse.
According to the parallelism analysis in (Naik et al, 2007), time delay in the received signal controls where the maximum received energy lies within the PRP and therefore determines the number of parallel PMF's required for acquisition and synchronisation operation for a particular channel condition. The channel taps (amplitudes of individual reflected paths) also contribute in determining the energy captured by each PMF.
The analysis simulates the acquisition and synchronisation mode using all 128 parallel PMFs and successive PNCs in operation. Transmit signal is passed through 100 different channel impulses generated using IEEE 802.15.4a channel model (Siwiak, 2004). The time delay is varied from 0ns to 50ns for each channel condition and the PMF number capturing the maximum energy as reported by the peak detector for each condition is determined. This number represents the least number of PMF's required to be in operation for successful acquisition and synchronisation operation for the current operating channel impulse and time delay. The analysis results show that:

- Number of PMF's required for processing the received signal for different channel impulses are different;
- For same channel impulses if time delay increases, PMF reported by the peak detector increases significantly; and
- In very few channel impulse cases and higher time delay values all the 128 parallel PMF's are required for operation.

The real time reconfigurability of the parallel blocks according to the changing channel condition and time delay has the potential to reduce the power consumption during the

acquisition and synchronisation mode without affecting the bit error rate performance of the receiver (Naik et al, 2007).

5.2 Real time reconfigurability algorithm proposal and design requirements

The majority of the parallelism of the digital UWB receiver is in the digital backend. The banks of 128 PMFs and 11 x 128 PNCs employed in the digital backend, constitute of more than 80% of its hardware (Chen, 2002). According to the receiver operation presented in section 4.2, the entire bank of 128 PMFs and 11 banks of 128 PNCs each, are in operation simultaneously during acquisition and synchronisation mode (during preamble). On the other hand, in tracking and data detection mode, only three adjacent PMFs and PNCs are in operation. This results in high power consumption in the acquisition and synchronisation mode as compared to the tracking and data detection.

From all the above considerations it can be concluded that, it will be most effective to use as many parallel PMFs and PNCs that are required for receiver operation for the current channel conditions and switch off the remaining ones, for the rest of the acquisition and synchronisation mode. In a very good channel condition only a few PMFs and PNCs would be required for correct receiver operation, therefore, the remaining ones can be switched off to save significant power consumption. This number will increase as the channel condition gets worse. As major percentage of the digital backend hardware will be reconfigured with this strategy, it has the potential to result in significant reduction in the average power consumption. Therefore, reconfiguration of the PMF and PNC banks according to the changing channel condition during majority of the acquisition and synchronisation mode is the most effective reconfiguration strategy.

Fig. 6 presents the block diagram for the proposed real time reconfigurability algorithm (RTRA) architecture. It consists of an estimation block which estimates significant energy received within the PRP and time delay in the received signal for current channel condition. The translation block translates this information into the number of PMF's required and the control block finally generates the enable/disable signals to turn on the required number of PMF's and successive PNCs in the bank and switch off the unwanted ones.

The primary aim of the RTRA is to facilitate average power saving in the acquisition and synchronisation mode of the receiver. The design constraints and important considerations for the RTRA are as follows:

- It should be simple and should introduce least hardware. Its power consumption should be low to justify the power saving;
- The algorithm should perform all the operations in the first few received pulses in order to save as much power as possible in the remaining preamble (acquisition and synchronisation mode); and
- The estimation and translation should be accurate in order to maintain the data detection error rate performance of the receiver.

6. RTRA design and implementation

6.1 Estimation algorithm

The transmitted signal in an indoor wireless channel undergoes reflections from various objects. Thus, the received signal is a collection of all reflected components at different times, called multipaths. Equation (1) represents the generalised channel response.

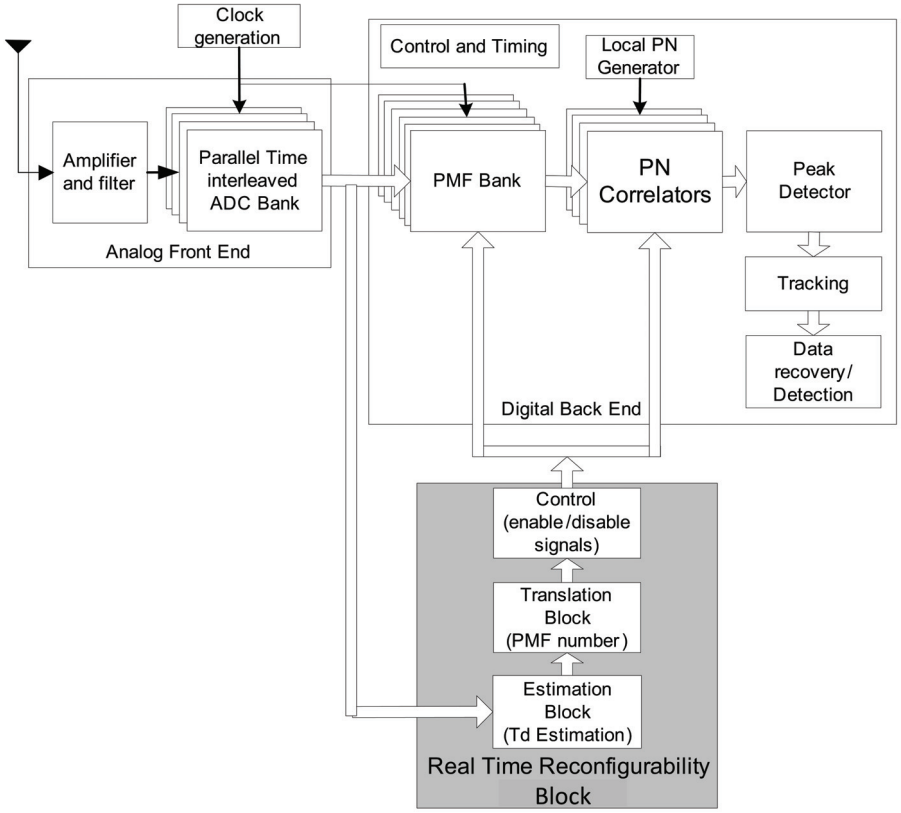

Fig. 6. Real time reconfigurability algorithm architecture

$$h(t) = \sum_{l=1}^{L} a_l \delta(t - t_l) \tag{1}$$

Where a_l is the attenuation, t_l is the time delay, L is the number of multipaths. In the channel response, values of attenuation and time delay change with respect to time and environment of operation Molisch, (2006). A pulse train of Gaussian 1st derivative pulses of width 3ns and PRP of about 128ns is used. Typical channel delay spread varies from 20-60ns (O'Donnell & Brodersen, 2005) (Cassioli et al, 2002), which means that the 3ns transmitted pulse has reflected components and the total energy received can be distributed over 20-60ns within the PRP. Also, due to time delay, the significant energy in the received signal can lie anywhere within the PRP.

For implementing the RTRA, some sort of channel and time delay estimation needs to be performed in order to obtain the information of significant energy received within the PRP. Traditional channel estimation methods are used for BER improvement. For estimation in this case, the aim is to extract sufficient information from the received signal in order to facilitate parallelism reduction. Implementing traditional, complex channel estimation algorithms would not server the purpose in this case as they require very high sampling

rates, additional pilot symbols and perform channel estimation over the entire preamble. Also, majority of them are implemented for offline processing where signal quantisation is not an issue. However, in our case the received signal is quantized for 1-bit resolution. This factor is one of the big challenges for RTRA implementation.

In the estimation block we propose to estimate the location of the last significant energy sample number within the PRP of the received pulse. This last significant sample information can be used to estimate the PMF capturing the maximum energy. This information can be obtained from the first few received pulses and used for translation.

As the received signal is sampled by 1-bit ADCs, the input data for the digital backend is a 256-bit long vector with each bit representing one sample in the received pulse. The last significant sample number estimation becomes as simple as determining the last sample which is '1' within the 256-bit long pulse sample vector and its sample number. For this we propose to use a priority encoder algorithm, which will take the 256-bit vector as input and output 8-bit last significant sample number.

In order to validate this estimation method, received signal pulses for 100 different channel impulses are obtained and last significant sample number is obtained for each case without any quantisation. Later, these received signals are quantized by 1-bit ADC and last significant sample number is estimated for each case using the 256-bit priority encoder algorithm. Fig. 7 presents the last significant sample number determined for no quantisation case and that determined by the priority algorithm after quantisation.

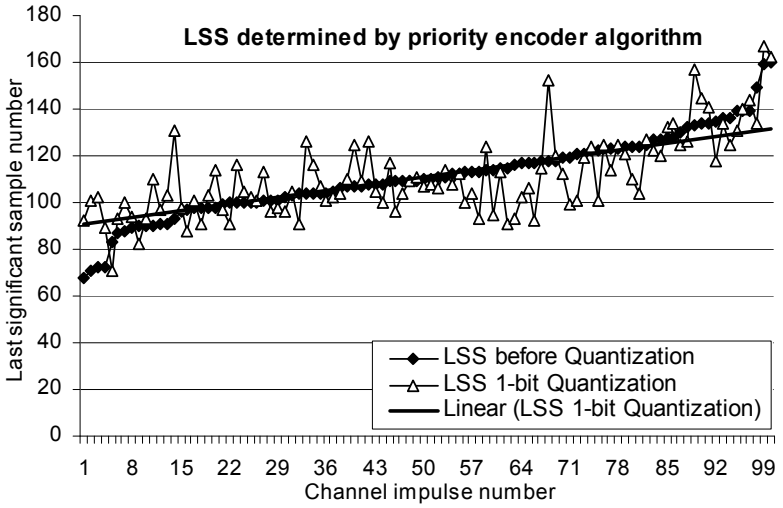

Fig. 7. Last significant sample results for priority encoder algorithm for 1 bit input

It can be seen in Fig. 7 that the last significant sample estimation for 1-bit quantisation by priority encoder algorithm resembles very closely to that with the one without quantisation for majority of the cases. The difference between the last significant sample number values is mainly due to quantisation. The priority encoder can be very easily implemented with less hardware and its processing is fast and simple. The small error between actual and estimated last significant sample numbers can be easily compensated in the translation block.

6.2 Translation and control algorithms

Translation is the process in which the last significant sample information obtained from the estimation block is translated to number of parallel PMFs required for the acquisition and synchronisation operation. For an effective translation, number of PMFs estimated by RTRA (*Tpmf*) should be equal to or more than the PMF reported to capture the maximum energy in a normal receiver (*pmf_ref*), for the same channel condition. If *Tpmf* < *pmf_ref*, then the translation method is said to fail and can cause an error in data detection. However, the probability of data detection error depends on the closeness of *Tpmf to pmf_ref*, due to the energy capture principle.

In translation of the last significant sample information to number of PMFs required for acquisition and synchronisation operation, we assume that the last significant sample lies in the centre of the PMF capturing the maximum energy. This ensures that the translated number of PMFs actually cover the part of the PRP where significant energy is received. Translation method 1 (TM1) is defined by Equation (2) where LSS is the last significant sample.

$$\begin{aligned} &\text{if } LSS \le 64 \text{ then, } \quad Tpmf = LSS/2; \\ &\text{if } LSS \le 191 \text{ then } \quad Tpmf = LSS - 64; \\ &\text{else } \quad Tpmf = 128 \end{aligned} \tag{2}$$

In order to validate the translation method, the transceiver is modeled in simulation environment. PMF numbers reported by the peak detector after acquisition and synchronisation operation for a normal receiver are determined for 100 different channel impulses and time delay varying from 0-50ns. Later, for each of these channel impulses and time delays, estimation is performed using priority encoder and translation is performed using the translation methods. Percentage of failure cases, the figure of merit used to validate the translation methods is the percentage of channel impulses in which *Tpmf* < *pmf_ref*. Fig. 8 presents the percentage failures cases for the translation methods.

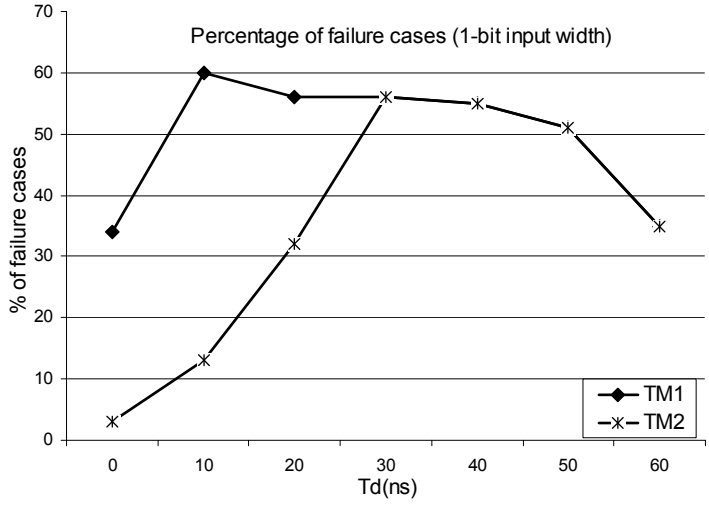

Fig. 8. Percentage failure cases for translation methods (TMs)

It can be seen from Fig. 8 that translation method 1 results in approximately 50% failure cases for most time delay values. However, individual simulations show that *Tpmf* values are very close to *pmf_ref*, which reduces probability of data detection error. Nevertheless, such a high percentage of failure cases for lower time delay values from 0-30ns, may lead to high data detection errors, as significant energy within the PRP may not be captured due to low value of *Tpmf*. However, for higher time delay values, this does not have such an effect as the chances of loosing significant energy is reduced due to higher values for *Tpmf*. Average relative power saving percentage after reconfiguration is estimated assuming that 100% power is consumed when all 128 PMFs are 'on' and is presented in Fig. 9. It shows that the average relative power saving percentage varies from 90% to less than 10% with increasing time delay.

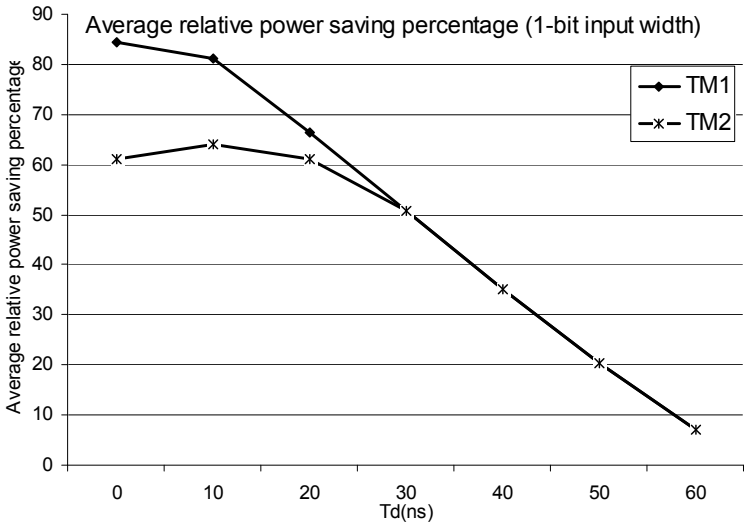

Fig. 9. Average relative power saving percentage

In order to reduce the percentage of failure cases for lower time delay values in translation method 1, translation method 2 uses a guard band of 32 PMFs and is defined by Equation (3)

$$\begin{aligned} &\text{if } \mathrm{Tpmf}_1 \le 32; \quad \text{then } \mathrm{Tpmf}_2 = \mathrm{Tpmf}_1 + 32; \\ &\text{else } \mathrm{Tpmf}_2 = \mathrm{Tpmf}_1 \end{aligned} \tag{3}$$

With the guard band, the percentage failure cases are reduced for lower values of time delays, as seen in Fig. 8. However, this improvement comes at a cost of reduced average power saving, as seen in Fig. 9. Also, probability of data detection error is considerably reduced for lower time delay values.

In order to validate the maintenance data detection error, 5000 sample data bits are used. The data detection error before reconfiguration and after reconfiguration is estimated. Fig. 10 presents the percentage data detection error comparison. The results of this analysis show that the proposed RTRA performs better than normal receiver with 0.5% reduction in the detection error for time delay values of 0-20ns, a marginal increase of 0.6% in detection

errors for time delays of 30-40ns and same detection error for remaining time delays. Therefore, translation method 2 maintains the data detection error. The small increase in data detection error for certain cases can be easily compensated in the error detection and correction block of the receiver.

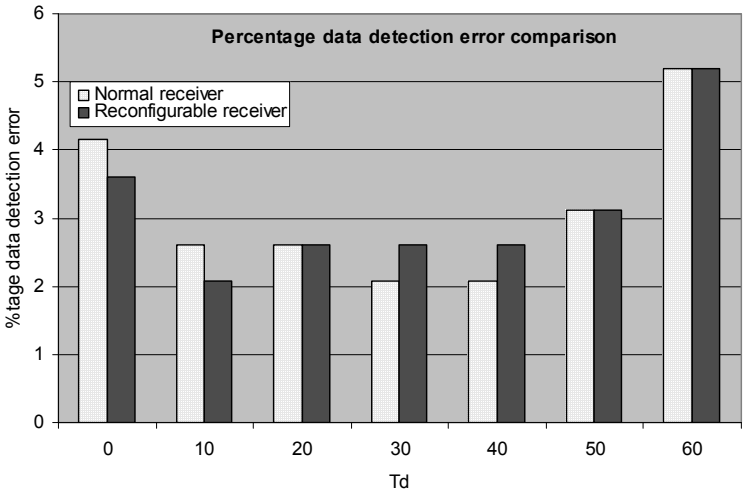

Fig. 10. Percentage data detection error comparison

The percentage data detection error comparison provides enough evidence that the proposed estimation and translation methods can efficiently reconfigure the UWB receiver digital backend and maintain the data detection error rate of the normal receiver. Once translation is done the control block generates enable/disable signals to switch off the unwanted PMFs and PNCs.

6.3 RTRA hardware design

The acquisition and synchronisation mode hardware, which include the PMF and PNC banks, constitutes of 80% of hardware of the receiver digital backend (Chen, 2002). The major percentage of this hardware is the PMF bank. Power efficient hardware design for a single PMF is presented in (Naik & Singh, 2007) is designed to suit the stringent low power design requirements.

In order to simulate the acquisition and synchronisation mode operation of a normal receiver and that with RTRA, a bank of 128 PMFs is implemented with each PMF having an enable signal. A 256-bit input buffer stores the received input samples from the ADC bank. Each PMF in the bank processes consecutive windows of 128 samples each, which are one sample apart. When all the 128 PMFs are enabled, this PMF bank implementation represents normal receiver operation. Fig. 11 presents the block diagram of the PMF bank implementation for the normal receiver. It also presents the RTRA blocks that are added to the normal receiver in order to reconfigure the PMF bank.

For the RTRA, a 256:8 bit priority encoder is implemented as the estimation block, which results in 8-bit last significant sample number. The translation methods presented in equations (2) and (3) are implemented using digital combinational and sequential logic. The translation block results in a 7-bit *Tpmf* value.

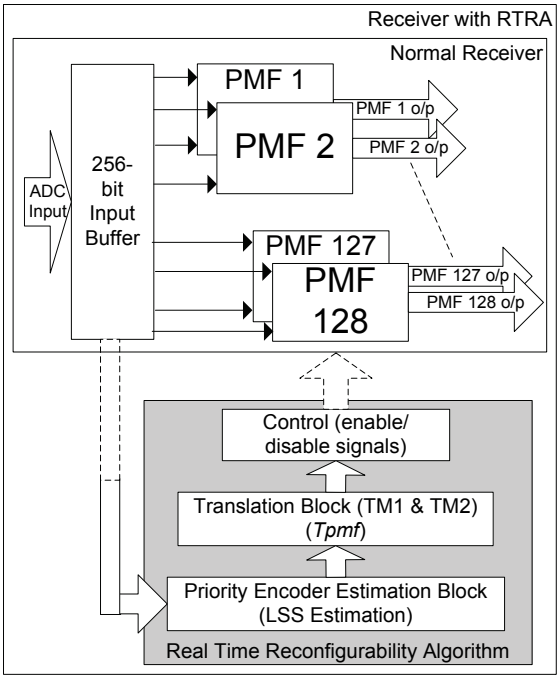

Fig. 11. PMF implementation bank for normal receiver and that with RTRA

Finally the control block is a decoder which decodes the 7-bit *Tpmf* value and generates 128 enable/disable signals which then enable/disable the PMFs according to the changing channel condition.

The PMF bank for acquisition and synchronisation operation for a normal receiver and that with RTRA, as presented in Fig. 11, is implemented using the semi-custom design flow using ST-Microelectronics 90nm technology. Both the designs process received data samples at the same pulse repetition frequency. Fig. 12 presents the post place and route view of the reconfigurable PMF bank for the UWB receiver with RTRA. Table 1 presents the hardware implementation results and the comparison of normal receiver to that with RTRA. The power consumption results are obtained by performing a simulation based power analysis with the input signal for different channel conditions and time delays.

It can be observed in Table 1, that the number of instances, nets, wire length and core area for PMF bank with RTRA implementation for reconfigurable receiver increases as compared to the normal receiver PMF bank due to additional hardware for the RTRA implementation. Due to the simplicity of the estimation, translation and control algorithms of this additional hardware results in a 3.75% increase in area.

The power consumption results show a 25.16% reduction in the core power consumption and 23.76% reduction in the average power for receiver with RTRA over the normal receiver for the test input data. As 90nm process technology is used, leakage power is high and dominates total average power consumption.

These two designs were also implemented on an Altera Stratix II Field Programmable Gate Array (FPGA) device to verify the power saving. A significant 28.57% reduction in the

average current consumption was observed by the PMF bank with RTRA for reconfigurable receiver as compared to that for the normal receiver. The FPGA implementation results correspond with those of the ASIC implementation.

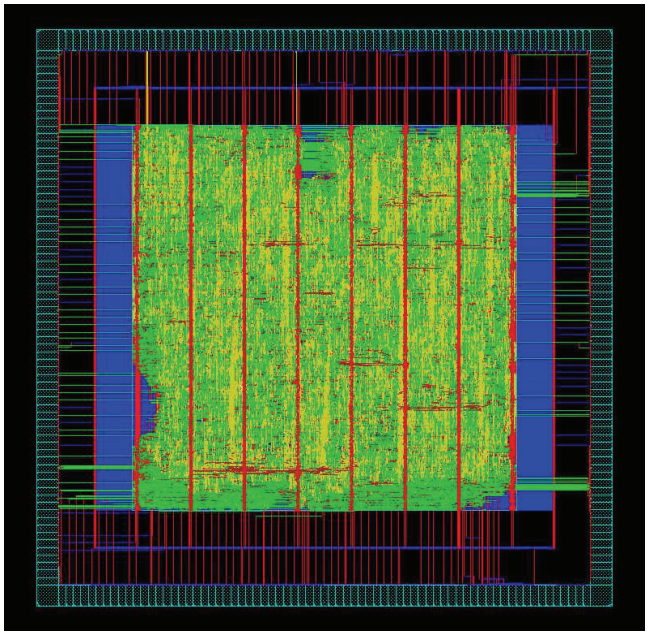

Fig. 12. PMF bank and RTRA post place and route view

Parameter	Normal Receiver	Receiver with RTRA	Relative Comparison
Number of Instances	1202852	1234395	2.55% ↑
Number of Nets	855647	872565	1.93% ↑
Total wire length (µm)	9792686	10495531	6.69% ↑
Area (µm²)	2517148	2611764	3.75% ↑
Core Power (mW)	181.72	135.99	25.16% ↓
IO power (mW)	10.67	10.67	↔
Avg power (mW)	192.38	146.67	23.76% ↓

Table 1. Hardware implementation results and comparision

7. Conclusion

This chapter presented a new paradigm of biosensors which have processing capability with an intelligent and adaptive wireless communication module. The adaptive communication module efficiently reconfigures its hardware components according to the changes in operating environment in order to reduce system power consumption and optimally utilise resources. The chapter presented several significant applications of wireless biosensor networks which hold enormous potential to benefit the community. It also identified that

low power consumption is one of the critical design parameters for biosensor node design due to battery operation and UWB communication is one of the most suitable technologies to be used for communication.

Further the chapter presented the potential challenges of parallel hardware and high power consumption in the UWB receiver architecture and proposed a real time reconfigurability algorithm to address that. The real time reconfigurability algorithm senses the current operating condition and intelligently reconfigures the receiver hardware to optimal size in order to reduce the average power consumption. The results show approximately 25% power saving in the receiver's digital backend with the implementation of the real time reconfigurability algorithm for ASIC as well as FPGA implementations. At the same time the reconfigurability maintains the data detection error rate as the normal receiver. This significantly contributes in reducing the overall system power consumption and makes UWB transceiver a better candidate to be used in the biosensor unit for WBSN applications.

Thus the proposed novel intelligence in the communication module of the biosensor unit is one of the important steps in the development of a sophisticated and smart biosensors and WBSN.

8. References

Cassioli, D.; Win, M. Z. & Molisch, A. R. (2002). The ultra-wide bandwidth indoor channel: from statistical model to simulations, IEEE Journal on Selected Areas in Communications, vol. vol.20, no.6, pp. 1247-1257.

Chen, M. S. W. (2002). Ultra Wide-band Baseband Design and Implementation, *vol. Masters of Science*, Department of Electrical Engineering and Computer Sciences, University of California-Berkeley.

IEEE (2009). IEEE 802.15 WPAN Low Rate Alternative PHY Task Group 4a (TG4a), http://www.ieee802.org/15/pub/TG4a.html.

Karl, H. & Willig, A. (2003). A short survey of wireless sensor networks, *Technical Report TKN-03-018*, Telecommunication Networks Group, University of Berlin, Berlin.

Molisch, A. F. (2006). Time variance for UWB wireless channels, *IEEE P802.15 Working Group for Wireless Personal Area Networks (WPANs),* IEEE P802.15-02/461r0.

Naik, R.; Singh, J. & Le, H. (2007). Investigation of Reconfigurability for the Digital Backend of Ultra Wideband Receiver, *The NASA/ESA Conference on Adaptive Hardware and Systems (AHS-2007),* ISBN: 978-0-7695-2866-3, pp184-189 Scotland, UK.

Naik, R. & Singh, J. (2007). Pulse Matched Filter Implementation for Reconfigurable Ultra-Wideband Receiver, *The International Symposium on Integrated Circuits (ISIC-2007),* ISBN: 978-1-4244-0797-2, pp 473 - 476, Singapore.

O'Donnell, I. D. & Brodersen, R. W. (2005). An ultra-wideband transceiver architecture for low power, low rate, wireless systems, *IEEE Transactions on Vehicular Technology*, vol. 54, pp. 1623-31.

O'Donnell, I. (2006). A Baseband, Impulse Ultra-Wideband Transceiver Front-end for Low Power Applications, *vol. Doctor of Philosophy*, Department of Electrical Engineering and Computer Sciences, University of California, Berkeley.

Porcino, D. & Hirt, W. (2003) Ultra-wideband radio technology: potential and challenges ahead, *IEEE Communications Magazine*, vol. 41, pp. 66-74.

Siwiak, K. (2004). UWB Channel Model for under 1 GHz (VHF and UHF), *IEEE P802.15 Working Group for Wireless Personal Area Networks (WPANs)* IEEE P802.15-04/505r4.

14

Design and Construction of a Distributed Sensor NET for Biotelemetric Monitoring of Brain Energetic Metabolism using Microsensors and Biosensors

Pier Andrea Serra, Giulia Puggioni, Gianfranco Bazzu, Giammario Calia, Rossana Migheli and Gaia Rocchitta
University of Sassari
Italy

1. Introduction

Neurochemical pathways involved in brain physiology or disease pathogenesis are mostly unknown either in physiological conditions or in neurodegenerative diseases. Nowadays the most frequent usage for biotelemetry is in medicine, in cardiac care units or step-down units in hospitals, even if virtually any physiological signal could be transmitted (FCC, 2000; Leuher, 1983; Zhou et al., 2002). In this chapter we present a wireless device connected with microsensors and biosensors capable to detect real-time variations in concentrations of important compounds present in central nervous system (CNS) and implicated in brain energetic metabolism (Bazzu et al., 2009; Calia et al., 2009).
Molecular Oxygen (O_2), an essential molecule for life, is utilized not only for cellular respiration but also for biosynthesis and metabolism of various important biomolecules such steroids, eicosanoids and neuroactive substances (Watanabe et al., 1997). It is also implicated in several biochemical reactions involving, for instance, ATP in the brain (Bazzu et al., 2009). To monitor istantaneous oxygen concentrations and relative variations could give important information about brain energetic metabolism related to glucose (Fillenz, 2005) or lactate consumption (Aubert et al., 2005). Eletrochemical reduction of oxygen is amperometrically obtained by means of complex transformations occurring at a carbon-epoxy sensor surface by applying a potential of -400 mV *vs* Ag/AgCl reference electrode (RE) (Bazzu et al., 2009; Calia et al., 2009) as follows:

$$O_2 + 2H^+ + 2e^- \rightarrow H_2O_2 \quad (1)$$

$$H_2O_2 + 2H^+ + 2e^- \rightarrow 2H_2O \quad (2)$$

Because of its anatomical characteristics and physiology, the central nervous system (CNS) is assumed to be particularly sensitive to oxidative stress (Emerit et al., 2005). Oxidative stress in CNS is now known as responsible for involvement of reactive oxygen species (ROS) and reactive nitrogen species (RNS). This particular kind of stress is crucial for the modulation of fundamental cellular functions as apoptosis, calcium mobilization, ion

transport and all phenomena involved in excitotoxicity (Emerit & Edeas, 2005). Oxidative stress takes place from a disparity, involving the physiological antioxidant capability and free radicals synthesis (Andersen, 2004), so the dynamics concerning antioxidants in CNS are extremely important.

Ascorbic acid (AA) is the most important component of antioxidant pool in the brain (Serra et al., 2002). Low molecular weight antioxidant AA is a water soluble vitamin that owns radical scavenger properties against ROS and RNS (Serra et al., 2002). As it is not produced in human organism but introduced with diet (Hediger, 2002), the presence of a specific transporter (SVCT2) allows its cytosolic internalization in neurons. Ascorbic acid is readily oxidized to dehydroascorbate (DHAA) which can undergo irreversible hydrolysis to 2,3-diketo-L-gulonic acid, but because of its crucial role in CNS, DHAA is easily converted to the reduced form for preventing vitamin C depletion. AA is as well implicated in the protection against excitotoxicity due to high glutamate concentration through ascorbate-glutamate hetero-exchange (Rice, 2000). Ascorbic acid is readily oxidized on epoxy-carbon electrode surface at + 120 mV against Ag/AgCl as follows:

$$\text{L-Ascorbic acid (+120 mV)} \rightarrow \text{DHAA} + 2e^- + 2H^+ \quad (3)$$

Several biologically interesting compounds are not directely oxidizable at a sensor surface, in this case it is needed a biosensor (Pantano et al., 1995). Biosensor combines a trasducer with an enzyme that is capable to give sensitivity and selectivity to the device (Scheller et al., 1997).

Glucose (GLU) is actively involved in ATP synthesis and its concentration in extracellular spaces is the most important factor for energetic metabolism (Lowry et al., 1998; Magistretti et al., 1999, Fillenz et al., 2005). GLU detection is possible by means of loading on a Pt surface transducer glucose oxidase (GOx) enzyme. GOx is covalently linked with flavin adenine dinucleotide (FAD) (Serra et al., 2007) and is extremely reliable because of its good sensitivity to the enzyme substrate and high stability when immobilized on Pt electrodes by means of poly-orthophenylenediamine (OPD) (Wilson et al., 1992; Lowry et al., 1998). The biosensor-based detection of GLU occurs as follows:

$$\beta\text{-D-Glucose} + \text{FAD}^+\text{-GOx} \rightarrow \text{D-Glucono-}\delta\text{-Lactone} + \text{FADH}_2\text{-GOx} \quad (4)$$

$$\text{FADH}_2\text{- GOx} + \text{O}_2 \rightarrow \text{FAD}^+\text{-GOx} + \text{H}_2\text{O}_2 \quad (5)$$

As glucose, lactate (LAC) is an important molecule involved in brain energetic metabolism as product of glicolysys (Fillenz, 2005) or energetic substrate for neurons (Magistretti et al., 1999). LAC is oxidized by lactate oxidase (LOx), an enzyme with a covalently-linked FAD cofactor (Serra et al., 2007). After the oxidation of the substrate, the further oxidation of $FADH_2$ to FAD^+ produces H_2O_2 in the presence of O_2.

$$\text{L-Lactate} + \text{FAD}^+\text{-LOx} \rightarrow \text{Pyruvate} + \text{FADH}_2\text{-LOx} \quad (6)$$

$$\text{FADH}_2\text{- LOx} + \text{O}_2 \rightarrow \text{FAD}^+\text{-LOx} + \text{H}_2\text{O}_2 \quad (7)$$

The application of a positive potential (+700 mV *vs* Ag/AgCl) to a Pt working electrode generates a current proportional to the concentration of the H_2O_2. Reactions occur as follows:

$$\text{H}_2\text{O}_2 \rightarrow \text{O}_2 + 2e^- + 2H^+ \quad (8)$$

where the amount of current produced by the previous oxidation (8) is proportional to the quantity of substrate (GLU or LAC) transformed by the enzyme. The intrinsic chemical characteristics of each indicated molecule allow using specific telemetric devices able to work in oxidation mode (Calia et al., 2009) or in reduction mode (Bazzu et al., 2009; Calia et al., 2009). In this chapter we describe the implementation of a distributed biosensor NET, composed by implantable biotelemetry devices and derived from previously published systems (Bazzu et al., 2009; Calia et al., 2009), successfully used in conjunction with micro-biosensors for the *in-vivo* measurement of brain O_2, AA, glucose and lactate. The analysis of signals derived from the above sensors allowed the real-time study of biochemical pathways involved in brain energetic metabolism. The design, construction and operation of the hardware, firmware and software are described. The proposed system, based on simple and inexpensive components, could be used as a rapid and reliable model for the real-time study of the effects of different drugs on brain neurochemicals and offers the possibility of expanding the biotelemetric NET simply and quickly.

2. Biotelemetric system hardware

The electronic circuit of the implantable biotelemetric device (Fig. 1) was built using surface mount components and comprised two different parts: the amperometric module and the microcontroller/transceiver module.

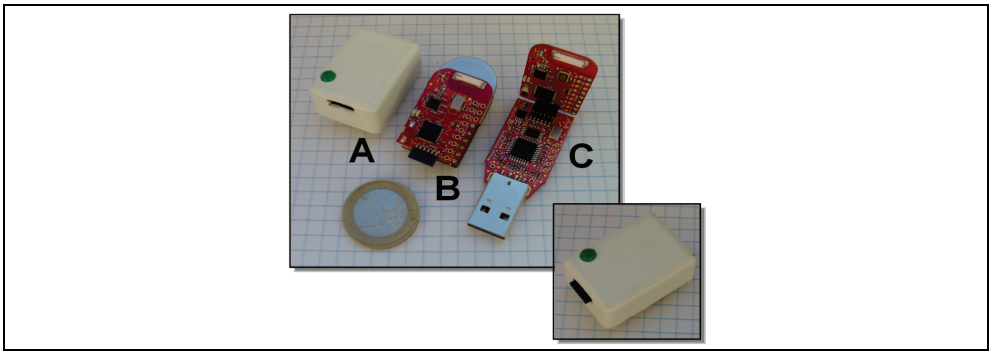

Fig. 1. Pictures showing the biotelemetry system developed during this study (see text).

As schematized in figures 2 and 3, the amperometric module was made soldering a quad operational amplifier (MCP6042), a Zener diode (ZXRE4001), two resistors, a potentiomenter and one capacitor on a 28 mm x 17 mm PCB. The MCP6042 can operate from a single-supply voltage with "rail-to-rail" inputs and outputs; it has been designed for micropower applications consuming only 600 nA per OPA with low input bias current (1 pA) and high input resistance (>$10^{13}\Omega$).

The zener diode plays a pivotal role in the amperometric circuitry; as bandgap voltage reference, it generates a fixed voltage (V_z = 1.22 V) consuming around 10 µA in virtue of a limiting resistance (150K).

The not inverting input of the potentiostat was connected to V_z (Bazzu et al., 2009; Calia et al., 2009) for working with O_2 microsensors (reduction mode, Fig. 2).

In oxidation mode (Fig. 3), the above mentioned input of the potentiostat was grounded resulting in a positive potential applied to working electrode (WE) ranging from ground

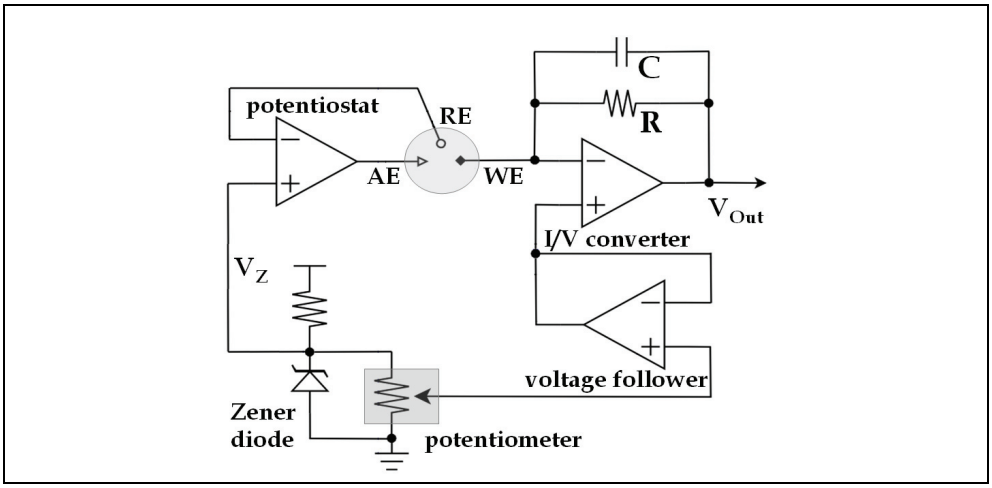

Fig. 2. Schematic of the amperometric module of the biotelemetric device working in "reduction mode".

(GND) to V_z. The inverting input of the potenziostat was directly connected to RE while its output wired to the auxiliary (AE) electrode. This allows the implementation of a feedback circuit in which RE and AE potentials are maintained at the same potential of the not-inverting input (potentiostatic circuit).
The buffered voltage divider, composed by the potentiomenter and the voltage follower, generated the potential necessary to polarize the WE in a range comprised between 0 and 1.22 V (V_z, controlled by ZXRE4001).

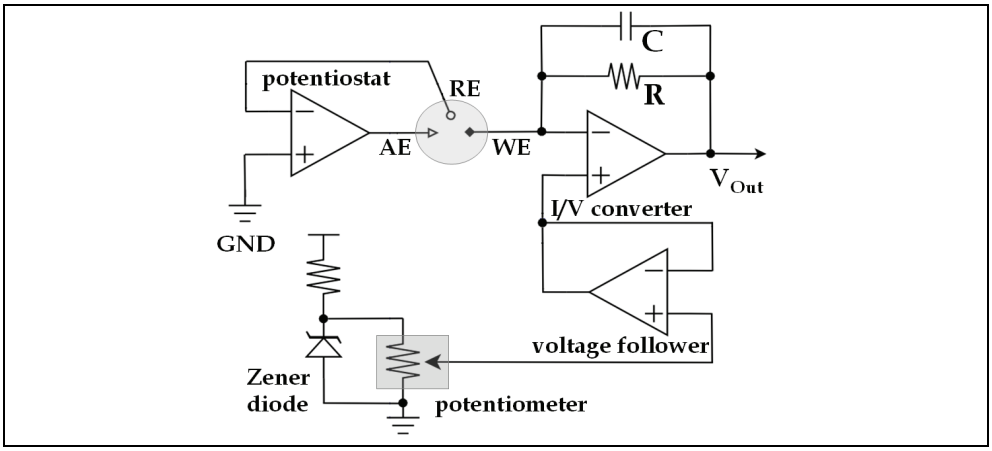

Fig. 3. Schematic of the amperometric module of the biotelemetric device working in "oxidation mode".

The current-to-voltage (I/V) converter is a single-supply adaptation of a classic transimpedance amplifier and derived form a previously-published design (Serra et al., 2007; Rocchitta et al., 2007). The transfer function of the I/V converter is:

$$V_{Out} = -(I_{redox} \cdot R) + V_{App} \quad (9)$$

in which I_{redox} is the current flowing through the WE, R is the feedback resistor and V_{App} is the potential applied to the WE (*versus* ground). For example, working in reduction mode, a current of 0 nA corresponds to V_{App} (0.8 V, -0.4 V *vs* V_z) while with a cathodic current of -30 nA V_{Out} is equal to 0.5 V (R=10MΩ). The maximum allowable current is ≈ -80 nA (V_{Out} = 0.0 V). Instead, when the system is configured in oxidation mode, a maximum anodic current of 18 nA can be read without saturation (V_{App} = 0.7 V; V_{Out} = 2.5 V; R =100MΩ). The feedback resistor (R) has a capacitor in parallel (C) to complete a low-pass filter with a cut-off frequency ($F_{cut-off}$) of 5 Hz. The value of C was calculated in Farads according to the equation:

$$C = 1 / (F_{cut-off} \bullet 2\pi \bullet R) \quad (10)$$

A dummy cell was made based on a previously published design (Serra et al., 2007) for testing the amperometric module of the biotelemetric device before sensors calibration. The aim of the design was to devise a Thevenin current source that would reproduce the constant amperometric response of a true electrochemical cell. The voltage applied to the dummy cell was generated between the WE and RE/AE and is equal to the voltage difference between the above electrodes. The resulting currents were converted in an output voltage (V_{Out}) as illustrated above. Data obtained from electronics calibration are similar to those obtained in previous studies (Bazzu et al., 2009; Calia et al., 2009).

The MSP430F2274 (Texas Instruments, TI) is the heart of the digital module. This is a 16-bit CMOS IC with ultra-low power features equipped with internal 10 bit ADCs. The microcontroller unit (MCU) performed the A/D conversion of V_{Out}, V_{Batt}, V_{App} and in-chip temperature using a 2.5 V internal reference. After the digital signal processing (DSP) of acquired raw data, a serial data packet was generated and sent to the transceiver: the TI CC2500 multi-channel RF transceiver, designed for low-power wireless applications (2.4 GHz).

Several pins of the microcontroller were connected to the CC2500 providing the data lines of the transceiver. In conjunction with the MCU, this component allows the realization of a serial data transmitter working at the speed of 9600 baud. A miniaturized chip antenna was integrated in the PCB board. The in-circuit-serial-programming (ICSP) bus provides the possibility of programming the MCU "on-board" in a few seconds. The digital module (Fig 1B; Fig. 1C) is commercially available pre-assembled by TI (eZ430-RF2500). A 210 mAh, 3 V lithium coin battery (Maxell CR2032) provided the power to the biotelemetric device for up to one week in continuous transmission (1 Hz). A small plastic enclosure (3.2 x 2.1 x 1.4 mm; Fig. 1A) completed the implantable device (Fig. 1B, inset). The weight of the implantable device (Fig.1, inset) is 12.4 grams including battery. A second digital module (wired unit, Fig. 1C), connected to a personal computer (PC) by means of an USB-programmer, coupled the implanted biotelemetric device with the software running on the PC side (Fig. 4).

3. Firmware and software

The firmware to drive the MSP430F2274 MCUs was realized in C language using IAR Embedded Workbench (version 5.20, KickStart) freely available from www.ti.com. The program, which runs on the biotelemetry device, consists of two routines: the main procedure and a timer-interrupt routine called every second as illustrated in Figure 5.

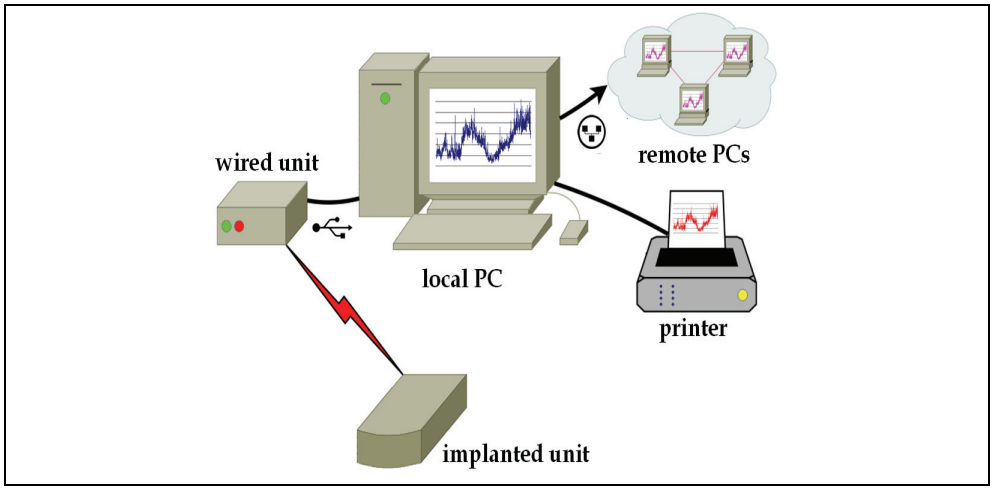

Fig. 4. Schematic of the biotelemetric system developed and used in this study.

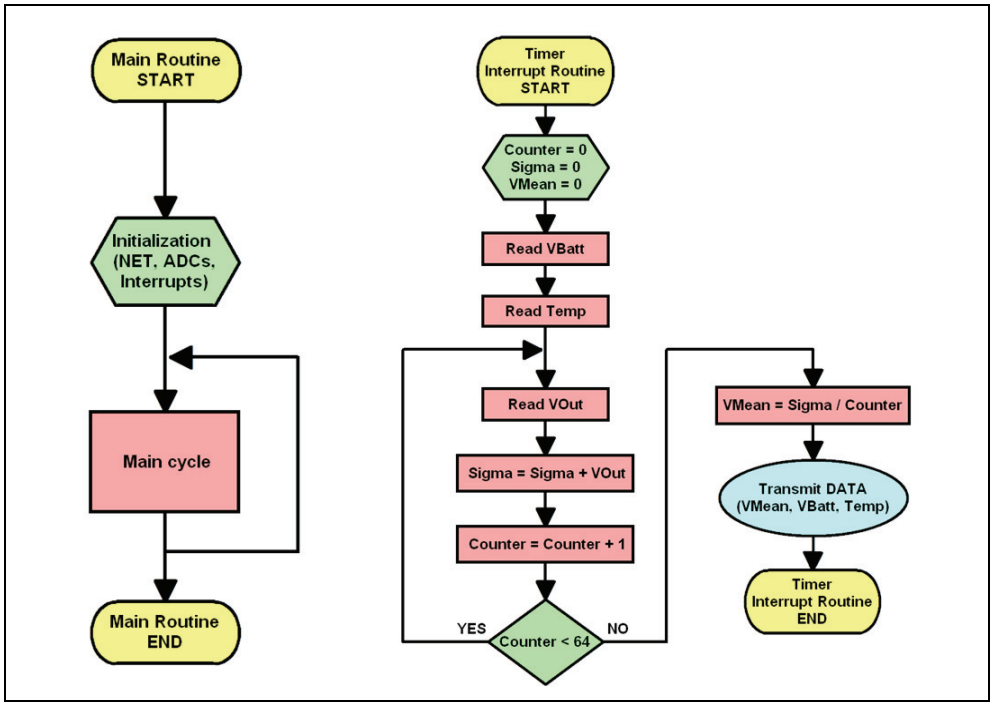

Fig. 5. Firmware running on the implantable biotelemetric device.

When the analogue signal V_{Out} was digitized, the hardware ADC resolution (10 bit) was improved following the oversampling and averaging method (Pagnacco et al., 1997):

$$F_{os} = 4^{w} \cdot F_{s} \tag{11}$$

where w is the number of additional bits of resolution (2), F_s is the sampling frequency (1 Hz) and F_{os} is the oversampling frequency. In accordance with the Nyquist's theorem F_s was calculated as follows:

$$F_s = 2 \cdot F_{max} \tag{12}$$

in which F_{max} has been fixed to 2 Hz. To do that, the MCU acquired and accumulated 64 consecutive samples then divided the result by 2^6 (Fig. 5). This technique increased the ADC resolution from 10 to 12 bits. The RF data packets (1 per second), sent by the MCU, were encapsulated in an Open Source Stack (SimpliciTI™), implemented by Texas Instruments for the development of low power wireless NETs. Up to 100 implantable units, with an 8 bit ID memorized in their E²PROM, can share the same transmission channel. The interrupt-driven routine on the receiver unit, mounting a second MSP430F2274, communicates to the PC using USB and filters the IN-OUT data. The firmware was downloaded to the MCUs using the TI USB programmer connected to the ICSP bus (Fig. 6).

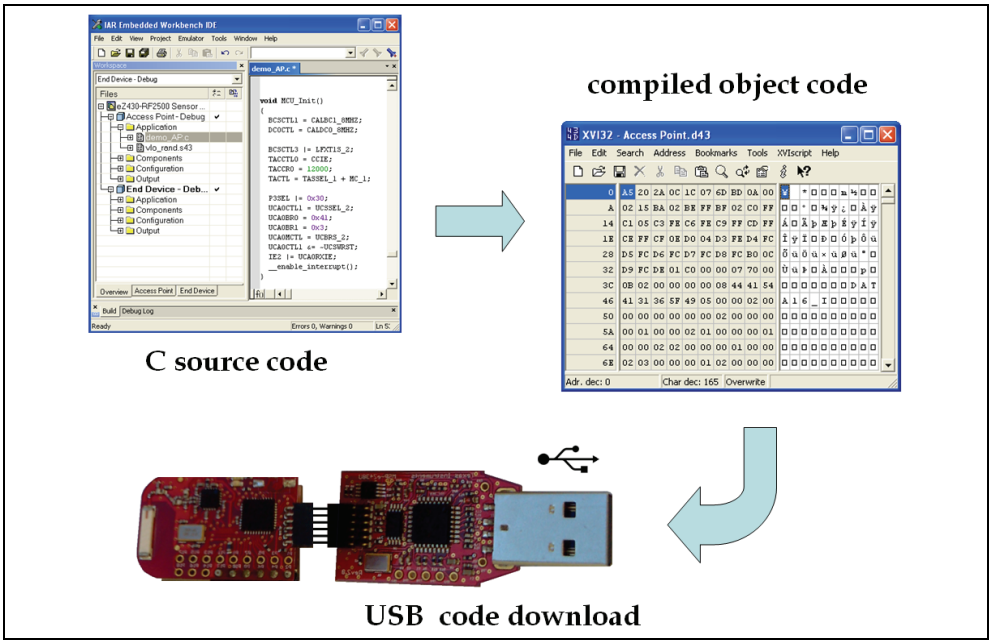

Fig. 6. Program process of MSP430F2274 consisting on edit-compile-download cycle.

The software, running on the PC under Windows XP Professional™ or Vista™, communicates thought the USB by using the low-level driver freely available from www.ti.com. The graphic user interface (Fig. 7) was developed using Profilab Expert® (version 4.0 from Abacom) while the dynamic link library (DLL) serial-data-parser was programmed in C (Dev-C++ ver. 4.9.9.2).

The application (capable of plotting, storing and retrieving data) interfaces the system with a printer via USB and a Local Area Network (LAN) and Internet via TCP/IP (Fig. 4). A software alarm was generated if V_{Batt}< 2.7 V, signal strength (RSSI) too low or a data reception time-out occurred.

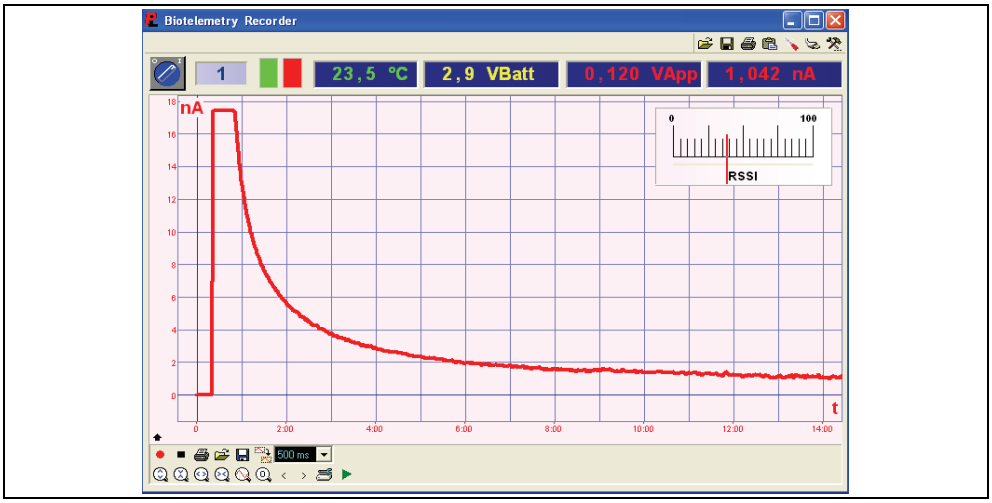

Fig. 7. Simple graphic user interface of the data-acquisition software running on the PC.

4. Statistical analysis

Concentrations of O_2 were expressed in µM while AA, glucose and lactate in mM. Oxygen, ascorbate and H_2O_2 signals were expressed in nA and given as baseline-subtracted data (ΔnA). The sensors *in-vitro* response was characterized immediately before implantation and the electrochemical parameters evaluated before *in-vivo* experiments. The changes of brain tissue neurochemicals were calculated as absolute variations *versus* the corresponding baselines and their striatal concentrations were estimated using pre-implantation *in-vitro* calibrations.

Statistical significance of changes was evaluated using paired t-tests between the means of 300 consecutive recordings before (baseline) and during the maximum magnitude of neurochemical changes as a result of physiological stimulation (tail pinch).

Pearson's correlation coefficient was used to show correlation significance of current variations induced by tail pinches among O_2, AA, glucose and lactate. Immediately after the stimulus application, the first five minutes of raw data (n=300) were compared point-by-point. The null hypothesis was rejected when $p < 0.05$.

5. Design, construction and calibration of oxygen and ascorbic acid microsensors

Oxygen microsensor construction and calibration were performed as previously described (Bazzu et al., 2009; Calia et al., 2009). Briefly, 1 mm silver wire (25 mm in length; Ø=125 µm, Advent Research Materials, Suffolk, UK) was introduced in a silica capillary tube (10 mm in length; I.D. Ø=180 µm, Polymicro Technologies, Phoenix, USA), partially filled with epoxy-carbon (EC) obtained mixing 450 mg of graphite with 350 mg epoxy resin (Araldite-M®, Sigma-Aldrich, Milan, Italy). A 180 µm diameter carbon composite disc electrode was made up and left 12 hours at 60°C. A conical shape was provided to the microsensor by drilling the tip.

The final oxygen microsensors (Fig. 8) had a length about 250 μm, a surface of 0.00145 cm^2 and a tip < 25 μm. Nitrocellulose (NC, collodion) treatment was carried out dipping the microsensor in the collodion solution (4% nitrocellulose in ethanol/diethyl ether) 3 times and drying it for 1 hour at 40 °C after each coating. Cellulose nitrate membrane, because of its hydrophobic properties, sets a barrier for large organic molecules, as proteins, avoiding poisoning of microsensor surface while can be crossed by small charged ions and gases (Bazzu et al., 2009).

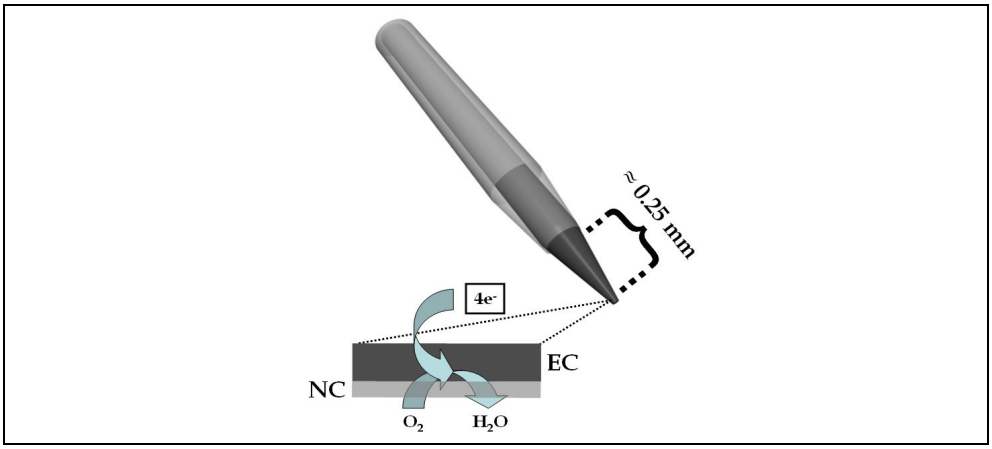

Fig. 8. Schematic representation of the oxygen microsensor used in this study.

O_2 reduction potential was experimentally determined in a previous study (Bazzu et al., 2009) using cyclic voltammetry and fixed at at -400 mV *vs* Ag/AgCl reference electrode. Constant potential amperometry (CPA) was used for *in-vitro* and *in-vivo* calibrations and experiments. No significant interferences were remarked on exposing sensors to other electroactive molecules (AA, UA, DA, DOPAC and HVA) present in the striatal extracellular fluid at pharmacologically significant concentrations (Calia et al., 2009). O_2 microsensor was calibrated by adding known volumes of a standard O_2 solution (100%) to nitrogenated PBS and only sensors with sensitivity lower than 10 μM were chosen. All *in-vitro* calibrations of oxygen microsensors were carried out 24 h after manufacture, immediately before implantation, using a previously-described electrochemical cell (Serra et al., 2007; Rocchitta et al., 2007) appropriately set for oxygen (Bazzu et al., 2009). The calibration (Fig. 9) exhibited good linearity showing a slope of -254 ± 32 pA μM^{-1} of O_2 (R^2=0.999; n=6), in line with previous observations (Calia et al., 2009).

AA microsensors (Fig. 10) were manufactured in the same way as oxygen microsensors without the collodion layer or any further surface modification.

In-vitro calibrations of ascorbic acid microsensors were carried out in fresh PBS at room temperature (25 °C) before implantation. A constant potential of +120 mV was applied and after a stabile baseline was reached, known amount of ascorbic acid stock solution were added to PBS in order to obtain concentrations ranging from 0 to 5 mM.

AA microsensors, calibrated before implantation (Fig. 11), showed good sensitivity and good linearity (2.96 nA ± 0.1 mM^{-1}, R^2= 0.998, n=6).

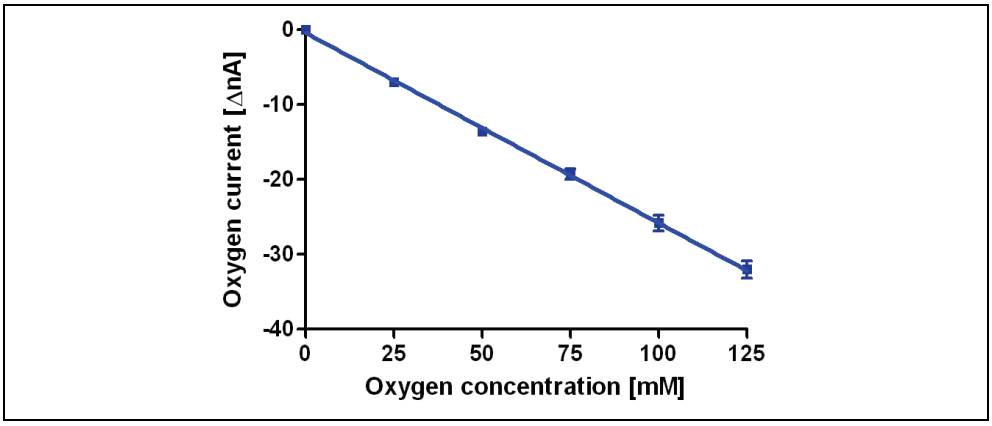

Fig. 9. Oxygen microsensor *in-vitro* calibration.

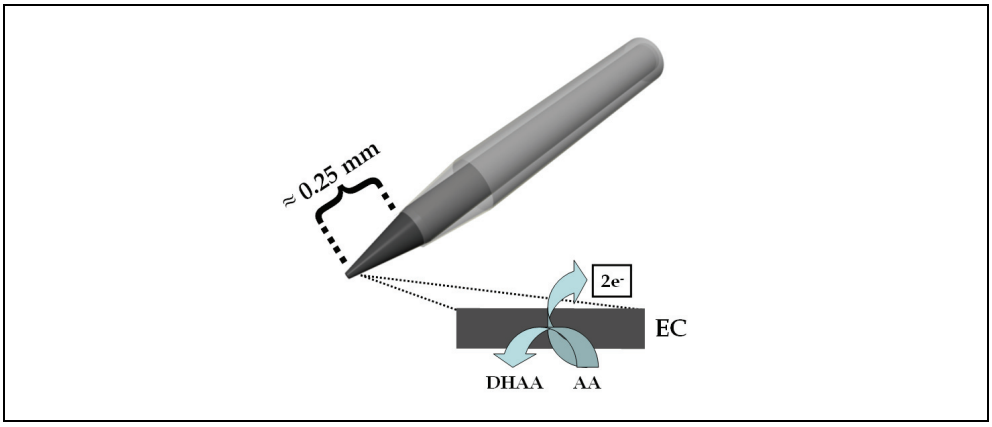

Fig. 10. Schematic representation of the ascorbic acid microsensor used in this study.

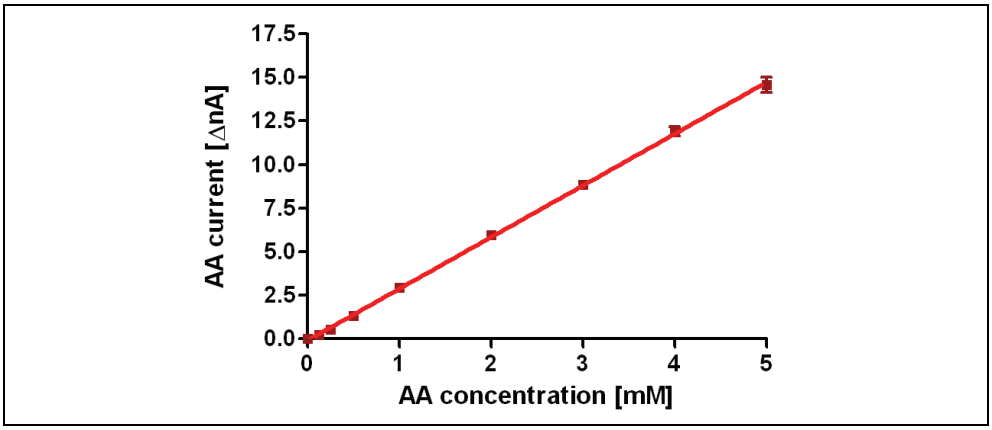

Fig. 11. Ascorbic acid microsensor *in-vitro* calibration.

6. Design, construction and calibration of glucose and lactate biosensors

The design of the glucose biosensors (Fig. 12) has been previously described in detail (Serra et al., 2007). Briefly, 1 mm platinum (Pt) cylinder, obtained cutting Teflon-insulated Pt wire (Ø=125 µm, Advent Research Materials, Suffolk, UK), was immersed for 5 min into a solution of glucose oxidase (GOx) to allow adsorption. After 10 min drying at room temperature, the biosensor was placed in the cell filled with 5 ml of nitrogenated PBS containing the o-phenylenediamine monomer (OPD, 250 mM). The electrosynthesis of poly-o-phenylenediamine (p-OPD) was carried out at +700 mV *vs* Ag/AgCl reference electrode for 15 min. After electropolymerization, the biosensor was stored in fridge (4°C).

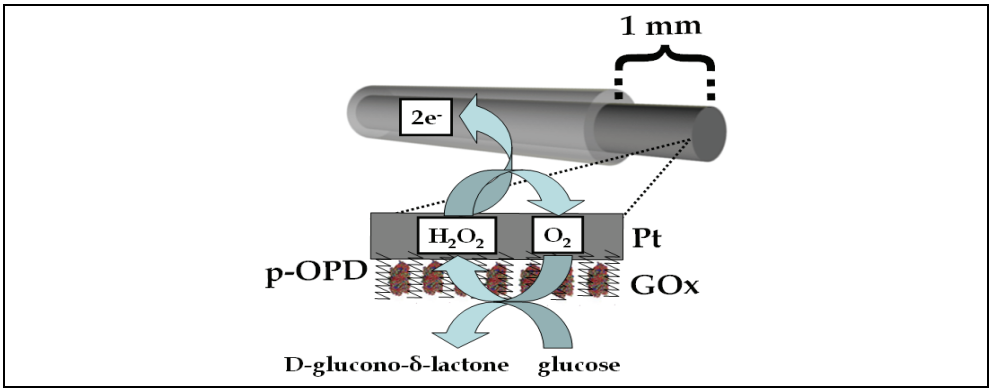

Fig. 12. Schematic representation of the glucose biosensor used in this study.

The *in-vitro* calibration of glucose biosensor was made in air-bubbled PBS performing ten successive injections of glucose (0.2, 0.4, 0.6, 1, 2, 10, 20, 60, 100, 140 mM). The calibration data (Fig. 13) well fitted with the Michaelis-Menten equation (R^2=0.984, n=6) with a V_{MAX} of 59.6±0.8 nA and a K_M of 5.6±0.4 mM. The response to low concentration of glucose (0-2 mM; Fig. 13, inset), revealed excellent linearity (R^2=0.999, n=6) and a slope of 8.9±0.08 nA mM^{-1}.

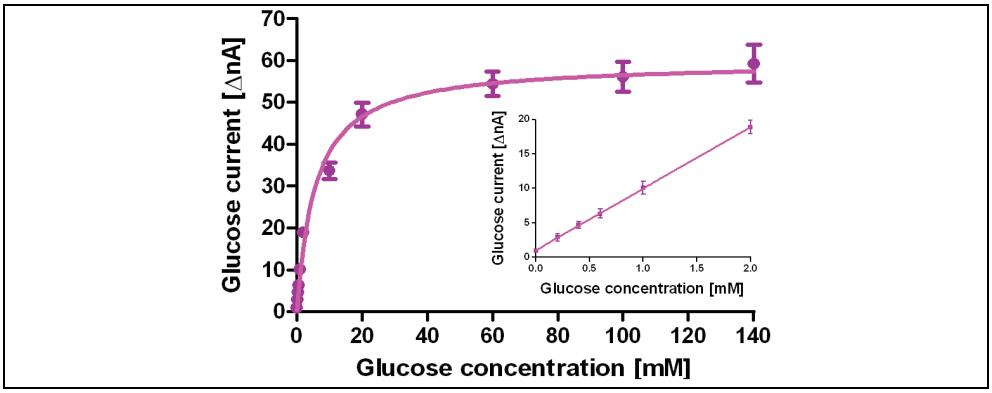

Fig. 13. *In-vitro* calibration of glucose biosensor (see text).

The fabrication of the lactate biosensors (Fig.14) has been derived from a previously described procedure used to make glutamate biosensors (McMahon et al., 2006). A Pt

cylinder (1 mm) was placed in the electrochemical cell containing nitrogenated PBS and OPD monomer and p-OPD was electrosynthesized as previously described for glucose biosensor. The Pt/p-OPD cylinder was immersed (quick dip) into a solution of polyethylenimmine (PEI, 0.5%in water)-LOx (25 U/50 µl of PBS) to allow oxydase adsorption. After 5 min drying at room temperature, the dipping procedure was repeated four times.

With the purpose of increasing the K_M of the biosensor, a diffusion-reducing membrane (Schuvailo et al., 2006) was applied on top of the PEI-LOx layers by dipping the biosensor in a polyurethane (PU) solution (2.5% in tetrahydrofurane). Finally, the biosensor was stored in fridge.

Constant potential amperometry (CPA) was used for *in-vitro* and *in-vivo* experiments fixing the H_2O_2 oxidation potential at +700 mV (Serra et al., 2007) *vs* Ag/AgCl.. All *in-vitro* calibrations were performed in fresh PBS 24 h from sensors' manufacture as previously described in detail (Rocchitta et al., 2007).

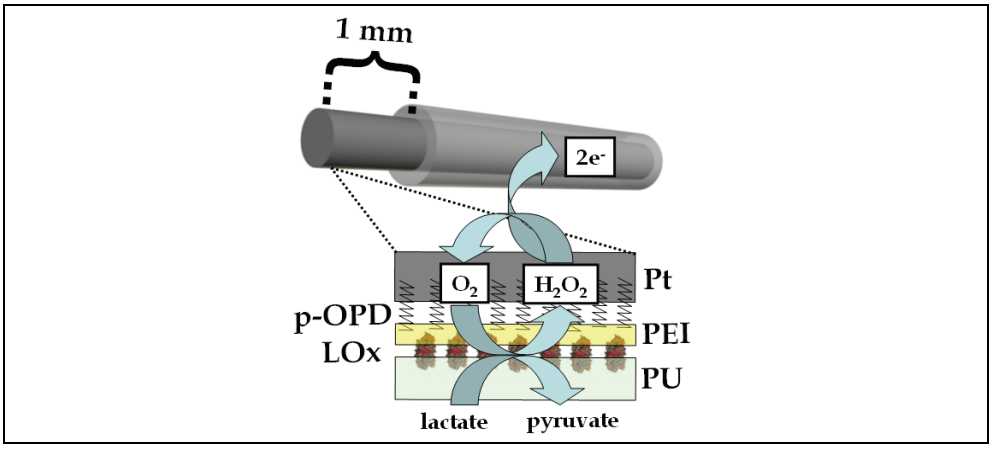

Fig. 14. Schematic representation of the lactate biosensor used in this study.

The *in-vitro* response of lactate biosensor was determined only before implantation adding known amounts of lactate in the electrochemical cell giving concentrations ranging between 0 and 150 mM.

Calibrations showed a classical Michaelis-Menten kinetic (R^2=0.944, n=6) with V_{MAX} and K_M equal respectively to 92.8±2 nA and 8.7±0.9 mM (Fig. 15). Linear region was evaluated at low concentration (0-5 mM) and it showed good linearity (R^2=0.997, n=6) with a slope of 6.7±0.2 nA mM^{-1} (Fig. 15, inset).

No significant interference signals were observed on exposing biosensors to AA or other electroactive molecules present in the striatal extracellular fluid, even at pharmacologically relevant concentrations (Calia et al., 2009).

7. Animals and neurosurgery

Male Wistar rats (Morini R. Emilia, Italy), weighing 250-350 g were used in all experiments. Rats were kept under standard animal care conditions with 12 h light/dark cycle, and room temperature 21°C, food and water ad libitum.

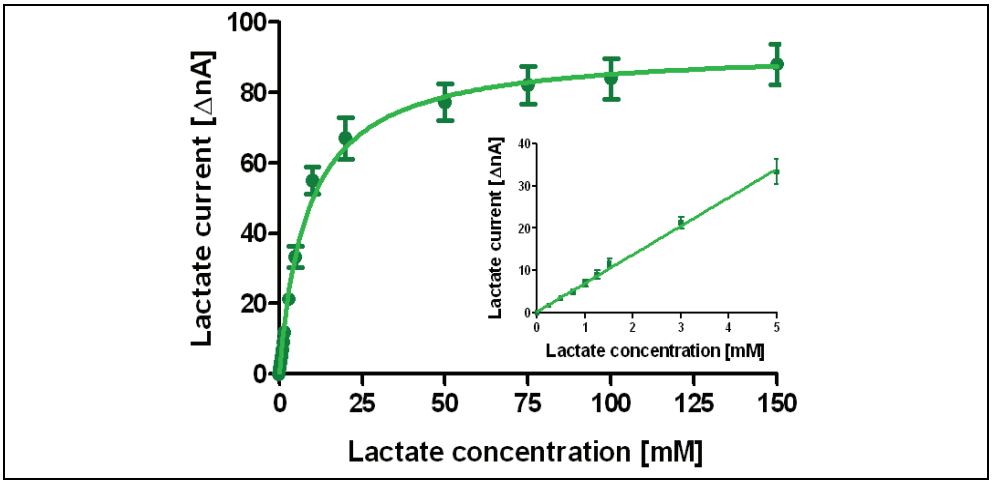

Fig. 15. *In-vitro* calibration of lactate biosensor (see text).

All procedures were licensed under the European Community directive 86/609 included in Decreto No. 116/1992 of the Italian Ministry of Public Health.

Stereotaxic surgery was performed under chloral hydrate (400 mg Kg^{-1} i.p.) anesthesia and body temperature during anaesthesia was maintained at 37 °C by means of an isothermal heating pad.

Before each experiment, the health of the animals was assessed according to published guidelines (Wolfensohn and Lloyd, 2003).

O_2 and AA microsensors, glucose and lactate biosensors were implanted in the right striatum (Fig. 16) using the following coordinates from the atlas of Paxinos & Watson (Paxinos & Watson, 2007): A/P +0.5 from bregma, +2.5 M/L, and -4.0 D/V from dura. Reference and Auxiliary electrodes were implanted in the parietal cortex.

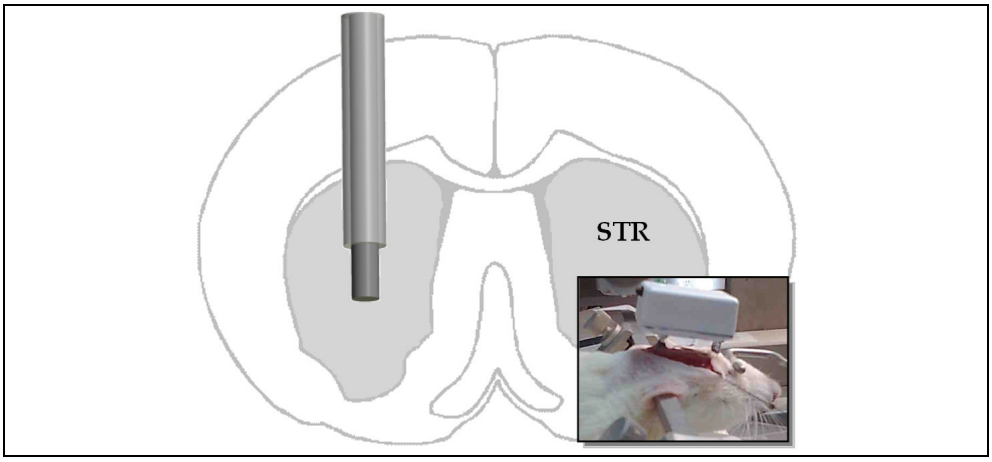

Fig. 16. Amperometric sensor inserted in the right striatum by means of sterotaxic surgery. The sensor was wired to the biotelemetric device fixed to the skull (inset).

The biotelemetric device was fixed by mean of two screws inserted in the skull (Fig. 16, inset), as previously described (Bazzu et al., 2009; Calia et al., 2009).
Following surgery, the animals were housed in large Plexiglas bowls (45 cm diameter), and maintained in a temperature- and light- controlled environment, with free access to food and water. The sensors were connected 24 h after surgery. The monitoring of neurochemicals started with the animal in its home bowl allowing the rat free movement (Fig. 17).

Fig. 17. Biotelemetric device implanted in a freely-moving rat.

8. *In-vivo* experiments and results

Baseline recordings and physiological stimulation were carried out within the first day after stereotaxic surgery, starting 24 h after implantation. The Oxygen microsensor reached a stable baseline (-24.3 ± 2.7 nA) after a period of about 50 minutes from the application of the working potential. Considering that the background current of the microsensor in nitrogen-saturated PBS was -14.2 ± 0.9 nA, it is possible to estimate the concentration of O_2 using *in-vitro* pre-calibration; this was found to correspond to 39.8 ± 7.1 μM, a value in agreement with previous results (Bazzu et al., 2009; Calia et al., 2009). Physiological stimulation as five-minute tail pinch (Fig. 18), administered in order to increase neural activity and to promote regional cerebral blood flow (rCBF), led to an increased motor activity yielding to a striatal O_2 current of -2.97 nA, corresponding to +11.69 μM, statistically different from baseline ($p<0.001$; Fig. 18, inset).
Striatal oxygen dynamics, following physiological stimulation, resulted in a rise in the local O_2 signal, mainly related to an increase of rCBF during neural activation in agreement with previous findings (Bazzu et al., 2009; Calia et al., 2009).
A stable AA baseline was reached after a period of about 25 minutes. The calculated AA baseline corresponded to a concentration of 566 μM, in line with previous findings (Calia et al., 2009). A physiological increase ($p<0.001$; Fig. 19, inset) of striatal AA current (+0.447 nA corresponding to +228 μM) was observed immediately after the administration of a 5 min tail pinch (Fig. 19).

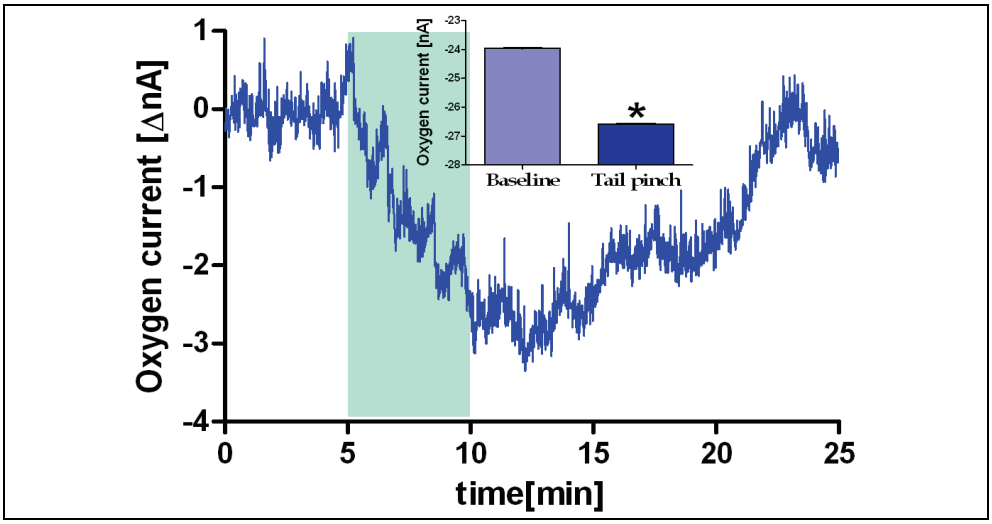

Fig. 18. Effect of physiological stimulation (5 min. tail pinch, vertical band) on striatal dissolved oxygen.

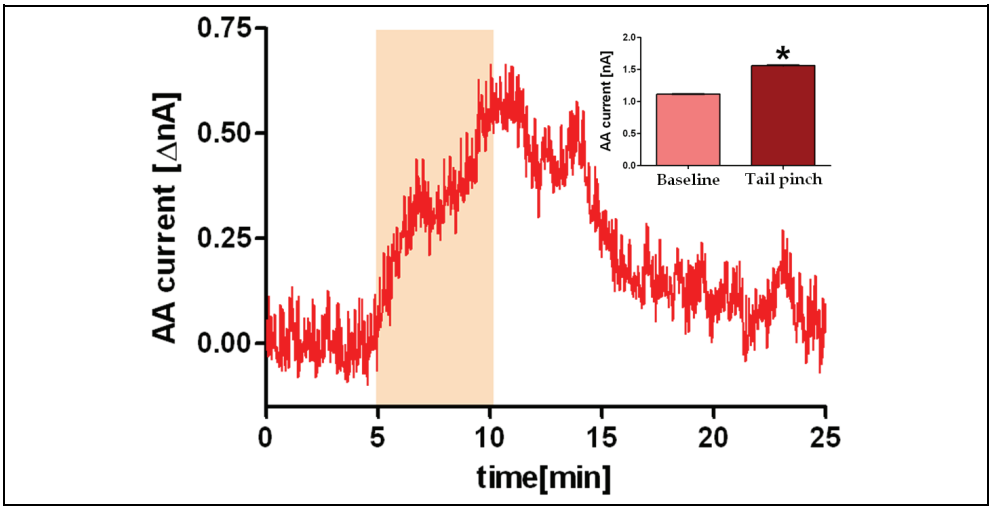

Fig. 19. Effect of a 5 min. tail pinch (vertical band) on striatal AA.

This result is consistent with the activation of the AA/glutamate heteroexchange system (Rice, 2000) in which AA release is related to glutamate release and uptake subsequent to neural activation (Miele et al., 2000).

Glucose biosensor *in-vivo* experiments were carried out using the same procedures as oxygen and AA ones. Thirty minutes after biosensor activation a stable anodic current corresponding to 4.6±0.24 nA (517±26 μM from *in-vitro* calibration) was reached. Physiological stimulation (Fig. 20) produced a significant decrease of glucose signal (-167 μM; Fig. 20, inset) followed by its increase after stimulus suspension.

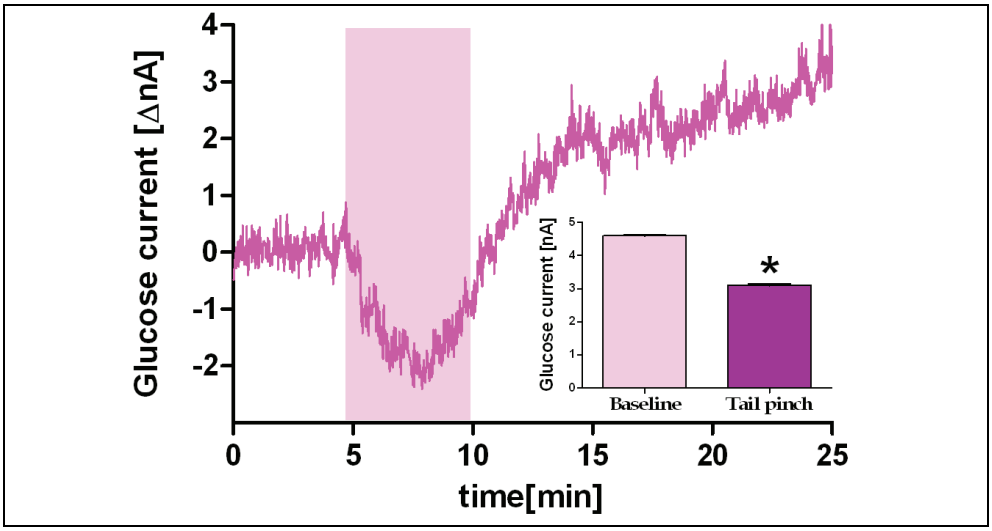

Fig. 20. Effect of a 5 min. tail pinch (vertical band) on striatal glucose.

A stable baseline was observed 40 min after lactate biosensor polarization and corresponded to 5.09±0.43 nA (759±62 μM from the above *in-vitro* calibration). A five-minute tail pinch (Fig. 21) resulted in a significant increase of lactate signal during stimulus administration and after stimulus suspension (+544 μM, $p<0.001$; Fig. 21, inset).

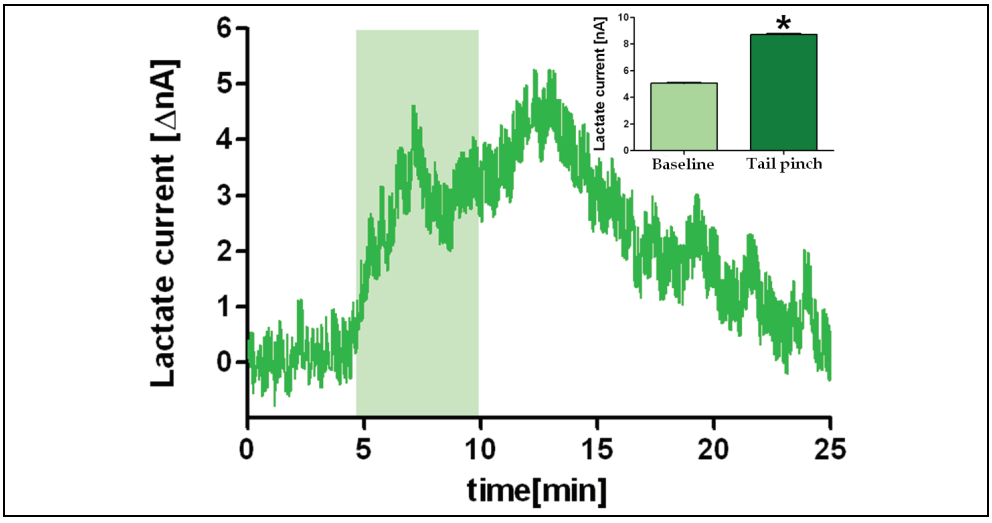

Fig. 21. Effect of a 5 min. tail pinch (vertical band) on striatal lactate.

These results are suggestive of glucose consumption and lactate production during neural activation followed by an increase of extracellular levels of glucose subsequent to astroglial glycogenolysis (Fillenz et al., 1999). Figure 22 shows Pearson's correlation analysis of current variations induced by tail pinches among O_2, AA, glucose and lactate.

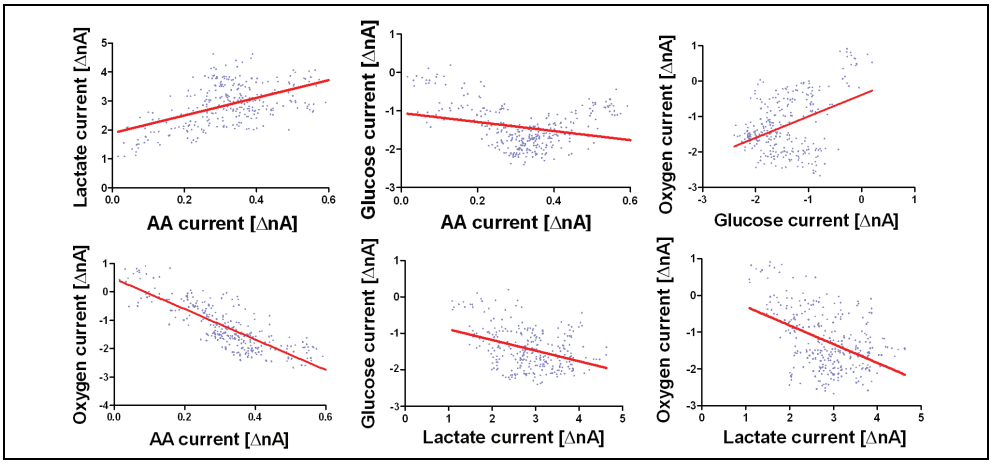

Fig. 22. Pearson's correlation analysis of striatal neurochemical changes during neural activation.

It is important to remember that an increase in anodic currents (AA, glucose and lactate) reflects a striatal increase of the above neurochemicals while an increase in extracellular dissolved O_2 levels, corresponds to an increase in cathodic oxygen current, resulting in a more negative signal. Results of correlation analysis are summarized in Table 1.

	Ascorbic Acid	**Glucose**	**Lactate**
Oxygen	**r = -0.819** P<0.0001	**r = 0.401** P<0.0001	**r = -0.457** P<0.0001
Ascorbic Acid		**r = -0.266** P<0.0001	**r = 0.518** P<0.0001
Glucose			**r = -0.388** P<0.0001

Table 1. Results of correlation analysys of striatal neurochemical changes during neural activation.

After each experiment, rats were sacrificed with an injection of chloral hydrate (800 mg Kg^{-1} i.p.). The location of each sensor was established by post-mortem histology. Brains were fixed in formal saline and 50 μm coronal sections were made with a cryostat. The slices were stained with cresyl violet and examined under a microscope.

9. Discussion and conclusion

In this chapter we have described the development of a distributed sensor NET for biotelemetric monitoring of brain neurochemistry using amperometric microsensors and biosensors. The implantable biotelemetric units, based on simple and inexpensive components, have been successfully used for accurate transduction of the electrochemical signals generated on the surface of the sensors implanted in the striatum of freely-moving rats. At this stage of development the system exhibits high stability and excellent linear response in the nanoampere current range. The choice of low-power CMOS technology makes the project suitable of further improvements such as the reduction of the power

consumption. The use of surface mount components and careful PCB design will make it possible to further miniaturize the circuitry. As result of *in-vivo* experiments, we have shown some preliminary data obtained monitoring important brain molecules during short-time neural activation (5' tail pinch). The study was carried out using new microsensors, biosensors and the newly-developed biotelemetric device in order to record real-time changes of key neurochemical markers of brain bioenergetic metabolism. Indeed, all studied species (oxygen, AA, glucose and lactate) are implicated in brain energetics.

Recently, Castro and coworkers (Castro et al., 2009) proposed a new pivotal role for AA as modulator in the *metabolic switch* between glucose and lactate as energetic substrate of neurons. This review paper, mainly based on *in-vitro* results, summarizes the evidences of the relationships among glutamate, AA, glucose and lactate during neural activation. In figure 23, we repropose the model suggested by Castro, updated on the basis of our *in-vivo* results. In brief, in normal conditions both neurons and astrocytes use glucose as energetic substrate. After neural activation, cortico-striatal endings release glutamate (1) in the striatal extracellular compartment (Miele et al., 2000). Immediately after, GLU is taken by astrocytes from the synaptic cleft and exchanged (Rice, 2000) with AA (2). The *in-vivo* increase of extracellular AA during tail pinch is in accord with this mechanism. The glutamate entry into astrocyte stimulates glucose internalization (3), glycolysis (4) and lactate efflux (5). We observed a reduction of extracellular glucose and an increase of lactate during tail pinch in agreement with this model. Finally, ascorbic acid enters neurons (6) through a specific transporter (SVCT2) and activates the *metabolic switch* (Castro et al., 2009), stimulating lactate uptake in neurons (7) and inhibiting glucose consumption (8). The rise in the local O_2 signal,

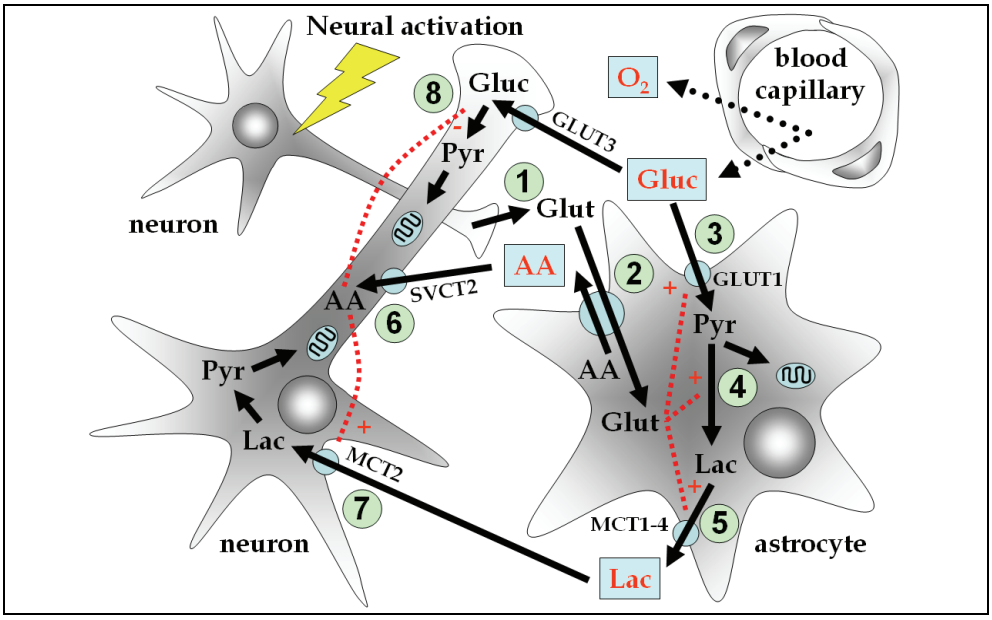

Fig. 23. Neurochemical pathway involved in brain energetic metabolism during neural activation. Glut: glutamate; Gluc: glucose; Lac: lactate; Pyr: pyruvate; GLUT: glucose transporter; SVCT: AA transporter; MCT: lactate transporter.

during neural activation, might reflect an increase of rCBF (Bazzu et al., 2009; Calia et al., 2009). Immediately after the end of the physiological stimulation, AA current inverted its trend and slowly (10 min) returned to baseline levels. Oxygen and lactate currents continued to rise for 5 min after the end of the tail pinch then slowly decreased to baseline levels. The drop of glucose during neural activation was followed by its increase as result of astroglial glycogenolysis (Fillenz et al., 1999). Post-activation data are complex to interpret and suggest the return to normal (inactive) condition with glucose as energetic substrate for neurons. It is important to remember that AA is oxidized to DHAA by ROS and RNS in neurons (Serra et al., 2002). DHAA, secreted in the extracellular space, enters astrocyte through GLUT1 transporter and is back-reduced to AA (Hediger, 2002). A sustained increase of extracellular glucose could interfere with AA/DHAA cycle resulting in oxidative stress, AA loss and neuron damage.
These *in-vivo* results indicate that, during neural activation in physiological conditions, extracellular striatal changes of the above neurochemicals mainly reflect astrocyte response to glutamatergic stimulation. Further *in-vivo* pharmacological studies are necessary to confirm *in-vitro* evidences on bioenergetic substrates used by neurons in different experimental conditions.

10. Acknowledgment

The authors acknowledge the Italian distributors of Texas Instruments for free samples of integrated circuits. The research was supported by the Ministero dell'Istruzione, dell'Universita` e della Ricerca (MIUR, PRIN 2007 fund), University of Sassari (ex 60% fund) and Fondazione Banco di Sardegna.
This work is dedicated to the beloved memory of Giovanna Pisanu who left us too early.

11. References

Andersen, J.K. (2004) Oxidative stress in neurodegeneration: cause or consequence? *Nat. Med.*, 10, 18-25.

Aubert, A.; Costalat, R.; Magistretti, P.J.; Pellerin, L. (2005) Brain lactate kinetics: modeling evidence for neuronal lactate uptake upon activation. *Proc. Natl. Acad. Sci.,* 102, 16448-16453.

Bazzu, G.; Puggioni, G.G.; Dedola, S.; Calia, G.; Rocchitta, G.; Migheli, R.; Desole, M.S.; Lowry, J.P.; O'Neill, R.D.; Serra, P.A. (2009). Real-time monitoring of brain tissue oxygen using a miniaturized biotelemetric device implanted in freely-moving rats. *Anal. Chem.*, 81, 2235–2241.

Calia, G.; Rocchitta, G.; Migheli, R.; Puggioni, G.G.; Spissu, Y.; Bazzu, G.; Mazzarello, V.; Lowry, J.P.; O'Neill, R.D.; Desole, M.S. & Serra, P.A. (2009) Biotelemetric Monitoring of Brain Neurochemistry in Conscious Rats Using Microsensors and Biosensors. *Sensors*, 9, 2511-2523.

Castro, M.A.; Beltrán, F.A.; Brauchi, S.; Concha, II. (2009) A metabolic switch in brain: glucose and lactate metabolism modulation by ascorbic acid. *J Neurochem.*,110(2),423-440.

Emerit, J. & Edeas, M. (2005) Neurodegenerative diseases and oxidative stress. *Eur. Neuropsychopharmacol.*, 15, 100-101.

FCC (Federal Communication Commission). (2000) Commission's Rules to Create a Wireless Medical Telemetry Service; *FCC* : Washington, DC, USA. FCC 00-211, 1-24.

Fillenz, M.; Lowry, J.P.; Boutelle, M.G.; Fray, A.E. (1999) The role of astrocytes and noradrenaline in neuronal glucose metabolism. *Acta Physiol. Scand.*, 167, 275-284.

Fillenz, M. (2005) The role of lactate in brain metabolism. *Neurochem. Int.*, 47, 413-417.

Hediger, M.A. (2002) New view at C. *Nat. Med.*, 8, 445-446.

Leuher, D.C. (1983) Overview of biomedical telemetry techniques. *Eng. Med. Biol.*, 3, 17-24.

Lowry, J.P.; Miele, M.; O'Neill, R.D.; Boutelle, M.G.; Fillenz, M. (1998) An amperometric glucose oxidase/poly(o-phenylenediamine) biosensor for monitoring brain extracellular glucose: In vivo characterisation in the striatum striatum of freely-moving rats. *J. Neurosci. Methods*, 79, 65-74.

Magistretti, P.J.; Pellerin, L.; Rothman, D.L.; Shulman, R.G. (1999) Energy on demand. *Science*, 283, 496-497.

McMahon C.P.; Rocchitta G.; Serra P.A.; Kirwan S.M.; Lowry J.P.; O'Neill R.D. (2006) The efficiency of immobilised glutamate oxidase decreases with surface enzyme loading: an electrostatic effect, and reversal by a polycation significantly enhances biosensor sensitivity. *Analyst*, 131(1), 68-72.

Miele, M.; Mura, M.A.; Enrico, P.; Esposito, G.; Serra, P.A.; Migheli, R.; Zangani, D.; Miele, E.; Desole, M.S. (2000) On the mechanism of d-amphetamine-induced changes in glutamate, ascorbic acid and uric acid release in the striatum of freely-moving rats. *Br. J. Pharmacol*., 129, 582-588.

Pagnacco, G.; Oggero, E.; Morr, D.R.; Berme, N. (1997) Oversampling data acquisition to improve resolution of digitized signals. *Biomed. Sci. Instrum.*, 34, 137–142.

Pantano, P. & Kuhr, W.G. (1995) *Electroanalysis,* 7, 405.

Paxinos, G. & Watson, C. (2007) *The Rat Brain in Stereotaxic Coordinates*, 6th Ed.; Academic Press: San Diego, CA, USA.

Rice, M.E. (2000) Ascorbate regulation and its neuroprotective role in the brain. *Trends Neurosci*., 23, 209-216.

Rocchitta, G.; Migheli, R.; Dedola, S.; Calia, G.; Desole, M.S.; Miele, E.; Lowry, J.P.; O'Neill, R.D.; Serra, P.A. (2007) Development of a distributed, fully automated, bidirectional telemetry system for amperometric microsensor and biosensor applications. *Sens. Actuat. B,* 126, 700-709.

Scheller, F. W.; Schubert, F.; Fedrowitz, J. (1997) Present state and frontiers in biosensorics. *EXS*, 80, 1-9.

Schuvailo, O.M.; Soldatkin O.O.;, Lefebvre, A.; Cespuglio, R.; Soldatkin, A.P. (2006) Highly selective microbiosensors for in vivo measurement of glucose, lactate and glutamate. *Analytica Chimica Acta,* 573, 110–116

Serra, P.A.; Sciola, L.; Delogu, M.R.; Spano, A.; Monaco, G.; Miele, E.; Rocchitta, G.; Miele, M.; Migheli, R.; Desole, M.S. (2002) The neurotoxin 1-methyl-4-phenyl-1,2,3,6-tetrahydropyridine induces apoptosis in mouse nigrostriatal glia. Relevance to nigral neuronal death and striatal neurochemical changes. *J Biol Chem.,* 277, 34451-34461.

Serra, P.A.; Rocchitta, G.; Bazzu, G.; Manca, A.; Puggioni, G.M.; Lowry, J.P.; O'Neill, R.D. (2007) Design and construction of a low cost single-supply embedded telemetry system for amperometric biosensor applications. *Sens. Actuat B*, 122, 118-126.

Watanabe, Y.; Hyllbrant, B.B.; Langstrom, B. (1997) Tracing oxygen metabolism by use of positron emitter Oxygen-15. *Biochem. Biophys. Res. Commun.,* 231, 131-134.

Wilson, R. & Turner, A.P.F. (1992) Glucose oxidase: an ideal enzyme. *Biosens. Bioelectron.,* 7, 165-185.

Wolfensohn, S. & Lloyd, M. (2003) *Handbook of Laboratory Animal Management and Welfare*, 3rd Ed.; Blackwell Publishing: Cornwall, ON, Canada.

Zhou, R.J; Hao, Z.Q. (2002) The present status and development of biotelemetry. *Zhongguo Yi Liao Qi Xie Za Zhi*, 26, 212-214.

15

Information Assurance Protocols for Body Sensors using Physiological Data

Kalvinder Singh[1] and Vallipuram Muthukkumarasamy[2]
[1]*IBM and Griffith University*
[2]*Griffith University*
Australia

1. Introduction

Wireless sensors and actuators have the potential to significantly change the way people live and interact. As the sensors permeate the environment they can monitor objects, space and the interaction of objects within a space. Sensors can monitor a wide range of diverse phenomena by collecting information such as vibrations, temperature, sound, and light. Different sensors have different associated costs. For example, a sensor simply detecting light will have different costs to a sensor recording sound. However, less costly sensors can be used to detect a phenomenon before alerting the more expensive sensors to start their monitoring.

The aging population and the increase of chronic diseases have placed an immense financial burden on health services. Body sensors can be used to help reduce their costs. Sensors can be used to remotely monitor elderly patients suffering from chronic diseases and allow them to have relatively independent lives. The uses of body sensor networks are inherently complex. For instance, blood pressure increasing due to exercise is normal. However, blood pressure increasing while at rest could mean a serious medical condition. Sensors may not just measure physiological values, but also body motions, which can lead to a number of different sensors needing to communicate with each other. As the number of heterogeneous sensors increases, so will the complexity of interactions between the sensors.

There are many different types of sensor environments, ranging from large areas covered by sensors, to many sensors in a small area (Kuorilehto et al., 2005). Different environments have a wide range of varying characteristics. For instance, sensors placed in large open area are not as physically secure as sensors implanted in an individual's body. The protocols proposed in this paper are mainly designed for our home health care system, although these protocols can also be applied to other environments that have similar security characteristics.

Context awareness is an important aspect of body sensor networks (Thiemjarus & Yang, 2006). For instance, blood pressure increasing due to exercise is normal. But if the blood pressure increases while at rest then that could mean a serious medical condition. Sensors may not just measure the physiological values, but also the body motions, and can lead to a number of different sensors needing to communicate with each other.

Figure 1 gives a diagrammatic representation of our proposed home health care system. The diagram shows a patient at home with a number of body sensors that can communicate with

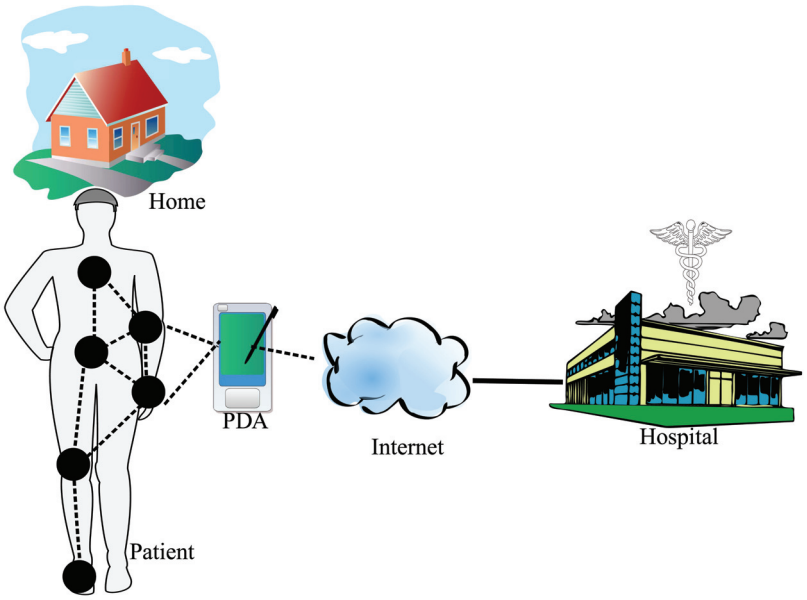

Fig. 1. Architecture and service platform of a BSN for telemedicine and m–health

a camera sensor, the health controller, and a PDA. The cameras may only start recording if the body sensors detect that there may be a medical emergency, such as the patient lying horizontal in the kitchen. Surveillance software, such as S3 (Hampapur et al., 2004), can be used to detect if the patient is cleaning the kitchen, or getting something from the ground, or there actually is an emergency. If the software does detect an emergency, the hospital staff are notified, examine the information, and decide on the best course of action. The PDA is used to give feedback to the patient about the condition of their body, as well as the status of the sensors. The PDA can notify the patient of any detected emergency, allowing the patient to report back a false alarm if one has occurred. The PDA can be replaced with a mobile phone or any other hand held communication devices.

Some of the data recorded from body sensors include the heart rate, blood pressure, temperature, and blood oxygen level. They require a data rate of around 2 bits per second (Balomenos, 2001; Yeatman & Mitcheson, 2006). However, other information sent with the message, such as the location of the sender node (8 bits), a MAC (we have specified the size to be the same as the size of the physiological data), and a counter to stop replay attacks (32 bits) raises the data rate to around 10 bits per second. This paper, therefore, assumes the data rate of 10 bits per second for body sensors. Another type of sensor is a surveillance camera, and the data rate requirement for video streams (Axis, 2007) is much greater than that of body sensors. A single camera normally requires 1–4 Mbits per second bandwidth. Providing secure data transfer between sensors is a requirement for our home health care system.

Health information collected from sensors needs to be secured and in some countries (for example the USA) security is mandated (USA, 2003). Securing a home health care system becomes more difficult mainly because of the different requirements for various components. For instance, the sensors have dramatically more resource constraints than the

constraints found in mobile phones, cameras or desktop computers. With differences in computing power, as well as differences in communication costs, different security protocols may be required throughout the entire system. For instance, an efficient key establishment mechanism specifically for body sensors was created using physiological data (Singh & Muthukkumarasamy, 2007). However, the home health system may send physiological data to medical staff, or to an analytics engine (Espina et al., 2006). The physiological data may also be sent to an actuator to release medicine into the body (Espina et al., 2006).

When the same physiological data is used for more than one purpose (as well as the complexity of a heterogeneous environment), it becomes important from a security or information assurance point of view to have a formal methodology. A formal methodology is also important to insure that the information sent to medical staff and actuators to dispense medicine is accurate, and the correct actions are taken. The formal methodology has a requirement that it can model both the security and privacy aspects as well as the application correctness. In this paper, we show that Behaviour Trees can be used as a formal methodology to verify both the system and the security.

A number of researchers have used environmental data as the only source of secret information to establish keys between body sensors (Bao et al., 2006; Poon et al., 2006; Bao et al., 2005; Bao & Zhang, 2005; Venkatasubramanian & Gupta, 2006). The major benefit of using environmental data is that body sensors can use this information to authenticate that the other sensor is also on the same person and not of another individual. However, these researchers have citepd a number of problems with that approach.

The problems include the following:

- only cryptographically strong environmental data can be used.
- the environmental values can become compromised, in which case the new session key is also compromised.

These problems limit the use of environmental data for establishing keys to only a few cases. The other difficulty our system encounters is in the key establishment scheme of the PDA with sensors at home and in the body. It is envisaged that the patient will simply be users of the system, and will not be able to set up security certificates or keys.

In this paper we propose and develop a number of protocols to address these problems. We show that password protocols can be used to establish keys between body sensors, if passwords are replaced by physiological data. A new protocol is developed to allow a patient to connect a PDA to the home health care system thus able to view information about each of the sensors (ranging from cameras to body sensors). The proposed protocol does not require traditional encryption to transport the new session key. We show that the sensor nodes can establish keys even if no previous shared keys exist between them.

2. Notation

This paper will use the notations shown in Table 2 to describe security protocols and cryptographic operations.

3. Background

A sensor network can consist of many different computing devices. Some have more computational power (and memory) than others. A Body Sensor Network (BSN) is a network of wearable heterogeneous sensors (Aziz et al., 2006). The sensors are spread over

Notation	Description
A, B	The two nodes who wish to share a new session key
S	A trusted server
N_A, N_B	Random numbers generated by nodes A and B respectively
$[[M]]_K$	Encryption of message M with key K to provide confidentiality
$[M]_K$	One–way transformation of message M with key K to provide integrity
K_{AB}, K'_{AB}	The long–term key initially shared by A and B and the new session key respectively
K_{AS}, K_{BS}	Long–term keys initially shared by A and S, and B and S respectively
X, Y	The concatenation of data strings X and Y
$A \rightarrow B$: m	A sends a message m to B
$\underline{m}$	Another way to define sending of message m
$\oplus$	Exclusive–or function

Table 1. Notations

the entire body, and monitor and communicate a range of health related data. BSNs are used in the health industry to monitor a patient's physical and biochemical parameters continuously, in different environments and locations where ever the patient needs to go. BSNs can also be used by athletes to measure their performance. Another use for BSNs is controlling characters in video games (Aziz et al., 2006). Health information collected from sensors needs to be secured and in some countries, for example the USA, security is mandated (USA, 2003).

Key establishment protocols are used to set up shared secrets between sensor nodes, especially between neighbouring nodes. When using symmetric keys, we can classify the key establishment protocols in WSNs into three main categories: Pair–wise schemes; Random key predistribution schemes; Key Distribution Center (KDC). The Pair–wise schemes and Random key predistribution schemes are designed for open environments, where there can be many individual sensors (Liu & Ning, 2007). A difficulty with the above schemes is that updating the keys between the nodes is still an unsolved problem. Another drawback is that, when using the random key predistribution schemes, the shared keys cannot be used for entity authentication, since the same keys can be shared by more than a single pair of nodes (Hämäläinen et al., 2006). The KDC mechanisms by themselves are not suitable for large scale WSN environments, although combinations of a KDC mechanism and the previously mentioned schemes have created hybrid protocols (Chan & Perrig, 2005). Some of the limitations with using a sensor node as a KDC mechanism are:

- The KDC scheme relies upon other schemes to create the trusted intermediary.
- The key sizes in sensor nodes are not large enough, so over a period the key between the sensor and the trusted intermediary may become compromised. If the KDC protocol messages were captured and saved by an adversary, then the adversary may calculate the new keys created.
- Some sensor networks may not need an encryption algorithm, although KDC protocols require an encryption algorithm to encrypt the new key.

A password has been proposed as a way to initiate key establishment (Singh et al., 2006). However, the use of a PIN code or a password is not applicable to BSNs since many of the sensors do not have a user-interface. Sensors also may be placed in hard–to–reach places, with some of the sensors implanted into the body. To complicate matters, the sensors may

harvest energy directly from the body (Kansal & Srivastava, 2005), thus allowing the sensors to exist for long periods of time. Updating keys is therefore an important function.
This paper uses the generic name Secure Environmental Value (SEV) referring to sensed data that can be obtained by sensors in an environment. The SEV is usually hard to obtain through other means. Examples of an environment where SEVs may be found include:

- Human body, where it is difficult to attach a device on the body without the knowledge of the person.
- A secured location, for instance a military base or unmanned vehicle, such as UAVs, or a secure home environment.
- Hard to reach places, for instance a satellite in orbit.

The example environment used in this paper is the human body, where BSNs have been developed to measure the physiological values found in individuals (Aziz et al., 2006). Health sensors can use Inter–Pulse–Interval (IPI) (Poon et al., 2006) or Heart Rate Variance (HRV) (Bao et al., 2005) as good sources for cryptographically random numbers and the physiological values can be used as a one–time pad. Protocols (Venkatasubramanian & Gupta, 2006; Bao & Zhang, 2005) have been developed that used these physiological values to encrypt a new key between a sensor pair. For instance, Venkatasubramanian and Gupta(Venkatasubramanian & Gupta, 2006) used a single message to send a new key to the neighbouring sensor node, as shown in Protocol 1.

Protocol 1 Venkatasubramanian BSN protocol

$A \rightarrow B : N_A, [N_A]_{RANDKEY}, RANDKEY \oplus SEV$

Venkatasubramanian and Gupta noted that finding additional cryptographically sound physiological values is still an open research problem. Only cryptographically strong physiological values, such as IPI and HRV, can be used. Also, modern wireless technology (ultra wideband – UWB, radar (Staderini, 2002)) may be used to remotely capture the heart rate. It may encounter security risks when only using IPI and HRV to secure the communication. Other cryptographically weaker physiological values, such as blood pressure, and iron count, are less susceptible to those remote attacks.

4. Using physiological data to establish keys

Even though PINs and passwords may not be used in body sensors, we show that password protocols can be used. Passwords have low randomness, and therefore have similar characteristics to many SEVs. A four digit PIN contains less than 14 bits of randomness and can be used in a password protocol. A typical password length of eight characters has less than 48 bit of randomness, if we randomly choose upper and lower case letters as well as the digits 0 to 9. We investigate the suitability of password protocols for the sensor environment. Password protocols have the special property of allowing secrets with small entropy to be used for key establishment. Password protocols are designed so that both off–line and on–line attacks are not feasible. A feature or by–product of most password protocols is that if the password is compromised, then any keys created before the password was compromised will not be compromised.
Key sizes in sensor networks are small, normally 64 bits, so that the encryption or integrity tests do not consume a large amount of energy (Karlof et al., 2004). Small key sizes lead to the need to update keys on a regular basis.

Researchers have shown that password protocols can be implemented in sensor networks (Singh et al., 2006). The password protocols were using either a human–entered password on the sensor, or an existing 64 bit key. Instead we propose that environmental data can be used in the absence of using small keys or passwords. Also, previous approaches for sensor environments only used elliptic curve cryptography. However, RSA password protocols that can be converted to ECC have large exponent such as 1024 bits. When the protocol is converted to use ECC, then 160 bit arithmetic is required.

We instead investigated the EKE protocol, which is an RSA based password protocol where the exponent only needs to be 160 bits (Bellovin & Merritt, 1992). The EKE protocol is chosen because other variants of password protocols require exponents of size 1024 bits. The EKE protocol is diagrammatically shown in Protocol 2. A drawback of the EKE protocol is that it cannot use ECC (Boyd & Mathuria, 2003).

Protocol 2 Diffie–Hellman–based EKE protocol

Shared Information: Generator g of G where $p - 1 = qr$

A		B
$r_A \in_R \mathbb{Z}_p$		
$t_A = g^{r_A}$	$\xrightarrow{A,[[t_A]]_{SEV_1}}$	$r_B \in_R \mathbb{Z}_p$
		$K_{AB} = t_A^{r_B}$
		$t_B = g^{r_B}$
$K_{AB} = t_B^{r_A}$	$\xleftarrow{[[t_B]]_{SEV_2},[[n_B]]_{K_{AB}}}$	
	$\xrightarrow{[[n_A,n_B]]_{K_{AB}}}$	Verify n_B
Verify n_A	$\xleftarrow{[[n_A]]_{K_{AB}}}$	

The EKE protocol contains four messages. Node A sends the first message to node B, the message contains the location of A (the location value is in the clear), and the first part of Diffie–Hellman, t_A, is encrypted by the weak key SEV_1. After the first message is sent, node B will calculate the second part of the Diffie–Hellman scheme and hence be able to calculate the session key K_{AB}. Node B then sends the second part of the Diffie–Hellman scheme encrypted by the weak key SEV_2 to node A. The nonce n_B is also sent, encrypted by the session key K_{AB}. The last two messages authenticate both A and B, as well as confirming that they have the session key K_{AB}. The encryption of t_A, t_B, n_A, and n_B can be implemented with an exclusive–or function, as originally described by (Bellovin & Merritt, 1992).

Depending on which environmental value is measured, and how long the protocol will run, different SEVs may be used for the request and response. However, if the SEV stays constant throughout the running of the protocol, then both SEV_1 and SEV_2 will be the same. The EKE protocol is designed for a constant password throughout the running of the protocol, so similar or same data for both SEV_1 and SEV_2 will not adversely affect the protocol.

The EKE protocol was originally designed to handle small entropy secrets, so that off–line and on–line dictionary attacks are infeasible for an adversary. Another useful feature is that even if the secrets SEV_1 or SEV_2 are compromised or available freely after the running of the key establishment protocol, the session key K_{AB} will remain secure and safe.

Both nonces n_A and n_B are cryptographically strong random numbers, allowing the exclusive–or function to be used for encryption. If any nonce was not cryptographically strong then either $n_A \oplus K_{AB}$ or $n_B \oplus K_{AB}$ operation would allow an adversary to significantly reduce the number of valid K_{AB} values. A characteristic of the EKE protocol is that the nonces are never sent out in the clear, since the nonces are used to encrypt the new key K_{AB}.
The value of p should be chosen wisely (Bellovin & Merritt, 1992).The value of p should be as close to $2^N - 1$ as possible for the best security.
Even though exclusive–or and block cipher symmetric cryptography is suitable in an RSA environment, it is not suitable when converting to elliptic curves (Boyd & Mathuria, 2003).The EKE (RSA) protocol is compared with a ECC based password protocol (Singh et al., 2006).
Using the RSA implementation (Dutta et al., 2006) from the Deluge system and porting it to the mica2 mote system, and only using 160 bit exponents, we found that the total number of cycles is 147879. Password protocols that can use an ECC implementation inherently require 1024 bit exponents when in RSA mode (Boyd & Mathuria, 2003). When measuring the number of cycles by using the ECC implementation for sensors (Liu et al., 2007), including an implementation of the square root function, we get a total number of 18790689. The key size was 160 bits, which is equivalent to 1024 bits in RSA. When moving to the ECC protocols, more secure keys are required. There is a significant number of extra cycles in a ECC implementation over the RSA implementation.
We also examine the memory of the application, as shown in Table 4. The combination of .bss and .data segments use SRAM, and the combination of .text and .data segments use ROM. The .text contains the machine instructions for the application. The .bss contains uninitialized global or static variables, and the .data section contains the initialized static variables.

Memory	RSA	ECC
ROM	1942	9720
RAM	177	859
.data	60	8
.bss	117	851
.text	1882	9712

Table 2. Memory Overhead In Bytes On MICA2 Platform

We used the values provided by the TOSSIM simulator (a part of the TinyOS installation) to obtain an indication of the power consumption when sending a message. In our calculations we do not take into account any collision avoidance times. On the mica2 mote, the cost of sending an extra 20 bytes is 28.1 microjoules. There is a substantial startup cost for each message sent, and then there is an added cost for every bit that is sent.

4.1 Securely connecting the PDA

When a patient starts up a PDA or obtains a new PDA. Keys need to be created with the PDA and the sensors (both body and camera sensors). The mechanism we use is that the patient, when starting up the PDA, will need to enter either a password or PIN. The remainder of this section discusses a protocol that can be efficiently used to establish keys with all the sensor devices in the household and one of the sensors on the body (normally the body control sensor).

We assume that the body sensors, especially any body sensors that are leader nodes, have obtained the session keys from other sensors in the house. It is envisaged that when the controller sensor was added to the body, it had embedded a key with a central server. Then by using a KDC protocol, it can obtain keys with all the other sensors in the house. When the body sensors establish or update keys between themselves, they can use the password protocols (as described earlier in this paper). However, a hand held device, such as a PDA or mobile phone, may be purchased from a local store and will not have any keys. If patients are required to set up certificates or keys themselves, then the security system may be set up incorrectly. Also, if the device becomes lost or stolen, then an adversary is able to physically obtain any long–term keys held on the device. Our solution is to propose a multiple server protocol that can create session keys between the sensors in the house and the body controller sensor, with the PDA. A multiple server protocol has previously been developed for normal sensor networks (Singh & Muthukkumarasamy, 2006). The main reason for a multiple server protocol is that if sensors exists in an open environment, then KDC nodes can be physically compromised. In our sensor environment, the sensors are less likely to be physically compromised (either they be sensors implanted in the body, or the cameras placed in the home). However, multiple server protocols are still important for a home health care system. The reasons for a multiple server protocol are:

- Increase the randomness of the new key, by having multiple parties adding randomness to the new key.
- A camera may break down, or run out of power. A multiple server protocol increases the availability of the key establishment service.
- The key between the camera and the sensor may become compromised. The keys used by the sensors are normally small in size, since cryptographic algorithms consume more energy when larger keys are used.

In our attempt to create an efficient multiple server protocol, we specified n servers where each server corresponds to a camera. The Proposed Protocol 1 shown below, represents each of the cameras as S_i. The PDA device is labelled as A, and sends the first message, A,B,N_A, to each of the cameras. Each camera sends their message to back to the PDA. The PDA will calculate the keys K_{AS_i} and the cross checksums, and sends the cross checksums as well as parts of the messages from the cameras to the body sensor. The body sensor creates its own cross–checksums and compares them against the cross– checksums created by the PDA. At this stage, the keys K_S and K_{AB} are created by the body sensor. The body sensor sends N_B, the keying data, and the its newly created cross–checksums to the PDA. The PDA can now also create the keys K_S and K_{AB}. The final message completes the key confirmation between the PDA and the body sensor, as shown in Proposed Protocol 1. If key confirmation is not vital, then the final message can be removed.

The Proposed Protocol 1 provides key authentication, key freshness and key confirmation, using multiple authentication servers. In our Proposed Protocol 1, the following constructs are used: π is the password or SEV, A is the PDA, B is a body sensor, S_i is a camera, t_{AS_i} and t_{S_iA} are the Diffie–Hellman values, $m_{AS_i} = [[t_{AS_i}]]_\pi$, $m'_{AS_i} = [[t_{S_iA}]]_\pi$, $AUTH_{Ai} = [A,B,K_i]_{K_AS_i}$, $MASK_{Ai} = [[AUTH_{Ai}]]_{K_{AS_i}}$, $AUTH_{Bi} = [A,B,K_i]_{KBS_i}$, and $MASK_{Bi} = [[AUTH_{Ai}]]_{K_{BS_i}}$

The PDA, the body sensor and the cameras contribute to the key value. The values N_A and N_B are generated by the PDA and the body sensor respectively as input to the MAC function, that determines the session key. The key used with the MAC function is generated by the servers. Both the PDA and body sensor compute the session key as $K_{AB} = [N_A,N_B]_{K_S}$.

Proposed Protocol 1 A Preliminary Multiple Server Protocol

$M1$	$A \rightarrow S_i:$	m_{AS_i}, A, B
$M2$	$S_i \rightarrow A:$	$m'_{AS_i}, S_i, AUTH_{Ai}, MASK_{Ai} \oplus K_i,$ $MASK_{Bi}, AUTH_{Bi} \oplus K_i$
$M3$	$A \rightarrow B:$	$S_1, MASK_{B1}, AUTH_{B1} \oplus K_1, \ldots,$ $S_n, MASK_{Bn}, AUTH_{Bn} \oplus K_n,$ $cc_A(1), \ldots, cc_A(n), N_A, A$
$M4$	$B \rightarrow A:$	$cc_B(1), \ldots, cc_B(n), N_B, [N_A]_{K_{AB}}$
$M5$	$A \rightarrow B:$	$[N_B]_{K_{AB}}$

The keys K_{AS_i} are generated by computing the diffie–hellman part of the protocol. The PDA and body sensor should have a minimum number of cameras returning valid results before confirming that the key is valid. The PDA will calculate $cc_A(i)$ $\forall i \in 1, \ldots, n$.

$$cc_A(i) = \begin{cases} [K_i]_{K_i} & \text{if valid,} \\ EM & \text{otherwise} \end{cases} \tag{1}$$

Where EM is an error message; an example will be the value zero. There is a remote chance a valid case may be zero. If the valid value is zero, the camera needs to be considered a compromised server (even though it is not a malicious server).
The body sensor will calculate $cc_B(i)$, and compare it with $cc_A(i)$. If they are the same, then the server S_i is valid. Below is a way the PDA and body sensor compare the cross checksum for $cc_A(i)$ and $cc_B(i)$.

$$cc_B(i) = \begin{cases} cc_A(i) = [K_i]_{K_i} & \text{if valid,} \\ EM & \text{otherwise} \end{cases} \tag{2}$$

After the comparison of the entire cross checksums, a set of valid keys $V_1, \ldots, V_m$ should remain. The creation of K_S is defined as follows.

$$K_S = V_1 \oplus \ldots \oplus V_m \tag{3}$$

Where V_i is the i^{th} valid key given by a server, and m is the total number of valid servers $t \leq m \leq n$, where t is the minimal number of trusted servers. Another advantage of the proposed protocol is that the cameras will not be able to calculate K_S. The calculated $cc_B(i)$ values are returned to the PDA, where the PDA performs similar checks as the body sensor and calculates K_S.
Once the PDA has established a key with one of the body sensors, then a KDC protocol can be used to establish keys with the other body sensors.

4.2 Analysis and discussion

Our Proposed Protocol 1 has a number of advantages, one of which is that the body sensor does not need good random number generators to create the nonces. The body sensor could even safely use a counter for their nonce values. Another advantage is that if a camera or a number of cameras are unavailable, the authentication service itself still exists through the working cameras. If one or more cameras become compromised, the authentication service or the security of the system is not compromised.

The proposed protocol only encrypts random information. If the encryption cipher uses an *IV* value (such as RC5 and SKIPJACK currently used in TinyOS (TinyOS, 2007)) then we can use a constant *IV* value. However, the constant *IV* value chosen for our protocol must only be used to encrypt the random data and should never be used to encrypt other information. Also, a wide variation of different ciphers can safely be used.

Some MACs have vulnerabilities when the message sizes are variable. All of our message sizes are of constant value, allowing us to safely use a wider range of MACs than previously available. The size of the MACs sent to the body sensor can be lower than that of conventional protocols. The integrity checking is performed by the body sensor. If x is the size of the MAC in bits, then an adversary has 1 in 2^x chance of blindly forging a valid MAC for a particular message. The adversary should be able to succeed in 2^{x-1} tries. Because of the low bandwidth of sensor nodes, a 4 byte MAC, requiring 2^{31} packets, will take years to complete. If an adversary did attempt this attack, the sensor node would be non–functional within that period. In addition, an adversary will need to forge $2t$ MACs; t MACs to A and t MACs to B, and stop traffic from the other base stations before they can determine the value of K_{AB}.

In the proposed protocol, the device that is most sensitive to energy restrictions is the body controller sensor. The message $M3$ is of the most concern, since it the largest message sent to the controller sensor. We calculate the size of the message as $M3 = (n+1)a_0 + a_1 + na_2 + na_3$ bytes. Where a_0 is the size of the location, a_1 is the nonce size, a_2 is the key size, a_3 is the MAC size, and n is the number of cameras. Assuming that the location is 1 byte in size (maximum 256 possible sensors), the nonce is 1 byte in size, the key is 8 bytes in size, and the MAC is 4 bytes in size, we get $M3 = 13n + 2$ bytes. If we assume that a packet size is 28 bytes, a configuration with more than two cameras will require multiple packets sent between the PDA and the body controller node. If there is no or little concern about whether the cameras or the camera keys are compromised, then the PDA can select two cameras to send to the body controller sensor.

The computational complexity for the body sensor depends on the number of valid servers the PDA forwards to the sensor, the number is defined as m. The computational cost of the MACs is $4m + 2$, and the cost of the encryption operations is m. The number of exclusive–or operations is $2m$.

5. Formal verification

Formal analysis of communication protocols for traditional networks has been used since at least 1978 (West, 1978), with significant improvements in recent decades (Clarke & Wing, 1996). Sithirasenan et al. (Sithirasenan et al., 2006) have compared different modeling techniques, and listed advantages for each of the techniques.

Verifying a protocol is proving that the claims for the protocol are correct and is a significant step in analysing the protocol. The complexity of security protocols makes their verification a difficult task. Informal arguments about protocol correctness are not reliable or acceptable, leading to a formal analysis to verify that a claim made by a protocol is correct.

Computer assisted formal methods for verifying security protocols can be divided into two major categories:

- Model Checking: considers a finite number of possible protocol behaviours and allows checking that satisfy a set of correctness conditions. This method works well for finding

attacks on a protocol, rather than proving their correctness Clarke et al. (2000); Lowe (1996); Mitchell et al. (1997).

- Theorem Proving: considers all possible protocol behaviours, and checks that they satisfy a set of correctness conditions. This method works well for proving protocol correctness, rather than finding attacks on protocols Meadows (1996); Paulson (1998); Song (1999).

Both model checking and theorem proving methods require computer assistance to aid with the analysis. However, methods based on theorem proving are less automated than those based on model checking.

A useful feature of model checking methods is that they can prove an attack when a protocol is found not to satisfy a correctness condition. The failure to find an attack indicates that the protocol is correct. However, model checkers do not provide a symbolic proof that can explain why a protocol is correct and thus are uninformative when checking a correct protocol. Another important limitation of model checking methods is that they only guarantee correctness of a scaled down version of the protocol.

Theorem proving mechanisms have their own strengths and limitations. One of the strengths of theorem proving methods is that they can provide a symbolic proof when a protocol is found to be correct. Their main limitation is that they generally require more expert human guidance than methods based on model checking.

Sitherasenan et al. Sithirasenan et al. (2006) have used Genetic Design Methodology to check the correctness of the 802.11i wireless security protocol. The requirements of the protocol was placed into a number of Requirement Behaviour Trees. The requirements were then verified by integrating them into a single Integrated Behaviour Tree. Thereafter, the Behaviour Tree model was translated into SAL formal notations for theorem proving. This mechanism shows that both model checking and theorem proving can be performed using the same analysis tool. However, the model checking was mainly focused on the protocol correctness and not the security. We will show that this analytical tool can perform both model checking and theorem proving on the security of a protocol.

One of the major advantages is that the genetic design methodology produces graphical models that are derived and integrated from the original requirements. The models can be used to verify that security protocols correctly work in a complex system. A home health care system is a complex system, where it is difficult to track how sensed data is used in the system. When the sensed data is also used in security protocols, tracking the use of sensed data becomes even more important. For example, some key establishment protocols require the sensed data never to be sent in the clear or to an untrusted third party, whereas other protocols do not need such restrictions.

The genetic design methodology creates behaviour trees, which in turn can generate SAL code (Sithirasenan et al., 2006). A model checker can then be used to verify the SAL code and thus verify the protocol in the sensor environment. The main steps with the genetic methodology are: translation of requirements to behaviour trees; integration of behaviour trees; architecture transformation; component behaviour projection; component design. When modelling the entire system, genetic design has significant advantages over UML, state charts or other methods. The advantages include:

- Allows designers to focus on the complexity and design of individual requirements while not having to worry about the detail in other requirements. The requirements can be dealt with one at a time (for both translation and integration).

- The component architecture and the component behaviour designs of the individual components are emergent properties of the design behaviour tree.
- The methodology concentrates on discovery behaviour gaps, which in turn discovers requirement gaps. The focus of direct translation of requirements to design makes it easier to see and find gaps.
- An automated method of mapping changes in requirements to changes in design.

An important part of the genetic design methodology is the behaviour trees. Dormey (Dromey, 2003) defined Behaviour Trees as: *a formal, tree–like graphical form that represents behaviour of individual or networks of entities which realize or change states, make decisions, respond–to/cause events, and interact by exchanging information an/or passing control*.

Each requirement can be represented as a behaviour tree; this representation is specifically called a Requirement Behaviour Tree.

Another mechanism to verify that a protocol is secure is to use a mathematical proof Canetti & Krawczyk (2001). Problems with using mathematical proofs include:

- With each small change in the protocol a new proof needs to be constructed.
- Security proofs run to several pages of mathematical reasoning and is difficult to understand to the average practitioner.
- There are relatively few protocols with mathematical security proofs.
- As a system becomes more complex, constructing mathematical proofs becomes more challenging.

Informal verification, machine analysis (either using model checking, or theorem proving), and mathematical proofs are all important approaches to gain assurance on the security of the protocol.

5.1 Modelling

In order to verify the BSN system, the Behaviour Tree technique is used to represent the home health care system. The modelling was completed after several stages. The initial stages involved obtaining the requirements of the Venkatasubramanian and Gupta protocol and EKE password protocol. The major requirement is to establish a cryptographic key between two nodes. The Venkatasubramanian and Gupta protocol properties include that SEV needs to be cryptographically strong, and the SEV should never be sent in the clear. The EKE protocol does not have as many restrictions because of the following properties:

- Sensor nodes only possess a secret of small entropy,
- Off–line dictionary attacks are not feasible,
- On–line dictionary attacks are not feasible, and
- The key must have forward secrecy.

From the properties of the key establishment protocols, we developed the Requirement Behaviour Trees (RBTs). While developing the RBTs, we found that the previous definitions and properties of the protocols did not have a consistent method to define the need for the sensor to sense the physiological data. The RBT is designed for, and has built–in syntax for, external events, so this requirement was easily added to our RBTs. The feature for quickly adding external events makes RBTs suitable for a sensor environment. The RBTs were then placed into an Integrated Behaviour Tree (IBT) to display the entire system. The IBT was then used to create other models for us to investigate and analyse. The Component Interaction Network (CIN) was used to show the relationship between the components in the system and gave a representation of the component architecture. The Component

Behaviour Trees (CBTs) and Component Interface Diagrams (CIDs) gave us views of each of the individual components. The final RBT for the EKE protocol is shown in Figure 2. The RBT for the Venkatasubramanian and Gupta protocol has a similar structure.

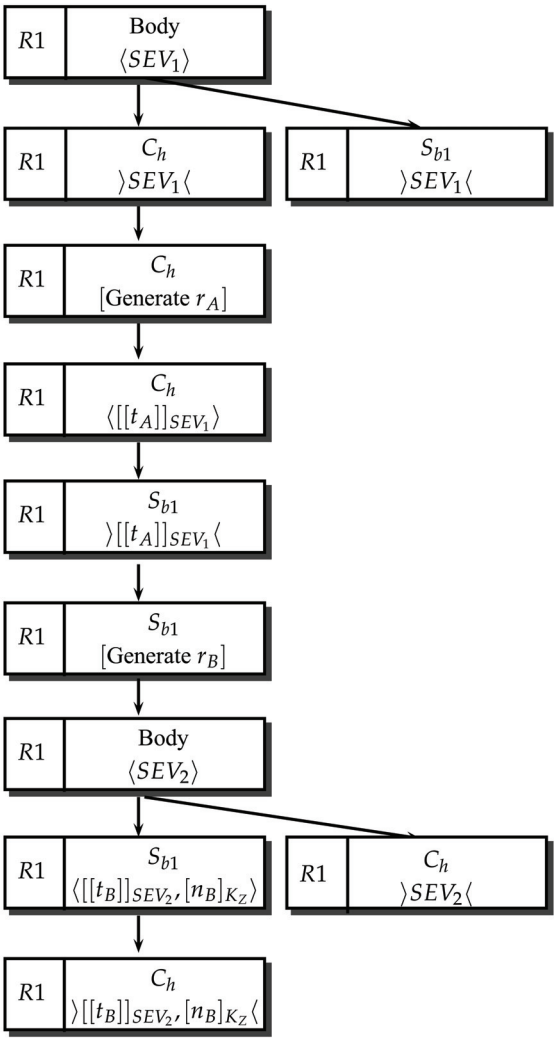

Fig. 2. EKE password protocol for Sensors

The RBT has four major components, the first three components belong to Requirement 1 (R1), whereas Sensor C sensing data belongs to Requirement 2 (R2):

- Sensor A sensing data every 10 seconds
- Sensor B sensing data every 10 seconds
- Sensors A and B Establishing a key
- Sensor C sensing data every 10 seconds

In the above diagram, establishment of the key is initiated by Sensor A. It will create t_A and then send it to Sensor B. In our RBT we have made the sending of the message from Sensor A to Sensor B non–deterministic. In this case, Sensor B could have received a malicious message from another node. Verification of the key is the last step. We have this as a separate RBT, since it overcomplicates the diagram. The verification of the key involves the key confirmation steps described in the protocol.
By using behaviour trees, we were quickly able to find all of the possible inputs and outputs that a sensor can obtain, either through wireless communication or through their sensing devices. This also helps us to verify that each component that we are developing has the needed features to run in our environment. When there are a large number of sensors, this requirement becomes difficult to track. The next step is to generate SAL code from this behaviour trees, and verify the protocol in a sensor environment.

5.2 Specification of SAL

Before we could test our requirements on the key establishment protocol, we first needed to specify the network and body into SAL code. To specify the network in SAL, we were able to utilize previous SAL libraries (Rushby, 2003). However, we found no existing SAL libraries to specify obtaining SEVs from the body. We defined the body within SAL as having two operations: getSEV; changeSEV. Sensors can obtain a SEV by calling getSEV and afterwards a changeSEV can be called to create a new SEV.
We then generated the SAL code from the RBTs. The first SAL code generated is for the Venkatasubramanian and Gupta protocol. Due to limitations in the SAL generation, we modified the SAL code to read the physiological data from our body SAL code. We have a requirement R2 where a sensor sends physiological data to an external third party system. We want to show that requirement R2 will break requirement R1, since for the protocol to be secure we needed to ensure that the sensed data is never sent in the clear. The following theorem is used to verify that no other sensor reads the same sensed data as the pair that is establishing the new session key.

```
prop_no_delay: THEOREM system |-
G(NOT((FORALL (x,y: principals):
(buffer.1.1=buffer.2))));
```

SAL code was also generated for the EKE protocol. Wemodified the SAL code to read the physiological data from our body SAL code. We have a requirement R2 where a sensor sends physiological data to an external third party system. We want to show that the requirement R2 will not break the requirement R1, since we also placed a delay into the sensors in requirement R1, where the sensor will wait 30 seconds before sending out the physiological data. It should be noted that the Venkatasubramanian and Gupta protocol still is broken if the physiological data is sent out with a delay. The following theorem is used to verify that another sensor delays its send when reading the same sensed data as the pair that is establishing the new session key.

```
prop_delay: THEOREM system |-
G(NOT((FORALL (x,y: principals):
(buffer.1.1=buffer.2 AND
delayed.2=true))));
```

6. Comparison of different implementation

We implemented and compared different cryptographic primitives that can be used in body sensor security protocols on a Crossbow mica2 MPR2600 mote (Crossbow, 2006). Before comparing the different cryptographic primitives, and the benefits that one implementation has over another, we created skeleton code based on TinyOS 2.x (TinyOS, 2007). The skeleton code initializes the sensor node, and after the sensor is initialized, we obtained the initial time in milliseconds. We then run a cryptographic primitive in a loop for 2000 iterations, before obtaining a new time. We subtracted the new time from the initial time to obtain the elapsed time in milliseconds to run our cryptographic primitive for 2000 attempts. The elapsed time was then sent via the serial connection, to a PC running a Linux® distribution where we have a Java® application reading the TinyOS packet from the serial port, and report that data to the user.

The key establishment protocols uses exclusive–or (xor) to encrypt the new session key. We compare this method with other methods of encrypting the new session key for body sensor networks. Singh et al. (Singh & Muthukkumarasamy, 2008; 2007) have shown how RC5, SKIPJACK, HMAC–MD5, RSA, and ECC cryptographic primitives can be used in BSNs, however, their work and comparisons were based on simulations, and on TinyOS 1.x. We have implemented these cryptographic primitives on real hardware, and for TinyOS 2.x. To our knowledge these cryptographic primitives have not (until now) been ported to the latest version of TinyOS. Previously, Singh et al. did not separate the square root function from the elliptic curve cryptography. However, in our comparison we found significant information when separating them.

Table 6 shows the time it takes to run 2000 iterations of each of the algorithms. We have ordered the algorithms on the time elapsed. The Lines of Code indicates the complexity for the coder to implement the algorithm. The Size (bytes) indicates the size in bytes of the application.

Algorithm	Time	Lines of Code	Size (bytes)
xor	2 milliseconds	80	6340
RC5	500 milliseconds	506	7168
SKIPJACK	700 milliseconds	697	8138
HMAC–MD5	20 seconds	507	19054
RSA	43 seconds	1456	7814
SQRT	80 seconds	3366	8610
ECC	78 minutes	5038	16328

Table 3. Time measurements for different algorithms

The RC5 application took considerable more effort than the exclusive–or (xor) application. We found an RC5 implementation for TinyOS 1.x in the TinySEC library (Karlof et al., 2004), however, it has yet to be ported to TinyOS 2.x. Most of our effort was spent porting the code to the new platform. The SKIPJACK application had similar problems as the RC5 application. Where there was an implementation for TinyOS 1.x in the TinySEC library but there was not one for TinyOS 2.x. Once again, most of our effort was spent porting the code to the platform. For HMAC–MD5 application we could not find any previous

implementations of HMAC–MD5 in any version of TinyOS. In this case we obtained code from RFC1321 (Rivest, 1992) and RFC2104 (Krawczyk et al., 1997) and ported the code to first the nesc language and then to the TinyOS application. This was considerably more effort then either RC5 or SKIPJACK implementations. The RSA application also had similar problems as the RC5 and SKIPJACK implementations. We found code in the Deluge System (Dutta et al., 2006), however, the RSA code was based off TinyOS 1.x. Effort was required to port this code to TinyOS 2.x. We used a 160 bit exponent as required by the EKE protocol. The SQRT application had the most difficulties since we implemented it from pseudo–code rather than porting any code. We used Newton's Method (Press et al., 2007) for finding square roots to implement the SQRT application. The ECC application also had similar problems to the RSA, RC5 and SKIPJACK implementations. We ported an ECC library (Liu et al., 2007) developed for TinyOS 1.x to TinyOS 2.x. The ECC application used a 160 bit points, since password protocols that could be converted to use ECC require stronger keys (Singh & Muthukkumarasamy, 2007).
The xor application is the quickest by several orders of magnitude compared to the other cryptographic primitives. The size of the application is smaller, and the number of lines is less then the other applications. The xor application is the quickest, whereas the ECC application is the slowest. This verifies existing research into the differences in speed for password protocols of RSA and ECC implementations in TinyOS simulators (Singh & Muthukkumarasamy, 2007). The HMAC–MD5 application is the largest, however the application was a straight port from the RFCs, where the code was not intended for sensors.

7. Future research directions

We have proposed a multi–server key establishment protocol that allows a PDA to obtain session keys with most of the sensors in our home health care system. We implemented salient features of the password protocols and compared the energy consumption of the nodes. The password protocols that could be converted to use ECC had a larger computational overhead than the EKE protocol, because of the stronger keys required by the ECC–based password protocols. Due to the EKE protocol only requiring 160 bit exponents, the message sizes of the EKE protocol were comparable to the ECC– based password protocols. The impact on memory by adding elliptic curves to a sensor application was analyzed, revealing that there is additional costs associated with an ECC solution over a RSA solution. Future work includes using cryptographic protocol verifiers to confirm that our protocols are secure.
Genetic design methodology is used to gather the requirements of the health care system. We examined two existing key establishment protocols that use physiological data to establish keys between body sensors, where the sensors have no other prior secret. We showed how the requirements of the EKE protocol can be placed into a Requirement Behaviour Tree. SAL code is generated from the behaviour tree, as well as SAL code created to model the events from the body. A SAL model checker is used to verify the protocol formally within our system. Implementation of the protocols involved either porting libraries or creating new libraries in TinyOS 2.x. The time elapsed, complexity of the code, and memory requirements are analysed in detail on mica2 sensors. The password protocols that use ECC had a larger computational overhead than the EKE protocol, confirming

existing work performed using simulations. Future work will include the full implementation and analysis of both the RBTs and code for each of the key establishment protocols on our sensor network.

8. Acknowledgments

Linux is a registered trademark of Linus Torvalds in the United States, other countries, or both. Java and all Java-based trademarks and logos are trademarks of Sun Microsystems, Inc. in the United States, other countries, or both. Other company, product, or service names may be trademarks or service marks of others.

9. References

Axis (2007). Setting up an ip–surveillance system using axis cameras and axis camera station software, http://www.axis.com/files/manuals/gd_ipsurv_design_en_070320.pdf.

Aziz, O., Lo, B., Darzi, A. & Yang, G.-Z. (2006). Introduction, *in* G.-Z. Yang (ed.), *Body Sensor Networks*, Springer–Verlag.

Balomenos, T. (2001). User requirements analysis and spcification of health status analysis and hazard avoidance artefacts, *Technical report*, DC FET Project ORESTELA, Delieverable D02.

Bao, S.-D. & Zhang, Y.-T. (2005). A new symmetric cryptosystem of body area sensor networks for telemedicine, *6th Asian–Pacific Conference on Medical and Biological Engineering*. http://ifmbe-news.iee.org/ifmbe-news/july2005/shudibaopaper.html.

Bao, S.-D., Zhang, Y.-T. & Shen, L.-F. (2005). Physiological signal based entity authentication for body area sensor networks and mobile healthcare systems, *27th Annual International Conference of the Engineering in Medicine and Biology Society, 2005*, IEEE Press, pp. 2455–2458.

Bao, S.-D., Zhang, Y.-T. & Shen, L.-F. (2006). A design proposal of security architecture for medical body sensor networks, *BSN '06: Proceedings of the International Workshop on Wearable and Implantable Body Sensor Networks (BSN'06)*, IEEE Computer Society,Washington, DC, USA, pp. 84–90.

Bellovin, S. M. & Merritt, M. (1992). Encrypted key exchange: Password-based protocols secure against dictionary attacks, *IEEE Symposium on Research in Security and Privacy*, IEEE Computer Society Press, pp. 72–84.

Boyd, C. & Mathuria, A. (2003). *Protocols for Authentication and Key Establishment*, Springer Berlin / Heidelberg.

Canetti, R. & Krawczyk, H. (2001). Analysis of key-exchange protocols and their use for building secure channels, *EUROCRYPT 2001: Proceedings of the International Conference on the Theory and Application of Cryptographic Techniques*, Springer-Verlag, London, UK, pp. 453– 474.

Chan, H. & Perrig, A. (2005). PIKE: Peer intermediaries for key establishment in sensor networks, *Proceedings of IEEE Infocom*, IEEE Computer Society Press.

Clarke, E. M., Jha, S. & Marrero, W. (2000). Verifying security protocols with brutus, *ACM Transactions Software Engineering Methodology* 9(4): 443–487.

Clarke, E. M. & Wing, J. M. (1996). Formal methods: state of the art and future directions, *ACM Comput. Surv.* 28(4): 626–643.

Crossbow (2006). Crossbow, http://www.xbow.com/.

Dromey, R. (2003). From requirements to design: Formalizing the key steps, *sefm* 00: 2.

Dutta, P. K., Hui, J. W., Chu, D. C. & Culler, D. E. (2006). Securing the deluge network programming system, *In the Fifth International Conference on Information Processing in Sensor Networks (IPSN'06)*.

Espina, J., Falck, T. & Mülhens, O. (2006). Network topologies, communication protocols, and standards, *in* G.-Z. Yang (ed.), *Body Sensor Networks*, Springer–Verlag.

Hämäläinen, P., Kuorilehto, M., Alho, T., H¨annik¨ainen, M. & H¨am¨al¨ainen, T. D. (2006). Security in wireless sensor networks: Considerations and experiments., *SAMOS*, pp. 167–177.

Hampapur, A., Brown, L., Connell, J., Haas, N., Lu, M., Merkl, H., Pankanti, S., Senior, A., Shu, C.-F. & Tian, Y. (2004). S3-r1: the ibm smart surveillance system-release 1, *ETP '04: Proceedings of the 2004 ACM SIGMM workshop on Effective telepresence*, ACM Press, New York, NY, USA, pp. 59–62.

Kansal, A. & Srivastava, M. (2005). Energy–harvesting–aware power management, *in* N. Bulusu & S. Jha (eds), *Wireless Sensor Networks: A Systems Perspective*, Artech House.

Karlof, C., Sastry, N. & Wagner, D. (2004). Tinysec: a link layer security architecture for wireless sensor networks, *SenSys '04: Proceedings of the 2nd international conference on Embedded networked sensor systems*, ACM Press, New York, NY, USA, pp. 162–175.

Krawczyk, H., Bellare, M. & Canetti, R. (1997). Hmac: Keyed-hashing for message authentication. http://tools.ietf.org/html/rfc2104.

Kuorilehto, M., H¨annik¨ainen, M. & Hämäläinen, T. D. (2005). A survey of application distribution in wireless sensor networks, *EURASIP J. Wirel. Commun. Netw.* 5(5): 774–788.

Liu, A., Kampanakis, P. & Ning, P. (2007). Tinyecc: Elliptic curve cryptography for sensor networks (version 0.3). http://discovery.csc.ncsu.edu/software/TinyECC/.

Liu, D. & Ning, P. (2007). *Security for Wireless Sensor Networks*, Springer Berlin / Heidelberg.

Lowe, G. (1996). Breaking and fixing the needham-schroeder public-key protocol using fdr, *TACAs '96: Proceedings of the Second International Workshop on Tools and Algorithms for Construction and Analysis of Systems*, Springer-Verlag, London, UK, pp. 147–166.

Meadows, C. A. (1996). The nrl protocol analyzer: An overview, *Journal of Logic Programming* 26: 113–131.

Mitchell, J. C., Mitchell, M. & Stern, U. (1997). Automated analysis of cryptographic protocols using mur/spl phi/, *SP '97: Proceedings of the 1997 IEEE Symposium on Security and Privacy*, IEEE Computer Society, Washington, DC, USA, p. 141.

Paulson, L. C. (1998). The inductive approach to verifying cryptographic protocols, *Journal of Computer Security* 6(1-2): 85–128.

Poon, C. C. Y., Zhang, Y.-T. & Bao, S.-D. (2006). A novel biometrics method to secure wireless body area sensor networks for telemedicine and m–health, *IEEE Communications Magazine* 44: 73–81.

Press, W. H., Teukolsky, S. A., Vetterling, W. T. & Flannery, B. P. (2007). Root finding and nonlinear sets of equation, *in* W. H. Press (ed.), *Numerical Recipes: The Art of Scientific Computing*, Cambridge University Press.

Rivest, R. (1992). Themd5 message-digest algorithm. http://tools.ietf.org/html/rfc1321.

Rushby, J. (2003). The needham-schroeder protocol in sal. http://www.csl.sri.com/users /rushby/ abstracts/needham03.

Singh, K., Bhatt, K.&Muthukkumarasamy, V. (2006). Protecting small keys in authentication protocols for wireless sensor networks, *Proceedings of the Australian Telecommunication Networks and Applications Conference*, Melbourne, Australia, pp. 31–35.

Singh, K. & Muthukkumarasamy, V. (2006). A minimal protocol for authenticated key distribution in wireless sensor networks, *ICISIP '06: Proceedings of the 4th International Conference on Intelligent Sensing and Information Processing*, IEEE Press, Bangalore, India, pp. 78–83.

Singh, K. & Muthukkumarasamy, V. (2007). Authenticated key establishment protocols for a home health care system, *Proceedings of the Third International Conference on Intelligent Sensors, Sensor Networks and Information Processing (ISSNIP)*, Melbourne, Australia.

Singh, K. & Muthukkumarasamy, V. (2008). Performance analysis of proposed key establishment protocols in multi–tiered sensor networks, *Journal of Networks* 3(6).

Sithirasenan, E., Zafar, S. & Muthukkumarasamy, V. (2006). Formal verification of the ieee 802.11i wlan security protocol, *Australian Software Engineering Conference (ASWEC '06)*, Sydney, Australia.

Song, D. X. (1999). Athena: a new efficient automatic checker for security protocol analysis, *CSFW '99: Proceedings of the 12th IEEE workshop on Computer Security Foundations*, IEEE Computer Society, Washington, DC, USA, p. 192.

Staderini, E. M. (2002). Uwb radars in medicine, *IEEE Aerospace and Electronic Systems Magazine* 21: 13–18.

Thiemjarus, S. & Yang, G.-Z. (2006). Context–aware sensing, *in* G.-Z. Yang (ed.), *Body Sensor Networks*, Springer–Verlag.

TinyOS (2007). An operating system for sensor motes, http://www.tinyos.net/.

USA (2003). Summary of hipaa health insurance probability and accountability act, US Department of Health and Human Service.

Venkatasubramanian, K. K. & Gupta, S. K. S. (2006). Security for pervasive health monitoring sensor applications, *ICISIP '06: Proceedings of the 4th International Conference on Intelligent Sensing and Information Processing*, IEEE Press, Bangalore, India, pp. 197–202.

West, C. (1978). General technique for communications protocol validation, *IBM Journal of Research and Development* 22(4).

Yeatman, E. & Mitcheson, P. (2006). Energy scavenging, *in* G.-Z. Yang (ed.), *Body Sensor Networks*, Springer–Verlag.

16

Symbolic Modelling of Dynamic Human Motions

David Stirling, Amir Hesami, Christian Ritz,
Kevin Adistambha and Fazel Naghdy
The University of Wollongong
Australia

1. Introduction

Numerous psychological studies have shown that humans develop various stylistic patterns of motion behaviour, or dynamic signatures, which can be in general, or in some cases uniquely, associated with an individual. In a broad sense, such motion features provide a basis for non-verbal communication (NVC), or body language, and in more specific circumstances they combine to form a Dynamic Finger Print (DFP) of an individual, such as their gait, or walking pattern.

Human gait has been studied scientifically for over a century. Some researchers such as Marey (1880) attached white tape to the limbs of a walker dressed in a black body stocking.

Humans are able to derive rich and varied information from the different ways in which people walk and move. This study aims at automating this process. Later Braune and Fischer (1904) used a similar approach to study human motion but instead of attaching white tapes to the limbs of an individual, light rods were attached. Johansson (1973) used MLDs (Moving Light Displays; a method of using markers attached to joints or points of interests) in psychophysical experiments to show that humans can recognize gaits representing different activities such as walking, stair climbing, etc. The Identification of an individual from his/her biometric information has always been desirable in various applications and a challenge to be achieved. Various methods have been developed in response to this need including fingerprints and pupil identification. Such methods have proved to be partially reliable. Studies in psychology indicate that it is possible to identify an individual through non-verbal gestures and body movements and the way they walk.

A new modelling and classification approach for spatiotemporal human motions is proposed, and in particular the walking gait. The movements are obtained through a full body inertial motion capture suit, allowing unconstrained freedom of movements in natural environments. This involves a network of 16 miniature inertial sensors distributed around the body via a suit worn by the individual. Each inertial sensor provides (wirelessly) multiple streams of measurements of its spatial orientation, plus energy related: velocity, acceleration, angular velocity and angular acceleration. These are also subsequently transformed and interpreted as features of a dynamic biomechanical model with 23 degrees of freedom (DOF).

This scheme provides an unparalleled array of ground-truth information with which to further model dynamic human motions compared to the traditional optically-based motion capture technologies. Using a subset of the available multidimensional features, several

successful classification models were developed through a supervised machine learning approach.
This chapter describes the approach, methods used together with several successful outcomes demonstrating: plausible DFP models amongst several individuals performing the same tasks, models of common motion tasks performed by several individuals, and finally a model to differentiate abnormal from normal motion behaviour.
Future developments are also discussed by extending the range of features to also include the energy related attributes. In doing so, valuable future extensions are also possible in modelling, beyond the objective pose and dynamic motions of a human, to include the intent associated with each motion. This has become a key research area for the perception of motion within video multimedia, for improved Human Computer Interfaces (HCI), as well as its application directions to better animate more realistic behaviours for synthesised avatars.

2. Dynamic human motions used in bodily communication

Bodily communication or non–verbal communication (NVC) plays a central part in human social behaviour. Non-verbal communication is also referred to as the communication without words. Face, hands, shrugs, head movements and so on, are considered as the NVC. These sorts of movements are often subconscious and are mostly used for:

- Expressing emotions
- Conveying attitudes
- Demonstrating personality traits
- Supporting verbal communication (McNeil, 205)

Body language is a subset of NVC. Body language is used when one is communicating using body movements or gestures plus, or instead of, vocal or verbal communication. As mentioned previously these movements are subconscious, and so many people are not aware of them although they are sending and receiving these all the time. Researchers have also shown that up to 80% of all communications is body language. Mehrabian (1971) reported that only 7% of communication comes from spoken works, 38% is from tone of the voice, and 55% comes from body language.
A commonly identified range of NVC signals have been identified (Argyle, 1988) such as:

- Facial expression
- Gaze and pupil direction
- Posture
- Non–verbal vocalizations
- Clothes, and other aspects of appearance
- Bodily contact
- Gesture and other bodily movements
- Spatial behaviour
- Smell

In addition to this as Argyle described the meaning of a non–verbal signal can be different from sender or receiver's points of view. To a sender it might be his emotion, or the message he intends to send and to the receiver can be found in his interpretation. Some NVC signals are common among all the different cultures where some others might have different meanings in different cultures. According to Schmidt and Cohn (2002) and Donato et al. (1999) there are 6 universally recognized facial expressions:

1. Disgust
2. Fear
3. Joy
4. Surprise
5. Sadness
6. Anger

But there are other emotions that could be recognized through body movements including anxiety, nervousness, embarrassment, lying, aggression, boredom, interest, tiredness, defensive, curiosity, agreement, disagreement, and even some states such as thinking and judging. Some emotions are expressed as a sequence of movements, so one will need to use prior or posterior information from movements in order to be able to recognize such specific emotions.

2.1 Body parts and related emotions

Certain movements of one body part often need to be associated with the movements of various other parts in order to be interpreted as an emotion. Table 1 details a basic list of the parts that one is is able to acquire data from their movements and the emotions related to those movements are described.

member	movement	interpretation
head	*lowering*	*defensive or tiredness.*
	raising	*interest, visual thinking.*
	tilting	*interest, curiosity.*
	oscillating up & down	*agreement.*
	oscillating left & right	*disagreement.*
	touching	*thinking.*
arms	*expanding*	*aggression*
	crossing	*anxiety*
hands	*holding behind*	*lying, self confidence*
	palms up or down	*asking*
	rubbing together	*extreme happiness.*
	repetitive movements	*anxiety, impatience..*
neck	*touching*	*fear.*
shoulder	*raised*	*tension, anxiety or fear.*
	lowered	*relax*
chest	*rubbing*	*tension and stress.*
belly	*Rubbing or holding*	*tension*
legs	*standing with feet together*	*anxiety*
	crossing	*tension and anxiety*
	repetitive movements	*anxiety, impatience*
thighs	*touching*	*readiness*
feet	*curling*	*extreme pleasure*
	stamping	*anger and aggression*
	moving	*anxiety, impatience, lying*

Table 1. Noted emotions for associated body movements (Straker, 2008).

These interpretations are acquired from different psychological researches through different web sites and dissertations. Interpretation would clearly depend on cultural and other context.

Table 1 infers a highly complex multidimensional space in which a human body can relay emotional expressions as various spatial articulations at any point in time. This together with any associated temporal sequence surrounding an observed postural state, combine to provide an extremely challenging context in which to capture and further model the

dynamics of human motions. A rich array of initial, contributory intentions further obfuscate matters. The decidedly successful analysis of facial micro expressions by Ekman and others (Ekman, 1999) has proven insightful for identifying the underlying emotions and intent of a subject. In a related but possibly more prosaic manner, it is the intended to establish three basic goals from the analysis and modeling of dynamic motions of a human body, these are to:

1. develop a sufficient model of dynamic finger printing between several individuals
2. model distinctive motion tasks between individuals
3. formulate a model to identify motion pretence (acting) as well as normal and abnormal motion behaviours

Successfully achieving some or all of these goals would provide invaluable outcomes for human behavioural aspects in surveillance and the detection of possible terrorism events as well as medical applications involving dysfunction of the body's motor control.

3. Motion capture data

Given the three distinct task areas it became prudent to utilise, were ever possible, any existing general motion capture data that may be available, as well as record specific motion data that addressed more specific task needs. To this end the Carnegie Mellon University (CMU) Motion Capture Database (2007) has been utilized explore the second goal, that is to investigate plausible models for the identification of distinctive motion tasks between individuals. This database was created with funding from NSF EIA-0196217, and has become a significant resource providing a rich array of motion behaviours that have been recoded over a prolonged period. Alternatively, the first and last goal objectives require more specific, or specialised captured motion data. For these areas, a motion capture system based on a network array of inertial wireless sensors, as opposed to the more traditional, optical multiple camera based system.

3.1 Inertial motion capture

Data recorded from this technology is being acquired using an inertial movement suit, Moven® from Xsens Technologies, which provides data on 23 different segments of the body kinematics such as position, orientation, velocity, acceleration, angular velocity and angular acceleration as shown in Fig. 1.

In capturing human body motion no external emitters or cameras are required. As explained by Roetenberg et al. (2007) mechanical trackers use Goniometers which are worn by the user to provide joint angle data to kinematic algorithms for determining body posture. Full 6DOF tracking of the body segments are determined using connected inertial sensor modules (MTx), where each body segment's orientation, position, velocity, acceleration, angular velocity and angular acceleration can be estimated. The kinematics data is saved in an MVNX file format which is subsequently read and used, using an intermediate program coded in MATLAB.

Using the extracted features, a DFP (Dynamic Finger Print) can be generated for each individual. DFP is used to identify the individual or detect departure from his/her expected pattern of behaviour. Using this comparison, it is possible to find the smoothness or stiffness of the movement and find out if the person is concealing an object. In order to recognize identity of an individual, different measurements will be made to extract the unique

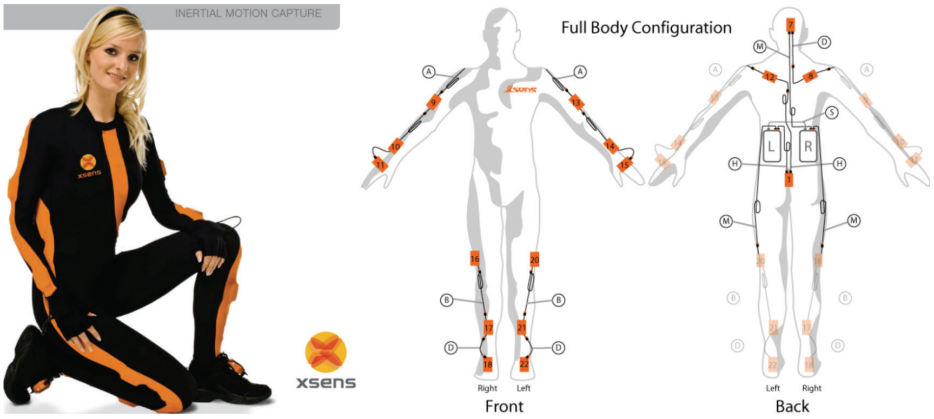

(a) (b)

Fig. 1. Inertial Motion Capture: (a) Moven®, light weight latex motion suit housing a network of 16 MTx inertial sensors (b) distribution of MTx sensors including the L and R aggregation and wireless transmitter units— adapted from (Xsens Technologies, 2007).

Dynamic Finger Print (DFP) for that individual. The data produced by the suit consists of kinematics information associated with 23 segments of the body. The position, velocity, acceleration data for each segment will be then analyzed and a set of feature of derived will be used in classification system.

3.2 Feature extraction

The determination/selection and extraction of appropriate features is an important aspect of the research. All the classification results would be based on the extracted features. The features should be easy to extract and also must contain enough information about the dynamics of the motion. The selected features should be independent of the location, direction and trajectory of the motion studied. In the case of a sequence of walking motions (or gait) it would be reasonable to deduce that the most decisive/important facets to consider would be the legs, feet and arms. Features are extracted in a gait cycle for each individual. The gait cycle is a complete stride with both legs stepping, starting with the right leg as shown in Fig. 2. A typical recording session of a participant wearing the suit is shown in Fig. 3.

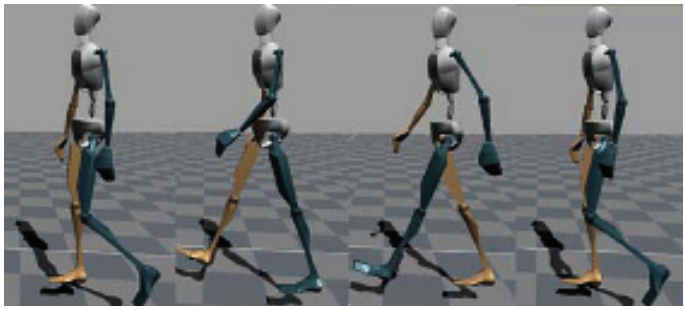

Fig. 2. A sample gait cycle: as received from the wireless inertial motion suit and animated on a 23 DOF avatar within the Moven Studio™ software.

The data produced by the Moven system is stored in rich detail within an MVNX (Moven Open XML format) file which contains 3D position, 3D orientation, 3D acceleration, 3D velocity, 3D angular rate and 3D angular acceleration of each segment in an XML format (ASCII). The orientation output is represented by quaternion formalism.

Fig. 3. Recording of the Body Motions; on average, each participant walked between ground markers, white to black, and return in some seven seconds.

The extracted features chosen are the subtended angles of the following body elements:

- Left and Right Foot Orientation,
- Left and Right Foot,
- Left and Right Knee,
- Left and Right Thigh,
- Left and Right Elbow,
- Left and Right Arm.

In total 12 features per individual was extracted, were each angle is given in radians. The location and interpretation of these features is illustrated on the animated motion avatar in Fig. 4.

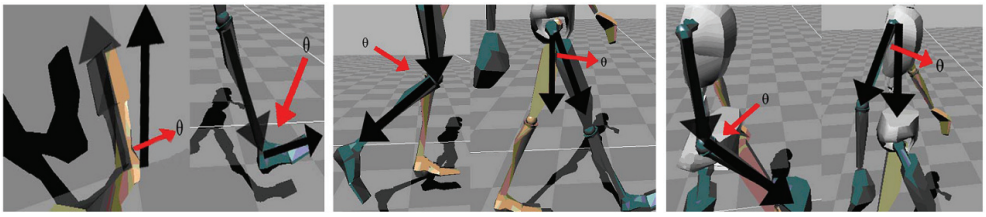

(a) (b) (c)

Fig. 4. Selected features annotated of the Moven avatar; (a) Foot Orientation Angle and Foot Angle, (b) Knee Angle and Thigh Angle (c) Elbow Angle and Arm Angle.

An example plot combining all of the 12 selected features, for five participants (p6-p10), can be seen in Fig. 5. These have been concatenated together for comparison; the extent of each individual is delineated by grey vertical lines—each individual marking some 3 to 4 gait cycles in-between. This amounted to some 3 to 4 seconds for a subject to walk from one marker to the other, and for a sample rate of 120Hz this equates to some 360 to 480 captured data frames per person.

One can readily appreciate several various differences in gait amongst these participants—such as the marked variations in angular extent of foot orientations (Left Foot O, Right Foot O), and their associated temporal behaviour. Despite this array of other differences the leg

period of each remains approximately similar as their variation of height is not significant, nor the distance each travelled between the markers during the recording sessions.

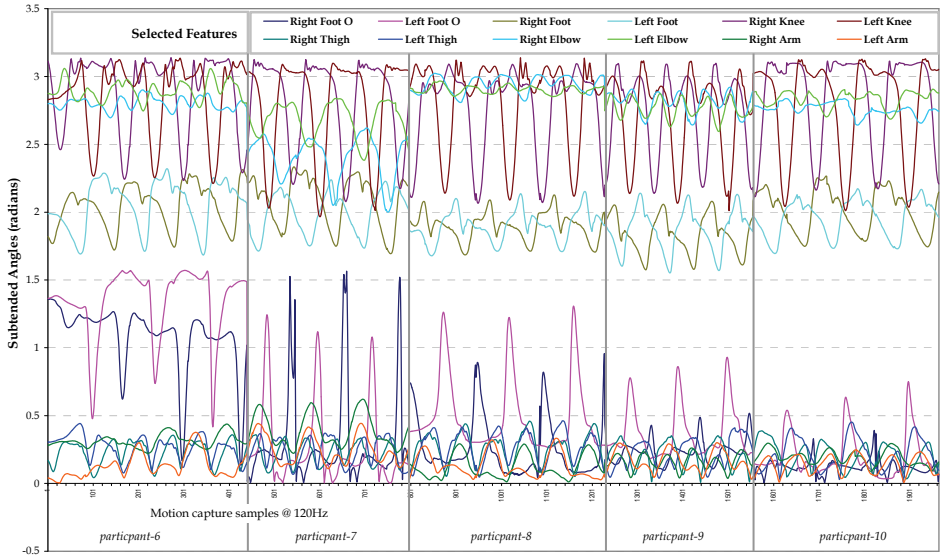

Fig. 5. Temporal trends for the 12 selected features across participants p6—p10.

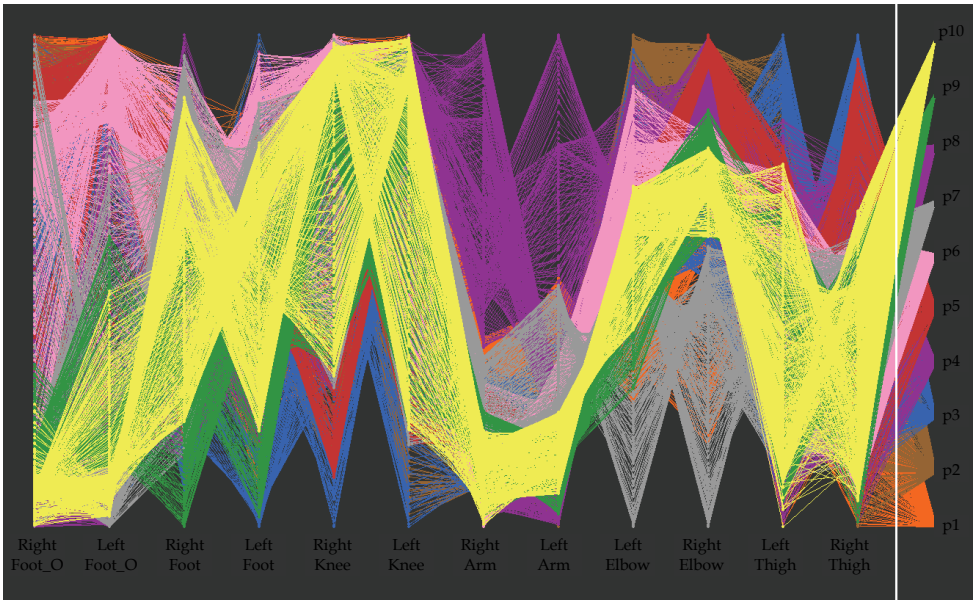

Fig. 6. Parallel Coordinate Plot: providing visualisation of all selected features, for all participants (p1-p10) —covering here, 3837 data frames.

Although there degrees of diversities between the trends in Fig. 5 of all selected features, one may still remain unconvinced that a set of dynamic finger prints ultimately exists, and if so how could they possibly be reliably extracted? Part of this difficulty arises from observing the distinct feature dissimilarities as a function of time. A more pragmatic approach would be to transform these into alternative domains such as FFT or Wavelets. However, an alternative to either of these might be to visualise the features through a Parallel Coordinate Plot (PCP), as illustrated in Fig. 6, in order to explore the multivariate data without the coupling effect of time.

The PCP of Fig. 6 obtained via a visualisation tool Ggobi (Cook and Swayne, 2007), here, arranges a series of parallel coordinates axes, one for each feature, scaled to represent the normalised range of each. The right-most axis of this plot further provides a numerically ordered array of the 10 participants. Every frame of the motion capture data, although constrained to the 12 selected features, is represented by a distinct line that intersects each feature coordinate axis at an appropriate (normalised) value. By colour coding (brushing) the data fames for each participant, one can more readily appreciate potentially unique signatures of profile patterns (or DFP) across the combined feature space. In comparison, both Fig. 5 and Fig. 6 are derived from the same data; however the participants in the former are essentially contrasted with each other (but only half of these for clarity) in the temporal domain. However, in the latter case of Fig. 6 all participants are explicitly compared with each other solely in the feature domain, which also reveals strong visual evidence for the existence of motion signatures amongst the various individuals.

4. Symbolic modelling of DFP

The principal benefit of symbolic machine-learning (modelling), as opposed to other approaches such as physical modelling (or knowledge-driven modelling), is that it is essentially an empirical, or data driven, modelling process which endeavours to represent only the patterns of relationships or process behaviours (here human movements). Hence, it is readily able to cope with significantly higher dimensionality of data. Non-symbolic machine learning approaches, such as artificial neural networks also address such problems, but lack the major benefits offered by symbolic modelling —these being the transparency of learnt outcomes or patterns, plus an adaptive process of the model structure to scale to accommodate data. These abilities are necessary in order to critique and understand patterns and knowledge that may be discovered.

In order to examine the Dynamic Finger Print hypothesis, the ten individuals wearing the Moven suit, undertook four repetitions of a simple walking task. From these tasks, the selected features, across the individuals were collected and recorded for an identification trial. For this trial, the goal was to clearly identify an individual based purely on a combination of the subtended joint angles. In addressing this recognition challenge, the machine learning, rule induction system known as See5 (RuleQuest, 2007) was used. This system, being a supervised learning algorithm was utilised to induce symbolic classification models, such as decision trees, and or rule sets, based on the range of chosen features (attributes), including a priori known classes. The final decision trees and rule sets were created through adjustment of the various pruning options, but primarily through the (major) pruning control for the minimum number of cases option (M).

Essentially a large tree is first grown to fit the data closely and then pruned by removing parts that are predicated to have relatively high error rate. The pruning option, M, is

essentially a stopping criterion to arrest the expansion formation of a decision tree and any associated rule set derived from it. It specifies the minimum number of cases that are required before any leaf classification node is formed and essentially constrains the degree to which the induced model can fit the data. In order to obtain a more reliable estimate of the predictive accuracy of the symbolic model *n–fold* cross validation is used as illustrated in Fig. 7.

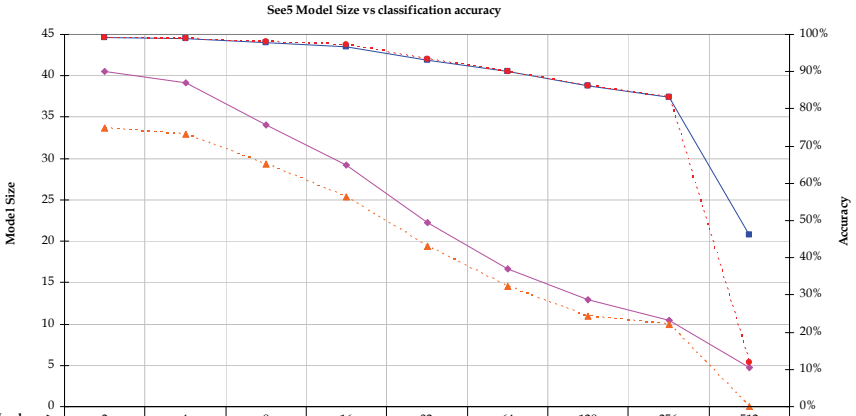

M value =>	2	4	8	16	32	64	128	256	512
Tree size	40.5	39.1	34	29.2	22.3	16.6	12.9	10.4	4.7
Rules size	33.7	32.9	29.3	25.4	19.4	14.5	11	10	0
Tree accuracy	99.3%	98.9%	97.9%	96.8%	93.1%	90.0%	86.1%	83.1%	46.0%
Rules accuracy	99%	99%	98%	97%	93%	90%	86%	83%	12%

Fig. 7. Model size and accuracy variations as measured by 10–fold cross validation.

The cases in the feature data file are divided into *n–blocks* of approximately the same size and class distribution. For each block in turn, a classifier model is induced from the cases in the remaining blocks and tested on the cases in the hold–out block. In this manner, every data frame is used just once as a test case. The error rate of a See5 classifier produced from all the cases is then estimated as the ratio of the total number of errors on the hold–out cases to the total number of cases (See5, 2002). Here, the number of folds has been set to 10.

As can been seen in Fig. 7 there is a nonlinear trade-off between model size and accuracy. Given that the intended use of the model can be guided as to the most dominant factor. Which at the two extremes can be either; a greater generalisation with a reduced model size or, alternatively, a larger, more sensitive model that is less likely to produce miss-classifications. The objective in this task was to model potential motion signatures, and as an example we have chosen a model size that generally reflects a 90~95% accuracy, here M=64. Once a suitable classifier performance level has been identified using the cross validation trends, the resultant model is generated as illustrated by the rule set model in Fig. 8.

For this task we are seeking to establish an individual motion signature for all participants, thus there are ten classes p1–p10. Participants undertaking the experiments were 5 males and 5 females between 18 to 40 years of age. According to Fig. 8, the average error rate achieved is some 6.8% and number of rules is 18.

Rule 1: (1119/728, lift 3.3) Left Foot O > 1.124812 Right Elbow <= 2.901795 => class p1 [0.350]	Rule 2: (296/28, lift 9.7) Left Foot O > 1.124812 Right Elbow > 2.901795 Left Elbow > 2.918272 => class p2 [0.903]	Rule 3: (66/28, lift 6.2) Right Foot O > 1.260007 Left Foot O <= 1.124812 Right Elbow > 2.640656 => class p2 [0.574]	Rule 4: (225/3, lift 10.7) Left Foot O > 1.124812 Right Foot <= 2.100667 Right Knee <= 2.866177 Right Elbow <= 2.901795 Left Elbow > 2.795459 Left Arm > 0.1387282 => class p3 [0.982]
Rule 5: (191/21, lift 9.6) Left Foot O > 1.124812 Right Foot <= 2.100667 Right Knee <= 2.866177 Right Elbow <= 2.901795 Right Arm <= 0.2898046 => class p3 [0.886]	Rule 6: (65/25, lift 6.7) Right Foot O > 1.053137 Left Foot O <= 1.124812 Right Elbow <= 2.640656 => class p3 [0.612]	Rule 7: (350, lift 10.9) Left Foot O <= 1.124812 Left Arm > 0.4538144 => class p4 [0.997]	Rule 8: (395, lift 9.4) Left Foot O > 1.124812 Right Elbow > 2.901795 Left Elbow <= 2.918272 => class p5 [0.997]
Rule 9: (224/15, lift 8.1) Left Foot O > 1.124812 Right Knee > 2.866177 Right Elbow <= 2.901795 Left Elbow > 2.795459 => class p6 [0.929]	Rule 10: (188/15, lift 8.0) Left Foot O > 1.124812 Right Elbow <= 2.901795 Left Elbow > 2.795459 Right Arm > 0.2898046 Left Arm <= 0.1387282 => class p6 [0.916]	Rule 11: (80/13, lift 7.2) Right Foot O > 1.00804 Right Foot O <= 1.260007 Left Foot O <= 1.124812 Right Elbow > 2.640656 => class p6 [0.829]	Rule 12: (615/311, lift 4.3) Left Foot O > 1.124812 Right Elbow <= 2.901795 Right Arm <= 0.3535621 => class p6 [0.494]
Rule 13: (326, lift 10.7) Right Foot O <= 1.053137 Left Foot O <= 1.124812 Right Elbow <= 2.640656 => class p7 [0.997]	Rule 14: (838/435, lift 4.3) Right Foot O <= 1.00804 Left Foot O > 0.1827743 Left Foot O <= 1.124812 Right Elbow > 2.640656 Left Arm <= 0.4538144 => class p8 [0.481]	Rule 15: (295/16, lift 11.1) Right Foot O <= 1.00804 Left Foot O > 0.1827743 Left Foot O <= 1.124812 Right Elbow > 2.640656 Left Elbow <= 2.852491 Left Arm <= 0.4538144 => class p9 [0.943]	Rule 16: (169/28, lift 9.7) Right Foot O <= 1.00804 Left Foot O <= 1.124812 Left Knee <= 3.004622 Right Elbow > 2.838296 Left Elbow <= 2.879424 Left Arm <= 0.4538144 => class p9 [0.830]
Rule 17: (302, lift 9.3) Right Foot O <= 1.00804 Left Foot O <= 0.1827743 Right Elbow > 2.640656 Left Arm <= 0.4538144 => class p10 [0.997]	Rule 18: (228/28, lift 8.2) Right Foot O <= 1.00804 Left Foot O <= 1.124812 Right Elbow <= 2.838296 Left Elbow > 2.852491 Left Arm <= 0.4538144 => class p10 [0.874]	Default class: p6 Evaluation on training data (3837 motion frames) Decision Tree / Rules Size / Errors / No / Errors 18 / 270(7.0%) / 18 / 261(6.8%)	

Fig. 8. An example motion signature model for participants, p1–p10.

Each rule in Fig. 8 consists of an identification number plus some basic statistics such as ***(n, lift x)*** or ***(n/m, lift x)*** these, in fact, summarize the performance of each rule. Here, ***n,*** is the number of training cases covered by the rule and ***m***, where it appears, indicates how many of the cases do not belong to the class predicted by the rule. The accuracy of each rule is estimated by the Laplace ratio ***(n − m +1)/(n + 2)*** . The ***lift x,*** factor is the result of dividing a rule's estimated accuracy by the relative frequency of the predicted class in the training set. Each rule has one or more antecedent conditions that must all be satisfied if the rule consequence is to be applicable. The class predicted by the rule is show after the conditions, and a value between 0 and 1 that indicates the confidence with which this prediction is made is here shown in square brackets (See5, 2002).

The overall performance of the signature model can be readily observed in the confusion matrix of Fig. 9 which details all resultant classifications and miss-classifications within the trial. The sum of values in each row of this matrix represents the total number of true motion frames that are derived from the associated participant (p1–p10). Any off-diagonal values in Fig. 9 represent miss-classification errors, such as 13 motion frames of participant p5 was very similar to those exhibited by p2. Here an ideal classifier would register only diagonal values in Fig. 9.

All extracted features were available to the induction algorithm as it constructed its various classifier models, however not all of these were ultimately utilised in the final rules. For

example considering the model of Fig. 8, the number of times that each feature has been referred in the rules, which reflects its importance in classifying a person, is shown in Table 2. According to Table 2 the features, Left Foot, plus the, Left Thigh and Right Thigh, angles have not been used in classifier at all, and the two most important features are angle of the Left Foot Orientation and that of the Right Elbow.

(p1)	*(p2)*	*(p3)*	*(p4)*	*(p5)*	*(p6)*	*(p7)*	*(p8)*	*(p9)*	*(p10)*	<= *classified as*
384	15				7					p1
	306	21			29					p2
		311			42					p3
			350							p4
	13			395						p5
		3			436					p6
6		25				326				p7
	28						347	28	28	p8
								327		p9
								16	394	p10

Fig. 9. Confusion matrix analysis of the motion signature model for participants p1–p10.

Feature	Usage	Percentage of usage of all features
Left Foot O	18	26.1%
Right Elbow	17	24.6%
Right Foot O	9	13.0%
Left Arm	8	11.6%
Left Elbow	8	11.6%
Right Arm	3	4.3%
Right Knee	3	4.3%
Right Foot	2	2.9%
Left Knee	1	1.4%
Left Foot	0	0%
Right Thigh	0	0%
Left Thigh	0	0%

Table 2. Usage of features, highlighting three redundant attributes.

Although we had originally included all of the apparently, seemingly important bodily attributes, the induced model has found these, Left to be redundant. These leads to an obvious suggestion of not manually selecting or limiting the range of available attributes, but rather allow the algorithm to choose an appropriate sub-set of these. This in fact is one of the specific approaches employed in Section 5.

Ultimately the various rules in such classifiers all define specific hyper-cubes within the multidimensional feature space. As an example, four rules from an initial version of the signature model are overlaid on a 2-dimensional projection of the 12-dimensional feature space. This was observed in some preliminary data visualisation work carried out on the motion data using Ggobi (Cook & Swayne, 2007). Using projection pursuit visualization, the rotating projection was paused whenever a significant 2D segmentation could be observed. Here, in Fig. 10 one can clearly identify participants 9 and 10, and also conceptualize four hyper-cubes encompassing the array of these points (motion data frames) with rules 13, 14, 23 and 24.

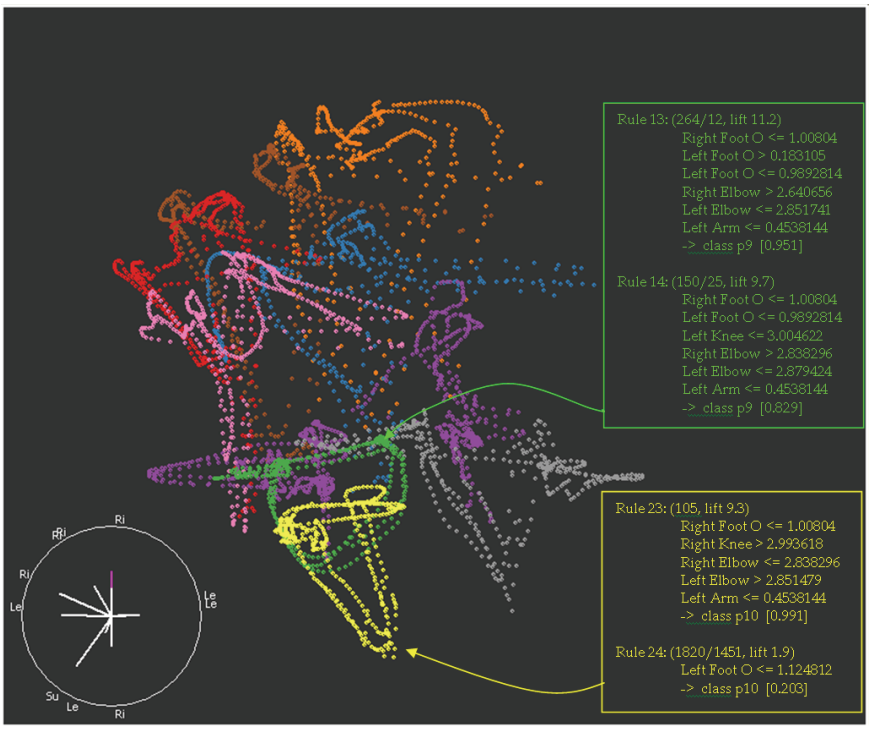

Fig. 10. Selective symbolic model rules identifying participants 9 and 10 with a 2D projection of the 12 dimensional feature–space.

The primary aim of this study was to identify a person based on a combination of subtended angles at the feet, knees, thighs, arms, and elbows. In this process 12 features were extracted and using a decision tree and converting this into a rule set classifier 93.2% accuracy was achieved. The participants were 5 males and 5 females between 18 to 40 years of age, indicating that the results obtained were not dependent to specific characteristics of participants. The extracted features could also be used in gender classification, or even different motion classifications. In order to be able to use the described method in a real application, an image processing and computer vision section for data acquisition should be added to the system. The goal in this section is only to test the hypothesis that a plausible

signature model to recognize specific individuals could be developed from an appropriate set of features.

5. Symbolic modelling of distinctive motion tasks

This section progresses the development of symbolic modelling to see if it can be used to model various distinctive tasks of human movement skills. As mentioned in Section 3, the CMU Motion Capture Database (2007) offers a significant array of general motions, which would take a considerable period of time to replicate. This data, however, is freely available from the Carnegie-Mellon Motion Capture Database, in the Acclaim ASF/AMC format (CMU Motion Capture Database, 2007).

The data consists of motion capture sequences for various activities such as sports, walking, running, dancing, and nursery rhyme actions. These are captured at a rate of 120 frames per second. For each frame, the optically inferred x, y and z axis rotation for each bone of the body are recorded with respect to the degrees of freedom available for the bone, e.g. the upper arm (humerus) has x, y and z rotations while the forearm (radius) has only x-axis rotation from the elbow.

In total, there are 28 bones in the model as shown in Fig. 11, with the 29th bone (root point) representing the rotation and translation of the whole body. This root point serves as the

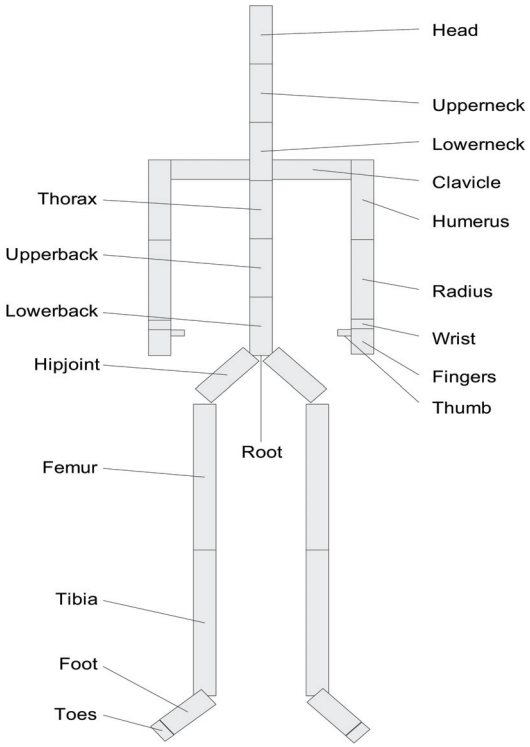

Fig. 11. Names and locations of the bones as per the CMU database used in this work.

point of origin for the whole skeleton and is situated between the lower back, left hip joint and right hip joint, as illustrated in Fig. 11. A plot showing an example of the dataset is shown in Fig. 12. In Fig. 12, the x-axis represents the frame number of the motion and the y-axis represents the degree of rotation applied to each bone in the skeleton. Fig. 12 shows the x, y, and z axis rotation of the lower back bone for two walking motions and a golf swing.
For the purposes of this work, four types of motions consisting of walking, running, golf swing and golf putt were used. The motions were chosen to provide visually similar motions (walking and running), visually dissimilar movements but which utilised a similar set of bones (golf swing and golf putt).

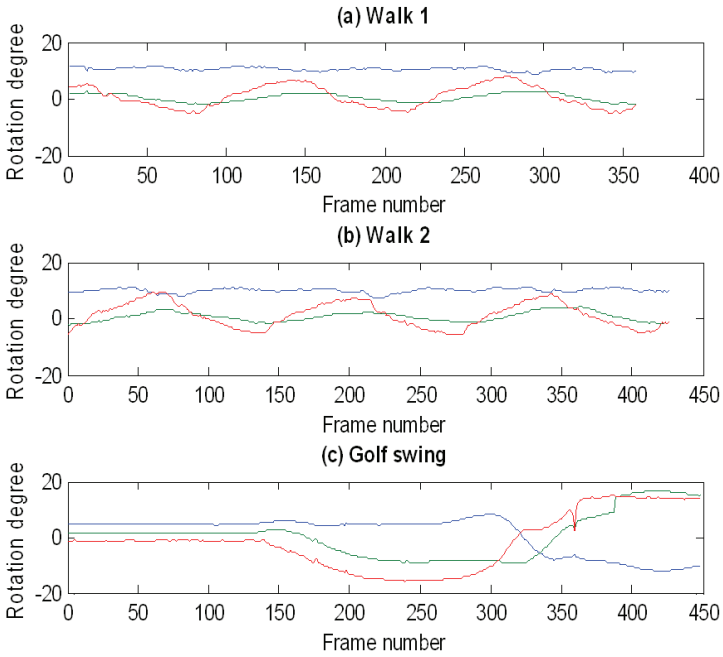

Fig. 12. The plots of x, y, and z axis rotations of the lower back bone of two walking motions and a golf swing with different lengths. Each curve represents rotation of the back bones in the skeleton vs. time.

5.1 Symbolic motion classification using see5

In this section, multiple experiments in developing symbolic models of the motion data using a See5 decision trees were performed where the M value was increased by power of 2 up to 32,768. For each experiment, the size of the decision tree, rule set and the average classification accuracy of each (which was confirmed by 10-fold cross-validation) were recorded. An example of the resulting decision tree for M=8 is shown in Fig. 13. In Fig. 13, a motion is classified by first looking at the root node of the tree, which contains a threshold decision about the left humerus, x-axis rotation. If the condition is not true, then the next node visited specifies that the left wrist, y-axis rotation be examined. Continuing down the

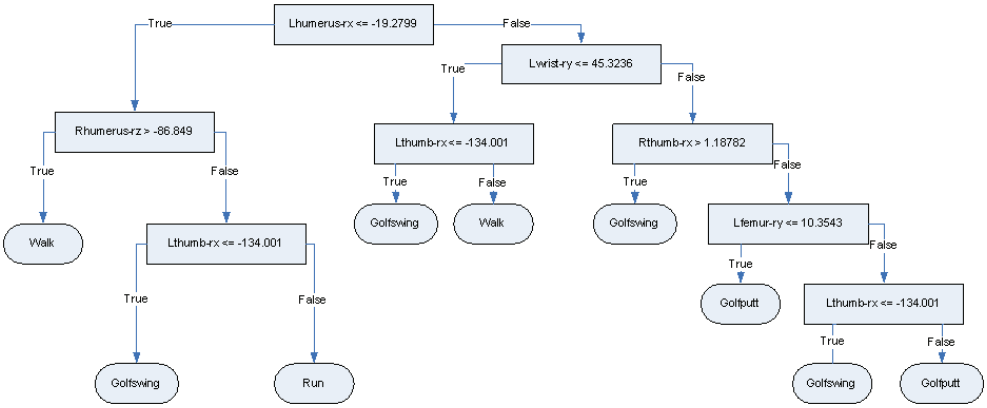

Fig. 13. Symbolic motion decision tree for: walk, run, golfswing and golfputt, using M=8.

tree to one of the leaf nodes, a data frame of a motion can be classified as a golf swing, golf putt, walk or run motion. It can be readily observed in Fig. 13 that to in order to classify these four motion classes, only seven bone tracks out of a possible 62 in the motion data base are actually used, and that these seven are the most important features for differentiating between the four motion classes.

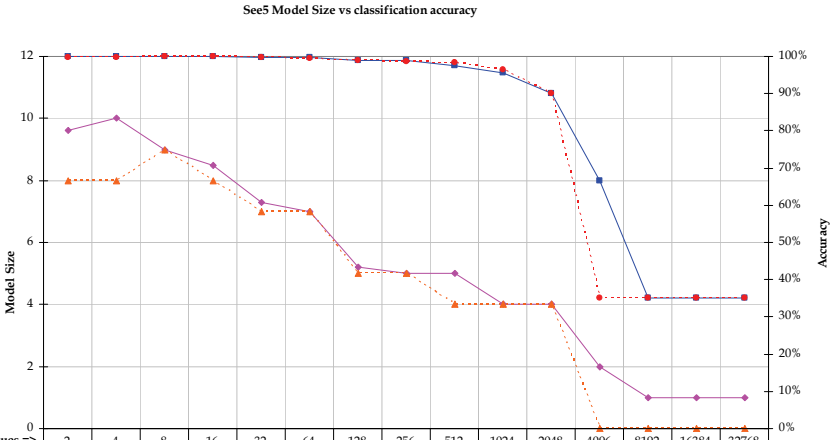

M values =>	2	4	8	16	32	64	128	256	512	1024	2048	4096	8192	16384	32768
Tree size	9.6	10	9	8.5	7.3	7	5.2	5	5	4	4	2	1	1	1
Rules size	8	8	9	8	7	7	5	5	4	4	4	0	0	0	0
Tree accuracy	100%	100%	100%	100%	100%	100%	99%	99%	98%	96%	90%	67%	35%	35%	35%
Rules accuracy	100%	100%	100%	100%	100%	100%	99%	99%	98%	96%	90%	35%	35%	35%	35%

Fig. 14. Symbolic Model size and accuracy variations as measured by 10–fold cross validation for four motion classes (walk, run, golfswing, and golfputt).

From the graph presented in Fig. 14, the tree in Fig. 13 would perform classification with 99.9% accuracy per-frame, which results in 100% accuracy in motion classification. Plots of the M value vs. tree size vs. classification accuracy are shown in Fig. 14.
It is evident that in Fig. 14 that, there is a knee point in the graph approximately where M=1024, beyond which the classification accuracy begins to decrease significantly i.e., for M=1024 and M=2048, classification accuracies are 96% and 90%, respectively. A typical confusion matrix for such models is illustrated in Fig. 15. In Fig. 14 there is a further observed knee point at around M=2048, after which for greater values of M the accuracy rate again drops significantly (67% for M=4096 and 35% for M=8192).

(golfswing)	*(golfputt)*	*(walk)*	*(run)*	<= *predicted as*
4463	4			golfswing
1	2507			golfputt
		6616		walk
			1608	run

Fig. 15. Typical confusion matrix of the motion model (M=128) for golfswing, golfputt, walk and run.

It is also of note that parameters of M=2 up to M=32 yields almost 100% classification results. Fig. 14 also shows that M=8 for this dataset provides the best classification performance (99.95%), where using smaller M values was not observed to improve classification performance. Using M=8, the resulting decision tree is relatively small with 17 nodes and seven bone motion tracks in total. Hence for the purpose of this work, experiments were performed using decision tree generated with M=8.

5.2 Symbolic modelling of normal and abnormal motion behaviours

In order to investigate the concept of being able to detect normal and abnormal motion behaviours, a further series of experiments, again involving the Moven inertial motion suit were designed. In this context individuals were asked to carry a back pack with a 5kg weight in it. From these tasks, the same range of features (as used in Section 3) was used again, for the various individuals undertaking the trial.
For this trial, the goal was to clearly identify if a person is carrying a weight or not. However, in addition to this each participant was invited to subtlety disguise their gait on occasions of their choosing, informing the investigators at the end of any recording trial if they had do so. Thus motion data was collected for individual walking gaits that were influenced, or not, by an unfamiliar extraneous weight and also, or not, by a deliberate concealing behaviour of the participant. Again symbolic models of these motion behaviours were induced using the See5 algorithm (RuleQuest, 2007) from the participants using various combinations of subtended joint angles. The algorithm formulates symbolic classification models in the form of decision trees or rule sets, based on a range of several concurrent features or attributes. The model development process followed the same procedure previously discussed in the pervious sections.
For this particular work it was decided to formulate two parallel classifiers to identify both the gender of an individual as well as attempting to deduce if the individual was in fact carrying a weight. The layout of the system is shown in Fig. 16.

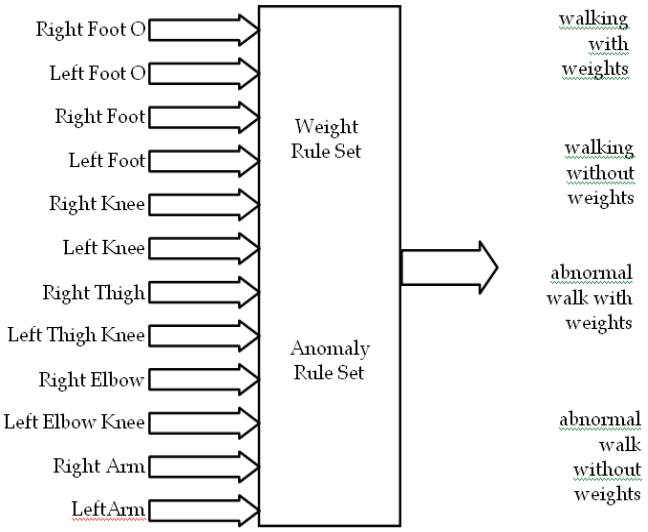

Fig. 16. Symbolic model proposal to identify: a weight induced gait anomaly; or an abnormally motion arising from some premeditated disguise.

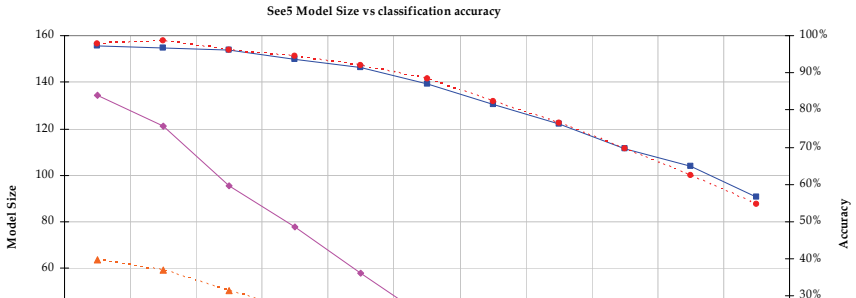

M value =>	2	4	8	16	32	64	128	256	512	1024	2048
Tree size	134.5	120.9	95.5	77.6	57.9	38.4	21.9	12.9	7.2	4.3	2
Rules size	63.7	59.1	50.5	42	33	24.4	14.7	8.3	5.5	2.1	0
Tree accuracy	97.3%	96.7%	96.1%	93.6%	91.3%	86.9%	81.4%	76.3%	69.6%	65.0%	56.5%
Rules accuracy	98%	99%	96%	95%	92%	88%	82%	77%	70%	63%	55%

Fig. 17. Symbolic Model size and accuracy variations as measured by 10–fold cross validation for detecting weight induced gait anomalies.

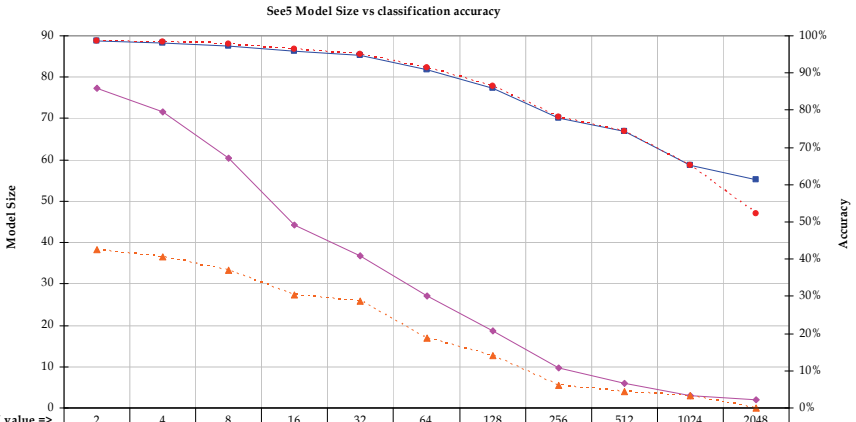

M value =>	2	4	8	16	32	64	128	256	512	1024	2048
Tree size	77.2	71.6	60.5	44.2	36.8	27	18.7	9.6	5.9	3	2
Rules size	38.2	36.5	33.3	27.3	25.8	17	12.8	5.5	3.9	3	0
Tree accuracy	98.5%	98.0%	97.1%	95.8%	94.7%	91.0%	86.0%	78.0%	74.2%	65.3%	61.3%
Rules accuracy	99%	98%	98%	96%	95%	91%	87%	78%	74%	65%	52%

Fig. 18. Symbolic Model size and accuracy variations as measured by 10–fold cross validation for detecting disguised gait related motion behaviours.

Motion data for all 12 subtended joint angles was used in both rule sets in an attempt to classify disguised motion behaviours, and or, individuals that may be carrying an extraneous weight. As in the Sections, 3 and 5, a series of plausible models were firstly analyzed as illustrated in Figs. 17 and 18, before their appropriate formal forms were realized as illustrated in Figs 19 and 20.

The participants undertaking these motion experiments were 4 males and 5 females between 18 to 40 years of age. The primary aim of this study was to identify if a person is carrying an object and maybe concealing the object under his clothes based on a combination of the subtended angles at their feet, knees, thighs, arms, and elbows. In this process, again 12 features were extracted and using decision tree and rule set classifier models, more than 87% accuracy was achieved for detecting individuals carrying an extraneous weight, and an accuracy of at least 89% was also achieved in detecting unnatural (pretense) in gait motions.

6. Conclusion

The results from Section 4 and Section 5 clearly support all of the three objectives discussed at the end of Section 2. These being to firstly; develop a plausible model for dynamic finger printing of motion data between individuals. Secondly, investigate a model that could to also identify distinctions between various motion tasks, and finally to formulate a model to identify motion pretence, or acting, as well as normal and (physically induced) abnormal motion behaviours.

Rule 1: (182, lift 2.2) Right Foot O <= 1.282073 Left Foot O <= 1.515643 Right Elbow > 3.057076 => WithWeights [0.995]	Rule 2: (479/6, lift 2.2) Right Foot O > 1.282073 Left Arm <= 0.1065039 => WithWeights [0.985]	Rule 3: (216/11, lift 2.1) Left Foot O <= 0.2262519 Left Foot <= 2.165244 Right Elbow > 2.876776 Left Elbow > 2.802877 => WithWeights [0.945]	Rule 4: (400/21, lift 2.1) Left Foot O <= 1.515643 Right Elbow > 3.027218 Left Elbow <= 3.027386 Right Arm <= 0.2105112 => WithWeights [0.945]
Rule 5: (175/26, lift 1.9) Left Elbow <= 2.605653 Left Arm <= 0.3550883 => WithWeights [0.847]	Rule 6: (475/74, lift 1.9) Right Foot O <= 0.05478672 => WithWeights [0.843]	Rule 7: (146/25, lift 1.8) Right Foot O > 0.05478672 Left Foot O > 1.515643 Left Elbow > 3.02983 Right Arm > 0.1455698 => WithWeights [0.824]	Rule 8: (260/49, lift 1.8) Right Foot O <= 1.282073 Right Elbow <= 2.399449 Left Elbow <= 2.802877 => WithWeights [0.809]
Rule 9: (528/139, lift 1.6) Left Foot O > 0.3129601 Left Foot O <= 1.515643 Right Knee <= 2.996378 Right Elbow <= 3.057076 Left Elbow <= 2.802877 Left Arm <= 0.3550883 => WithWeights [0.736]	Rule 10: (1092/294, lift 1.6) Right Foot O > 1.282073 Left Foot O <= 1.515643 Left Elbow <= 3.027386 Left Arm <= 0.3550883 => WithWeights [0.730]	Rule 11: (297/80, lift 1.6) Right Foot O <= 1.282073 Left Foot O > 1.422201 Left Foot O <= 1.515643 Left Elbow > 2.802877 Right Arm <= 0.3095023 => WithWeights [0.729]	Rule 12: (141, lift 1.8) Left Foot O > 1.515643 Left Elbow > 3.02983 Right Arm <= 0.1455698 =>WithOutWeights [0.993]
Rule 13: (259/7, lift 1.8) Right Foot O <= 1.282073 Left Foot O > 1.422201 Right Arm > 0.3095023 =>WithOutWeights [0.969]	Rule 14: (267/17, lift 1.7) Right Foot O > 1.282073 Right Elbow > 3.027218 Right Elbow <= 3.083863 Right Arm > 0.2105112 Left Arm > 0.1065039 =>WithOutWeights [0.933]	Rule 15: (556/77, lift 1.6) Right Foot O > 0.05478672 Right Foot O <= 1.282073 Left Foot O > 1.422201 Right Elbow <= 3.057076 Left Arm > 0.1278452 =>WithOutWeights [0.860]	Rule 16: (6287/2659, lift 1.1) Right Foot O > 0.05478672 =>WithOutWeights [0.577]
		Default class: WithOutWeights	
		Evaluation on training data (6762 motion frames)	
		Decision Tree	Rules
		Size / Errors	No / Errors
		26 / 926(13.7%)	16 / 819(12.1%)

Fig. 19. An example motion model for detecting subjects carrying an additional 5kg weight.

Rule 1: (145, lift 2.1) Right Arm > 0.6420745 Left Arm <= 0.432619 => Abnormal [0.993]	Rule 2: (344/12, lift 2.0) Right Foot O <= 0.9345771 Left Foot O > 0.206346 Left Foot O <= 1.478905 Right Knee <= 3.012932 Right Arm > 0.2752825 Left Arm <= 0.432619 => Abnormal [0.962]	Rule 3: (298/12, lift 2.0) Right Elbow <= 2.419674 Left Arm > 0.432619 => Abnormal [0.957]	Rule 4: (246/12, lift 2.0) Right Elbow > 2.905675 Right Elbow <= 3.027221 Left Elbow <= 3.013905 Left Arm <= 0.432619 => Abnormal [0.948]
Rule 5: (395/59, lift 1.8) Right Foot O > 1.3187 Right Foot O <= 1.408431 Left Foot O > 0.206346 Right Elbow <= 3.027221 Right Arm > 0.2752825 => Abnormal [0.849]	Rule 6: (4467/2094, lift 1.1) Left Foot O > 0.206346 => Abnormal [0.531]	Rule 7: (144, lift 1.9) Left Thigh > 0.5184123 Left Arm <= 0.432619 => Normal [0.993]	Rule 8: (655/80, lift 1.7) Left Foot O <= 0.206346 => Normal [0.877]
Rule 9: (371/58, lift 1.6) Right Knee > 2.892806 Right Elbow > 2.419674 Left Arm > 0.432619 => Normal [0.842]	Rule 10: (3128/1117, lift 1.2) Right Arm > 0.1541919 Left Arm <= 0.432619 => Normal [0.643]	Rule 11: (202/73, lift 1.2) Left Foot > 1.776459 Right Elbow <= 3.032689 Right Arm <= 0.1541919 => Normal [0.637]	
		Default class: Normal	
		Evaluation on training data (5122 motion frames)	
		Decision Tree	Rules
		Size / Errors	No / Errors
		19 / 606(11.8%)	11 / 554(10.8%)

Fig. 20. Motion model for detecting subjects manifesting disguised gait motion behaviours.

Motion capture data of human behaviour is necessarily by its nature highly complex and dynamic. Alternative approaches often seek to avoid where ever possible the so-called "curse of dimensionality" (Bellman, 1957) by developing methods to reduce this dimensionality to a tractable lower number of dimensions. Whilst these methods made succeed to various degrees they essentially smother or aggregate out fine detail and various nuances of motion behaviours.

In contrast, the application of symbolic machine learning is able to readily cope with the multidimensional properties of motion data, as evidenced by the example models developed in the previous sections. In effect, an appropriate (symbolic and inductive) DM algorithm will structure and or adjust numerous internal relationships between all of the input features that relate to and support the corresponding output, thereby avoiding, or significantly mitigating, the "curse of dimensionality".

However, whilst such models were often pruned significantly, which may also reduce the domain dimensionality the models address, this process always provides a transparent view of any resultant rules, patterns—often leading to new discovered knowledge. Thus the developer is able to readily critique and further explore various properties and consequences, often through a visualization process, that an individual element of existing or discovered knowledge poses in relation to any reduction in a models resolution (Asheibi, 2009).

Apart from this, motioning the induced symbolic patterns also provides a diagnostic ability guiding the often cyclic and interactive nature of applying machine learning in general. Previous other studies have validated this approach by combining together with unsupervised mixture modelling for gait recognition (Field et al., 2008)(Hesami et al., 2008).

The premise of this proposed work is that all humans have, by the stage of adolescence (or maturity) developed various stylistic signatures or patterns of motion behaviour that can be typically (uniquely) associated with an individual. These become (fundamentally) imprinted as patterns within the central nervous system (CNS) and govern everyday motions such as walking gaits, various gesticulations and other dynamic movements (trunk rotations) of an otherwise static body (Cuntoor et al., 2008). As is obvious, much of these motions can be unconsciously affected or modulated by underlying emotions (Dittrich et al., 1996) or by some conscious intent in order to conceal one's true identity.

In particular, the highly coupled nature of such complex data provides numerous opportunities for the discovery of actionable knowledge patterns, which in turn can be adapted for abnormal motion detection and tracking in two-dimensional (2D) video streams.

It is conjectured that the study of these dynamic (spatiotemporal) multidimensional manifestations will facilitate a new approach to anomaly pattern detection for human motions. By employing (symbolic) machine learning and other related data mining techniques, on a comprehensive range of motion capture trials, it is envisioned that a unique ontology ("structure or science of being", or taxonomy) of such manifest anomaly patterns could be formulated. This would provide a valuable resource structure of (manifest) pattern relationships. Amongst other future goals this research should address is that the motion ontology framework should be utilized to facilitate the derivation of various 2D images and silhouette maps to be subsequently utilized in video pattern analysis for anomaly identification and ultimately tracking.

7. References

Argyle, M. (1988). Bodily Communication, Routledge publishing.

Asheibi, A., Stirling. D. & Sutanto, D. (2009). Analysing Harmonic Monitoring Data using Supervised and Unsupervised Learning, Paper ID: TPWRD-00394-2007. IEEE Trans. On Power Delivery, vol 24, No 1, January.

Bellman, R. (1957). Dynamic Programming, Princeton Univ. Press, Princeton, New Jersey.

Braune, W., Fischer, O. (1904). Der Gang Des Menschen/The Human Gait, Springer, Berlin.

Cook, D., and Swayne, D. F., (2007). Interactive and Dynamic Graphics for Data Analysis With R and GGobi, Springer, www.springerlink.com/content/978-0-387-71761-6.

Donato, G.; Bartlett, M.S.; Hager, J.C.; Ekman, P. & Sejnowski, T.J. (1999), Classifying facial actions, IEEE Transactions on Pattern Analysis and Machine Intelligence, Volume 21, Issue 10, Oct. 1999 Page(s): 974 – 989.

Ekman, P. (1999). Facial Expressions, In T. Dalgleish and T. Power (Eds.), The Handbook of Cognition and Emotion. Pp. 301-320. Sussex, U.K.: John Wiley & Sons, Ltd.

Field, M., Stirling, D. Naghdy, F. & Pan, Z. (2008). Mixture Model Segmentation for Gait Recognition, Symposium on Learning and Adaptive Behaviours for Robotic Systems, LAB-RS '08. ECSIS, 6-8 Aug. 2008 Page(s): 3 - 8.

Hesami, A., Stirling, D., Naghdy, F. & Hill, H. (2008). Perception of Human Gestures through Observing Body Movements , Proc. of the International Conference on Intelligent Sensors, Sensor Networks and Information Processing, ISSNIP2008, Sydney, Dec.

Johansson, G. (1973). Visual Perception of biological motion and a model for its analysis, Percept. Psycophys. 14 (1973) 210-211.

McNeill, D. (2005). Gesture and Thought, The University of Chicago.

Marey, E.J. (1904). Centre Nationale d'Art Moderne, E-J Marey 1830/1904: La Photofraphie Du Movement Paris Centre Georges Pompidou, Musee national d'art moderne, Paris.

Mehrabian, A. (1971). Silent messages, Wadsworth publishing, Belmont, California.

CMU Motion Capture Database. (2007). CMU Graphics Lab Motion Capture Database, http://mocap.cs.cmu.edu/.

Cuntoor, N., Yegnanarayana B. & Chellappa, R. (2008) Activity Modeling Using Event Probability Sequences, IEEE Transactions on Image Processing, Volume: 17, Issue: 4, April 2008.

Dittrich, W., Troscianko T, Lea S. & Morgan D. (1996). Perception of emotion from dynamic point-light displays represented in dance. Perception, 25,727-738.

Roetenberg, D., Luinge, H. & Slycke, P. (2007). Moven: Full 6DOF Human Motion Tracking Using Miniature Inertial Sensors, Xsen Technologies, December, 2007.

RuleQuest Research (2007). Data mining tools, www.rulequest.com.

Schmidt, K. & Cohn, J. (2002). Human facial expressions as adaptations: Evolutionary questions in facial expression. Yearbook of Physical Anthropology, 44:3–24.

See5. (2002). See5: An Informal Tutorial, RuleQuest Research, www.rulequest.com.

Straker, D. (2008) . Changing Minds: in Detail, Published by Syque Press (October 2008).
Xsens Technologies (2009). Moven®/MVN®, wireless inertial motion capture www.xsens.com.